High Repetition Rate Tunable Lasers

by

Ian Jason Evans

Jesus College

Oxford

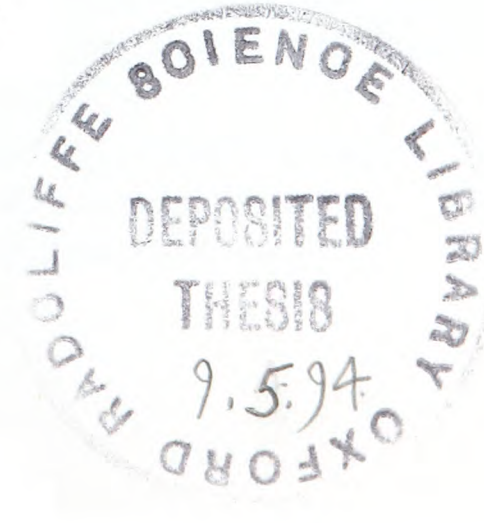
A thesis submitted for the degree of

Doctor of Philosophy

at the University of Oxford.

The Clarendon Laboratory

Trinity Term, 1993.



For my family.

Without them, none of this would be possible.

Abstract

High Repetition Rate Tunable Lasers

I.J.Evans, Jesus College, Oxford.

A Thesis Submitted for the degree of Doctor of Philosophy.
Trinity Term 1993.

Copper vapour laser (CVL) pumped dye lasers offer a source of high power, kilohertz repetition rate, tunable narrow-bandwidth radiation suitable for many spectroscopic applications in the visible and infra-red. Furthermore, the nonlinear frequency conversion of CVL-pumped dye laser radiation extends the wavelength range of these laser sources into the blue and ultra-violet.

A series of experimental investigations have been undertaken to gain a physical understanding of the fundamental parameters necessary for the optimization of the CVL-pumping of dye lasers. Issues addressed include the influence of the CVL cavity design, the pump beam polarization and geometry, the dye oscillator cavity design, the choice of grating materials, and the dye flow rate. A model based on the rate equation analysis of the kinetic processes relevant to optical amplification in dye lasers has been developed, and the results have been used to design amplifiers with extraction efficiencies in excess of 45%.

As a result of the aforementioned investigations, three commercially available pulsed dye lasers have been successfully optimized for CVL-pumping for the first time. Once modified, these dye lasers have typically shown conversion efficiencies in excess of 20%, with frequency bandwidths as narrow as 800MHz, and beam qualities approaching the diffraction limit.

The theory of second harmonic generation is reviewed, and a suite of corresponding computer models have been developed to form the basis for a coherent experimental investigation of UV generation using the CVL and CVL-pumped dye lasers. CVL SHG has been demonstrated in β-barium borate (BBO) and lithium tri-borate (LBO), with SHG efficiencies in excess of 18% realized for the CVL 511nm line in BBO. For the first time, an experimental comparison of spherically and elliptically focused second harmonic generation has been undertaken. Optimized elliptical focusing is found to be up to 30% more efficient than using conventional spherical focusing in agreement with theoretical predictions.

The superior divergence and transverse coherence of CVL-pumped dye lasers, in comparison to those of the CVL, is reflected in the SHG efficiencies achieved in BBO, LBO and lithium iodate. Conversion efficiencies approaching 40% have been demonstrated in lithium iodate, with harmonic conversion coefficients approaching 2400mW/W^2 realized at low input powers. The Boyd and Kleinman theory of SHG with focused Gaussian beams is found to provide an excellent description of SHG with CVL-pumped dye laser radiation, and accurately predicts the optimum strength of focusing and harmonic conversion coefficient. For the first time, sum frequency mixing (SFM) of the CVL with a dye laser has been demonstrated, and found to provide a potentially efficient source for tunable UV radiation.

Finally, the application of CVL-pumped dye lasers to resonant ionization mass spectrometry and tropospheric hydroxyl (OH) radical detection is discussed, and the spectroscopic potential of a frequency doubled CVL-pumped dye is demonstrated by recording the absorption spectrum of OH at 308nm.

Acknowledgements

I welcome the opportunity to thank

Professors Christopher Llewelyn-Smith, Roger Cowley and Pat Sandars, for the use of the facilities of the Clarendon Laboratory.

Professor Colin Webb, for his untiring supervision, infectious enthusiasm, and countless *optimistic* research proposals.

Dr. Tony Andrews, for many useful discussions, and introducing me to the practical side of high voltage circuitry, and the copper vapour laser.

Mr. Chris Goodwin, for the occasional production of high quality optical coatings.

Mr. George Mathews, for much practical advice, and for mopping up the mess after a milling machine started an argument with my thumb.

Oxford Lasers Ltd., for their technical help, loan of optics, and lucrative consultancy opportunities.

Sarah, for introducing me to grammar, punctuation, split-infinitives and the English Language!

Past and present members of the laser group for many useful and distracting discussions.

Members of Jesus College and Oxford University Boat Clubs, who have provided ample distraction from research.

The SERC/DTI LINK initiative, and the EC environmental programme for financial support.

Jason Evans,
Clarendon Laboratory,
August 1993.

High Repetition Rate Tunable Lasers
Contents

Chapter 1 : Introduction. **1**

1.1	Context and Purpose of The Current Research.	2
1.2	Layout of This Thesis	4

Chapter 2 : The Copper Vapour Laser. **6**

2.1	Introduction.	7
2.2	History of the Copper Vapour Laser.	8
2.3	Atomic Physics of the CVL.	9
2.4	The Effect Of Pressure and Temperature.	11
2.5	Practical Details.	12
2.6	Cavity Design.	14
2.6.1	Plane-Plane Cavities.	14
2.6.2	Unstable Cavities.	15
2.7	Pulse Timing of the 511nm and 578nm Lines.	19
2.8	The Oxford Lasers Cu40.	20
	References	22

Chapter 3 : Dye Lasers **24**

3.1	Introduction.	25
3.2	The Photophysics and Photochemistry of Dyes.	26
3.3	Challenges to Dye Lasers.	29
3.4	Broad Bandwidth Pulsed Dye Laser Oscillators.	30
3.5	Narrow Linewidth Pulsed Dye Laser Oscillators.	31
3.6	Injection Locked Systems.	39
3.7	The Modeless Dye Laser.	41
	References	43

Chapter 4 : Optical Amplification In Dye Lasers. **45**

4.1	Introduction.	46
4.2	Theory of CVL Pumped Dye Lasers.	48
4.3	Physical Interpretation.	52
4.4	Computation and Results.	53
4.4.1	Longitudinally Pumped Amplifier.	53
4.4.2	Transversely Pumped Amplifier.	55
4.5	Comparison With Experiment.	59
4.6	Results.	62
4.7	Practical Details and Conclusion.	65
	Appendix 4.1: Spectroscopic data for Rhodamine 6G	67
	References.	68

Chapter 5 : Practical CVL Pumped Dye Lasers. **69**

5.1	Introduction.	70
5.2	CVL Pump Laser Optimization.	71
5.2.1	Cavity Design.	71
5.2.2	Choice of 511nm and 578nm Pump Wavelengths.	73
5.2.3	Spatial Filtering.	74
5.2.4	Pump Beam Geometry.	76
5.2.5	Pump Beam Polarization.	76
5.3	Dye Laser Optimization.	80
5.3.1	General Considerations.	80
5.3.2	ASE in Pulsed Laser Systems.	84
5.3.3	Choice of Grating Material.	85
5.4	Characterization Measurements.	87
5.4.1	Beam Divergence Measurements.	88
5.5	Commercially Available Pulsed Dye Lasers.	92
5.5.1	The Russian Dye Laser LZhI-504.	93
5.5.2	The Lambda Physik LPD3000.	105
5.5.3	The Lumonics Hyperdye HD-350.	118
5.6	Conclusion	130
	Appendix 5.1: Lifetime Against Stimulated Emission	132
	Appendix 5.2 : Gaussian Beam Focusing.	133
	References.	136

Chapter 6 : The Theory of Harmonic Generation. **138**

6.1	Introduction.	139
6.2	Crystal Optics.	140
6.2.1	Fresnel's Equation.	141
6.2.2	The Ellipsoid of Wave Normals and Crystal Classes.	143
6.2.3	Ray Directions.	146
6.3	Nonlinear Optics.	148
6.3.1	Plane Wave Treatment of Second Harmonic Generation	148
6.3.2	Phase Matching.	150
6.3.2a	Phase Matching In Uniaxial Crystals.	151
6.3.2b	Phase Matching In Biaxial Crystals.	154
6.4	SHG with Focused Gaussian Beams.	157
6.4.1	Theoretical Harmonic Efficiencies.	166
6.5	SHG With Non-Ideal Laser Beams.	169
6.6	Concluding Remarks.	174
	Appendix 6.1 : The effective Nonlinear Coefficient.	175
	References.	178

Chapter 7 : Second Harmonic Generation and Sum Frequency Mixing : Practical Results. **181**

7.1 Introduction. 182
7.2 CVL Second Harmonic Generation. 184
7.2.1 Calibration. 186
7.2.2 Results 187
7.2.3 Elliptical Focusing. 193
7.3 SHG of CVL-Pumped Dye Laser Radiation. 198
7.3.1 Results. 199
7.4 Sum Frequency Mixing The Dye and CVL Radiation. 207
7.5 Comparison With Theory. 210
7.5.1 CVL SHG : Comparison With Theory. 211
7.5.2 Dye Laser SHG : Comparison With Theory. 215
7.6 Conclusion and Discussion. 217
7.7 Future Design Considerations and Suggested Work. 218
7.7.1 SHG With Air-Cooled CVLs. 218
7.7.2 Enhancement Cavities and Parametric Oscillation. 219
References. 221

Chapter 8: Applications Of High Repetition Rate Tunable Lasers And Conclusion. **223**

8.1 Introduction. 224
8.2 RIMS - Resonant Ionization Mass Spectrometry. 224
8.3 Tropospheric Hydroxyl Radical Detection. 228
8.4 Conclusions. 234
8.5 The Future Direction For High Repetition Rate Tunable Laser Research. 237
References 239

Appendix A : Computer Model Listings. **240**

A.1 Longitudinally pumped amplifier calculations. 241
A.2 Gain length scaling for transversely pumped amplifiers. 243
A.3 Seed power scaling for transversely pumped amplifiers. 245
A.4 Pump power scaling for transversely pumped amplifiers 247
A.5 Type I phase-match calculations in BBO. 249
A.6 Type II phase-match calculations in BBO. 251
A.7 Type I phase-match calculations in lithium iodate. 253
A.8 Type I phase-match calculations in the crystal LBO. 255
A.9 Type II phase-match calculations in the crystal LBO. 257
A.10 Type I phase-match calculations in LBO at θ=90. 259
A.11 Boyd & Kleinman theory : variation of SHG efficiency with phase mismatch and strength of focusing. 261
A.12 Non-collinear SHG interaction model. 262
A.13 Type I sum frequency calculations in BBO. 264

Abbreviations Used In This Thesis.

ADP	-	Ammonium Dihydrogen Phosphate.
AR	-	Anti-Reflection.
ASE	-	Amplified Spontaneous Emission.
AVLIS	-	Atomic Vapour Laser Isotope Separation.
BBO	-	Beta-Barium Borate.
CCD	-	Charge Coupled Device.
CVL	-	Copper Vapour Laser.
CW	-	Continuous Wave.
DC	-	Direct Current.
ESA	-	Excited State Absorption.
$\mathcal{F}$	-	Finesse.
FSR	-	Free Spectral Range.
FWHM	-	Full Width Half Maximum.
GEC	-	General Electric Company.
GPIB	-	General Purpose Interface Bus.
GSA	-	Ground State Absorption.
He-Ne	-	Helium Neon.
HMPGI	-	Hybrid Multiple Prism Grazing Incidence.
HR	-	High Reflectivity.
IEEE	-	Institute of Electronic and Electrical Engineers.
IOP	-	Institute Of Physics.
IR	-	Infra-Red.
KDP	-	Potassium Dihydrogen Phosphate.
LBO	-	Lithium Tri-Borate.
LIF	-	Laser Induced Fluorescence.
$LiIO_3$	-	Lithium Iodate.
LLNL	-	Lawrence Livermore National Laboratory.
LPA	-	Longitudinally Pumped Amplifier.
MOPA	-	Master Oscillator Power Amplifier.
MPL	-	Multiple Prism Littrow.
MVL	-	Metal Vapour Laser.
Nd:YAG	-	Neodymium doped Yttrium Aluminium Garnet (laser).
NBA	-	Narrow Band Amplifier.
NCPM	-	Non Critical Phase Matching.
OH	-	Hydroxyl Radical.
OL	-	Oxford Lasers.
OPO	-	Optical Parametric Oscillator.

Abbreviations Used In This Thesis (Continued)

PC	-	Personal Computer.
PRF	-	Pulse Repetition Frequency.
QEG	-	Quantum Electronics Group.
RIMS	-	Resonant Ionization Mass Spectrometry.
RIS	-	Resonance Ionization Scheme.
SCL	-	Short Cavity Laser.
SFM	-	Sum Frequency Mixing.
SFUR	-	Self Filtering Unstable Cavity.
SH	-	Second Harmonic.
SHG	-	Second Harmonic Generation.
SLM	-	Single Longitudinal Mode.
TPA	-	Transversely Pumped Amplifier.
UV	-	Ultra-Violet.

Glossary of Symbols Used in This Thesis

Unfortunately, owing to the large number of parameters required to describe many of the laser and nonlinear phenomena contained in this work, several symbols have different meanings according to their context. Thus, at the risk of unnecessary repetition, the symbols and their meanings are listed by chapter :

Chapter 2

N	-	Density of copper atoms.
E	-	Electric field strength.
M	-	Unstable cavity magnification.
f	-	Focal length.

Chapter 3

S_0	-	Singlet ground state of an organic dye.
S_i	-	i^{th} excited singlet state of an organic dye.
T_i	-	i^{th} excited triplet state of an organic dye.
τ	-	Lifetime.
N	-	Number of electrons.
λ	-	Wavelength.
$\Delta\lambda$	-	Bandwidth.
$\Delta\theta$	-	Divergence.
$(\partial\theta/\partial\lambda)$	-	Dispersion.
θ	-	Grating angle.
M	-	Telescope magnification.
ϕ	-	Angle of incidence.
ψ	-	Angle of refraction.
n	-	Refractive index.
$\mathscr{F}$	-	Finesse.
R	-	Reflectivity.
FSR	-	Free spectral range.

Chapter 4

S_i	-	i^{th} excited singlet state.
L	-	Length of dye amplifier.
h	-	Height of pump beam focus at the dye amplifier.
d	-	Width of amplifier dye cell.
x,y,z	-	Cartesian coordinates.
k_{st}	-	Intersystem (S→T) crossing rate constant.
n_i	-	Population density of the singlet state S_i.
τ_s	-	Lifetime of S_1 against spontaneous emission.
τ_{21}	-	Radiationless decay time for $S_2 \rightarrow S_1$ relaxation.
I_l	-	Dye laser intensity.
I_p	-	Pump (CVL) laser intensity.
$\sigma_{01}(\lambda_p)$	-	Absorption cross-section at the pump laser wavelength $S_0 \rightarrow S_1$.

Chapter 4 (continued)

$\sigma_{01}(\lambda_l)$	-	Absorption cross-section at the dye laser wavelength $S_0 \rightarrow S_1$.
$\sigma_e(\lambda_l)$	-	Emission cross-section at the dye laser wavelength $S_1 \rightarrow S_0$.
$\sigma_{12}(\lambda_p)$	-	Absorption cross-section at the pump laser wavelength $S_1 \rightarrow S_2$.
$\sigma_{12}(\lambda_l)$	-	Absorption cross-section at the dye laser wavelength $S_1 \rightarrow S_2$.
n	-	Total number of dye molecules.
t	-	Time.
α_0	-	Small signal gain coefficient.
α_l	-	Saturated gain coefficient at the dye laser wavelength.
α_p	-	Saturated gain coefficient at the pump laser wavelength.
I_s	-	Saturation Intensity.
ξ	-	ESA Parameter.
η	-	Extraction efficiency.
G	-	Amplifier gain.
T	-	Dye transmission at the pump laser wavelength.
ρ	-	$\sigma_{12}(\lambda_p)/\sigma_e(\lambda_l)$.
d_p	-	Penetration depth.
f	-	Pulse repetition frequency.
τ_{CVL}	-	CVL pulse length.
τ_{DYE}	-	Dye pulse length.
Wp	-	Height of pump beam cylindrical focus.
Ad	-	Area of dye laser beam.

Chapter 5

f	-	Focal length.
$\Delta\theta$	-	Beam divergence (full angle).
η	-	Solvent viscosity.
τ_{ROT}	-	Rotational re-orientation time for the dye dipoles.
k	-	Boltzmann constant.
T	-	Temperature.
w_i	-	Beam waist.
d_i	-	Distance.
λ	-	Wavelength.
n	-	Refractive index.
m	-	Grating order.
d	-	Grating ruling separation.
D	-	Angular dispersion ($\partial\theta/\partial\lambda$).
θ	-	Grating angle.
M	-	Magnification.
R	-	Number of cavity round trips.
$\Delta\nu$	-	Bandwidth (frequency).
$\Delta\lambda$	-	Bandwidth (wavelength).
N^*	-	Population inversion.
n/v	-	Photon density.
t	-	Time.
σ	-	Cross-section for stimulated emission.

Chapter 5 (continued)

c	-	Speed of light.
τ_{LASE}	-	Lifetime against stimulated emission.
ν	-	Frequency.
h	-	Planck's constant.
A	-	Area.
q	-	Gaussian beam parameter.
b	-	Confocal parameter.
w_0	-	Beam waist.

Chapter 6

E	-	Electric field intensity vector.
D	-	Electric displacement vector.
B	-	Magnetic induction vector.
H	-	Magnetic field intensity.
t	-	Time.
μ_r	-	Relative permeability.
μ_0	-	Permeability of a vacuum.
ϵ_0	-	Permittivity of a Vacuum.
ϵ_{ij}	-	Permittivity tensor (anisotropic media).
x,y,z	-	Cartesian coordinates.
$\epsilon_{x,y,z}$	-	Principal dielectric constants.
ω	-	Angular frequency.
k	-	Wave vector.
k	-	Wave number.
r	-	Position vector.
s	-	Unit vector in the direction of **k**.
S	-	Poynting vector.
v_p	-	Phase velocity.
n	-	Refractive index.
$n_{x,y,z}$	-	Principal Refractive Indices.
v_i	-	Phase velocity for a wave propagating in direction i.
n_o	-	Refractive index for an ordinary wave (uniaxial crystal).
n_e	-	Refractive index for an extraordinary wave (uniaxial crystal).
β'	-	Angle subtended between the optic axes in a biaxial crystal.
θ	-	Polar angle.
ϕ	-	Azimuthal angle.
ρ	-	Walk-off angle.
c	-	Speed of light.
P	-	Polarization vector.
$\chi_{i,j,k}$	-	Electric susceptibility tensor.
d_{eff}	-	Effective nonlinear coefficient.
α_ω	-	Electric field loss coefficient.
κ'	-	$\omega d_{eff}/(nc)$.
σ_R	-	Real component of the surface charge density.
Δk	-	Phase mismatch.

Chapter 6 (continued)

P	-	Power.
L	-	Crystal length.
T	-	Temperature.
B_i, C_i	-	Dummy parameters used to calculate phase matching in biaxial crystals.
x',y',z'	-	Cartesian coordinates describing Gaussian beam propagation.
w_0	-	Beam waist.
b	-	Confocal parameter.
τ'	-	Gaussian beam parameter.
f	-	Focal length.
C	-	Lumped SHG constants.
h	-	Boyd and Kleinman efficiency parameter
ξ	-	Boyd and Kleinman focusing parameter.
μ	-	Boyd and Kleinman focus position parameter.
β	-	Boyd and Kleinman birefringence parameter.
σ	-	Boyd and Kleinman phase match parameter.
κ	-	Boyd and Kleinman absorption parameter.
B	-	Boyd and Kleinman beam walk-off parameter.
l_a	-	Beam-walk-off length.
l_f	-	Diffraction length.
e	-	Elipticity.
ξ_x	-	Elliptical focus parameter.
θ_{acc}	-	Acceptance angle.
l_{max}	-	Maximum interaction length.
$\Delta\theta$	-	Beam divergence (half angle).
G(i,j)	-	Second order correlation function.
γ(i,j)	-	First order correlation function.

Chapter 7

f	-	Focal length.
$l\Delta T$	-	Phase match temperature bandwidth.
c	-	Harmonic conversion coefficient.
P	-	Power.
θ	-	Polar angle.
ϕ	-	Azimuthal angle.
d_{eff}	-	Effective nonlinear coefficient.
σ	-	Boyd and Kleinman phase match parameter.
B	-	Boyd and Kleinman walk-off parameter.
ξ	-	Boyd and Kleinman focusing parameter.
h	-	Boyd and Kleinman efficiency parameter.
I	-	Intensity.
E	-	Electric field intensity.
l	-	Crystal length.
n	-	Refractive index.
c	-	Speed of light.
ϵ_0	-	Permittivity of a vacuum.

Chapter 7 (continued)

ω	-	Angular frequency.
κ	-	Lumped SHG constants.
k	-	Wave number.
λ	-	Wavelength.
ρ	-	Walk-off angle.
e	-	Elipticity.
d	-	Distance.

Chapter 8

I_{SAT}	-	Saturation intensity.
ω	-	Angular frequency.
σ	-	Absorption cross-section.
τ	-	Lifetime.
$\hbar$	-	Planck's constant ($h/2\pi$).
M	-	Unstable cavity magnification.

Chapter 1 : Introduction

1.1 Context and Purpose of the Current Research.

1.2 Layout of This Thesis.

Chapter 1 : Introduction

1.1 Context and Purpose of the Current Research

The laser research detailed in this thesis forms part of the SERC/DTI LINK collaborative programme to develop a resonant ionization mass spectrometer (RIMS). The aim of the research undertaken at the Clarendon Laboratory was to develop a tunable, narrow-bandwidth source of high repetition rate laser radiation suitable for the resonance ionization of elemental species in the vapour phase for RIMS detection.

To ensure sensitivity and selectivity in the RIMS process, the laser source must fulfil several requirements. The laser system must produce high repetition rate (5-10kHz) pulsed laser radiation at an adjustable, but otherwise stable, wavelength; the pulse energy should be constant, and sufficient to saturate the resonance ionization transitions (intensities of order 20kW/cm^2); the pulse length should also be short and the pulse timing reproducible. Finally, the beam should be homogeneous, possess a frequency bandwidth comparable to the Doppler broadened transition profiles of the elemental species to be detected, and have good beam divergence characteristics. (The full reasoning underpinning these requirements will become apparent later.)

Whilst high repetition rate radiation is possible from cavity dumped Nd:YAG lasers, the technology in this area is in its infancy, and the pulse length is too long ($\sim$200ns) for application to RIMS. Suitable sources of high repetition rate tunable laser radiation are, however, provided by the family of intrinsically pulsed metal vapour lasers, of which the copper vapour laser (CVL) is the best known example. The CVL forms an excellent starting point in the design of a spectroscopic laser system; laser pulses of several millijoules can be produced at repetition rates in the range 2-32kHz with pulse energy jitter of only a few percent. Furthermore, the CVL pulse shape is reproducible and lasts for about 30ns, with timing jitter less than 1ns.

However, the CVL operates at a pair of fixed wavelengths (511nm and 578nm), and conversion of the laser output into tunable radiation is necessary. Three

promising means of converting the fixed CVL frequencies into tunable laser output suitable for RIMS were identified as research goals:

(1) The CVL-pumping of dye lasers.
(2) The CVL-pumping of Ti:Sapphire lasers.
(3) The second harmonic generation (SHG) of dye laser radiation, and the sum frequency mixing of the CVL beam with tunable radiation generated by methods (1) and (2).

The present work considers the generation of high repetition rate tunable laser sources by the CVL-pumping of dye lasers, the SHG of the CVL and CVL-pumped dye lasers, and the sum frequency mixing of the CVL and CVL-pumped dye laser radiation. CVL-pumped Ti:Sapphire lasers have been studied at the Clarendon Laboratory, and are the subject of another thesis by Knowles.

Whilst in recent years, the potential of the copper vapour laser as a high repetition rate source for laser spectroscopy has been recognized, the physics and technology is still in its infancy. Little published work is available to suggest how to optimize a dye laser for CVL pumping, let alone which nonlinear crystals, or focusing geometries, are best suited to achieve efficient harmonic conversion of the resulting laser radiation. The purpose of this thesis is, therefore, to address the fundamental issues affecting the design and operation of CVL-pumped dye lasers and their second harmonic generation. The initial research goals were to achieve 10% conversion of the CVL radiation into tunable dye laser radiation, and then to achieve 10% conversion of the dye radiation into its second harmonic. As will be shown, significantly better results have been achieved, and in many cases represent the best results published to date.

Whilst the work described in this thesis has been motivated by the development of a high repetition rate tunable laser source for RIMS, the results and conclusions are of general relevance to the spectroscopic application of the CVL to a number of areas of scientific and technical importance. Indeed, during the course of the research programme, both CVL-pumped dye lasers and their nonlinear

frequency conversion have been applied to a number of applications including laser TV, and hydroxyl radical detection.

1.2 Layout of this thesis

The copper vapour laser forms the basis of the laser systems reported in the present work, and an understanding of its characteristics and operation is essential for the design of CVL-based high repetition rate tunable laser systems. Chapter 2 reviews the principles and operation of the CVL, and discusses the merits of plane-plane and unstable cavity designs. Design modifications to the Oxford Lasers CU40, used for the present investigations, are detailed, and the implications of using such a laser as a source of high repetition rate radiation for dye laser pumping and second harmonic generation are discussed.

Chapters 3 to 5 are concerned with the CVL-pumping of dye lasers, and their optimization. Chapter 3 reviews the photophysics and photochemistry of laser dyes and illustrates how, using dispersive optics, dye oscillator cavities may be constructed to provide tunable narrow-bandwidth laser output. The relative merits of numerous cavity designs are discussed, and the spectral output of a number of CVL-pumped dye oscillator cavity designs are presented.

In chapter 4 a rate equation analysis of the laser kinetics relevant to optical amplification in dye lasers is developed. Unlike the classical analysis of Hargrove and Kan, the effect of excited state absorption at both the pump and dye laser wavelengths is included. The merits of longitudinally-pumped and transversely-pumped amplifiers are discussed, and the ESA model predictions are compared with experiment.

Chapter 5 reports a series of experiments conducted to ascertain the parameters of the CVL, the dye laser, and their optical coupling, necessary to optimize dye laser systems for CVL-pumping. Using the physical understanding gleaned from these investigations, the design modifications necessary for the optimum CVL-pumping of three commercially available dye lasers are detailed. The modified

commercial systems, the Lambda Physik LPD3000, Lumonics HD-350 and one of Russian manufacture, the LZhI-504, are characterized, and their suitability as a spectroscopic tool is discussed.

Chapter 6 reviews the theory of second harmonic generation using plane waves, Gaussian beams, and partially coherent beams. Computer model predictions of the optimum focusing strengths, expected harmonic conversion efficiencies, and phase-match angles for both uniaxial and biaxial crystal are presented. Chapter 7 describes the experimental investigation of second harmonic generation in beta-barium borate (BBO), lithium tri-borate (LBO) and lithium iodate using both CVL, and CVL-pumped dye laser, radiation. Conventional spherically focused SHG is compared with elliptically focused SHG geometries, and the results are compared with the theoretical predictions of chapter 6. Chapter 7 also reports a preliminary investigation of sum frequency mixing of the CVL and CVL-pumped dye laser radiation, which may provide a valuable source of high repetition rate tunable radiation. The factors restricting the harmonic conversion efficiency are discussed, and future work is suggested.

Chapter 8 discusses the spectroscopic value of CVL-based high repetition rate lasers by illustrating their application to resonance ionization mass spectrometry and the detection of tropospheric hydroxyl radicals. The chapter also reports the use of a frequency doubled CVL-pumped dye laser to record the 308nm absorption spectrum of hydroxyl radicals produced in a flame. The current work is concluded and the direction of future research in the field of high repetition rate tunable lasers is considered.

For clarity, the computer models developed to predict the behaviour of optical amplification in dye lasers and the second harmonic processes are collected and listed in Appendix A at the end of the thesis, rather than allowing them to detract from the main body of the research.

Chapter 2 : The Copper Vapour Laser

2.1 Introduction.

2.2 The History of The Copper Vapour Laser.

2.3 The Atomic Physics of The CVL.

2.4 The Effect of Pressure and Temperature.

2.5 Practical Details.

2.6 Cavity Design.

2.6.1 Plane-Plane Cavities.

2.6.2 Unstable Cavities.

2.7 Pulse Timing of The 511nm and 578nm Lines.

2.8 The Oxford Lasers CU40.

References.

Chapter 2 : The Copper Vapour Laser

2.1 Introduction

The copper vapour laser (CVL) is the most powerful source of visible laser radiation currently available, and offers an efficient source of high repetition rate laser radiation at two wavelengths simultaneously - 510.6 nm (green) and 578.2 nm (yellow). The CVL is typically capable of pulse repetition rates (prfs) in the range 2-32 kHz, with pulse energies of several millijoules delivered in pulse durations of 10-50 ns. The physics and technology of the CVL has advanced significantly over the last 15 years, such that now, single unit CVLs capable of average powers in excess of 650 W [2.1] are available. Moreover, commercial units capable of average output powers approaching 200 W, with nearly 1% electrical input to light conversion efficiency, are procurable [2.2].

The CVL may also be used in an amplifier configuration, and, in fact, possesses better extraction characteristics when used as an amplifier than when used as an oscillator. Thus, by passing the laser beam from a master CVL oscillator through a chain of amplifier CVLs, light beams of very high average power may be generated. This very scheme is used at the Lawrence Livermore National Laboratory to generate laser beams with average powers in excess of 7 kW for use in dye laser pumping.

To understand how CVLs may be used to pump tunable laser media, and so generate sources of high repetition rate tunable laser radiation, it is important to understand both the physics of the CVL and its technological limitations. This chapter reviews the basic physics of both the CVL and CVL cavity design, and illustrates how best the lasers may be operated when used for dye laser pumping and second harmonic generation.

2.2 The History Of The Copper Vapour Laser

The copper vapour laser belongs to a family of "self-terminating" pulsed metal vapour lasers (MVLs) which includes, amongst others, the manganese, lead, and gold vapour lasers. The first report of laser action in this family of metal vapour lasers was made by Fowles & Silfvast (1965) [2.3], who observed lasing on the 723 nm transition of neutral lead excited in a pulsed discharge containing lead vapour and a noble gas. Laser oscillation on the 510.6 nm and 578.2 nm lines of atomic copper was demonstrated the following year, in 1966, by Walter *et al* [2.4]. Walter's laser used an external furnace to produce the atomic copper vapour, and, despite only limited operation at the lasing temperature of ~ 1500°C, it was established that the CVL was capable of both high repetition rate and high efficiency. Walter subsequently identified five criteria relating to the atomic term diagram necessary for the high gain and high efficiency operation of MVLs [2.5] - all five are upheld for the CVL.

A significant milestone in the development of CVL technology was set by Isaev *et al.* [2.6], who developed a system in which the power necessary to maintain the CVL at its ~ 1500°C operating temperature was supplied by the discharge itself. Further work by Petrash, Isaev and the group at the Lebedev Institute succeeded in promoting the output powers of discharge-heated CVLs to 40W, although the lifetime of these early lasers tended to be rather brief [2.7]. In parallel with the Russian work, an extensive CVL research programme was undertaken at the Lawrence Livermore National Laboratory (LLNL) in collaboration with the General Electric Company (GEC). Their aim was to develop a high power, high repetition rate tunable laser system suitable for the Atomic Vapour Laser Isotope Separation (AVLIS) of uranium 235 from its natural mixture. In spite of all these efforts, the output power of practical CVLs remained at the 20 W level. In 1978, however, contrary to expectations, Smilanski *et al* [2.8] successfully demonstrated the high prf operation of a stable, discharge-heated CVL in plasma tubes as wide as 40 mm, and so established the volumetric scalability of the CVL.

Following Smilanski's key demonstration of volumetric scaling in discharge-heated CVLs, further research and development at the LLNL on plasma tube and

circuit design has resulted in single CVL modules capable of several hundred watts.

2.3 The Atomic Physics of The CVL

A partial term diagram of copper in the LS-coupled central field approximation is illustrated in figure 2.1. The lowest configuration of the copper atom contains one 4s valence electron outside of a full $3d^{10}$ subshell, and consequently, the excited states corresponding to the promotion of the 4s electron resemble those of Group I alkali metal atoms. There is, however, one important difference between the term diagram of copper as compared with that of an alkali metal: some of the excited levels corresponding to the excitation of one of the inner-core 3d electrons lie well below the ionization energy. In particular the $3d^9 4s^2$ configuration gives rise to $^2D_{3/2}$ and $^2D_{5/2}$ levels only 1.6 and 1.4 eV above the ground state, as shown below.

Laser operation involves the promotion of $3d^{10}4s\ ^2S_{1/2}$ ground state population

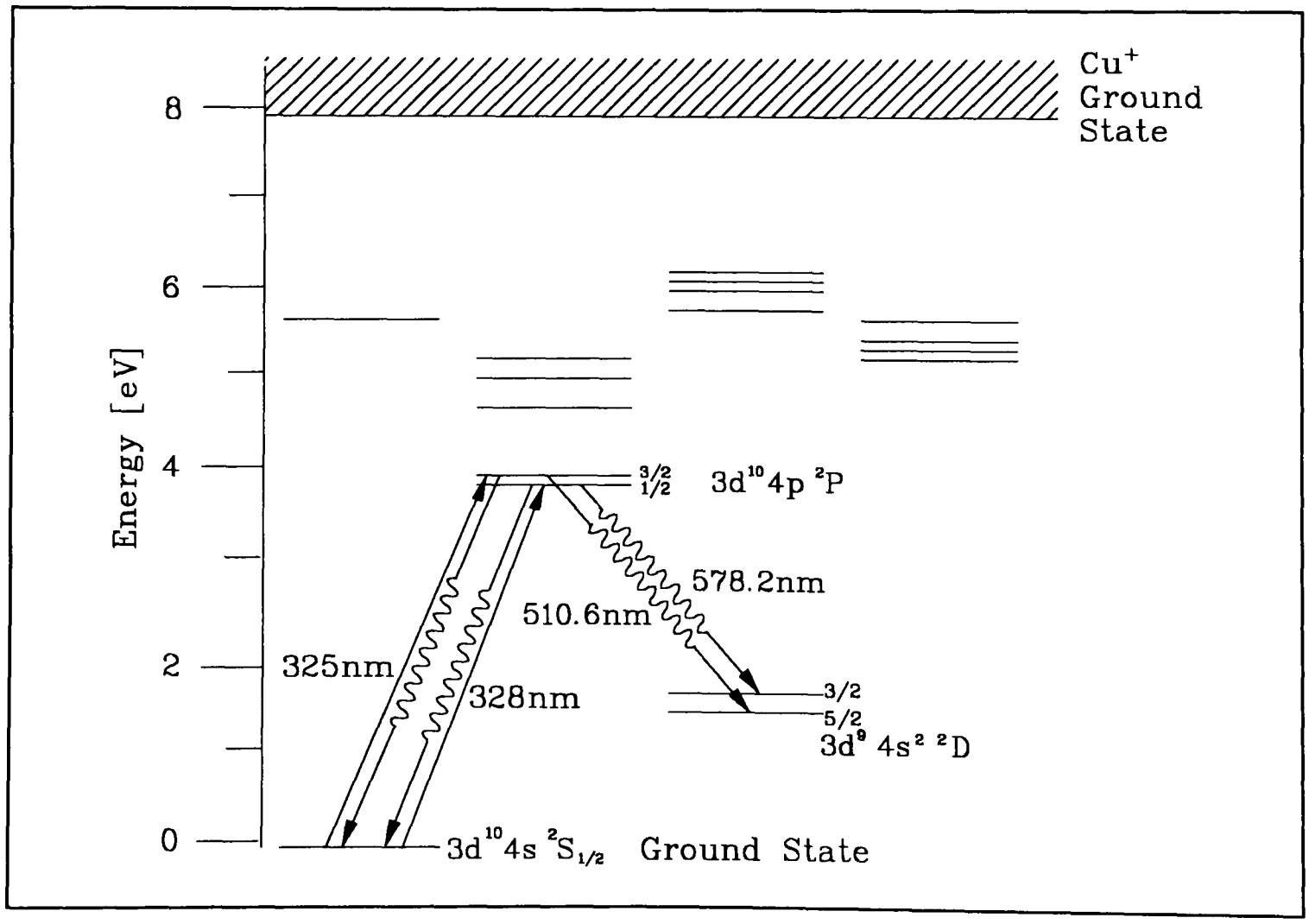


Figure 2.1 Partial term diagram for neutral copper, showing the key transitions relevant to CVL operation

to the $3d^{10}4p\,^2P_{1/2,\,3/2}$ upper laser levels, which initially have an automatic population inversion with respect to the thermally empty $3d^9 4s^2\,^2D_{3/2,\,5/2}$ lower laser levels. Whilst the upper laser levels are connected to the ground state by strong resonance transitions at 325 and 328 nm, under practical laser conditions, the density of copper atoms is such that these resonance transitions are trapped, and so the only effective decay route open to the upper laser level is via the laser transitions. If the central field approximation provided a good description of the copper atom, the 510.6 nm and 578.2 nm laser transitions would be strictly forbidden, since they require the simultaneous jump of 2 electrons. However, there is sufficient configuration mixing to provide moderate transition probabilities for the two laser lines :-

$$3d^{10}4p^2P_{3/2} \;-\; 3d^9 4s^2\,^2D_{5/2} \qquad \lambda = 511 \text{ nm} \qquad \tau = 450 \text{ ns}$$

$$3d^{10}4p^2P_{1/2} \;-\; 3d^9 4s^2\,^2D_{3/2} \qquad \lambda = 578 \text{ nm} \qquad \tau = 600 \text{ ns.}$$

The lower laser levels are metastable since they have the same parity as the ground state, and electric dipole transitions to the ground state are, therefore, strictly forbidden. The lower laser levels can only decay via collisional processes, which occur on relatively long timescales in the low pressure CVL discharge. Thus, the laser is self-terminating through population "bottlenecking" in the lower laser level, and so the CVL is an intrinsically pulsed laser system.

Excitation of the laser levels occurs via inelastic electron-copper atom collisions in an electrical discharge containing copper vapour and a rare gas buffer. The peak cross-section for the excitation of the upper laser level is some 50 times larger than that of the lower laser level; this is because the lower laser level collisional excitation involves the rearrangement of an inner-core, rather than a valence electron. Efficient and preferential pumping of the upper laser level is ensured by limiting the electron temperature to the range 4 - 8 eV. The lower limit is determined by populating the lower laser levels at a rate comparable to that of the upper laser levels; the upper limit is determined by the pumping of higher energy levels, which do not contribute to the lasing process, and represent a loss mechanism. Thus, if a fast-rising current pulse is applied to a discharge tube containing copper vapour ($\sim$0.1-1 mbar) and a buffer gas (eg. neon 20-100 mbar), a substantial population inversion may be transiently sustained, before the rate of pumping of the upper laser level is insufficient to overcome the bottlenecking in the lower laser level.

Typically, the discharge current may last between 300 and 500 ns, whilst the population inversion will only be sustained on the super-linear rising edge of the current pulse, lasting a few tens of nanoseconds.

2.4 The Effect of Pressure and Temperature

Initially, the buffer gas is required so that a discharge may be sustained at room temperature. The discharge heats the plasma tube until the copper melts and evaporates (melting point 1083°C), whereupon the discharge switches to the copper vapour, owing to its lower ionization potential. Under running conditions, the buffer gas is responsible for stabilizing the discharge by anchoring it to the electrodes rather than the gas ports. The gas also reduces the copper diffusion rate, thus limiting the rate of loss of copper from the plasma tube, and discourages the copper from plating out on the tube windows. Finally, the buffer gas also plays a role in the CVL dynamics by cooling the electron temperature between discharge pulses; this enables the lower laser levels to be efficiently depopulated by collisions with cool electrons, with energies ~ 1.5eV.

The optimum operating temperature of the CVL is a compromise between two conflicting tendencies. As the temperature of the CVL is increased, the copper vapour pressure increases, and so more ground state copper atoms become available for excitation and contribute toward laser action. However, as the copper ground state density increases, so the electron energy decreases. This is because the mean electron energy is determined by E/N, where E is the accelerating electric field, and N is the number of species (copper atoms) with which the electrons may undergo inelastic collisions. Thus, the cross section for electron collisional excitation to the ^{2}P upper laser level will decrease, and the excitation of the lower ^{2}D laser levels will increase with increasing laser temperature, until the upper laser level is no longer populated in preference to the lower level.

Because of the energy difference between the two ^{2}D lower laser levels, and the different gain for the two laser transitions, the optimum temperature for the green laser line is not the same as that of the yellow laser line. For a 40 mm bore plasma

tube and neon buffer gas, the optimum temperature for the green is 1500°C whilst the optimum temperature for the yellow is 1600°C; however, the greatest total power is extracted at ~1520°C where the ratio of green to yellow is 2:1. Under steady running conditions, there is a radial temperature variation, with the average gas temperature on axis being some 200°C higher than at the tube walls. For a uniform copper vapour pressure, there will be a corresponding radial variation in the copper density, with the highest density at the "cool" tube walls. For this reason, the gain in a copper laser first exceeds threshold at the tube walls, and this explains why, when a CVL is run-up, lasing first occurs at the tube walls, seen as a green annulus, which gradually closes in, and later increases its yellow content as the temperature increases. This radial variation in the gain has important consequences for resonator design, and is discussed further in §2.6.2.

2.5 Practical Details

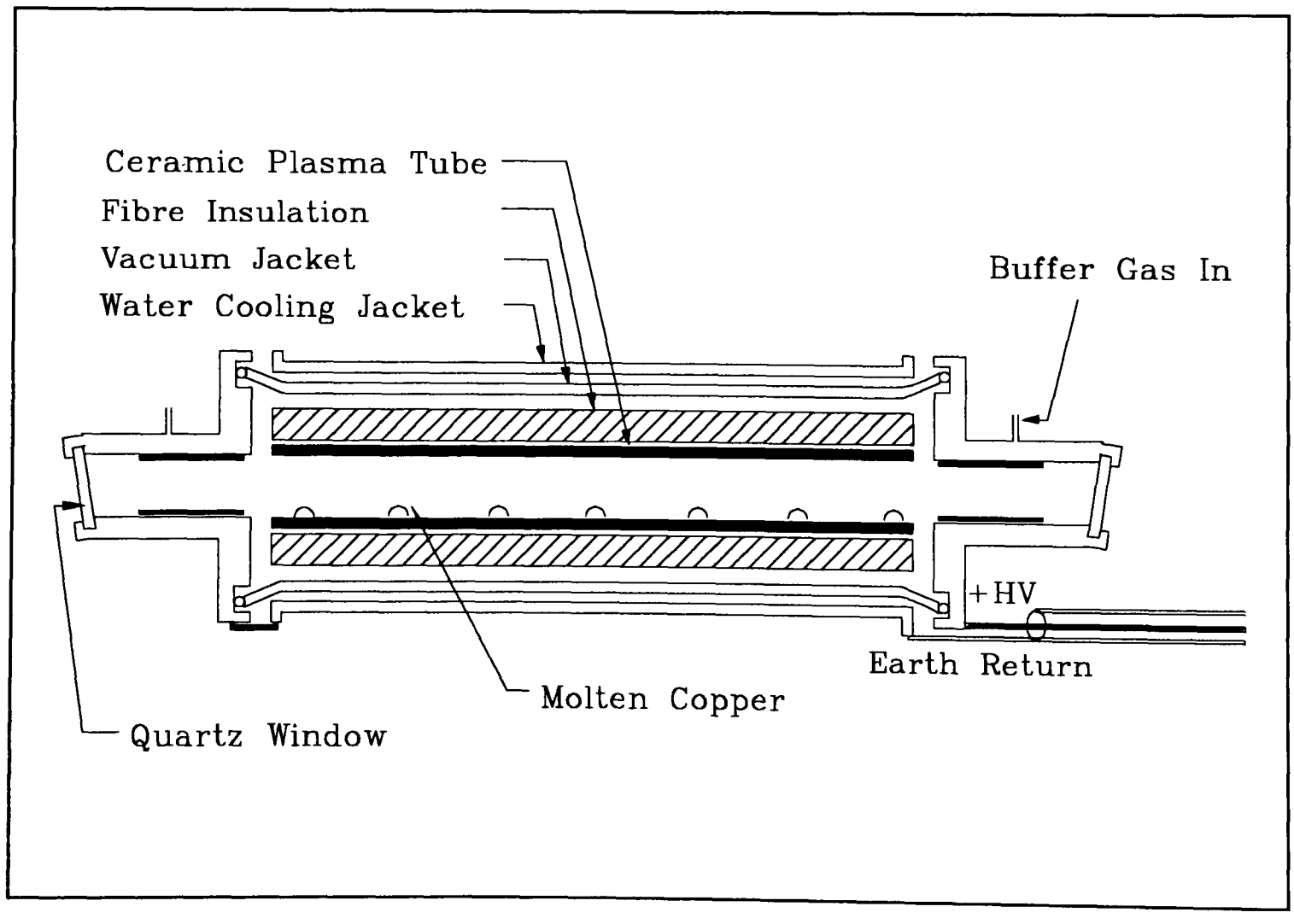


Figure 2.2 : Schematic illustration of the construction of a CVL head.

A schematic diagram illustrating the construction of a longitudinally excited CVL is shown in figure 2.2. The laser head is based upon a ceramic tube, typically of some 20-40 mm in diameter and 1 m in length, surrounded by a thick layer of alumina fibre insulation. The copper load is in the form of a few tens of grammes of coiled copper wire, uniformly distributed along the length of the discharge tube. The whole assembly is enclosed in a silica / Pyrex vacuum tube, with stainless steel end flanges completing the vacuum system. The end flanges contain foil electrodes, and one of them is electrically connected to the co-axial water cooling jacket, which also acts as a low inductance current return path. Finally, gas fittings at the end flanges allow the steady flow of neon buffer gas through the discharge tube at a rate of ~ 1 litre atmosphere / hour, and at a pressure of ~ 30 mbar.

The electrical charging circuit of the CVL must produce a fast rising current pulse for efficient operation of the laser, and consequently, great care must be taken to minimize the inductance of the circuit. A commonly used charging circuit is

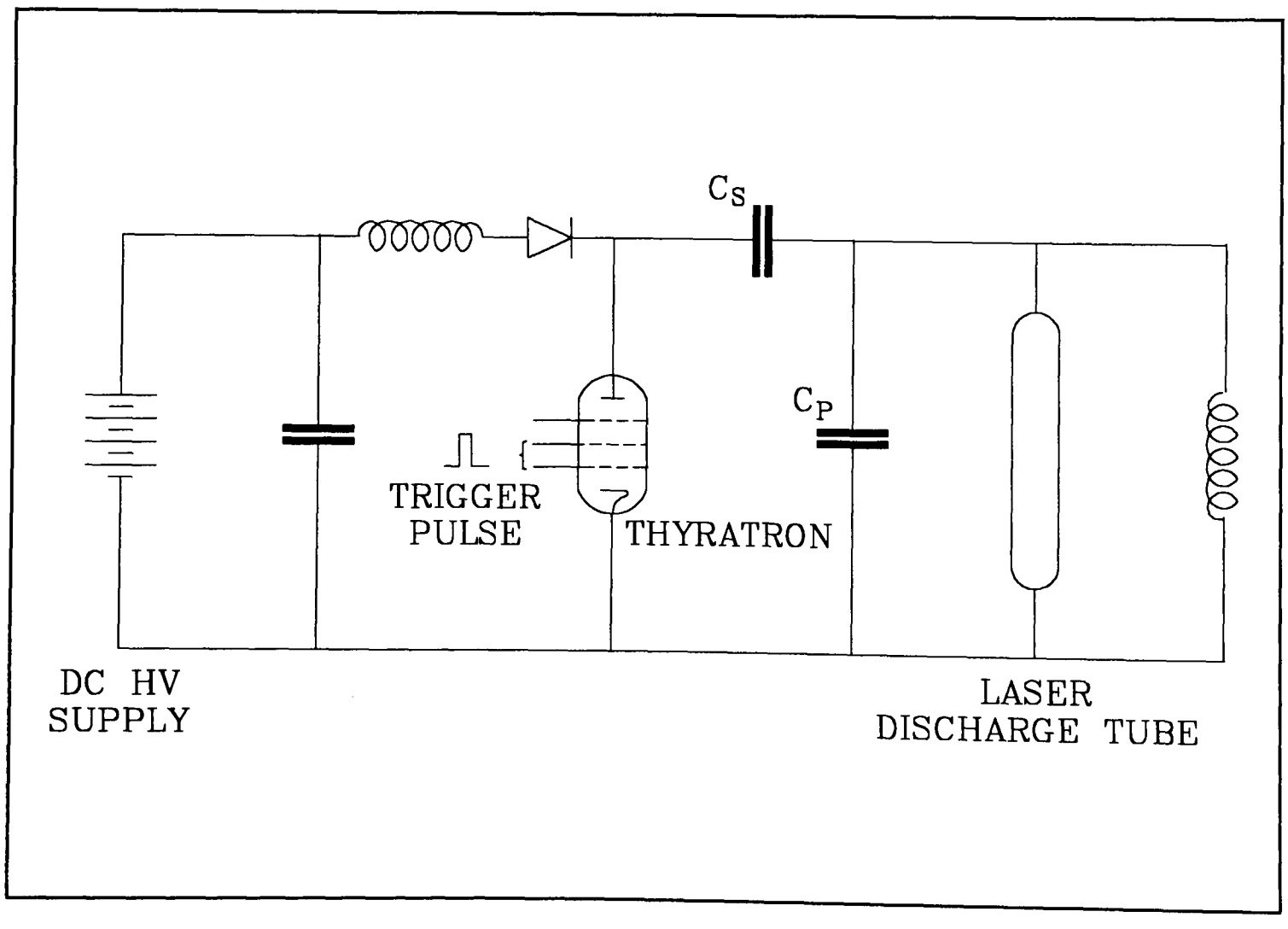


Figure 2.3 : High voltage charging circuit commonly used in copper vapour lasers.

illustrated in figure 2.3, where a thyratron is used as a fast, high voltage, high current switch. A high voltage DC supply is used to resonantly charge the storage capacitor, C_S, to a voltage of 10-20 kV. Then, when the thyratron triggers, this charge is transferred to the peaking capacitor, C_p, connected across the discharge tube. As the voltage across the peaking capacitor increases, the gas in the discharge tube breaks down, and the energy from the storage capacitors is deposited in the discharge. By changing the values of C_S and C_P, it is possible to achieve operation between $\sim$2-32 kHz.

2.6 Cavity Design

The low divergence output offered by stable resonator designs relies upon mode evolution over many cavity round trips, whereupon low order TEM modes dominate over the high diffraction-loss high order modes. Whilst suitable for cw systems, these cavities are unsuitable for the high gain, short-pulse CVL. The CVL exhibits gain for typically 50 ns, and so for a 2 m cavity, only $\sim$5-6 cavity rounds trips are possible before the medium becomes absorbing, and the laser pulse terminates. In addition, the small mode volumes characteristic of stable resonator geometries offer poor extraction efficiencies from the large cross-sectional area gain volume of the CVL. For efficient energy extraction from the CVL, it is necessary to use large mode volume plane-plane or unstable cavity designs; the choice of cavity design depends very much upon the application for which the CVL is to be used.

2.6.1 Plane-Plane Cavities

The greatest power extraction from a CVL is achieved with a plane-plane cavity. The cavity consists of a high reflectivity flat and a quartz flat, AR-coated on one side, so as to provide 96% output coupling. An estimate of the beam divergence may be made by considering a small volume of spontaneous emission seeding the gain at the centre of the tube (figure 2.4). The divergence of the laser beam will then be given by the diameter of the plasma tube divided by the total distance travelled before the beam exits from the cavity. For a 40 W CVL with a plasma tube diameter of 42 mm, and a cavity length of 2 m, this implies a beam divergence of $\sim$5 milliradians.

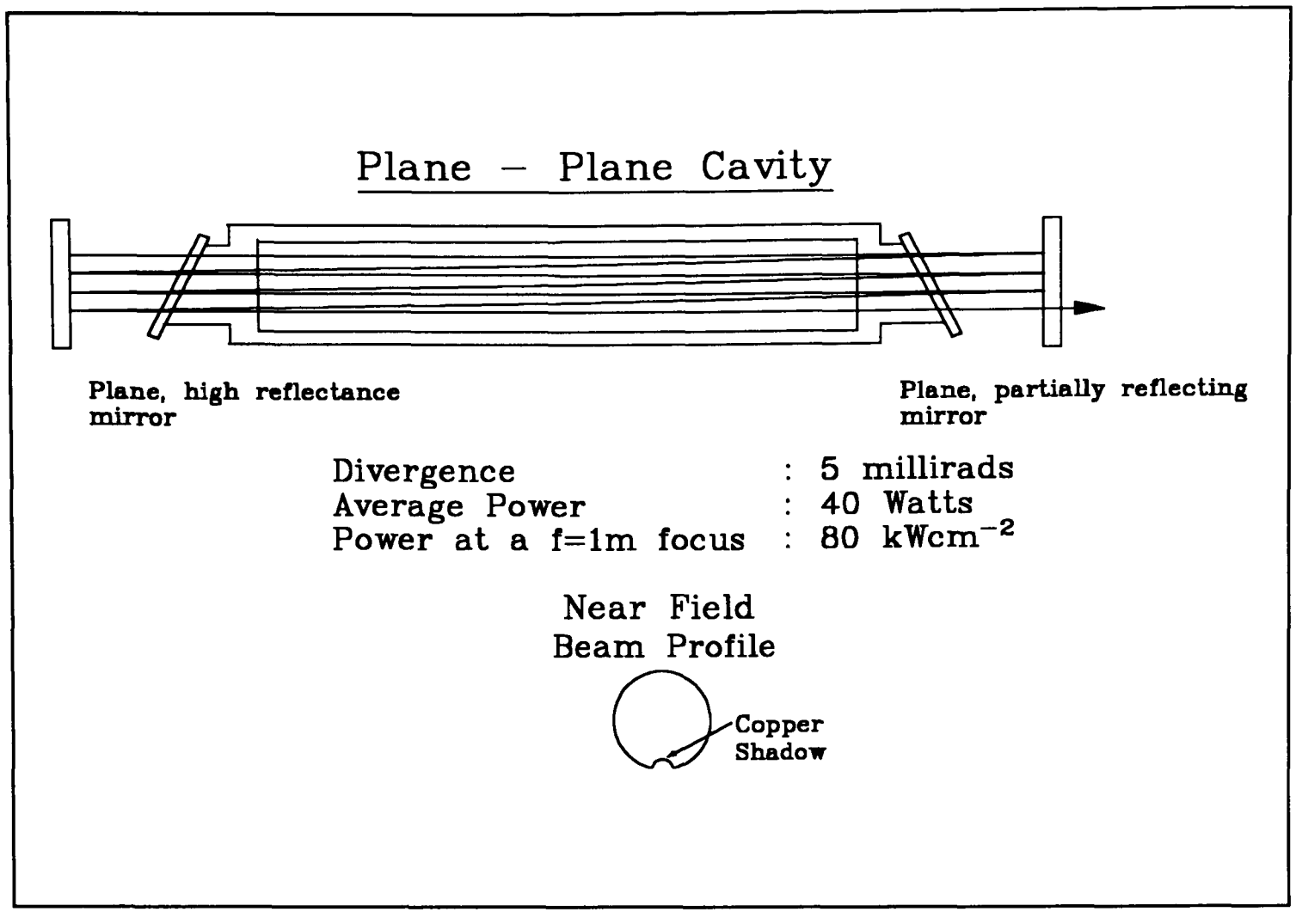


Figure 2.4 : Plane-plane cavity design for a nominal 40 W CVL.

For applications such as high speed photography, where the CVL is merely used as a high repetition rate, short pulse-length strobe, the relatively poor divergence is unimportant. However, for dye laser pumping and/or nonlinear frequency conversion, it is the focusable power that is important. Thus, alternative cavity geometries must be considered which provide both a high extraction efficiency and a low divergence output.

2.6.2 Unstable Cavities

Unstable cavities have proved to be highly successful in their applications to copper vapour lasers, and are capable of :-

. Producing laser beams of high brightness.
. Controllable mode volumes.
. Rapid mode evolution.

Also, unstable cavities are capable of novel geometries, and are well suited to

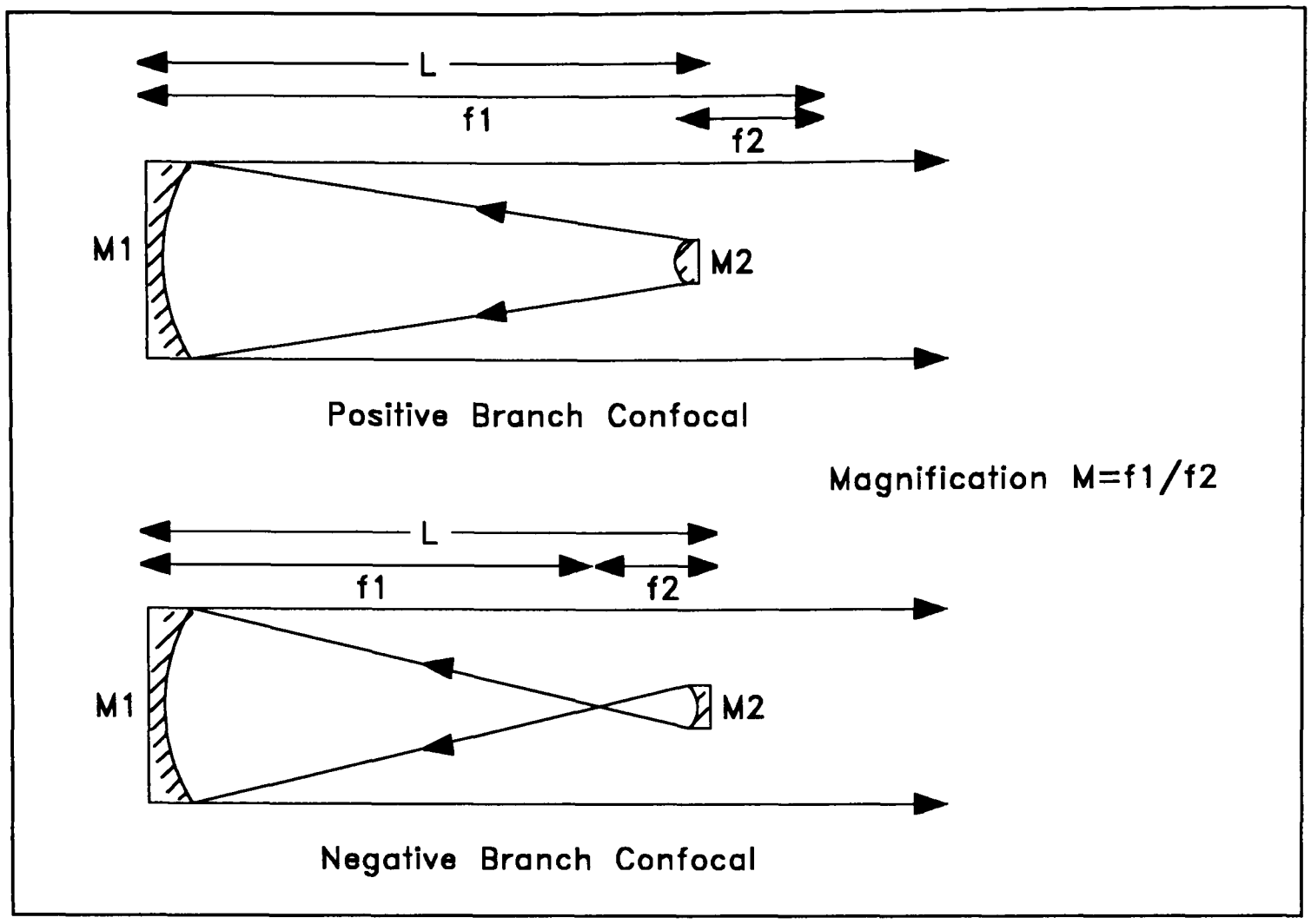


Figure 2.5 : Positive & negative branch confocal unstable resonator designs frequently employed with copper vapour lasers.

injection locking.

The first report of an unstable cavity used with a CVL was made by Zemskov *et al* in 1973 [2.9]; the publication reported sub-milliradian beam divergence, and has paved the way for the CVL to be used in a number of high brightness applications. The most common form of unstable cavity used for CVLs is that formed by a pair of confocal mirrors, used in either a positive or negative branch confocal resonator arrangement, as shown in figure 2.5. The magnification, M, of such a cavity is defined by the ratio of the focal lengths of the mirrors M1 and M2, $M=f_1/f_2$. A valuable way of visualizing the operation of a positive branch unstable resonator is to consider the build-up from spontaneous emission. The spontaneous emission originating from an arbitrary point in the gain medium will travel in both directions. Some of the radiation travelling in the forward direction will be reflected by the convex spot mirror, and on its return pass, will appear to diverge from an image point source located between the mirror and its focal point. This image acts as a virtual source seeding the cavity in the direction of the concave mirror. Of the

radiation subsequently reflected by the concave mirror, most leaves the cavity, but some is intercepted and reflected back by the convex spot mirror. This time the light reflected by the convex spot mirror appears to diverge from a virtual point source even nearer to its focal point. Thus, with each cavity round trip, the virtual point source moves closer and closer to the confocal point, and the divergence of the light exiting from the cavity is reduced by the magnification of the cavity. This cavity build-up continues until the diffraction-limit is reached or the laser pulse terminates.

The light which exits from the cavity on the first pass is little more than amplified spontaneous emission (ASE) which has escaped any cavity control. Only the radiation which exits after three or four cavity round trips approaches the diffraction limit, and is of low divergence. Thus, of the total CVL output, only ~50% (corresponding to the latter half of each laser pulse) may be considered as low divergence. This evolution of the CVL beam quality during the laser pulse may be demonstrated by analysing the pulse shape of the CVL radiation passing through

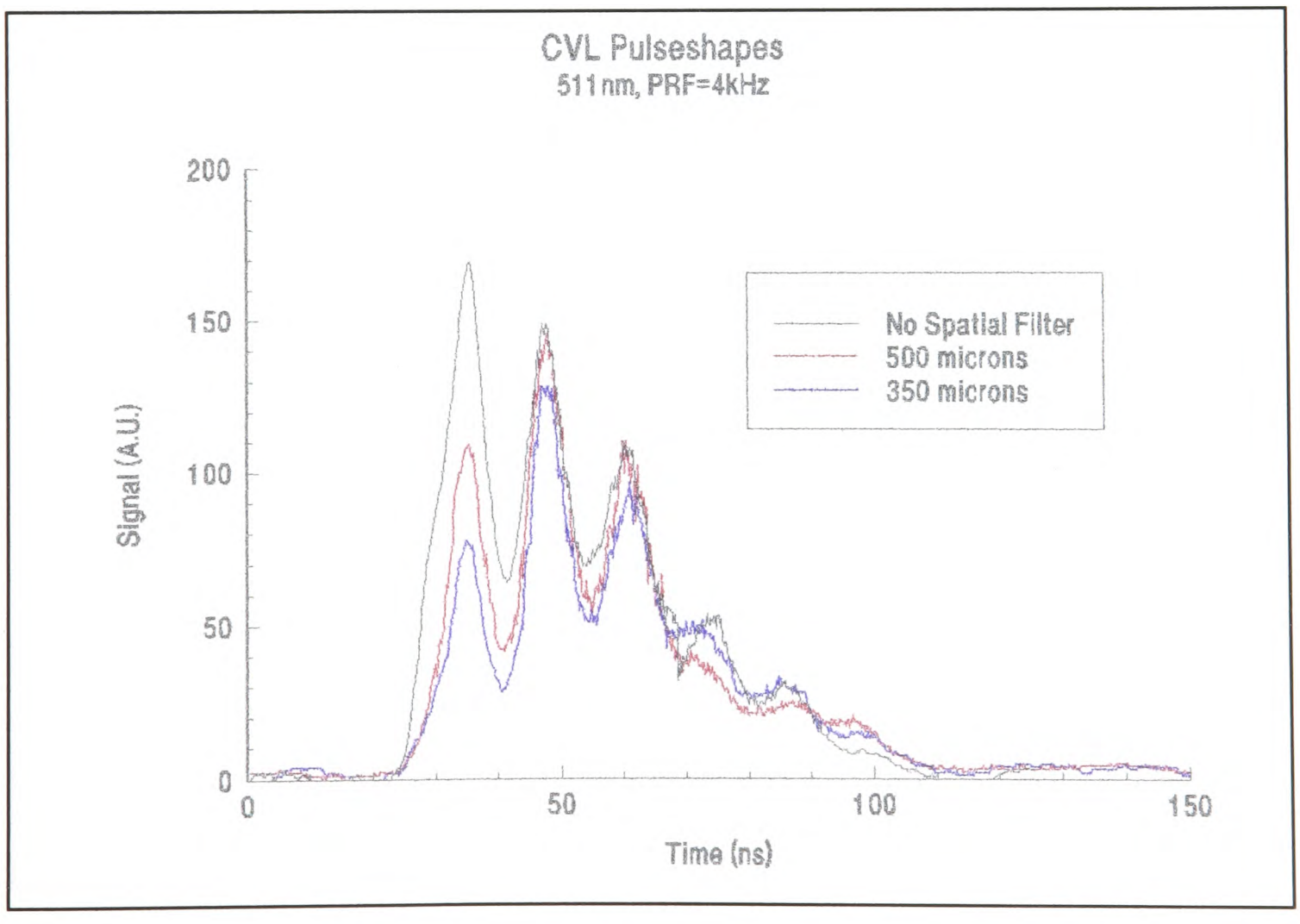


Figure 2.6 : Pulse shapes of the CVL beam spatially filtered at the focus of a lens, f=1 m, by pinholes of size (a)no pinhole, (b) 500 microns, (c) 350 microns.

different diameter pinhole spatial filters at the focus of a lens. CVL pulse shapes of the light passing through 500μm and 350μm spatial filters at the focus of a $f=1$ m lens, recorded using a fast vacuum photodiode, are shown in figure 2.6. The CVL pulse shape can be seen to contain microstructure with a periodicity of $\sim$10ns corresponding to the round trip transit time. It can clearly be seen that the high divergence radiation at the pulse onset is increasingly suppressed by smaller and smaller spatial filters, whilst the low divergence pulse-tail is relatively unaffected.

The fraction of the light-pulse output which may be considered as low divergence is influenced by the magnification of the unstable cavity. High magnification cavities offer rapid mode and transverse coherence evolution, but offer poor extraction efficiencies, whilst the converse is true of low magnification cavities [2.10]. A significant improvement in the beam quality, and in the extraction efficiency of the low divergence radiation, has been achieved by using an off-axis unstable cavity [2.10], as depicted in figure 2.7. Owing to the radial variation in the copper

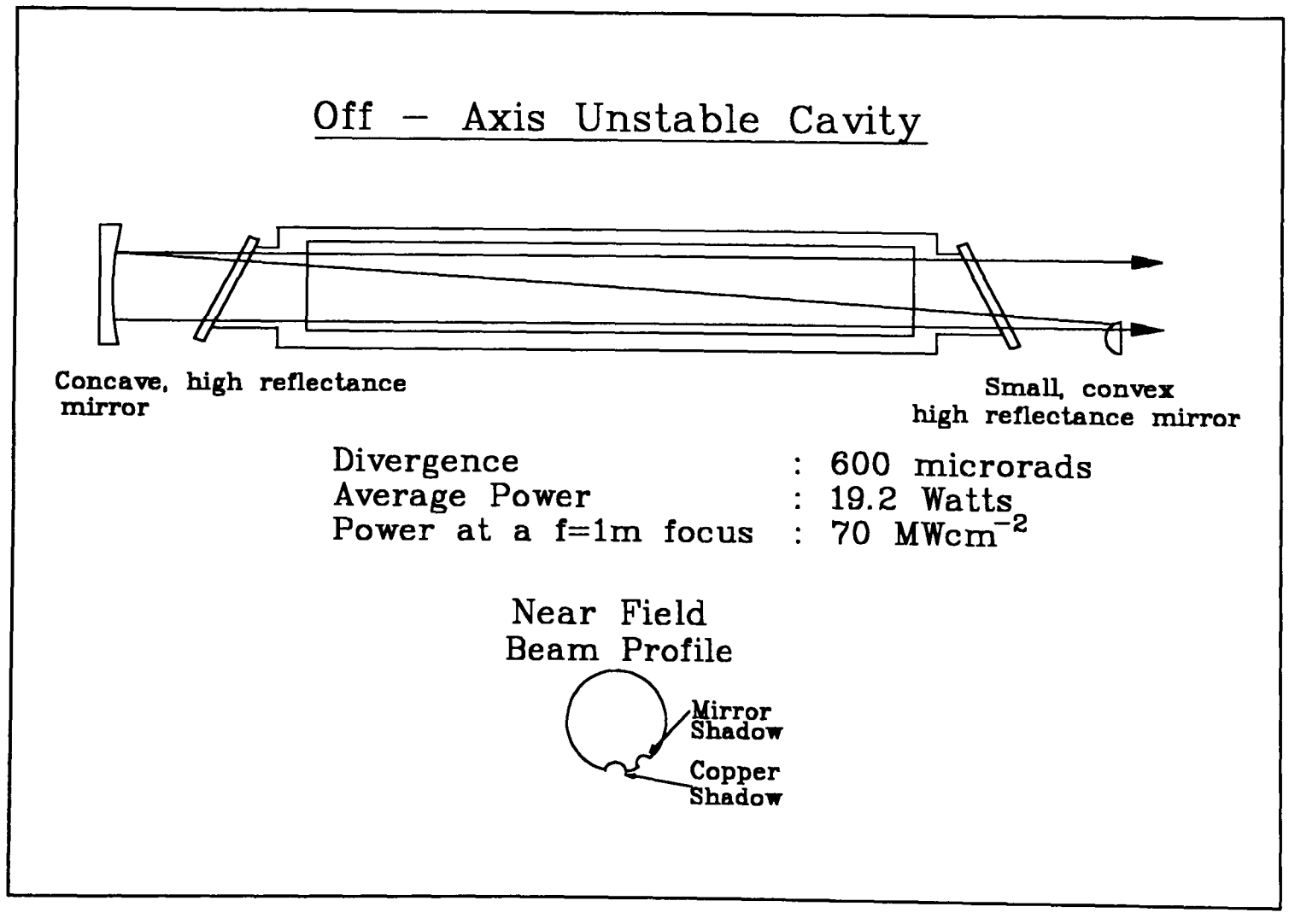


Figure 2.7 : Off-axis unstable cavity (M=40) used with a nominally 40W CVL tube during the course of the following experiments.

density (§2.4), when the CVL is pulsed, gain first appears at the tube walls a few nanoseconds before the gain picks up on the tube axis. Thus, if the front convex spot mirror is positioned at the edge of the tube wall, the cavity may be seeded earlier, allowing more cavity round trips during the gain period. Such an off-axis cavity provides 75% of the power extracted by a plane-plane cavity, and of the total output power, 80% of the radiation has a divergence of less than 600 μrad [2.11].

2.7 The Pulse Timing of the 511 nm and 578 nm Lines

Because of the different transition probabilities for the CVL 511 nm and 578 nm lines, the build-up time for the gain to exceed the cavity losses on the two laser transitions is different. The lower gain of the CVL yellow line causes the 578 nm radiation to be delayed by ~7.5 ns with respect to the 511 nm radiation. The relative timing of the green and yellow lines was investigated by using a dichroic mirror to separate the CVL wavelengths, and a fast response photodiode connected to a digital

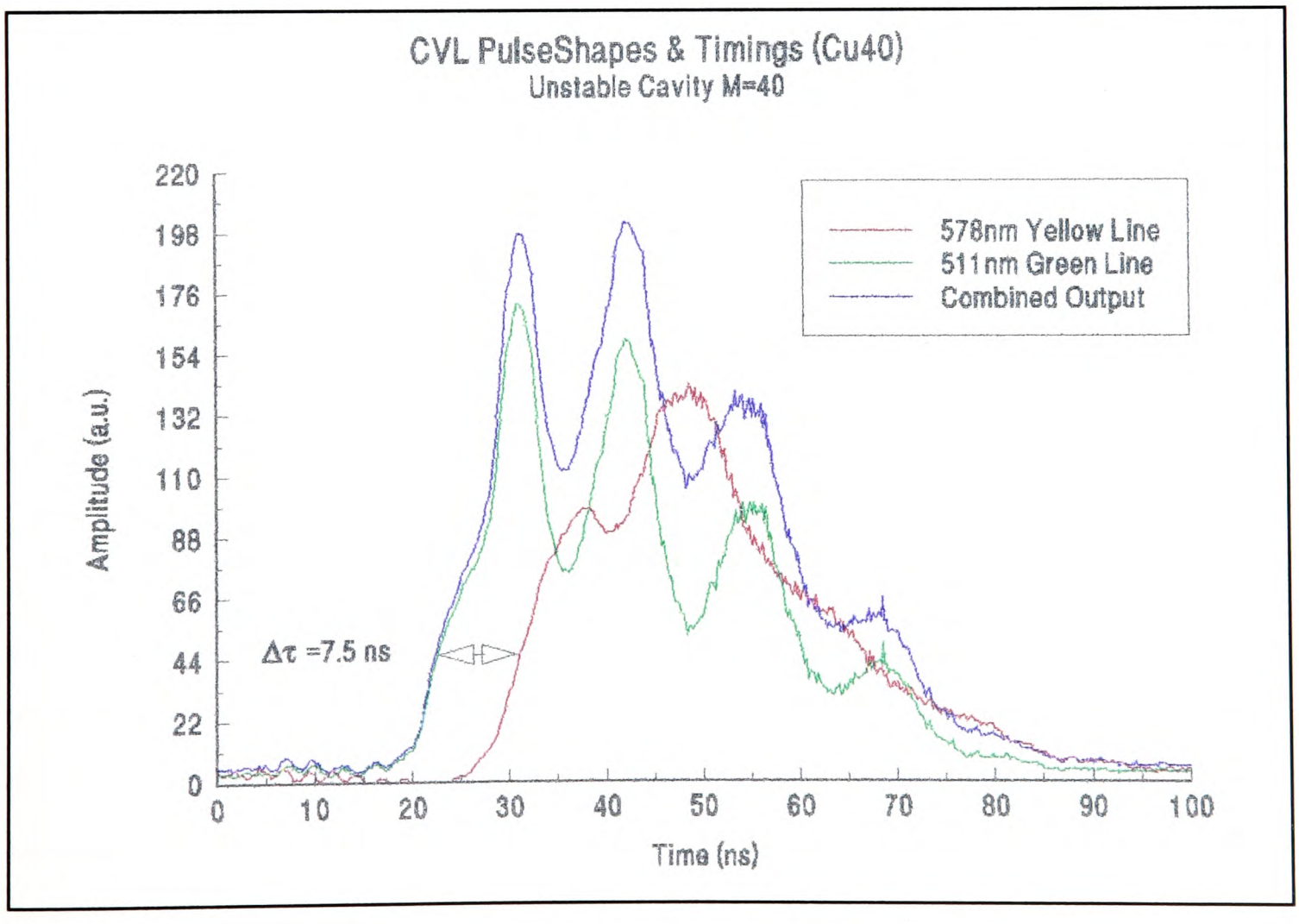


Figure 2.8 : Green and yellow pulse shapes and relative timings from a 42mm bore CVL.

oscilloscope to observe the pulse shapes. The recorded pulse shapes, illustrating the delay, are shown in figure 2.8. Whilst, for many purposes, this delay is of little consequence, it is important in applications such as the nonlinear sum frequency mixing of the CVL wavelengths, where a good spatial and temporal overlap in the nonlinear crystal is required for efficient mixing.

2.8 The Oxford Lasers CU40

The copper vapour laser used in all of the experiments reported in this thesis was an Oxford Lasers CU40. The laser comfortably met its specification of delivering an average power of 40W (combined 511 nm & 578 nm output) when used with a plane-plane cavity, and, in practice, powers approaching 45 W were possible.

The three-phase mains input is transformed up to 10 kV before being bridge-rectified and smoothed by a large capacitor bank. This supply is then used to resonantly charge a thyratron modulator unit of the type described in section §2.5. The power supply is remote from the laser head, and the pulsed high voltage is conducted between the two via an "umbilical" which also carries the gas and control lines. Following consultation with Oxford Lasers, it was decided to move the high voltage modulator to a position next to the laser head, so eliminating the high inductance umbilical current path. Additionally, by using magnetic pulse compression techniques, the rising edge of the current / voltage waveforms was reduced from 105 ns to 55 ns (figure 2.9). The result of these modifications was an increase in the output power from 40 W to nearly 60 W for the same electrical input power; additionally, a reduction in the electrical RF noise radiated by the laser was observed, owing to the removal of the long umbilical connection, which acted as an aerial. The electrical noise was further reduced by solidly earthing the CVL, and the optical breadboard, to an external earthing stake; the residual electrical RF pick-up by laser diagnostic tools was suppressed by the use of coaxial connecting leads wound on saturable inductors.

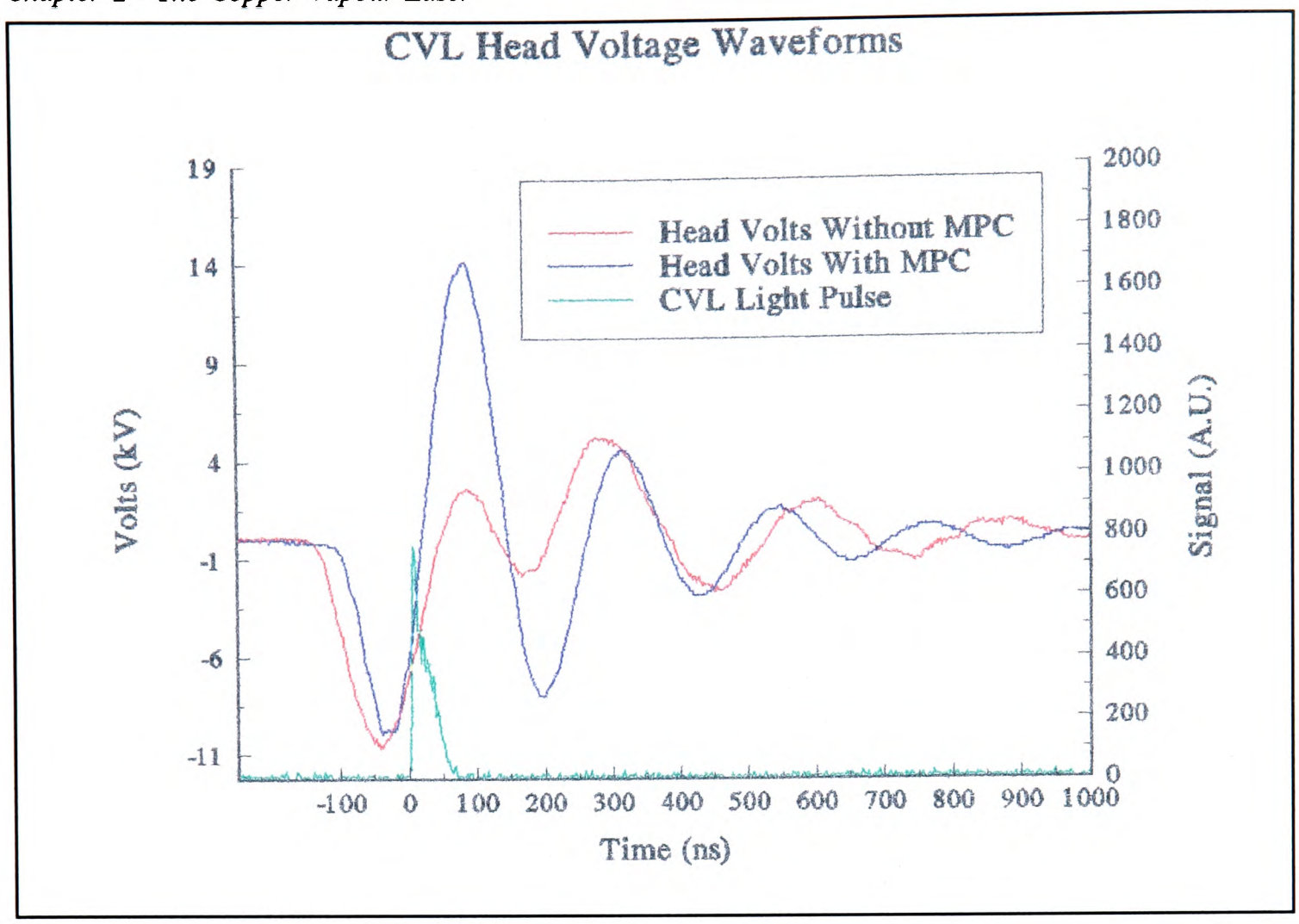


Figure 2.9 : CVL head-voltage with and without magnetic pulse compression techniques. Also shown is the CVL laser pulse.

Chapter 2 : References

2.1 B.E. Warner

Status of copper vapour laser technology at Lawrence Livermore National Laboratory

Tech. Dig. Conf. Las. & Elec. Opt. ***CFH4*** *(1991)*

2.2 G.A. Naylor

Private Communication

Oxford Lasers Ltd., Abingdon Science Park, Oxfordshire.

2.3 G.R. Fowles & W.T. Silfvast

High gain laser transition in lead vapour

Appl. Phys. Lett. ***6*** *236 (1965)*

2.4 W.T. Walter, M.Piltch, N. Solimene & G.Gould

Pulsed laser action in atomic copper vapour

Bull. Am. Phys. Soc. ***11*** *113 (1966)*

2.5 W.T. Walter, N. Solimene, M.Piltch & G.Gould

Efficient Pulsed Gas Discharge Lasers

IEEE J.Q.E. 2 474-479 (1966)

2.6 A.A. Isaev, M.A. Kazaryan & G.G. Petrash

Effective pulsed copper vapour laser with high average power generation

JETP Lett. ***16****, 27 (1972)*

2.7 A.A. Isaev & G.Yu. Lemmerman

Investigation of a copper vapour pulsed laser at elevated powers

Sov. J.Q.E. 7 799 (1977)

2.8 I. Smilanski, A. Kerman, L.A. Levin & G. Erez

Scaling of the discharge heated copper vapour laser

Opt. Commun. ***25*** *79 (1978)*

2.9 K.I. Zemskov, A.A. Isaev, M.A. Kazaryan, G.G. Petrash & S.G. Rautian

Use of unstable resonators in achieving the diffraction divergence of the radiation emitted from high-gain pulsed gas lasers

Sov. J.Q.E. ***4*** *474-477 (1974)*

2.10 T.G.M. Freegarde

Spectroscopic Applications of Pulsed Metal Vapour Lasers

D.Phil Thesis, Oxford 1989

2.11 G.A. Naylor, A.J. Kersley & R.R. Lewis

Cavity designs for metal vapour lasers

Oxford Lasers Technical Note #1, Oxford Lasers Ltd., Abingdon Science Park

Chapter 3 : Dye Lasers

3.1 Introduction.

3.2 The Photophysics and Photochemistry of Dyes.

3.3 Challenges to Dye Lasers.

3.4 Broad-Bandwidth Pulsed Dye Laser Oscillators.

3.5 Narrow-Linewidth Pulsed Dye Laser Oscillators.

3.6 Injection Locked Systems.

3.7 The Modeless Dye Laser.

References.

Chapter 3 : Dye Lasers

3.1 Introduction

Ever since the pioneering demonstration of ruby laser-pumped dye laser operation by Sorokin and Lankard in 1966 [3.1], organic dyes have been extensively used as laser media. Typical laser dyes show high optical gain over a bandwidth of several tens of nanometres and are usually used in solution; however, some recent work has been carried out in the gas phase, and even solid state hosts, are currently under investigation [3.2]. The physics and technology, both of laser dyes and dye lasers, has advanced rapidly over the past sixteen years, until today, dye lasers are capable of :-

i) Tunable continuous wave oscillation from 400 nm to 1000 nm.
ii) Stable cw single mode operation at linewidths less than 1 kHz.
iii) Tunable pulsed operation from 300 nm to 1200 nm.
iv) High conversion efficiencies : $>50\%$ for some pulsed systems.
v) High pulse energies : 800 J in a 500 ns excimer-pumped dye laser pulse has been reported.
vi) Ultrashort pulses : <30 fs.
vii) Very long pulses : several microseconds.
viii) High repetition rates : >10 kHz.
ix) High average power : >1 kW at LLNL AVLIS programme.
x) Broad bandwidths.
xi) Narrow linewidth pulsed operation including SLM operation.

but not, of course, simultaneously !

The applications of dye lasers are diverse. As tunable intense light sources, dye lasers find many applications in chemistry and medicine. Narrow bandwidth dye lasers have revolutionized spectroscopy by providing tunable high spectral intensity sources. These sources now enable the investigation of weak or nonlinear effects,

which had hitherto been impossible.

However, whilst the physics is mature in many areas of dye lasers, at the onset of the present studies, comparatively little work had been published concerning the optimization of dye laser performance at high repetition rates. (The extensive CVL-pumped dye laser research carried out at the LLNL has only recently been declassified, and is only now filtering through to scientific journals.) CVL-pumped dye lasers offer tunable sources of kilohertz repetition rate radiation, with pulse energies sufficient to saturate many atomic transitions. This unique combination yields an increased signal to noise ratio / data acquisition rate over that offered by other dye laser systems. For this very reason, high power CVL-pumped dye laser chains find applications in the Atomic Vapour Laser Isotope Separation (AVLIS) [3.3] of fissile uranium from its natural mixture by resonant multi-step ionization; the same principle is used at lower energies for the ultra-sensitive trace analysis of materials in Resonance Ionization Mass Spectrometry (RIMS) [3.4].

3.2 The Photophysics & Photochemistry of Dyes

Laser dyes are organic molecules which contain a chain of conjugated double bonds with an appropriate termination group at each end. The physics of interest here is associated with the conjugated carbon chain; this consists of a σ-bonded carbon framework with an uniform electronic charge distribution running the length of the chain, displaced above and below the plane of the molecule by approximately half an atomic spacing, due to the π-interaction. The eigenfunctions of the π-electron distribution have been successfully modelled on those of free electrons confined to an uniform potential well of similar dimensions to that of the conjugated chain [3.5], (figure 3-1). In the ground state, the first N/2 levels are filled by the N π-electrons and the first excited state corresponds to the promotion of an electron from the highest occupied level to the lowest unoccupied level. The energy of the transition is proportional to the dimensions of the potential well and consequently to the length of the conjugated chain. The highest excitation energies correspond to wavelengths around 200 nm which arise from the shortest bonds; in this regime, the photon

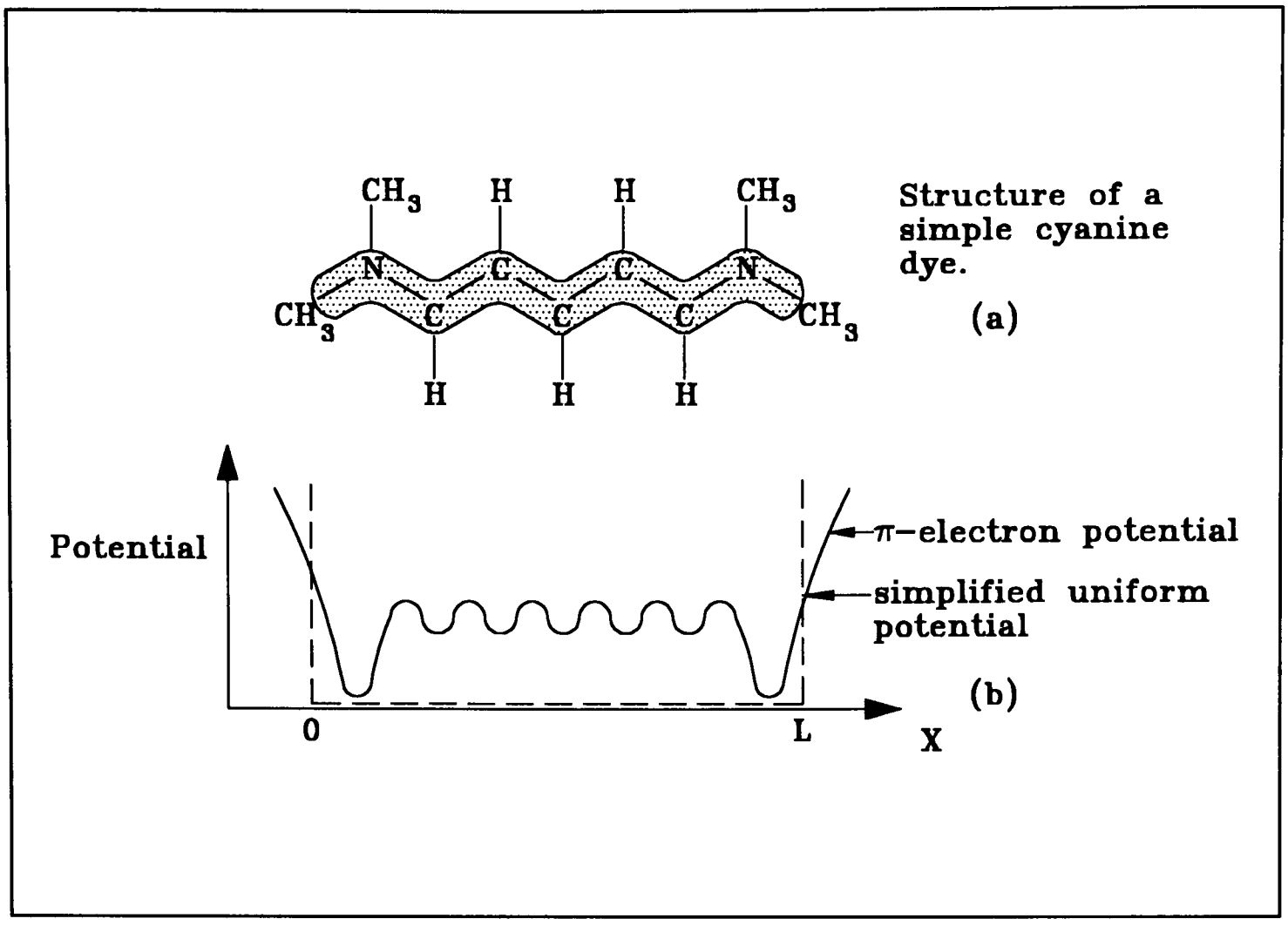


Figure 3.1 : The structure of a simple cyanine dye. The π-electronic potential arising from the conjugated chain may be approximated by a square well to model the electronic transitions.

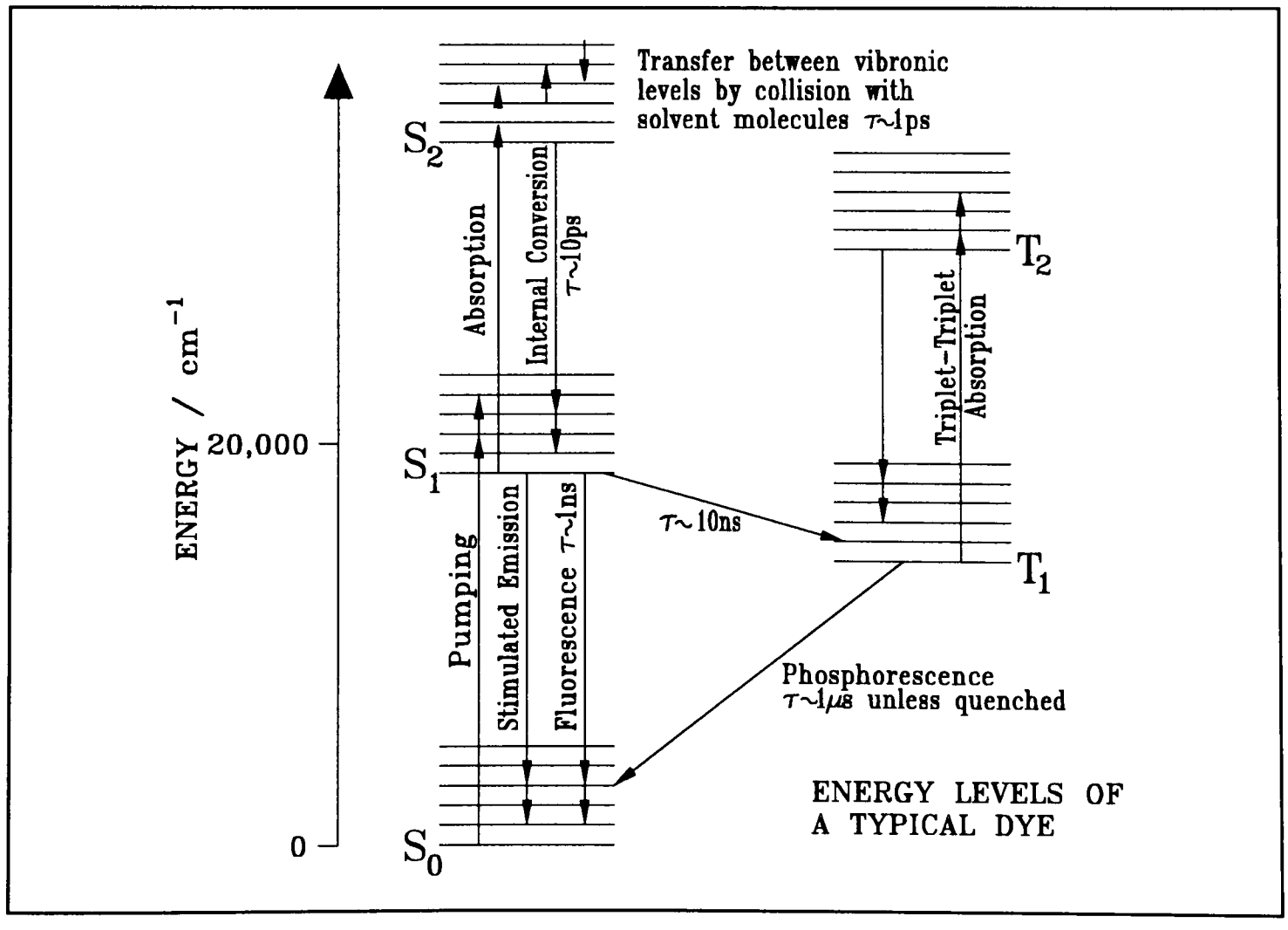


Figure 3.2 : The energy levels of a typical laser dye and the associated kinetic processes relevant to dye laser operation.

energy is comparable to the binding energy of the molecule and photochemical decomposition is an alternative to radiative decay. This limits practical laser dyes to operation above 250 nm.

Associated with each electronic level is a fine ladder of vibrational levels, to which are coupled even more densely spaced rotational sub-levels, and give rise to a quasi-continuum of states, as depicted in figure 3.2. Furthermore, the dye suffers collisional and electrostatic perturbations due to the solvent molecules on picosecond time scales; this results in the closely spaced framework of energy levels being washed out into a continuum, and gives rise to the continuous tunability of laser dyes.

With each excited singlet state, there is an associated triplet state of slightly lower energy; these triplet states have two unpaired electrons of the same spin and thus have a highly reactive, chemical biradical character. Optical electric-dipole transitions are highly forbidden between singlet and triplet states, owing to the associated change of electron spin. Consequently, the lowest triplet level is metastable with respect to the ground singlet state, and so most of the population which reaches the triplet states will decay non-radiatively through chemical decomposition. Thus, the population of these chemically reactive triplet levels can be seen to directly influence the stability and lifetime of a dye solution. Also related to triplet state decomposition is the long wavelength absorption limit - long wavelength dyes have a low-lying singlet level and thus, an even lower-lying triplet level which may be thermally populated at room temperature. Chemical kinetics calculations show that for a dye shelf life of a few months, the long wavelength limit is around 1 μm, and so practical dye laser operation is limited between 250 nm and 1 μm. The lifetime of a dye is also influenced by the means of excitation : UV sources, such as excimer pump lasers, can induce photodissociation of the dye molecules, whilst long-pulse pump sources, such as flashlamps or cw lasers, cause a build up of triplet state population (inter-system crossing time $\sim$ 10 ns), and so chemical decomposition results. The CVL pump pulse, typically 40 ns, is short compared with typical inter-system crossing times and so dye degradation through population building up in the triplet states is negligible. Additionally, due to the absence of UV radiation from the CVL pump, active dye lifetimes are significantly

longer than those associated with many other forms of pump laser.

Within each band, solvent-collision-induced thermalization to a Boltzmann distribution occurs within a few picoseconds. This results in a homogeneously broadened fluorescence band, being the mirror image of the absorption band as reflected about the energy of the purely electronic transition. The basic dynamics of laser action involve population from the lower thermally populated states of the ground level being optically excited to vibrational/rotational states of the first excited singlet S_1. These excited states then quickly thermalize giving a population inversion with respect to all but the thermally populated states of the ground level S_0. Thus, a homogeneously broadened gain will be apparent over a range of wavelengths corresponding to different lower laser levels throughout the band S_0 - typically, a range of some 30-40 nm is covered by a single dye. A more detailed account of the dye laser kinetics, including the effects of higher excited states, is included in the rate equation analysis of chapter 4.

3.3 Challenges to Dye Lasers

With the advent of solid state crystals such as Ti:Al_2O_3, Cr:LiSAF (Cr^{3+}:$LiSrAlF_6$) and Cr:LiCAF (Cr^{3+}:$LiCaAlF_6$) providing tunable laser action in the near infra-red region of the spectrum, several of the disadvantages of dye lasers which have hitherto been tolerated are now questioned. The main problems associated with laser dyes are :-

1. Finite lifetime through photodegradation.

This is particularly acute with excimer and frequency-tripled Nd:YAG laser pumps, where the high photon energy UV laser radiation causes some photodissociation of the dye molecules. Also, for cw and long pulse length pump lasers, the triplet population can become appreciable and without the use of appropriate quenching agents non-radiative chemical decomposition results. However, recent developments at the molecular level have come some way in solving these problems by providing new, more stable, more efficient, and more soluble dyes [3.6].

2. Chemical hazards.

The majority of laser dyes are highly toxic and/or carcinogenic and/or mutagenic, and so great care must be taken in their preparation, use and storage. Additionally, the dye solvents are frequently toxic and sometimes highly flammable.

The aforementioned solid state alternatives offer chemical inertness, no photodegradation and a larger gain bandwidth - some 400 nm in the case of $Ti:Al_2O_3$. However, currently available solid state laser crystals are only capable of lasing beyond 650 nm, and whilst they provide a valuable source for the near infra-red, the important region of the spectrum between 500 and 650 nm is unattainable without the use of inefficient and exotic nonlinear schemes. Additionally, solid state host materials are prone to permanent optical damage which, unlike the liquid host for laser dyes is not "self healing". Consideration should also be given to the expense of the lasing medium, currently laser dyes cost a minute fraction of the cost of solid state laser crystals.

With the low pulse energy and long duty cycle of a CVL pump source, the stored energy and gain in solid state materials is small (typically, α, the single pass gain is of order 1) and so low loss cavity designs are necessary for oscillation. This poses problems for narrow-bandwidth operation where lossy dispersive elements must be employed, and so careful cavity design is necessary. Even where successful narrow-bandwidth CVL pumped solid state lasers have been realized [3.7], an inescapable consequence of the low gain is the long, and sometimes erratic build-up time which pose synchronization problems for many applications Thus, at this time, tunable solid state lasers should be considered as a complement to dye lasers, but not as an alternative for the immediate future.

3.4 Broad-Bandwidth Pulsed Dye Laser Oscillators

The early dye lasers were essentially little more than a dye solution enclosed by a pair of mirrors. The corresponding bandwidth was typically a few nanometres,

with crude tuning achieved by changing the dye concentration and mirror reflectivities. The first reported work with a CVL pumped dye laser [3.8] revolved around a broadband design utilizing Brewster angled prisms as the dispersive element, as shown in figure 3.3b. Tuning was achieved by rotating the rear cavity mirror and despite offering a modest 2 nm bandwidth, the efficiency of the oscillator was an impressive 57% at the peak of Rhodamine 6G. It is also possible to use the dispersion of a diffraction grating to provide a narrow-bandwidth tunable output. By replacing one of the mirrors of a plane-plane cavity with a diffraction grating sub-nanometre bandwidths may be realized, but at the expense of the conversion efficiency, which is reduced to $\sim 15\%$.

Bandwidth measurements of several laboratory built CVL-pumped dye oscillator designs supporting these reports are presented in figure 3.3. Here a 1 m computer controlled monochrometer, with a dynamic range greater than 2×10^5, and with an instrumental resolution better than 5 GHz, was used to measure the laser spectral features. Generally, the uses for such a coloured light source are rather limited, although broadband dye lasers do find applications in medicine and biology, where molecular spectral features of interest are usually wide.

3.5 Narrow Linewidth Pulsed Dye Laser Oscillators

In a pulsed dye laser oscillator incorporating dispersive elements, the single pass linewidth is given, to a first approximation, by :-

$$\Delta\lambda \approx \Delta\theta\left(\frac{\partial\theta}{\partial\lambda}\right)_c^{-1} \qquad (1)$$

where $(\delta\theta/\delta\lambda)_c$ is the total dispersion provided by the optical components of the cavity, and $\Delta\theta$ is the beam divergence. Thus, to minimise the bandwidth, the beam divergence must be reduced and/or the dispersion of the cavity increased. For a

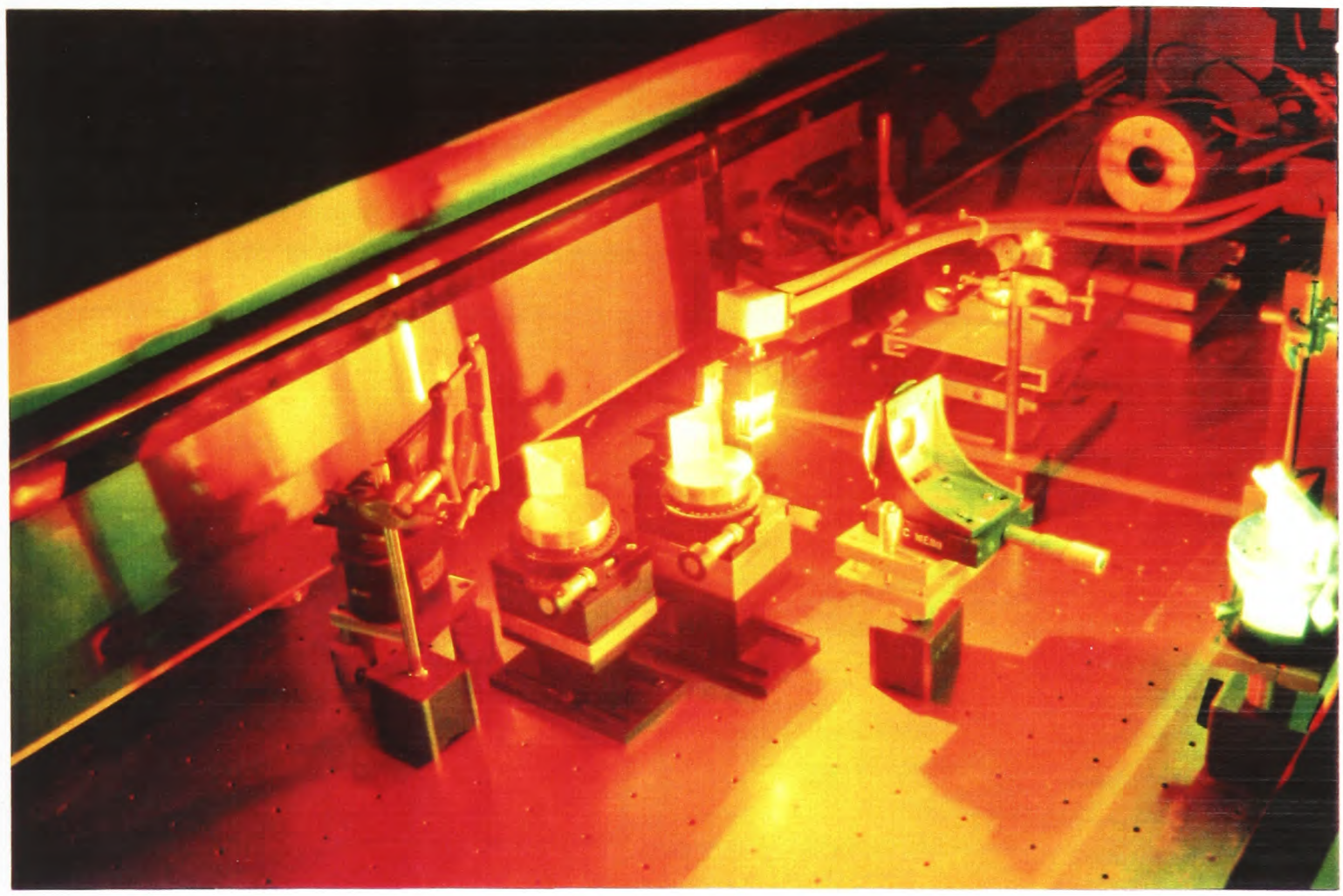


Plate 3.1 : A CVL-pumped dye oscillator used for the bandwidth studies presented in this chapter. The oscillator contains two Brewster-angled prisms and the corresponding frequency bandwidth is ~2nm.

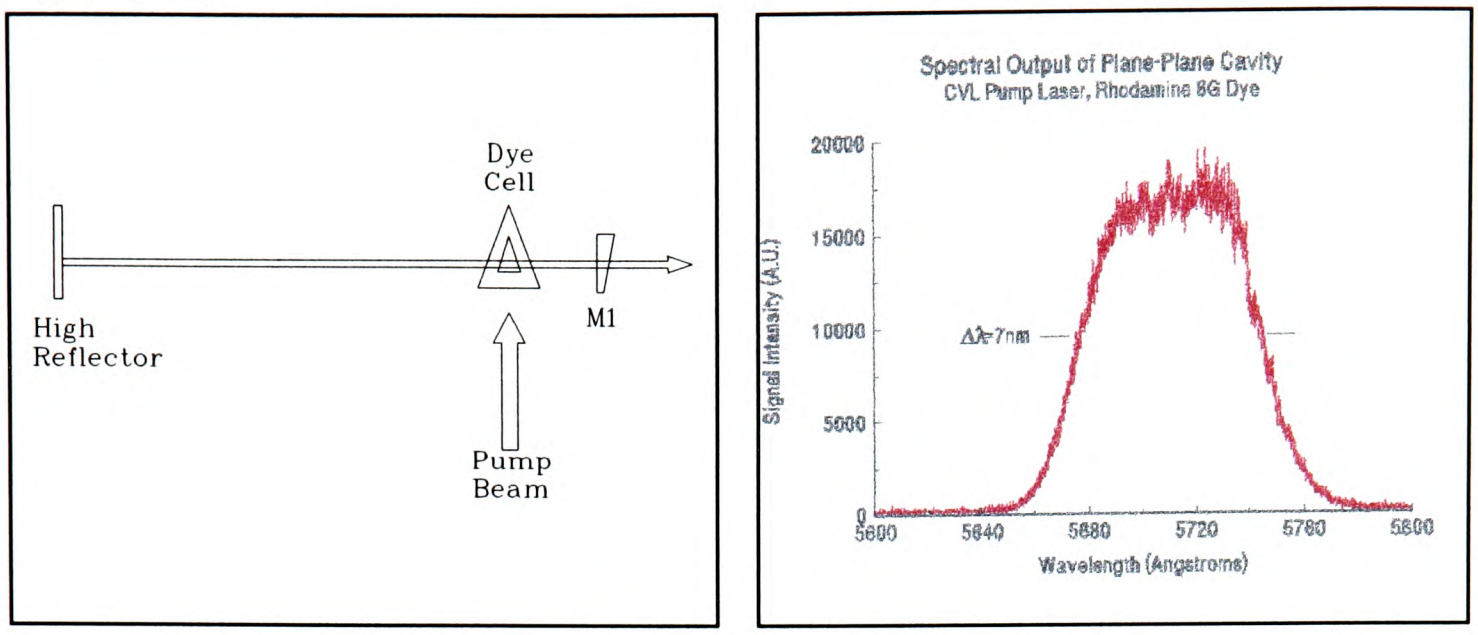


Figure 3.3a : Spectral output of a CVL pumped plane-plane cavity. No frequency selective elements are present and the cavity lases broadband at the peak of the Rhodamine 6G fluorescence band.

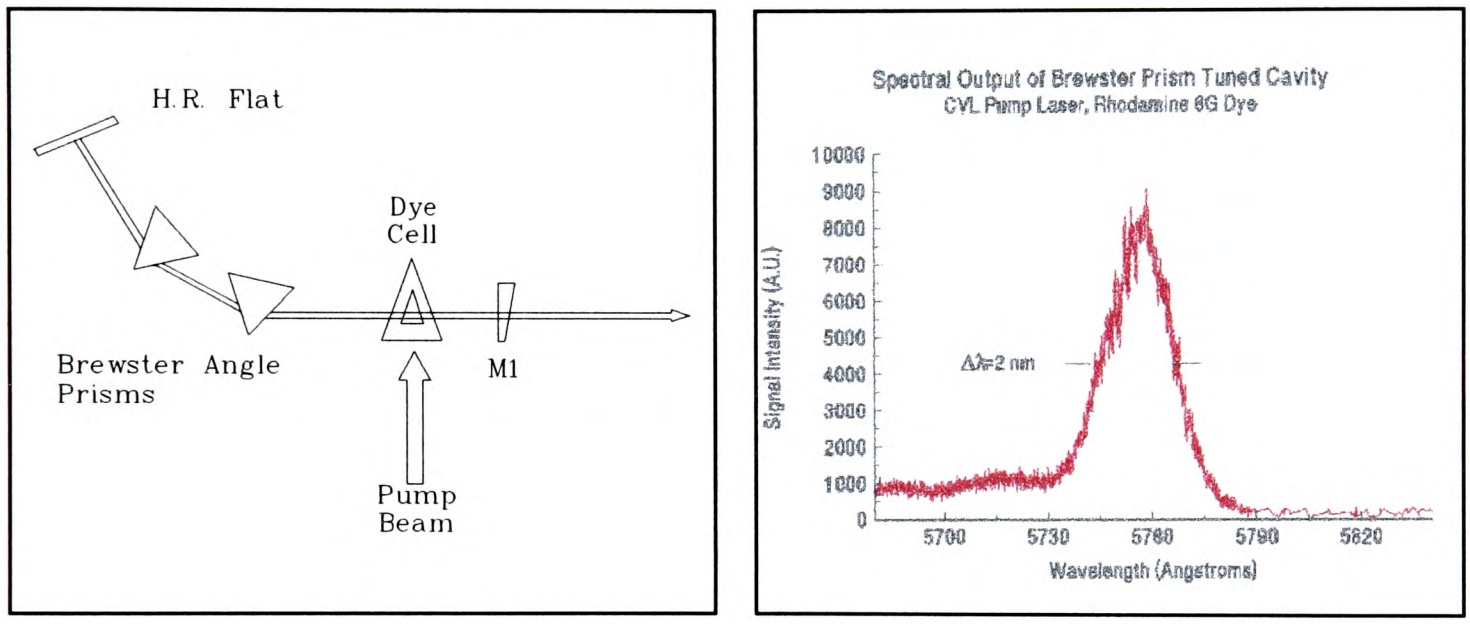


Figure 3.3b : Spectral output of a CVL pumped cavity incorporating two dispersive Brewster-angled prisms. Tuning of the wavelength is achieved by rotating the rear cavity mirror about the horizontal.

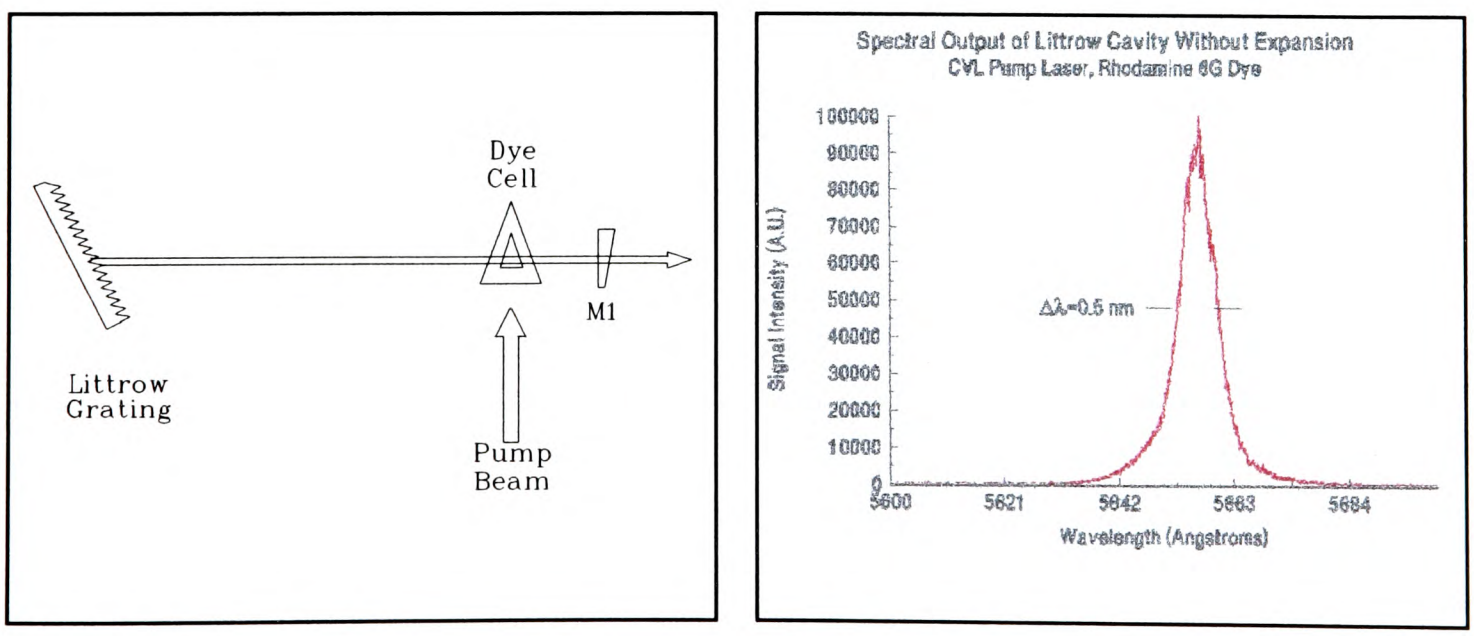


Figure 3.3c : Spectral output of a CVL pumped Littrow grating dye oscillator - tuning of the output wavelength is achieved by rotating the grating.

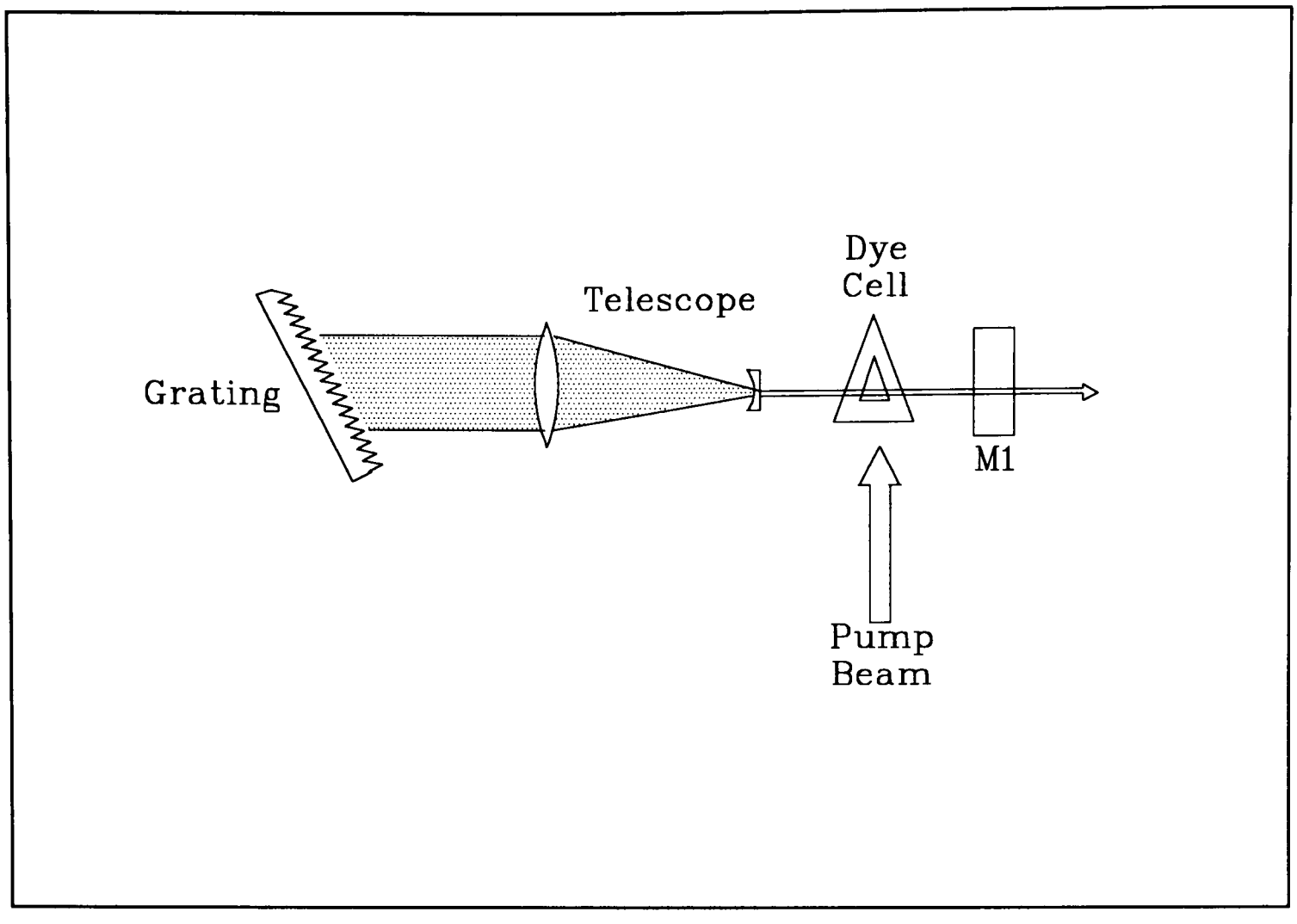


Figure 3.4 : Hänsch type Littrow grating dye oscillator incorporating an intra-cavity telescope to provide narrow linewidth operation.

Littrow grating-mirror cavity, the dispersion can be shown to be :-

$$\left(\frac{\partial\theta}{\partial\lambda}\right)_G = \frac{\tan\theta}{\lambda} \qquad (2)$$

Hänsch [3.9], realized in 1972, that the Littrow grating cavity bandwidth could be reduced by employing an intra-cavity telescopic beam expander, as shown in figure 3.4. The telescope serves to illuminate a greater fraction of the grating and to decrease the beam divergence by the telescope magnification factor. For such a system, the linewidth equation is modified to :-

$$\Delta\lambda = \Delta\theta\left(M\frac{\partial\theta}{\partial\lambda}\right)^{-1}_G \qquad (3)$$

where M is the magnification factor. The Hänsch telescopic device produced linewidths of about 2.5 GHz, but had a range of associated problems: the high magnification factors needed for narrow-linewidth operation require long cavities,

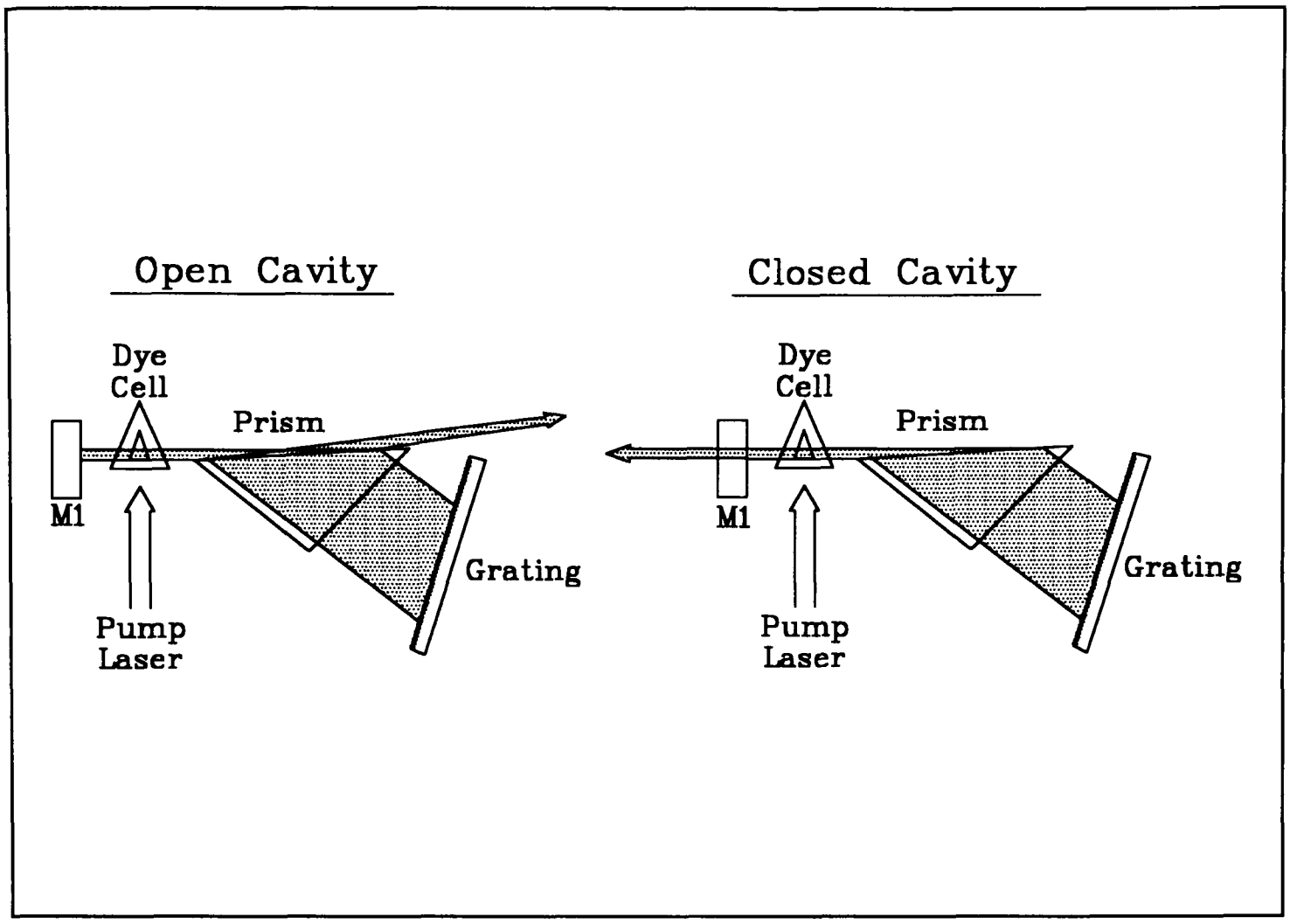


Figure 3.5 : Open and closed cavity designs of a Littrow cavity incorporating prismatic expansion of laser beam before the grating.

and consequently lead to a large amount of dead space; additionally, the telescope lenses must be used slightly off-axis to prevent the oscillation of parasitic modes, and so the output beam possesses a certain amount of astigmatism.

An alternative to Hänsch's telescope is to use a prism as a compact one dimensional beam expander. The grazing incidence reflection from such a prism beam expander allows the laser to be operated in either of an open-cavity or closed-cavity mode as shown in figure 3.5. Characteristic of the open-cavity design is a good extraction efficiency but, is unfortunately accompanied by a large component of amplified spontaneous emission (ASE), appearing as a broad background of noise in the spectral profile. The converse is true of the closed-cavity design where good spectral purity is obtained at the expense of high efficiency. This dichotomy is due to the high Fresnel losses associated with the high angles of incidence at the prism faces necessary for narrow linewidth operation. For a single prism, the reflection losses for the p-component of polarization presented by the prism surface is given by

:-

$$l_p = \frac{\tan^2(\phi_1 - \psi_1)}{\tan^2(\phi_1 + \psi_1)} \tag{4}$$

where ϕ_1 is the angle of incidence and ψ_1 is the angle of refraction. The beam expansion coefficient, for a right angled prism designed for orthogonal beam exit, can be written as

$$M = \frac{\cos\psi_1}{\cos\phi_1} = \left[\frac{(n^2 - \sin^2\phi_1)}{(n^2 - n^2\sin^2\phi_1)}\right]^{1/2} \tag{5}$$

These two equations clearly illustrate the conflict of interest between large beam expansion and the requirement for low reflection losses. In an effort to avoid this problem, Shoshan [3.10] realized that by tilting the grating into a grazing-incidence

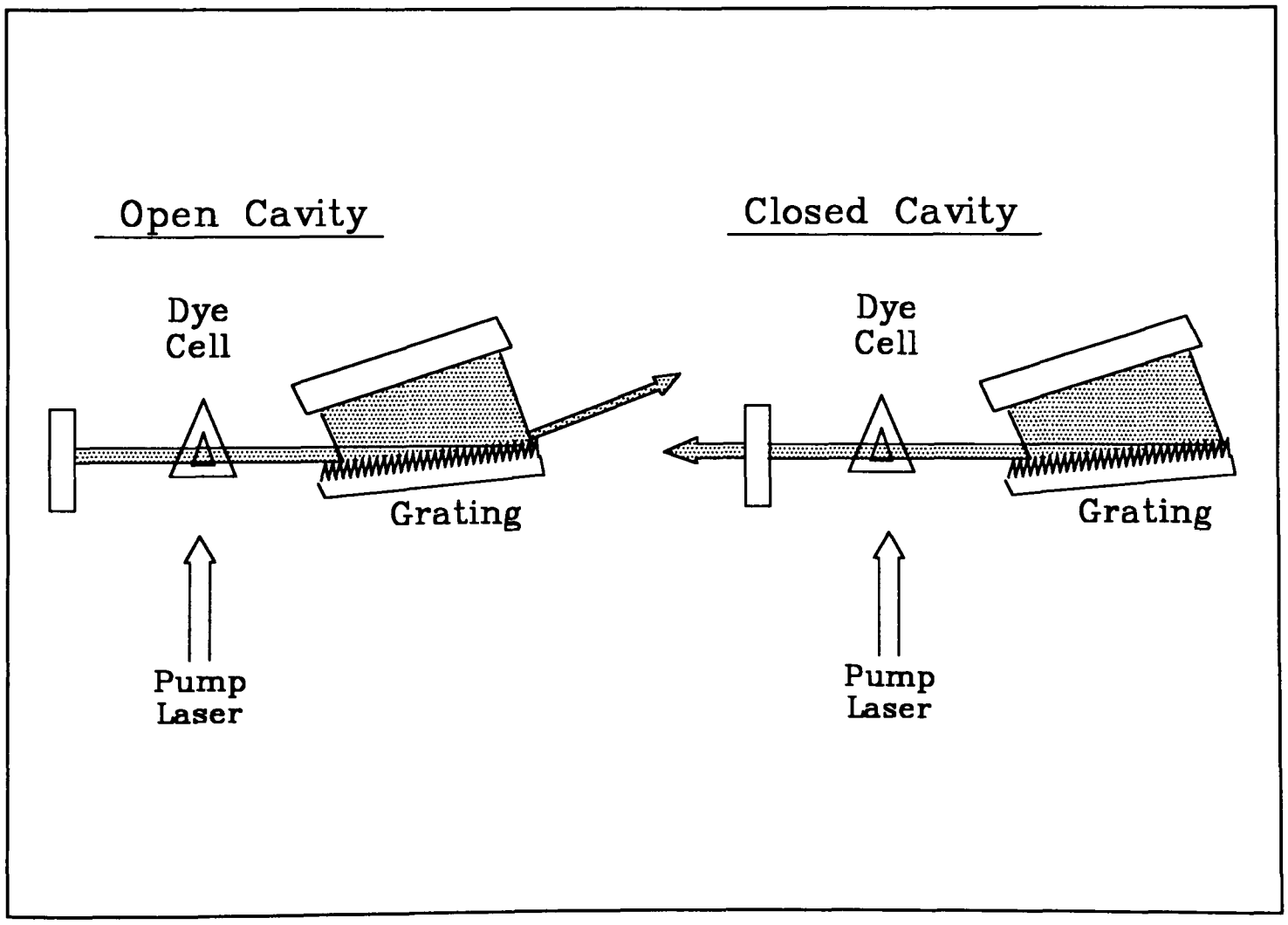


Figure 3.6 : Open- and closed-cavity designs for grazing incidence dye oscillators, here the beam expansion and dispersion is provided by the same optical element.

orientation, the dispersion and beam expansion could be provided by the same optical element (figure 3.6). Unfortunately, the efficiency of the grating tends to deteriorate rapidly at the high angles of incidence required for narrow-linewidth operation, and the same dilemma associated with the use of open- and closed-cavity designs, with respect to efficiency and ASE, is also true of grazing incidence dye lasers.

Littman [3.11] capitalized upon Shoshan's design by shortening the cavity, thereby increasing the longitudinal mode separation, and increasing the number of cavity round trips to give sub-gigahertz bandwidths and single longitudinal mode operation. The tuning of such a grazing-incidence oscillator cavity is particularly simple; there are only two frequency selective parameters : the grating, and the cavity length. By careful positioning of the grating pivot point, it is possible to provide tunable SLM operation without mode hopping.

The efficiency and ASE problems of single prism Littrow and grazing incidence cavities can be substantially overcome with designs incorporating multiple stages of prism expansion. For a closed-cavity multiple-prism-Littrow (MPL) cavity Duarte and Piper [3.12] have achieved a conversion efficiency of nearly 14% with a reduction in the ASE of more than two orders of magnitude as compared to a single prism open-cavity design of similar efficiency. In this case, the single pass Fresnel prism losses were 90% in the single prism case and only 70% in the MPL device. Similarly a hybrid multiple-prism grazing incidence (HMPGI) cavity design offers efficiency and ASE advantages over the pure grazing incidence alternative. Here, the prismatic beam expansion before the grating allows more efficient operation at grating angles of $\approx 85^{\circ}$ yielding efficiencies close to 10%, as compared to 2% typical of a pure grazing incidence design.

Advantages of multiple prism beam magnification over telescopic expansion include compactness, ease of alignment, and the availability of a polarized output beam. The main disadvantage of prism beam expansion is the introduction of an additional chromatic component into the cavity, and now the dispersion is no longer dependent solely upon the grating. It is possible [3.13], however, that by appropriate choice prism refractive indices, in each prism pair, a near achromatic beam expansion

may be produced. In practice, however, this is of little consequence since the tuning of the cavity is often performed electronically, and wavelength calibration may be built into the control software.

A further avenue to linewidth narrowing is provided by the introduction of intra-cavity etalons. The choice of plate separation and reflectivity are determined by two key etalon parameters : the free spectral range (FSR) and the finesse ($\mathscr{F}$) :-

$$FSR = \frac{1}{2nd_{cm}}(cm^{-1}) = \frac{c}{2nd_{m}}(Hz) \qquad (6)$$

$$\mathscr{F} = \frac{\pi\sqrt{R}}{(1-R)} \qquad (7)$$

where n is the refractive index, d is the plate separation and R is the reflectivity of the etalon plates. In dye lasers, intra-cavity etalons are usually used to provide increased linewidth-narrowing beyond that offered by other intra-cavity dispersive elements. The FSR of the etalon is chosen in relation to the dispersive bandwidth of the cavity : a commonly used approach is to choose the FSR to be at least twice the dispersive linewidth, this condition then ensures that only one etalon mode will oscillate at any one time. The finesse, and hence the reflectivity, of the etalon is then determined by the ultimate desired bandwidth according to the relation : linewidth $\Delta\nu \approx [(\text{FSR})/\mathscr{F}]$.

It should be noted, however, that the fundamental bandwidth limit of any pulsed dye laser cavity is limited by the Fourier transform of the laser pulse length. Frequently, even for single longitudinal mode dye lasers, the time-averaged bandwidth often falls short of the fundamental limit due to thermal instabilities and fluctuations in the dye which occur on millisecond time scales. At Kilohertz repetition rates in particular, SLM performance is not trivial due to the requirement of maintaining a homogeneous dye flow on the one hand, and achieving a clearing ratio of the pumped volume greater than unity on the other. Berry *et al.* [3.14] have demonstrated SLM operation at 1 kHz with a longitudinally-pumped Littman

oscillator, but dye fluctuations in the 2×2 mm dye cell caused the output to go multi-mode at higher repetition rates. Again, the spectral characteristics, recorded by a 1m monochrometer, of several of the CVL-pumped dye oscillator cavities considered in this section have been measured, and are presented in figure 3-7.

3.6 Injection Locked Systems

To avoid dye laser frequency jitter, two approaches may be adopted, either the dye laser cavity length may be actively stabilized by locking the output to an external frequency standard or, a design incorporating injection locking in conjunction with cavity stabilization may be employed. Injection locking improves the performance of a dye laser by controlling the initial excitation of individual modes by providing an initial seed signal well above the spontaneous emission noise level in one or a small set of desired modes. The efficiency of a locked oscillator is generally higher than if the same laser medium were used as a linear amplifier for the same injected source. Additionally, injection seeding has the advantage that not only does the oscillator output possess the same frequency format as the injected signal but also, the polarization and beam divergence of the oscillator are determined by the seed.

CVL-pumped dye laser oscillators using Rhodamine 640 Perchloride dyes have been successfully locked to Helium-Neon lasers (both 612 nm & 633 nm lines) [3.15] for use in laser projection video systems. Here, the frequency format, & polarization are critical for the acousto-optic deflectors and a low divergence beam is required for projection over the large distances from projector to screen.

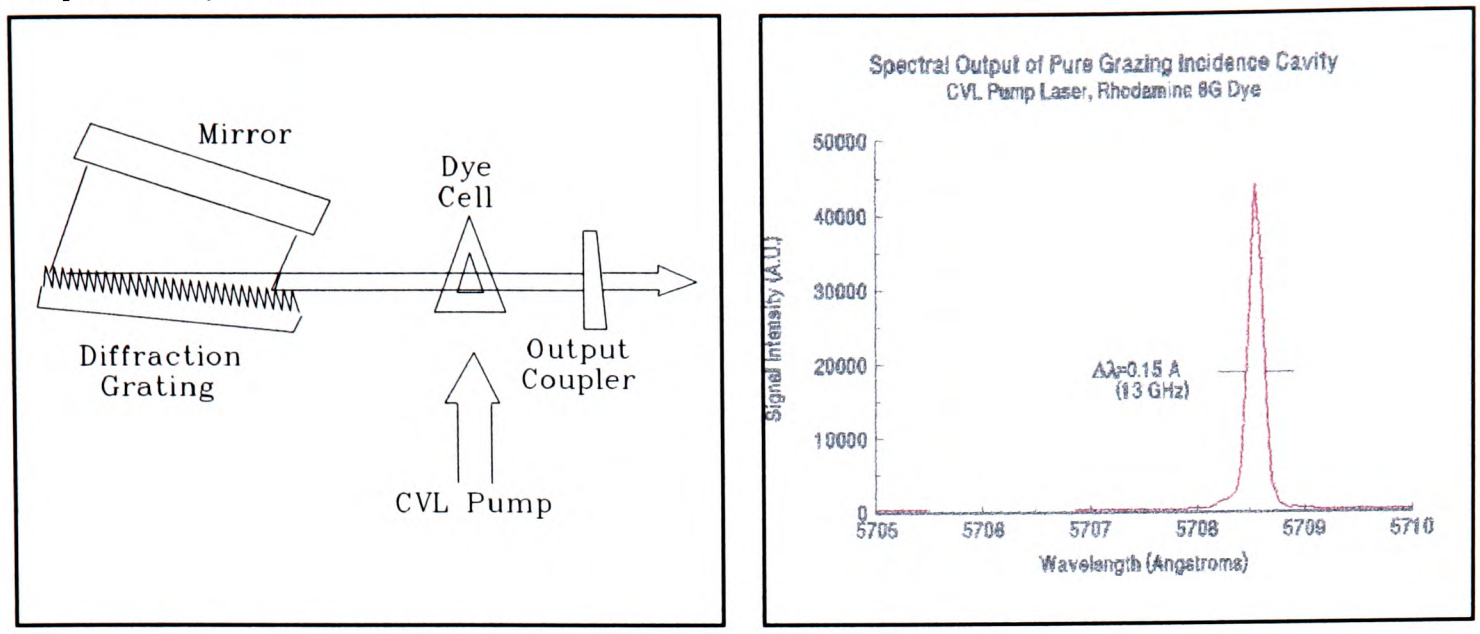


Figure 3.7a : Spectral Output of a CVL pumped grazing incidence dye laser - tuning of the cavity is achieved by rotating the feedback mirror relative to the fixed grating.

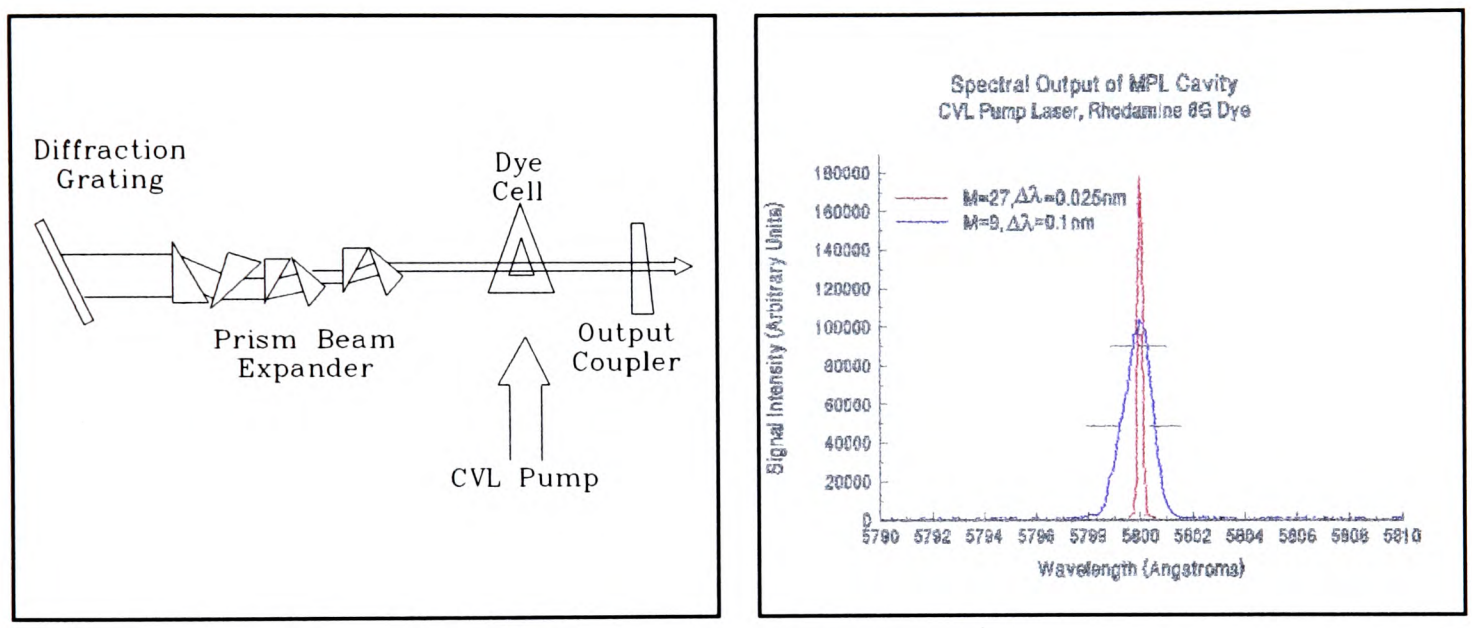


Figure 3.7b : Spectral output of a CVL pumped MPL cavity for intra-cavity prismatic expansions of 9 and 27, achieved by 2 and 3 prism pairs respectively.

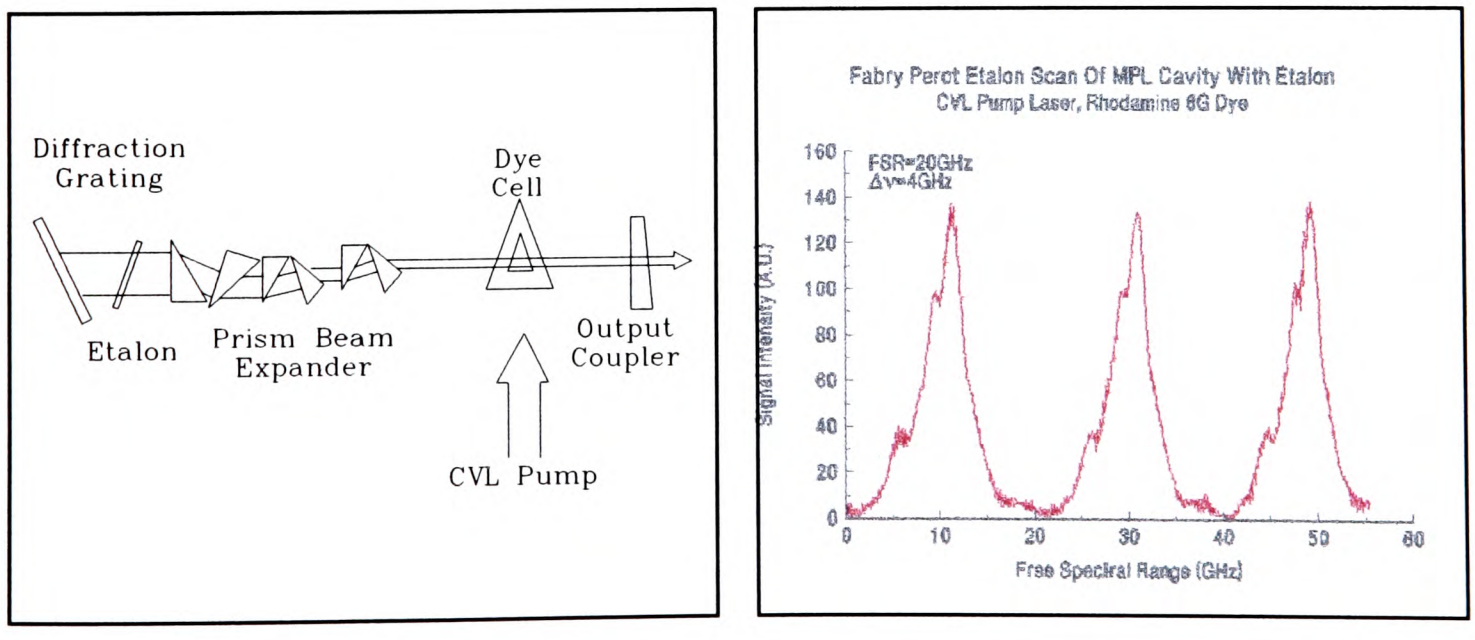


Figure 3.7c : Spectral output of a MPL cavity with a prism beam expansion ratio of 27 and an intra-cavity etalon (FSR=20 GHz) which limits oscillation to one etalon mode, $\Delta\nu$ is then finesse limited.

3.7 The Modeless Dye Laser

A novel design of single longitudinal mode dye laser has been developed by Ewart and Meacher [3.16]. Unlike the SLM Littman cavity where the grating pivot must be positioned with $\lambda/2$ accuracy, the Ewart design is both elegant and relatively easy to manufacture.

A small fraction of the pump beam is split off and used to pump a short cavity laser (SCL) formed by a pair of mirrors, M1, M2, separated by a distance, d=1-2 mm. Here, due to the short cavity length, well defined cavity modes, widely separated in frequency ($\Delta\nu$=c/2d), are generated even from short pump excitation pulses. The output of the SCL is directed toward a modeless narrow band amplifier (NBA) [3.17] as shown in figure 3.8. SLM operation is achieved by adjusting the bandwidth of the NBA so as to amplify only one of the modes arising from the SCL.

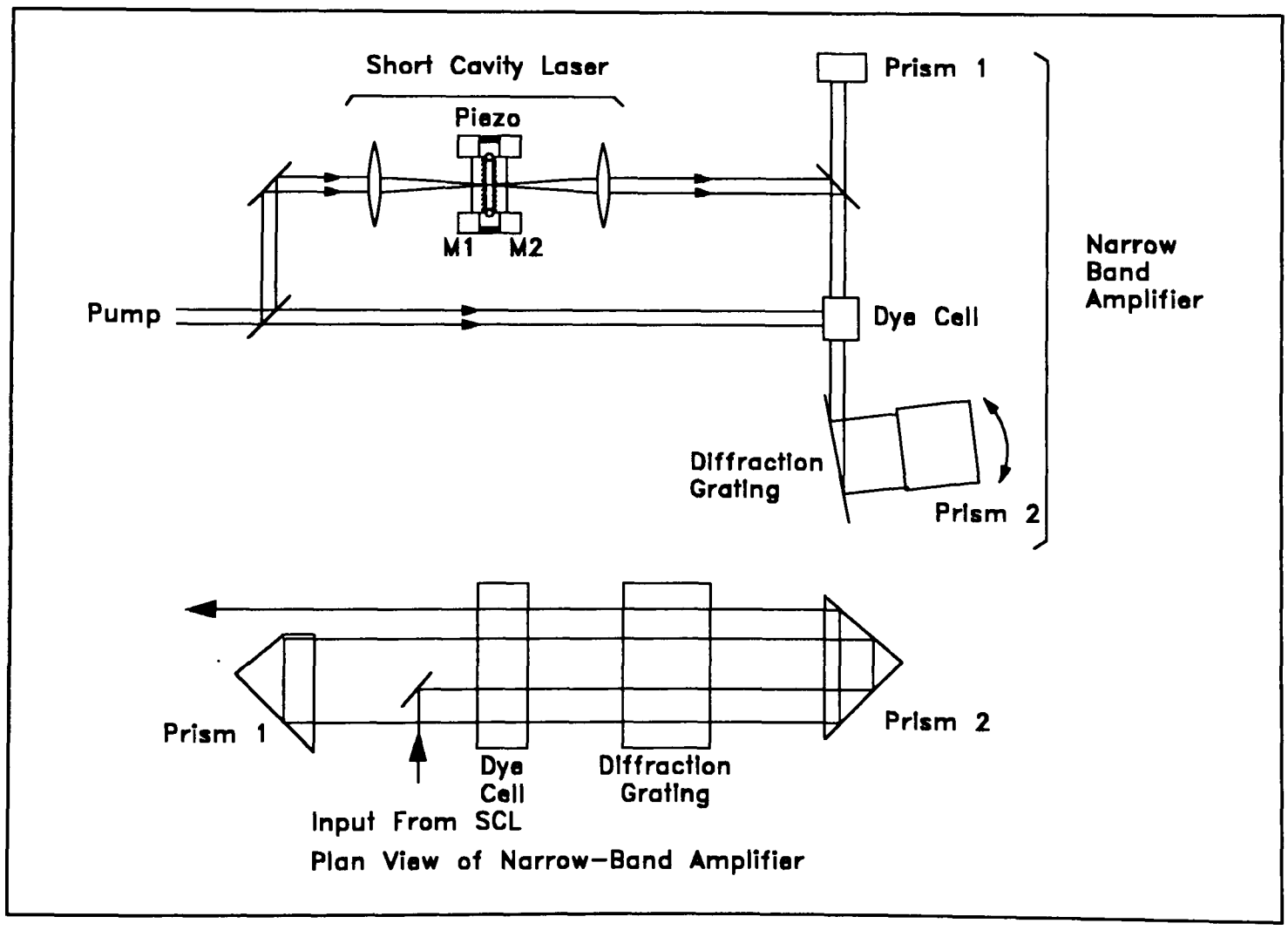


Figure 3.8 : Ewart Laser - One of the widely spaced modes from the short cavity laser (SCL) is amplified by the modeless narrow band amplifier (NBA).

Tuning of the laser is performed by synchronously adjusting the SCL cavity length and rotating the NBA tuning prism M2 to prevent mode-hopping of the SLM output.

With a 10 Hz frequency-doubled Nd:YAG pump, tunable SLM output has been achieved with (transducer limited) tuning over 1 THz without mode-hopping. The time-averaged bandwidth of 250 MHz was limited by dye turbulence in the SCL. Best frequency stability of the output was achieved using a static dye solution, where the solvent (ethylene glycol and water) was chosen to provide a high thermal conductivity. Whilst suitable for 10 Hz pumping, a static dye solution is wholly unsuitable for 10 kHz CVL-pumping. The high average power and comparatively high duty cycle of the CVL cause thermally induced refractive index gradients in the dye and necessitates a flowing dye solution (as is discussed in chapter 5). Thus considerable design modifications would be necessary for high repetition rate operation of the Ewart laser, such as the use of a pneumatically isolated dye flow pump, and temperature stabilizing the dye solution.

Chapter 3 : References

3.1 P.P. Sorokin & J.R. Lankard

Stimulated emission observed from an organic dye, chloro-aluminium pthalocyanine

IBM J. Res. Develop. ***10*** *162-163 (1966)*

3.2 W.E. Davenport & J.J. Ehrlich, U.S. Army

Characterization of dye impregnated solid host materials applicable to flashlamp pumped dye lasers

Proc. Intnl. Conf. on Lasers 1991 ***THI-6***

3.3 R.S. Hargrove & T. Kan

Laser Isotope Separation Program

LLNL Laser Prog. Annual Rep. 1976 8.48-8.42

3.4 N. Trautmann et al.

Trace detection of Plutonium by three-step photoionization with a laser system pumped by a copper vapour laser

App. Phys. ***B 38*** *249-253 (1985)*

3.5 H. Kuhn

Progress in the chemistry of organic natural products

Springer Verlag ***16*** *17- (1959)*

3.6 C.H. Chen et al.

Lasing characteristics of new coumarin analog dyes : broadband and narrow linewidth performance

Appl. Opt. ***27*** *443-445 (1988)*

3.7 M.R.H. Knowles & C.E. Webb

Efficient high-power copper-vapor-laser-pumped Ti:Al_2O_3 laser.

Opt. Lett. ***18*** *607-609 (1993)*

3.8 W.M. Morey

Copper vapour laser pumped dye laser

Proc. Intnl. Conf. on Lasers 1979 365-372

3.9 T.W. Hänch

Repetitively pulsed tunable dye laser for high resolution spectroscopy

Appl. Opt. ***11*** *895-898*

3.10 I. Shoshan, M.M. Damon & U.P. Oppenheim

Narrowband operation of a pulsed dye laser without intra-cavity beam expansion

J. Appl. Phys. ***48*** *4495-4497*

3.11 M.G. Littman

Single mode pulsed dye laser

Appl. Opt. ***23*** *4465-4468*

3.12 F.J. Duarte & J.A. Piper

A double prism beam expander for pulsed dye lasers

Opt. Comm. ***35*** *100-104*

3.13 F.J. Duarte

Note on achromatic multiple-prism beam expanders

Opt. Comm. ***53*** *259-262*

3.14 A.J. Berry, I.T. McKinne & T.A. King

Narrow linewidth operation of a pulsed grazing-incidence dye laser

J. Mod. Opt. ***37*** *463-471 (1990)*

3.15 I.J. Evans

CVL pumped injection locked oscillators for laser projection TV

Report to COLOR 1992

3.16 P. Ewart & D.R. Meacher

A novel, widely tunable, single mode pulsed dye laser.

Opt. Comm. ***71*** *197-201 (1989)*

3.17 P. Ewart

A modeless, variable bandwidth, tunable laser.

Opt. Comm. ***55*** *124-126 (1985)*

Chapter 4
Optical Amplification in Dye Lasers

4.1 Introduction.

4.2 Theory of CVL-Pumped Dye Lasers.

4.3 Physical Interpretation.

4.4 Computation and Results.

4.4.1 Longitudinally Pumped Amplifier.

4.4.2 Transversely Pumped Amplifier.

4.5 Comparison With Experiment.

4.6 Results.

4.7 Practical Details and Conclusion.

Appendix 4.1.

References.

Chapter 4 : Optical Amplification in Dye Lasers

4.1 Introduction

Many of the narrow-bandwidth pulsed dye laser oscillators described in the previous chapter are unsuitable for scaling to high power. At high pump powers the increased gain enables off-axis parasitic modes to oscillate. Such modes result from stray or grazing incidence reflections off intra-cavity components, such as dye cell windows. These off-axis modes increase the bandwidth of the oscillator, owing to the increased range of angles presented to the intra-cavity dispersive elements. The only efficient route to a narrow-bandwidth high power dye laser is via Master Oscillator Power Amplifier (MOPA) configuration. In this configuration, a low power, relatively inefficient oscillator is used to generate the desired tunable (narrow-bandwidth) light, whose power is then increased by means of a high efficiency amplifier.

Two generic amplifier configurations exist for coherently pumped dyes: the longitudinally pumped amplifier (LPA) geometry and the transversely pumped amplifier (TPA) geometry, shown in figures 4.1 and 4.2 respectively. The gain characteristics of these devices are best evaluated from a rate equation analysis of the system dynamics. At the onset of the work described in this thesis, the most comprehensive theoretical account of CVL pumped dye lasers, based on such an analysis, was that of Hargrove and Kan [4.1]. Their treatment followed that of Teschke *et al.* [4.2], originally developed for cw or long pulsed dye lasers, but, significantly, does not take into account the effect of excited state absorption (ESA) at the dye laser wavelength.

The effect of ESA in coherently pumped dye amplifiers has recently been considered by a number of authors [4.3, 4.4, 4.5]. Unlike the model proposed by Hargrove and Kan, which predicts saturation of the amplifier extraction efficiency with increasing input dye laser seed power, the effect of ESA and ground state absorption (GSA) at the dye laser wavelength is to give rise to an optimum in the

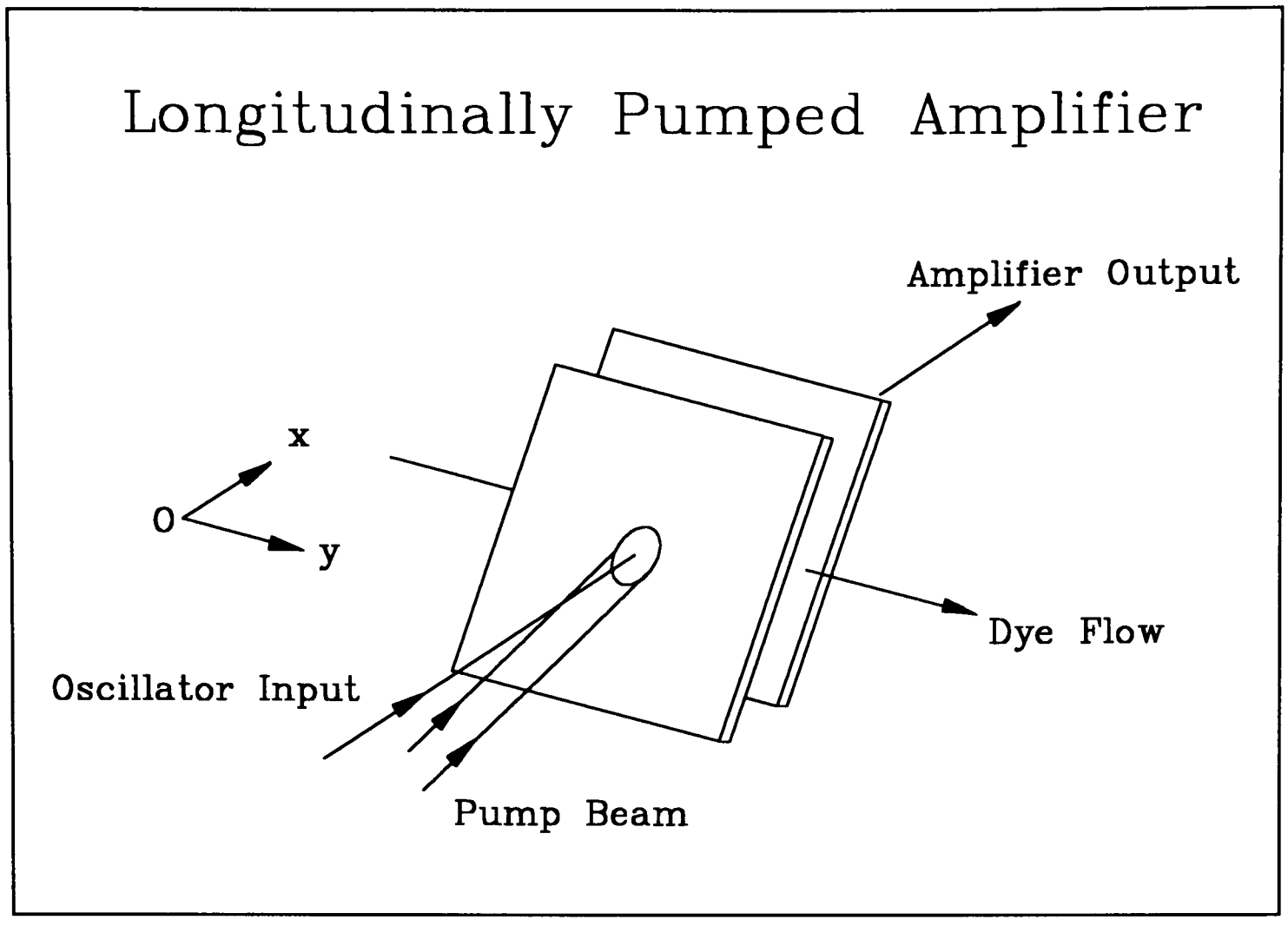


Figure 4.1 : The longitudinally pumped amplifier (LPA) geometry; here the pump and amplifier beams are collinear, and orthogonal to the direction of the dye flow.

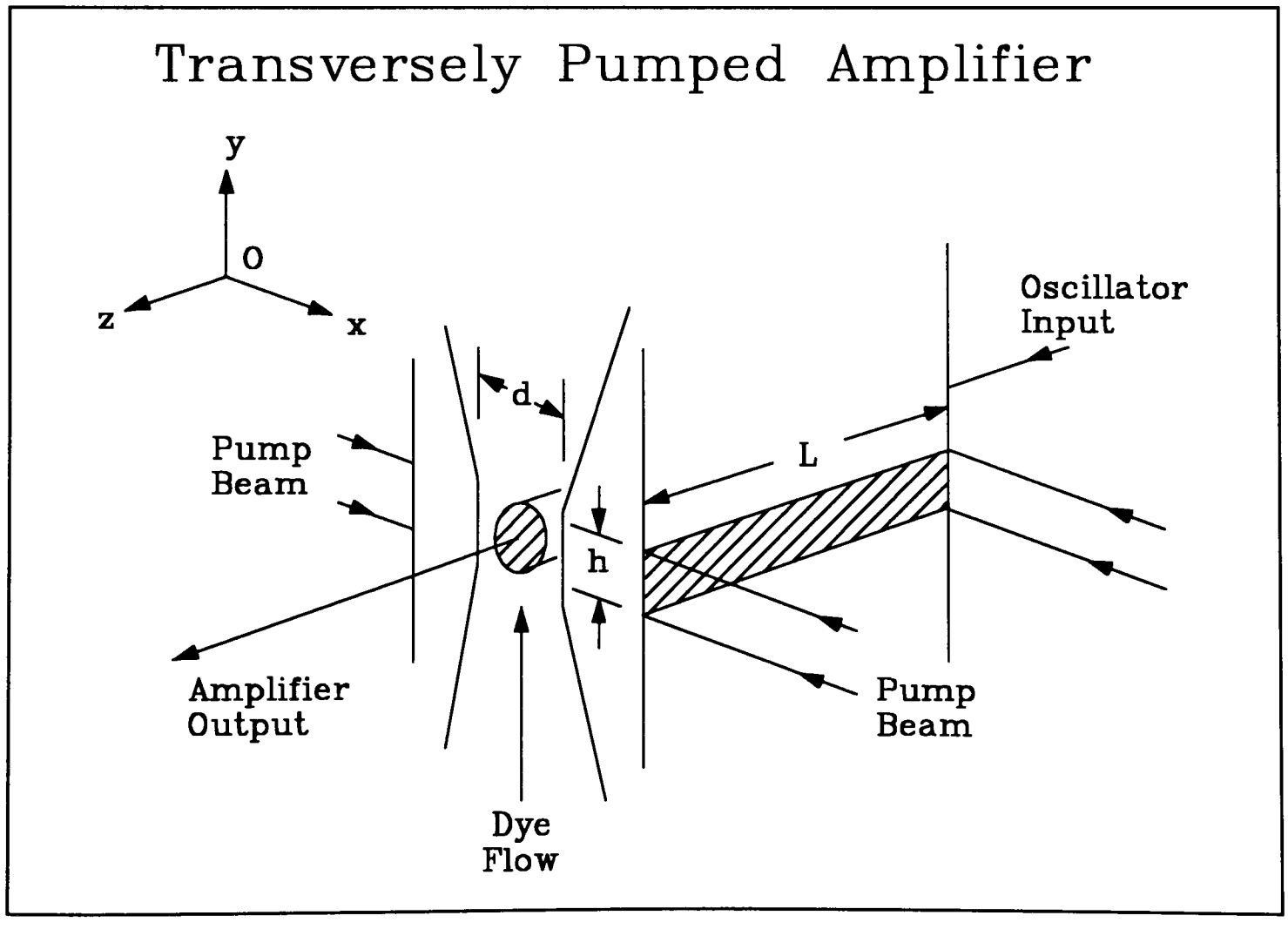


Figure 4.2 : The transversely pumped amplifier (TPA) geometry; here the pump beam(s), amplifier beam and direction of dye flow are mutually orthogonal.

extraction efficiency with respect to the dye laser seed power. This chapter reviews the theory of CVL-pumped dye laser amplifiers, and shows that, under certain conditions, extraction efficiencies greater than 50% are possible. The model predictions both of the Hargrove and Kan theory, and the ESA theory detailed below, are compared with experimental results achieved in this laboratory, and conclusions regarding optimum amplifier design are discussed.

4.2 Theory of CVL-Pumped Dye Lasers

The dye laser kinetics described in the previous chapter, are greatly simplified by several assumptions particular to the case of CVL pumping:-

1. Triplet absorption effects can be neglected, since the CVL pump pulse duration ($\sim$50 ns) is considerably shorter than the singlet to triplet inter-system crossing time constant, k_{st}^{-1}.
2. The population n_2 of the second excited singlet is taken to be zero, since the radiationless decay time, τ_{21}, typically of order a few picoseconds, is considerably shorter than the CVL pump pulse.
3. The cross-section for stimulated emission at the pump wavelength, $\sigma_e(\lambda_p)$, is assumed to be negligible (in the absence of the 578 nm pump line).[1]
4. The presence of amplified spontaneous emission is neglected; although this is not strictly valid, if the dye laser seed intensity is large enough to saturate the gain throughout the amplifier, it is a reasonably good assumption.

In the case of a LPA geometry, with reference to the simplified energy level diagram shown schematically in figure 4.3, the relevant rate equations are :

$$\frac{dn_1}{dt} = \sigma_{01}(\lambda_p)n_0 I_p + \sigma_{01}(\lambda_l)n_0 I_l - \frac{n_1}{\tau_s} - \sigma_e(\lambda_l)n_1 I_l \qquad (1)$$

GSA PUMP WAVELENGTH	GSA SIGNAL WAVELENGTH	SPONTANEOUS EMISSION	STIMULATED EMISSION

[1] The consequences of utilising both the 511 nm and 578 nm pump wavelengths of the CVL in dye laser / amplifier pumping will be considered in Chapter 5; here we consider using only one pump wavelength which does not lie in the fluorescence band of the dye.

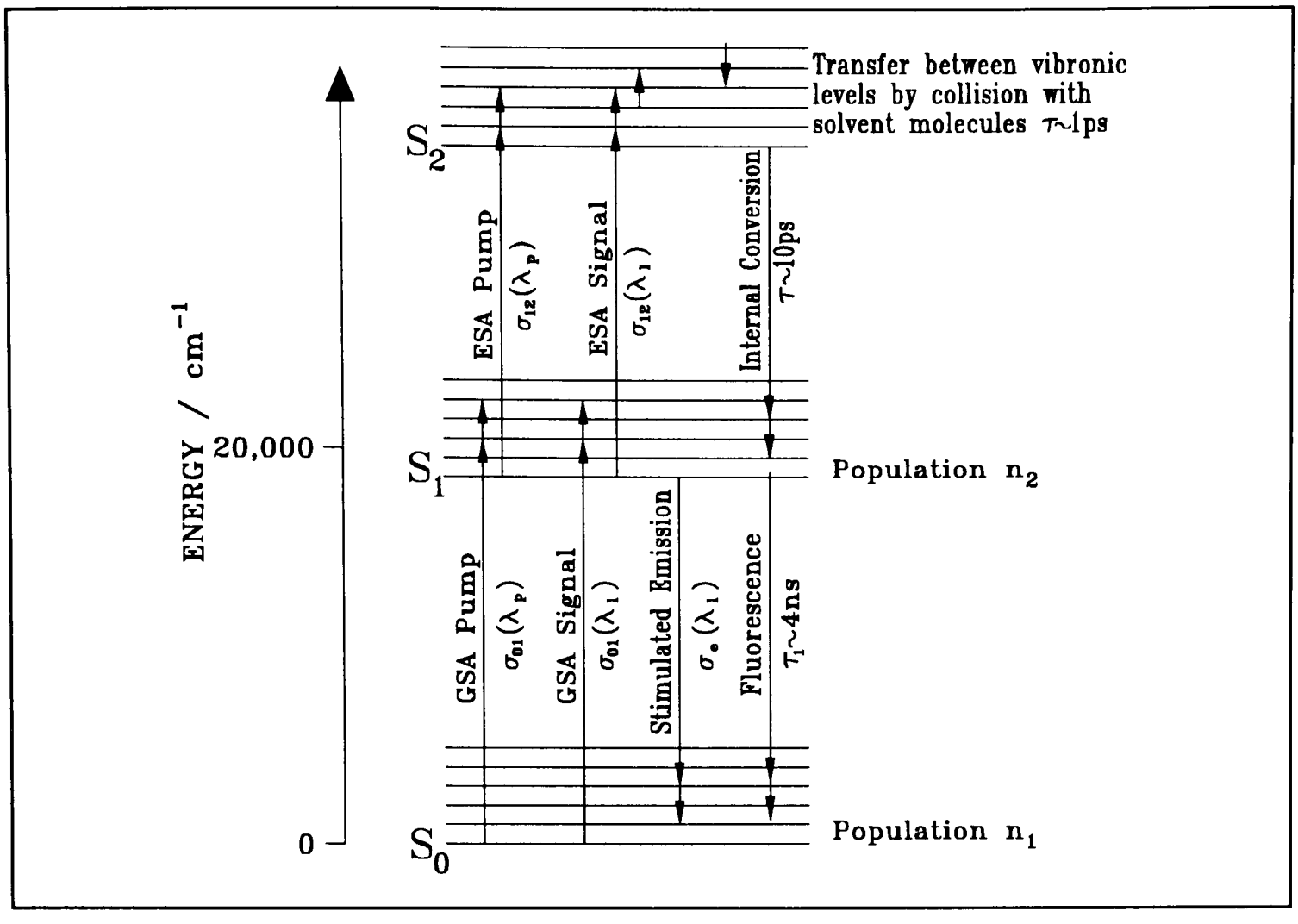


Figure 4.3 : The simplified dye energy levels and optical transitions relating to the kinetics of CVL pumped dye amplifiers.

$$\frac{1}{c}\frac{\partial I_p}{\partial t} + \frac{\partial I_p}{\partial x} = -\left[\sigma_{01}(\lambda_p)n_0 + \sigma_{12}(\lambda_p)n_1\right]I_p \quad , \tag{2}$$

GSA PUMP WAVELENGTH — ESA PUMP WAVELENGTH

$$\frac{1}{c}\frac{\partial I_l}{\partial t} + \frac{\partial I_l}{\partial x} = \left[\sigma_e(\lambda_l)n_1 - \sigma_{01}(\lambda_l)n_0 - \sigma_{12}(\lambda_l)n_1\right]I_l \quad , \tag{3}$$

STIMULATED EMISSION — GSA SIGNAL WAVELENGTH — ESA SIGNAL WAVELENGTH

where σ_{01}, σ_{12}, and σ_e are the ground state absorption, excited state absorption and stimulated emission cross sections respectively; n_0 and n_1 are the dye population densities of the ground and first excited singlet states S_1 and S_2 respectively; τ_s and τ_{21} are the spontaneous and radiationless decay lifetimes; and I_p and I_l are the pump laser and dye laser photon fluxes (photons/s/cm^2). The equations for the TPA case are similar, except that $\partial I_l/\partial x$ must be replaced by $\partial I_l/\partial z$ in equation (3).

Due to the fast radiationless decay between S_2 and S_1, only states S_0 and S_1 are

populated, and the total dye population density, n, may be expressed as :

$$n = n_0 + n_1 \ . \tag{4}$$

Furthermore, to a good approximation for the dye systems studied, the CVL pump pulse length is much longer than the lifetime of the first dye singlet level with respect to spontaneous emission ($\sim$4 ns for Rhodamine 6G). Therefore, a steady state solution may be assumed, and the time derivatives in equations (1) to (3) may be set to zero, yielding in the case of (1) and (3) :

$$\sigma_{01}(\lambda_p)n_0 I_P - \sigma_e(\lambda_l)n_1 I_l + \sigma_{01}(\lambda_l)n_0 I_l - \frac{n_1}{\tau_s} = 0 \ , \tag{5}$$

$$\frac{1}{I_l}\frac{dI_l}{dx} = \sigma_e(\lambda_l)n_1 - \sigma_{01}(\lambda_l)n_0 - \sigma_{12}(\lambda_l)n_1 \ , \tag{6}$$

whereupon, eliminating n_0 from (4) using (5), an expression for the population of the upper laser level, n_1, may be shown to be :

$$n_1 = \frac{n\tau_s[\sigma_{01}(\lambda_p)I_p + \sigma_{01}(\lambda_l)I_l]}{1 + \tau_s I_l[\sigma_e(\lambda_l) + \sigma_{01}(\lambda_l)] + \sigma_{01}(\lambda_p)I_p\tau_s} \ . \tag{7}$$

Since S_1 quickly thermalizes to give a population inversion with respect to all, but the thermally populated vibrational states of the ground level S_0, n_1 is also the population inversion density. Substituting this expression for the population inversion into equation (6), with a little algebraic manipulation, the saturated-signal gain can be shown to given by:

$$\alpha_l \equiv \frac{1}{I_l}\frac{dI_l}{dx} = \frac{\alpha_0}{1+\frac{I_l}{I_s}} - \frac{\xi I_l}{1+\frac{I_l}{I_s}} \ , \tag{8}$$

where the ESA parameter, ξ, the small signal gain, α_0, and the saturation intensity, I_s, are given by:

$$\xi = \frac{n\sigma_{12}(\lambda_l)\sigma_{01}(\lambda_l)\tau_s}{1+\sigma_{01}(\lambda_p)I_p\tau_s} \quad , \tag{9}$$

and

$$\alpha_0 = \frac{\sigma_{eff}n\left(\sigma_{01}(\lambda_p)I_p\tau_s - \dfrac{\sigma_{01}(\lambda_l)}{\sigma_{eff}}\right)}{1+\sigma_{01}(\lambda_p)I_p\tau_s} \quad , \tag{10}$$

where

$$\sigma_{eff} = \sigma_e(\lambda_l) - \sigma_{12}(\lambda_l) \quad , \tag{11}$$

and

$$I_s = \frac{1 + \sigma_{01}(\lambda_p)I_p\tau_s}{\sigma_e(\lambda_l)\tau_s\left(1 + \dfrac{\sigma_{01}(\lambda_l)}{\sigma_e(\lambda_l)}\right)} \cdot \tag{12}$$

It is worthy to note that the second term on the right of equation (8) does not appear in the analysis of Hargrove and Kan, and represents a nonlinear fractional loss coefficient owing to the ESA at the dye laser wavelength. It is reassuring that in the limit of no ESA, $\sigma_{12}(\lambda_l)=0$, this second term vanishes, and equation (8) reduces to the classical form of the saturated gain presented in [4.1].

A similar analysis results in a corresponding relationship for the saturated signal absorption that characterizes the pump photon flux I_p :

$$\alpha_p = \frac{I}{I_p}\frac{\partial I_p}{\partial x} = \frac{-n\sigma_{01}(\lambda_p)\left[1 + \left(1 + \dfrac{\sigma_{01}(\lambda_l)\sigma_{12}(\lambda_p)}{\sigma_e(\lambda_l)\sigma_{01}(\lambda_p)}\right)\sigma_e(\lambda_l)\tau_s I_l + \sigma_{12}(\lambda_p)\tau_s I_p\right]}{1 + \left(1 + \dfrac{\sigma_{01}(\lambda_l)}{\sigma_e(\lambda_l)}\right)\sigma_e(\lambda_l)\tau_s I_l + \sigma_{01}(\lambda_p)\tau_s I_p} \cdot \tag{13}$$

4.3 Physical Interpretation

To establish the origin of the nonlinear absorption at the signal wavelength, the rate equations must be reconsidered in the limit of a small dye laser signal and a low pump power, ie. $I_l \ll I_S$ and $I_P \ll (\sigma_{01}(\lambda_p)\tau_s)^{-1}$; whence, using the steady state limits of equations (1), (2) and (3), an approximate form for both the upper laser level population, n_1, and the small signal gain, α_0, may be shown to be :-

$$n_1 \approx n\sigma_{01}(\lambda_p)I_p\tau_s + n\sigma_{01}(\lambda_l)I_l\tau_s \equiv n_1(\lambda_p) + n_1(\lambda_l) \quad , \tag{14}$$

GSA PUMP WAVELENGTH — GSA SIGNAL WAVELENGTH

$$\frac{1}{I_l}\frac{dI_l}{dx} \approx \sigma_e(\lambda_l)n_1(\lambda_p) + \sigma_e(\lambda_l)n_1(\lambda_l) - \sigma_{12}(\lambda_l)n_1(\lambda_p) - \sigma_{01}(\lambda_l)n_0 - \sigma_{12}(\lambda_l)n_1(\lambda_l) \tag{15}$$

in which the two components contributing to the population of the upper laser level, namely GSA at the pump and signal wavelengths, are represented by $n_1(\lambda_p)$ and $n_1(\lambda_l)$ respectively. Equation (15) is the low power extreme of (8), but now the physical origin of the component parts is clear. The first two terms represent stimulated emission due to population inversion created by GSA at the pump and signal wavelengths respectively; the third term represents a loss mechanism for the population inversion created by the pump laser through ESA - this term is included in σ_{eff} in equation (10). The fourth term describes the linear absorption at the signal wavelength by the ground state molecules, and is included in the expression for α_0. Finally, the fifth term represents the nonlinear absorption of the signal wavelength by the molecules $n_1(\lambda_l)$ excited by GSA of I_l itself - this last term gives rise to the parameter ξ of equation (8), not included in the Hargrove and Kan analysis.

The effect of scaling this analysis to higher powers is to multiply these component parts by a saturation factor of $(1+I_l/I_s)^{-1}(1+I_p/I_{ps})^{-1}$. Thus, the ESA term can be seen to be responsible for a decrease in the net gain coefficient, $(\alpha_0-\xi I_l)$, at high signal fluxes; such high fluxes may result from high initial seed intensities or progressive amplification. Finally, it is worth noting that the nonlinear ESA

absorption depends upon GSA at the signal wavelength, and if $\sigma_{01}(\lambda_l)=0$, then the effect is negligible.

4.4 Computation and Results

The machine calculations for the case of TPA and LPA geometries were carried out with the aid of the Mathcad package executed on a PC host. Mathcad is a high level mathematical interpreter which allows programs to be written in an algebraic format; it also includes subroutines for numerical integration, and the solution of transcendental equations, by means of Simpson's Rule and the Newton Raphson technique respectively. The ESA dye amplifier model is readily translated into a form suitable for Mathcad, and can be found in appendices A1 to A4. By changing the model iteration variables, the dependence of the amplifier efficiency can be investigated with respect to a number of parameters including seed power, pump power, and gain length.

4.4.1 Longitudinally Pumped Amplifier

The pump and dye laser beams are collinear in a LPA geometry, and in the case of $\sigma_{01}(\lambda_l)=0$, combining equations (8) and (13) yields:

$$\frac{\partial I_p(x)}{\partial I_l(x)} = -\frac{I_p(x)}{I_l(x)}\frac{\sigma_{12}(\lambda_p)}{\sigma_e(\lambda_l)} - \left(1 + \frac{1}{\sigma_e(\lambda_l)\tau_s I_l(x)}\right). \qquad \textbf{(16)}$$

The power extraction efficiency, η, is then obtained by integrating (16) with the aid of an integrating factor ρ :

$$\eta = \frac{P_{OUT} - P_{INP}}{P_{PUMP}} = \frac{(G-1)I_l(x=0)\lambda_p}{I_p(x=0)\lambda_l} \qquad \textbf{(17)}$$

$$\eta = \frac{\lambda_p(1+\rho)(G-1)}{\lambda_l(G^{(1+\rho)}-1)}\left[1 - TG^{\rho} - \frac{(G^{\rho}-1)}{\rho\sigma_e(\lambda_l)\tau_s I_p(x=0)}\right], \qquad \textbf{(18)}$$

where G is the amplifier gain, $I_l(x=l)/I_l(x=0)$; T is the pump transmission,

$(I_p(x=l)/I_p(x=0))$; and $\rho=\sigma_{12}(\lambda_p)/\sigma_e(\lambda_l)$. The LPA computer model predictions are shown in figure 4.4, which shows the amplifier efficiency as a function of the pump intensity for two different values of the gain, G. The model is based on an amplifier using Rhodamine 590 Chloride dye operating near the peak of the fluorescence band (λ_l=570 nm), and with CVL green-only pumping, λ_p=510.6 nm. The extraction efficiency of a LPA geometry is strongly influenced by the presence of very small values of ESA at the pump wavelength - for example, when operated with a gain $G=10$, the efficiency is approximately half of its potential maximum when $\rho=0.25$. From appendix 4.1, which details the relevant cross sections for Rhodamine 590 Chloride, we see that the ratio $\sigma_{12}(\lambda_p)/\sigma_e(\lambda_l)\approx 0.5$, and the corresponding extraction efficiency is only 25% compared to a possible 80% in the case of no ESA.

Excited state absorption also determines the pump beam penetration depth. In the case of a dye with $\sigma_{12}(\lambda_P)=\sigma_{01}(\lambda_P)$, then, independent of the pump or dye laser intensity, equation (13) shows that the 1/e pump beam penetration depth is

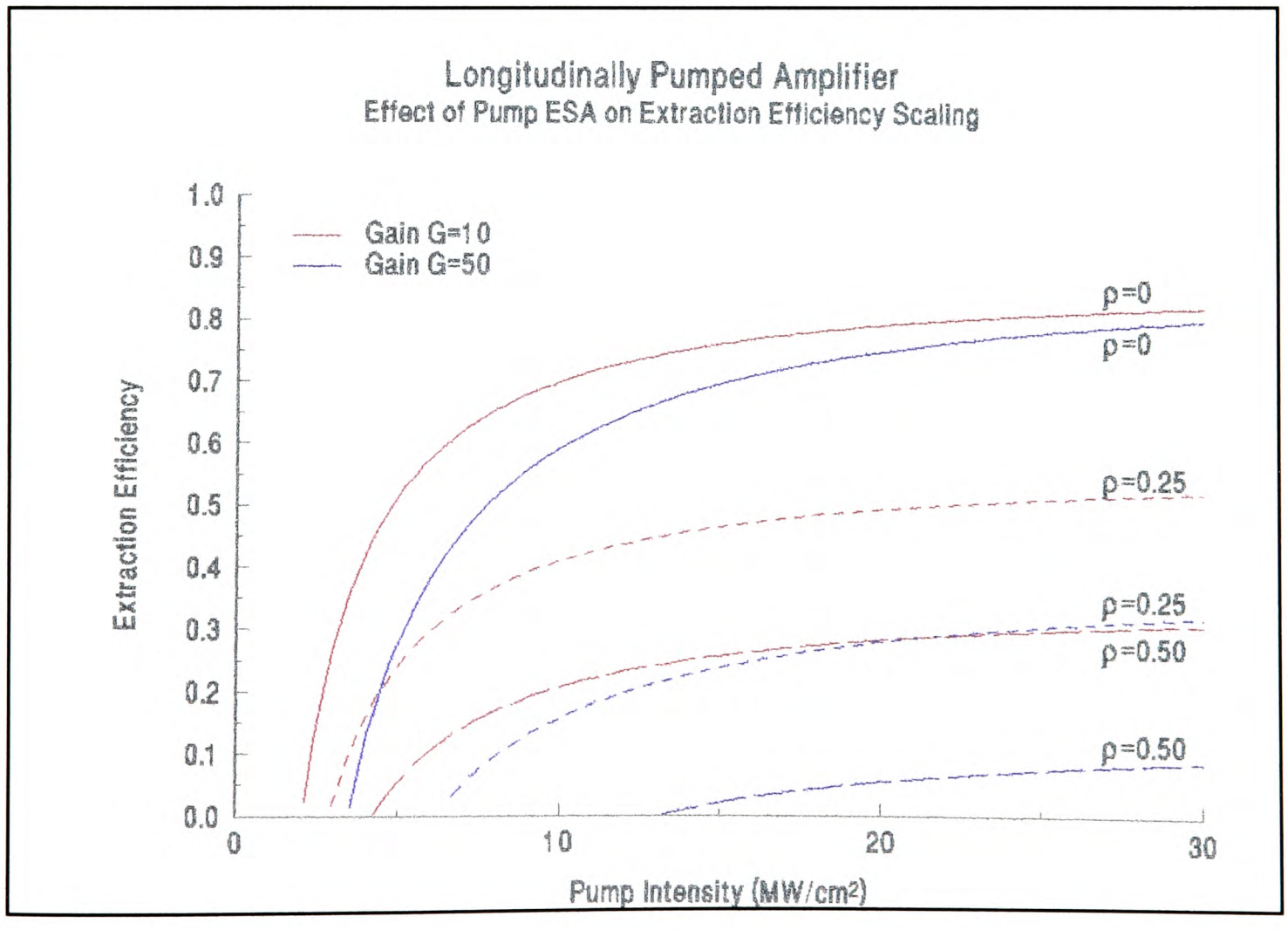


Figure 4.4 : Calculated LPA photon extraction efficiency as a function of the pump intensity for gains $G=10$ & 50 and for three values of the ESA parameter $\rho=0$, 0.25 & 0.5.

$d_p=(n\sigma_{01}(\lambda_p))^{-1}$. Thus, ESA prevents the pump beam bleaching its way into the medium and restricts the gain length of the LPA to values of order d_p; consequently, by considering the limit of equation (10) at high pump intensities, the maximum value of the gain G, may be shown to be given by the expression:-

$$g_{\max} \sim \alpha_{0\max} d_p \sim \frac{\sigma_e(\lambda_l)}{\sigma_{01}(\lambda_p)} \qquad (19)$$

Therefore, the maximum small signal gain with strong ESA is restricted to values of order unity, and efficient energy extraction is only realized at very high seed fluxes. It is for these reasons that the LPA geometry is not used for practical application, and longitudinal pumping is restricted to oscillators, where the exact spatial overlap of the pump and dye laser beams results in excellent dye laser beam quality.

4.4.2 Transversely Pumped Amplifier

The transversely pumped amplifier (TPA) geometry offers an additional degree of freedom to the laser designer: the device aspect ratio ($I_l/I_p \approx L/d$) may be selected, a choice not available in the case of a LPA geometry. The saturated gain G, of a TPA of length L, is obtained by integrating (8) with respect to the propagation distance, z, to give the transcendental relationship:

$$G = \frac{I_{OUT}}{I_{INP}} = \frac{\alpha_0}{\xi I_{INP}} - \left[\frac{\alpha_0}{\xi I_{INP}} - 1\right] \exp\left[\frac{\ln G - \alpha_0 L}{1 + \frac{\alpha_0}{\xi I_S}}\right] , \qquad (20)$$

where I_{INP} is the input dye amplifier seed photon flux and I_{OUT} is the amplified laser photon flux.

The energy extraction efficiency is given by :

$$\eta = \frac{P_{OUT} - P_{INP}}{P_{PUMP}} = (G-1)\frac{P_{INP}}{P_{PUMP}} , \qquad (21)$$

in which P_{INP}, P_{OUT} and P_{PUMP} are the average values of the dye laser seed input power, the amplifier output power and the CVL pump laser power respectively.

The precise spatial variation of the pump intensity along its propagation direction x is closely coupled to the dye laser intensity distribution along z. To simplify the calculations, we assume the pump beam does not bleach its way through the dye, and that the intensity varies exponentially as :

$$I_P(x) = I_P(x=0)\exp\left[-n\sigma_{es}(\lambda_P)x\right] . \tag{22}$$

The assumption is exact if $\sigma_{12}(\lambda_P)=\sigma_{01}(\lambda_P)$. For sufficiently small GSA at the signal wavelength ($\sigma_{01}(\lambda_l)\sim 0$), as is nearly always the case, it is also approximately correct if

$$\left[\sigma_{01}(\lambda_p) - \sigma_{12}(\lambda_p)\right]\tau_s I_p << \left(1+\sigma_e(\lambda_l)\tau_s I_l\right) . \tag{23}$$

That is, the pump intensity will vary exponentially if it is unsaturated ($\sigma_{01}\tau_s I_P \ll 1$), or if $\sigma_e\tau_s I_l$ is sufficiently large. Since the aspect ratio for efficient TPAs is large, typically 20-100, then this latter condition is satisfied throughout most of the gain volume due to the high dye laser signal intensities, even if the pump saturation level is greater than unity. The condition may not be satisfied, however, in the first few inverse small signal gain lengths ($1/\alpha_0$) at the amplifier input, but this represents a small fraction of the total gain volume. So, for the purpose of machine calculations, the average value of the pump laser photon flux over a 1/e absorption depth is used :

$$I_P = \left[\frac{\int_0^{d_p} e^{-d_p x}dx}{d_p}\right]\frac{P_P}{f\tau_{CVL}h\nu A} , \tag{24}$$

where f is the pulse repetition frequency, τ_{CVL} is the CVL pulse length, $h\nu$ is the photon energy, and A is the area (cm^2) to which the CVL pump is focused. A similar expression is used for calculating I_{IN}, the dye laser seed photon flux, but this time, without the exponential averaging factor.

The computer model predictions of the TPA amplifier efficiency scaling with respect to seed input, pump power, and gain length are presented in figures 4.5, 4.6 and 4.7 respectively; also shown, for comparison, are the corresponding predictions of the Hargrove and Kan model. Despite predicting different absolute efficiencies,

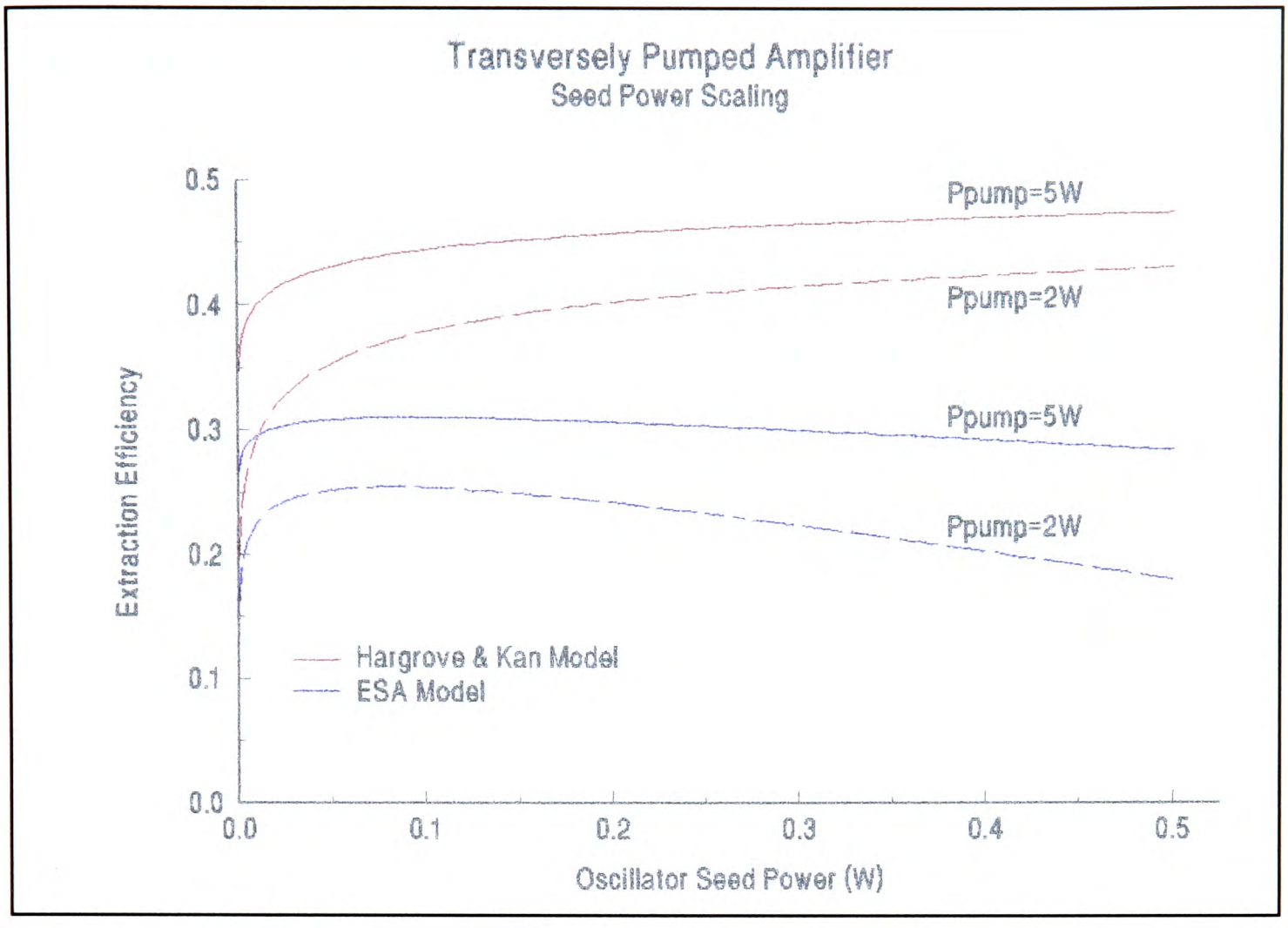


Figure 4.5 : Calculated TPA efficiency as a function of the oscillator seed power at two pump powers. Note that the ESA model predicts an optimum seed power, contrary to the Hargrove & Kan model.

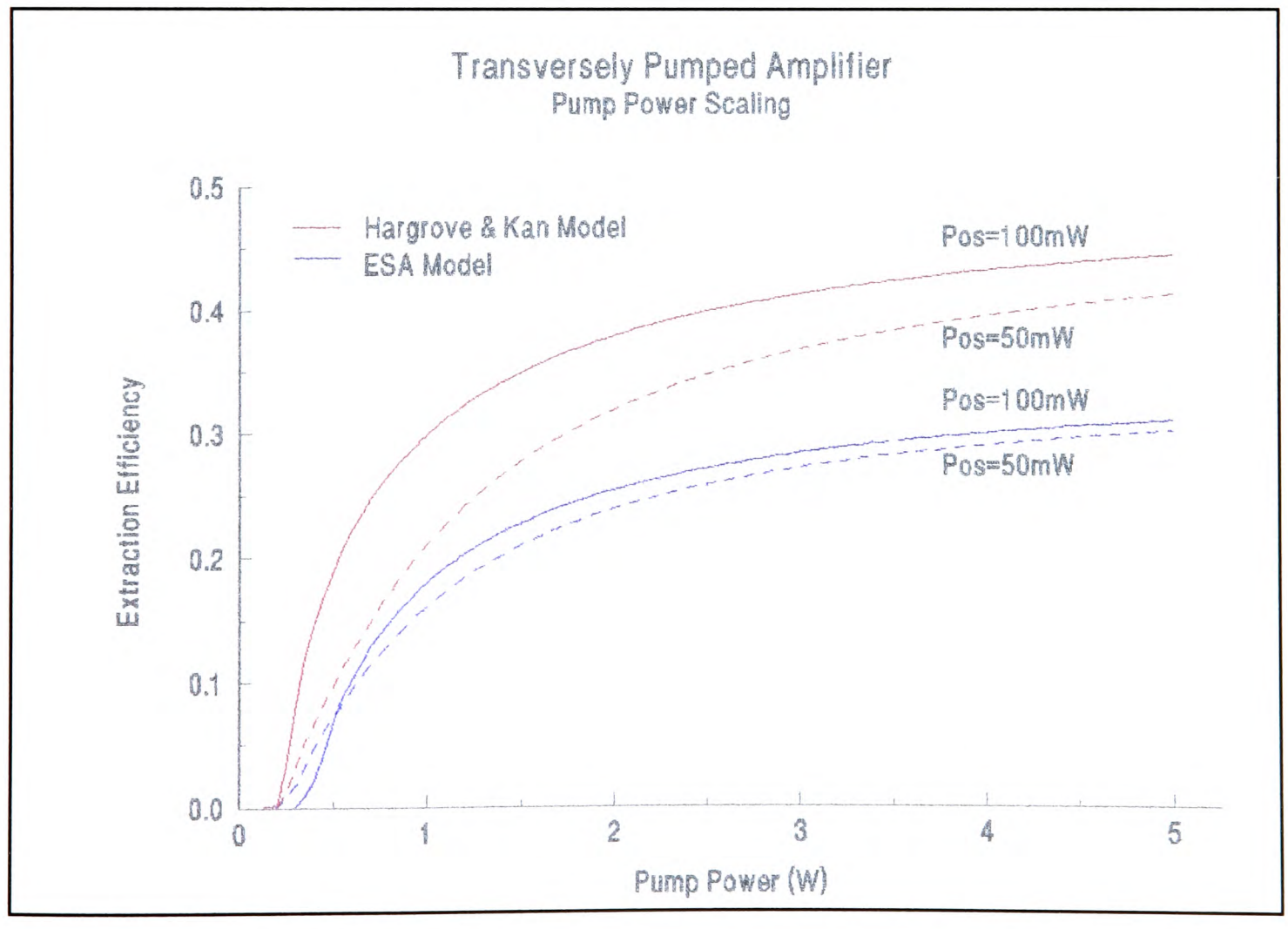


Figure 4.6 : Calculated TPA efficiency as a function of the pump power for two values of the seed input power.

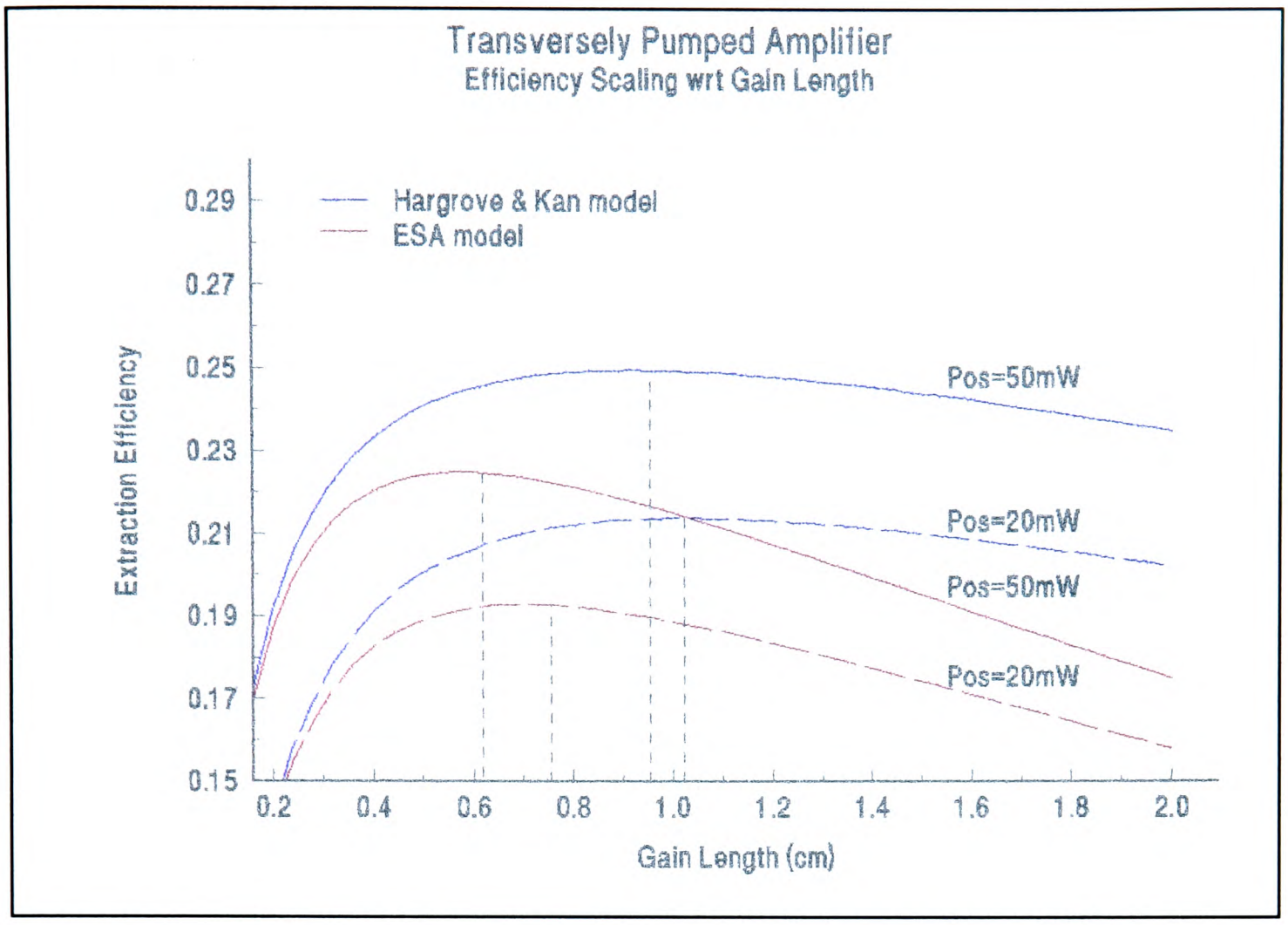


Figure 4.7 : Calculated TPA efficiency as a function of gain length for a pump power of 4 W and for differing seed powers - note the optimum gain length is $\leq$ 10 mm.

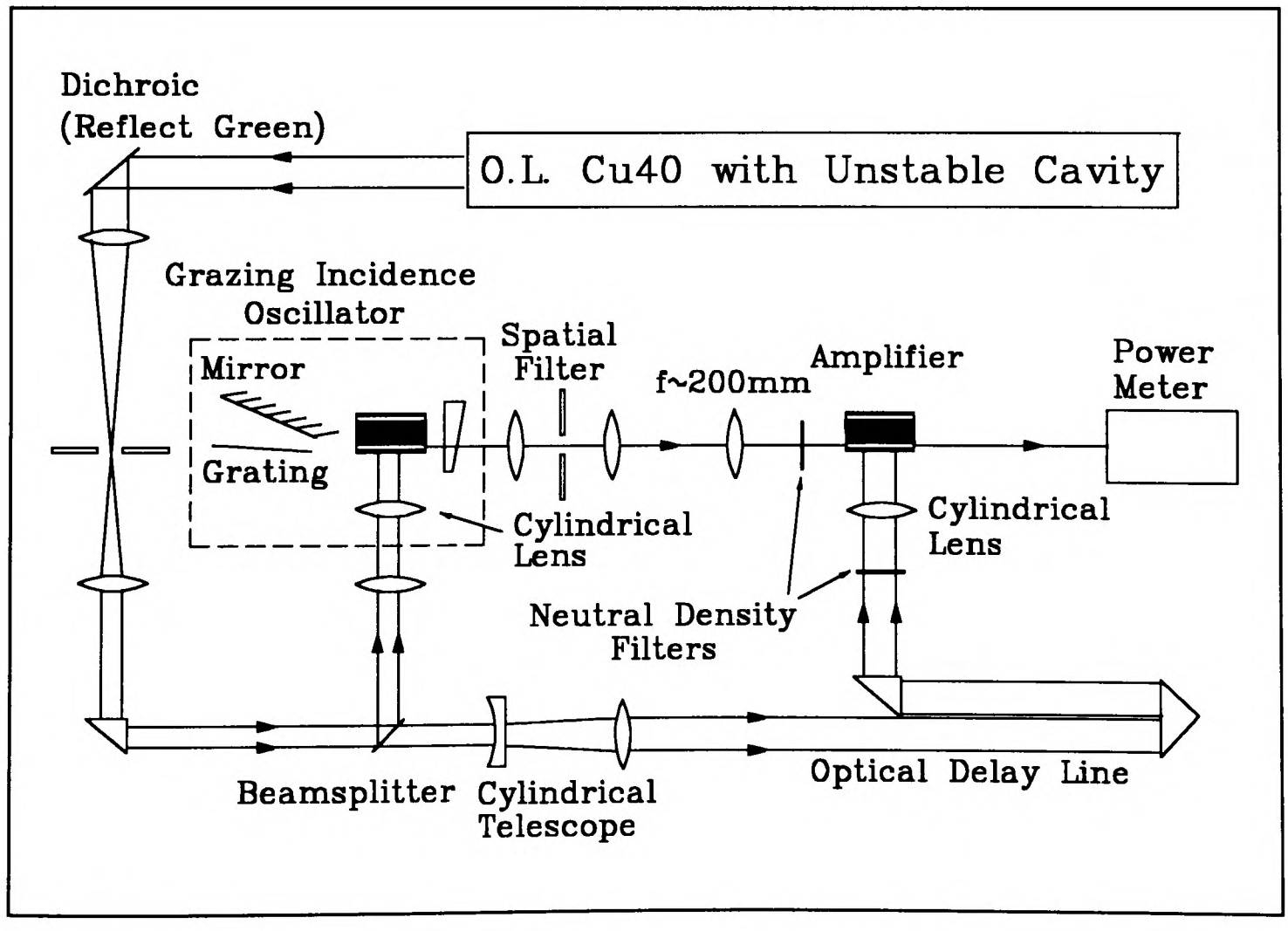


Figure 4.8 : Experimental set-up used for CVL pumped dye amplifier studies.

both models predict saturation of the extraction efficiency with respect to pump power. The biggest difference between the models is the prediction of an optimum value of the oscillator seed input by the ESA model, whereas the Hargrove and Kan model predicts saturation in the extraction efficiency with respect to oscillator input power.

It is interesting to note that both models predict an optimum for the amplifier gain length. For typical laboratory CVL pump and seed powers, the optimum amplifier length is of the order 5-10 mm. This should be compared to the usual 20-40 mm gain lengths of dye cuvettes conventionally used in commercial pulsed dye lasers, which are better suited to the very much higher peak powers of Nd:YAG or Excimer pumped systems.

4.5 Comparison With Experiment

The experimental set-up used to investigate the amplifier characteristics is shown in plate 4.1, and schematically in figure 4.8. The vertically polarized output from a 40 W CVL (Oxford Lasers Cu40), incorporating a polarized unstable cavity, was directed to a dichroic beamsplitter where the yellow, 578.2 nm, component was removed. Approximately one third of the remaining green, 510.6 nm, component was split off, and used to pump a grazing incidence dye oscillator (using a flowing solution of Rhodamine 590 Chloride (0.15 g/litre) in methanol). The dye oscillator output was typically 100 mW at 570 nm, with a corresponding bandwidth of 7 GHz. The output was spatially filtered, to remove ASE, before being focused to a variable spot-size in the amplifier dye cell.

The dye amplifier cuvette used was of a laminar flow design (Radiant Dye Chemie RDVC20), with the active dye channel measuring 20 mm by 1 mm. The dye solution consisted of Rhodamine 590 Chloride in methanol, flowing at a rate of 5 litres/minute. When used with the 6.5 kHz CVL pump focused into the dye cell by a f=10 cm cylindrical lens, this flow rate provided a clearing ratio greater than 2.5:1. This flow rate prevents thermal distortion of the dye medium and the associated reduction in beam quality. An optical delay line was incorporated in the amplifier

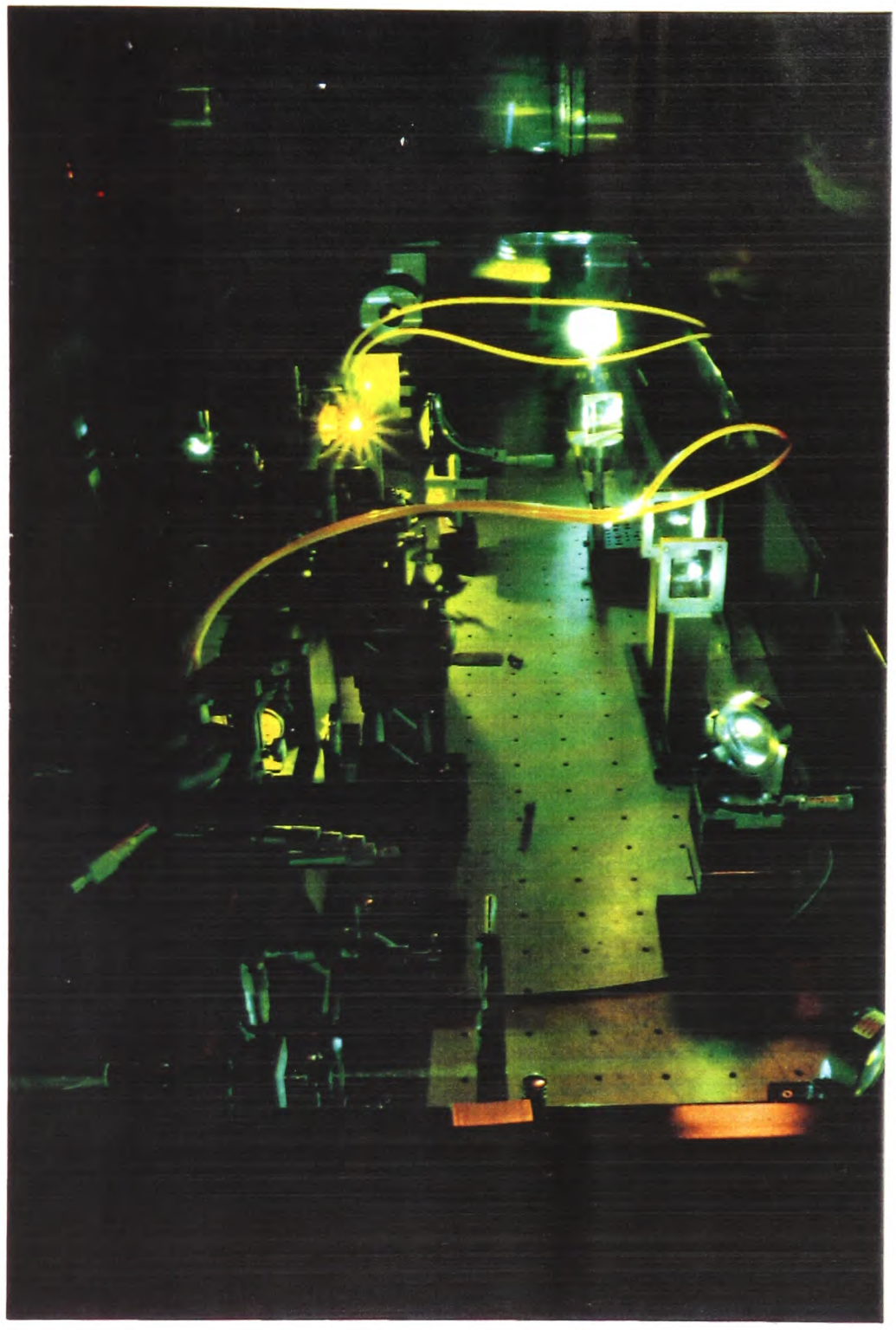


Plate 4.1 : The CVL-pumped Master Oscillator Power Amplifier (MOPA) configuration used for the dye-amplifier studies presented in this chapter. One third of the CVL 511nm radiation is used to pump a Littman dye oscillator (seen in the foreground), whilst the remaining CVL 511nm radiation is directed to the dye amplifier via an optical delay line.

pump beam path such that the pump and oscillator pulses arrived at the amplifier simultaneously, so ensuring efficient amplification, and minimum ASE.

The average cw powers of the CVL-pump, oscillator and amplifier output were measured using a thermopile type power meter (Laser Instrumentation model 9000), which was calibrated at manufacture against standards traceable to the National Physical Laboratory. The pulse shapes were recorded using fast response vacuum photodiodes (ITL-TF085M20UV), and displayed on a digital oscilloscope (Tektronix 2440), which was, in turn, connected to a PC via an IEEE interface for data acquisition and archiving. Frequency bandwidth measurements of the oscillator seed and amplifier output were recorded by focusing the fringe pattern from a scanning Fabry Perot interferometer (Technical Optics FP-25) onto a pinhole in front of a photomultiplier. The pinhole dimensions were an order of magnitude smaller than the central order fringe, so as not to impair the instrumental resolution. The photomultiplier output was displayed on an oscilloscope triggered by the etalon ramping voltage, and again, an IEEE link to a PC provided a means of data archiving.

A set of calibrated neutral density reflective filters was used to attenuate the laser beams, and permit gain scaling measurements with respect to both the pump and oscillator input powers. Neutral density filters were used to achieve variable pump and seed powers, rather than change the electrical input power to the CVL or the pump power to the oscillator, since the latter changes not only the power, but also, more importantly, the pulse length and beam quality of the laser radiation.

The dye concentration used was close to the optimum value. At low dye concentrations, the pump intensity is relatively uniform throughout the dye cell volume. The amplifier output increases with increasing concentration, as more pump power is deposited in the active volume; however, as the concentration is increased beyond its optimum, the majority of the pump power is deposited near to the pump input face of the cuvette, and strong fluorescence can be seen. In the present experiments, the amplifier was operated at slightly below optimum concentration to give small signal absorption depths of approximately 0.2 mm, and greater than 95%

of the peak efficiency. Such operation results in a favourable compromise between beam spatial homogeneity and efficiency.

4.6 Results

The results of the frequency bandwidth measurements are displayed in figure 4.9; the amplifier bandwidth closely follows that of the oscillator, although there is a very slight change in the frequency. It is thought that this frequency shift is due to gain-pulling in the amplifier - those frequency components closer to the fluorescence maximum will be amplified more than those further away. Similarly, the amplifier pulse shape closely mimics that of the oscillator seed (figure 4.10). When correctly aligned, the amplifier output contains very little ASE, and the small fraction present arises from periods when there is no temporal overlap between the seed and pump pulses in the amplifier.

Experimentally, it was found that the spot size to which the oscillator is focused in the amplifier has a large influence on the dye extraction efficiency; with the highest extraction efficiencies achieved by tight focusing of the seed into the amplifier to give small spot sizes. This is entirely consistent with theory: typical saturation intensities of laser dyes are of the order $1MW/cm^2$, and so, to sweep out all of the available gain, the low power oscillator seed must be focused into the amplifier cuvette.

The experimental data points for the output power and extraction efficiency plotted in figures 4.11, 4.12 and 4.13 show excellent agreement between the ESA theory and experiment. The only fitted parameters of the model are the spot sizes to which the seed and pump lasers are focused; these are estimated from a knowledge of the focusing optics and the beam divergence of the oscillator and CVL laser beams. Also shown on the plots are the theoretical predictions of the Hargrove and Kan model, which is seen to overestimate the efficiency for the same model parameters.

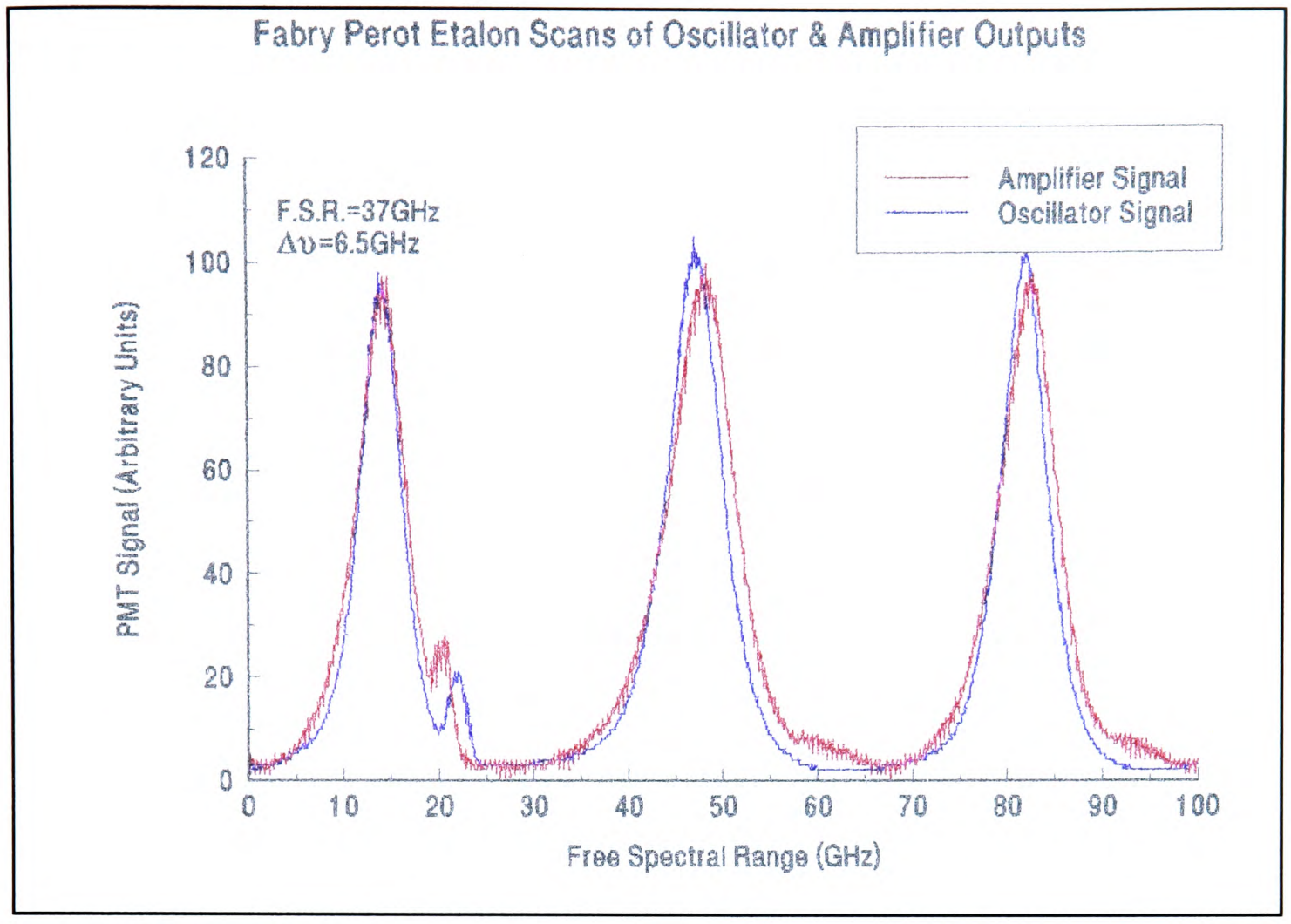


Figure 4.9 : Fabry Perot scans of the seed and amplified beams. Note the slight wavelength shift of the amplified beam relative to the seed, seen as a different fringe separation, owing to gain pulling.

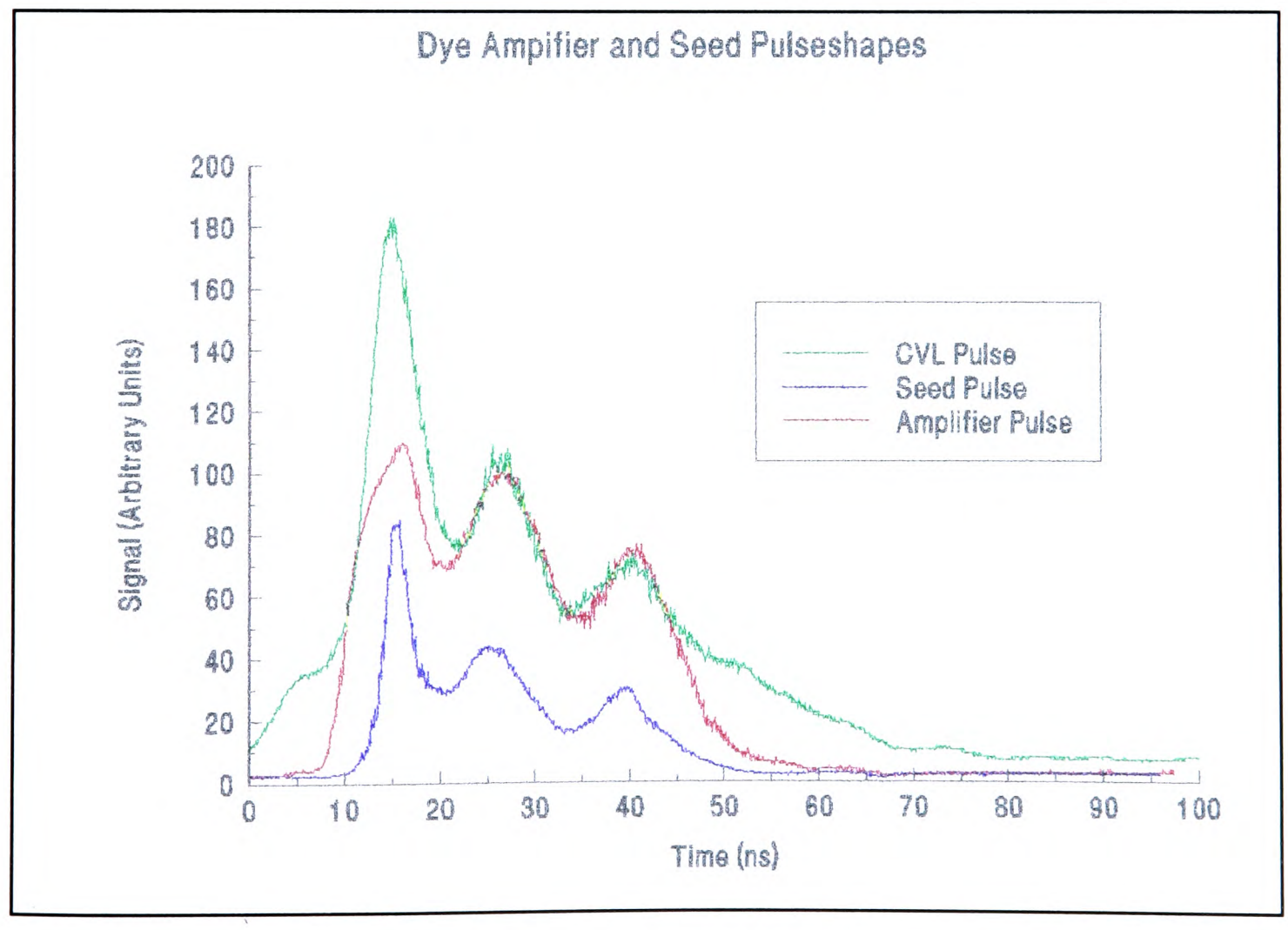


Figure 4.10 : Measured pump, seed and amplifier pulse shapes.

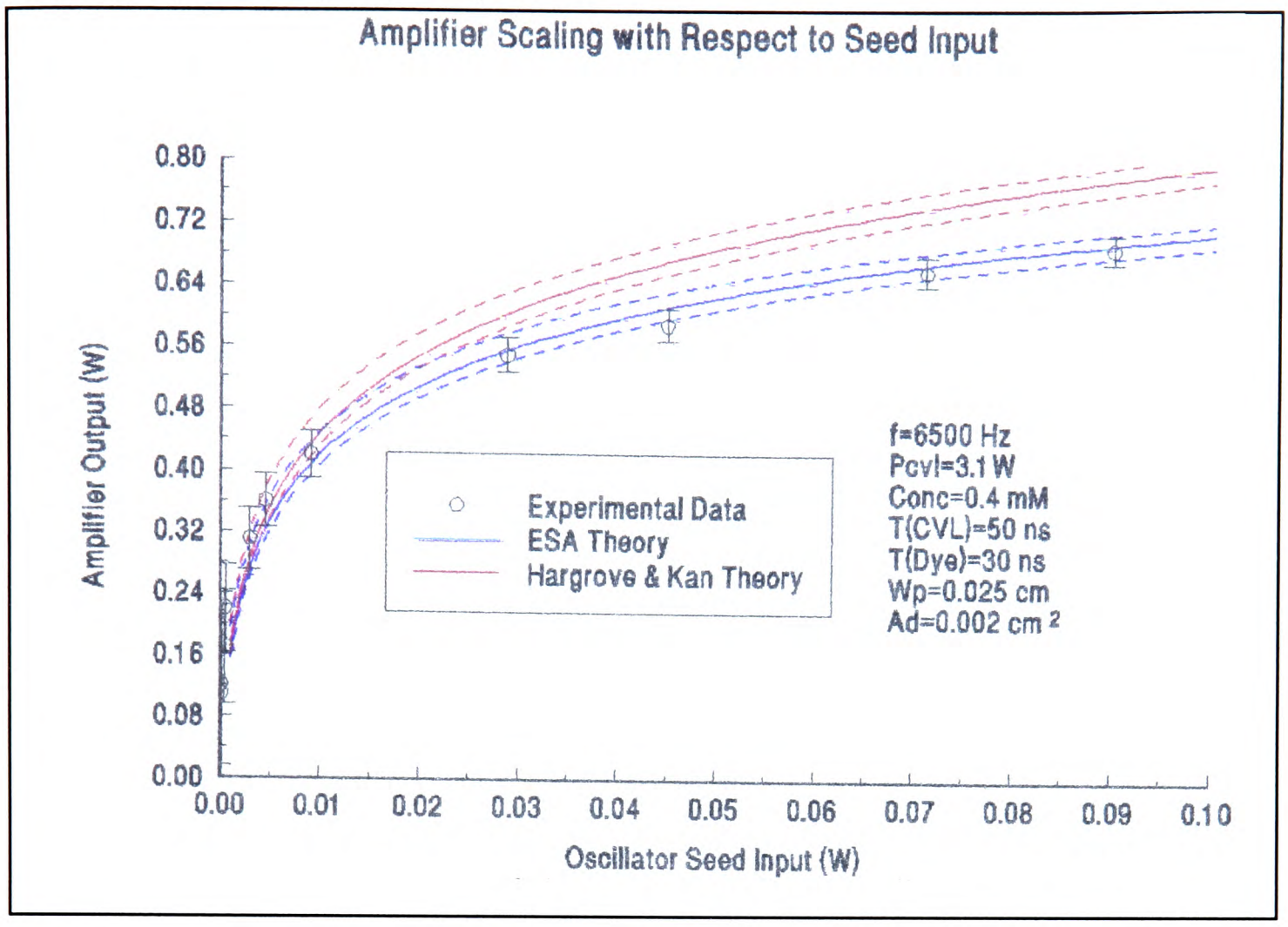


Figure 4.11 : Theoretical and measured TPA output power as a function of the seed input power for a 20 mm gain length of Rhodamine 6G pumped by 3.1 W of 511 nm CVL.

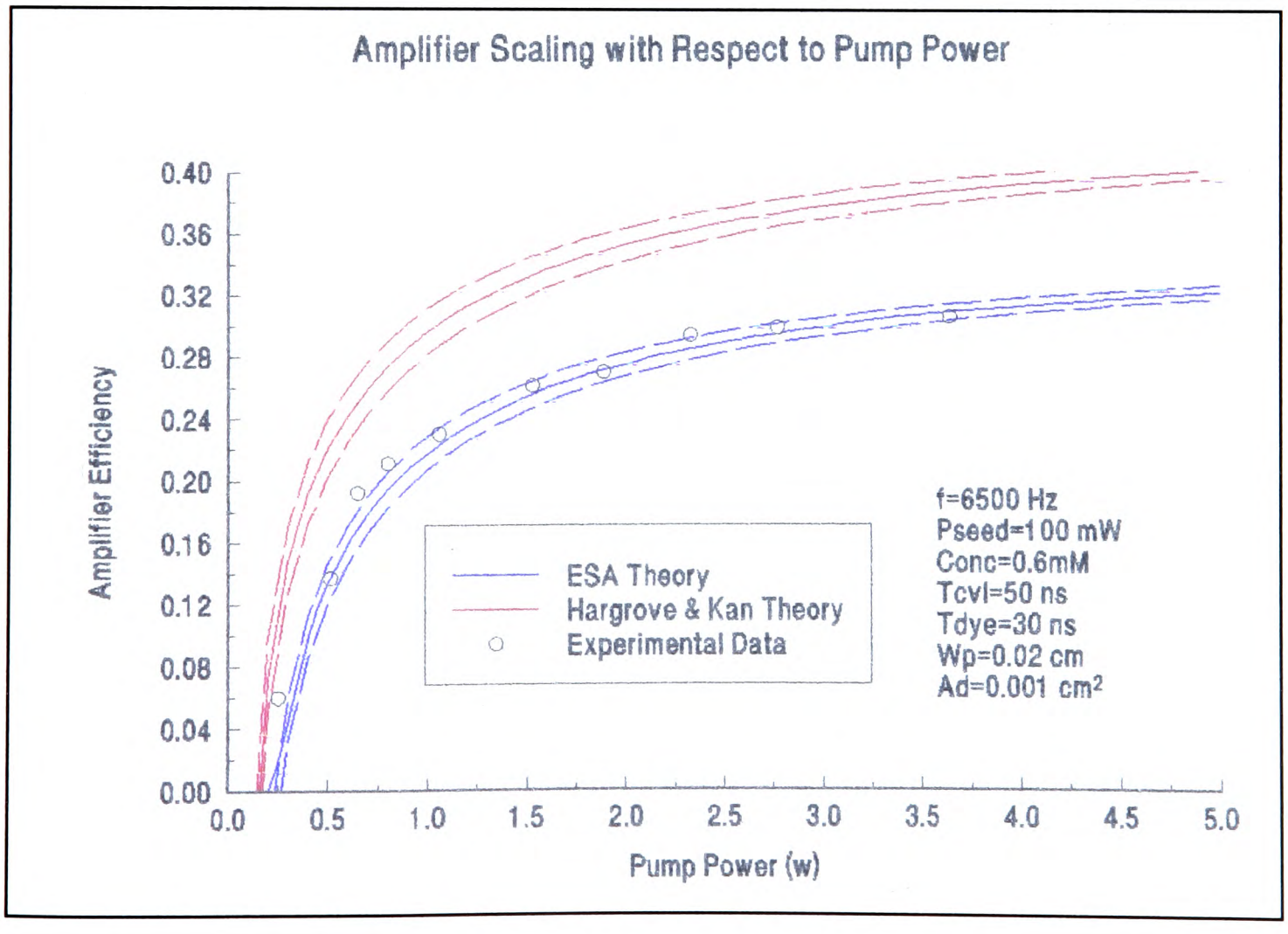


Figure 4.12 : Theoretical and calculated TPA efficiency scaling with respect to pump power for a 20mm gain length of Rhodamine 6G and a 100 mW seed input.

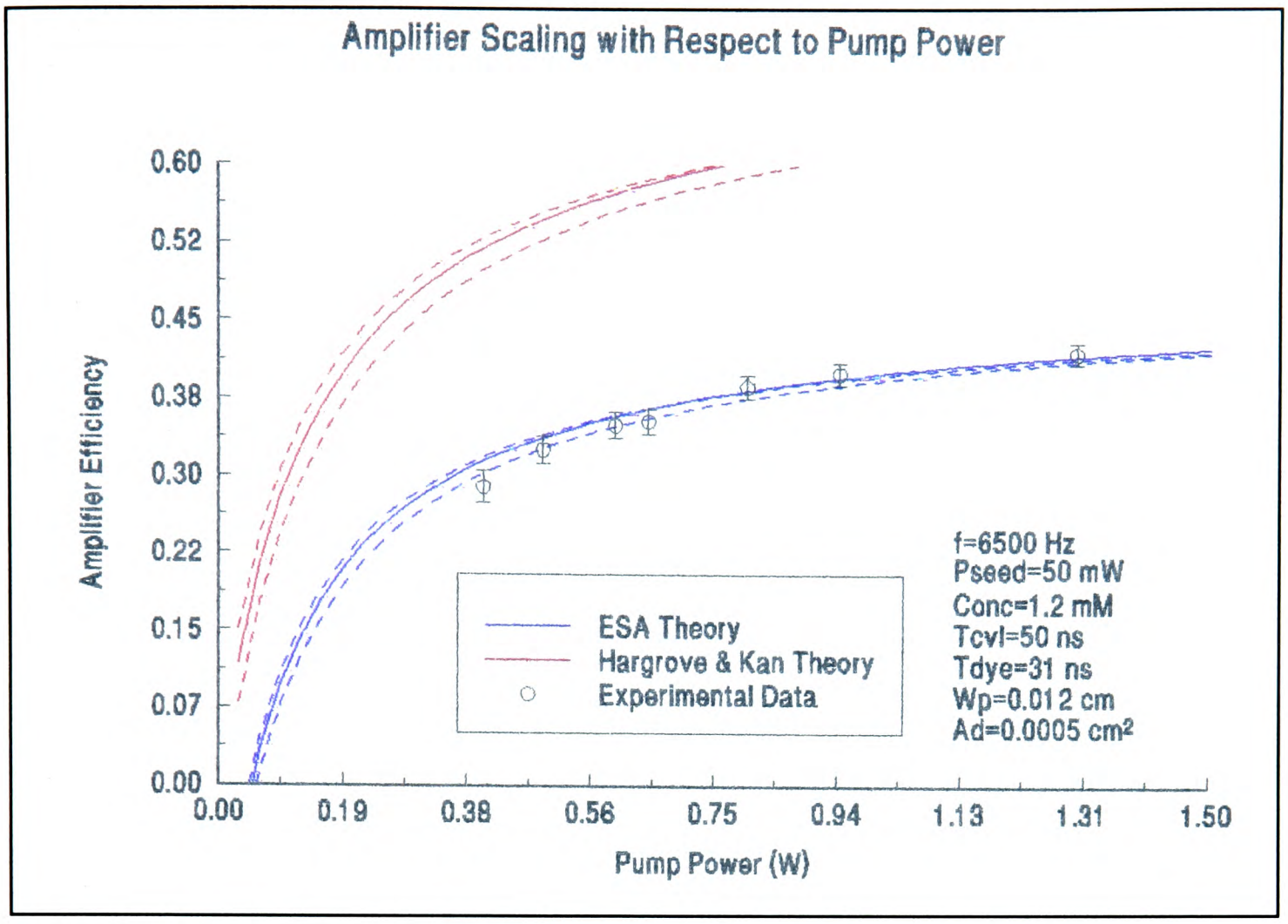


Figure 4.13 : Theoretical and calculated TPA efficiency scaling with respect to pump power for a 20mm gain length of Rhodamine 6G and a 80 mW seed input. At high pump powers, the efficiency exceeds 45% !

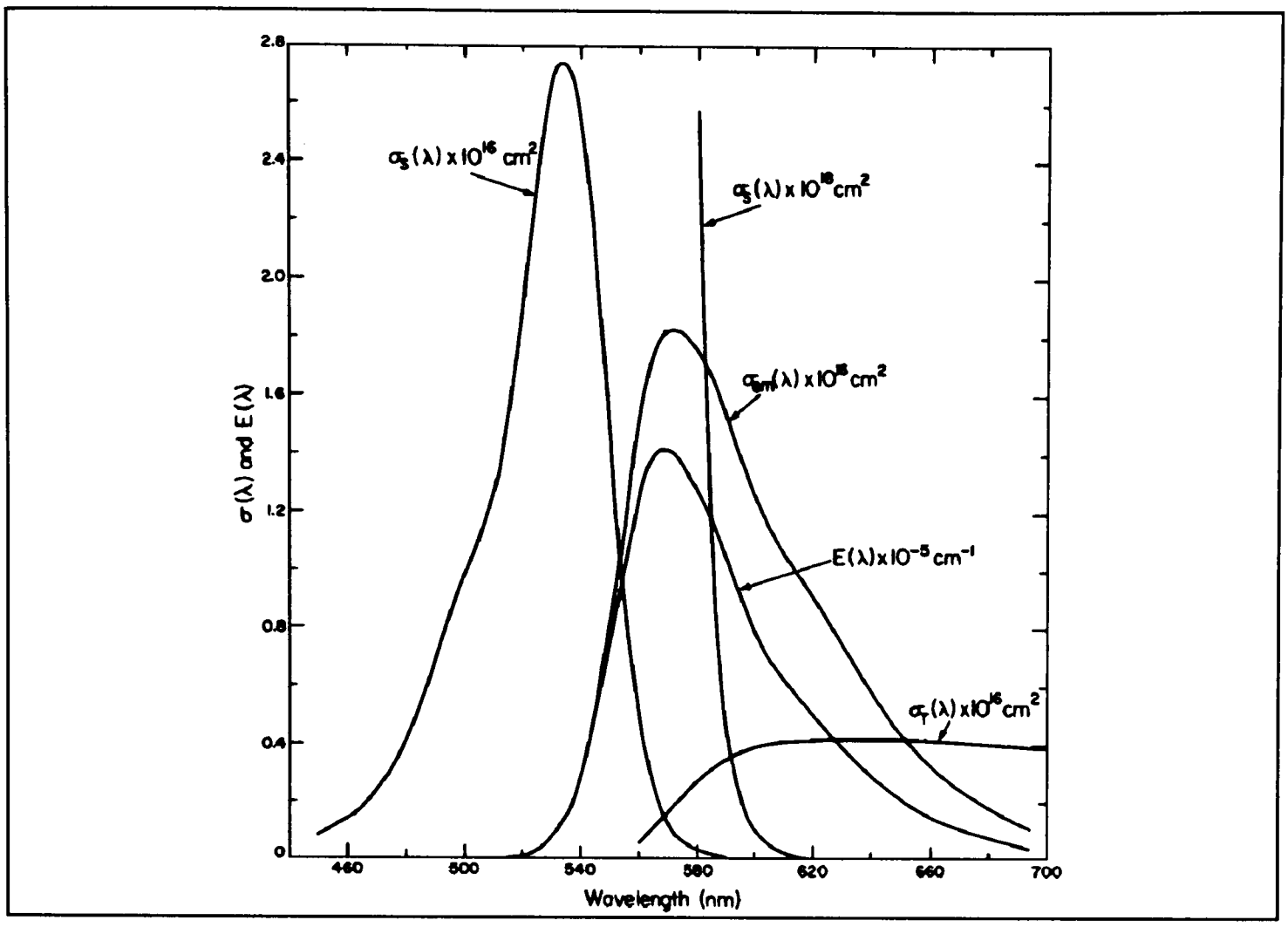
4.6 Practical Details and Conclusion

Longitudinal pumping is not of interest for practical amplifiers. With the TPA geometry, single pass dye amplification efficiencies in excess of 45% have been demonstrated, and with increased pump power, theory predicts that conversion efficiencies in excess of 50% are attainable. Excellent agreement is obtained between the ESA theory detailed here and experiment.

Both theory and experiment suggest that to obtain the highest efficiencies, it is best to focus the seed radiation into the amplifier, and ensure small pump absorption depths in the dye medium; in this instance there is little point in using dye cells greater than a few hundred microns wide. Wider dye channels merely cause problems with ASE feedback - here, the pump beam which is not absorbed in the first few inverse small signal absorption depths, and which does not play a part in seed amplification, merely generates ASE. The ASE generated has the opportunity of reflecting back into the amplifier dye cell off oscillator/amplifier coupling optics, and,

unless care is taken, this ASE can overwhelm the seed radiation in the amplification region. Theory also suggests that optimum dye amplifier gain lengths are of order 10 mm rather than the 20 mm or greater gain lengths typical of most pulsed dye laser designs, so for typical laboratory CVL pump lasers, the optimum amplifier cuvette dimensions would be a dye channel some 10 mm long and 300-500 μm wide.

Appendix 4.1 : Spectroscopic Data For Rhodamine 6G



Spectrophotometric data for the dye Rhodamine 6G taken from [4.5]

Alternative Name	:	Rhodamine 590 Chloride
Synonym(s)	:	2-[6-(ethylamino)-3-(ethylamino)-2,7-dimethyl-3H-xanthen-9-yl]-benzoic acid, ethyl ester, chloride.
Molecular Weight	:	479.02
Fluorescence Lifetime	:	4.8 ns

Optical Cross-sections [4.6]

GSA Pump	σ_{01}(510.6 nm)	:	1.66×10^{-16}cm^2
GSA Signal	σ_{01}(570.0 nm)	:	1.25×10^{-18}cm^2
Stimulated Emission	σ_e(570.0 nm)	:	1.76×10^{-16}cm^2
ESA Pump	σ_{12}(510.6 nm)	:	0.37×10^{-16}cm^2
ESA Signal	σ_{12}(570.0 nm)	:	0.91×10^{-16}cm^2

Chapter 4 References

4.1 R.S. Hargrove & T. Kan

High power efficient dye amplifier pumped by copper vapour lasers

IEEE J.Q.E. ***16*** *10 1180 (1980)*

4.2 O. Teschke, A.Dienes & J.R. Whinnery

Theory and operation of high power CW and long pulse dye lasers

IEEE J.Q.E. ***12*** *7 383 (1976)*

4.3 E. Sahar & D. Treves

Excited singlet-state absorption in dyes and their effect on dye lasers

IEEE J.Q.E. ***13*** *12 962 (1977)*

4.4 K. Dasgupta & L.G. Nair

Effect of excited state absorption at signal wavelength in pulsed dye laser amplifiers

IEEE J.Q.E. ***26*** *1 189 (1990)*

4.5 B.B. Snaverly

Continuous-Wave Dye Lasers I

Dye Lasers, Springer Topics in Applied Physics 1 Ed. F.P. Schafer (1989)

4.6 P.R. Hammond *et al.*

Spectra of the lowest excited states of Rhodamine 6G and Rhodamine B

IEEE J.Q.E. ***15*** *7 624 (1979)*

Chapter 5
Practical CVL-Pumped Dye Lasers

5.1 Introduction.

5.2 CVL Pump Laser Optimization.

5.2.1 Cavity Design.

5.2.2 Choice of 511nm and 578nm Pump Wavelengths.

5.2.3 Spatial Filtering.

5.2.4 Pump Beam Geometry.

5.2.5 Pump Beam Polarization.

5.3 Dye Laser Optimization.

5.3.1 General Considerations.

5.3.2 ASE in Pulsed Laser Systems.

5.3.3 Choice of Grating Material.

5.4 Characterization Measurements.

5.4.1 Beam Divergence Analysis.

5.5 Commercially Available Pulsed Dye Lasers.

5.5.1 The Russian Dye Laser LZhI-504.

5.5.2 The Lambda Physik LPD 3000.

5.5.3 The Lumonics Hyperdye HD-350.

5.6 Conclusion.

Appendix 5.1 : Lifetime Against Stimulated Emission.

Appendix 5.2 : Gaussian Beam Focusing.

References.

Chapter 5 : Practical CVL-Pumped Dye Lasers

5.1 Introduction

CVL-pumped dye lasers offer a source of high power, kilohertz repetition rate, tunable, narrow-bandwidth radiation suitable for many spectroscopic applications. Such applications include resonant ionization mass spectrometry (RIMS), where, because atoms effuse from an ion-beam-sputtered source at thermal velocities, and cross the irradiation zone in a typical RIS apparatus on sub-millisecond timescales, it is necessary to pulse a dye laser at several kilohertz if every atom is to be exposed to laser radiation.

This chapter reports the experimental investigations performed to determine the parameters of the CVL pump laser, the dye laser, and the optical coupling of the two, which are critical to the design and optimization of CVL-pumped dye lasers. The parameters investigated / optimized, and the dye laser characteristics measured, include:-

- Use of unstable and plane-plane CVL cavities
- 511 and/or 578 nm pumping
- Effect of spatially filtering the CVL pump
- Effect of polarizing the CVL pump
- Optimum pump beam geometry and delivery
- Optimum dye concentrations
- Optimum beamsplitter reflectivities
- Optimum output coupler reflectivities
- Choice of dye oscillator cavity materials
- Threshold and slope efficiencies
- Dye tuning ranges
- Dye pulse lengths
- Cavity build-up times
- Frequency bandwidths
- Frequency stability
- Pulse energy jitter
- Spectral purity and ASE content
- Beam divergence

The physical understanding acquired from these experimental investigations has been used to successfully modify several commercial dye lasers for CVL-pumping; the commercial systems examined include the Lambda Physik LPD3000, the Lumonics Hyperdye HD-350 and one of Soviet manufacture, the LZhI-504. The

design modifications to these commercial dye lasers necessary for optimum CVL-pumping are detailed, and their performance characteristics are reported. The modified units have shown conversion efficiencies in excess of 20%, frequency bandwidths as narrow as 800MHz, excellent frequency stability and, in some cases, a beam quality approaching the diffraction limit. These modified commercial dye lasers show themselves to be ideally suited for resonant ionization spectroscopy, and one such modified laser (a Lambda Physik LPD3000) has been installed at U.C. Swansea by the present author for this very application.

An overview of CVL-pumped dye lasers can be found in a recent publication by Webb and Duarte [5.1] where some of the present data is reported. Additionally, the present work has been reported at the IOP QEG topical meeting on tunable lasers (1990) and at the International Conference of Lasers '91, San Diego [5.2].

5.2 CVL Pump Laser Optimization

5.2.1 Cavity Design

The successful operation of a dye laser necessitates clearing the active pumped dye volume between shots, and, consequently, a dye laser pumped by a high repetition rate CVL requires correspondingly high dye flow rates. Practical flow rate considerations impose a limit on the height of the pumped active volume, and, thus, on the divergence of the CVL - the linear dimension of the smallest focal spot attainable in the focal plane of a lens is $f.\Delta\theta$, where f is the focal length of the lens and $\Delta\theta$ is the full angle divergence of the pump laser. Additionally, a tight line focus formed in the dye by a low divergence CVL is desirable to achieve the high gain necessary to overcome the high losses associated with dispersive oscillator cavities, and to achieve high efficiencies in dye amplifiers.

The greatest power extraction from a CVL is provided by a plane-plane cavity, but unfortunately, whilst offering high average power, the resulting CVL output beam is of poor quality. An alternative is to use an off-axis unstable cavity, of the type described in chapter 1. Here, the rapid mode evolution yields a low divergence beam and, whilst only half of the power of the plane-plane alternative is

extracted, the focusable power is increased by several orders of magnitude [5.3].

To see what effect the CVL cavity has on dye laser pumping, the slope efficiency of a HMPGI dye oscillator pumped by a CVL (Oxford Lasers CU40) fitted with a plane-plane cavity was measured, and compared with that of the same dye oscillator when pumped by the same CVL, but this time fitted with an off-axis unstable cavity. For these measurements calibrated neutral density filters were used to vary the pump power, rather than alter the electrical input to the CVL, since the latter varies not only the power, but also the pulse length and, more importantly, the cavity divergence of the pump beam. The ASE present in the dye laser output was removed by a mask before the power was recorded with a thermopile power meter (Laser Instrumentation Model 9000).

The results, plotted in figure 5.1, show the slope efficiency of the dye oscillator when pumped by a CVL fitted with an unstable cavity to be more than

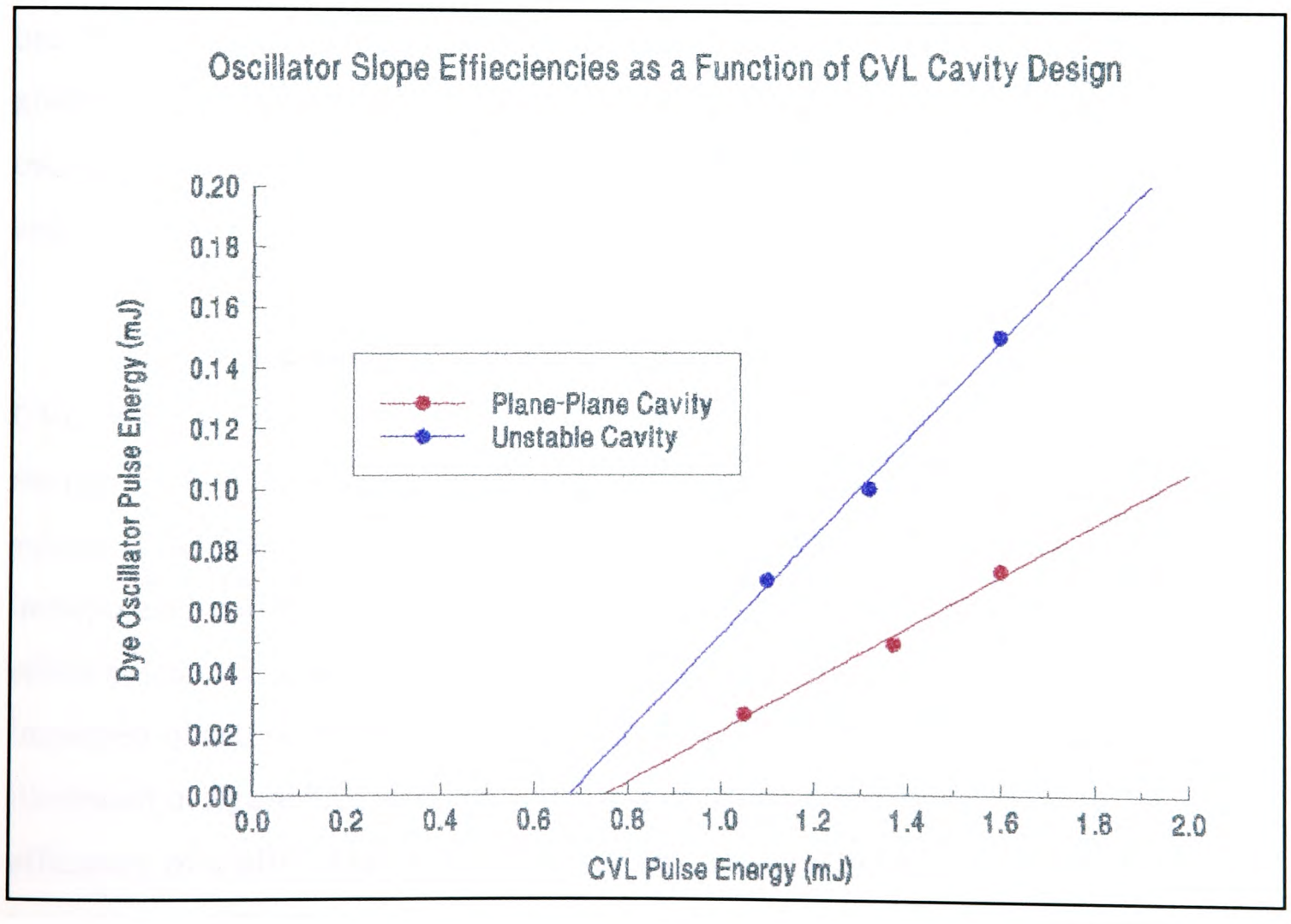


Figure 5.1 : Slope efficiency measurements of a HMPGI dye oscillator when pumped by a CVL fitted with (a) a plane-plane cavity, (b) an off-axis unstable cavity of magnification M=40.

double that of the same oscillator when pumped by a CVL operating with a plane-plane cavity. Thus, the use of the CVL unstable resonator offers an improvement in the wall-plug efficiency of the dye laser and, consequently, in all of the following experiments, the CVL cavity used was an off-axis unstable cavity (M=40).

5.2.2 Choice of 511nm and 578nm Pump Wavelengths

For dyes lasing in the range 550 - 600 nm, it was found to be detrimental to use the yellow (578 nm) component of the CVL for dye laser pumping since, for these dyes, the yellow CVL line lies within the fluorescence band. In the case of a longitudinally-pumped dye laser, the yellow component causes a loss of tunability, with the dye laser locking to the 578 nm line rather than to the cavity dispersion selected wavelength [5.4]. In the case of a transversely-pumped geometry and Rhodamine 6G, quenching of the laser action was observed when the 578nm pump line was used, with the output decreasing by a factor of about 2 as compared with green-only pumping. This is due to the depletion of the gain available to the dye oscillator through stimulated emission at 578 nm in the direction of the pump laser axis.

In all the experiments where the dye has dictated green-only pumping, the CVL 578 nm line has been separated from the green by use of multiple dichroic mirrors and/or a dispersing prism. However, for dyes lasing above 600 nm, the yellow CVL line (which then lies in the dye absorption band) can be successfully incorporated into the pumping scheme. Indeed, the 578 nm component is often more efficient than the green 511 nm line in pumping red fluorescing dyes, because of the improved quantum efficiency and the better match to the dye absorption bands, as illustrated in figure 5.2. Indeed, in the case of Rhodamine 640 Perchlorate, the slope efficiency of a MPL dye oscillator cavity was measured to be 7.5% with green-only pumping, and 20.3% in the case of yellow-only pumping - roughly in proportion to the ratio of the absorption cross sections at 510 nm and 578 nm respectively.

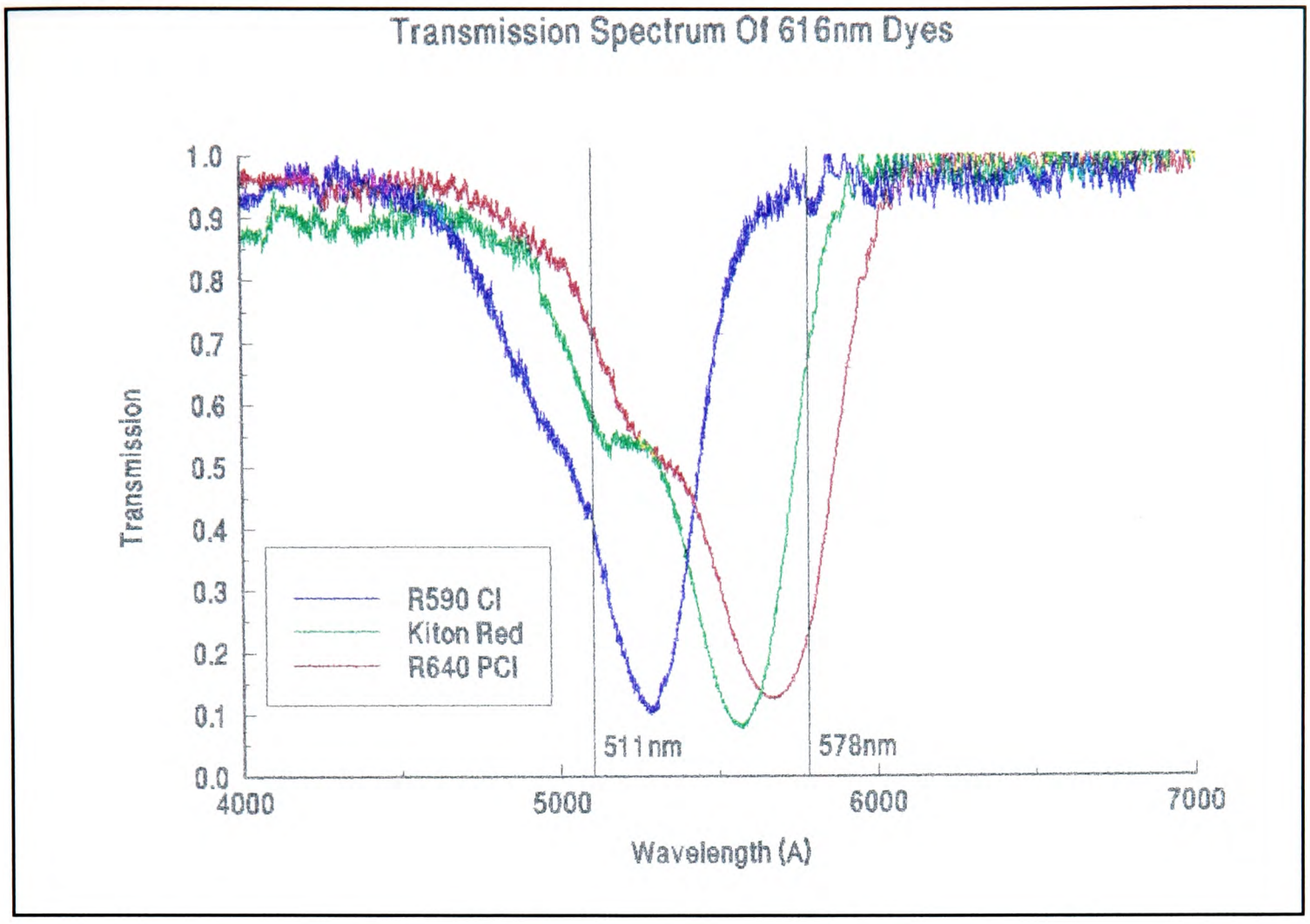


Figure 5.2 : Absorption bands for the dyes (a) Rhodamine 6G, (b) Kiton Red (c) Rhodamine 640 Perchlorate, measured with a spectrophotometer. Overlaid are the CVL pump wavelengths.

5.2.3 Spatial Filtering

In addition to the low divergence output from a CVL operated with an unstable cavity, there is an appreciable ASE component arising from radiation emitted on the first cavity round trip which escapes any cavity control. This ASE component is highly divergent and does not focus as tightly as the better mode quality radiation found toward the tail of the CVL pulse. The ASE does not play an effective role in dye laser pumping, and if it is not removed, the softer focusing ASE irradiates the dye before it flows into the active region. Whilst the dye relaxes at the molecular level on nanosecond timescales, thermal gradients persist on timescales longer than the CVL inter-pulse period. Thus, this ASE preheating of the dye induces unwanted thermal refractive index gradients which result in thermal lensing and beamsteering. However, the ASE can be removed from the pump beam by spatially filtering the CVL beam before the dye laser.

By using a variable iris stop placed near a focus in the pump beam path to a

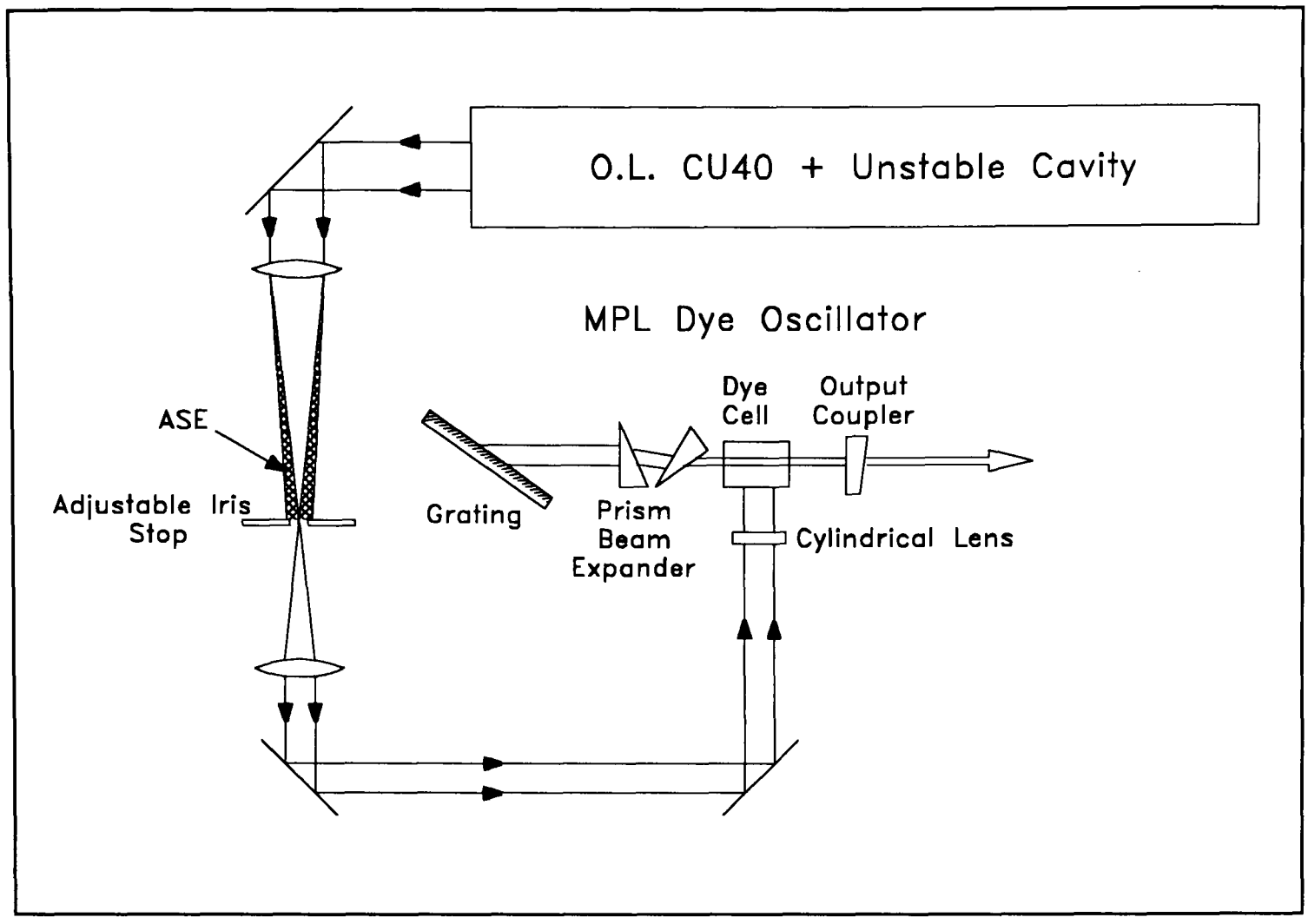


Figure 5.3 : The ASE component present in the CVL beam may be successfully removed by a suitable aperture placed at the common focus of the beam-shaping telescope illustrated above.

MPL dye laser (figure 5.3), the effect of removing the ASE component on the dye laser performance was investigated. It was found that by closing the iris stop down, and removing the majority of the ASE, the dye laser output power increased by up to 20%. This suggests that spatially filtering the CVL before pumping the dye laser would be beneficial. However, when the CVL beam was spatially filtered using a 300 μm pinhole at the focus of a $f=500$ mm lens, it was found that, in addition to the ASE, some of the better mode-quality light was lost. This was due to CVL beam pointing dither, resulting from the random thermal refractive index variations in the air near the hot CVL plasma tube windows. Consequently, the efficiency of the dye laser in terms of the total available power decreased when spatial filtering was employed. In the following investigations, true spatial filtering was not implemented, although a large part of the highly divergent component of the ASE was removed by aperturing the pump beam slightly, for safe and convenient beam delivery.

5.2.4 Pump Beam Geometry

In the case of transverse pumping geometries, the line focus produced in the dye, either by imaging the output of a tapered waveguide, or by cylindrical focusing, must fill the whole length of the dye cell. Experimentally, it was found that failure to fill the whole length of the dye cuvette resulted in a loss of efficiency. This is due to GSA and ESA at the signal wavelength occurring in the unpumped regions of the dye. This loss mechanism is also responsible for limiting the dye tuning range, especially toward the low wavelength end, where there is a significant overlap between the fluorescence and absorption bands. Here the high GSA and ESA at the signal wavelength was found to be sufficient to send many cavities below threshold.

5.2.5 Pump Beam Polarization

Dye laser oscillator cavities frequently favour one state of polarization due to the inclusion of intra-cavity polarization-sensitive elements; such elements include multiple prism beam expanders, Brewster-angled dye cells and diffraction gratings. The question of interest for maximizing laser performance, is whether the excited dye molecules diffuse rotationally from their initial excited orientation faster than they undergo stimulated emission.

According to Phillion [5.5], the interaction of most asymmetric dye molecules with polarized light can be described by a linear electric dipole oscillator model, in which the dipole is along one of the molecular axes. The orientational relaxation time for such dipoles in a solvent of viscosity η is accurately described by the Debye-Stokes-Einstein hydrodynamic model [5.6] :-

$$\tau_{ROT} = \frac{\eta V_m}{kT} , \qquad (1)$$

where V_m is the volume of the rotating dipole. This relationship has been verified for laser dyes [5.7] by passing the vertically polarized, picosecond output of a frequency doubled, modelocked Nd:YAG laser through a dye cell. A small fraction of the light passing through the dye cell is subsequently retro-reflected by a quarter wave plate,

and used as a circularly polarized probe. By moving the position of the quarter wave plate and measuring the intensities of the vertical and horizontal components of the return probe beam, the rotational relaxation time can be deduced.

In the case of Rhodamine 6G in methanol, theory predicts an orientational relaxation time of 100 ps, which is of the same order of magnitude as the lifetime against stimulated emission, as predicted by a rate equation analysis [Appendix 5.1]. This indicates that the dipoles retain some memory of their initial excitation orientation before they undergo stimulated emission. In addition, several mechanisms have been proposed which suggest that excited dye molecules may retain their polarization state for longer times (nanoseconds) than that predicted by the Debye-Stokes-Einstein model. These mechanisms include electrostriction whilst the pump laser pulse is present [5.8], and an enhancement of the solvent viscosity because of dye-solvent hydrogen-bonding [5.7]. This suggests that the memory of the dipoles' initial orientation is not completely lost before stimulated emission occurs, and that the maximum efficiency from a dye laser can be obtained only when the pump beam polarization is aligned to the preferred polarization axis of the oscillator.

The experimental arrangement used for the investigation of polarization effects in CVL-pumped dye lasers is depicted in figure 5.4. The 42 mm CVL beam was polarized using a 2" cemented Glan-Taylor polarizing cube mounted in a rotation stage, so as to enable the easy selection of either horizontally or vertically polarized pump beams. To avoid polarization effects experienced with dichroic and dielectric beam steering mirrors, anti-reflection coated right-angled prisms were used for pump beam delivery. Strictly, the use of total internal reflection in the prisms causes a phase change between the two orthogonal polarization components, which lie along the principal axes of the internally reflecting plane, but this is not of concern here. The dye oscillator cavity used for the polarization investigation contained two Brewster-angled prisms; these prisms act both as a dispersive element, and to define a preferred polarization axis - the two prisms present no loss for horizontally polarized light, but offer an 80% round trip loss for vertically polarized light.

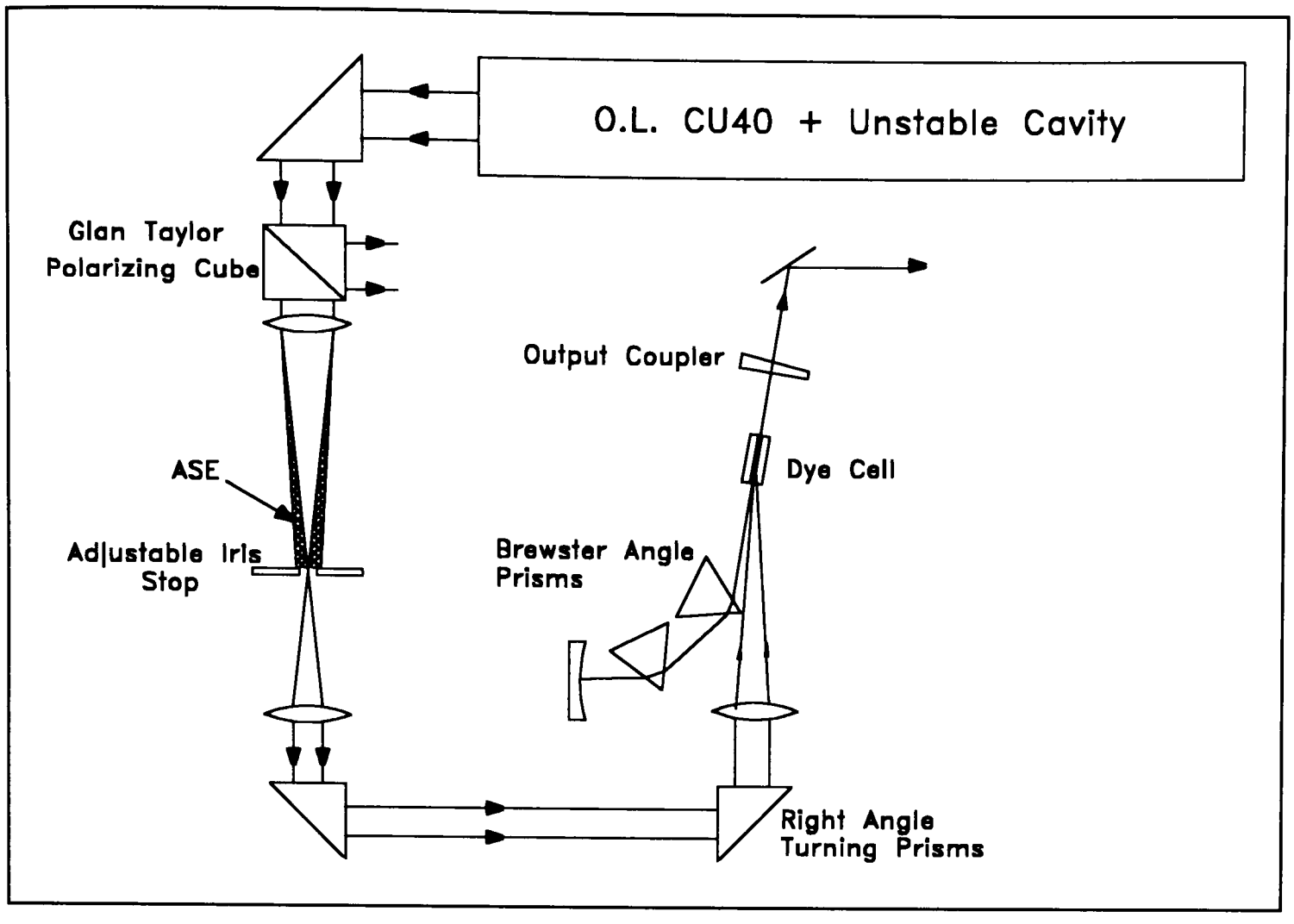


Figure 5.4 : Dye oscillator cavity used for pump beam polarization investigations.

By using reflective neutral density filters to attenuate the CVL beam, the slope efficiency of the oscillator was recorded when pumped by horizontally and vertically polarized CVL radiation; the results are presented in figure 5.5. A similar investigation was performed with respect to matching and mis-matching the CVL pump beam polarization relative to the seed polarization in a transversely-pumped saturated-gain amplifier. The results, plotted in figure 5.6, are qualitatively similar to those of the oscillator investigations and there appears to be a 20-30% improvement in the output power when the polarizations are matched. In the case of transverse pumping geometry, this requires the plane of polarization to be orthogonal to both the pump and dye laser axes.

The CVL unstable cavity may be successfully modified to give a polarized output, either by the inclusion of a large polarizing cube in the rear leg of the cavity [5.9], or by means of a smaller (and less expensive) one incorporated into a cavity side arm (figure 5.7) - the latter was employed here to give an output beam with $>95\%$ of the output power being vertically polarized, and with a negligible drop in CVL output power.

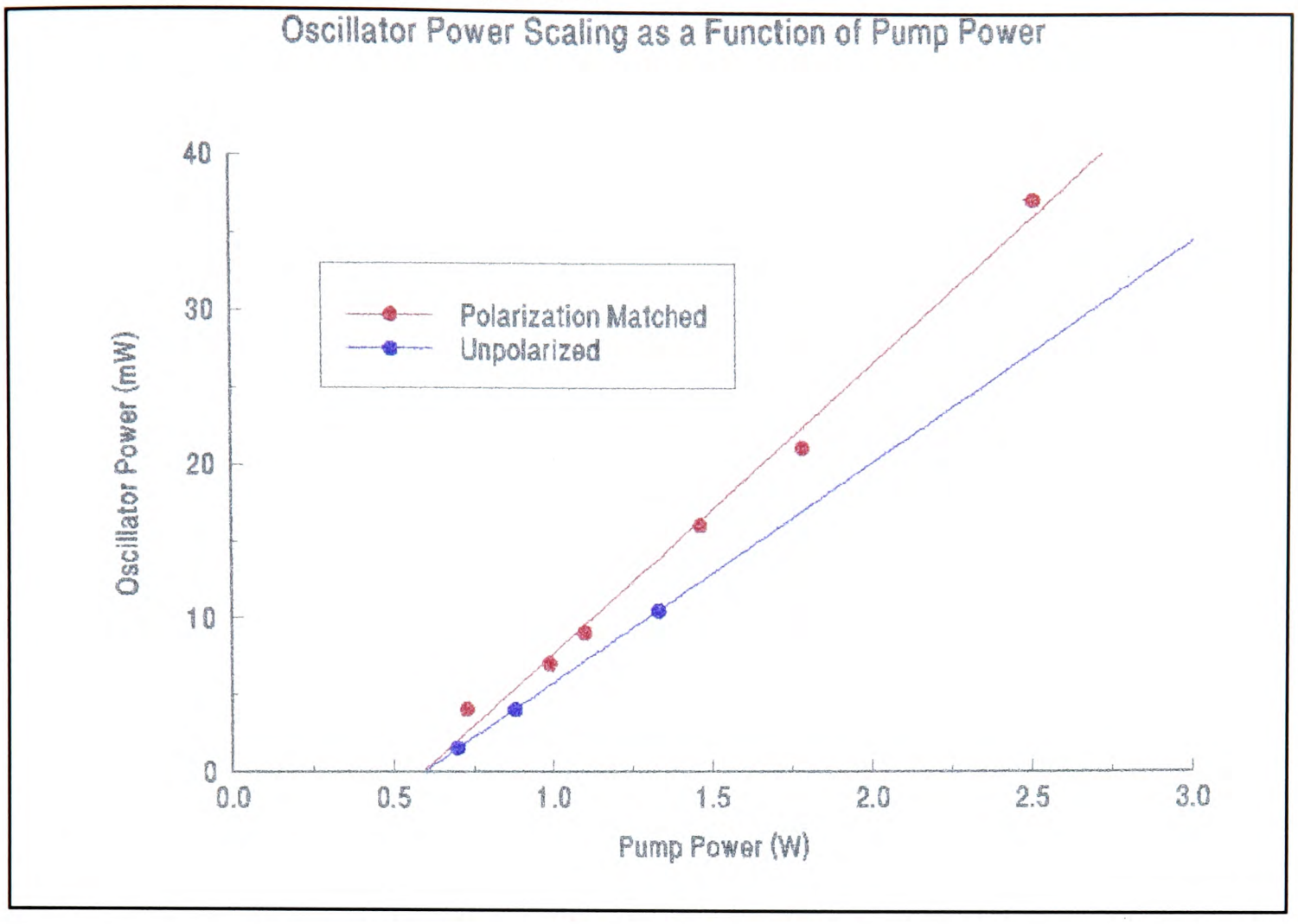


Figure 5.5 : Slope Efficiencies for a Brewster angled prism dye laser when pumped by (a) vertically polarized CVL, (b) horizontally polarized CVL.

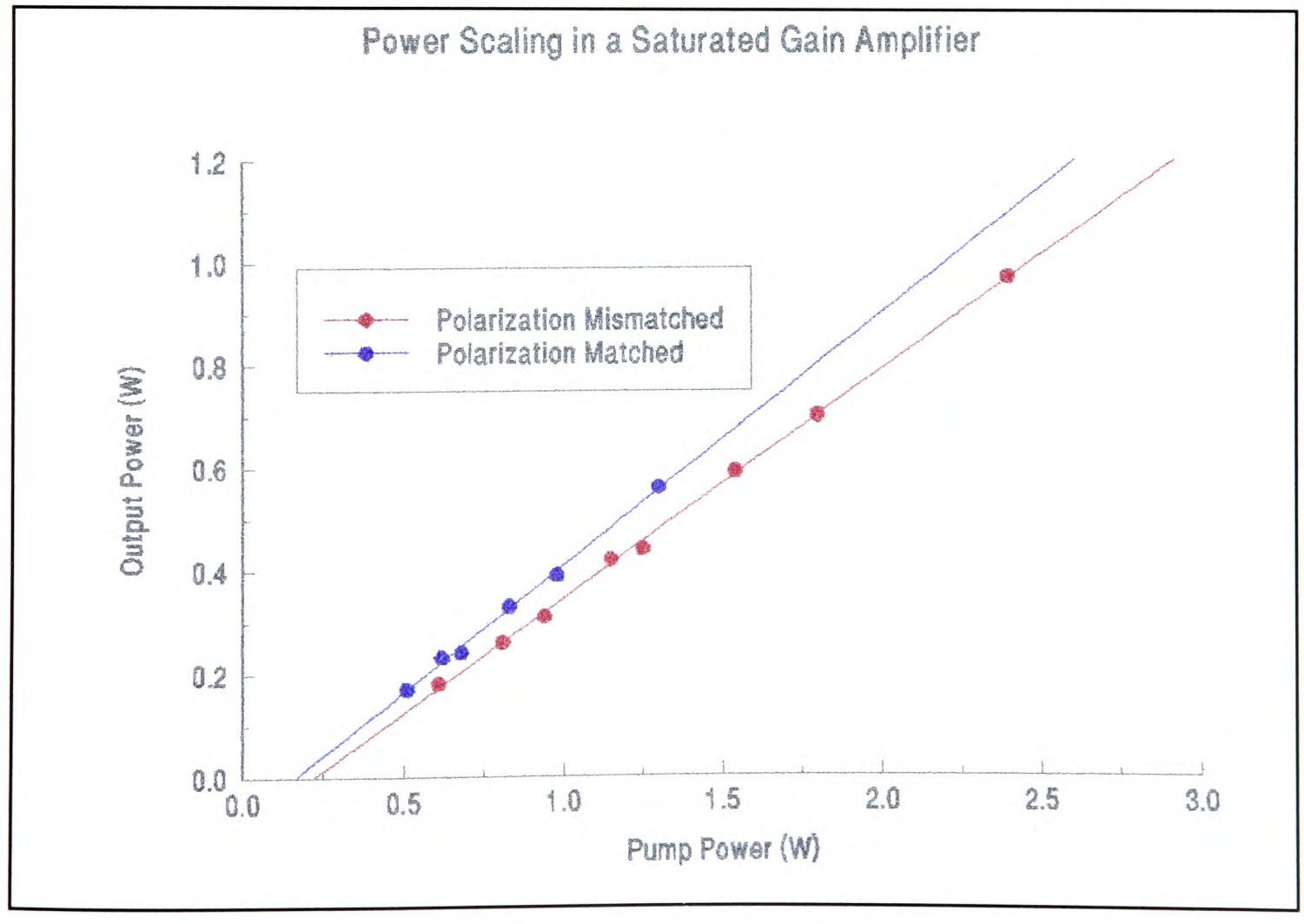


Figure 5.6 : Slope efficiencies of a saturated-gain optical dye amplifier when pumped by (a) vertically polarized CVL, (b) a horizontally polarized CVL. The seed input is vertically polarized.

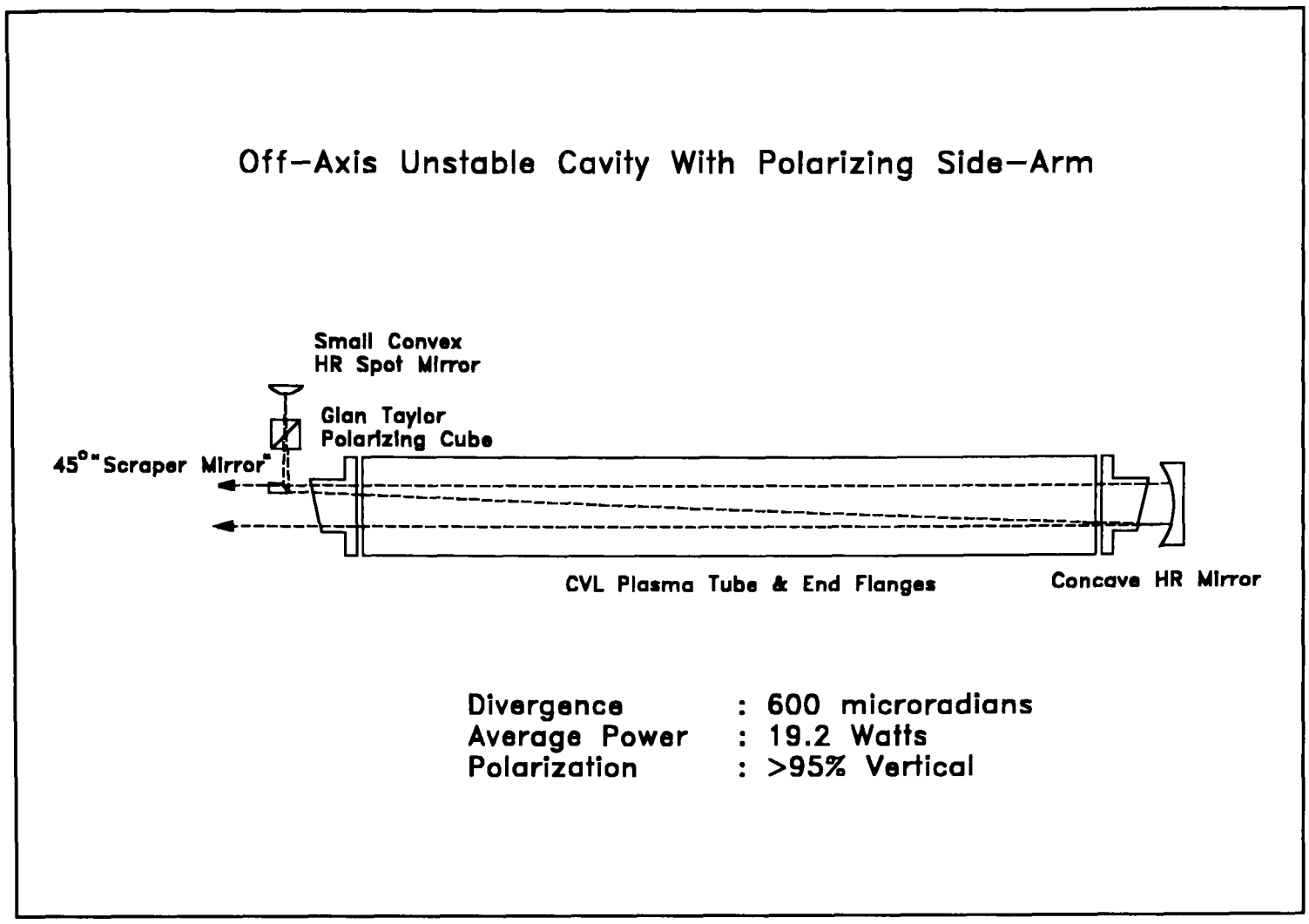


Figure 5.7 : The incorporation of a high power Glan-Taylor polarizing cube in a CVL side arm results in a (>95%) polarized output with a negligible drop in output power. Here the 45° "scraper mirror" is only ~3 mm in diameter, and is positioned at the tube wall in an off-axis unstable cavity geometry.

5.3 Dye Laser Optimization

5.3.1 General Considerations

As discussed in the previous chapter, the route to a high power narrow-bandwidth dye laser is via a master oscillator power amplifier (MOPA) configuration, in which the problem of ensuring narrow-bandwidth operation (determined by the oscillator) is decoupled from the high efficiency and high power generation (determined by the amplifier). There are two key parameters which affect the efficiency of such a system :-

1. the beamsplitter reflectivity, which determines the ratio in which the available pump power is split between the oscillator and the amplifier;
2. the oscillator output coupler reflectivity, which determines the Q of the oscillator cavity and influences oscillator parameters such as the cavity threshold, the slope efficiency, the pulse length, build-up time, and ASE content.

Usually, the optimization of such a MOPA system requires that the pump power delivered to the oscillator should be restricted to a value just above threshold for the oscillator section, and the remainder used for high efficiency amplification. However, when this criterion was adopted for beamsplitter optimization in a CVL-pumped dye laser, it was found that the oscillator was sent transiently above threshold for some fraction of the CVL pump pulse length. This then lead to a poor temporal overlap between the seed and pump pulses in the amplifier stage and, consequently, resulted in poor extraction efficiency, with most of the pump pulse length/energy being wasted as ASE. Figure 5.8 depicts a typical CVL pump pulse (with microstructure corresponding to the cavity round-trip time) and typical oscillator pulse shapes corresponding to different pump powers (determined by different beamsplitter reflectivities). Thus, a compromise must be found between delivering the maximum pump power to the amplifier, and, at the same time, ensuring that the oscillator has a suitable temporal profile and pulse energy to ensure efficient amplification.

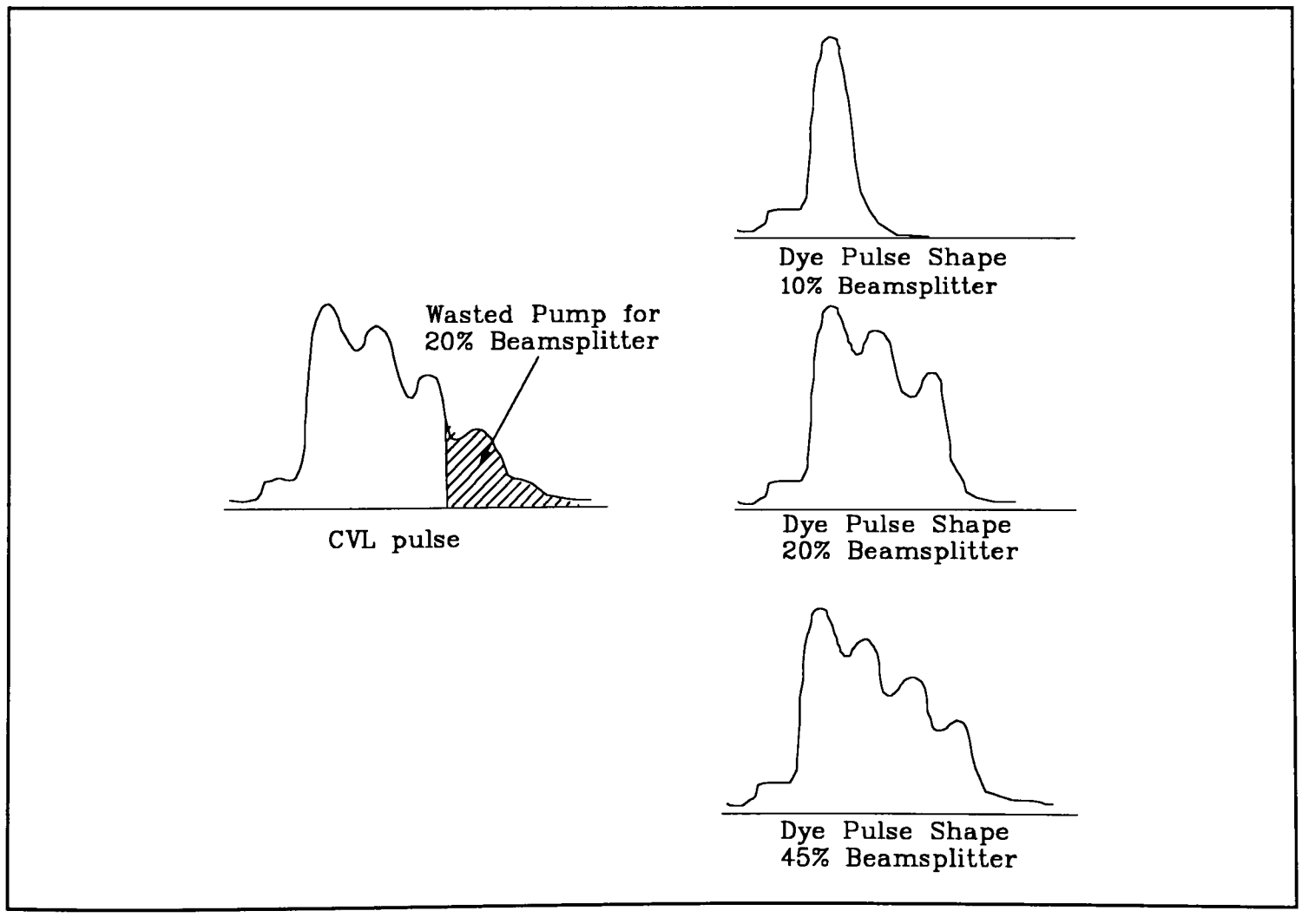


Figure 5.8 : Typical dye oscillator pulse shapes when pumped by a CVL

If the oscillator is of a closed-cavity design, then an additional degree of freedom for dye laser optimization is provided by the choice of output coupler reflectivity. The oscillator output coupling influences the pulse length, build-up time, cavity oscillation threshold, slope efficiency and ASE content of the oscillator beam independently of the beamsplitter reflectivity in a MOPA system. For high gain media, such as laser dyes, maximum efficiency is realized with large output coupling (typically, the 4% reflection off a quartz wedge is used to provide cavity feedback). However, by increasing the output coupler reflectivity, and decreasing the efficiency, the pulse length may be increased for a given pump power, which may result in more efficient amplification because of a better temporal overlap with the amplifier pump pulse. Clearly there is an optimum to be found, and ideally, the oscillator of a MOPA system should produce :-

1. Stable, narrow-bandwidth, tunable radiation with minimal ASE.
2. An output pulse shape with a similar temporal profile to that of the CVL pump.
3. Sufficient output power to saturate the gain in the amplifier stage(s).

Additionally, since the amplified beam profile is predominantly determined by the oscillator seed beam, attention must be paid to the method of pumping the oscillator, and to the optical coupling of the oscillator to the amplifier. The spatial profile of the oscillator beam is generally good in the case of longitudinally-pumped geometries, but in the case of transversely-pumped geometries, particularly single-sided pumping schemes (Figure 5.9), the beam has a poor spatial profile, reflecting the asymmetric gain profile (Figure 5.10). It is possible, however, to clean up the oscillator output beam before it is used to seed the amplifier. There are two proven methods: transport in multimode optical fibre [5.10], or spatial filtering. The use of an optical fibre has the advantage that less oscillator power is lost; however, the beam polarization may be scrambled by the fibre which results in inefficient polarization-matched amplification, and potentially disastrous consequences if the dye laser is to be frequency converted in a non-linear crystal. In the experiments conducted here, spatial filtering was used to clean up the oscillator beam before amplification, and the slight reduction in oscillator seed power was compensated by pumping the oscillator unit slightly harder.

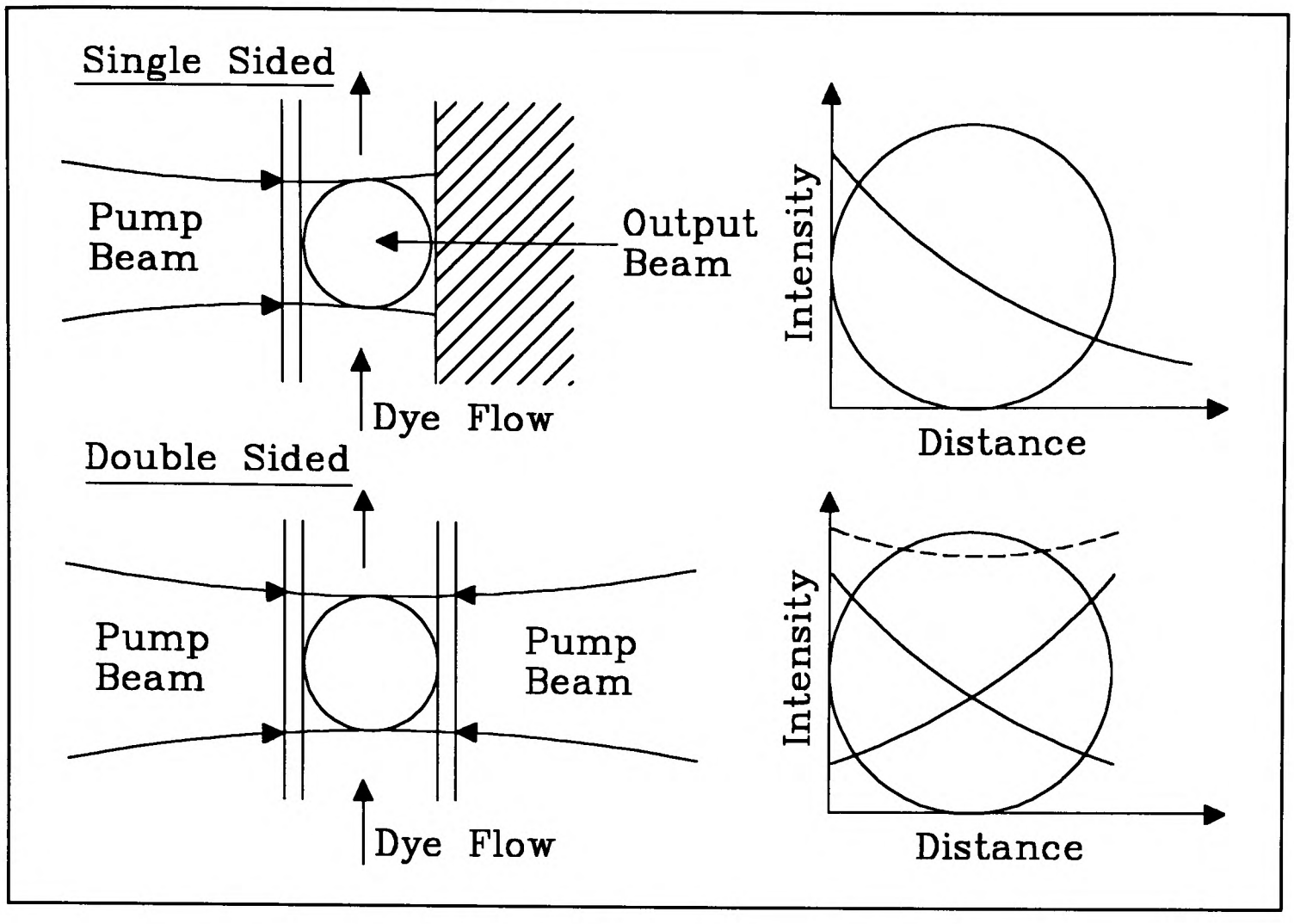


Figure 5.9 : Comparison of the gain profile in (a) single-sided and (b) double-sided transversely-pumped dye laser geometries.

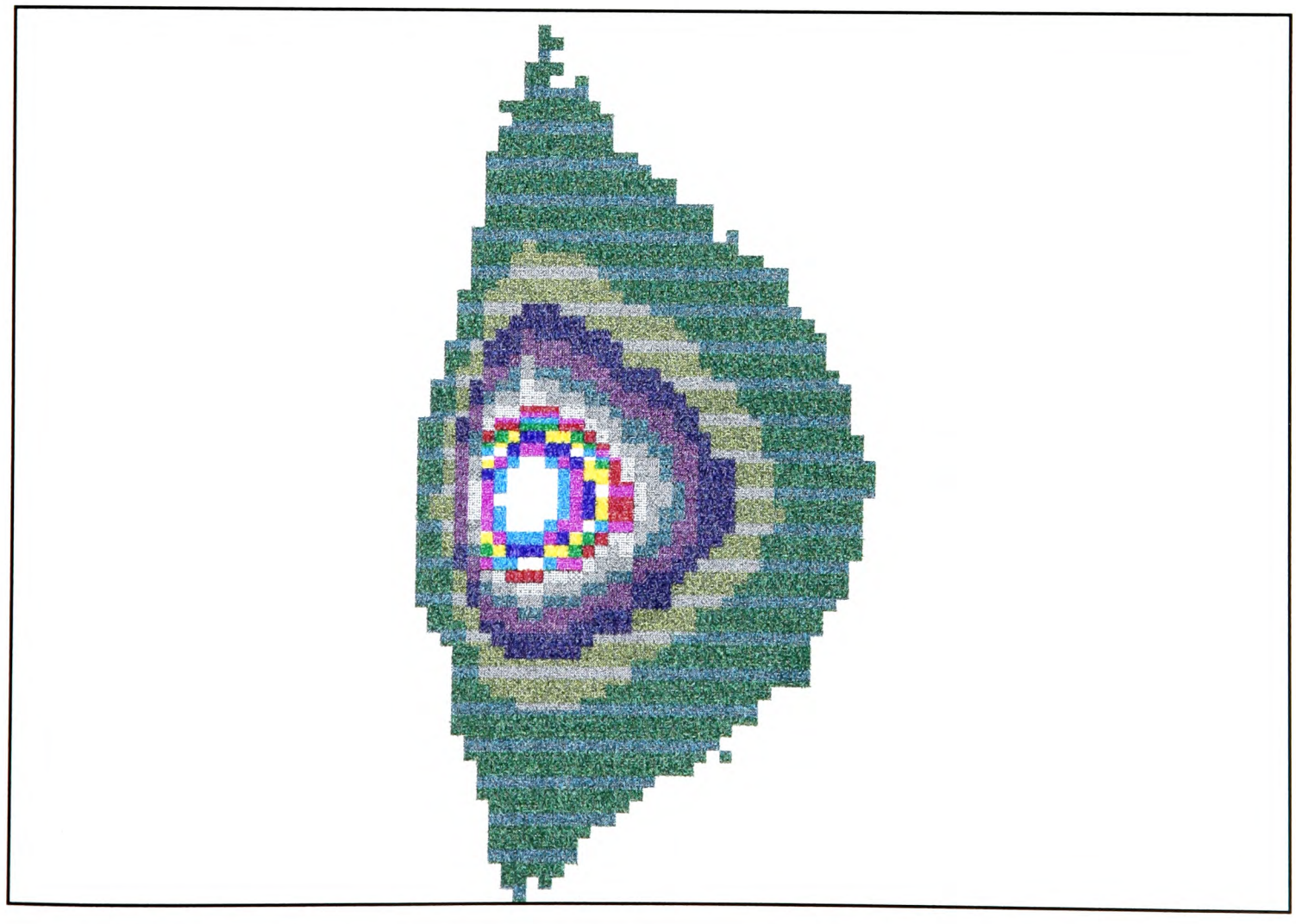


Figure 5.10 : Asymmetric beam profile arising from a single-sided transversely-pumped dye oscillator.

5.3.2 ASE in Pulsed Laser Systems

Pulsed dye lasers do not emit exclusively at the cavity-selected wavelength, but show a spectrally broad background of spontaneous emission which is amplified by the gain medium (ASE). Generally, in a pulsed dye laser, two kinds of ASE can be distinguished :-

1. A first component which is released immediately after excitation.
2. A second component which coincides with the build-up of the optical feedback in the oscillator cavity.

The first component of the ASE is easily suppressed by an appropriate delay between the excitation of the oscillator and the amplifier. Here, an optical delay line can be incorporated into the pump beam path to the amplifier, such that the excitation of the amplifier coincides with the arrival of the oscillator seed pulse (after the oscillator build-up time). The second component of the ASE is more difficult to remove, and, in general, requires some form of spectral filter between the oscillator and the amplifier. This is realized in the design of the Lambda Physik pulsed dye laser systems (FL2000 & LPD 3000 series), where a diffraction grating is used to couple the oscillator to the dye laser amplifier in the patented LambdaPure© configuration.

In practice, however, several techniques have proved useful in suppressing ASE :

1. The use of closed-cavity rather than open-cavity designs.
2. Anti-reflection coating of all intra-cavity components which may cause unwanted optical feedback, such as dye cell windows, and the back surfaces of the beam-expanding prisms.
3. Increasing the cavity Q by decreasing the output coupling, thus making conditions more favourable for lasing.
4. Spatially filtering the oscillator output - the ASE does not focus as tightly as the coherent laser output, and can so be removed before amplification.

5. Rotating the pump line focus relative to the oscillator axis - the direction of the ASE is determined by the orientation of maximum gain, and so the ASE will follow the pump line rather than follow the laser output. The ASE will then walk away from the laser output and may be effectively removed by a crude mask before amplification.

A novel technique devised by the present author capitalizes upon the fact that the ASE has random polarization, whilst the oscillator frequently has a preferred polarization. By inserting a polarizing cube aligned for the preferred cavity polarization in front of the output coupler, ASE of the wrong polarization will be prevented from being output and, equally importantly, the polarizing cube prevents ASE of the wrong polarization from being reflected back into the cavity, where it will be amplified, and depopulate the gain available for laser oscillation. This technique has been employed with great success both in suppressing ASE and in enhancing dye laser conversion efficiency.

5.3.3 Choice of Grating Material

Conventionally, dye laser diffraction gratings are aluminium-coated to allow dye laser operation in the UV and blue region of the spectrum permitted by excimer or frequency tripled Nd:YAG pumping. In the case of CVL-pumping, however, the 511nm pump line restricts operation to dyes lasing at wavelengths greater than ~520nm. Thus, it may be beneficial to use materials which offer a higher reflectivity than aluminium in the red region of the spectrum, even if they do not offer the same UV spectral coverage.

From figure 5.11 [5.11], silver can be identified as a potential grating material which offers a higher reflectivity than aluminium in the CVL-pumped dye laser operational range (> 520nm), despite not offering the UV spectral coverage. To see what effect the grating material has on dye laser performance an over-coating of 1000Å of silver was evaporated onto an aluminium holographic diffraction grating

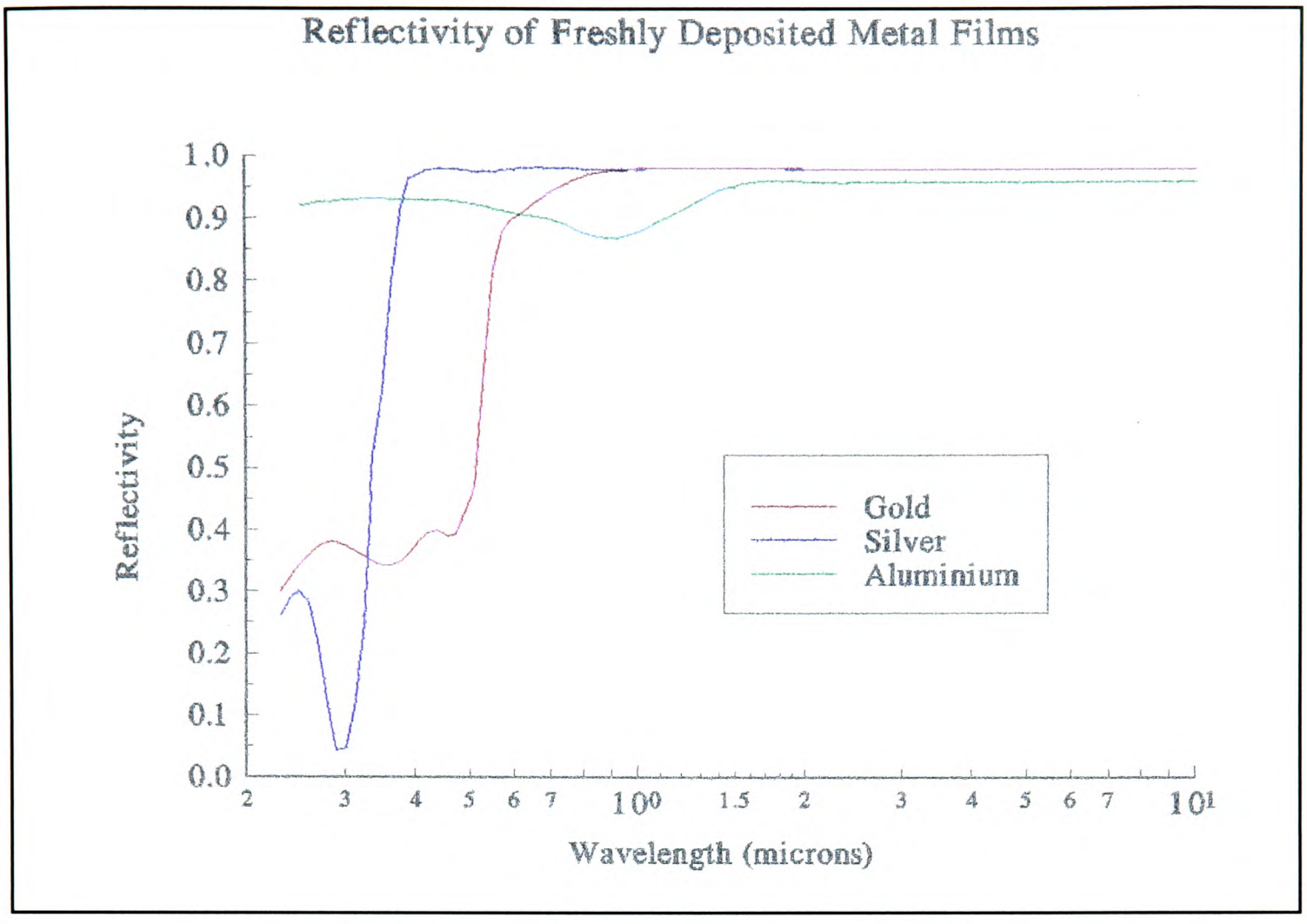


Figure 5.11 : Spectral response of potential dye laser grating materials [5.11]. Whilst aluminium offers a good response in the visible, and into the UV, silver is a better candidate at the restricted CVL-dye range.

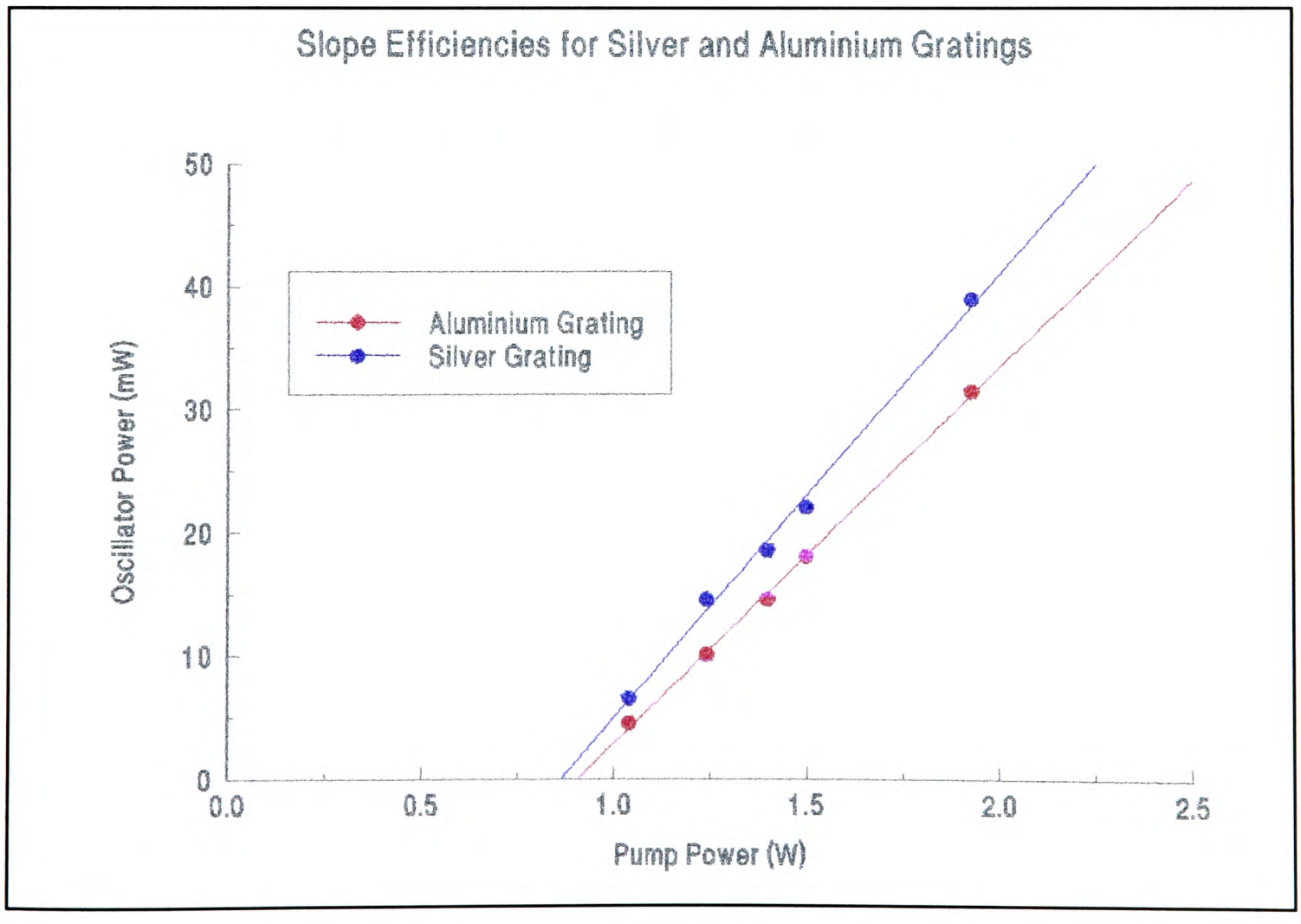


Figure 5.12 Slope efficiencies of a CVL-pumped HMPGI dye oscillator with (a) an aluminium-coated grating and (b) a silver-coated grating.

(2400 lines/mm) under vacuum. The slope efficiencies of a hybrid multiple prism grazing incidence (HMPGI) oscillator incorporating the holographic diffraction grating, before and after coating, were measured. As is evident from figure 5.12, there was nearly a 20% improvement in the slope efficiency, and a slight reduction in oscillation threshold, when the grating is silver-coated. The main problem encountered with the silver grating was that of atmospheric oxidation, and a further overcoat of magnesium fluoride was found necessary for long term operation with the grating. Another attractive grating material may be gold, which offers a similar reflectivity in the red as silver, but does not extend so far into the blue. Indeed, gold may be a preferred alternative since it is resistant to corrosion, although, that option has not been investigated here.

5.4 Characterization Measurements

In all of the following characterization measurements made on commercial or laboratory-built dye lasers, slope efficiency measurements were made using calibrated neutral density filters to attenuate the CVL pump beam, and the laser powers were measured using a thermopile-type power meter (Laser Instrumentation Model 9000). Pulse lengths and build-up times were examined using fast response vacuum photodiodes (ITL TF085M20UV) and displayed on a 500 MHz digital oscilloscope (Tektronix 2440), which was, in turn, connected via an IEEE interface to a PC host for data archiving and analysis.

The frequency bandwidth was measured by focusing the fringes of a scanning Fabry Perot interferometer (Technical Optics FPI-25) onto a pinhole at the input of a photomultiplier. The pinhole size used was more than an order of magnitude smaller than the diameter of the central order fringe, so as not to inhibit the instrumental resolution. The photomultiplier signal was displayed on a digital oscilloscope (Tektronix 2440), which was connected to a computer for data archiving. Frequency jitter and drift measurements were made using a Burleigh Wavemeter connected to a PC host : the wavemeter shown schematically in figure 5.13 splits the input beam between a Fizeau wedge and a solid Fabry Perot etalon. The parallel

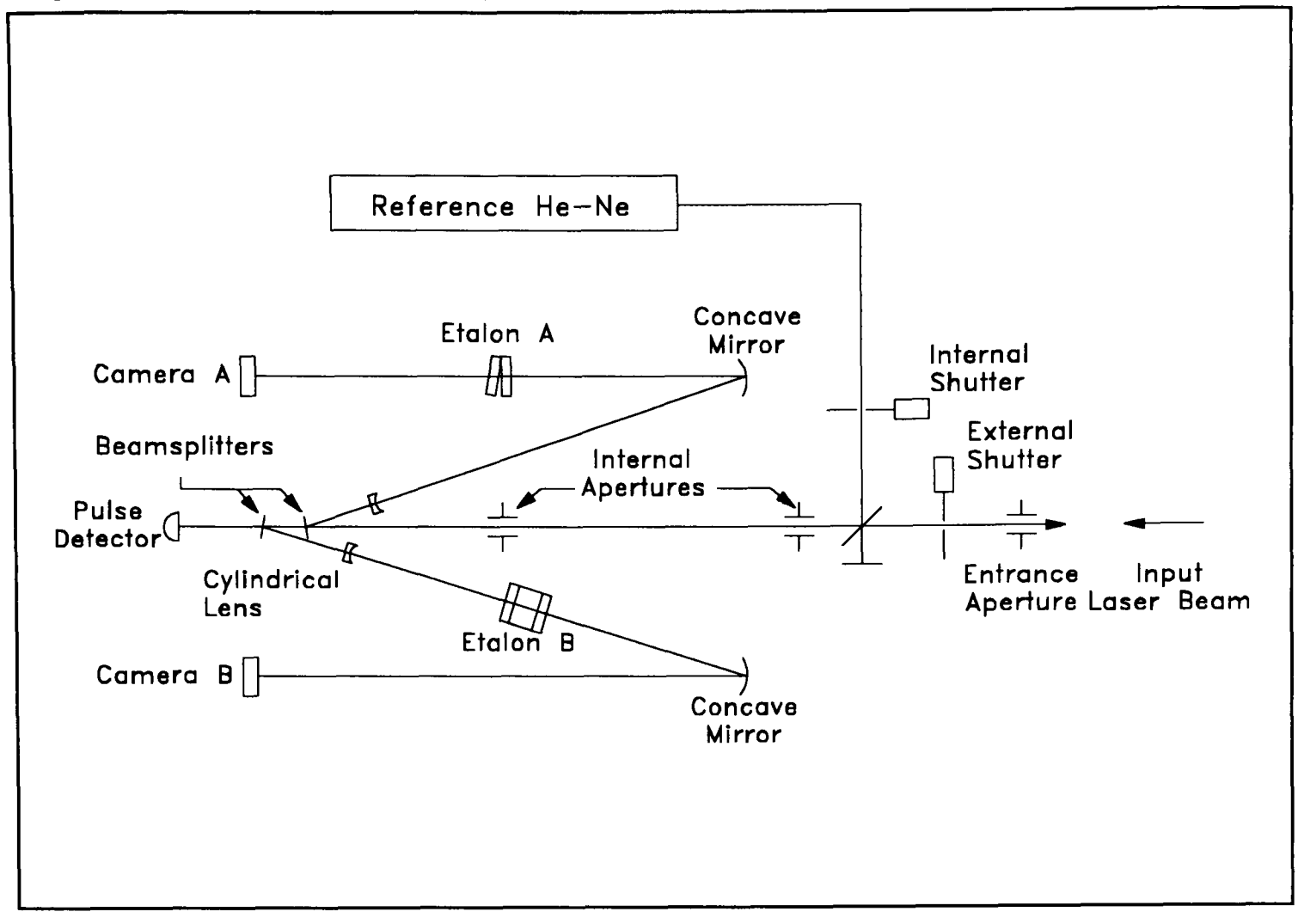


Figure 5.13 : Optical layout of the Burleigh wavemeter, illustrating the Fizeau wedge and Fabry-Perot etalon used for wavelength calculation.

fringes from the wedge are imaged onto a linear CCD array, and provide wavelength data with an accuracy to 1 in 10^4. This wavelength information is then used to interpret the fringes from the etalon (also imaged onto a CCD linear array), so removing the ambiguity with respect to etalon fringe orders. The etalon fringe pattern provides wavelength information with an accuracy better than 1 part in 10^6, which corresponds to an instrumental resolution better than 1 GHz. The spectral content of the dye laser beams was investigated using a remote, computer-controlled 1 m monochrometer, to which the laser beams were transported by a 1 mm diameter plastic optical fibre. The monochrometer offered a dynamic resolution of 2×10^5 and a frequency resolution of 5 GHz (tested using a He-Ne laser), and so, when scanned across the fluorescence band of the dye, it enabled any ASE profiles to be identified along with the laser output.

5.4.1 Beam Divergence Analysis

In addition to its intrinsic diffraction-associated divergence, the output from many types of pulsed dye laser oscillator shows an extra divergence due to lensing

arising from the refractive index gradients in the dye medium [5.12]. Indeed, the refractive index profile of the pumped dye region makes the medium look like a concave lens, and causes the laser cavity to become unstable. It is this unstable cavity action which, in part[1], gives rise to the excellent beam quality characteristic of many pulsed dye lasers (in much the same way as an unstable cavity improves the divergence characteristics of a CVL). The refractive index lensing does not affect the minimum spot size to which the laser beam can be focused, but does cause the laser output to diverge with an appreciable cone angle. To ensure that only the intrinsic component is examined, a novel alignment technique was devised by the present author to overcome errors associated with non-collimation and any intrinsic astigmatism in the laser beam.

It can be shown [Appendix 5.2] that for a Gaussian beam with a beam waist, w_1, a distance d_1 from a lens of focal length f, the beam is focused to a new waist, w_2, beyond the lens by a distance d_2 where :-

$$\frac{1}{w_2^2} = \left(1-\frac{d_1}{f}\right)^2 . \frac{1}{w_1^2} + \frac{1}{f^2} . \left(\frac{\pi w_1}{\lambda}\right)^2 , \qquad (2)$$

and

$$d_2 - f = \frac{(d_1 - f).f^2}{(d_1 - f) + \left(\frac{\pi w_1}{\lambda}\right)^2} . \qquad (3)$$

From (3) it can be seen that when $d_1 = f$, the location of the focused beam waist w_2 moves into the focal plane of the lens, and also, from (2), we see that the spot size becomes independent of the initial beam waist location, and :-

---

[1] Another contributory factor in the good beam quality radiation from dye lasers is that the pumped active region is usually long and narrow, which forces a long Rayleigh length on the dye laser beam, and correspondingly results in a low divergence Gaussian beam.

$$w_2 = f.\left(\frac{\lambda}{\pi w_1}\right), \tag{4}$$

where $\lambda/\pi w_1$ is the diffraction limited beam divergence. Thus, if a beam waist formed by the dye laser can be located, the intrinsic divergence of the dye laser may be established by measuring the spot size in the focal plane of a lens of focal length f, placed a distance f from the beam waist.

The experimental arrangement is depicted schematically in figure 5.14. The dye laser beam is collimated by a telescope formed by two convex lenses (f=5cm), and spatially filtered at their common focus. The resulting circular beam is focused onto a CCD camera located in the focal plane of a lens f, positioned a focal length away from the collimation telescope as shown below. The collimation telescope is then adjusted to give the minimum spot size / maximum intensity on the CCD camera; in this position the telescope exactly collimates the dye laser beam, and the

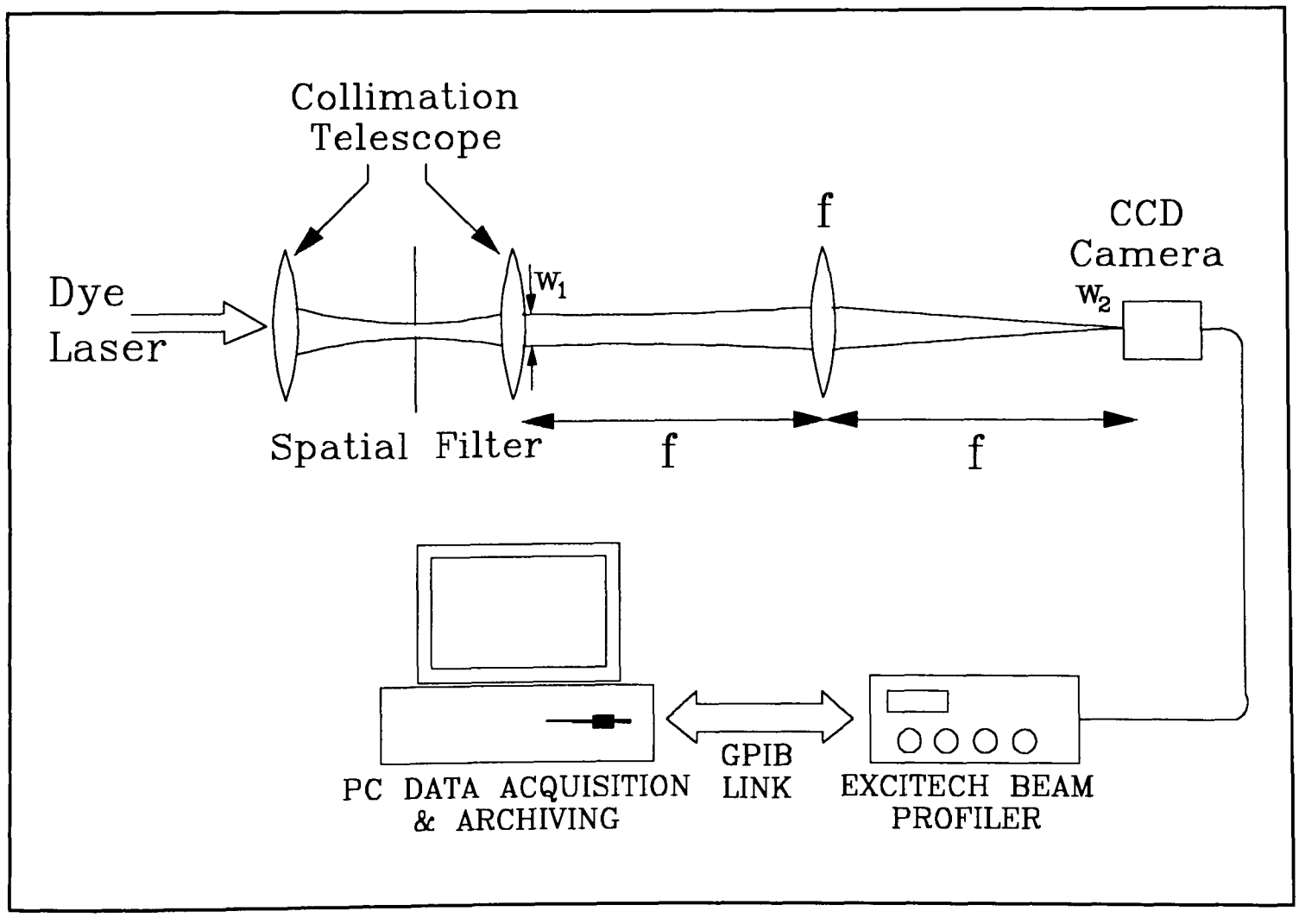


Figure 5.14 : The experimental layout used for the analysis of dye laser beam divergence.

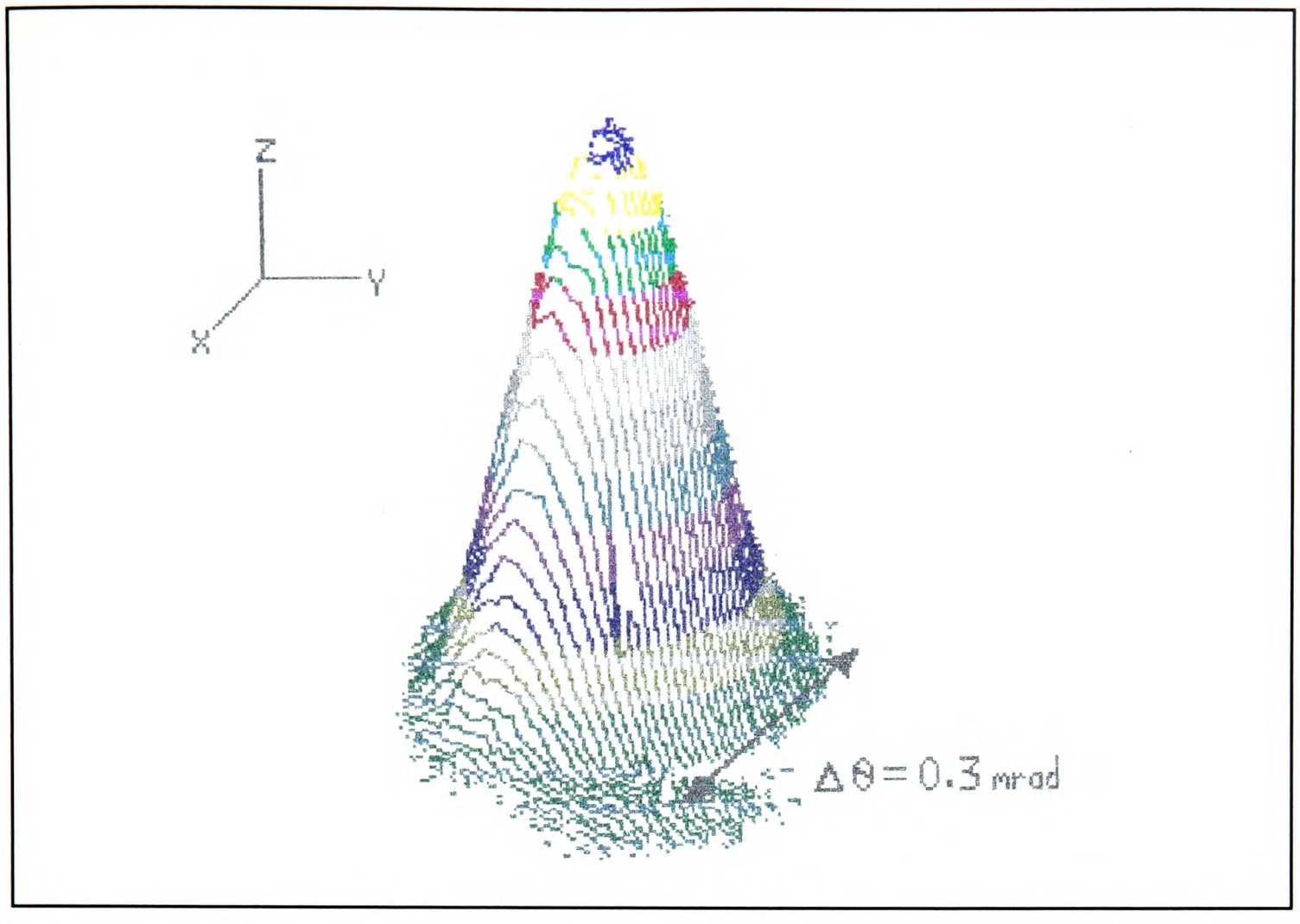


Figure 5.15 : Spatially filtered dye laser beam profile used for setting up the beam analysis lens positions.

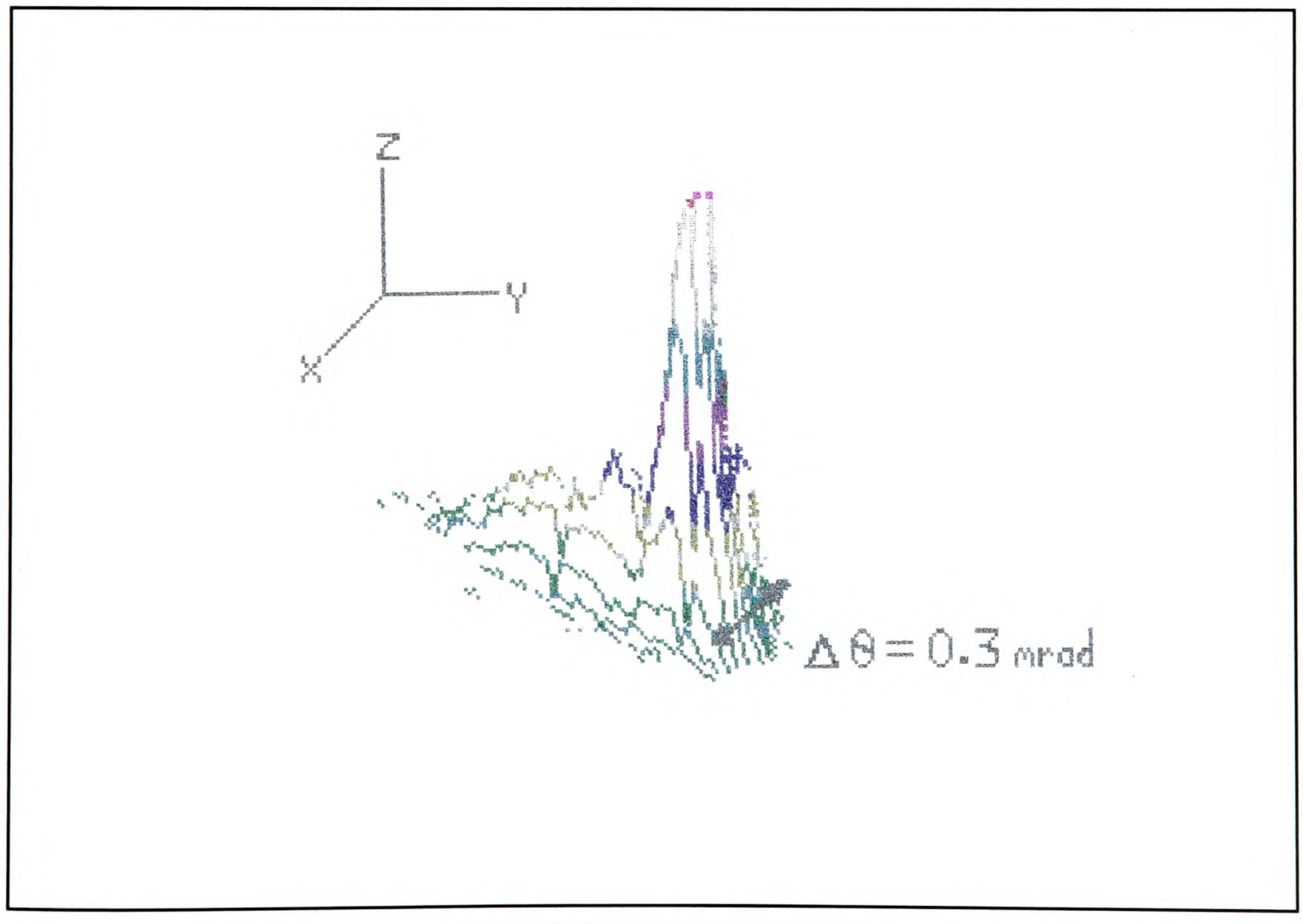


Figure 5.16 : The same dye laser beam as shown above, but this time, without the spatial filter.

beam waist w_1 is located at the exit plane of the telescope. Once collimation has been achieved the spatial filter can be removed and the true dye laser far-field profile can be examined. This technique allows the analysis of laser beams, which may be of irregular shape and / or possess an astigmatic component, for which it would otherwise be difficult to identify the true waist, w_2. Figure 5.15 shows the far field pattern of a spatially-filtered dye laser beam used for collimation purposes, and figure 5.16 shows the far field pattern of the same laser beam, but without the spatial filter in place. The near field pattern of the dye laser was also recorded by imaging the waist w_1 onto the CCD, so enabling the beam diameter $\times$ divergence product to be calculated.

The laser beams analyzed must be heavily attenuated, so as not to saturate the CCD camera, which operates in the nanojoule/pulse regime. This was accomplished by using multiple high reflectivity dielectric mirrors and reflective, neutral density filters to attenuate the dye laser beams under analysis to an appropriate intensity. Care was taken to ensure that neither thermal lensing induced by the attenuation optics, nor any astigmatism in the collimation/focusing optics, affected the recorded beam profile. The CCD camera used was a 256×256 array connected to a frame grabbing unit (Excitech Profiler 256), which was, in turn, connected to a PC for data analysis. PC software allowed cross-sectional analysis of the recorded beam profiles, and facilitated Gaussian and super-Gaussian curve fitting to the profiles, in addition to providing $1/e^2$ divergence measurements.

5.5 Commercially Available Pulsed Dye Lasers

Commercially available pulsed dye laser systems are primarily designed for use with Nd:YAG or excimer pump lasers, both of which are generally characterized by low repetition rates, typically tens of Hertz, and large pulse energies, typically of order 1 J. To optimize these lasers for use with a CVL pump, characterized by high repetition rate and low pulse energies, requires not only a change of the reflectivity of the optical components, but changes to the dye circulation system, and a rethink of the oscillator and amplifier design. In the following sections, the application of

the aforementioned laser physics is applied to three commercial systems, and the modifications necessary for CVL pumping are detailed.

5.5.1 The Russian Dye Laser LZhI-504

The LZhI-504 is a commercially available unit in the former USSR; the particular unit evaluated here was modified at the Institute of Spectroscopy, Troitzk to include some very attractive calibration features. The unit is solely an oscillator based upon a modified Hänsch design, and so amplification to high powers must be performed externally. A schematic diagram of the transversely pumped cavity is shown in figure 5.17. A multiple prism beam expander and an intra-cavity lens expand the oscillator flux onto a ruled aluminium grating (1200 lines/mm) mounted in first order Littrow configuration. The prism beam expander consists of a total of six prisms (Theta=30°, n=1.73), each mounted at Brewster's angle relative to the incident oscillator flux, and are designed for orthogonal beam exit from the anti-

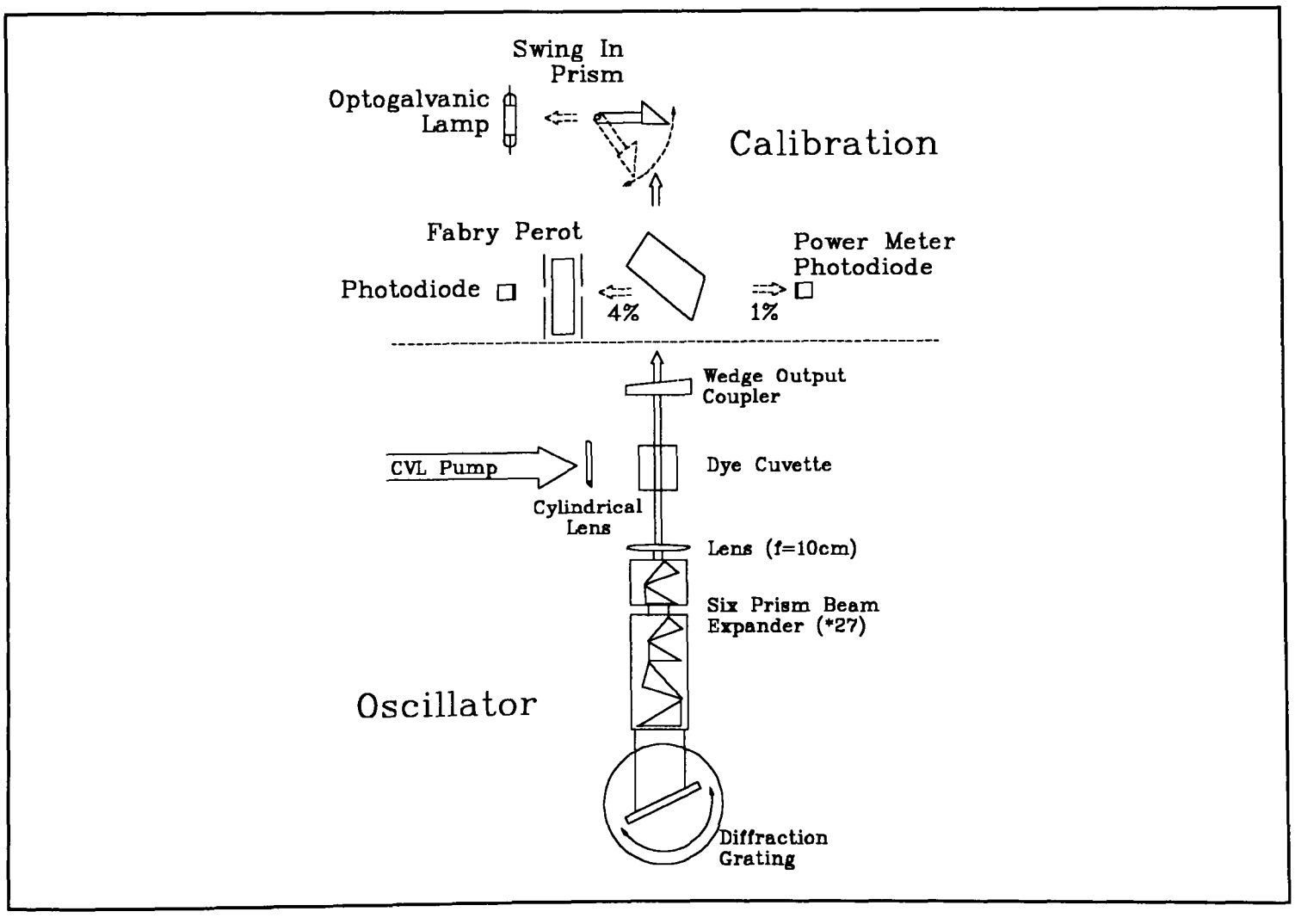


Figure 5.17 : The optical layout of the LZhI-504 dye laser and the on-board calibration facilities.

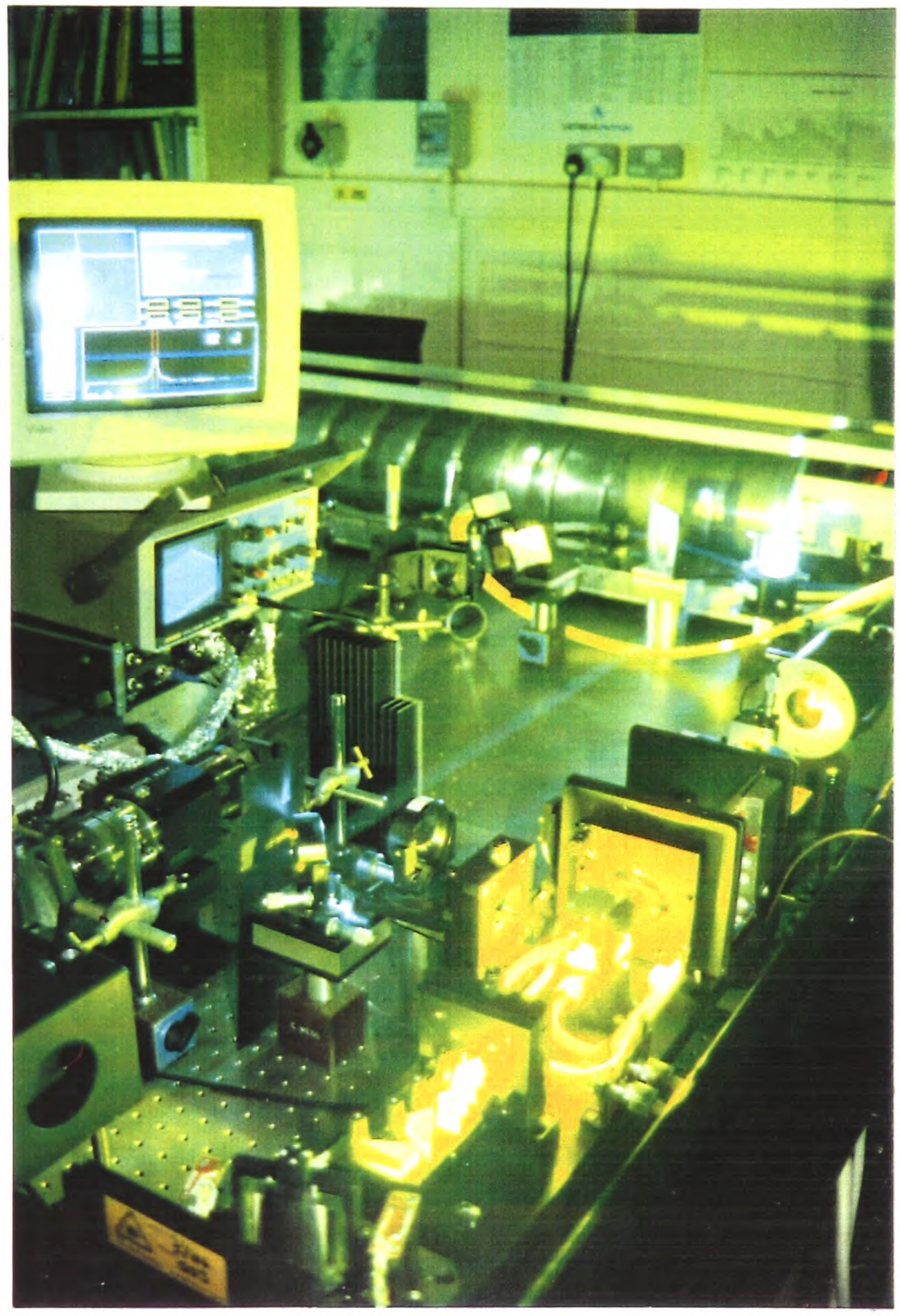


Plate 5.1 : The CVL-pumped LZhI-504 dye oscillator; the six-prism beam expander can be clearly identified in the foreground. The remainder of the plate contains the CVL and the associated diagnostic equipment used in characterizing CVL-pumped dye lasers.

reflection-coated back faces. Unfortunately, besides providing a beam-expansion ratio of 27, the prism beam expander defines the preferred polarization axis of the cavity to lie in the horizontal plane, which does not lend the oscillator to polarization-matched pumping. The purpose of the intra-cavity lens is two-fold : firstly, the lens serves to collimate the output beam by compensating for the thermal lensing in the dye cell and, secondly, the lens enhances the efficiency [5.13] of the oscillator by focusing the grating flux into the 0.5 mm wide dye cuvette.

Tuning of the oscillator is achieved by rotating the grating about the vertical axis. This may be effected crudely by using a screw drive or, more accurately, by using a purpose built electrodynamic drive [5.14]. The electrodynamic drive exploits the magnetic field generated by a pair of Helmholtz coils to rotate the grating; small sense coils mounted on the grating complete a feedback loop and enable the fast and accurate selection of wavelength. A purpose-built microprocessor control unit, utilizing a 14-bit analogue to digital converter, controls the grating magnetic field and enables wavelength steps of 1 GHz over a 30 nm range (typically the range of one dye).

A very attractive feature of the device is provided by the on-board calibration facilities, which make use of both optogalvanic and Fabry Perot referencing. A small swing-in prism diverts the output beam through a small argon hollow cathode discharge lamp, from which an optogalvanic signal is derived. Argon is rich in transitions across the visible spectrum, containing over 200 lines in the 500-700 nm region alone, which may be used as absolute frequency markers for calibration purposes. Figure 5.18 illustrates the optogalvanic peaks detected over the operating range from 565 nm to 595 nm of the Rhodamine 6G dye. Additionally, a small fraction of the dye laser output ($\sim 1\%$) is directed to a solid etalon (FSR$=3\text{cm}^{-1}$), and the resulting fringe pattern is recorded using a silicon photodiode as the wavelength is scanned. The recorded fringes provide an accurate means of interpolation between the absolute optogalvanic frequency markers, so that a wavelength scale may be

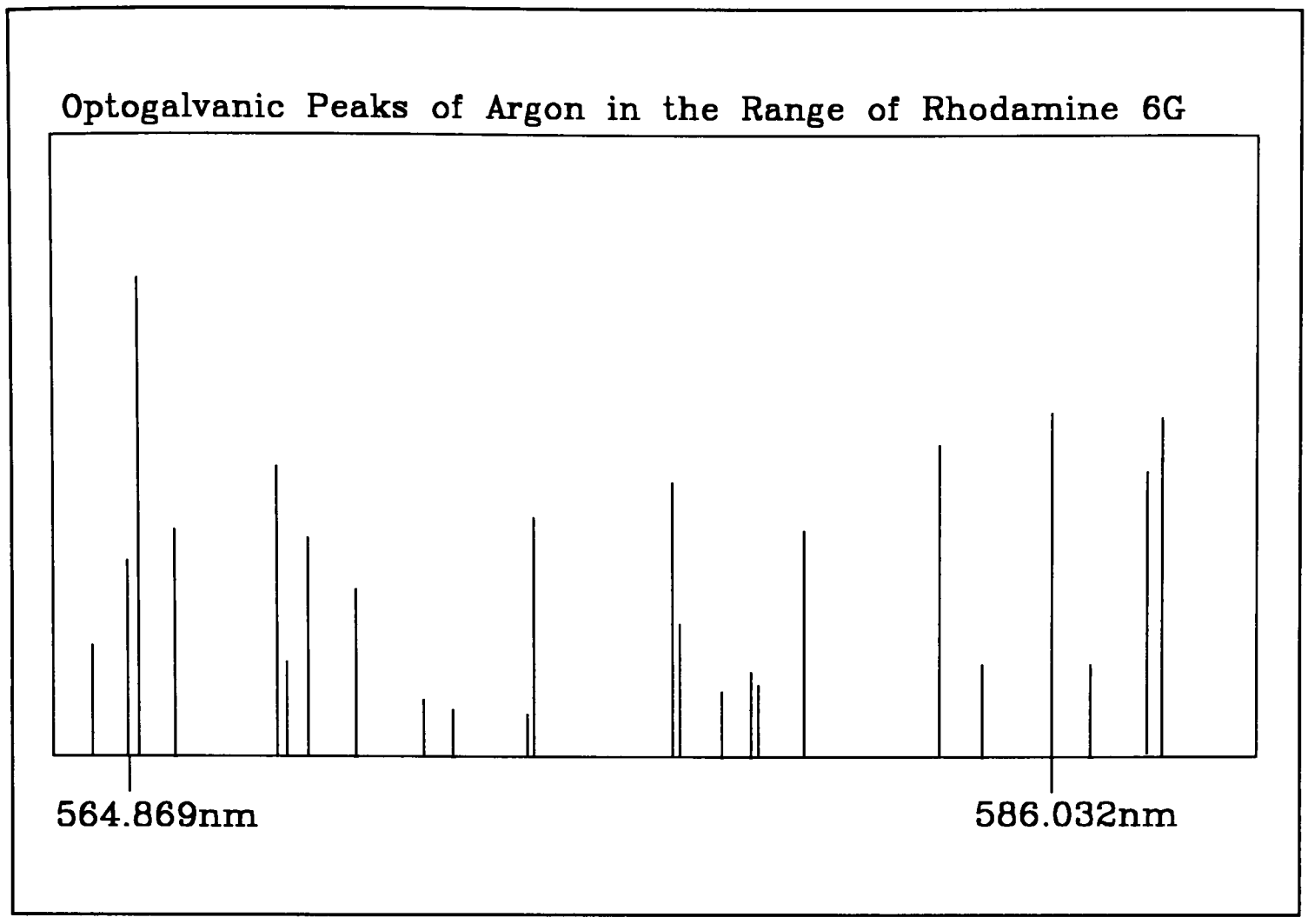


Figure 5.18 : Argon transitions detected in the lasing range of Rhodamine 6G which may be used for optogalvanic calibration.

defined. Calibration at dye laser power-up is achieved by scanning the laser over the 16384 (2^{14})-step range of the AD converter, whereupon the wavelength scale is calculated automatically by the control unit, using a polynomial fit algorithm to interpret the optogalvanic and etalon fringe data.

The limiting aperture in the LZhI-504 dye laser for the CVL pump beam is defined by the 10 mm long dye cell, and so the 42 mm wide CVL beam was conveniently demagnified by a $\times 0.25$ $f=500$ mm, $f=12$ mm Keplerian telescope external to the dye laser enclosure. The use of such a telescope enabled the convenient removal of the CVL ASE by a 500 μm pinhole placed at the telescope focus, and when the LZhI-504 was operated with Rhodamine 6G dye, transmit yellow-reflect green dichroic beam-steering mirrors were used in the pump beam path to remove the 578 nm CVL component.

The efficiency and bandwidth of the LZhI-504 were found to be critically dependent upon the alignment of the cavity, and so a careful alignment procedure was

devised:

1. Remove the intra-cavity prisms, lens and output coupler.
2. Rotate the cuvette until a single spot output is achieved from the feed-back off the grating.
3. Insert the output coupler, and align for maximum lasing output power.
4. Adjust the pump beam cylindrical focusing for optimum lasing.
5. The prism beam expander is aligned externally to the cavity using a horizontally polarized He-Ne laser. The prisms are inserted and secured one at a time, such that there is no reflection off the front surface (so ensuring alignment close to Brewster's angle), and that the very weak reflection off the AR-coated back face is directed back to the He-Ne.
6. Now, the prisms and lens should be inserted into the dye laser cavity. Dye fluorescence should be clearly visible as a stripe on the grating. Next, the height of the lens must be adjusted, such that the grating feedback is coincident with the single pass fluorescence. At this point lasing should occur. If not, the angle of the grating should be finely tuned.
7. Final alignment with a power meter.

By using a set of calibrated, neutral-density filters to attenuate the CVL beam, the slope efficiency and threshold pump power were measured to be 13% and 0.8 W respectively. The efficiency of the LZhI-504 was improved by configuring the oscillator such that efficient polarization-matched CVL pumping could be employed. This was accomplished by using a half-wave plate to rotate the horizontally polarized dye laser flux through 90° between the prism beam expander and the dye cell, so enabling pumping with vertically polarized CVL radiation. The modified oscillator is illustrated in figure 5.19, and the power scaling characteristics of the LZhI-504 with and without the wave plate, when pumped with a vertically polarized CVL are shown in figure 5.20. The design incorporating the wave plate shows a 25% increase in the slope efficiency, and a reduction in the oscillation threshold from 0.8 W to 0.7W.

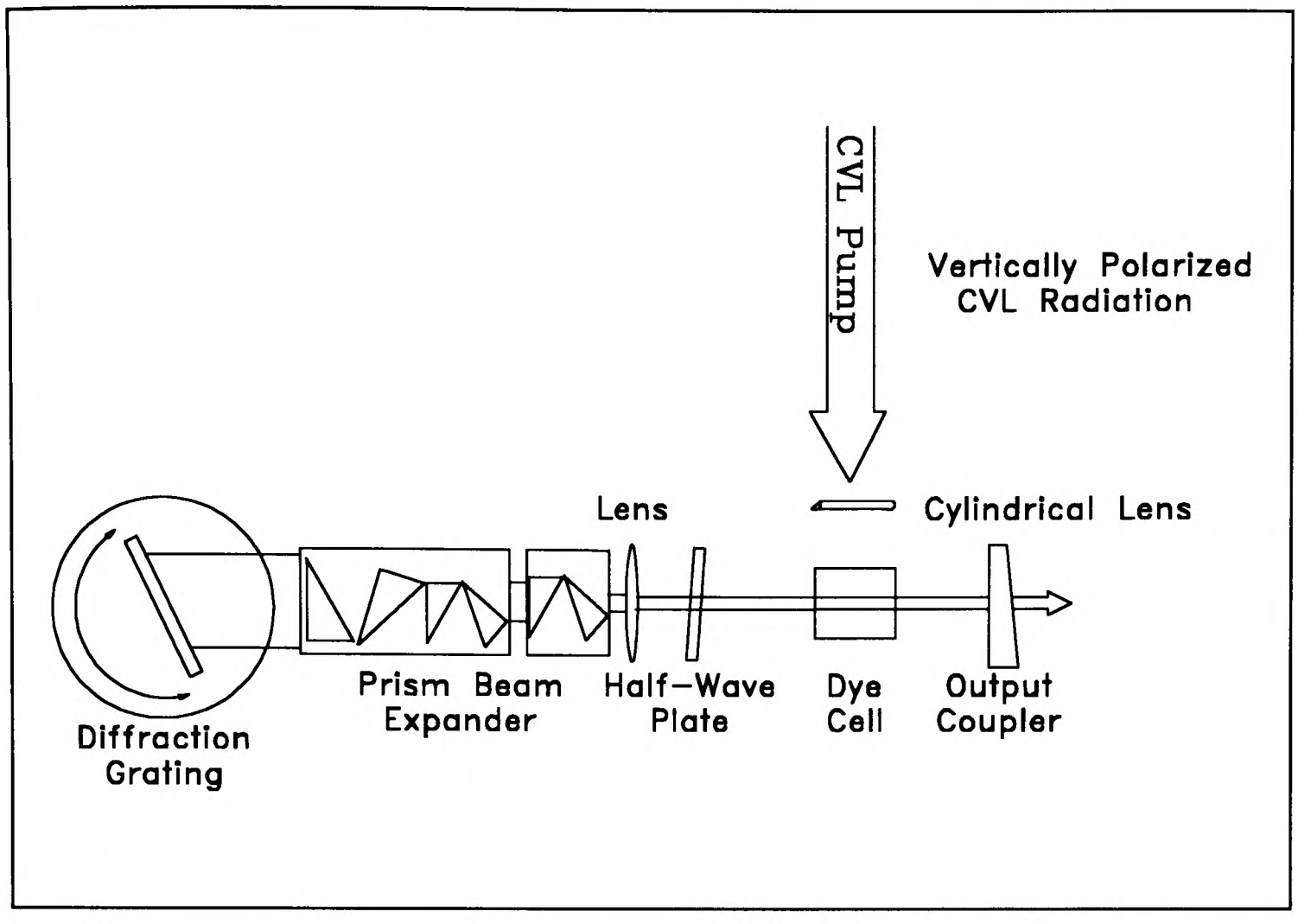


Figure 5.19 : Modified LZhI-504 dye laser with intra-cavity wave plate to enable polarization-matched CVL pumping

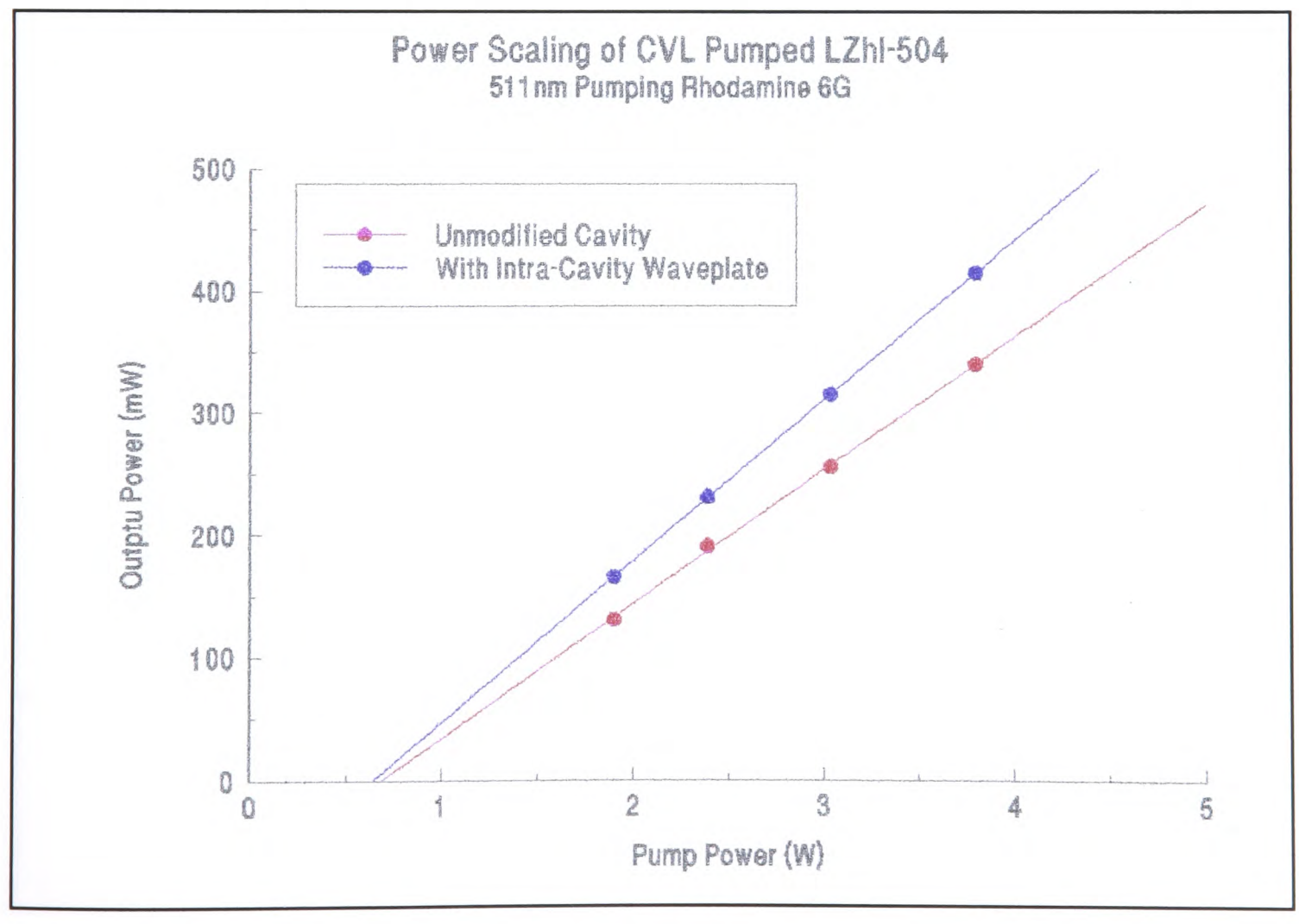


Figure 5.20 : Slope efficiencies of the wave-plate-modified, and unmodified, LZhI-504 cavity.

The time-averaged bandwidth of the CVL-pumped LZhI-504 was measured using a scanning Fabry Perot interferometer with a plate separation of 2 mm (FSR=75 GHz). The recorded fringe pattern shown in figure 5.21 indicates a bandwidth of some 22 GHz (0.75 cm^{-1}), in reasonable agreement with that predicted by theory. For a grating used in Littrow configuration:

$$m\lambda = 2d\sin\theta \ , \tag{5}$$

so the angular dispersion, D, is given by :

$$D = \frac{\partial\theta}{\partial\lambda} = \frac{\tan\theta}{\lambda} \ . \tag{6}$$

With the 1200 lines/mm ruled grating used in 1st order Littrow, and a dye laser wavelength of λ=570 nm, the angular dispersion may be calculated to be

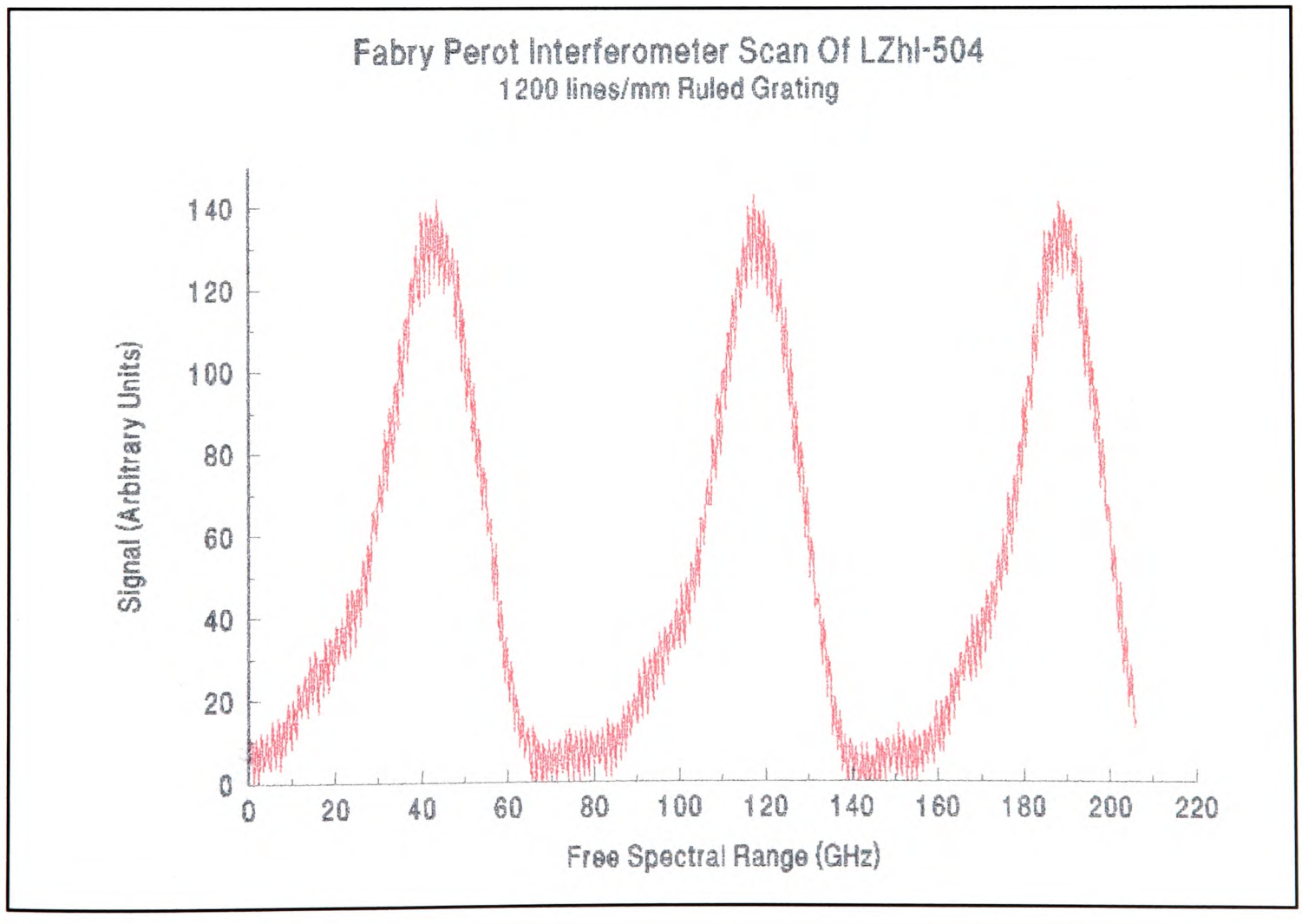


Figure 5.21 : Fabry Perot Scan of the LZhI-504 dye laser bandwidth.

$D \sim 0.364/\lambda$. Thus, with an intra-cavity beam expander of magnification M, and a total of R cavity round trips (limited by the duration of the laser pulse), according to the multi-pass line-width analysis of Duarte [5.15], the bandwidth is given by :

$$\Delta\lambda = \Delta\theta\left[RM\left(\frac{\partial\theta}{\partial\lambda}\right)\right]^{-1} . \qquad (7)$$

In this particular instance, $\Delta\theta \sim 2$ mrad and $R \sim 6$, which yields $\Delta\lambda \sim 0.02$ nm or $\Delta\nu \sim 18$GHz, in reasonable agreement with the measured time-averaged bandwidth of 22 GHz.

For many spectroscopic applications, a bandwidth in excess of a few gigahertz (the Doppler-width of typical spectral profiles) is undesirable, and so efforts were made to narrow the bandwidth of the LZhI-504 dye laser. In the first instance, the 1200 lines/mm ruled grating was replaced with a 2400 lines/mm holographic grating, so improving the angular dispersion by a factor of 2.58 over that offered by the Russian grating ($D \sim 0.928/\lambda$). Fabry Perot interferometer measurements of the bandwidth of the new cavity (figure 5.22) indicate a narrowed bandwidth of 9 GHz - an improvement parallelled by the increased angular dispersion. To narrow the bandwidth further, either the magnification of the multiple prism beam expander must be increased, or an intra-cavity etalon used. The latter option was tried here. The free spectral range of the etalon was chosen to be greater than the 10 GHz grating-cavity bandwidth to ensure that only one etalon mode would oscillate. Thus, a 6 mm thick solid spectrosil B etalon was inserted into the cavity between the prism beam expander and the grating, and tilted relative to the oscillator axis to prevent parasitic oscillation. The measured bandwidth of the etalon-cavity is displayed in figure 5.23; the bandwidth of 3 GHz is limited by the rather poor finesse of the solid etalon and, in principle, narrow line-width operation below 1 GHz is possible. Slope efficiency measurements of all three cavity configurations are shown in figure 5.24. The slope efficiencies of the 1200 lines/mm and 2400 lines/mm grating cavities are very nearly the same, illustrating the homogeneous nature of the dye gain profile. The slope efficiency of the etalon cavity is, however, correspondingly lower, and the oscillation threshold higher, owing to the increased cavity losses.

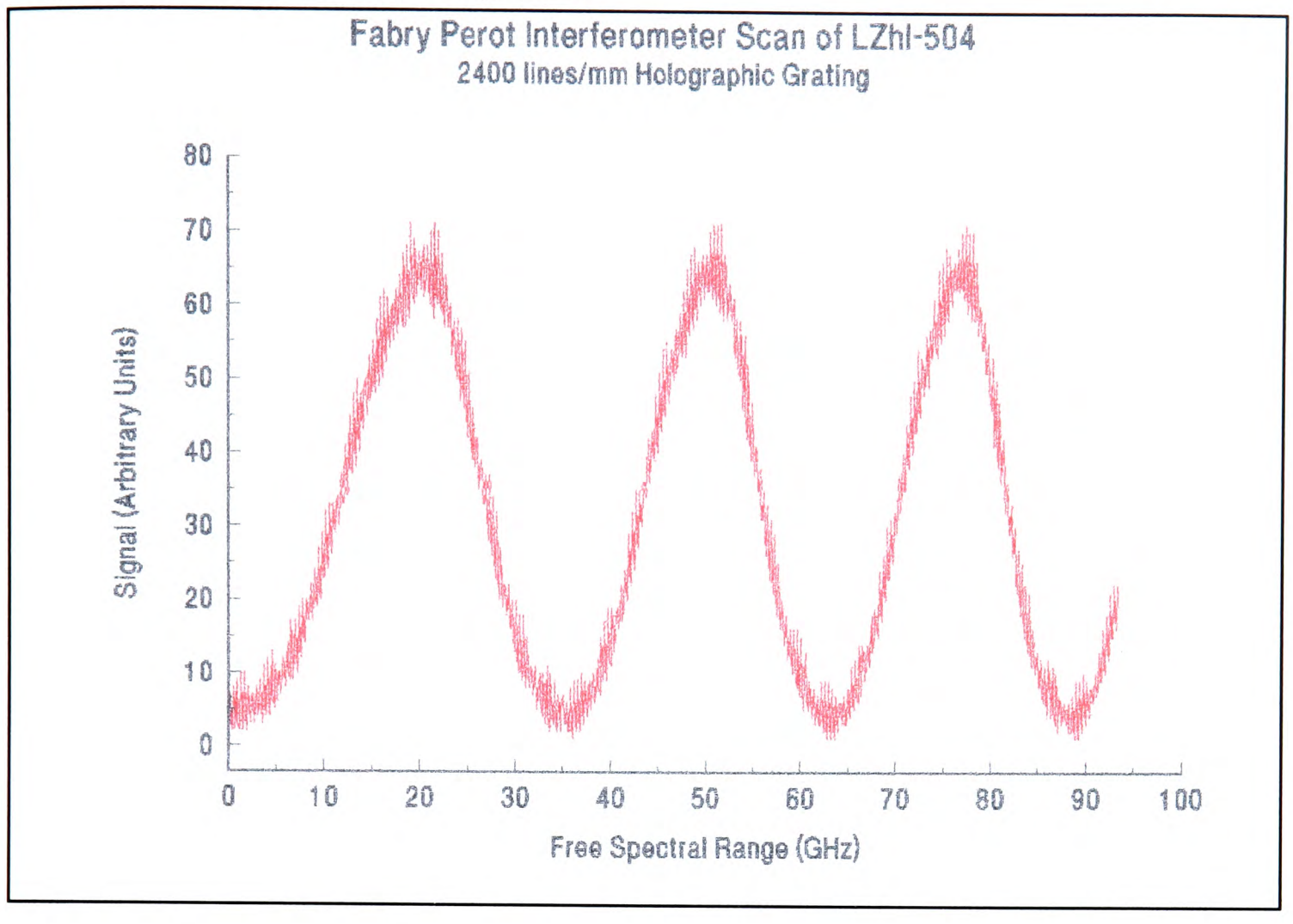


Figure 5.22 : Fabry Perot interferometer scan of the LZhI-504 dye laser with a 2400 lines/mm grating.

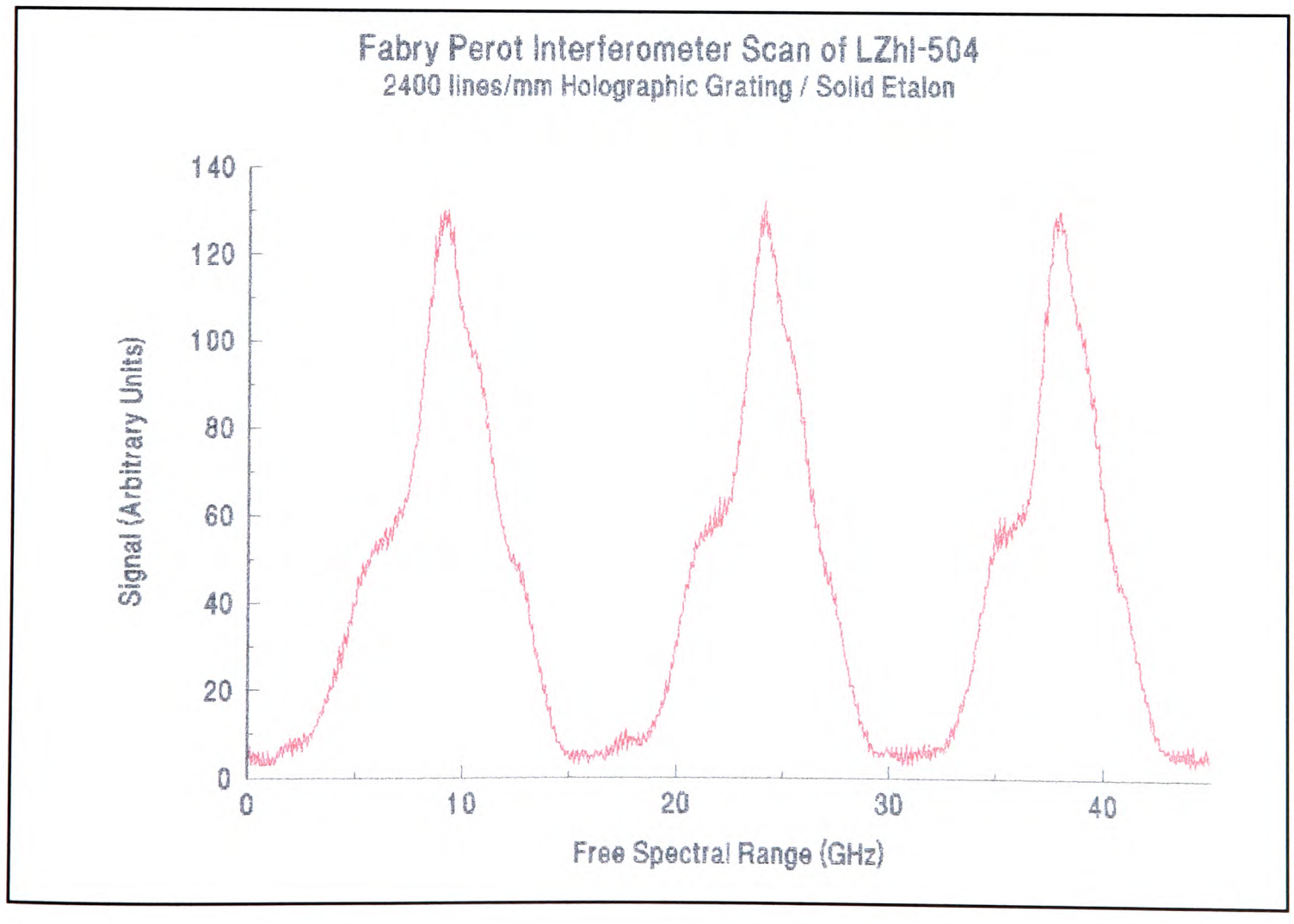


Figure 5.23 : Fabry Perot interferometer scan of LZhI-504 with a 2400 lines/mm holographic grating and intra-cavity etalon.

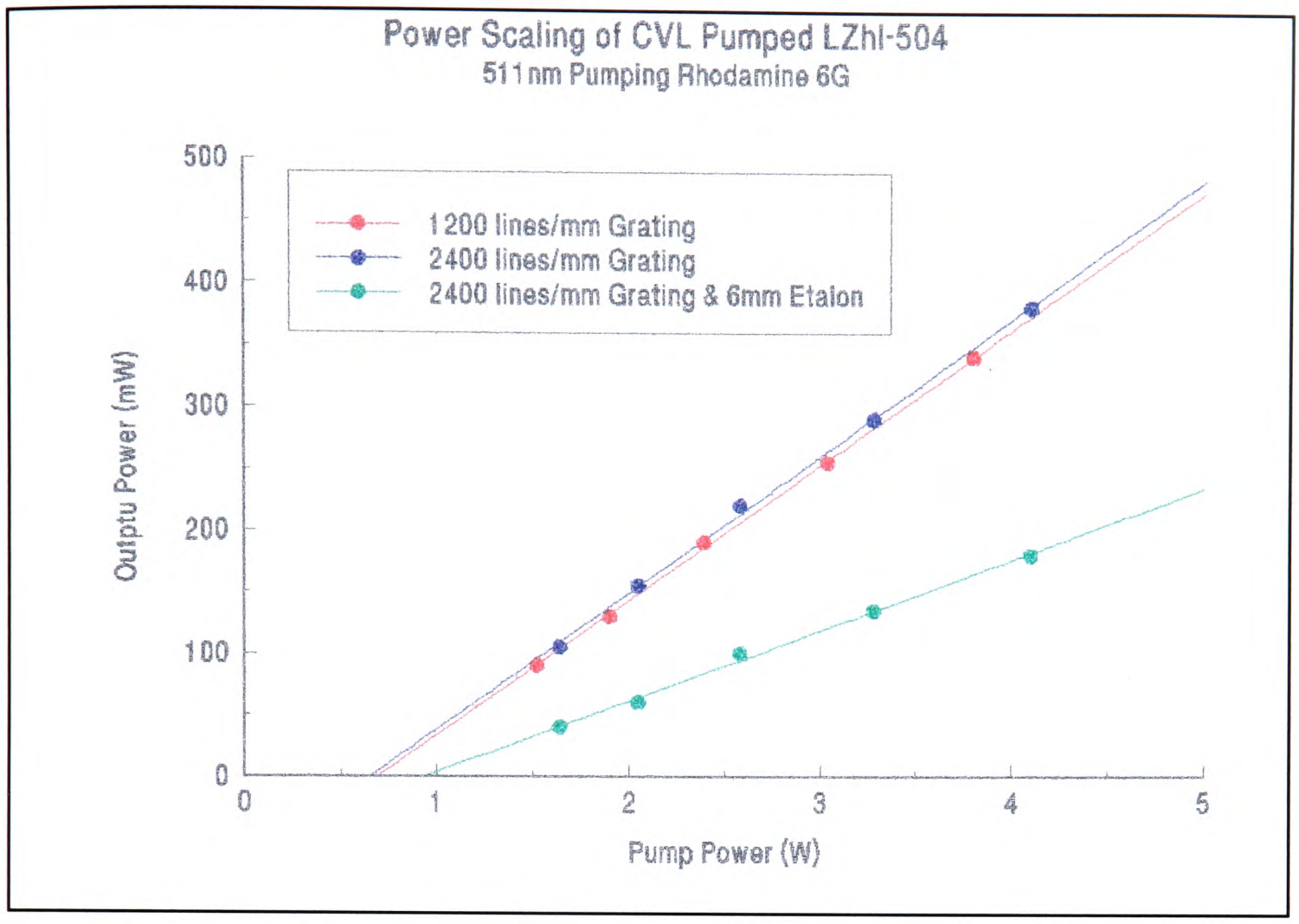


Figure 5.24 : Slope efficiency measurements of the LZhI-504 (a) unmodified, (b) with 2400 lines/mm grating and (c) with 2400 lines/mm grating and intra-cavity etalon.

The frequency stability of the LZhI-504 dye laser was measured using the Burleigh pulsed wavemeter, which acquired the wavelength and bandwidth every 20 seconds for 30 minutes. The wavelength data presented in figure 5.25 illustrates the excellent frequency stability of the LZhI-504, with sub-gigahertz frequency jitter and very little thermal drift, resulting from the robust solid steel / invar construction of the oscillator cavity.

The temporal behaviour of the LZhI-504 was investigated using fast response vacuum photodiodes, and the recorded dye and CVL pulse shapes are shown in figure 5.26. For these measurements the dye laser was operated near the fluorescence peak of Rhodamine 6G, and resulted in a pulse length and build-up time of 35 ns and 2-3ns respectively. When the laser was operated further away from the fluorescence maximum, where the gain is substantially less, the build-up time was seen to increase to 10 ns, whilst the dye laser pulse length shortened to 20 ns.

Beam quality / divergence measurements were investigated using the Excitech

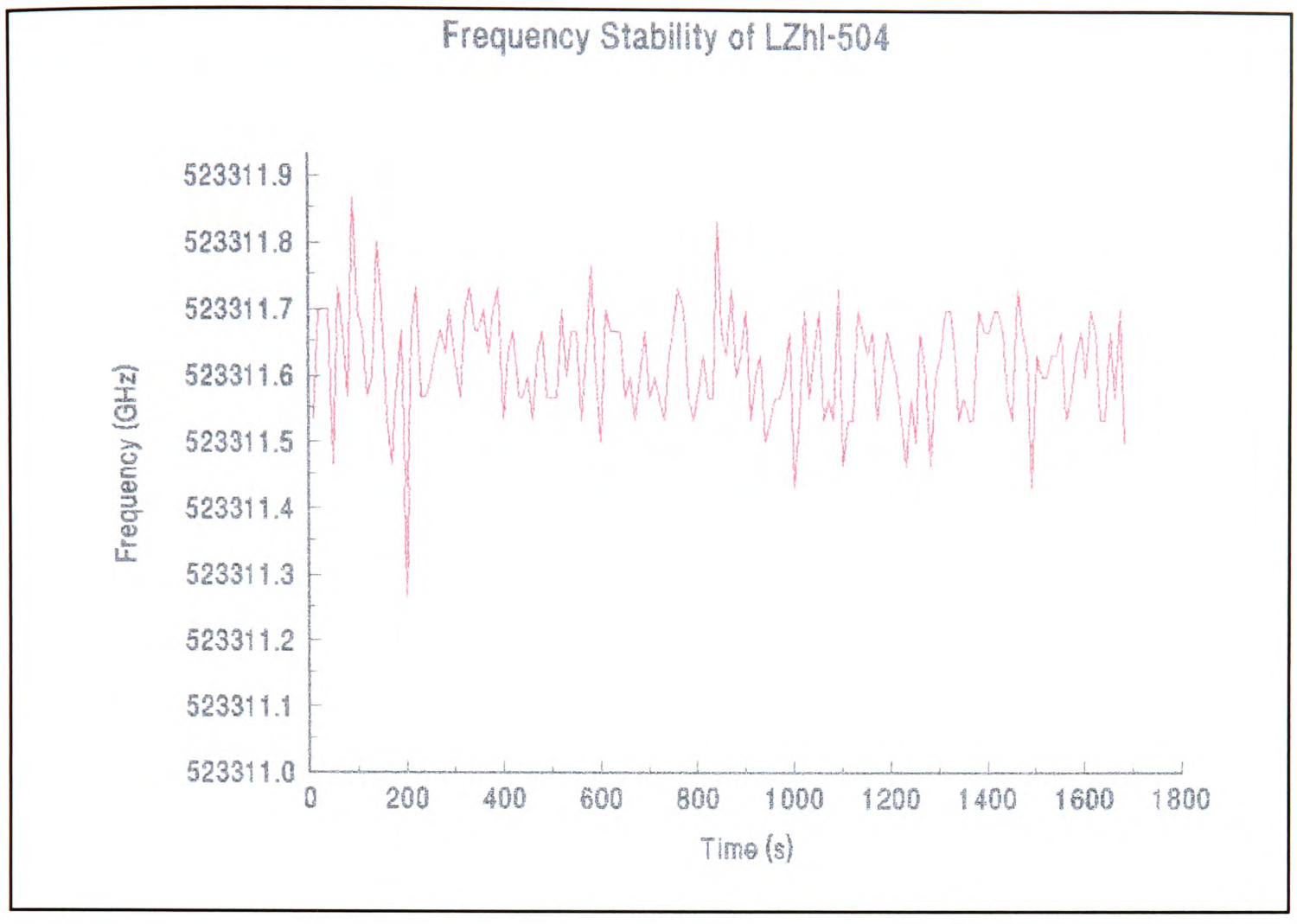


Figure 5.25 : Frequency stability of the LZhI-504 measured using the Burleigh wavemeter.

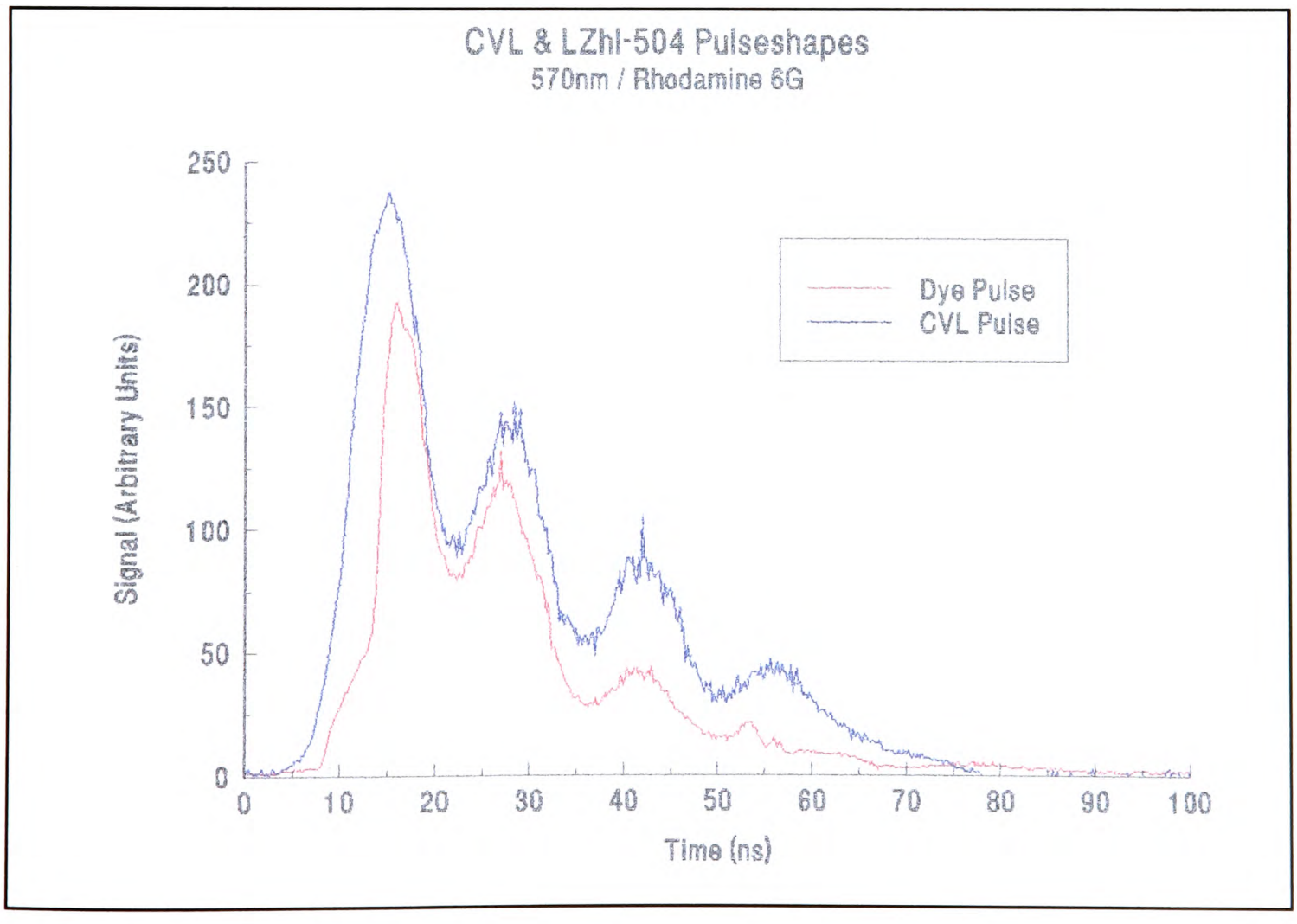


Figure 5.26 : Pulses shapes of the CVL and dye laser output from the LZhI-504.

beam profiler, using the alignment technique described in §5.4.1. The near and far field profiles are depicted in figure 5.27 and 5.28 respectively. Analysis of the far-field profile indicates a beam divergence of 0.3 mrad vertically and 0.25 mrad horizontally. The near-field profile shows the dye laser beam to be approximately 3mm in diameter, and, thus, indicates a beam quality of ~ 1.4 times the diffraction limit.

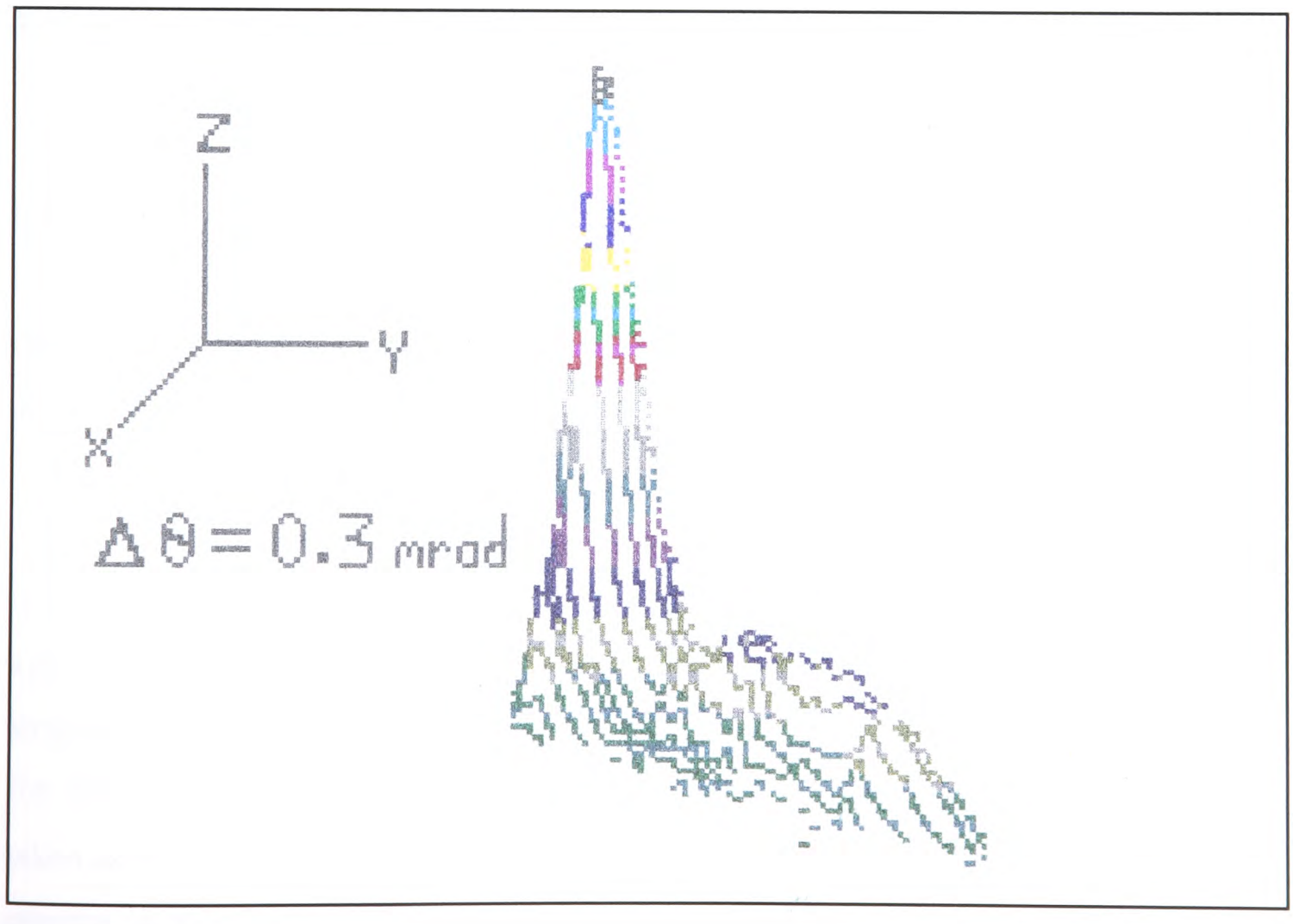


Figure 5.27 : Far field profile of the LZhI-504.

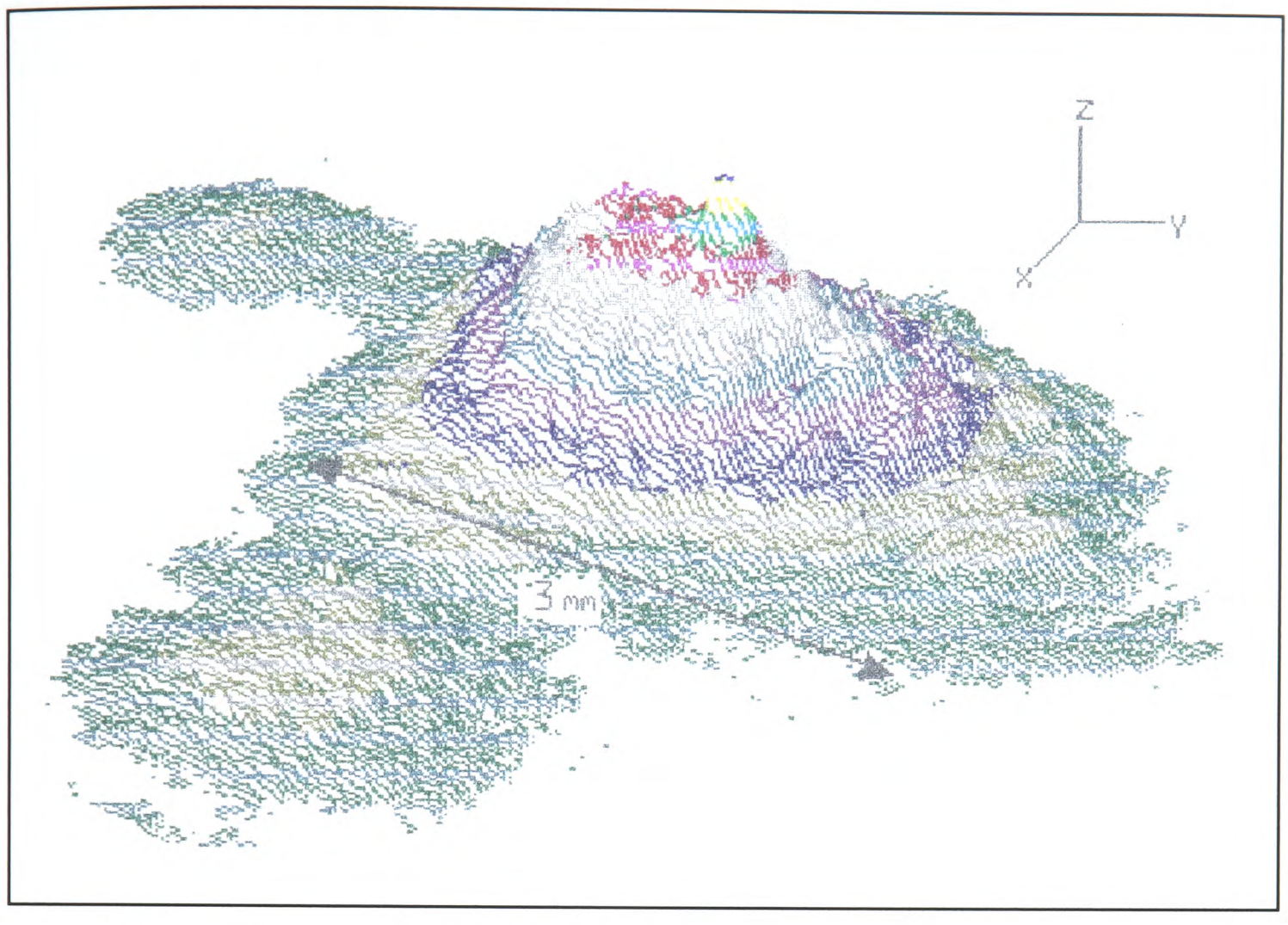


Figure 5.28 : Near field profile of the LZhI-504.

5.5.2 The Lambda Physik LPD 3000

The pump beam path of the LPD3000 is depicted in figure 5.29. On entering the interlocked entrance port of the dye laser, the pump beam is incident upon a beamsplitter which directs a fraction of the pump radiation toward the oscillator. The remainder of the pump beam is directed to the pre-amplifier via an optical delay line of approximately 4 ns (to minimise ASE).

A special feature of the Lambda Physik LPD3000 is that a single dye cuvette is used for both the oscillator and pre-amplifier, with a second cuvette available as a power amplifier. The pump laser is cylindrically focused to give two separate gain stripes in the dye cuvette, the lower one being used for the oscillator, and the upper for the pre-amplifier. The oscillator itself is an open-cavity design, with the output taken as a 25% reflection off the entrance prism of the multiple prism beam expander present in the multiple prism Littrow (MPL) grating cavity (Figure 5.30). The grating has a constant of 600 lines/mm with a 2.7μm blaze, and can be tilted between

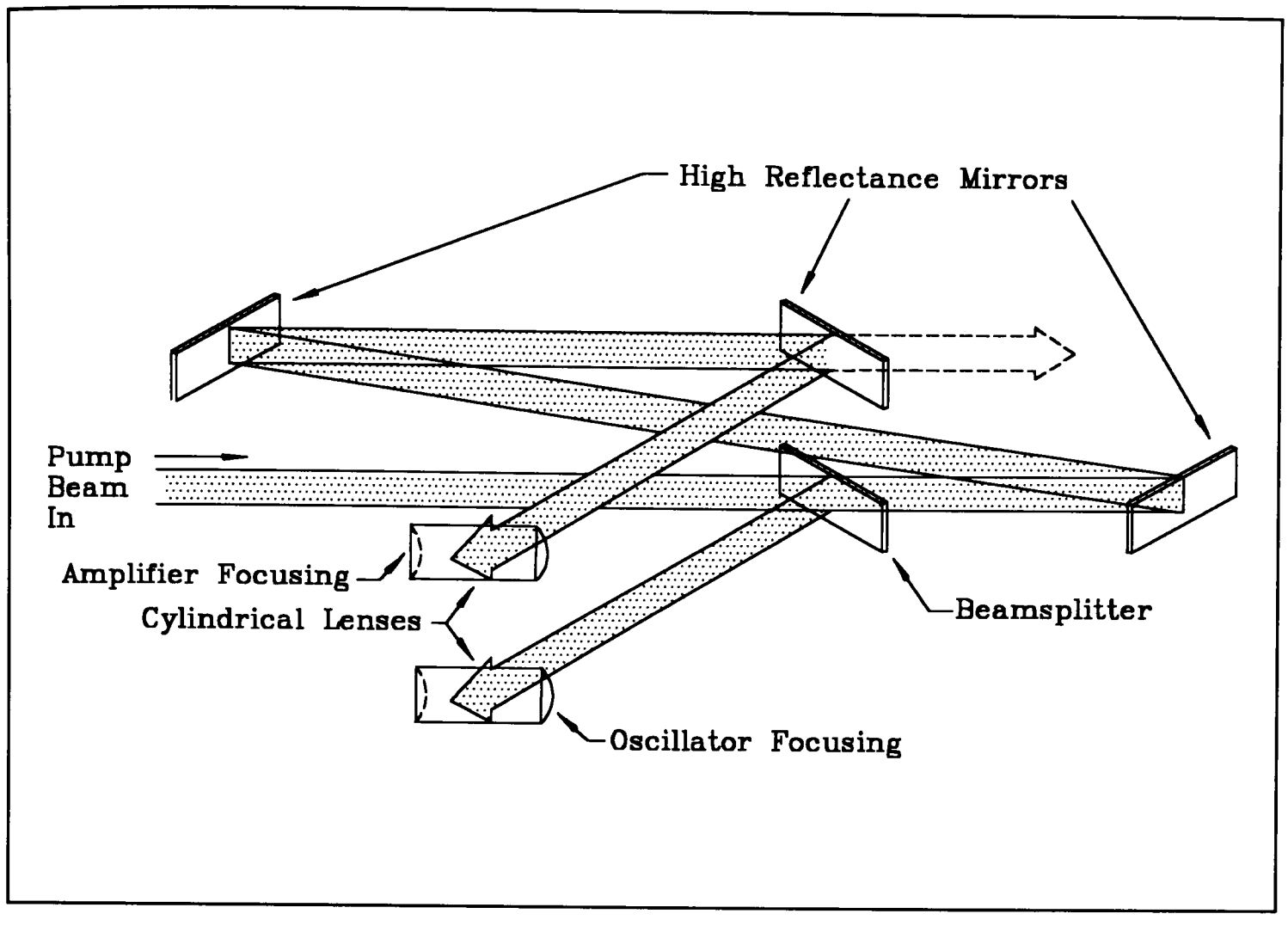


Figure 5.29 : Optical pump beam path of the Lambda Physik LPD3000

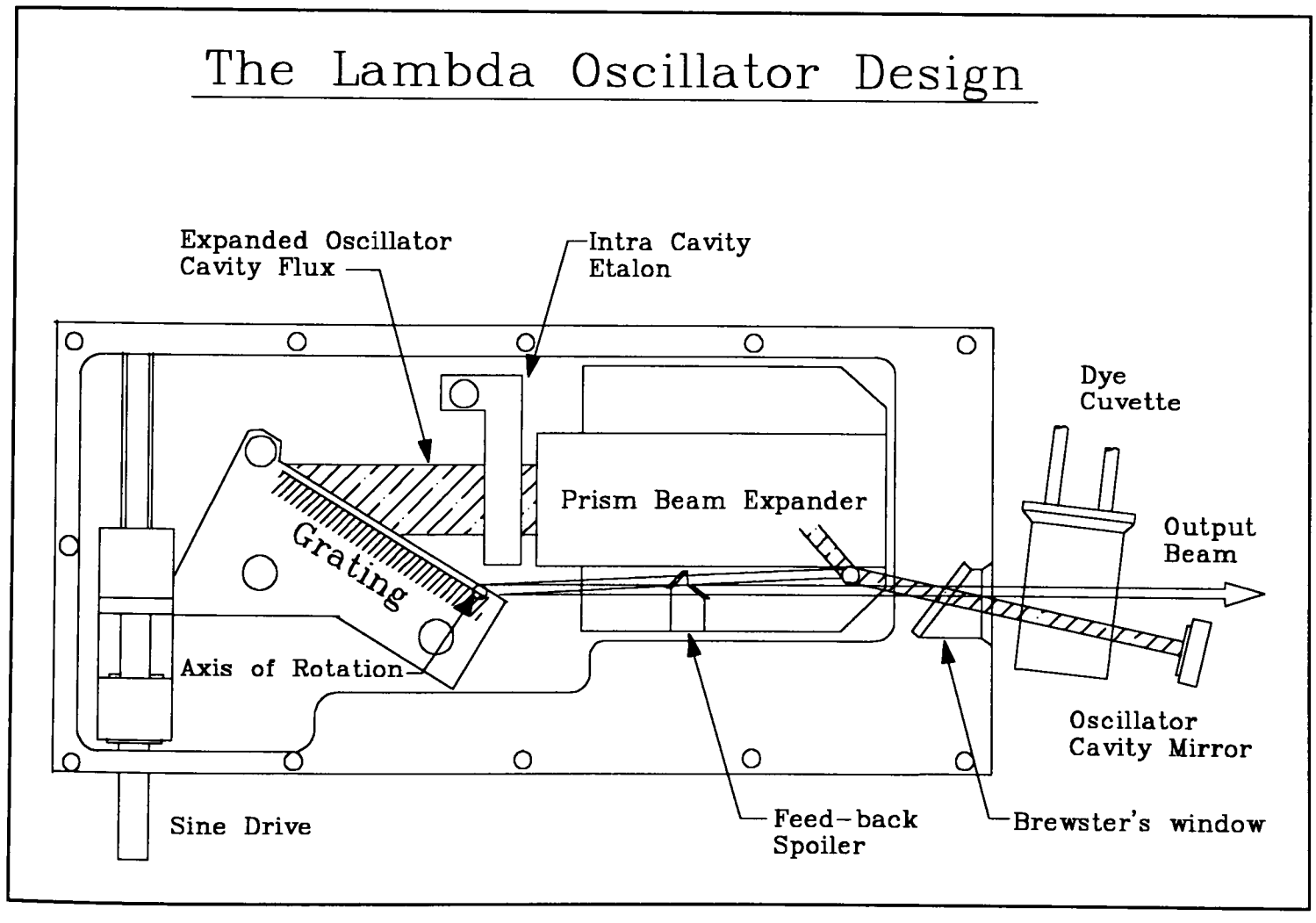


Figure 5.30 : Detail of the Lambda Physik LPD3000 oscillator block.

the Littrow angles of 42.5° and 72.5°, thus providing continuous tunability between 320 nm and 1.05 μm when used in third to eighth order. The grating is mounted on a precision sine drive which is coupled to a stepper motor by a fine lead screw. This drive mechanism provides minutely variable linear tuning with frequency steps of 0.85 GHz, although pressure tuning in the hermetically sealed oscillator block is possible, to provide finer adjustments if required. The possibility exists for mounting a synchronously-scanned etalon into the oscillator block which enables sub-gigahertz operation if required.

The intra-cavity prism beam expander not only serves to narrow the oscillator bandwidth through a beam expansion factor of 66, but also acts as a 20:1 polarizer. The output beam is highly vertically polarized, and so easy polarization-matched pumping with a vertically polarized CVL is possible to provide enhanced conversion efficiencies. The output taken off the entrance prism of the prism beam expander is directed to the grating in the Lambdapure© configuration before amplification. In this arrangement the grating is used as a spectral filter at the cavity selected wavelength before the oscillator beam arrives at the pre-amplifier. The use of such a coupling spectral filter both suppresses ASE from the oscillator being amplified, and prevents ASE from the amplifier feeding back and seeding the oscillator; the net result is a highly spectrally pure amplified output beam, with the signal to noise (ASE) ratio better than 10^6 [5.16]. Finally, provision exists for the inclusion of non-linear crystals and harmonic separators before the dye laser beam exits from the enclosure.

The basic dye laser was modified for CVL pumping by using appropriately coated pump optics, and shorter focal length cylindrical lenses, so as to form tighter line foci in the dye, and compensate for the low pump pulse energy of the CVL as compared with the intended excimer pump laser - $f=25$ mm and $f=46$ mm cylindrical lenses were used for the oscillator and amplifier respectively, rather than the standard $f=108$ mm optics for excimer laser pumping. With the limited pulse energy of the CVL, only the oscillator and pre-amplifier sections were pumped, and the second power-amplifier dye cell was removed from the dye laser enclosure. In an effort to clear the active volume between laser pulses, a high flow rate circulation pump with a laminar flow dye cuvette was used. The dye channel measured 1 mm

wide, and 20 mm long, whilst the height of the CVL line focus produced by the f=46mm cylindrical lens was about 110 μm (divergence of CVL=0.6 mrad/40 mm beam). Thus, the active volume which must be cleared between pump pulses is 2.2×10^{-3} cm^3, and at a repetition rate of 6.5 kHz, a minimum flow rate of 1 litres/minute is required to clear the active volume - this was comfortably met with the 4.2 litres/minute dye circulation pump used, providing a clearing ratio of ~4:1. However, since the same cuvette is used for the oscillator and pre-amplifier, the dye excited in the oscillator region is used in the amplifier 2.5 ms later. Although this time interval is sufficient for the excited dye molecules to relax back to the ground state, strong thermal gradients persist, which give rise to refractive index fluctuations, and corresponding lensing and beamsteering of the amplifier output. This is not a problem for low repetition rate pump lasers, where the whole cuvette volume can be exchanged between shots, but is a serious limitation of the single cuvette design at high repetition rates. A possible solution is to use miniature rhombs to divert the oscillator beam around the pre-amplifier section, and then to use a second dye cell for amplification.

Pump Beam Delivery - Size and Shape

The pumping scheme used in the characterization experiments is shown schematically in figure 5.31, the rather tortuous pump beam path being a result of the limited space on the optical table. The limiting aperture of the LPD3000 is defined by the cylindrical focusing lenses in the vertical direction, which are only 15 mm high (so as to enable two pump stripes to fit into the same cuvette), and the dye cuvette in the horizontal direction, which is 20 mm long. Whilst this does not pose a problem for the rectangular beam typical of the excimer pump laser, in order to fill the whole cuvette with the CVL pump, and not suffer the restricted efficiency and tuning range described in section §5.2.4, an elliptical pumping geometry should be used.

A number of different pump beam geometries were investigated, to couple the CVL to the LPD 3000 (lasing with a solution of Rhodamine 6G dye in methanol), and

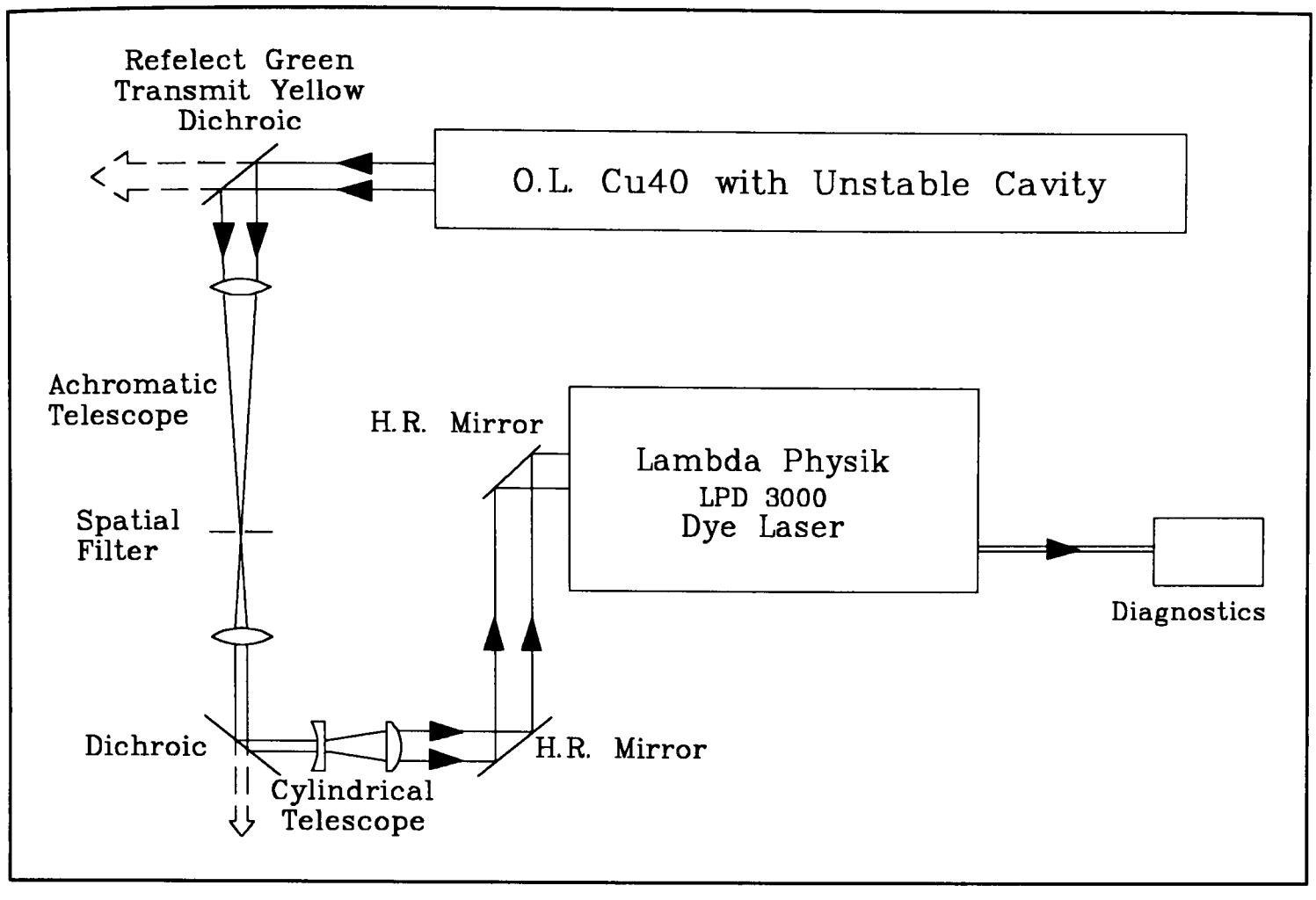


Figure 5.31 : Optical geometry used to couple the CVL to the Lambda Physik LPD3000.

are compared in table 5.1 :-

Table 5.1

Keplerian Telescope Magnification	Cylindrical Telescope Magnification	Tuning Range /nm	Best Efficiency* Rhodamine 6G 0.15g/litre
×0.25 50cm,12.5cm	---	559-590	16.3%
×0.25 50cm,12.5cm	×2 -10cm,20cm	557-603	21.5%
×0.25 2m,50cm	---	559-595	19.7%
×0.40 5m,2m	---	559-597	23.0%

* A dichroic mirror was used to remove the CVL 578 nm from the pump beam path.

As might be expected, those geometries which do not fill the whole length of the dye cell are inefficient and have restricted tuning ranges. It is interesting to note the differing efficiencies between the use of a 2 m/50 cm telescope and a 50 cm/12.5 cm telescope, both of which offer the same magnification and provide a 10.5 mm pump beam to the dye laser. It is thought that this was due to the spatial filter at the telescope focus acting as a spectral filter - the chromatic aberrations of the telescope

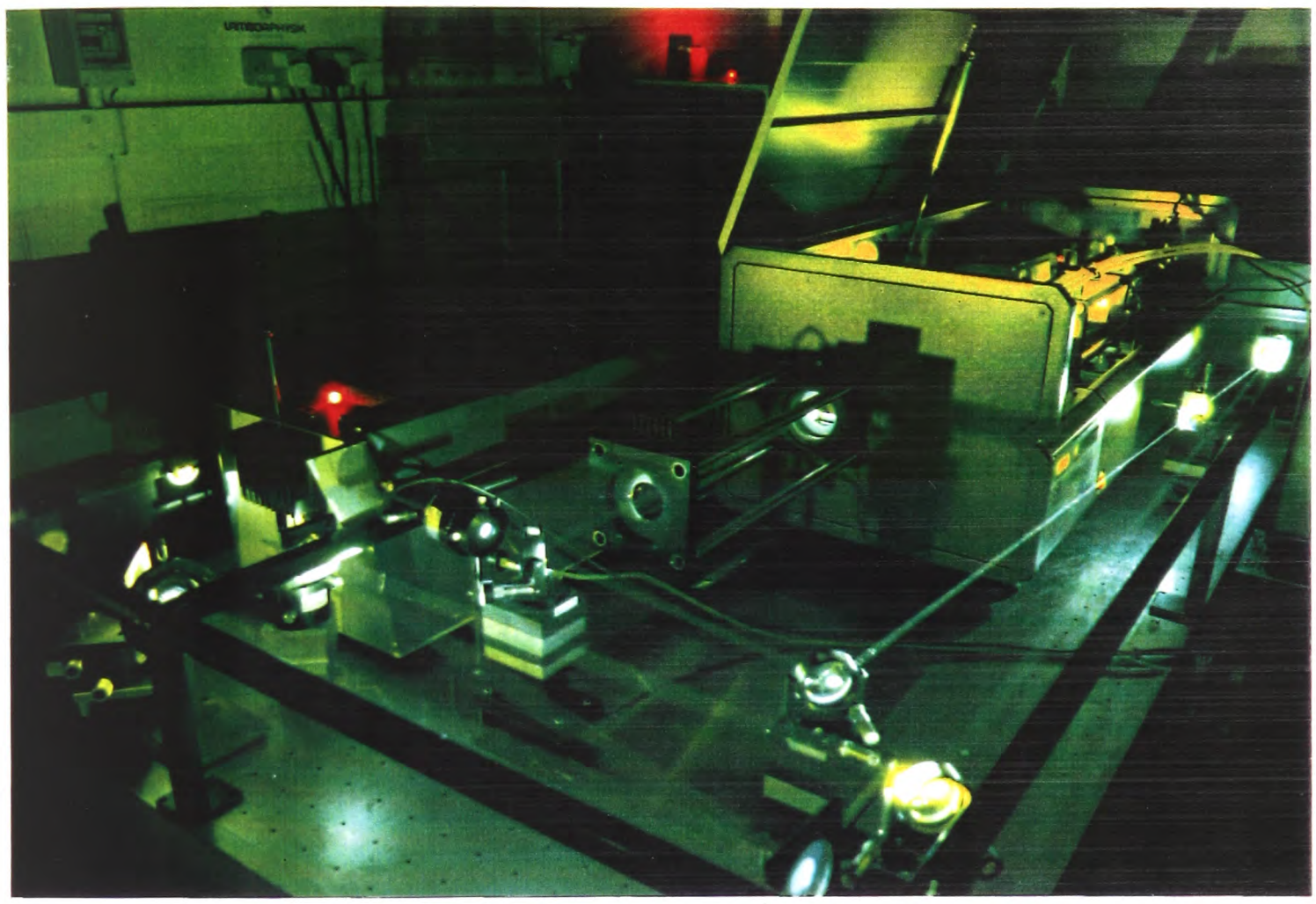


Plate 5.2 : The CVL-pumped Lambda Physik LPD3000 dye laser. Here, a 7m beam-shaping telescope (a combination of a 5m and a 2m lens) is used to demagnify the 42mm CVL beam, and couple the CVL to the dye laser.

singlet lenses cause the CVL yellow (which was not completely removed by the dichroic beamsplitter) to walk away from the green, where it was stopped at the spatial filter. By removing the residual yellow pump component at the spatial filter, an important depopulation mechanism for the dye laser gain is obviated, and the efficiency is not impaired. This mechanism also explains why the 5 m/2 m telescope was seen to be so efficient - in this case the yellow from the CVL pump was visibly seen to miss the steering mirrors because of singlet lens aberrations

The use of the $\times 2$ cylindrical telescope with the $\times 0.25$ Keplerian telescope provided a pump beam 21 mm wide and 10.5 mm high, which was near-ideal to both pass cleanly through the dye laser cylindrical pump optics, and fill the dye cuvette. The elliptical beam geometry resulted in a relatively high efficiency and wide tuning range; the situation may have been further improved by the use of better dichroic mirrors to remove the residual yellow from the pump beam, and a slightly different geometry - a 15 mm high and 20 mm wide pump beam would have been ideal, since this geometry gives the minimum vertical beam divergence (beam diameter $\times$ divergence = constant), and, hence, the best focus in the dye.

Beamsplitter Reflectivity and Dye Concentration

The choice of beamsplitter reflectivity is critical to the overall efficiency of the laser, but in changing the ratio of the pump power delivered to the oscillator relative to the amplifier, it is not unreasonable to expect a change in the optimum dye concentration. Thus, with a constant pump power of 8.6 Watts, the dye concentration and beamsplitter reflectivities were systematically varied. The results are plotted in figure 5.32, and show that a 25% beamsplitter is best for pump powers around the 10W level. That is, about 0.4 mJ is required to pump the oscillator so as to provide a seed signal with a pulse energy and temporal profile suitable for efficient amplification, as described in §5.3.1.

With the 25% beamsplitter, the optimum dye concentrations and tuning ranges for a number of dyes lasing in the visible region of the spectrum were investigated,

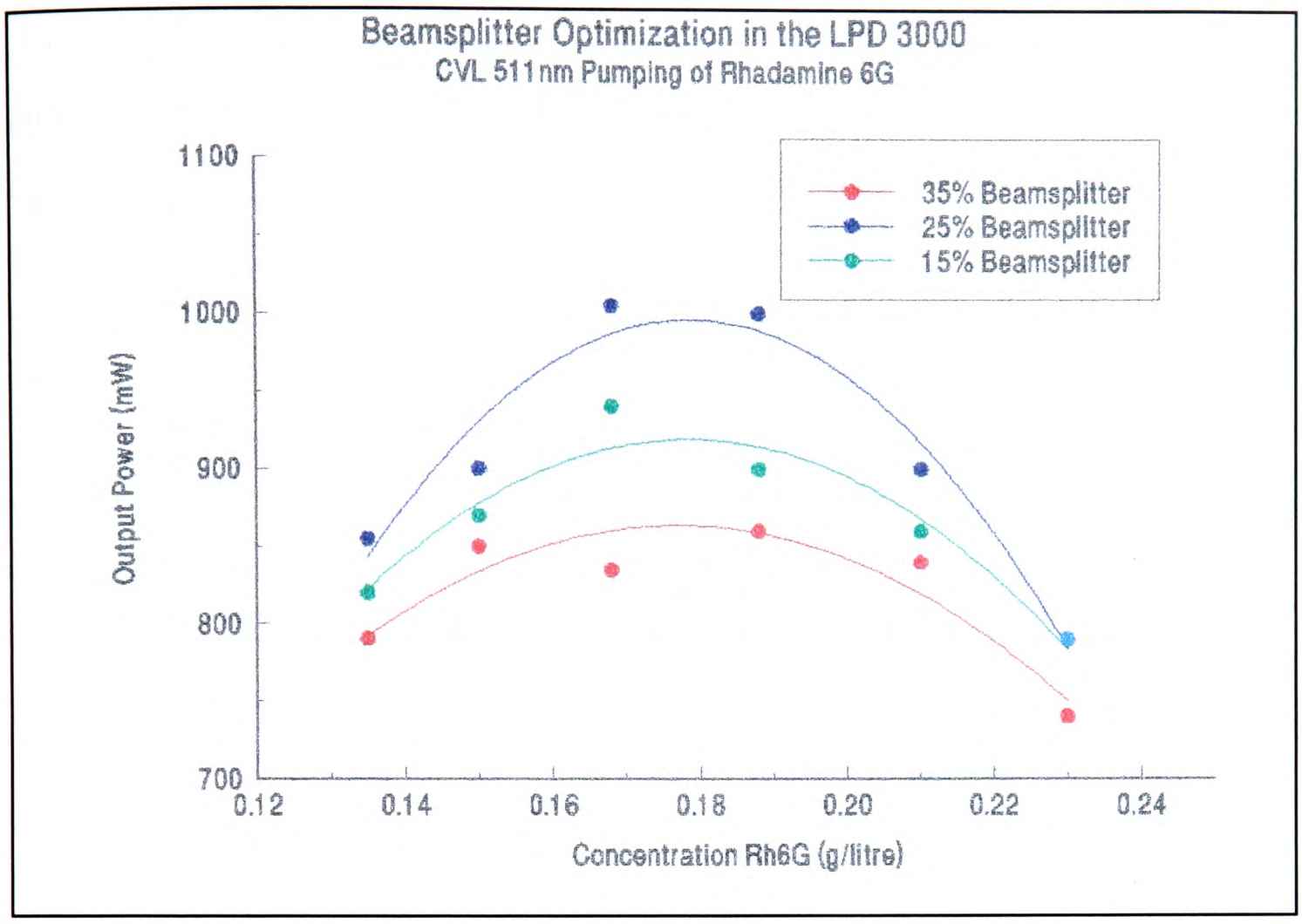


Figure 5.32 : Optimization of the beamsplitter reflectivity and Rhodamine 6G dye concentration in the CVL pumped Lambda Physik LPD3000 dye laser.

and the results are presented in table 5.2.

Table 5.2

Laser Dye	Concentration (g/l)	Maximum Wavelength (nm)	Peak Efficiency (%)	Pump Wavelengths
Rh 560 Cl	0.08	542 nm	22.8	Green
Rh 590 Cl	0.15	568 nm	23.2	Green
Rh 610 Cl	0.30	595 nm	10.4	Green
Kiton Red	0.45	600 nm	14.3	Green/Yellow
Rh 640 PCl	0.15	615 nm	20.3	Yellow
DCM	0.23	640 nm	11.8	Green

In an effort to further improve the efficiency of the LPD3000, an interception mirror was positioned in the oscillator block to reflect the oscillator beam directly to the amplifier, so avoiding the lossy grating reflection incurred in the Lambdapure© scheme. This arrangement, however, offered only slightly improved efficiencies (~10%), but at the expense of the spectral purity. Now, ASE feed back from the amplifier was seen to seed the oscillator, and a significant increase in ASE output was observed. The amount of ASE, as might be expected, is proportional to how hard the oscillator is pumped in relation to the amplifier and, consequently, to the beamsplitter reflectivity. To investigate this problem, the spectral profile of the modified dye laser output was recorded using a computer-controlled monochrometer for a number of beamsplitter reflectivities - the results are plotted in figure 5.33. The ASE, seen as a broad feature next to the narrow laser line, was greatest for the 15% beamsplitter, where strong ASE from the amplifier was easily able to seed the weakly-pumped oscillator. For comparison, the spectral profile of the LPD3000 with a 15% beamsplitter, but this time incorporating the LambdaPure© filter, is shown in

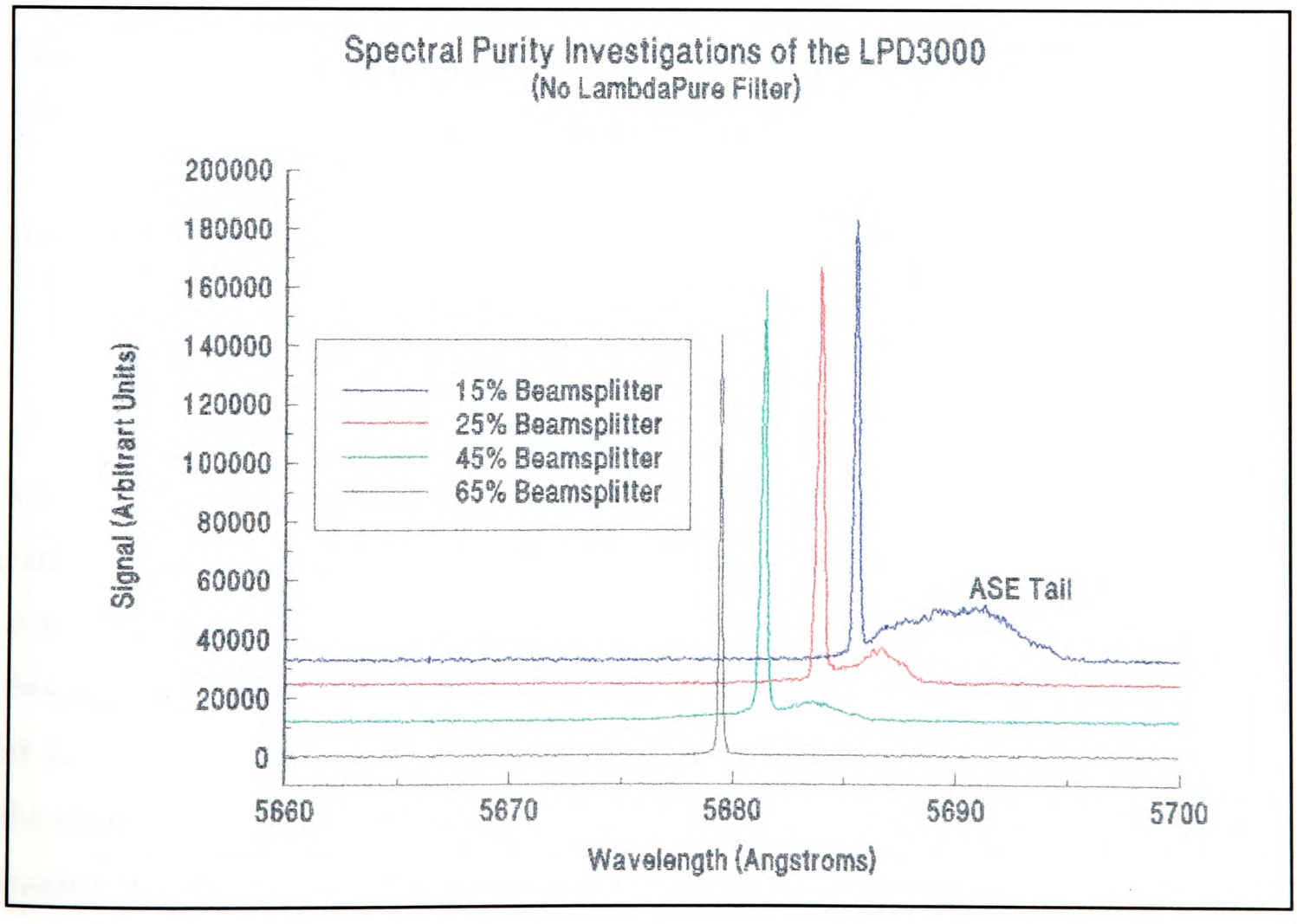


Figure 5.33 : Spectral Profiles of the modified LPD3000 with 15%,25%,45% and 65% beamsplitters

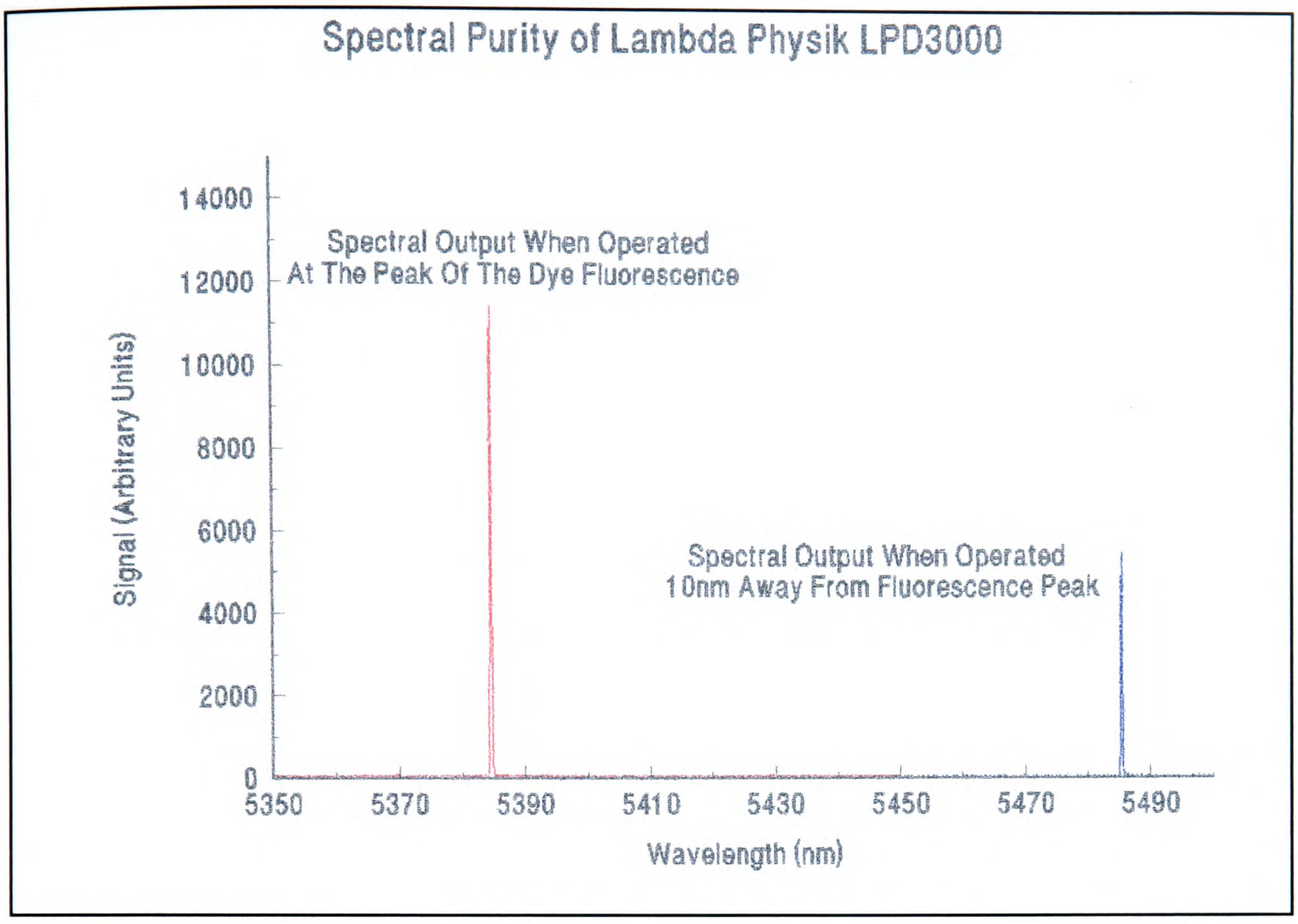


Figure 5.34 : Spectral profile of the LPD3000 incorporating the LambdaPure filter (a) operating near the dye fluorescence maximum (b) 15 nm away from the fluorescence maximum

figure 5.34. Here, the ASE is lost in the detector noise, even when the oscillator was operated away from the gain peak.

Dye Laser Characteristics

The time-averaged frequency bandwidth measurements of the LPD3000 lasing at 570 nm with a Rhodamine 590 Chloride dye are displayed in figure 5.35. Successive measurements, with different etalon free spectral ranges, indicate a bandwidth of 7 ± 0.5 GHz - similar to the Lambda Physik specification for the dye laser when used with an excimer laser pump. A subsequent measurement made at this laboratory by Abbot [5.17] using a 4W CVL pump laser indicated a bandwidth of 12.4GHz. In this instance, however, the oscillator was operating much closer to the cavity threshold, resulting in a short dye pulse length with correspondingly few transits to the cavity grating. Insertion of an 1cm solid etalon into the oscillator cavity narrowed the bandwidth to 800 MHz (figure 5.36), but at the expense of the efficiency, causing a $\sim 20\%$ drop in output power. The LPD3000 displayed excellent

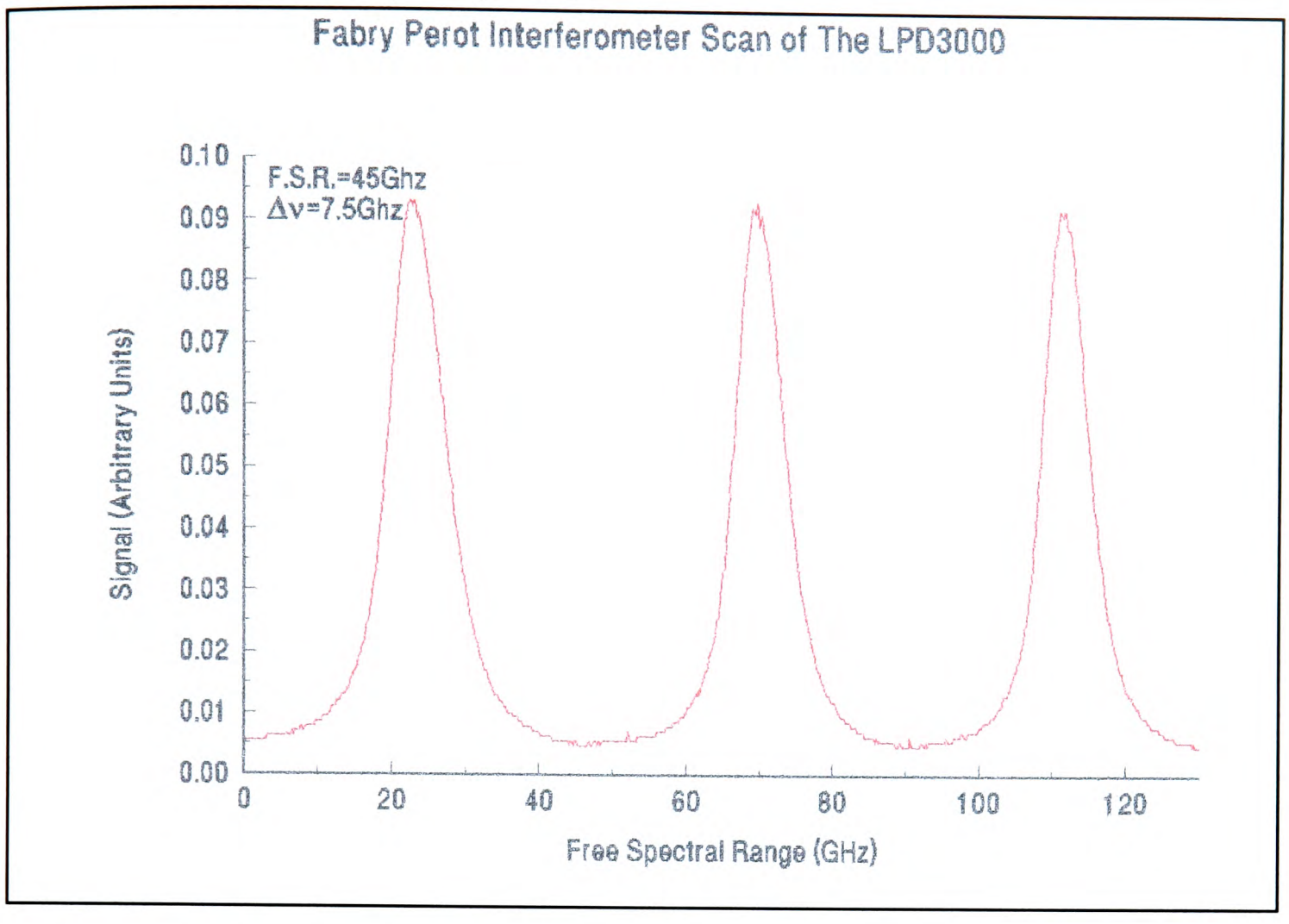


Figure 5.35 : Fabry Perot interferometer scan of the CVL-pumped LPD3000 dye laser.

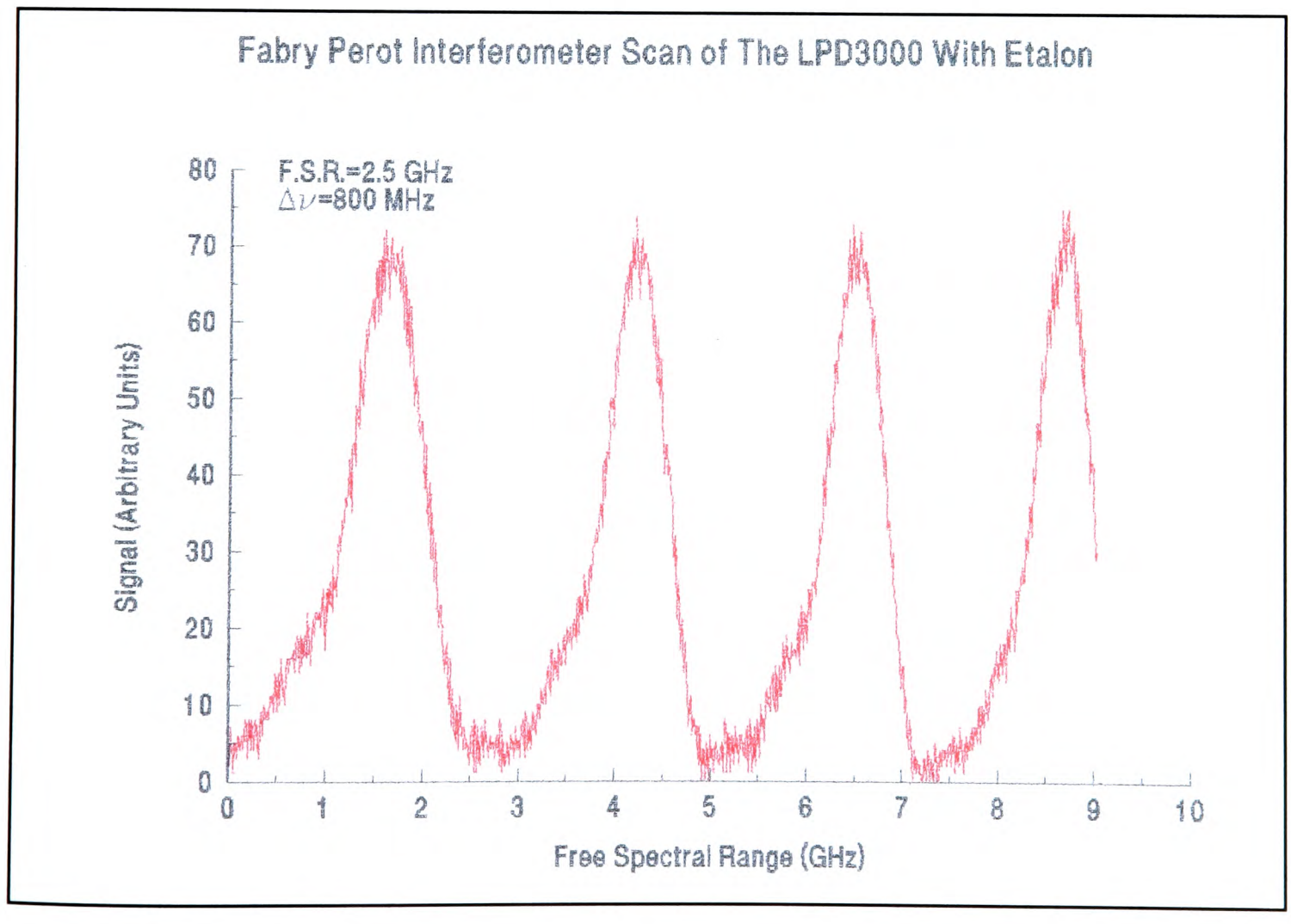


Figure 5.36 : Fabry Perot interferometer scan of the LPD3000 dye laser incorporating an intra-cavity etalon.

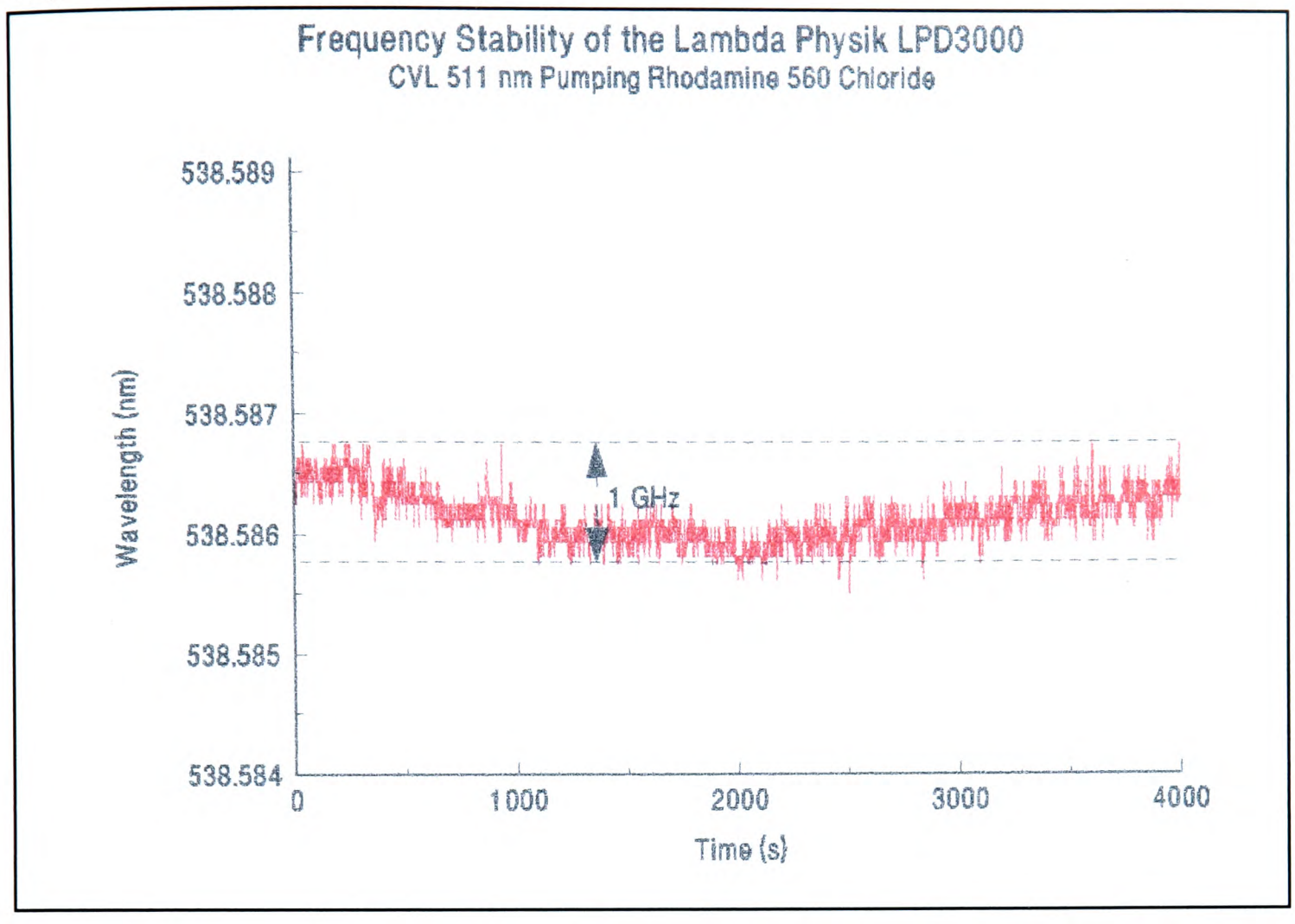


Figure 5.37 : Frequency stability of the CVL-pumped LPD3000, measured using the Burleigh wavemeter.

frequency stability, with sub-gigahertz shot-to-shot jitter, and less than a 2 GHz drift over an hour (monitored using the Burleigh wavemeter), as shown in figure 5.37 .

The temporal profile of the LPD3000 laser pulses (figure 5.38) was measured using fast response vacuum photodiodes. When the laser was operated near the fluorescence maximum of a dye, typical pulse lengths and build-up times were observed to be 35 ns and 2 ns respectively . Further away from the fluorescence maximum the dye pulse length decreases, and the build-up time increases to nearly 10ns.

The near and far field beam profiles of the CVL-pumped LPD3000, acquired using the CCD camera and the Excitech frame grabber, are presented in figures 5.39 and 5.40 respectively. These profiles show the asymmetric 1.5×0.7 mm laser beam to have a divergence of 0.7 mrad vertically and 0.8 mrad horizontally, indicating a beam quality of $\sim 1.8\times$ that of the diffraction limit. It is likely that the beam quality of the dye laser is impaired at high repetition rates due to the thermal refractive index fluctuations experienced because of the single dye cuvette design peculiar to the

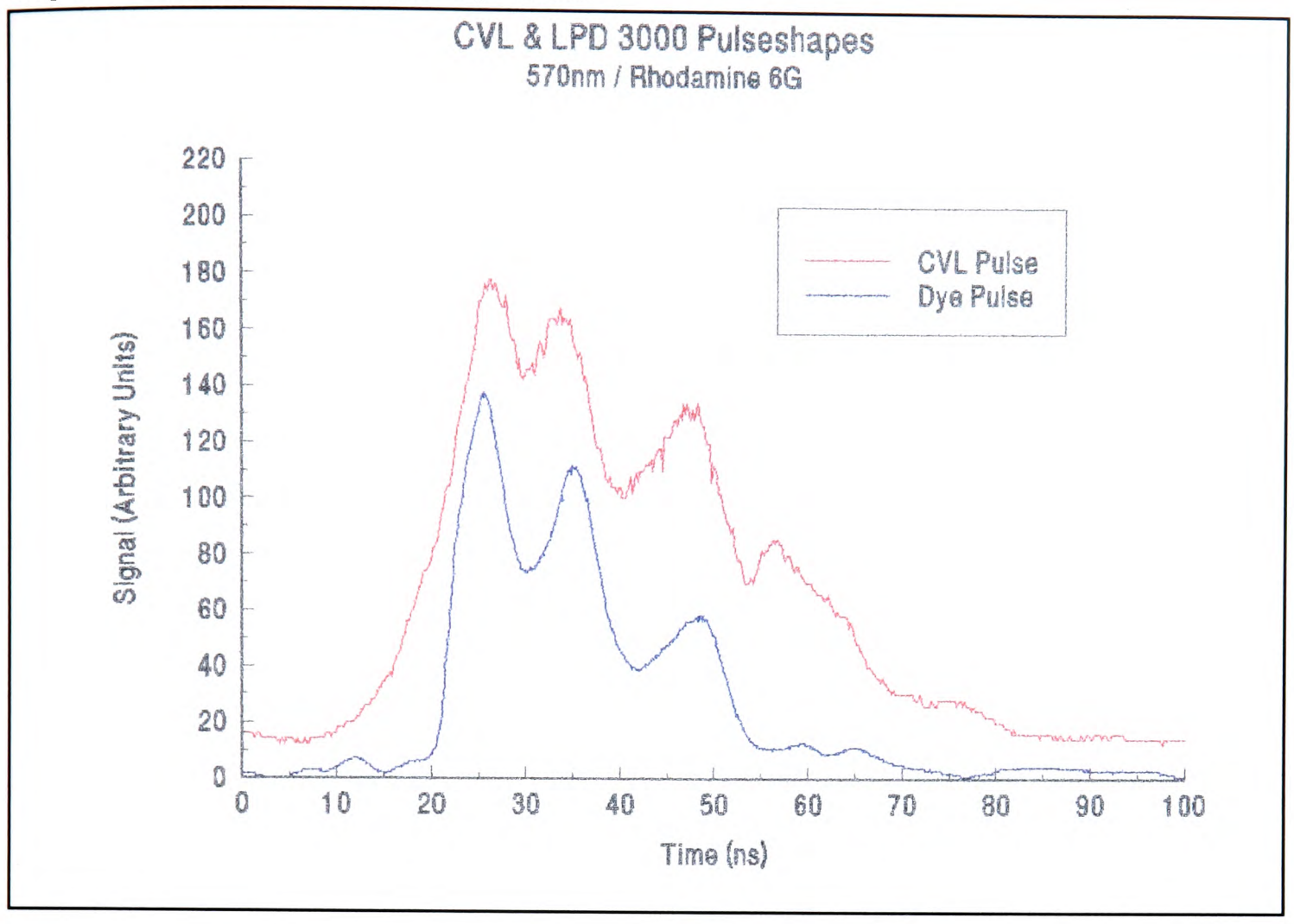


Figure 5.38 : CVL and dye laser pulse shapes from the LPD3000.

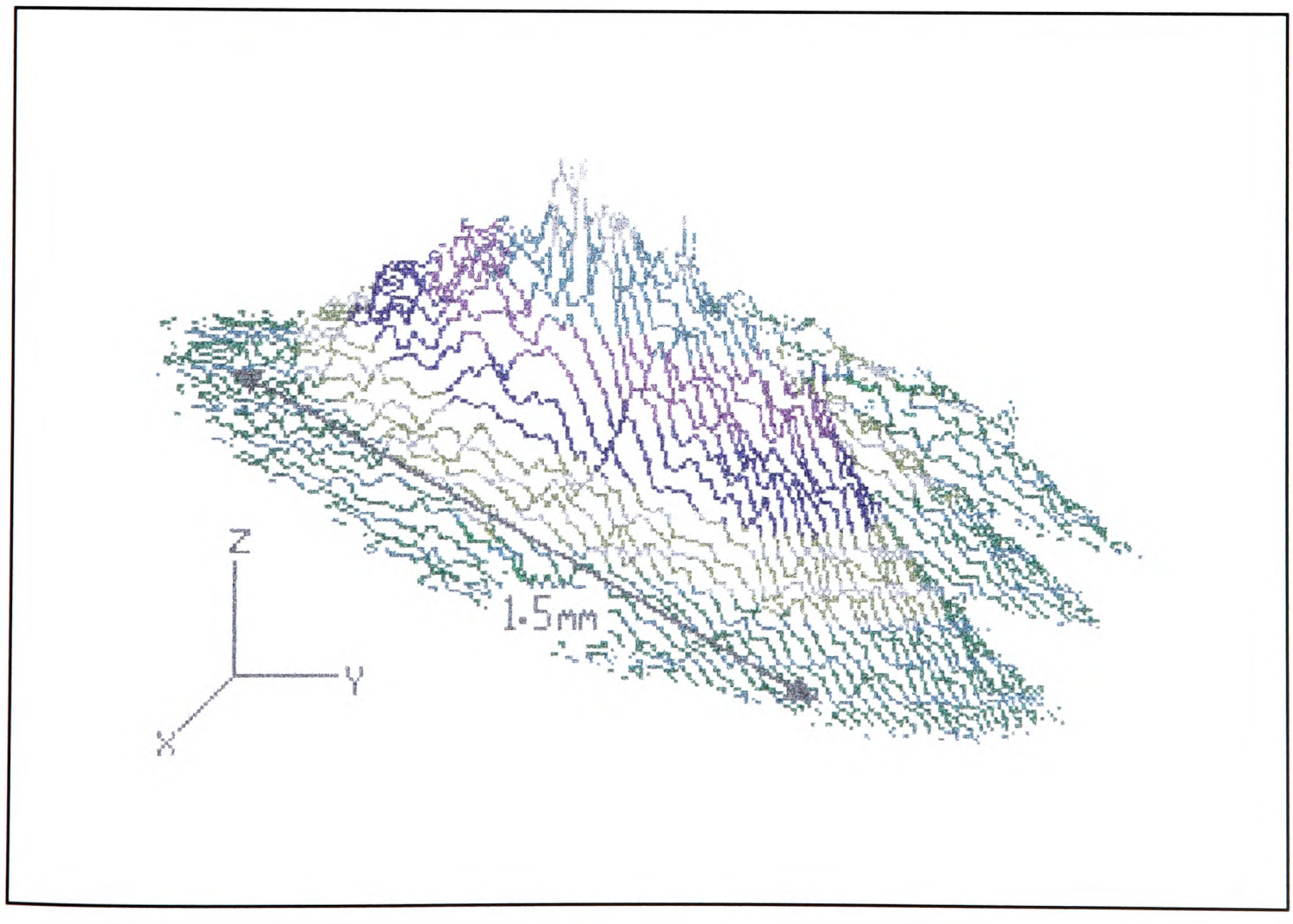


Figure 5.39 : Near field pattern of the LPD3000 dye laser beam.

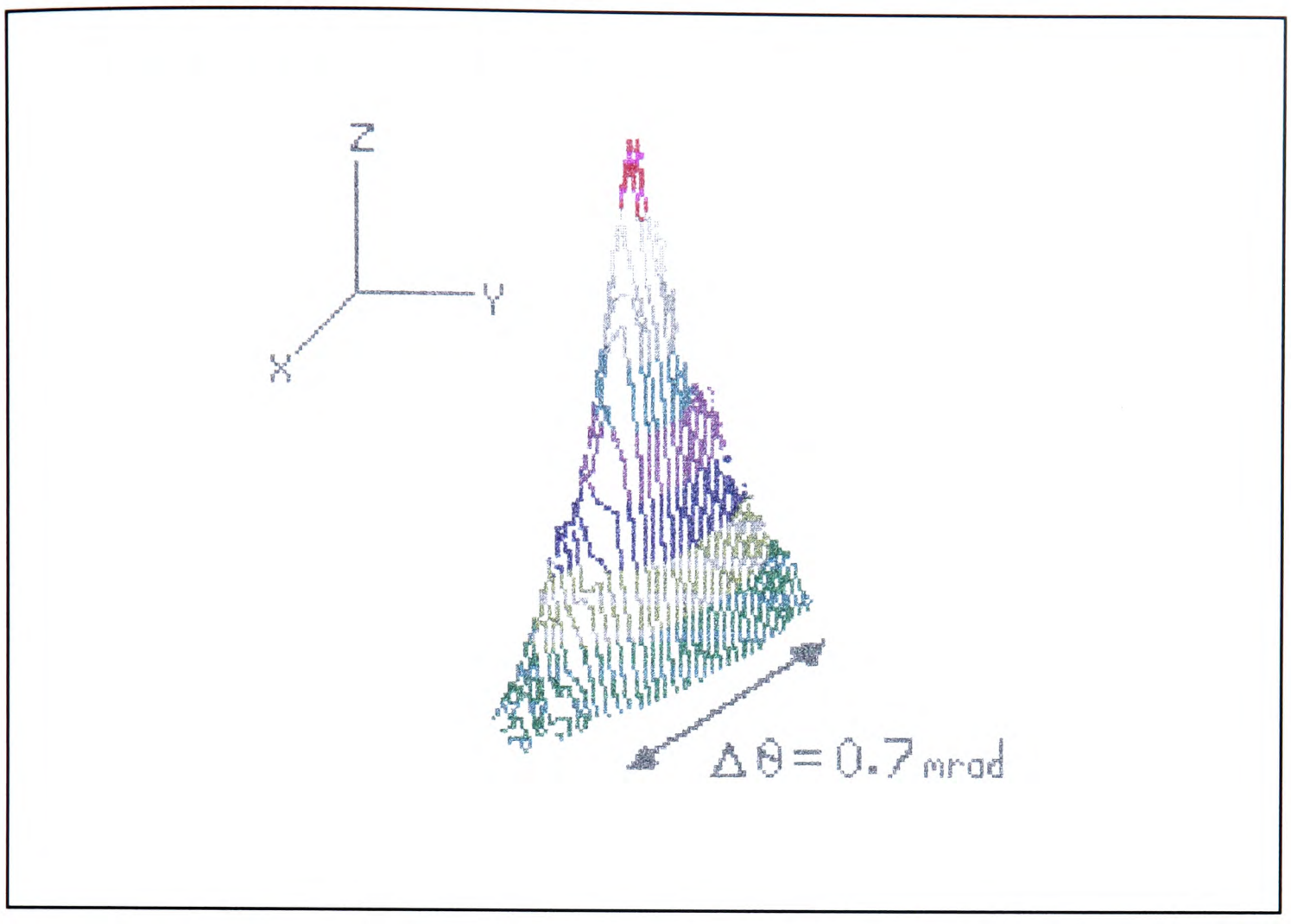


Figure 5.40 : Far field pattern of the LPD3000 dye laser.

5.5.3 The Lumonics Hyperdye HD-350

The Lumonics HD-350 dye laser [5.18] utilizes two dye cuvettes, a 20 mm long oscillator cuvette and a 40 mm long amplifier cuvette. The design is intended for use with a 40 mm wide excimer pump beam, which overfills the oscillator, but is matched to the amplifier. The pump beam path, shown in figure 5.41, is similar to that of the LPD3000, with a beamsplitter reflecting a fraction of the incident pump radiation to the oscillator, and the remainder directed to the amplifier cell via an optical delay line of $\approx$4 ns.

The oscillator (figure 5.42) is a closed-cavity hybrid multiple prism grazing incidence (HMPGI) design, with a low loss four-prism beam expander (magnification = $\times$15) used to allow operation at the more efficient grating angle of 86°, rather than the 89° typical of pure grazing incidence designs. The combination

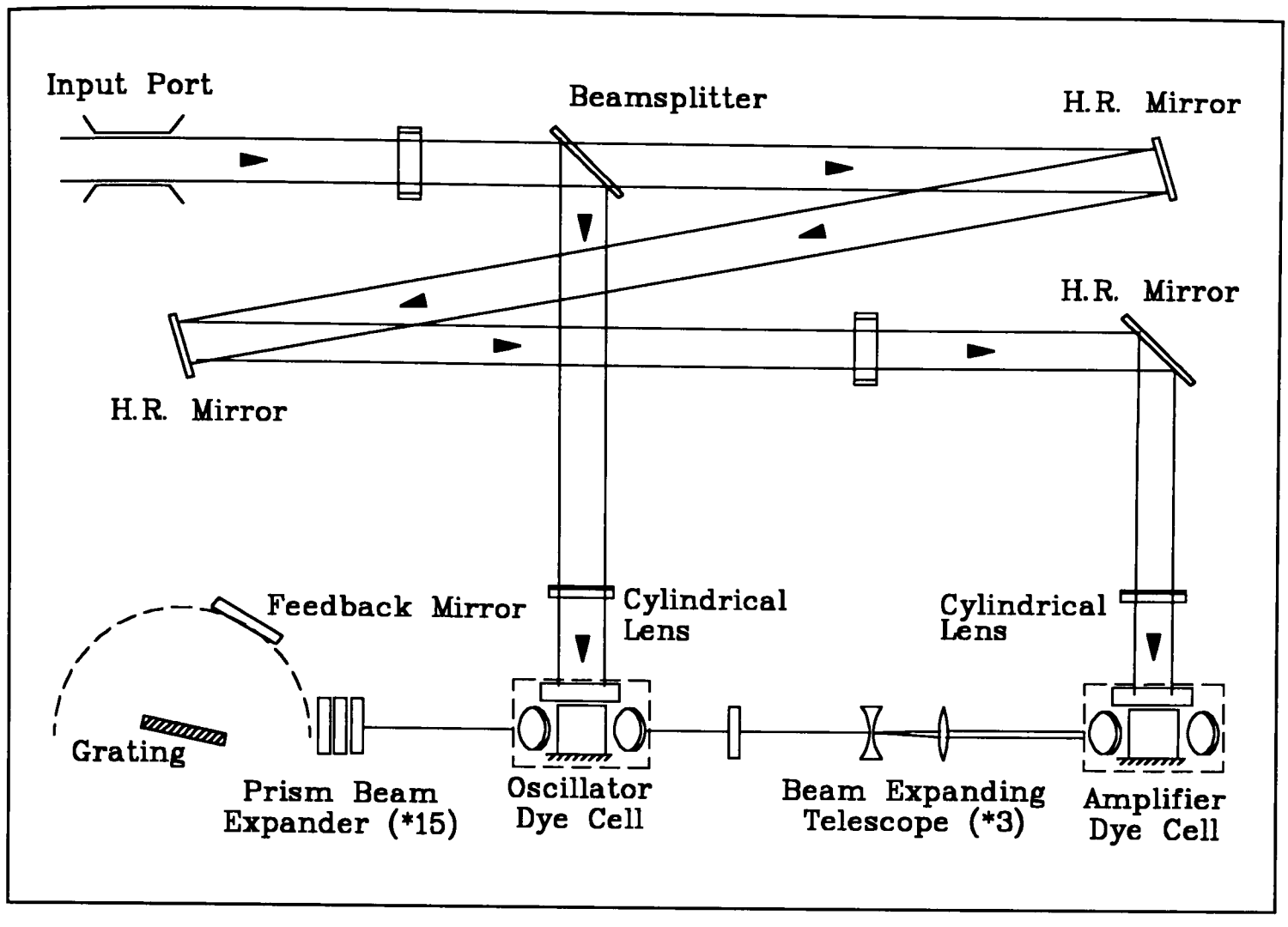


Figure 5.41 : Pump beam path of the Lumonics HD-350 dye laser.

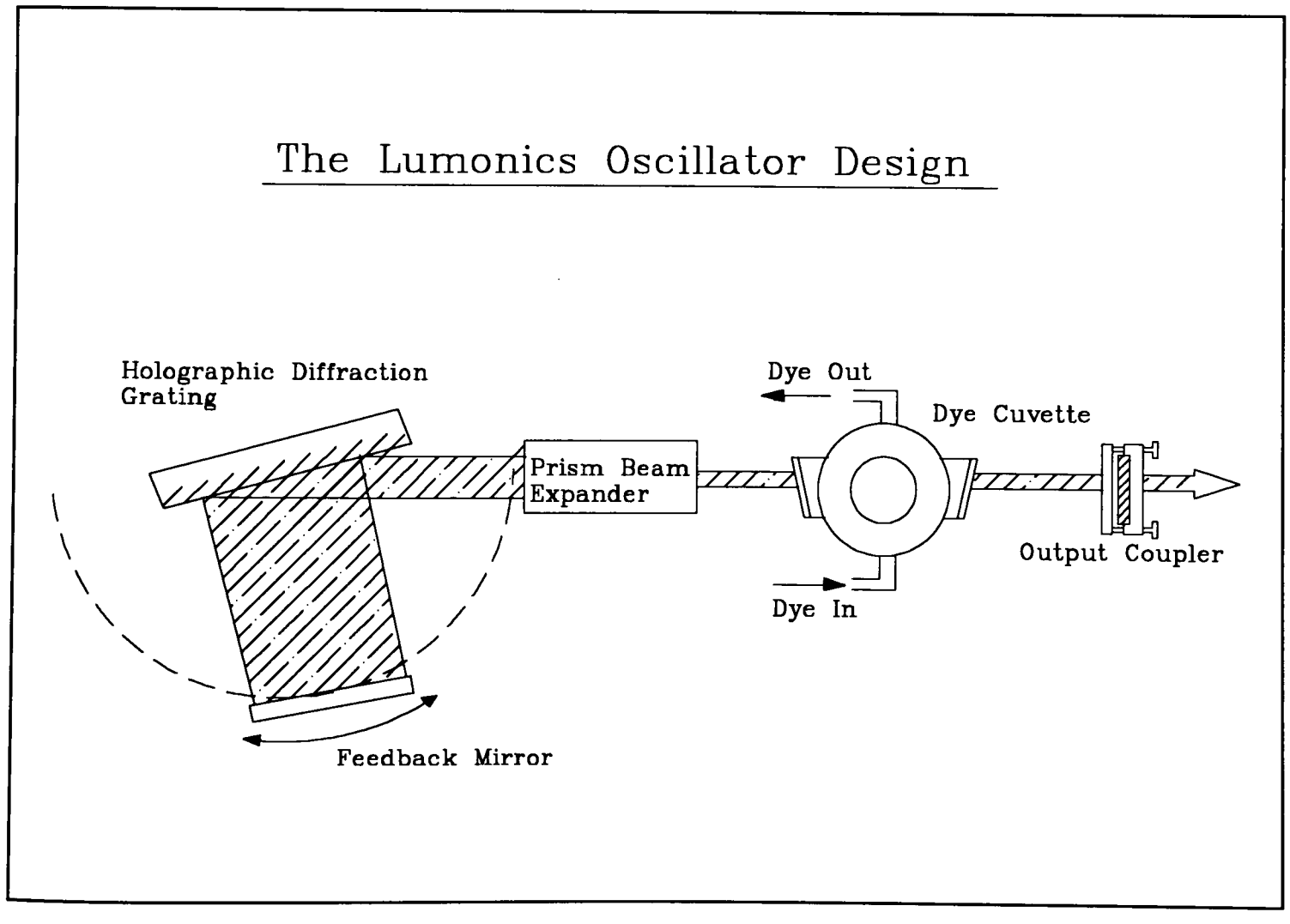


Figure 5.42 : Detail of the HMPGI dye oscillator in the Lumonics HD-350 dye laser.

of the prisms and the grating results in a highly vertically polarized output beam (>95%), which enables matched vertically polarized CVL pumping. Tuning between 320 nm and 720 nm is achieved by rotating the feedback mirror to reflect the first order diffracted from the 2400 lines/mm holographic diffraction grating back along the cavity axis. The mirror is scanned using a precision worm-and-pinion rotary drive stage, which, together with a close coupled incremental shaft encoder, permits accurate tuning with frequency steps of 0.3 GHz. However, tuning beyond 720 nm requires replacing the grating with one of 1800 lines/mm.

For the present studies, modifications to the HD-350 consisted of replacing the optics for ones coated for the CVL wavelengths, and using a high flow-rate dye circulator with wide bore flow tubes so that the active dye volume may be cleared between shots. The cuvette design in the Lumonics system is fundamentally different from the laminar flow designs found in the LPD3000 or LZhI-504 dye lasers. Here, a knife edge near the cell window (figure 5.43) is used to accelerate the dye.

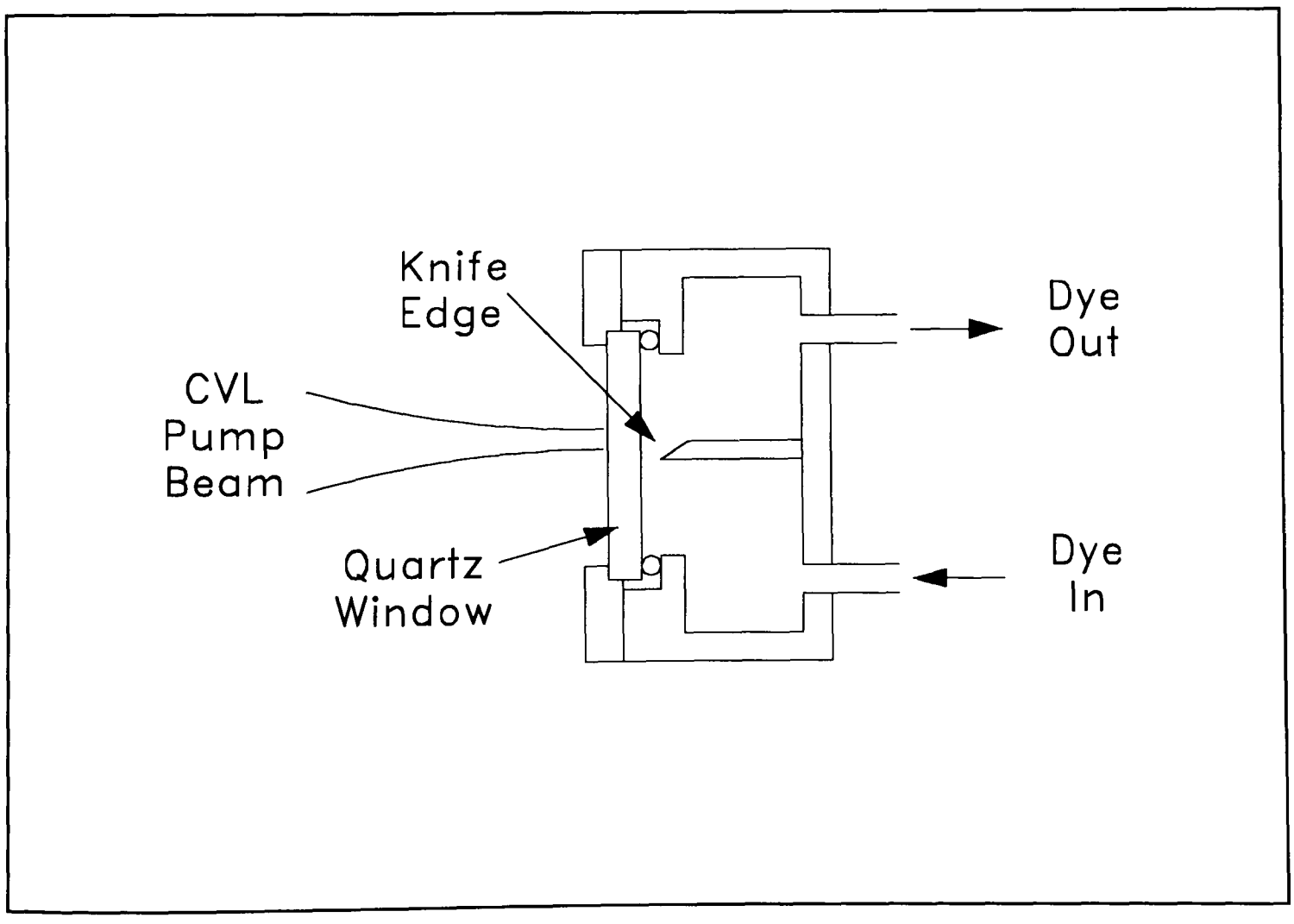


Figure 5.43 : Detail of the knife-edge cuvette design in the HD-350 dye laser.

However, the minimum knife edge-window separation is limited to 2 mm by the onset of turbulence and cavitation [5.19]; any turbulence in the dye medium destroys the optical homogeneity necessary for a good output beam and frequency stability. Thus, with the 2 mm deep, 20 mm long HD-350 dye channel, the required flow rate to clear active volume between shots is ~ 3.3 l/min when pumped by a CVL at 6.5 kHz with $f = 15$cm cylindrical lens pump optics (0.6 mrad/42mm beam) - this flow rate was comfortably met with a circulator capable of 11 litres/minute.

The use of two dye cuvettes eliminates the problem encountered with the Lambda laser of using preheated dye in the amplifier, and the associated problems of refractive index variations causing instabilities in the output beam. However, the 40mm long Lumonics amplifier cell is wholly unsuitable for the low pulse energy characteristic of the CVL pump - the ESA model of dye amplification presented in chapter 4 predicts an optimum gain length close to 10 mm for the CVL, and at 40mm the efficiency is only $\approx 50\%$ of its potential maximum. Thus, the internal amplifier was removed, and amplification was performed externally using a 20 mm long laminar flow cuvette (Radiant Dye Laser Associates RDVC 20), with a $f = 10$ cm cylindrical lens used to focus the pump beam into the dye.

The internal optics of the dye laser permit pumping with a 40×20 mm laser beam, and so the 42mm CVL beam was telescoped down to 21mm by a $\times 0.5$ Keplerian telescope external to the dye laser enclosure. Otherwise, the pumping scheme used for the HD-350 is similar to that used for the LPD3000, and again, multiple dichroic beam-steering mirrors were used to remove the yellow component of the CVL pump when using Rhodamine derivative dyes lasing in the range 550-600nm.

An early problem encountered with the HD-350, however, was the rapid deterioration of the laser dye, which manifested itself as a decrease in the output power, and a restriction of the dye tuning range. Freshly-mixed laser dye would typically last for only a few hours, after which the efficiency would be reduced to less than half of its original value. Upon investigation, a fine suspension of particles was found to contaminate the dye, even though the dye circulation loop was flushed

thoroughly with solvent before each dye change. The small particles must have been created in-situ by a chemical reaction between the solvent and/or dye with the materials comprising the dye circulation loop. Further investigation, and consultation with Lumonics, revealed the problem to lie in the dye circulation pump itself - the pump head gears were made of the material RYTON which was attacked by the methanol solvent and, gradually, fragments broke away to contaminate the dye solution. Once the pump head gears were replaced with a PTFE type polymer (PEEK) alternative, the problem was alleviated, and dye lifetimes were extended to several weeks.

Alignment, ASE and Oscillator Optimization

Because the HD-350 uses a separate oscillator and amplifier it was possible to undertake a full characterization to determine the best beamsplitter and output coupler combination to optimize the slope efficiency, pulse length and build-up time of the oscillator alone. Oscillator alignment with the standard 4% reflectivity output coupler by maximizing the output power resulted in the cavity locking onto ASE rather than lasing. Optimum cavity alignment was achieved by examining a 10% reflection of the oscillator output on a blackened screen, and adjusting until lasing was observed. Once lasing, the cavity was tuned toward longer wavelengths, where the gain is smaller, and, consequently, the cavity alignment is more critical. When the laser output started to flicker the cavity was finely realigned and tuned even further into the red, and the alignment process repeated. By the iterative use of this technique toward longer and longer wavelengths, the cavity was aligned for optimum laser action and not ASE. However, even with careful alignment, the ASE content in the output was still unacceptably high, and efforts to minimize the ASE centred around three techniques:-

1. Increasing the reflectivity of the output coupler (increasing the cavity Q) to make conditions more favourable for lasing.
2. Spatially filtering the oscillator output before amplification.

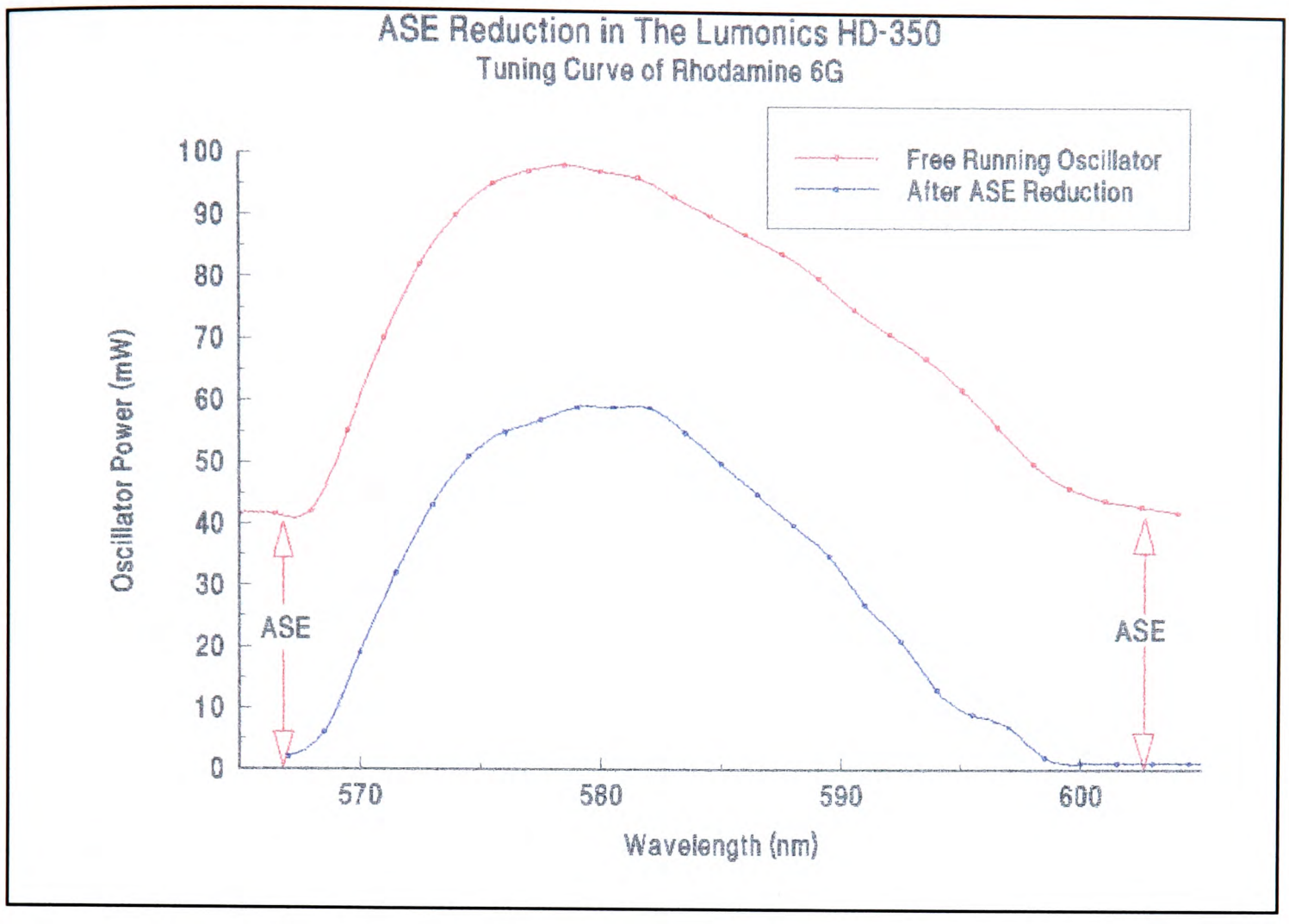


Figure 5.44 : HD-350 tuning range with and without ASE reduction techniques (Rhodamine 6G).

3. Rotating the pump line focus relative to the oscillator axis - the ASE then follows the pump line rather than the oscillator beam, and is removed by a crude mask.

The net result of these efforts can be seen in the tuning curve displayed in figure 5.44, where the previously large ASE background has been significantly reduced.

With a 25% reflectivity beamsplitter, the slope efficiency, threshold, build-up time and pulse length were recorded as a function of the output coupler reflectivity. As can be seen from table 5.3, and figures 5.45a,b,c,d, as the Q of the cavity is increased by increasing the output coupler reflectivity, the threshold, slope efficiency and build-up time decrease, whilst the pulse length and tuning range increase.

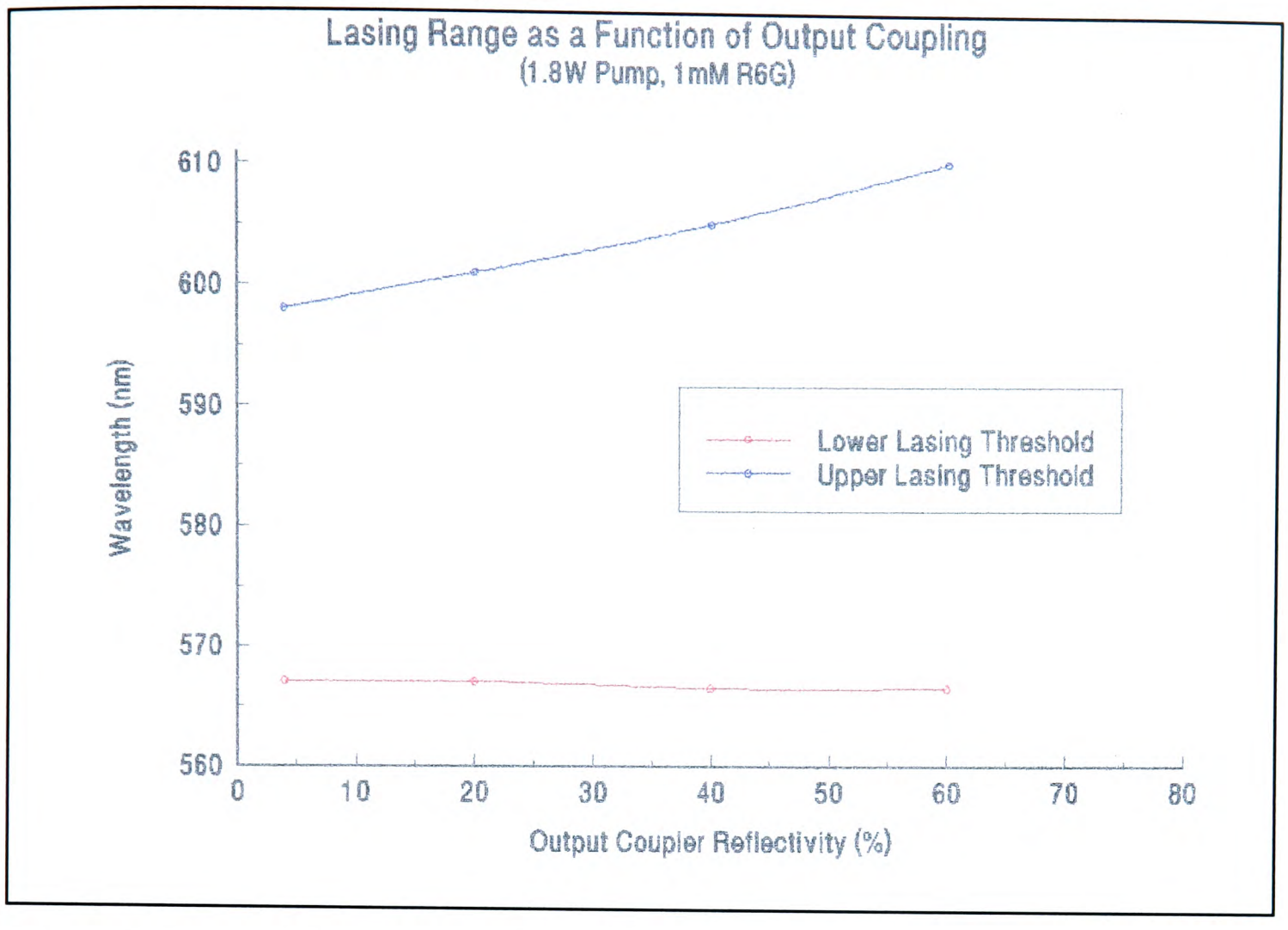


Figure 5.45a : HD-350 tuning range as a function of output coupling.

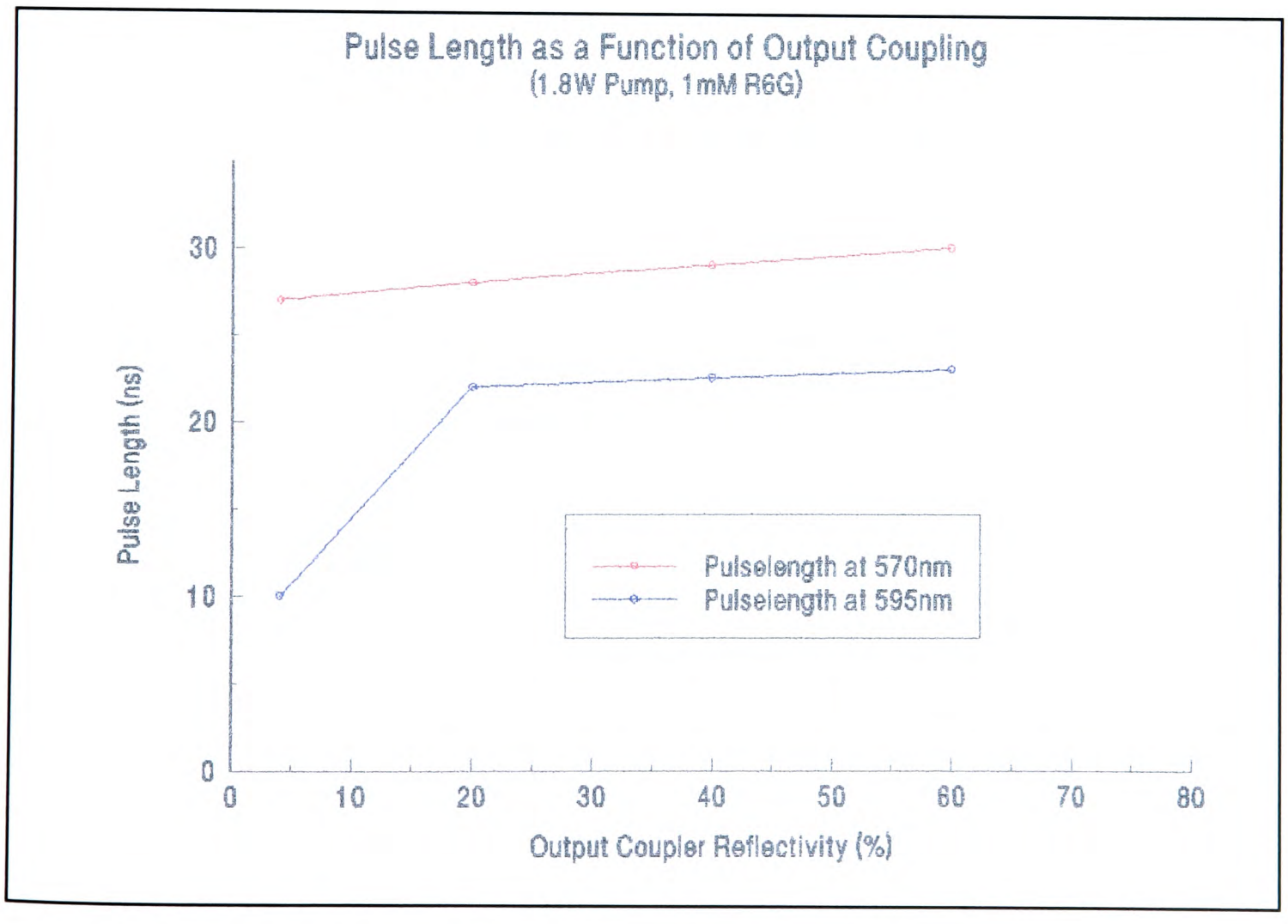


Figure 5.45b : HD-350 oscillator pulse length as a function of output coupling.

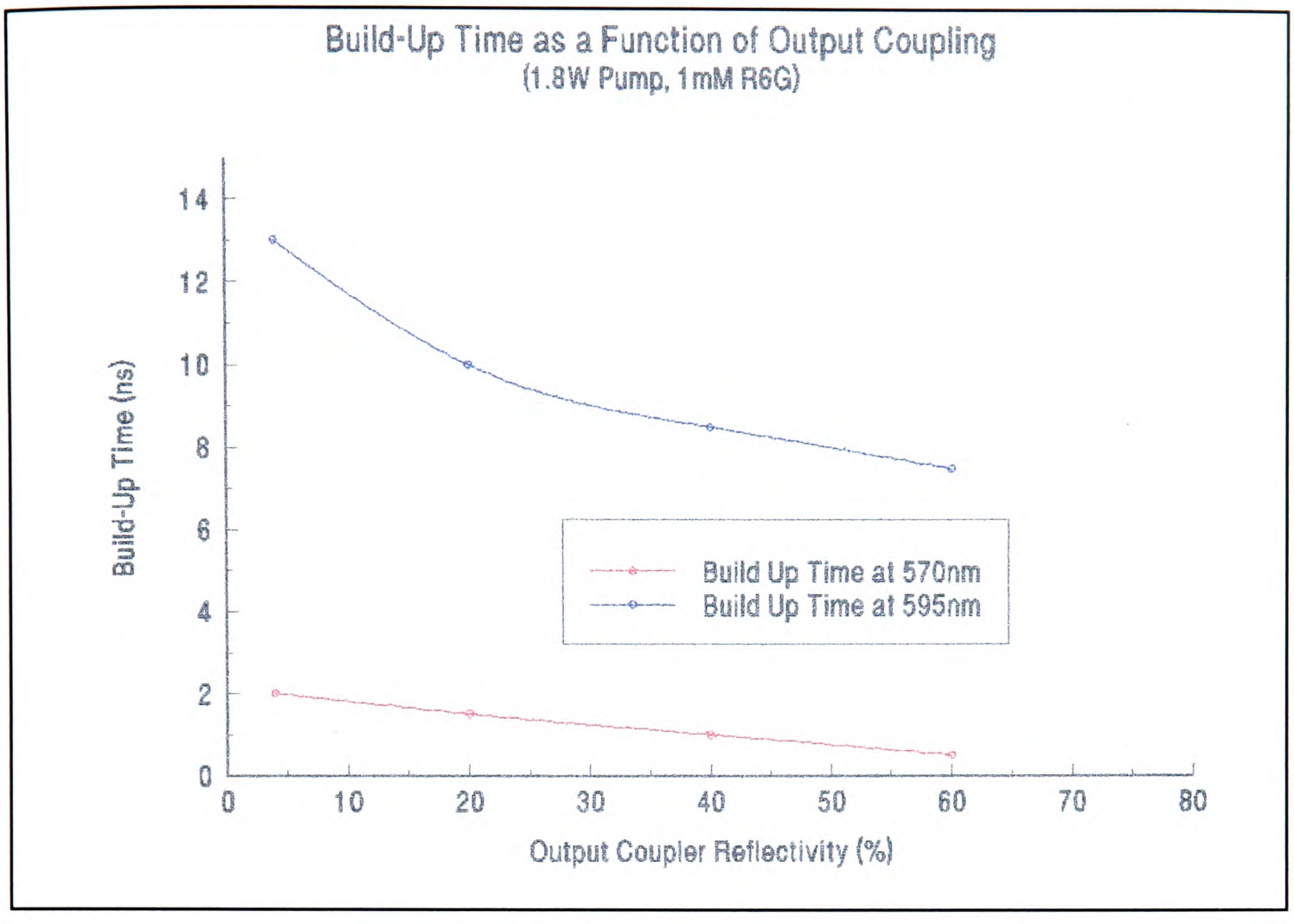


Figure 5.45c HD-350 Oscillator build-up times as a function of output coupling.

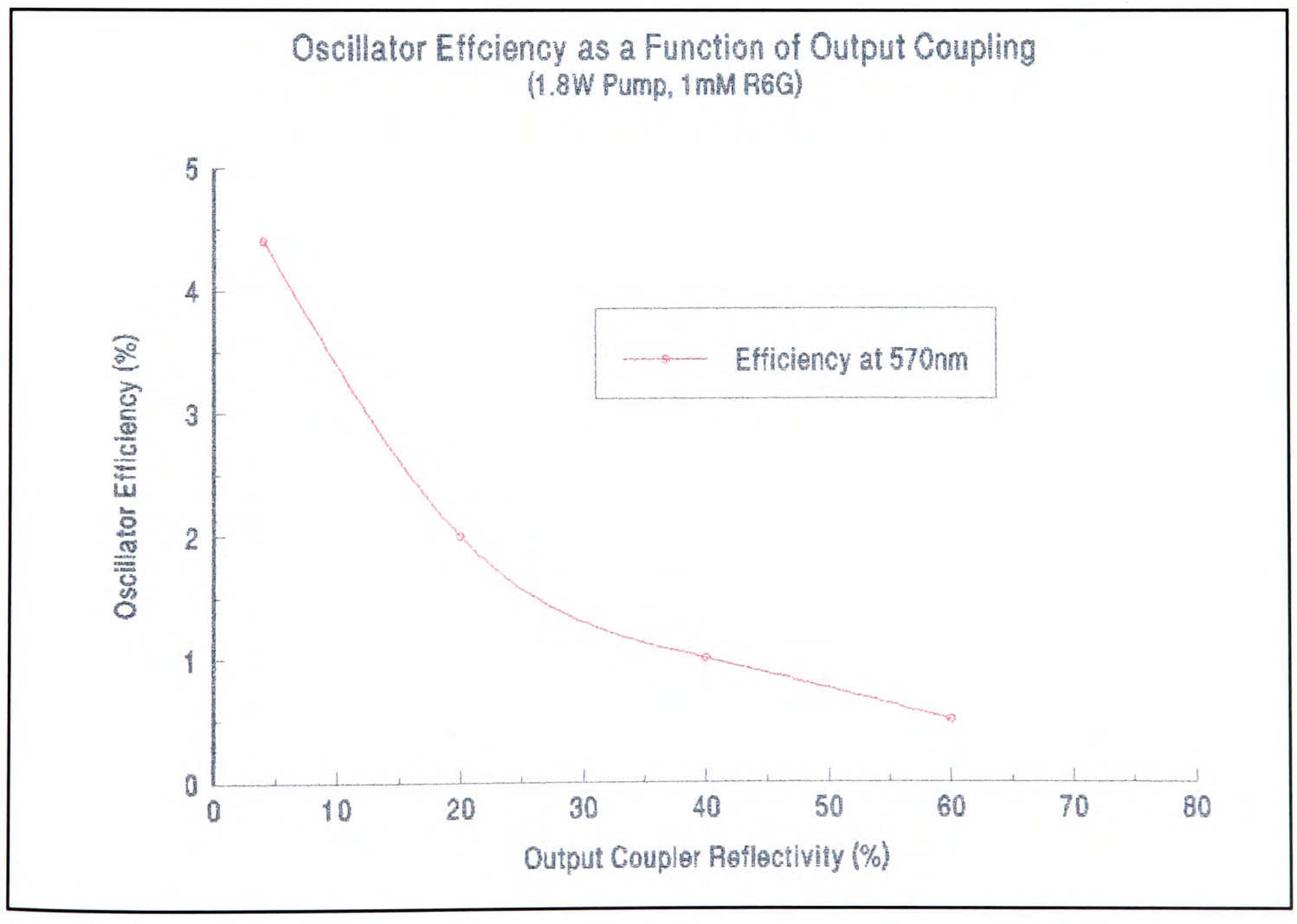


Figure 5.45d : HD-350 oscillator slope efficiency as a function of output coupling.

Table 5.3

Output Coupler Reflectivity	Slope Efficiency	Threshold [Watts]	Pulse length [ns]		Build-up Time [ns]		Tuning Range [nm] (Rhodamine 6G)
			τ_{571}	τ_{595}	τ_{571}	τ_{595}	
4%	4.4%	0.63	27	10	2	13	567 - 598
20%	2%	0.60	28	22	1.5	10	567 - 601
40%	1%	0.58	29	22	1	8.5	566.5 - 605
60%	0.5%	0.52	30	23	<1	7.5	566.5 - 610

The choice of optimum output coupling is not obvious. The main criteria are that the oscillator build-up time and pulse length should be matched to the amplifier excitation, and that 50-100 mW of oscillator seed radiation should arrive at the amplifier in order to saturate the gain (Chapter 4). With the 10 W of green CVL power available, the 20% reflectivity output coupler was chosen, since this equips the oscillator with a pulse length in excess of 20 ns across nearly the whole of the tuning range, and sufficient output power to saturate the amplifier gain. Optimization of the dye concentration to 1 mM and polarization matching the CVL pump to the oscillator cavity yielded a slope efficiency of 5.1% with the 20% output coupler; further improvements by silvering the grating resulted in a slope efficiency in excess of 6%.

It was noticed that, in the factory pre-set configuration, the flux from the intra-cavity prism beam expander overfilled the grazing incidence grating, and so the grating angle was increased from 86° to 80°. This resulted in the slope efficiency increasing by greater than a factor of two (to 13%), and the build-up times and pulse lengths at 595 nm changed from 10 ns to 4 ns, and from 22 ns to 30 ns respectively.

External amplification of the oscillator output in a 1.2 mM Rhodamine 6G solution in methanol was performed at efficiencies in excess of 40%, which gave an overall conversion efficiency approaching 30% at the peak of Rhodamine 6G.

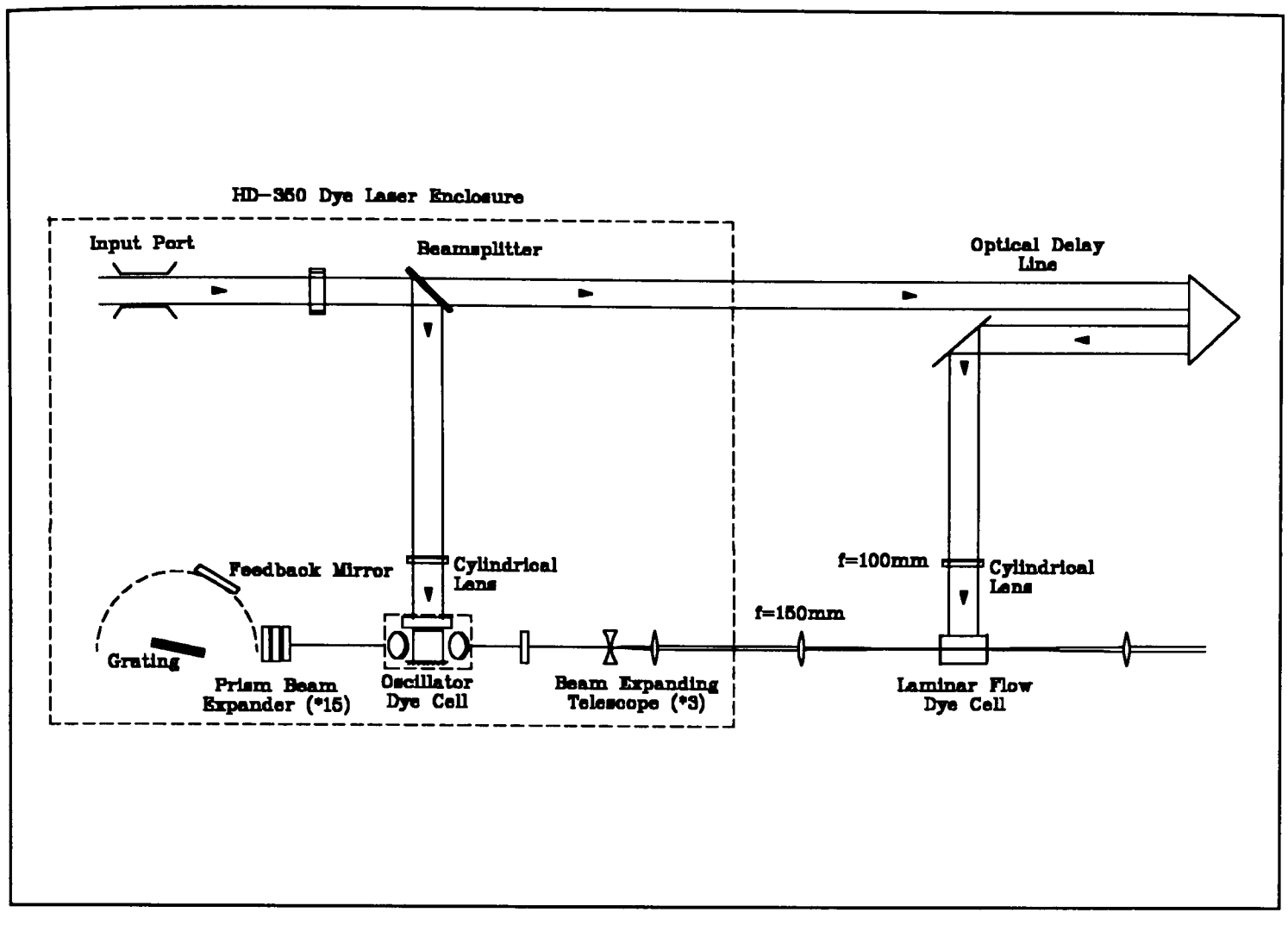


Figure 5.46 : Amplification of the HD-350 in an external laminar flow dye cell.

Dye Laser Characteristics

The time-averaged frequency bandwidth measurements made using a scanning Fabry Perot etalon are shown in figure 5.47. Successive measurements with different free spectral ranges indicate a bandwidth of 2.6 GHz for the oscillator with the grating angle=86°, and 4-6 GHz when the grating angle is increased to ~80°. There was no degradation in the frequency bandwidth during amplification, although there was a slight shift in absolute frequency, as described in chapter 4. The bandwidth measurements also agree with those measured using the Burleigh Wavemeter, and the frequency stability (figure 5.48) proved to be better than 0.5 GHz shot-to-shot and less than a 1 GHz drift in frequency was observed over an hour. The near and far field beam profiles recorded using the Excitech Profiler 256 are displayed in figures 5.49 and 5.50. These show a beam divergence of 0.4 mrad vertically and 0.5 mrad horizontally, and correspond to a beam diameter×divergence product of $1.28\times10^{-6}m^2$ (1.7 × diffraction limit).

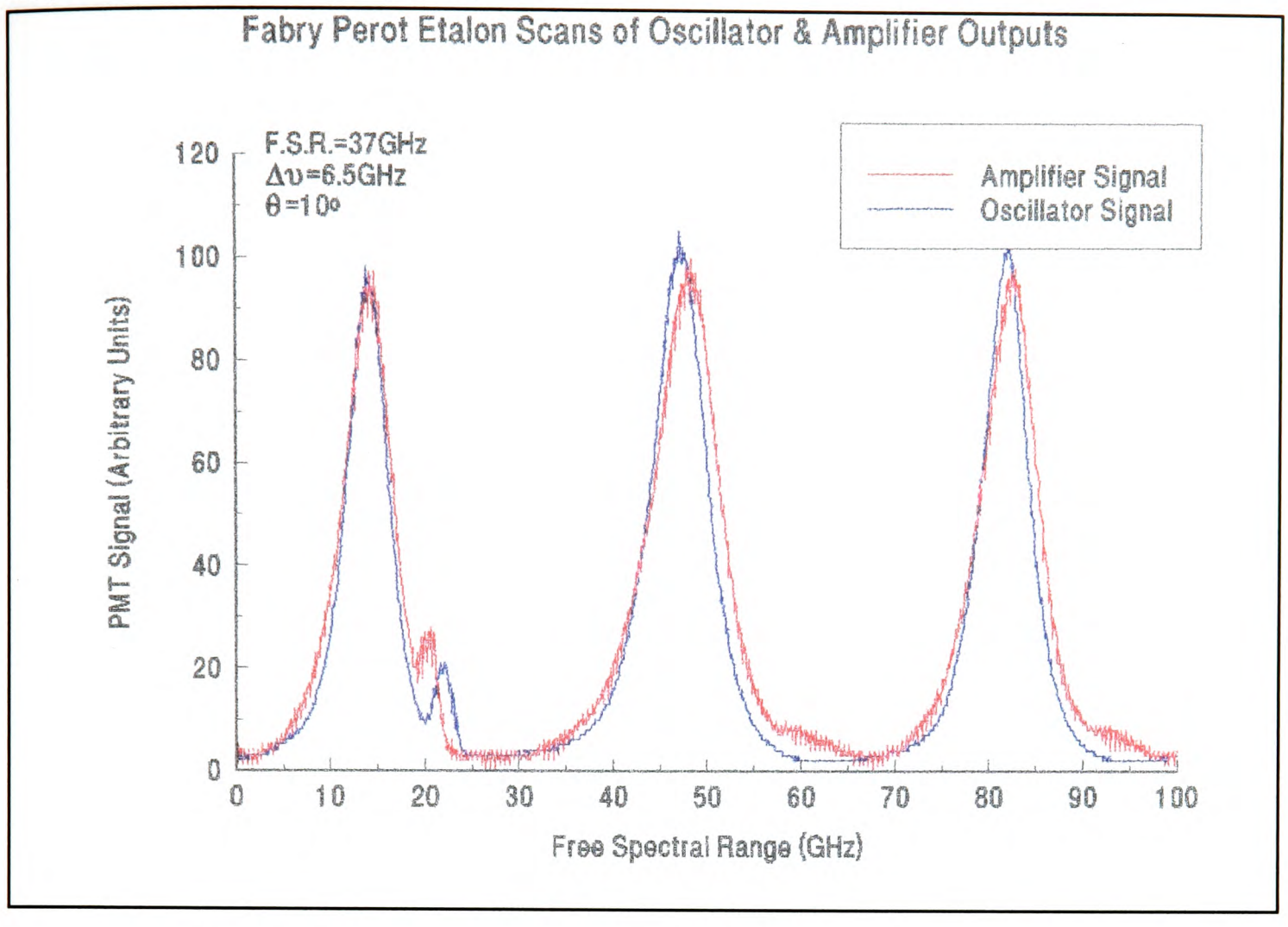


Figure 5.47 : Fabry Perot interferometer scan of the HD-350 laser bandwidth.

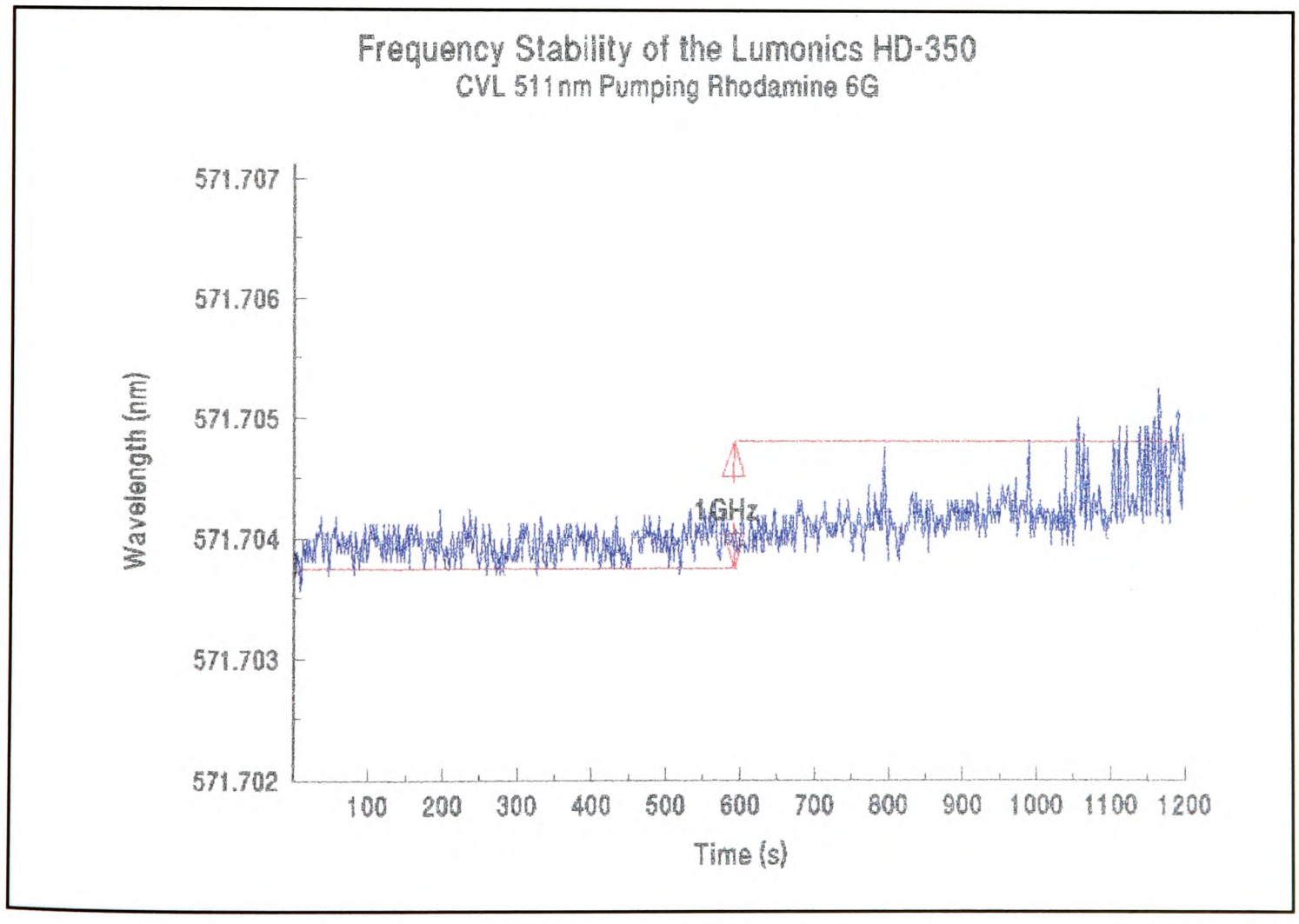


Figure 5.48 : Frequency stability of the HD-350 measured using the Burleigh wavemeter.

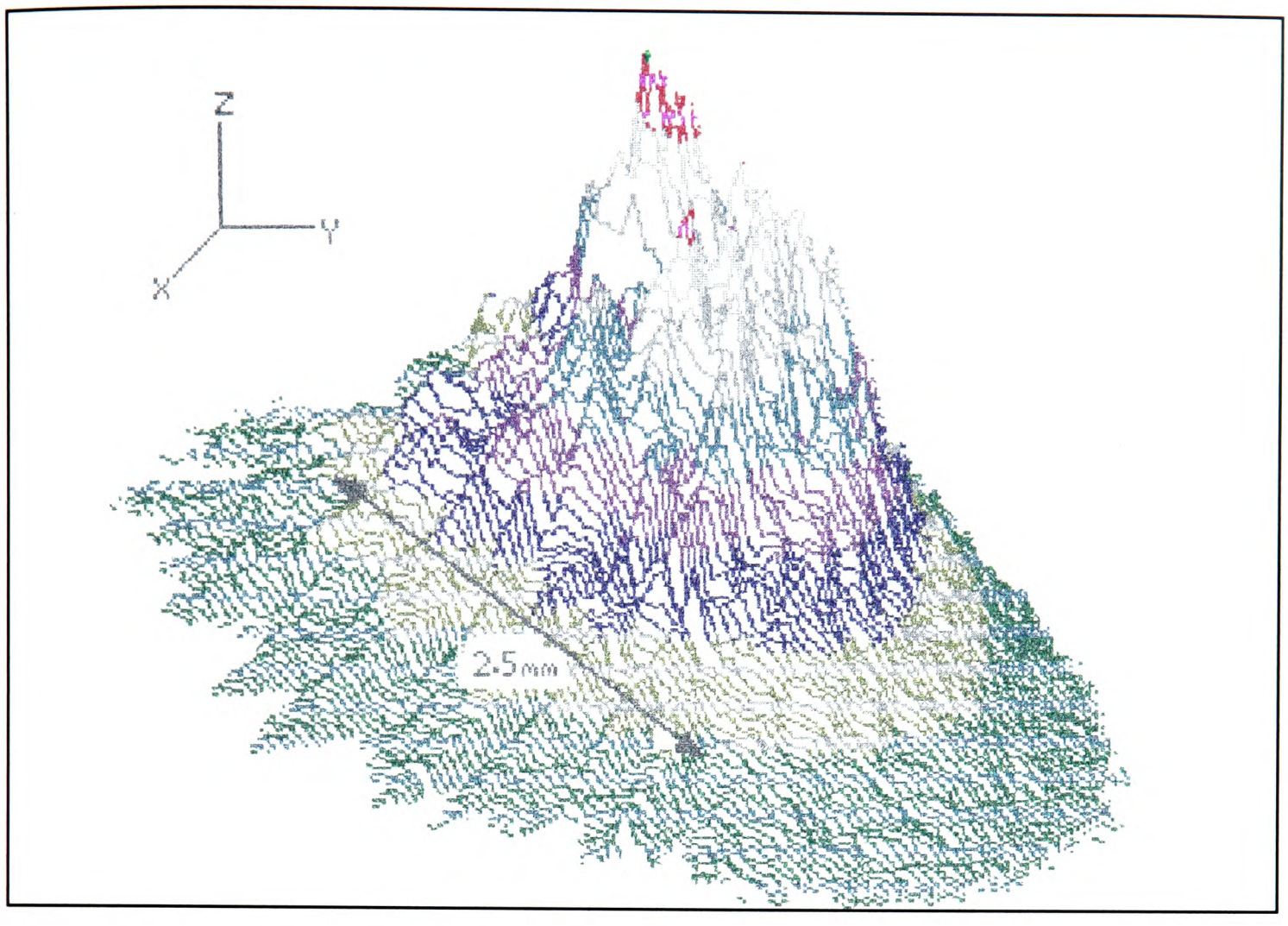


Figure 5.49 : Near field pattern of the HD-350 laser beam.

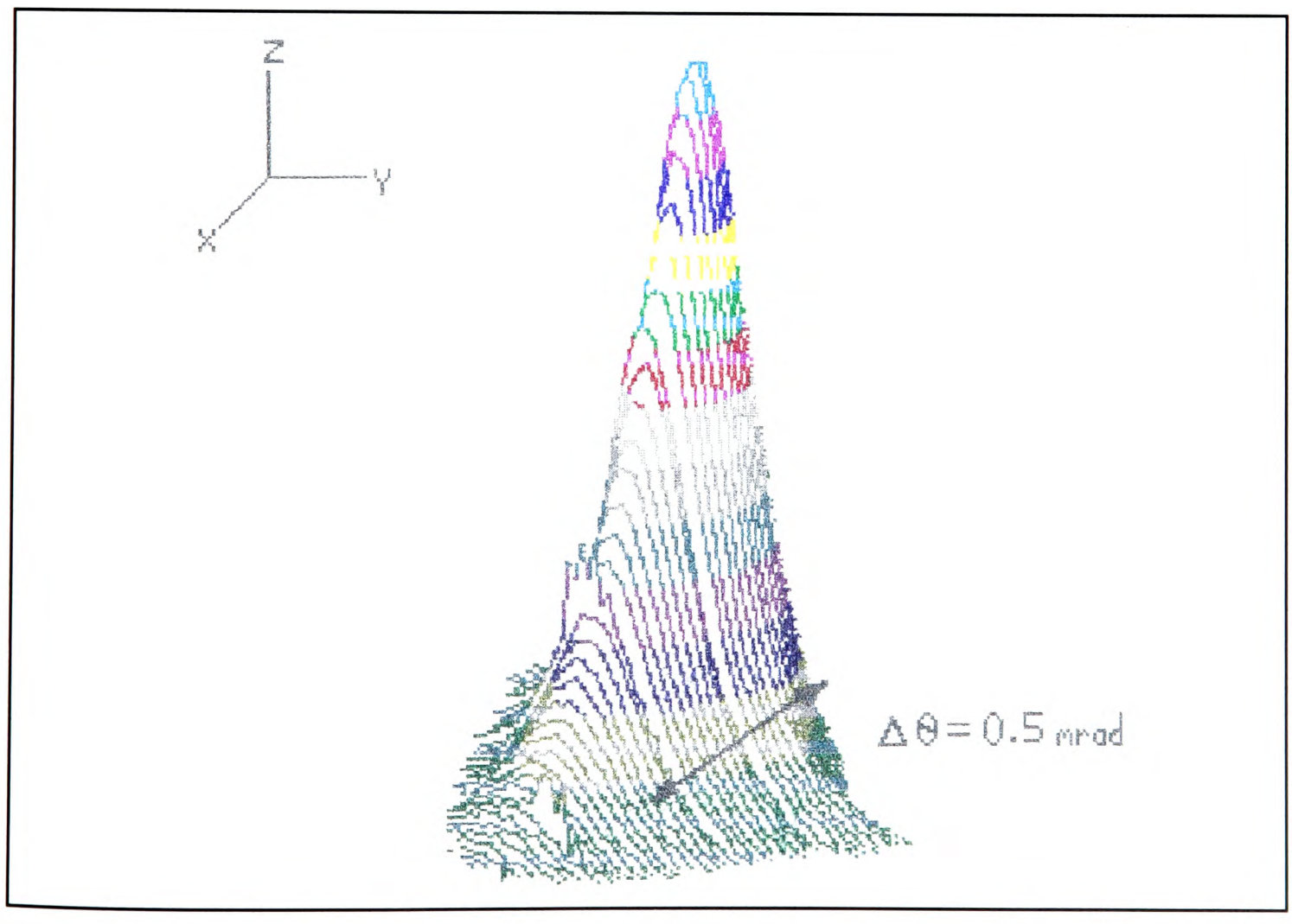


Figure 5.50 : Far field pattern of the HD-350 laser beam

5.6 Conclusion

A series of experiments has been conducted to gain a physical insight into the laser and optical parameters necessary for the optimum operation of dye lasers at kilohertz repetition rates. By using a polarized unstable CVL cavity, whose polarization is matched to the preferred polarization of the dye oscillator, the efficiency of operation may be improved by a factor of nearly three over that offered by a CVL operated with a plane-plane cavity. Furthermore, it has been demonstrated that CVL-pump-beam ASE removal enhances the conversion efficiency, and that careful choice of oscillator grating materials is required, depending upon the spectral range of operation.

Once modified, the three commercial dye lasers show themselves to be useful sources of high repetition rate tunable laser radiation, and are ideally suited to RIMS. A summary of the dye laser characteristics for CVL pumping are presented in table 5.4 below.

Table 5.4

	Lambda Physik LPD3000	Lumonics HyperDye HD-350	LZhI-504
Conversion Efficiency	23%	30%[1]	13%[2]
Bandwidth with etalon	7GHz 800MHz	2-6GHz[3]	24GHz 4GHz
Frequency Stability	<1GHz	<1GHz	<1GHz
Beam Divergence Vert: Horiz:	0.7mrad 0.8mrad (1.8×Diff.)	0.4mrad 0.5mrad (1.7×Diff.)	0.3mrad 0.25mrad (1.4×Diff.)
Build-Up Time	1 ns (570nm)	1ns (570nm)	1 ns (570nm)
Pulse Length	33 ns (570nm)	33ns (570nm)	30ns (570nm)

[1] With external amplification. [2] Oscillator only. [3] Dependent upon grating angle.

The choice of best CVL-pumped dye laser is determined by the application. Undoubtedly, the best calibration facilities are offered by the LZhI-504, although the dye laser bandwidth is rather large, and additional frequency narrowing schemes must be employed to compare with the Lambda Physik or Lumonics dye lasers. The best efficiency is offered by the Lumonics HyperDye HD-350, although, to reach these conversion efficiencies, significant modification to the oscillator was required, and the amplification was performed externally to the dye laser enclosure. The Lambda Physik LPD3000 dye laser offers a compromise between the Lumonics and Russian lasers, by offering good overall performance whilst requiring "minimal" modifications for CVL-pumping.

Appendix 5.I : Lifetime Against Stimulated Emission

From simple rate equation analysis, the life time against stimulated emission may be shown to be given by :-

$$\frac{dN^*}{dt} = -\frac{n}{V}N^*\sigma(\omega)c \qquad \textbf{A1.1}$$

and

$$\tau_{(L.A.S.E.)} = \frac{1}{\frac{n}{V}\sigma c}\ , \qquad \textbf{A1.2}$$

so, for a typical dye oscillator with the following parameters :

P_{OUT}	$\approx$ 100 mW
Output Coupler Reflectivity	= 25%
Pulse length	= 25 ns
Repetition Rate	= 6.5 kHz,

the intra-cavity peak power will be $\approx$ 2.46 kW.

Now, in the dye cuvette, the beam will typically be circular, with a diameter of 0.1 mm (at 1mM dye concentration, the absorption depth for the CVL is $\sim 50\mu$m). Thus, the peak intensity $I_{Pk} = P_{Pk}/A \approx 78\ GW/m^2$.

For coherent, collimated laser radiation,

$$I = c\frac{n}{V}h\nu\ , \qquad \textbf{A1.3}$$

and, therefore, for a dye oscillator operating at 570 nm with a Rhodamine 6G dye ($\sigma \approx 1.8\times10^{-16}cm^2$), we have a photon flux $n/V \approx 7.5\times10^{20}$ and a lifetime against stimulated emission of

$$\tau_{LASE} \approx 250\ ps\ ,$$

which is of the same order of magnitude as the lifetime of a dipole against collisional reorientation (100 ps).

Appendix 5.II : Gaussian Beam Focusing

A Gaussian beam is characterized by a complex radius q :

$$q = z - ib \quad , \qquad \textbf{A2.1}$$

where b is the confocal parameter, and z is the distance from the beam waist. The spot size of the beam at point z is then given by :-

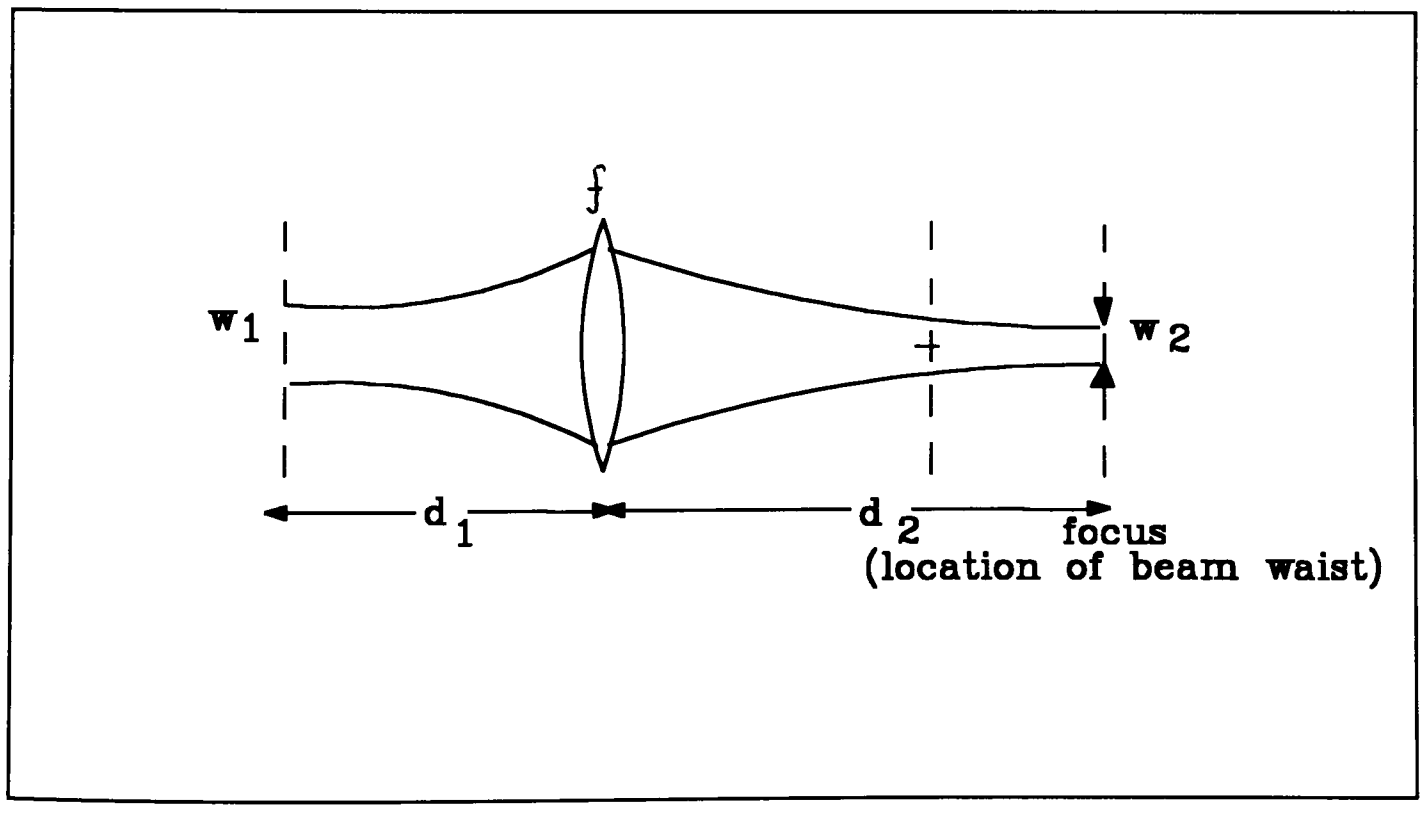
$$w(z)^2 = w_0^2 . [1 + \frac{z^2}{b^2}] \quad , \qquad \textbf{A2.2}$$

where

$$w_0 = \frac{2.b}{k} = \frac{|b|.\lambda}{\pi} \quad . \qquad \textbf{A2.3}$$

Therefore, at the beam waist:-

$$w(z) = w_0 = \sqrt{\frac{2.b}{k}} \quad . \qquad \textbf{A2.4}$$



According to the ABCD law of Gaussian beams, the transformation of the complex radius of a Gaussian beam propagating through an optical system is governed by the same optical transfer matrices as for classical light (in the paraxial approximation).

The transfer matrices are:-

$$Translation = \begin{pmatrix} 1 & d \\ 0 & 1 \end{pmatrix} \qquad \textbf{A2.5}$$

and

$$Lens = \begin{pmatrix} 1 & 0 \\ \frac{-1}{f} & 1 \end{pmatrix}. \qquad \textbf{A2.6}$$

Therefore, the system matrix for a translation through a lens to the focus is given by:-

$$M = \begin{pmatrix} 1 & d_2 \\ 0 & 1 \end{pmatrix}.\begin{pmatrix} 1 & 0 \\ -\frac{1}{f} & 1 \end{pmatrix}.\begin{pmatrix} 1 & d_1 \\ 0 & 1 \end{pmatrix} \qquad \textbf{A2.7}$$

$$= \begin{pmatrix} 1 & d_2 \\ 0 & 1 \end{pmatrix}.\begin{pmatrix} 1 & d_1 \\ -\frac{1}{f} & 1-\frac{d_1}{f} \end{pmatrix} = \begin{pmatrix} 1-\frac{d_2}{f} & d_1+d_2-\frac{d_1.d_2}{f} \\ -\frac{1}{f} & 1-\frac{d_1}{f} \end{pmatrix}, \qquad \textbf{A2.8}$$

and so, according to the ABCD law of Gaussian beams :-

$$q_2 = \frac{(1-\frac{d_2}{f}).ib_1+d_1+d_2-\frac{d_1.d_2}{f}}{\frac{-i.b_1}{f}+1-\frac{d_1}{f}} = \frac{f.ib_1-d_2.ib_1+d_1.f+d_2.f-d_1.d_2}{f-d_1-ib_1} \qquad \textbf{A2.9}$$

$$= \frac{(f-d_2).ib_1+(d_1+d_2).f-d_1.d_2}{(f-d_1)^2+b_1^2}.((f-d_1)+ib_1), \qquad \textbf{A2.10}$$

$$q(z=0) = ib_2 = \frac{f^2.ib_1+(d_1+d_2).(f-d_1).f-d_1.d_2.(f-d_1)-b_1^2.(f-d_2)}{(f-d_1)^2+b_1^2}, \qquad \textbf{A2.11}$$

so, comparing the real and imaginary components :-

$$b_2 = \frac{f^2.b_1}{(f-d_1)^2+b_1^2} \quad , \quad 0 = (d_1+d_2).(f-d_1).f-d_1.d_2.(f-d_1)-b_1^2(f-d_2) \qquad \textbf{A2.12}$$

and so, since we're looking at the focus and, hence, the beam waist of q_2, and the beam waists are related to the complex parameters via :-

$$w_2^2 = \frac{\lambda.b_2}{\pi} \qquad w_1^2 = \frac{\lambda.b_1}{\pi} \; . \qquad \textbf{A2.13}$$

Hence, we arrive at the equation :-

$$\frac{1}{w_2^2} = (1-\frac{d_1}{f})^2.\frac{1}{w_1^2}+\frac{1}{f^2}.(\frac{\pi.w_1}{\lambda})^2 \; . \qquad \textbf{A2.14}$$

Using the equality resulting from comparing the real coefficients,

$$0 = d_1.f^2-d_1^2.f+d_2.f^2-d_1.d_2.f-d_1.d_2.f+d_1^2.d_2-b_1^2.f+b_1^2.d_2 \qquad \textbf{A2.15}$$

$$\Rightarrow \quad d_2.f^2-2d_1.d_2.f+d_1^2.d_2+b_1^2.d_2 = d_1^2.f-d_1.f^2+b_1^2.f \qquad \textbf{A2.16}$$

$$d_2-f = \frac{(d_1-f).f^2}{(d_1-f)+b_1^2} \; . \qquad \textbf{A2.17}$$

Hence:-

$$d_2-f = \frac{(d_1-f).f^2}{(d_1-f)+(\frac{\pi}{\lambda}.w_1)^2} \; . \qquad \textbf{A2.18}$$

Chapter 5 : References

[5.1] C.E. Webb
High Power Dye Lasers Pumped by Copper Vapor Lasers
High Power Dye Lasers, Springer Optical Sciences **65** *Ed. F.J. Duarte (1992)*

[5.2] I.J. Evans & C.E. Webb
CVL Pumped Dye Lasers For Resonance Ionization Spectroscopy
Proc. Intnl. Conf. Lasers 1991 STS Press McLean VA (1992)

[5.3] T.G.M. Freegarde
Spectroscopic Applications of Pulsed Metal Vapour Lasers
D.Phil Thesis, Oxford University (1989)

[5.4] D.W. Coutts, M.D. Ainsworth & J.A. Piper
Efficient Green/Yellow Conversion of the Copper Vapour Laser Output
Opt. Commun. **75** *301 (1990)*

[5.5] D.W. Phillion, D.J. Kuizenga, A.E. Seigman
Rotational Diffusion and Triplet State Processes in Dye Laser Solutions
J. Chem. Phys. **61** *3828 (1974)*

[5.6] P. Debye
Polar Molecules
Dover Publications, London (1929) p. 84

[5.7] T.J. Chuang & K.B. Eisenthal
Studies of Effects of Hydrogen Bonding on Orientational Relaxation Using Picosecond Light Pulses
Chem. Phys. Lett. **11** *368*

[5.8] P. Ewart Oxford University
Private Communication

[5.9] D.W. Coutts, M.D. Ainsworth, J.A. Piper
Enhanced Efficiency of UV Second Harmonic & Sum Frequency Generation From Copper Vapour Lasers
IEEE J.Q.E. **26** *1555 (1990)*

[5.10] W. Ruster et al.

A Resonance Ionization Mass Spectrometer as an Analytical Instrument for Trace Analysis

Nuc. Instr. & Meth. in Phys. Res. A 281 547 (1989)

[5.11] G. Hass.

Filmed Surfaces For Reflecting Optics.

JOSA 45 945-95 (1955)

[5.12] M. Amit, G. Bialolenker, D. Levron & Z. Burshtein

Refractive Index Gradients and Dye Solution Flow Characteristics in Pulsed Copper Vapour Laser Pumped Dye Laser Cells

J. Appl. Phys. 63 1293 (1988)

[5.13] J.A. Lisboa et al

A Grazing Incidence Dye Laser With an Intra-Cavity Lens

Opt. Commun. 44 393 (1983)

[5.14] I.N. Nesteruk, O.N. Kompanets & V.I. Mishin

Pulsed Dye Laser with Precision Automatic Wavelength Tuning by Rotation of a Diffraction Grating with an Electrodynamic Drive

Sov. J.Q.E. 18 288 (1988)

[5.15] F.J. Duarte

Narrow Linewidth Pulsed Dye Laser Oscillators

Dye Laser Principles, Academic Press Ed. F.J. Duarte, L.W. Hillman P 161

[5.16] M. Przybylski, B. Otto & H. Gerhardt

Spectral Purity of Pulsed Dye Lasers

Appl. Phys. B 49 201 (1989)

[5.17] J.E. Abbot

Manganese Vapour Lasers

D.Phil Thesis, Oxford University (1990)

[5.18] The HD-350 Dye Laser

Lumonics Inc. Kanata

[5.19] J. Montgomery Lumonics Inc. Kanata

Private Communication

Chapter 6
The Theory of Harmonic Generation

6.1 Introduction.

6.2 Crystal Optics.

6.2.1 Fresnel's Equation.

6.2.2 The Ellipsoid of Wave Normals and Crystal Classes.

6.2.3 Ray Directions.

6.3 Nonlinear Optics.

6.3.1 Plane Wave Treatment of Second Harmonic Generation.

6.3.2 Phase-Matching.

6.3.2a Phase-Matching in Uniaxial Crystals.

6.3.2b Phase-Matching in Biaxial Crystals.

6.4 SHG with Focused Beams.

6.4.1 Theoretical Harmonic Efficiencies.

6.5 SHG With Non-Ideal Laser Beams.

6.6 Concluding Remarks.

Appendix 6.1 : The Effective Nonlinear Coefficient.

References.

Chapter 6 : The Theory of Harmonic Generation

6.1 Introduction

When an electromagnetic wave propagates through a linear medium, the induced polarization is directly proportional to the electric field that induces it. However, in certain crystals (and in particular, non-centrosymmetric crystals[1]), in addition to the linear response, the induced polarization is proportional to ascending powers of the electric field strength. This nonlinear response allows the exchange of energy between electromagnetic fields of differing frequencies which propagate through the medium, and is responsible for second harmonic generation, sum frequency mixing, parametric amplification, the linear electro-optic effect and a number of higher order processes.

This chapter reviews the linear and nonlinear properties of crystals and their role in second harmonic generation. The theory explains why efficient nonlinear frequency conversion depends on a number of parameters, of both the interacting laser beam, the crystal, and the crystal orientation, and illustrates how to maximize harmonic generation under practical constraints. The nonlinear crystals beta-barium borate (BBO) and lithium triborate (LBO) are presented as examples of uniaxial and biaxial crystal types respectively, in which it is possible to achieve efficient harmonic generation. Computer model predictions for the optimum crystal orientations (to achieve phase-matching), optimum focusing geometries and SHG conversion efficiencies are presented for BBO and LBO.

The treatment given in this chapter follows that of the ideal Gaussian laser beam analysis of Boyd and Kleinman [6.1]. A comparison is made with a recent non-collinear interaction model developed by Omatsu *et al* [6.2]; this latter theory

[1]Only in non-centrosymmetric crystals is the induced polarization proportional to the square of the electric field, and consequently, second harmonic generation can only be observed in materials which do not possess a centre of symmetry.

considers the effect of incomplete transverse coherence in the interacting laser beams and, thus, may provide a more appropriate account of the frequency conversion of copper vapour lasers. Additional reviews of the basic theory of second harmonic generation have been made by Yariv [6.3], Byer [6.4] and Franken and Ward [6.5]. Similarly, excellent reviews on crystal optics and the properties of crystals are provided by Born and Wolf [6.6] and Nye [6.7].

6.2 Crystal Optics

The behaviour of light waves in crystals is well documented [6.6], and may be derived from Maxwell's equations and the corresponding linear constitutive relations for a given medium. The theory, however, introduces concepts and notation important in the theory of second harmonic generation, and so an overview of the salient features of crystal optics relevant to second harmonic generation is presented here.

For an uncharged, non-conducting transparent crystal at rest, Maxwell's equations can be written as :-

$$\underline{\nabla}.\underline{D} = 0 \tag{1}$$

$$\underline{\nabla}.\underline{B} = 0 \tag{2}$$

$$\underline{\nabla}\times\underline{H} = \frac{\partial \underline{D}}{\partial t} \tag{3}$$

$$\underline{\nabla}\times\underline{E} = -\frac{\partial \underline{B}}{\partial t} \; . \tag{4}$$

We consider only homogeneous and magnetically isotropic (**B** parallel to **H**) crystals, but allow the crystals to be electrically anisotropic, in which case the constitutive relations may be written as:-

$$\underline{B} = \mu_r \mu_0 \underline{H} \tag{5}$$

$$D_i = \epsilon_0 \epsilon_{ij} E_j \; . \tag{6}$$

Where, in the last equation, the summation convention is assumed. At optical frequencies, the relative permeability $\mu_r \approx 1$. The dielectric tensor, ϵ_{ij}, must be

symmetric to conserve electromagnetic energy [6.6] - this restricts ϵ_{ij} to having 6 instead of 9 independent components. It is possible to find a crystallographic basis in which ϵ_{ij} is diagonal, in which case $D_x=\epsilon_x\epsilon_o E_x$ etc.; such a basis defines the principal dielectric axes, and $\epsilon_{x,y,z}$ are called the principal dielectric constants.

6.2.1 Fresnel's Equation

Consider a plane wave propagating through such a crystal with phase velocity $v_p=c/n$, in a direction specified by the unit wave-normal vector **s**; in this case, the vectors **E**,**D**,**H**,**B** will be proportional to the harmonic field, $\exp(i\omega(t-\mathbf{r}.\mathbf{s}/v_p))$, and Maxwell's equations become:

$$\underline{s}.\underline{D} = 0 \qquad (7)$$

$$\underline{s}.\underline{H} = 0 \qquad (8)$$

$$\frac{1}{v_p}\underline{s}\times\underline{H} = -\underline{D} \qquad (9)$$

$$\frac{1}{v_p}\underline{s}\times\underline{E} = \mu_0\underline{H}\ . \qquad (10)$$

Thus, **H** (and also **B**) is perpendicular to **E**,**D** and **s**, which must therefore be coplanar; additionally, **D** is orthogonal to **s**, so therefore **H** and **D** are perpendicular to the direction of propagation, but **E** is not. This illustrates that the ray direction (ie. the direction in which the energy propagates, specified by the Poynting vector **E**×**H**) is not in general the same as that of the wave normal, **s**. This "beam walk-off" has important consequences for second harmonic generation and will be considered later. The relationship between the vectors is illustrated in figure 6.1, where the walk-off angle, ρ, can be clearly identified. Eliminating **H** from (9) and (10) yields

$$\underline{D} = -\frac{1}{\mu_0 v_p^2}\underline{s}\times(\underline{s}\times\underline{E}) = \frac{1}{\mu_0 v_p^2}[\underline{E}-\underline{s}(\underline{s}.\underline{E})]\ . \qquad (11)$$

Using a coordinate system coincident with the principal dielectric axes such that $D_x=\epsilon_x\epsilon_0 E_x\ldots$, we have :

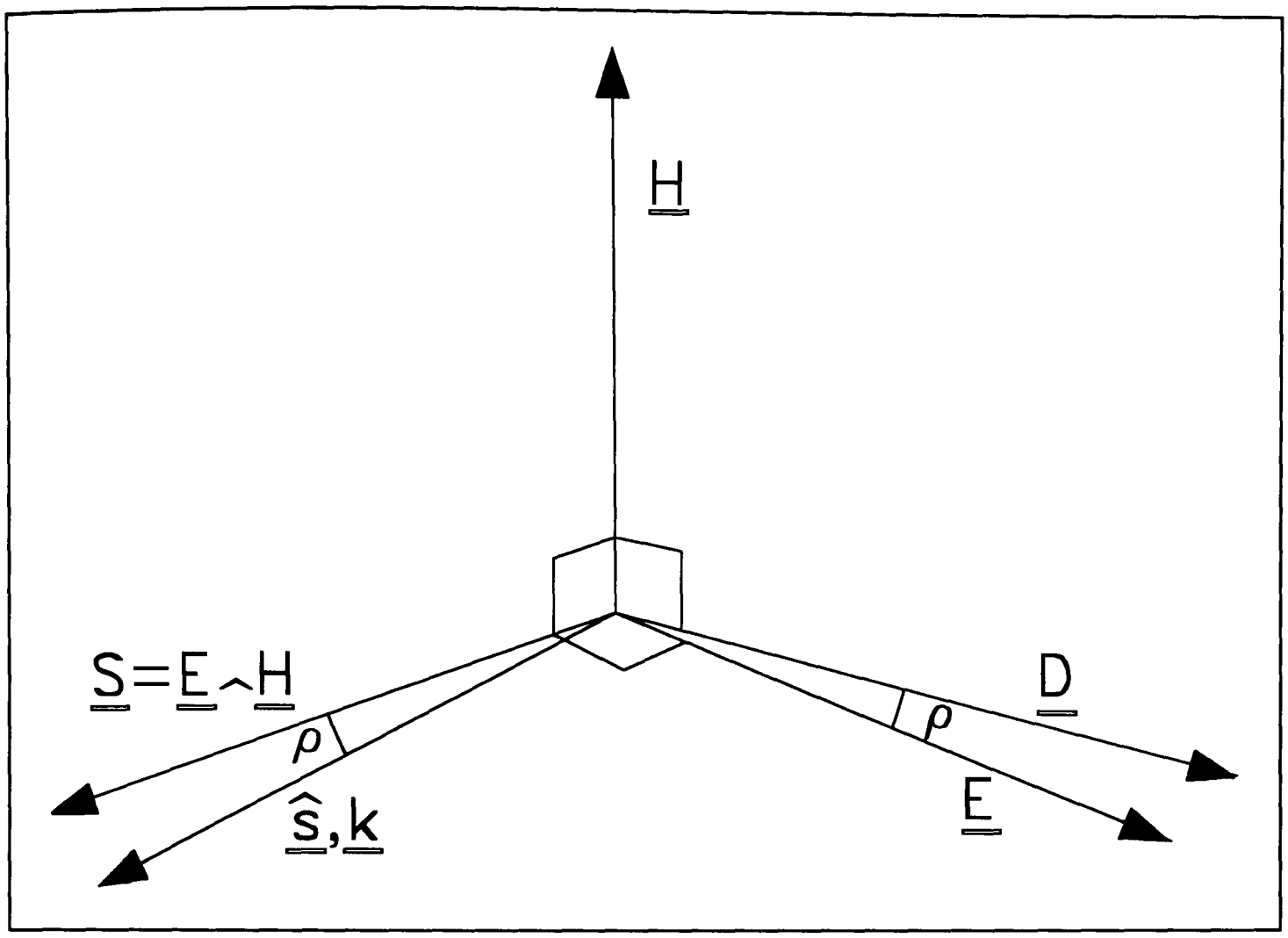


Figure 6.1 : Directions of the wave-normal **s**, field vectors **E,D,H** and the energy flow (**S=E×H**) in an electrically anisotropic medium.

$$E_k = \frac{n^2 s_k (\underline{E}.\underline{s})}{n^2 - \epsilon_k} \tag{12}$$

and, with a little algebraic manipulation, it may shown :-

$$\frac{s_x^2}{\frac{1}{n^2}-\frac{1}{n_x^2}} + \frac{s_y^2}{\frac{1}{n^2}-\frac{1}{n_y^2}} + \frac{s_z^2}{\frac{1}{n^2}-\frac{1}{n_z^2}} = 0 \tag{13}$$

where

$$v_k = \frac{1}{\sqrt{\epsilon_k \epsilon_0 \mu_0}} = \frac{c}{n_k}\,, \tag{14}$$

and so

$$\frac{s_x^2}{v_p^2 - v_x^2} + \frac{s_y^2}{v_p^2 - v_y^2} + \frac{s_z^2}{v_p^2 - v_z^2} = 0 \,. \qquad \textbf{(15)}$$

Equations (13) and (15) are equivalent forms of Fresnel's equation of wave normals. This is a quadratic equation in v_p^2, and for each wave normal direction, **s**, there correspond two phase velocities (the two values $\pm v_p$ corresponding to any value v_p^2 are counted as one since the negative value corresponds to propagation in the opposite direction -**s**). From equations (11) and (12) it can be seen that the ratios of the components $E_x : E_y : E_z$ are real, and so the **E** and **D** fields are linearly polarized. That is, the structure of an anisotropic medium allows two monochromatic plane waves with different linear polarizations and two different phase velocities to propagate in any direction. The two allowed **D**-vectors, corresponding to a given direction of propagation, can be shown to be perpendicular to each other [6.6], and their directions may conveniently be found from the optical indicatrix, as shown in the next section §6.2.2.

6.2.2 The Ellipsoid of Wave Normals and Crystal Classes

The ellipsoid of wave normals, or optical indicatrix, is the quadratic representation of the 2-symmetric tensor, $1/\epsilon_{ij}$, defined by the ellipsoidal surface

$$\frac{x^2}{n_x^2} + \frac{y^2}{n_y^2} + \frac{z^2}{n_z^2} = 1 \,. \qquad \textbf{(16)}$$

The semi-axes of the ellipsoid coincide with the directions of the principal dielectric axes and their magnitudes are equal to the principal refractive indices. The indicatrix has the useful property that the semi-axes of the elliptical cross-section through the ellipsoid, perpendicular to the direction of propagation **s**, define the magnitude of the refractive indices for the two allowed polarizations when an electromagnetic wave travels through the crystal in a direction **s**. Additionally, the semi-axes of the elliptical cross-section define the directions of the **D**-vectors of the two allowed solutions of the electromagnetic field. The geometric construction is

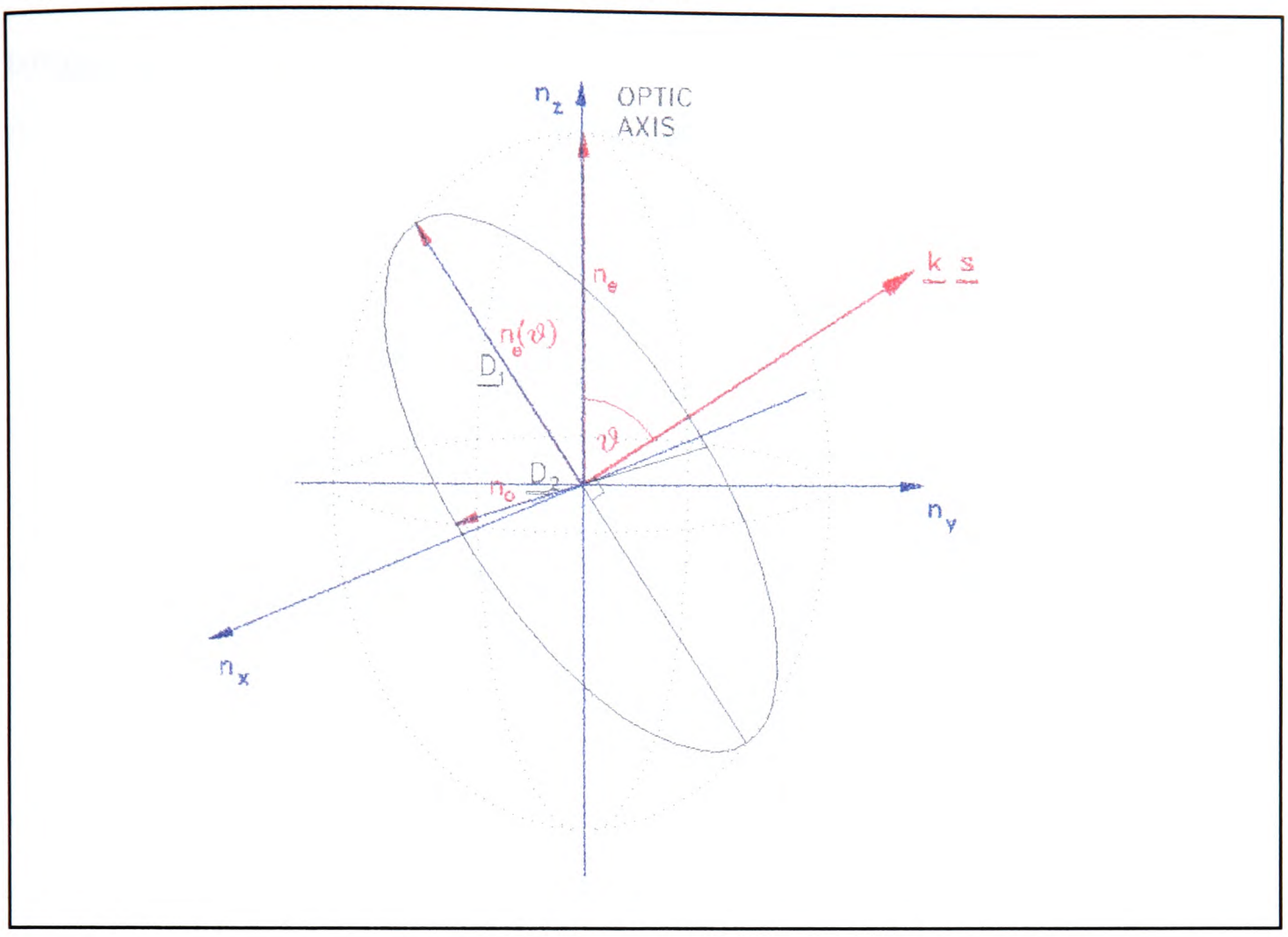


Figure 6.2 : The optical indicatrix showing the construction for determining the directions of vibrations of the **D** vectors and the associated refractive indices belonging to a wave-normal **s**.

illustrated in figure 6.2 for the case of a wave propagating in an uniaxial crystal; the formal proof may be found in Yariv [6.3] or Born and Wolf [6.6].

The symmetry of the crystal lattice is reflected in the symmetry of the optical indicatrix, since, according to Neuman's principle : the symmetry elements of any physical property of a crystal must include the symmetry elements of the point group of the crystal. There are three distinct crystal classes to consider :-

Group I : $n_x = n_y = n_z = n$

These are optically isotropic crystals, in which three crystallographically-equivalent mutually orthogonal axes may be chosen eg. cubic - the three directions specify the principal dielectric axes.

Group II : $n_x = n_y \neq n_z$

These are crystals not belonging to group I, in which two or more crystallographically-equivalent directions may be chosen in one plane - eg. hexagonal,

tetragonal, and trigonal crystals. The indicatrix is an ellipsoid of revolution about the principle symmetry (z) axis defined by :-

$$\frac{x^2}{n_o^2} + \frac{y^2}{n_o^2} + \frac{z^2}{n_e^2} = 1 \ . \qquad (17)$$

For a wave propagating along the z axis, the two allowed polarizations have the same refractive index and there is no double refraction. This principal symmetry axis is called the optic axis, and the crystal is said to be optically uniaxial. n_o and n_e are called the ordinary and extraordinary refractive indices respectively, and the crystal is termed positive when $(n_e\text{-}n_o)$ is positive and negative when $(n_e\text{-}n_o)$ is negative.

Group III : $n_x \neq n_y \neq n_z$

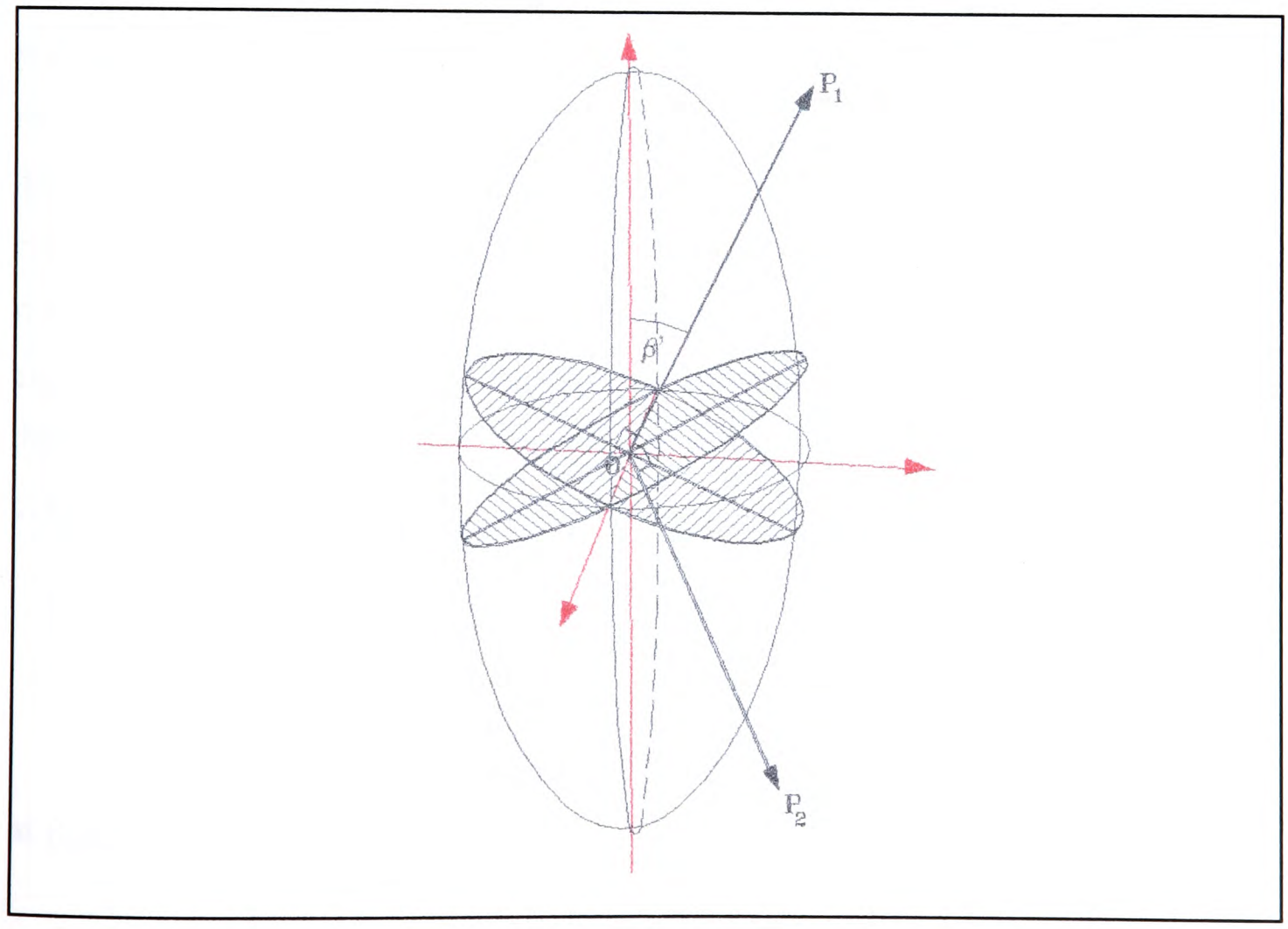


Figure 6.3 : The optical indicatrix for a biaxial crystal is a general ellipsoid and contains two circular cross-sections and, therefore, two optic axes.

These are crystals in which no two crystallographically-equivalent directions may be chosen - eg. orthorhombic, monoclinic and triclinic crystals. Here the optical indicatrix is a triaxial ellipsoid which contains two circular sections (Figure 6.3), and hence, there are two wave normal directions for which there is no double refraction. These two directions define two optic axes and the crystals are termed optically biaxial. The angle β' between the optic axes and the z axis can be shown to be given by [6.6] :-

$$\tan^2\beta' = \frac{(n_x)^{-2}-(n_y)^{-2}}{(n_y)^{-2}-(n_z)^{-2}} \qquad \textbf{(18)}$$

6.2.3 Ray Directions

In general, the ray direction is not the same as the wave front normal, and is responsible for the efficiency-limiting mechanism in second harmonic generation, where the SH wave walks away from the fundamental. The angle between the ray and wave normal, termed the "walk-off" angle, can be calculated by considering the ray velocity surface for an extraordinary wave in an uniaxial crystal - this surface describes the shape of the wave front resulting from a point disturbance within the crystal (figure 6.4). The propagation of a plane wave through a birefringent crystal may then be visualized by forming a Huygens-type construction of the wave fronts emanating from point sources, as shown in figure 6.5. In the principal axes of the dielectric tensor $D_x=\epsilon_o\epsilon_x E_x.....$, we may define the ray velocity surface in an uniaxial crystal as

$$\omega = \frac{x^2}{c/n_e^2} + \frac{y^2}{c/n_e^2} + \frac{z^2}{c/n_o^2} \,. \qquad \textbf{(19)}$$

The normal to this ellipsoid, ie. the wave normal, or wave vector direction, at (x,y,z) has direction cosines

$$\underline{s} = \underline{\nabla}\omega = \left(\frac{\partial\omega}{\partial x}, \frac{\partial\omega}{\partial y}, \frac{\partial\omega}{\partial z}\right) = (xn_e^2, yn_e^2, zn_o^2) \qquad \textbf{(20)}$$

so, with reference to figure 6.4,

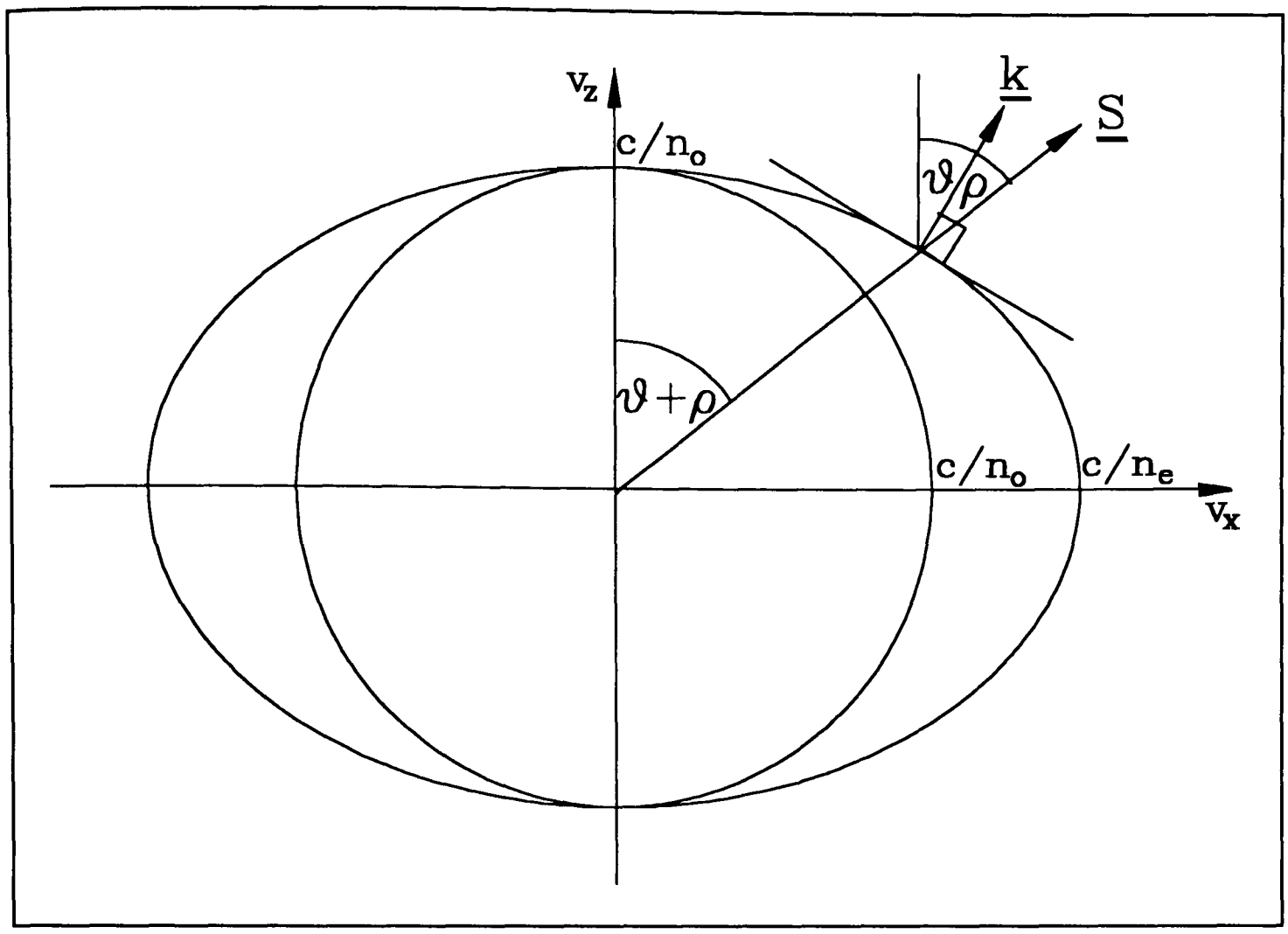


Figure 6.4 : The ray velocity surface describing the wave front arising from a point disturbance in an electrically anisotropic medium. The wave-normal is not generally coincident with the Poynting vector and leads to beam walk-off.

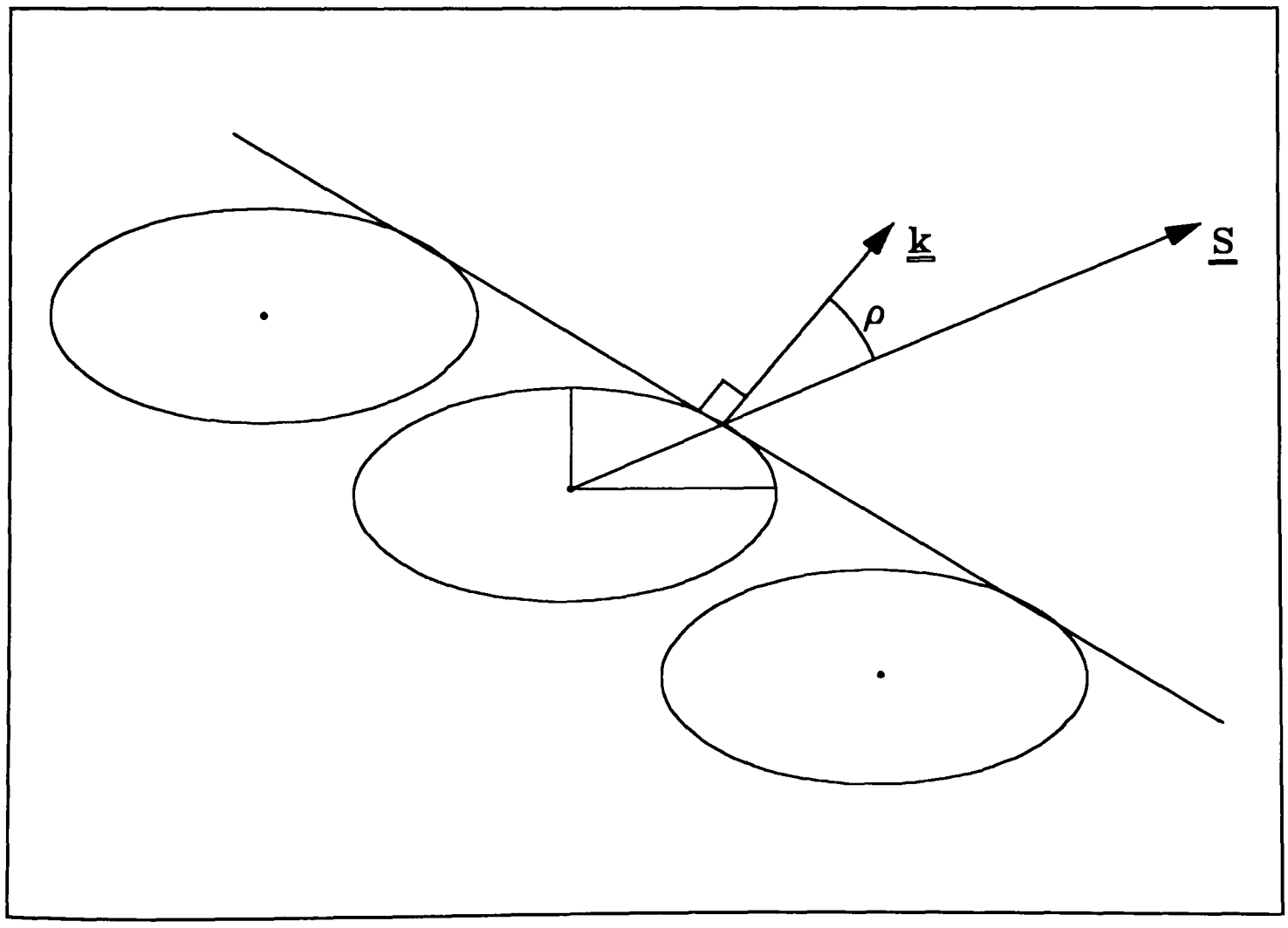


Figure 6.5 : The Huygens construction for the wave-normal in an electrically anisotropic medium.

$$\underline{s} = \left(n_e^2 \cos(\theta+\rho) \; , \; 0 \; , \; n_o^2 \sin(\theta+\rho)\right) \tag{21}$$

and, so

$$\tan(\theta+\rho) = \left(\frac{n_o}{n_e}\right)^2 \tan\theta \; . \tag{22}$$

The angle ρ thus represents the angle subtended between the ray directions of o- and e-waves propagating through the crystal, and since, as we shall see, most common SHG geometries involve the fundamental and second harmonic wave propagating as different polarizations, this beam walk-off represents an efficiency-limiting mechanism.

5.3 Nonlinear Optics

6.3.1 Plane Wave Treatment of Second Harmonic Generation

The electric fields within laser beams can be of the same order of magnitude as the electric fields within atoms, and consequently, the usual assumption of a linear relationship between the polarization, **P**, and the applied electric field, **E**, breaks down. The electric polarization induced in a crystal by a laser beam is more correctly expressed as a tensor expansion in ascending powers of the applied electric field :

$$P_i(\omega_3) = \epsilon_0\left[\chi_{ij}^{(1)}(\omega_3)E_j(\omega_3) + \chi_{ijk}^{(2)}(-\omega_3,\omega_2,\omega_1)E_j(\omega_2)E_k(\omega_1=\omega_3-\omega_2)+....\right] . \tag{23}$$

SHG arises from the $\chi_{ijk}^{(2)}$ term, which is responsible for inducing a second order polarization, $\mathbf{P}(2\omega)$, when an electric field, $\mathbf{E}(\omega)$, propagates through the (non-centrosymmetric) crystal. For fixed polarizations of **E** and **P**, we may introduce an effective scalar nonlinear coefficient, d_{eff} [Appendix 6.1], such that the second order polarization (ie. the component arising from the $\chi_{ijk}^{(2)}$ term) may be written as:

$$P = \epsilon_0 d_{eff} E^2(\omega) \; . \tag{24}$$

Thus, for a wave $E(\omega)=E.\cos(k_1x-\omega t)$ propagating through the crystal, the second order polarization is:

$$P = \frac{d_{eff}}{2}\epsilon_0 E^2\left[1 + \cos 2(k_1x-\omega t)\right] . \qquad (25)$$

This polarization contains a component at twice the original frequency and acts as a source for radiation at the second harmonic frequency. To see how the second harmonic generation efficiency depends on crystal and laser parameters, we must reconsider Maxwell's equations in the light of the nonlinear polarization response. For a steady state plane wave approximation, it is possible [Yariv 6.3] to derive a set of coupled differential equations which describe the propagation of the fundamental and harmonic waves through a nonlinear medium. In the case of SHG, and assuming slowly varying amplitudes, these equations become :-

$$\frac{dE(\omega)}{dz} = -\alpha_\omega E(\omega) - i\kappa' E(2\omega)E^*(\omega)\exp[-i\Delta kz] \qquad (26)$$

$$\frac{dE(2\omega)}{dz} = -\alpha_{2\omega} E(2\omega) + i\kappa' E(\omega)E(\omega)\exp[i\Delta kz] , \qquad (27)$$

where $\kappa'=\omega d_{eff}/nc$; the electric field loss coefficient, $\alpha=\mu_o\sigma_R c/2$; and $\Delta k=k(2\omega)-2k(\omega)$ is the phase mismatch between the fundamental and second harmonic. In the low conversion limit there is no significant depletion of the fundamental wave ($dE(\omega)/dz=0$), and so, for transparent, lossless crystals ($\alpha_\omega=\alpha_{2\omega}=0$), the second harmonic power generated in a length L is found by integrating (27) to be :-

$$\frac{P^{2\omega}}{P^{\omega}} = 2\left(\frac{\mu_0}{\epsilon_0}\right)^{3/2}\frac{\omega^2(d_{eff})^2L^2}{n^3}\left(\frac{P_\omega}{Area}\right)\frac{\sin^2\left(\frac{\Delta kL}{2}\right)}{(\Delta kL/2)^2} . \qquad (28)$$

When $\Delta k=0$, the fundamental and the SH wave have the same phase throughout the crystal and phase-matching is said to occur; in this situation, all the contributions to the second harmonic wave add coherently and the efficiency is maximized. Equation (28) suggests that high efficiencies are realized for long crystals with high laser intensities, $(P_\omega/Area)$ - this latter condition may be achieved through focusing the laser beam into the crystal. The theory of harmonic generation

with focused Gaussian laser beams including the effects of beam walk-off will be considered in section §6.4.

6.3.2 Phase-Matching

In general $n(2\omega) > n(\omega)$, and so $\Delta k = 2\omega/c.[n(2\omega) - 1/2[n(\omega) + n'(\omega)]]$ is non-zero, owing to normal dispersion in the crystal. Fortunately, however, it is possible to offset the normal dispersion by using the natural birefringence of uniaxial or biaxial crystals: by appropriate choice of polarization of the fundamental and harmonic waves, it is often possible to specify a direction of propagation through the crystal and/or a temperature (since $dn_2/dT - dn_1/dT \neq 0$) for which $\Delta k = 0$. The process of choosing the crystal-orientation, at some fixed temperature such that $\Delta k = 0$, is termed angle-tuning, and similarly, the process of choosing the crystal temperature, T, such that $\Delta k = 0$, for a fixed orientation, is termed temperature-tuning.

The most efficient type of phase-matching is called non-critical or 90° phase-matching (NCPM) - here, the fundamental wave propagates at 90° to one of the crystal optic axes. The crystal geometry is illustrated in figure 6.6. The two ellipsoids, corresponding to the refractive index at the fundamental and second harmonic, share a common tangent, and consequently, this geometry offers a large angular acceptance angle[2] for phase-matching. Additionally, there is no walk-off between the fundamental and harmonic waves in this crystal orientation, and so high conversion efficiencies are possible. In general, however, NCPM is attainable only at discrete wavelengths, determined by the crystal birefringence, although, in practice, some small adjustment of the wavelength is possible by temperature-tuning. Most crystals are not perfectly transparent, particularly in the UV, and will absorb some small fraction of the fundamental or SH, and so a thermal gradient, and consequently, a refractive index gradient, will appear across the beam. This can prove to be a limiting feature of temperature-tuned phase-matching in crystals with high average power lasers. Here, the refractive index gradient causes incomplete

[2]The angular acceptance angle is defined as the angular range within which the phase mismatch between the fundamental and harmonic is less than 2π.

phase-matching (thermal dephasing), and is responsible for conversion efficiencies below those theoretically predicted.

For other crystal orientations there will be a small angle between the direction of the power flux from the fundamental and SH, and the geometry is termed critical phase-matching. The directions for phase-matched SHG can be obtained by considering the intersection of the index surfaces at the harmonic and fundamental frequencies, as depicted in figure 6.7. There are two types of phase-matching corresponding to two possible orientations for the polarization vectors of the fundamental beams : in type I phase-matching, both polarization vectors are parallel, whilst in type II the polarization vectors are orthogonal (ie. the fundamental radiation is polarized at 45° to the optic axis, giving equal amounts of o- and e- waves).

6.3.2a Phase-Matching in Uniaxial Crystals

In a negative uniaxial crystal, there are two loci where the index surfaces of the fundamental and SH intersect and $\Delta k=0$:

$$n^e(2\omega,\theta_m) = n^o(\omega) \qquad Type\ I \tag{29}$$

$$n^e(2\omega,\theta_m) = \frac{1}{2}\left[n^e(\omega,\theta_m) + n^o(\omega)\right] \qquad TypeII\ . \tag{30}$$

The refractive index for a wave at an angle θ to the optic axis may be derived from the indicatrix (17), and in the case of type I phase-matching the locus can be shown to be a symmetric cone of directions at θ_m about the optic axis. Solving (29) with the aid of (13), the phase-match angle, θ_m, can be shown to be given by :-

$$\sin^2\theta_m = \left(\frac{\frac{1}{(n^o(\omega))^2} - \frac{1}{(n^o(2\omega))^2}}{\frac{1}{(n^e(2\omega))^2} - \frac{1}{(n^o((2\omega))^2}} \right). \tag{31}$$

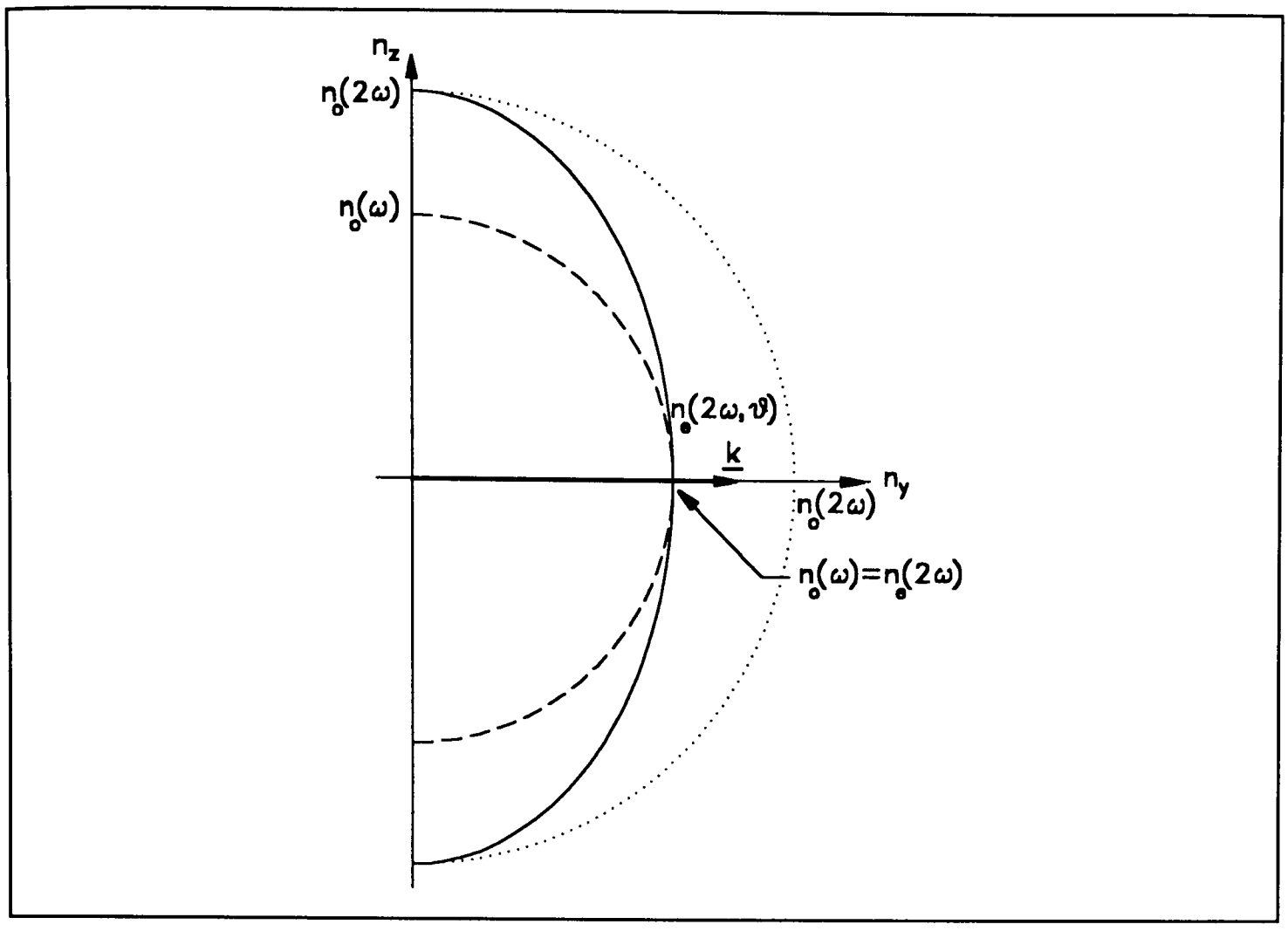


Figure 6.6 : NCPM phase-matching in a negative uniaxial crystal. Propagation at $\theta=90°$ results in $n_o(\omega)$ and $n_e(2\omega)$ sharing a common tangent resulting in large angular insensitivity.

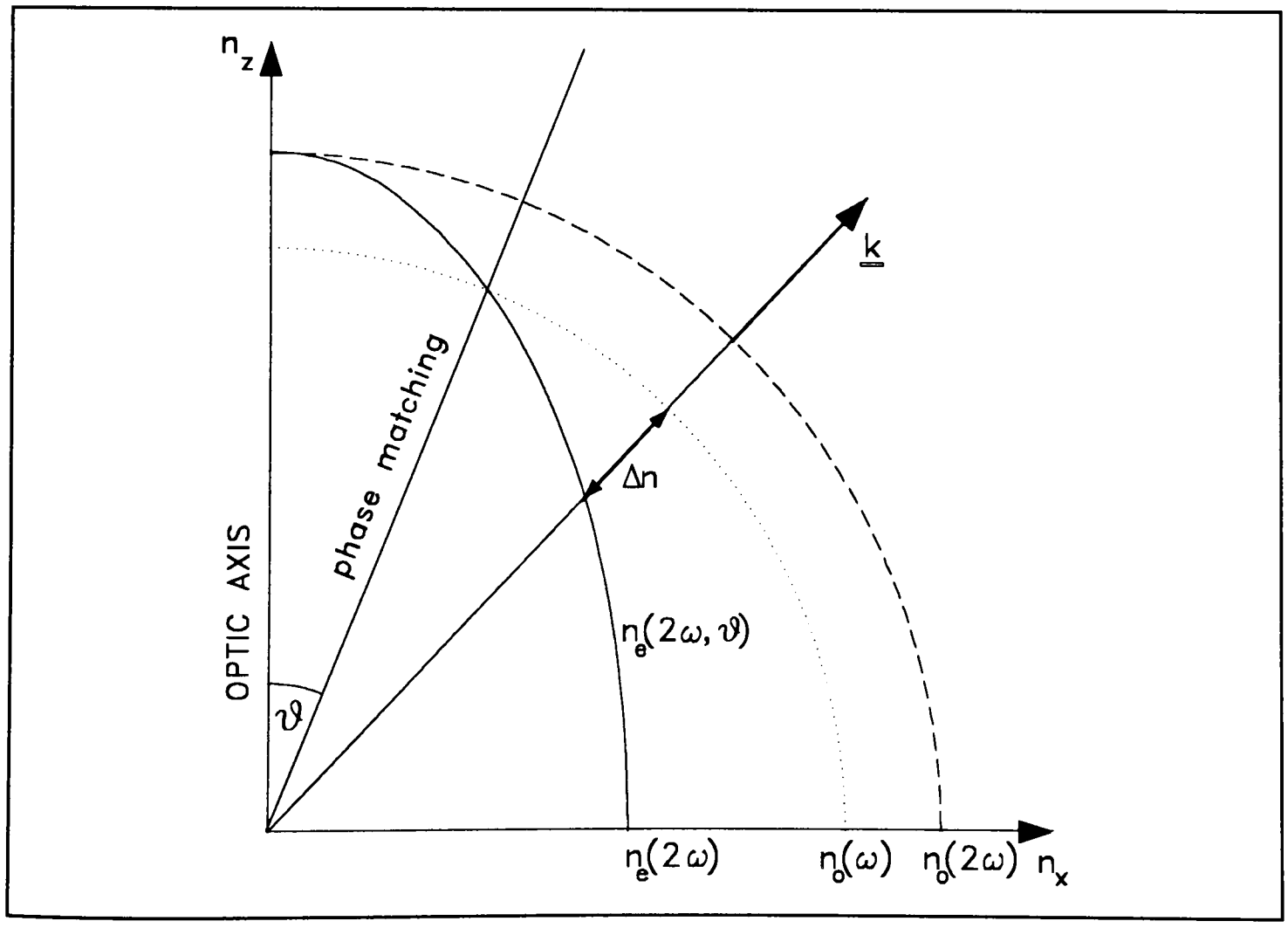


Figure 6.7 : Critical phase-matching in a negative uniaxial crystal. Only at the phase-match angle θ does $n_e(2\omega,\theta)=n_o$ and $\Delta k=0$.

The phase-match angle for type II phase-matching may be found in a similar manner. However, this time (30) and (13) yield a transcendental, and the phase-match angle is most conveniently found by machine calculation. In the case of the negative uniaxial crystal BBO, the variation of phase-match angle with wavelength for both type I and type II phase-matching may be computed [Appendix A.4, A.5], using the Sellmier data of [6.8] to give the phase-match curves plotted in figure 6.8. Whilst the azimuthal angle, ϕ, does not feature in the phase-matching calculations, there is, in general, an optimum azimuthal orientation determined by maximizing the effective nonlinear coefficient which is a function of crystal orientation (θ,ϕ). The value of d_{eff} should be considered, along with the angular, bandwidth and temperature sensitivities, when considering one particular phase-matching orientation in preference to another.

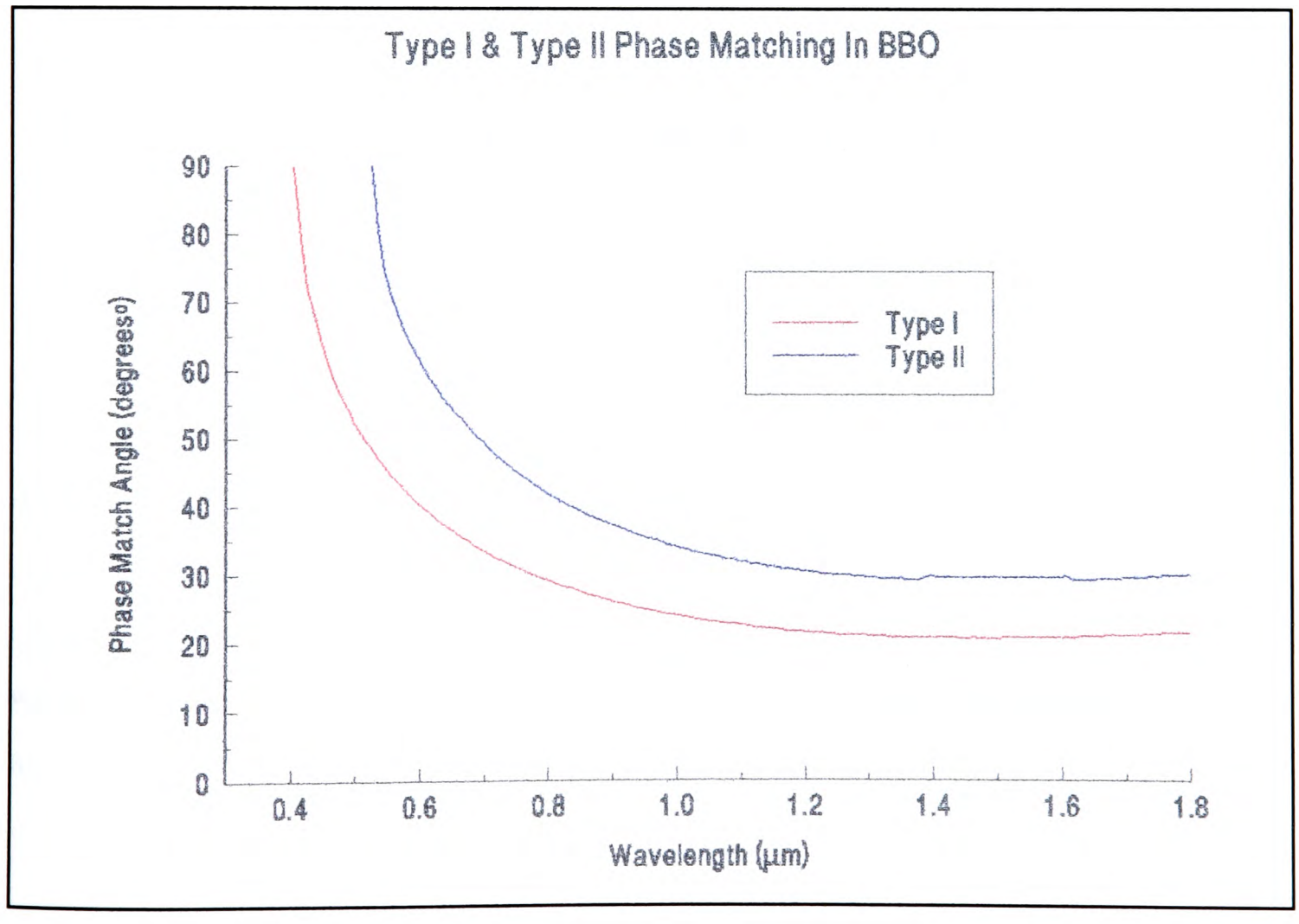


Figure 6.8 : Calculated phase-match angles for type I & II interactions in BBO as a function of wavelength.

6.3.2b Phase-Matching in Biaxial Crystals

Again, the direction for phase-matching can be conveniently calculated by considering the intersection of the index surfaces at the fundamental and harmonic frequencies. However, here the index surfaces (figure 6.9) and the intersection loci (figure 6.10) are generally more complex. Let us consider only optically well-behaved crystals, ie. those whose principal basis set is not a function of frequency and whose dispersions are normal, small, and approximately equal between the fundamental and harmonic frequencies :-

$$n_2^z > n_1^z, \quad n_2^y > n_1^y, \quad n_2^x > n_1^x \tag{32}$$

$$n_2^z - n_1^z \approx n_2^y - n_1^y \approx n_2^x - n_1^x \ll n_1^x \ . \tag{33}$$

Where, for simplicity of notation, $n_z(2\omega)$ is abbreviated to n_2^z.
Consider the situation, depicted in figure 6.9, where

$$n_2^z > n_1^z > n_2^y > n_1^y > n_2^x > n_1^x \quad , \tag{34}$$

$$n_2^x > \frac{1}{2}\left(n_1^x + n_1^y\right) \quad , \quad n_2^y > \frac{1}{2}\left(n_1^y + n_1^z\right) \ . \tag{35}$$

Type I phase-matching is seen to occur in a cone of directions about the optic axis, whilst type II phase-matching is seen to occur in a cone of directions enclosing both the z axis and optic axis. Analytically, the index surface can be derived from Fresnel's equation of wave normals, but the locus of directions for a given type of phase-matching has no simple form, and is best found by numerical computation. There are, in general, thirteen topologically distinct patterns of phase-matching loci, depending upon the ratios of the refractive indices n_x, n_y, n_z - these phase-matching classes have been characterized and detailed by Hobden [6.9]. Let us consider the calculation of the phase-match angles for type I phase-matching in LBO; we may write Fresnel's equation of wave normals [6.10] for the fundamental and harmonic as:-

$$x_1^2 + B_1 x_1 + C_1 = 0 \tag{36}$$

$$x_2^2 + B_2 x_2 + C_2 = 0 \ , \tag{37}$$

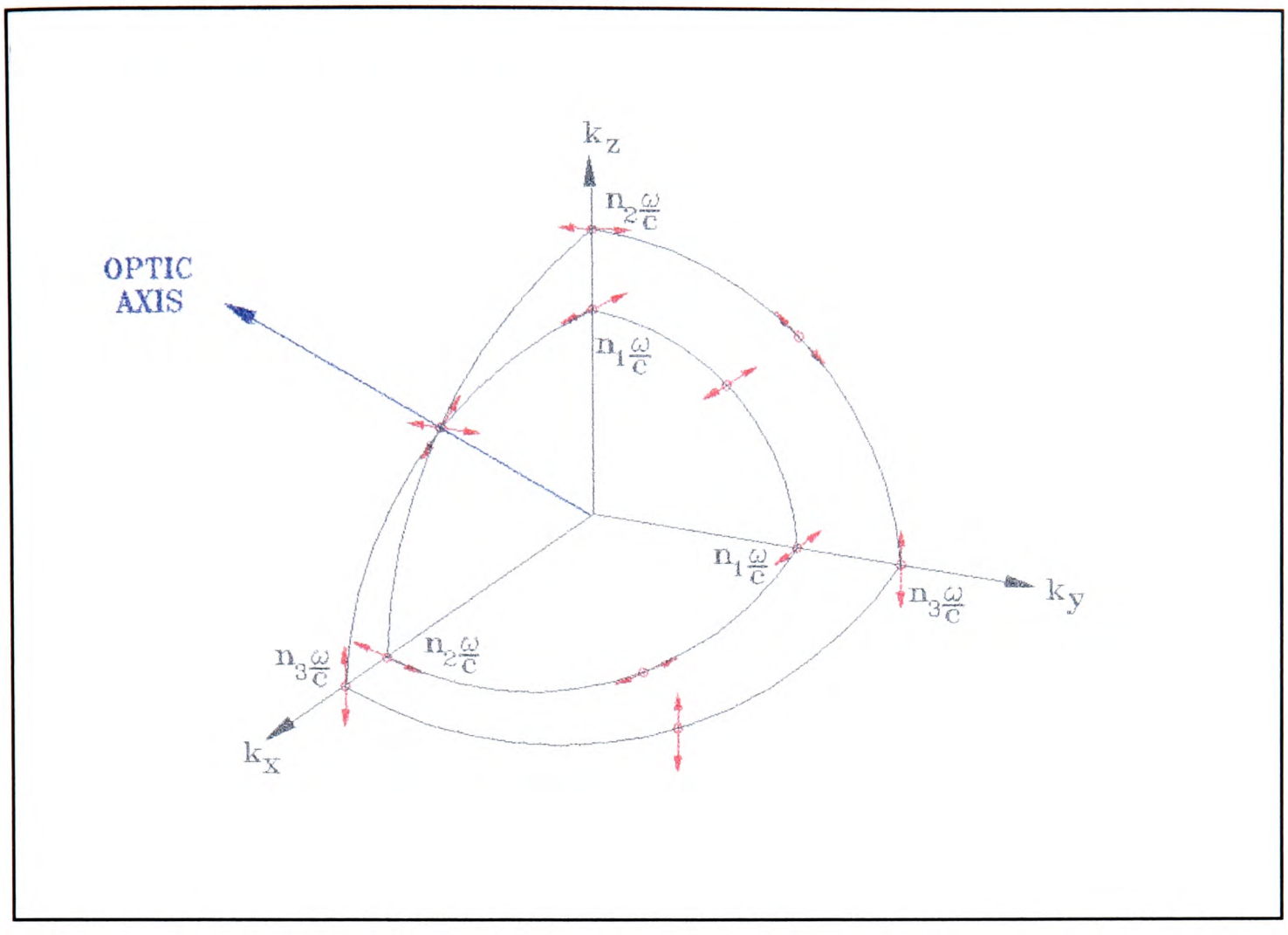


Figure 6. 9 : The wave-vector surface for a biaxial crystal.

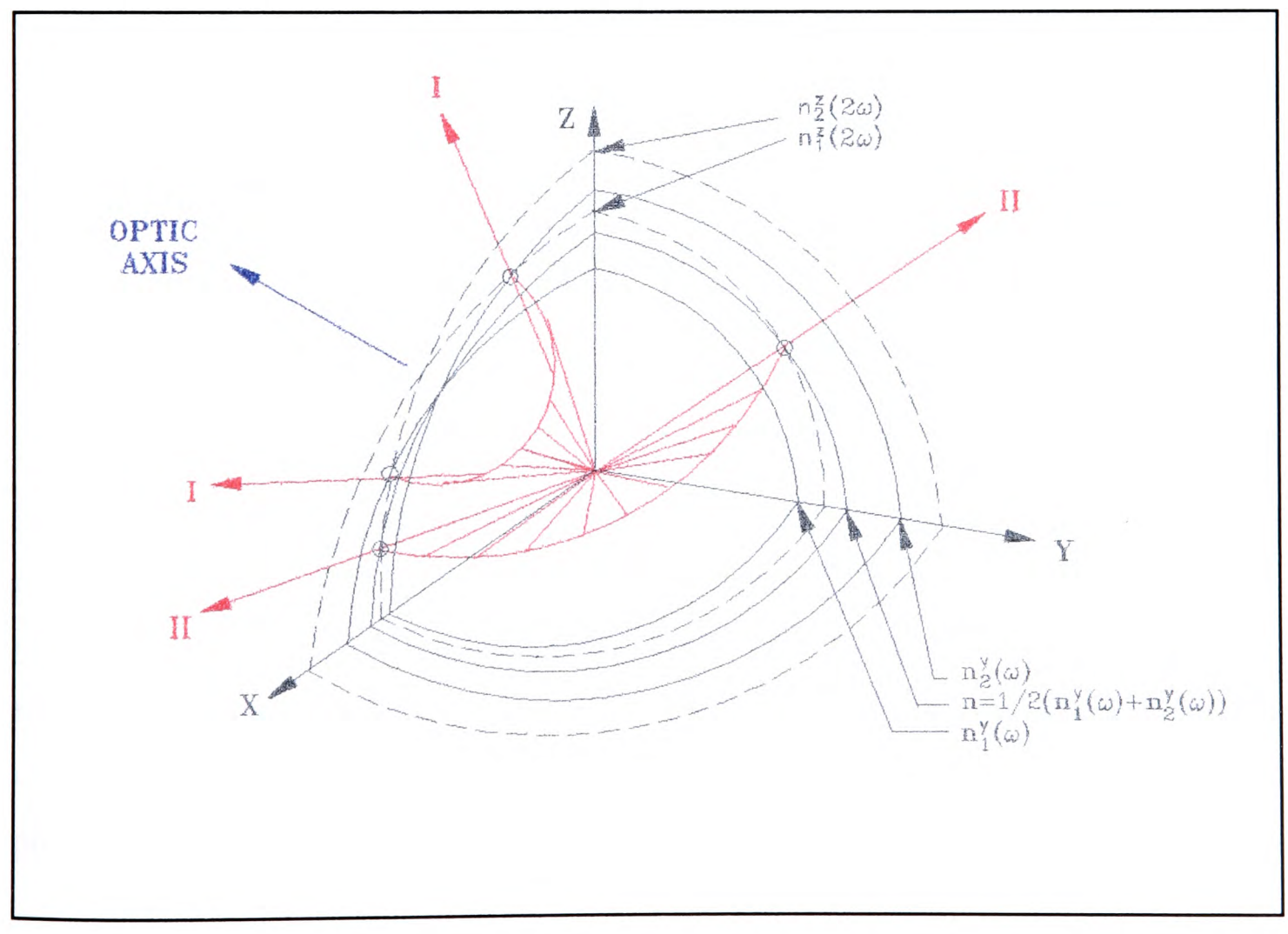


Figure 6.10 : Directions for phase-matched SHG in a biaxial crystal, visualized by the intersection of the index surfaces for the fundamental and second harmonic frequencies.

where

$$x_1 = n_\omega^{-2} \quad , \quad x_2 = n_{2\omega}^{-2} \tag{38}$$

$$B_i = \left[-s_x^2(b_i + c_i) - s_y^2(a_i + c_i) - s_z^2(a_i + b_i)\right] \tag{39}$$

$$C_i = \left[s_x^2 b_i c_i + s_y^2 a_i c_i + s_z a_i b_i\right] \tag{40}$$

$$a_1 = n_{x,\omega}^{-2} \quad , \quad b_1 = n_{y,\omega}^{-2} \quad , \quad c_1 = n_{x,\omega}^{-2} \tag{41}$$

$$a_2 = n_{x,2\omega}^{-2} \quad , \quad b_2 = n_{y,2\omega}^{-2} \quad , \quad c_2 = n_{z,2\omega}^{-2} \; . \tag{42}$$

Equations (36) and (37) may be solved for n, yielding :

$$n_{\omega,j} = \frac{\sqrt{2}}{\sqrt{-B_1 \pm \sqrt{B_1^2 - 4C_1}}} \tag{43}$$

$$n_{2\omega,j} = \frac{\sqrt{2}}{\sqrt{-B_2 \pm \sqrt{B_2^2 - 4C_2}}} \; , \tag{44}$$

where, as $j=1$ or 2, the symbols under the square root sign take on plus or minus values respectively. Clearly, $n_{\omega,2} > n_{\omega,1}$ and $n_{2\omega,2} > n_{2\omega,1}$; for type I phase-matching $n_{\omega,2} = n_{2\omega,1}$ ie. :

$$\frac{1}{\sqrt{-B_1 - \sqrt{B_1^2 - 4C_1}}} = \frac{1}{\sqrt{-B_2 + \sqrt{B_2^2 - 4C_2}}} \; . \tag{45}$$

Using the Sellmier data for LBO of [6.11], the phase-matching angles (θ,ϕ) for type I and type II doubling can be numerically calculated [Appendix A.7, A.8], and are plotted in figure 6.11. In the special case of beam propagation along one of the principal crystal axes, the phase-matching calculations are greatly simplified, and the situation is analogous to the problem of calculating the phase-match angles in uniaxial crystals. For LBO cut at $\theta=90°$ (where d_{eff} is maximized), it can be shown that the phase-matching angle, ϕ, is given by:

$$\sin\phi = \sqrt{\left(\frac{n_y^2(2\omega) - n_z^2(\omega)}{n_y^2(2\omega) - n_x^2(2\omega)}\right)}\cdot\frac{n_x(2\omega)}{n_z(\omega)} \quad . \tag{46}$$

The variation of ϕ with wavelength can be seen in figure 6.12. It is interesting to note that the birefringence of the crystal prevents phase-matched SHG below 552 nm for type I SHG, despite the crystal remaining transparent to below 180 nm. Thus SHG of the CVL green, 511 nm, line is not possible in LBO, and generation of wavelengths below 275 nm in LBO can only be realized by sum frequency mixing. For type II SHG, the situation is even more unfavourable, with the short wavelength SHG cut-off occurring at 778 nm.

6.4 SHG with Focused Gaussian Beams

Thus far, we have considered the interaction of plane waves of infinite extent in an electrically anisotropic medium. Usually, the intense light beams are generated by laser sources, and possess a Gaussian profile; in addition, the beams are usually focused into the nonlinear medium to increase the power density and maximize the conversion efficiency. The theory of second harmonic generation with focused Gaussian beams in uniaxial crystals, including the effects of beam walk-off, has been considered by Boyd and Kleinman [6.1]. The theory is also applicable to biaxial crystals when the waves propagate along one of the principal planes. The theory has been extended by Freegarde [6.12] to include elliptical focusing, and suggests that for crystals exhibiting large walk-off angles, optimum elliptical geometries offer a significant improvement ($>30\%$) in the SHG efficiency over conventional spherical focusing geometries.

Here, an overview of the salient features of the theory is presented to illustrate the parameters important in the optimization of focused SHG geometries, and to calculate the expected SHG conversion efficiencies. The fact that neither the CVL, nor the CVL-pumped dye laser beams possess Gaussian profiles will be considered in the next chapter.

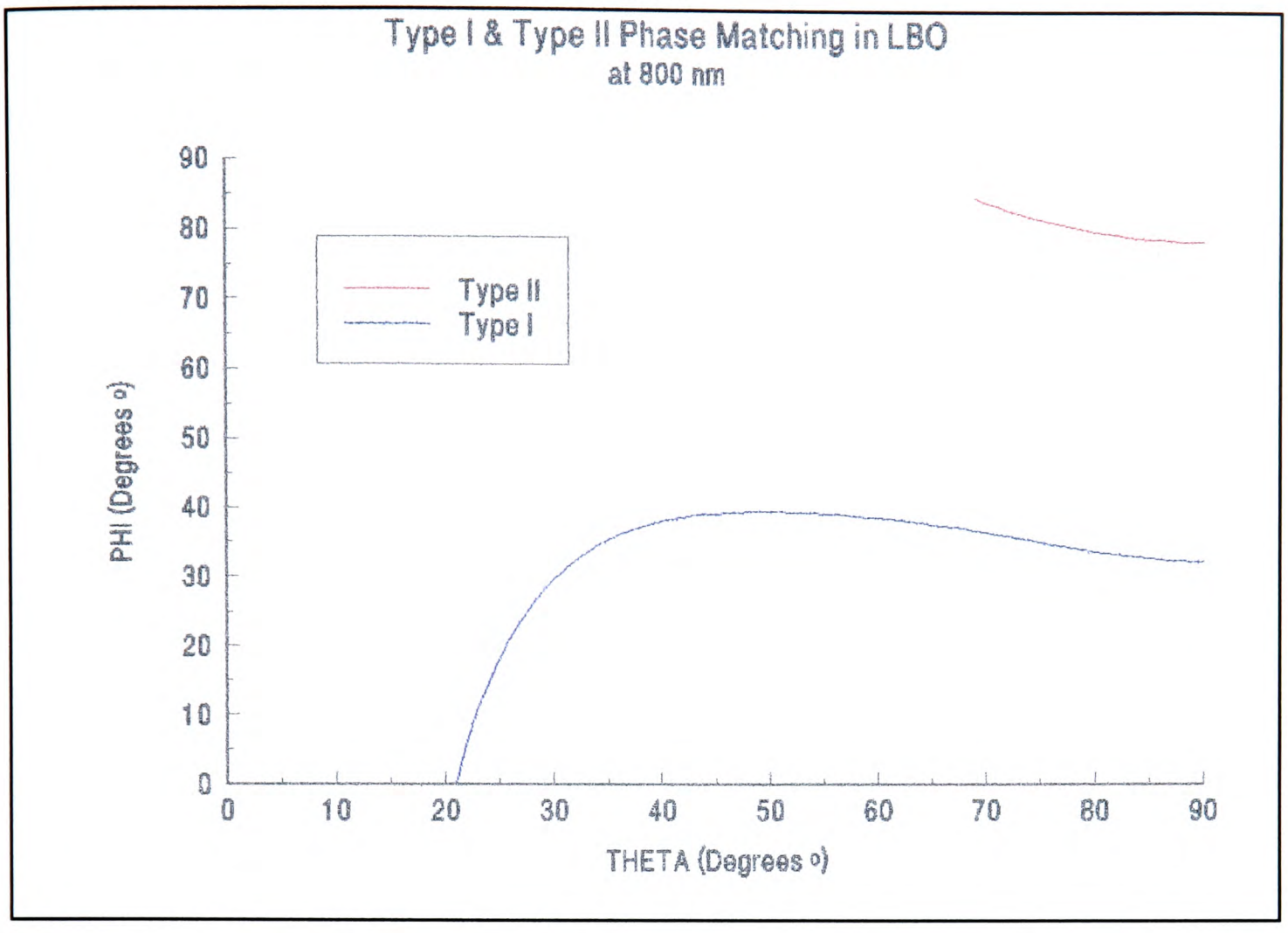


Figure 6.11 : Calculated phase-match angles (θ,ϕ) for type I & II interactions in LBO at a fundamental wavelength of 800 nm.

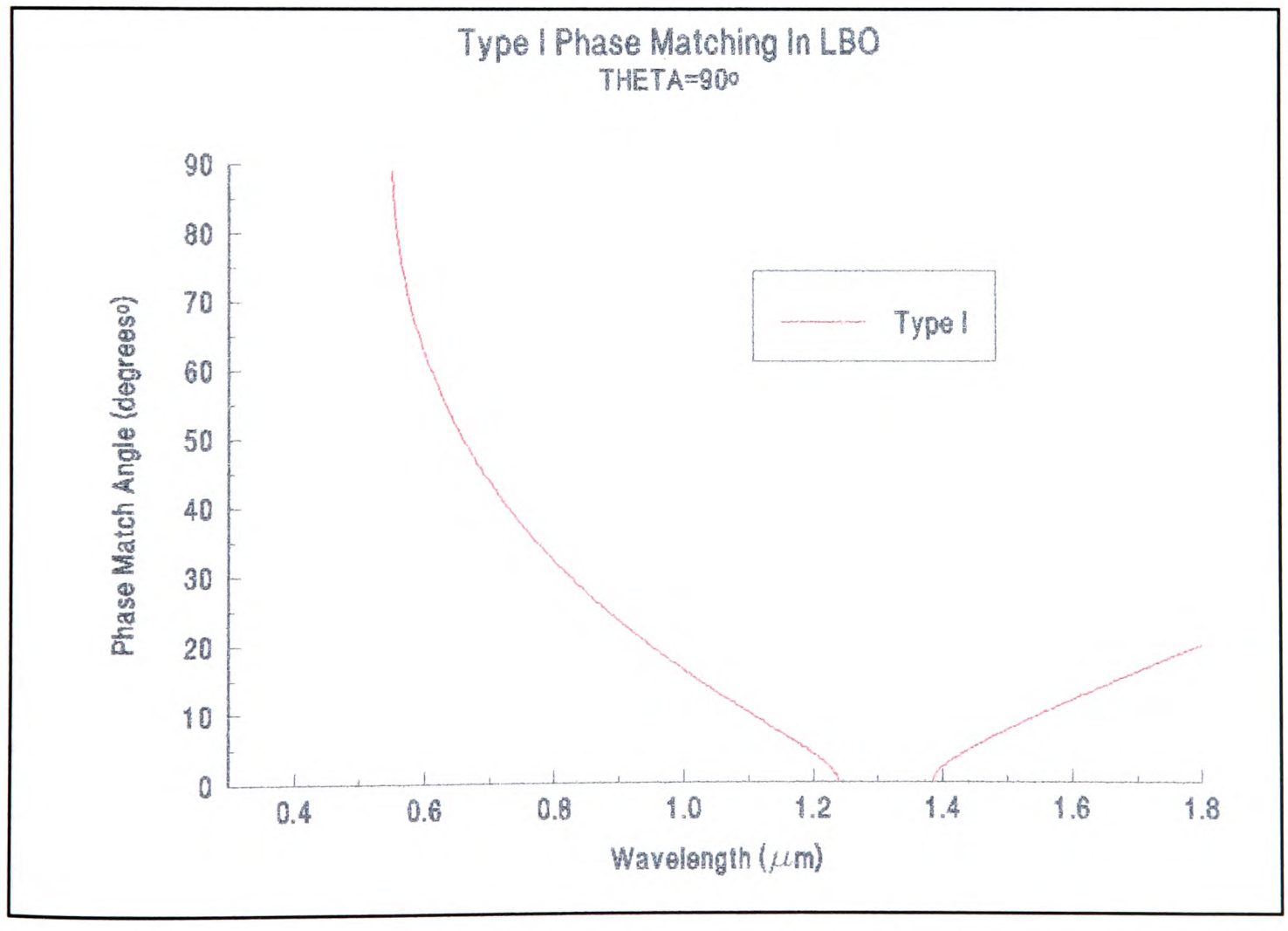


Figure 6.12 : Calculated phase-match angles for type I interaction in LBO for $\theta = 90°$ as a function of wavelength - in this case, the problem reduces to that of a uniaxial crystal.

The nonlinear crystal, cut for ordinary phase-matching ($\Delta k=0$) perpendicular to its surface, is assumed to be surrounded by index matching fluid - the situation is shown schematically in figure 6.13. The Gaussian beam, characterized by confocal parameter b and focus position f (specified in the crystal medium), which propagates through the crystal as an ordinary wave is assumed to be of the form :

$$E_1(x',y',z') = \frac{E_0}{1+i\tau'}\exp(ik_1 z')\exp\left[\frac{-((x')^2+(y')^2)}{w_0^2(1+i\tau')}\right]\exp(-\frac{1}{2}\alpha_1 z') \ , \qquad (47)$$

where

$$\tau' = 2\frac{(z'-f)}{b} \ ; \qquad (48)$$

α_1 is the absorption coefficient at the fundamental wavelength; and w_0 is the beam waist. The polarization, which oscillates at the second harmonic frequency in a small slab of thickness dz', may be found from (27). This induced polarization radiates electromagnetic energy into an extraordinary Gaussian beam characterized by the fundamental confocal parameter b, but has a spot size $\sqrt{2}$ smaller than the fundamental. The total harmonic field is obtained by integrating over all the slab contributions within the crystal $0 \le z \le l$; Boyd & Kleinman show that the SHG power is given by :

$$P_2 = Ck_1 l P_1^2 e^{-\alpha' l}.h(\sigma,\beta,\kappa,\xi,\mu) \ , \qquad (49)$$

where

$$h(\sigma,\beta,\kappa,\xi,\mu) = \frac{1}{4\xi}e^{\mu\alpha l}\int\int_{-\xi(1-\mu)}^{\xi(1+\mu)} d\tau d\tau' \exp\left[\frac{-\kappa(\tau+\tau')+i\sigma(\tau-\tau')-\beta^2(\tau-\tau')^2}{(1+i\tau)(1-i\tau')}\right] ,$$

(50)

and where $C=(2/\pi).Z_0.d_{eff}^2.\omega^2/(n_{2\omega}n_\omega^2 c^2)$; $\xi = l/b$ describes the strength of focusing; $\mu=(l-2f)/l$ locates the focus position within the crystal; $\beta=B\xi^{-1/2}$ describes the crystal birefringence and walk-off through the parameter $B=\rho(lk_1)^{1/2}/2$; $\sigma=1/2b\Delta k$ describes the phase mismatch; and $\kappa=1/2\alpha b$ describes the crystal absorption at the fundamental and harmonic wavelengths.

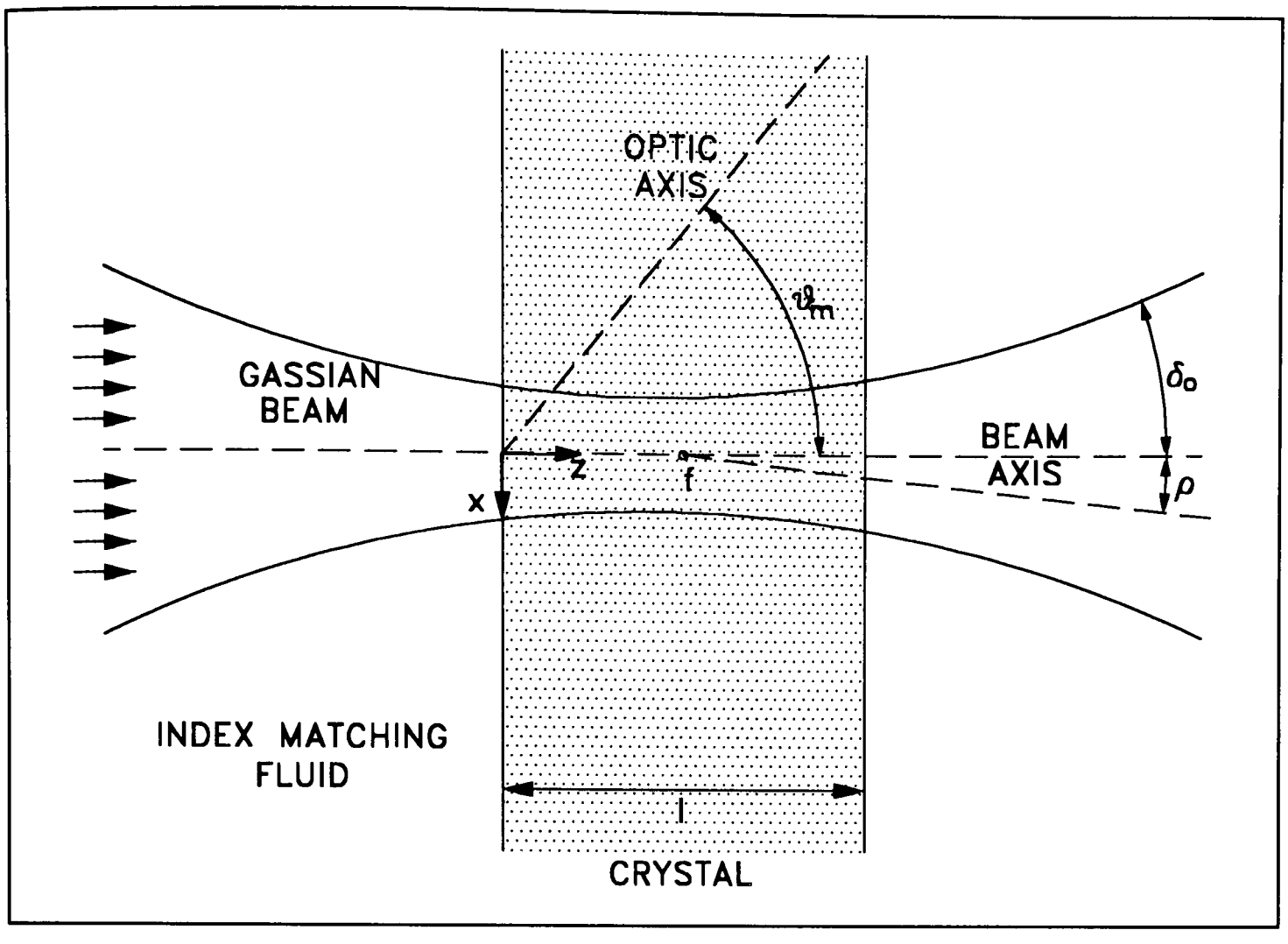


Figure 6. 13 : Schematic illustrating the parameters relevant to the Boyd & Kleinman theory of focused Gaussian beams interacting in non-linear media.

If the absorption is zero, as one might expect, the optimum focus position is located at the centre of the crystal, in which case :

$$\kappa = \mu = 0 \, . \tag{51}$$

In such a case, we may numerically integrate (50) [Appendix A.10] to yield the surface plots shown in figure 6.14,15. It is interesting to note that the optimum SHG efficiency for a given strength of focusing does not in general occur at $\Delta k=0$ $(\sigma=0)$; in practice, the optimum phase-match condition is achieved by slightly changing the crystal temperature or orientation about $\Delta k=0$ to maximize P_2. However, for soft focusing, $\xi=l/b \gg 1$, the phase-match condition reduces to the classical plane-wave limit of $\Delta k=0$, as can be seen from the trend of the contours in the figures 6.14,15. The maximum value of h corresponding to a given strength of focusing and crystal walk-off, $h(\sigma_m,\xi,B)$, is found by interpolation of the surface plots to find the optimum phase-matching; the variation of the optimized SHG efficiency,

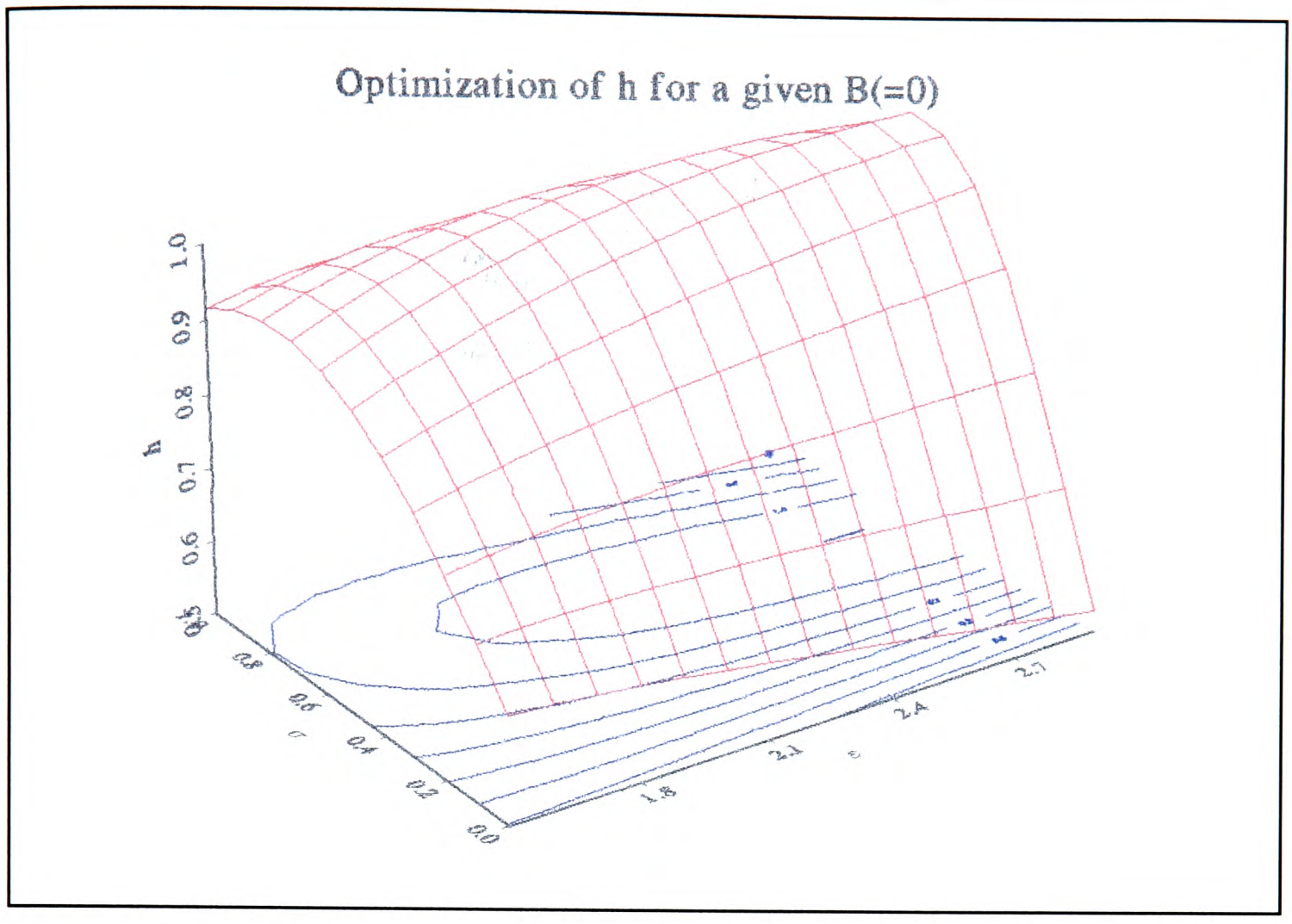


Figure 6.14 : Variation of the SHG power, h, as a function of focusing, ξ, and phase mismatch, σ, for $B=0$. Note that in general h_{OPT} does not occur for $\Delta k=0$.

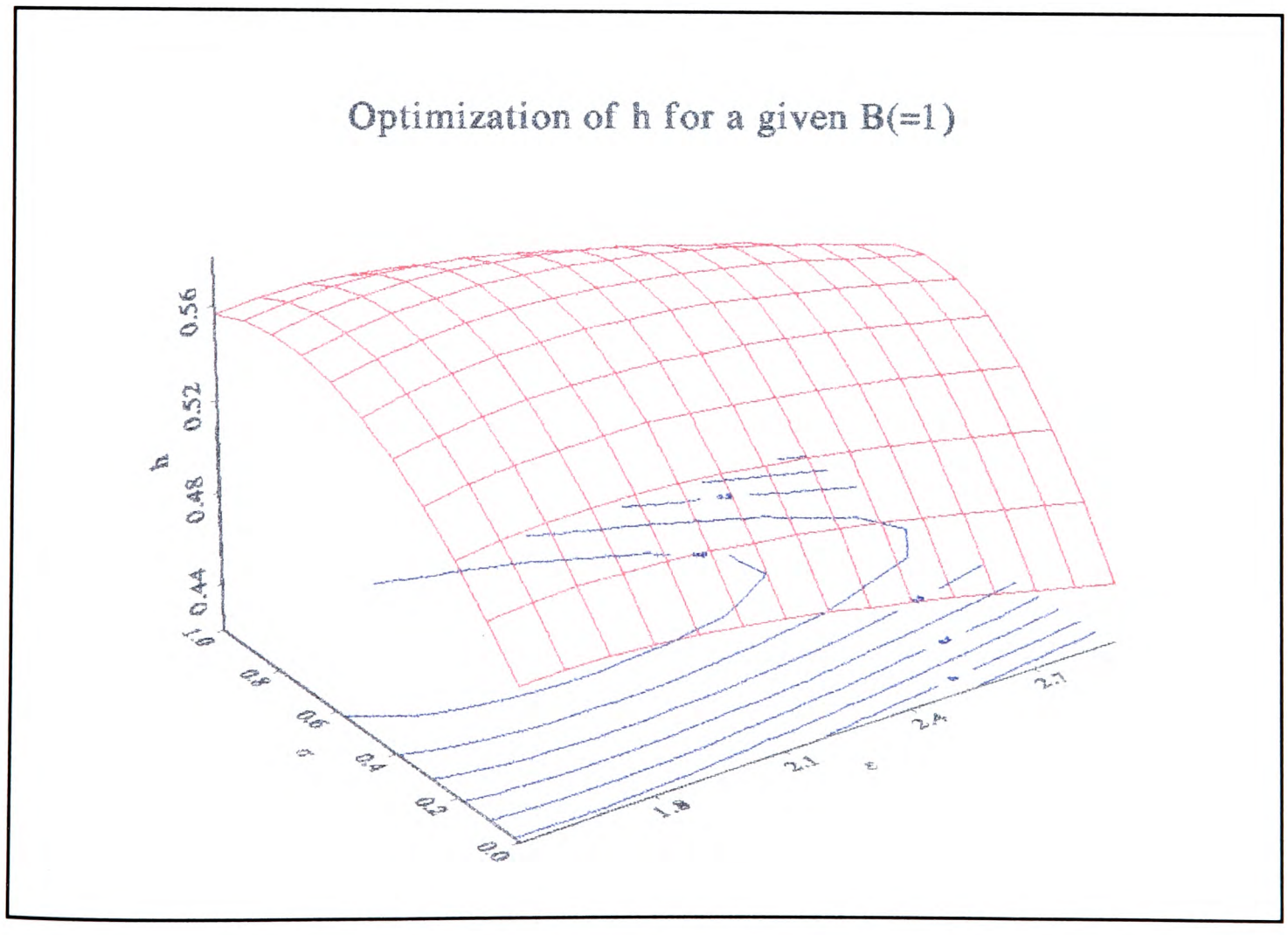


Figure 6.15 : Variation of the SHG power, h, as a function of focusing, ξ, and phase mismatch, σ, for $B=1$. Note that in general h_{OPT} does not occur for $\Delta k=0$.

described by $h_m=h(\sigma_m,\xi,B)$, as a function of the focusing parameter ,$\xi=l/b$, for several values of the double refraction parameter, B, is displayed in figure 6.16.

Figure 6.14 illustrates how insensitive the SHG optimization is with respect to ξ, since, for the sharpest curve $B=0$ (ie $\rho=0$), the maximum value of h_m, $h_{MAX}=1.068$ occurs at $\xi=2.84$, but h_m is approximately within 10% of its maximum value within the range $1.52\leq\xi\leq5.3$, indicating the focusing to be non-critical. Thus, one may achieve close to maximum conversion efficiencies at weaker than optimum focusing, thereby reducing thermal dephasing and the risk of crystal damage when using high power lasers. For large B, the optimum focusing parameter, $\xi_m(B)$, asymptotically tends toward 1.392, and for $B>2$:

$$h_m = h[B,\xi_m(B)] = 0.714/B \ . \qquad (52)$$

Boyd & Kleinman show that the asymptotic forms of (49) are conveniently

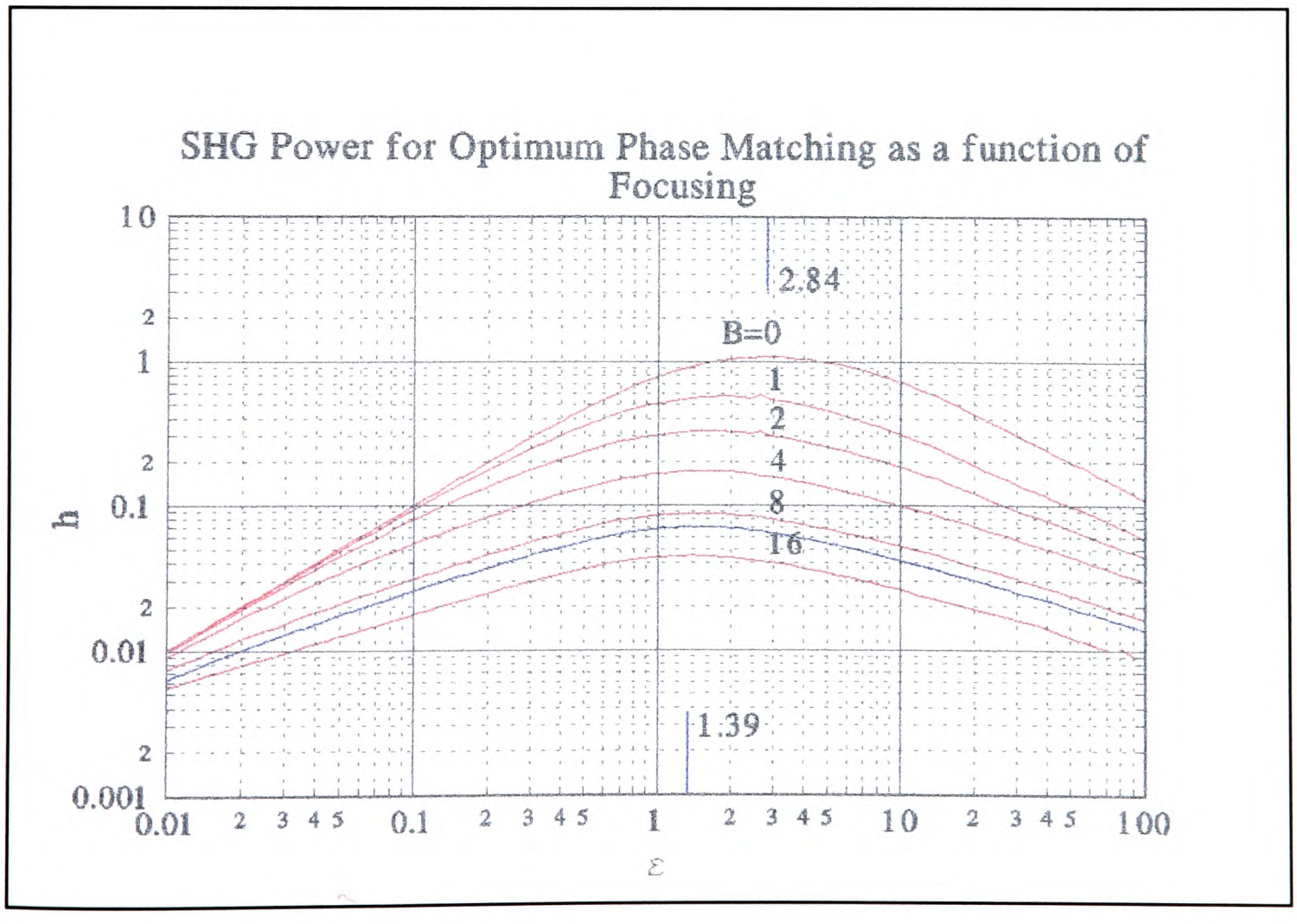


Figure 6.16 : Optimized SHG power, described through h_m, as a function of the focusing parameter $\xi=l/b$, for several values of the double refraction parameter B

expressed in terms of four characteristic lengths which are particularly useful for visualizing qualitative trends in SHG optimization. The four lengths are:

i) The crystal length, l.

ii) The beam radius, $w_0=(l/k_1)^{1/2}\xi^{-1/2}$.

iii) The aperture length, $l_a=\pi^{1/2}\omega_0/\rho=(\pi/4)^{1/2}(l/B)\xi^{-1/2}$. This is approximately the distance over which the fundamental and second harmonic beams become separated due to beam walk-off within the crystal.

iv) The effective length of focus, $l_f=(\pi/2)b=(\pi/2)l\xi^{-1}$; a Gaussian beam expands to $\sqrt{2}w_0$ at distances $\pm b/2$ from the beam waist on account of diffraction.

The asymptotic forms of the second harmonic power may be written as :

$$P_2 = \frac{CP_1^2}{w_0^2} \times \begin{cases} l^2 & l_a ; l_f \gg l & (i) \\ l l_a & l_f \gg l \gg l_a & (ii) \\ l_f l_a & l \gg l_f \gg l_a & (iii) \\ 4 l_f^2 & l \gg l_a \gg l_f & (iv) \\ 4.75 l_f^2 & l_a \gg l \gg l_f & (v) \end{cases} . \qquad (53)$$

These limits correspond respectively to :

(i) Weak focusing in a crystal in which the birefringence causes little beam walk-off ($B \approx 0$); the solution closely resembles the classical plane-wave form (29), where w_0^2 represents the area to which the fundamental beam is focused.

(ii) Again, weak focusing, but now the crystal birefringence is sufficient to cause complete beam walk-off with the crystal ($B \gg 0$); in such a case, the second harmonic power, P_2, is inversely proportional to w_0, and so P_2 increases with strength of focusing until case (iii).

(iii) Strong focusing in a crystal with large beam walk-off ($B \gg 0$) such that l_a is always less than l_f, even though the effective length of the focus is now less than the crystal length; now P_2 scales as w_0, and stronger focusing reduces the SHG efficiency.

(iv) Strong focusing in a crystal with small beam walk-off, such as close to a NCPM geometry where $B \rightarrow 0$; here the SHG power becomes limited by the effective focal length in the crystal, and $P_2 \propto w_0^2$.

(v) NCPM geometry $B=0$ and strong focusing; the second harmonic power is proportional to w_0^2.

An estimate of the optimum focusing geometry for crystals exhibiting a small walk-off angle ($B \rightarrow 0$, $B \simeq 0$) may be found by examining the cross over between the limiting cases of (i) and (iv); this occurs at $l=2l_f$ or $\xi=\pi$, close to the true value of $\xi_m(0)=2.84$. Similarly, to estimate the optimum focusing for SHG in crystals characterized by a large walk-off angle and a large B coefficient, such as is the case of CVL SHG in BBO ($B \simeq 14$ for $l=1$cm), the relevant intersection is between the limiting cases of (ii) and (iii), which occurs at $l=l_f$ or $\xi=\pi/2$, again, reasonably close to the true value $\xi_m=1.392$.

The theory of SHG with elliptical beams follows the same Boyd & Kleinman analysis, except, now as our starting point, we assume the Gaussian beam electric field is specified by

$$E_1(x',y',z') = \frac{E_0 \exp(-ikz')}{\left[(i+i\tau_x')(1+i\tau_y')\right]^{\frac{1}{2}}} \exp\left[-\left[\frac{(x')^2/w_x^2}{1-i\tau_x'} + \frac{(y')^2/w_x^2}{1-i\tau_y'}\right]\right] \exp(-1/2\alpha z') \quad (54)$$

where

$$\tau_x' = \frac{2(z'-f)}{kw_x^2} \qquad \tau_y' = \frac{2(z'-f)}{kw_y^2} \quad . \quad (55)$$

Freegarde has shown that in such a case, the second harmonic power is given by equation (49), except now, the function h is modified to :

$$h = \frac{\pi^2}{\epsilon_x} \exp(\mu\alpha l)\left[\frac{2}{\sqrt{\pi}} e \int_{-\infty}^{\infty} \exp(-4s^2)|H|^2 ds\right] , \quad (56)$$

where :

$$H = \frac{1}{2\pi}\int_{-\xi_x(1-\mu)}^{\xi_x(1+\mu)} \frac{\exp(-\kappa\tau_x')\exp(i\sigma\tau_x')}{(1+i\tau_x')^{\frac{1}{2}}(1+ie^2\tau_x')^{\frac{1}{2}}}\,d\tau_x' \,. \qquad (57)$$

Where e is the elipticity of the Gaussian beam waist given by $e=w_x/w_y$, and $\xi_x=l/b_x$. For optimum phase-matching and location of the focus in the crystal, the second harmonic efficiency is a function of B, ϵ_x, and e, of which the latter two parameters can be optimized for a given crystal type. The optimum elipticity of the Gaussian beam is plotted as a function of the crystal B parameter in figure 6.17, and the corresponding improvement in the harmonic conversion efficiency, represented by the function h_m, offered by optimal elliptical focusing over conventional spherical focusing is shown in figure 6.18.

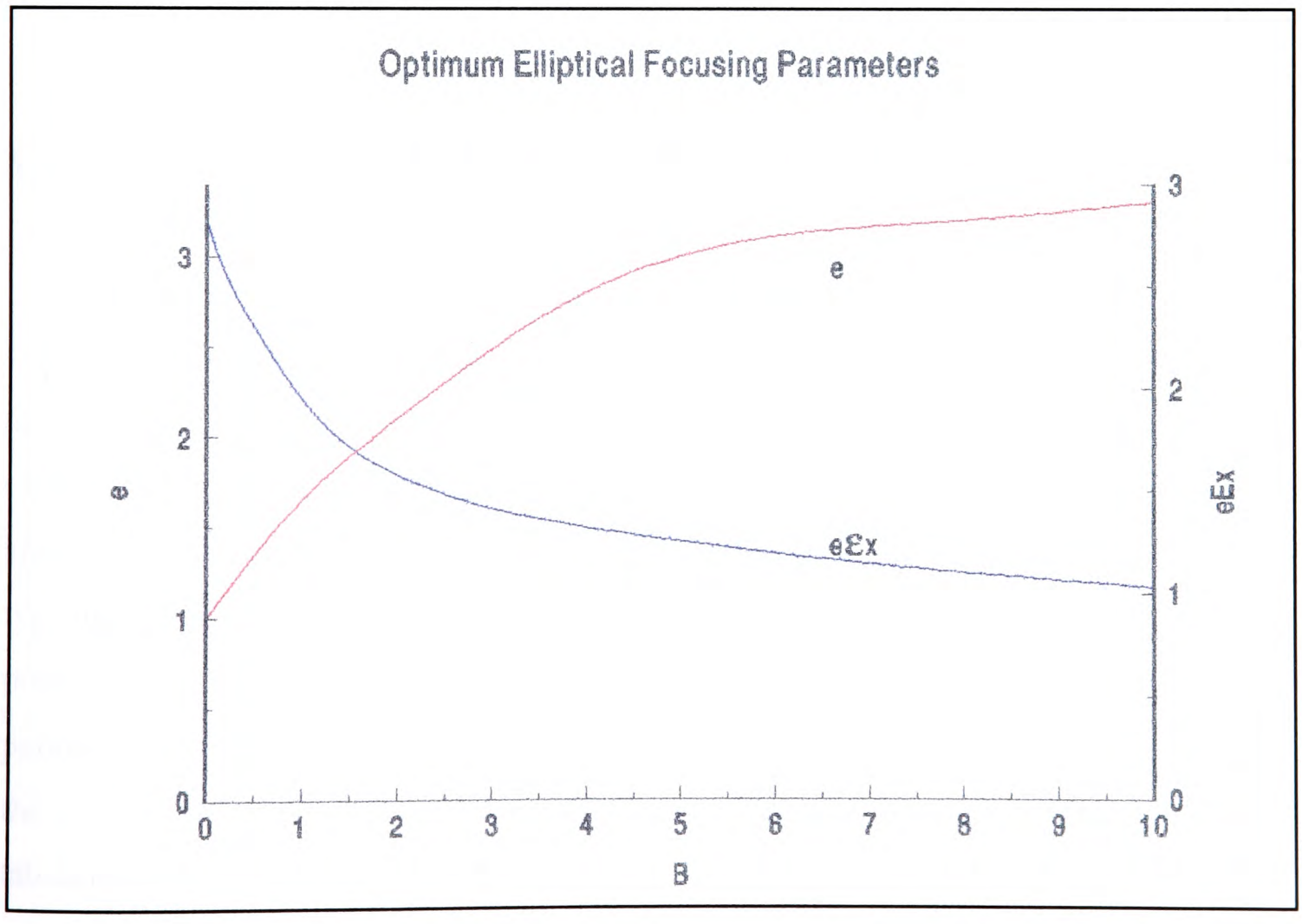


Figure 6.17 : Optimum elipticity of the focused Gaussian beam as a function of the crystal walk-off parameter B to achieve maximum harmonic conversion efficiency [6.12].

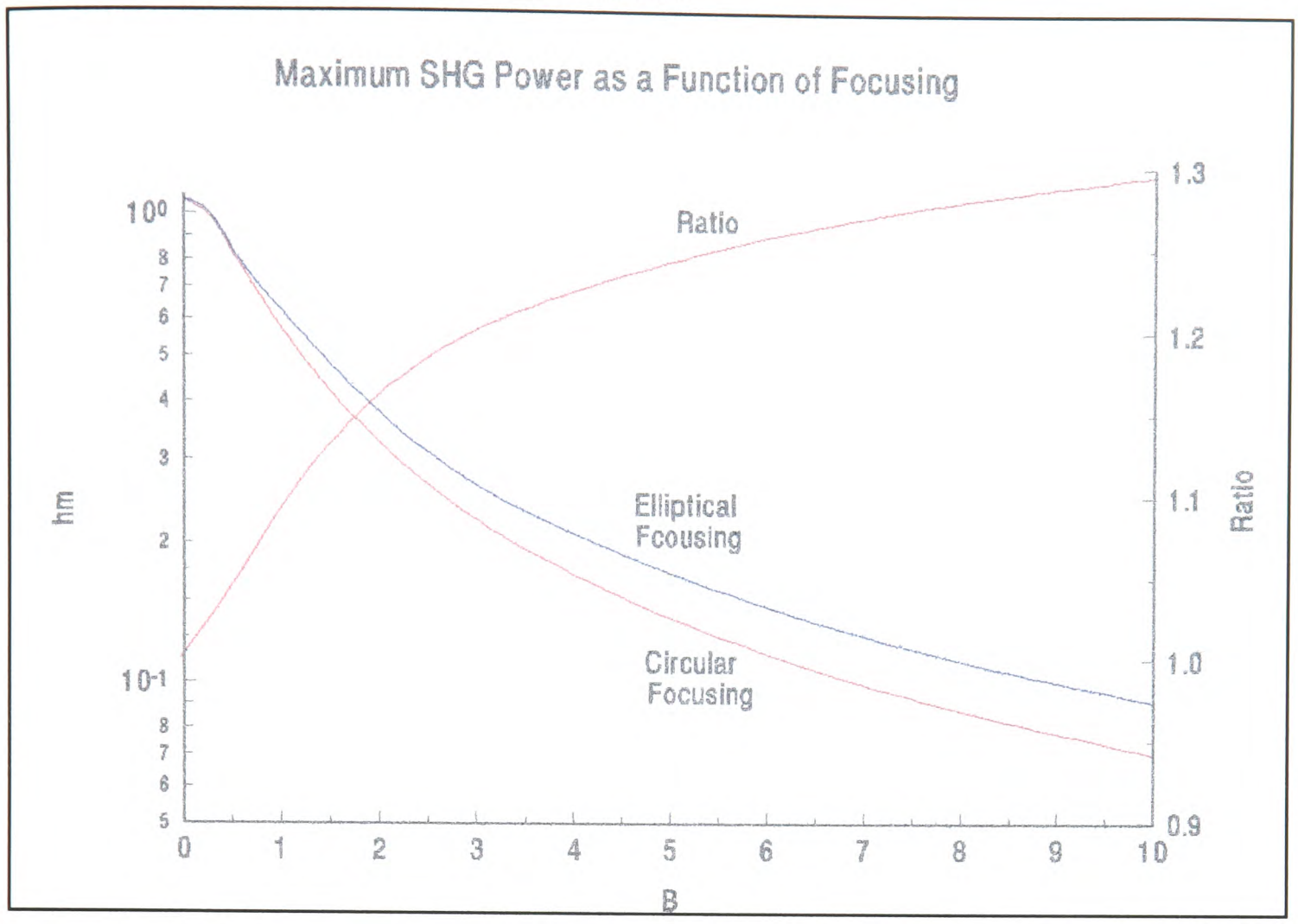


Figure 6.18 : Conversion efficiency parameter h_m for elliptical focusing as a function of the walk-off parameter B. Also shown is the function h_m arising from conventional focusing and the improvement ratio [6.12].

6.4.1 Theoretical Harmonic Efficiencies

Using published Sellmier data, the phase-matching angles and, hence, the Poynting vector walk-off angles, may be calculated for any nonlinear crystal. Once the walk-off angle, ρ, is known, the Boyd and Kleinman B parameter may be calculated, and used to find h_m, the harmonic conversion parameter. Then, with a knowledge of the functional dependence of the effective nonlinear coefficient on the type of phase-matching and crystal orientation, the ratio of the instantaneous harmonic power to the square of the fundamental power, $P_{2\omega}/P_{\omega}^{2}$, can be calculated. The parameters relevant to SHG in KDP, BBO, LBO and $LiIO_3$ are listed in table 6.1, and the calculated theoretical conversion efficiencies are presented for comparison. Also tabulated are the acceptance angles for the various phase-match geometries - these are computed using the theory developed by Blit *et al.* [6.13] to include the effects of focused Gaussian beams.

Table 6.1

	KDP	BBO	LBO	$LiIO_3$
Crystal Class	$_4$2m Uniaxial	R3c Uniaxial	mm2 Biaxial	C_6 Biaxial
d (pm/V)	$d_{36}=0.39$	$d_{11}=1.6\pm0.4$	$d_{32}=1.16$	$d_{31}=4.1$
Refractive Index	$no_{578}=1.51$ $ne_{578}=1.469$	$ne_{511}=1.557$ $no_{511}=1.677$ $ne_{578}=1.553$ $no_{578}=1.671$	$nx_{578}=1.576$ $ny_{578}=1.604$ $nz_{578}=1.618$	$no_{616}=1.88$ $ne_{616}=1.736$
Phase-Match Angle - Type I	$\theta_{578}=64°$	$\theta_{511}=50.5°$ $\theta_{578}=42.0°$	$\phi_{578}=69^0$ $\theta_{578}=90^0$	$\theta_{616}=67.6°$
Walk-Off Angle	$\rho_{578}=2.2°$	$\rho_{511}=4.1°$, $\rho_{578}=4.2°$	$\rho_{578}=0.7°$	$\rho=3.15°$
B	$B_{578}=7.7$	$B_{511}=10.5$ $B_{578}=10.1$	$B_{578}=2.0$	$B_{616}=8.8$
h_m	$h_{m\ 578}=0.091$	$h_{m\ 511}=0.7$ $h_{m\ 578}=0.7$	$h_{m\ 578}=0.34$	$h_{m\ 616}=0.081$
d_{eff} (pm/V)	$d_{eff}=d_{36}\sin\theta$ $.\sin2\phi$ $d_{eff}=0.35$	$d_{eff}=d_{11}\cos\theta\cos\phi+d_{31}\sin\theta$ $d_{eff\ 511}=1.1$ $d_{eff\ 578}=1.26$	$d_{eff}=d_{32}\cos\phi$ $(\theta=90°)$ $d_{eff}=0.42$	$d_{eff}=d_{31}\sin\theta$ $d_{eff}=3.8$
P_2/P_1^2	$15\mu W/W^2$ (578nm)	$56\mu W/W^2$ (511nm) $54\mu W/W^2$ (578nm)	$47\mu W/W^2$ (578nm)	$449\mu W/W^2$ (616nm)
θ_{acc}	0.05° (578nm)	0.013° (511nm) 0.022°(578nm)	0.12° (578nm)	0.021° (616nm)

In the above calculations, the nonlinear optical coefficients for KDP, BBO, LBO and $LiIO_3$ are taken from [6.14],[6.15],[6.16] and [6.14] respectively; similarly, the corresponding Sellmier coefficients can be found in [6.17], [6.8], [6.11] and [6.18]. Whilst it is not possible to achieve phase-matched SHG in $LiIO_3$ at the CVL wavelengths, the crystal promises to be very efficient for frequency doubling to 308nm for OH spectroscopy, as is considered in chapter 8, and so its nonlinear characteristics are presented here.

The laser beams used for second harmonic generation in the present studies (both CVL and CVL pumped dye laser beams) are far from TEM_{00}, and so we would expect the observed harmonic conversion efficiencies to fall rather short of the theoretical values of table 6.1. In practice, there are a number of crystal parameters, expressible as figures of merit, which indicate the suitability of a particular crystal for harmonic generation with non-ideal laser beams. Taking into account the walk-off and divergence of a nominal Gaussian beam, the efficiency may be written as $\eta \propto (d_{eff}.l_{max})^2/[n^2(\omega)n(2\omega)]$ [6.19], where l_{max} is the maximum interaction length. For walk-off limited conversion $l_{max} \propto 1/\rho$, whilst in the case of beam divergence-limited conversion $l_{max} \propto (\partial k/\partial\theta)^{-1}$. The figures of merit for an ideal plane wave interaction, walk-off limited interaction, and divergence-limited interaction are defined as $(d_{eff})^2/[n^2(\omega)n(2\omega)]$, $(d_{eff})^2/[n^2(\omega)n(2\omega)].1/\rho^2$, and $(d_{eff}.\quad)^2/[n^2(\omega)n(2\omega)].(\partial k/\partial\theta)^{-2}$ respectively. For KDP, BBO, LBO and $LiIO_3$ the figures of merit for type I phase-matching are listed in table 6.2. The damage threshold of a crystal is frequently a limiting factor for harmonic conversion, and so the single shot damage thresholds are also tabulated in table 6.2.

Table 6.2

	Figure Of Merit (FOM)			
Limitation Type	KDP	BBO	LBO	$LiIO_3$
none	1	7.5	1.2	70.9
divergence	1	1.57	7.5	13.1
walk-off	1	2.15	11.9	34.6
Damage Threshold [1]	7 GW/cm^2	15.6 GW/cm^2	25 GW/cm^2	See Next Chapter.

[1] The damage thresholds quoted are single-shot thresholds [6.20]; the high repetition rate damage threshold will generally be less than the figures quoted.

6.5 SHG With Non-Ideal Laser Beams

Thus far, harmonic generation with plane waves and focused Gaussian beams have been considered. However, the laser beams emanating from many high gain, pulsed lasers such as the CVL do not fall into either of these categories - the CVL intensity distribution is not Gaussian, and its divergence and transverse coherence evolve during the laser pulse. Thus, a theory of SHG with partially coherent laser beams whose divergence is in excess of the diffraction limit must be sought after. One such theory has recently been developed by Omatsu *et al* [6.2], based on a non-collinear interaction model.

The CVL beam, of divergence $\Delta\theta$ (half angle), is focused into the nonlinear crystal by a lens of focal length f; in the focal plane of the lens, the spot size of the CVL is $w_0 = 2\Delta\theta f$. The CVL beam is considered as being made up of "ray-bundles" of diameter w_0, such that the jth bundle, of power $P_{\omega j}$, propagates through the crystal with wave vector $\mathbf{k}_j$, as shown in figure 6.19. The CVL power is divided amongst the ray-bundles according to :

$$P_\omega = \sum_j P_{\omega j} \,. \tag{58}$$

Consider the interaction of two ray bundles, with wave vectors $\mathbf{k}_i$ and $\mathbf{k}_j$, in the non linear crystal, as depicted in figure 6.20. A nonlinear polarization will be induced in the crystal where the bundles overlap, and the resulting second harmonic wave will propagate along the direction $\mathbf{k}_i + \mathbf{k}_j$ with wave vector $\mathbf{k}_{2\omega}$. The phase-mismatch Δk is given by :

$$\Delta k = 2|k_i|\cos\phi - k_{2\omega} \tag{59}$$

where ϕ is the angle between $\mathbf{k}_{2\omega}$ and $\mathbf{k}_i$. As shown in figure 6.20, the direction of the second harmonic ray does not follow $\mathbf{k}_{2\omega}$ because of beam walk-off, but instead, travels at an angle ρ relative to $\mathbf{k}_{2\omega}$. The nonlinear interaction which gives rise to the second harmonic occurs only while the SH ray remains within the interaction region. The intensity of the second harmonic generated by the interaction of ray-bundles $\mathbf{k}_i$ and $\mathbf{k}_j$ is assumed to be given by the plane-wave theory; ie

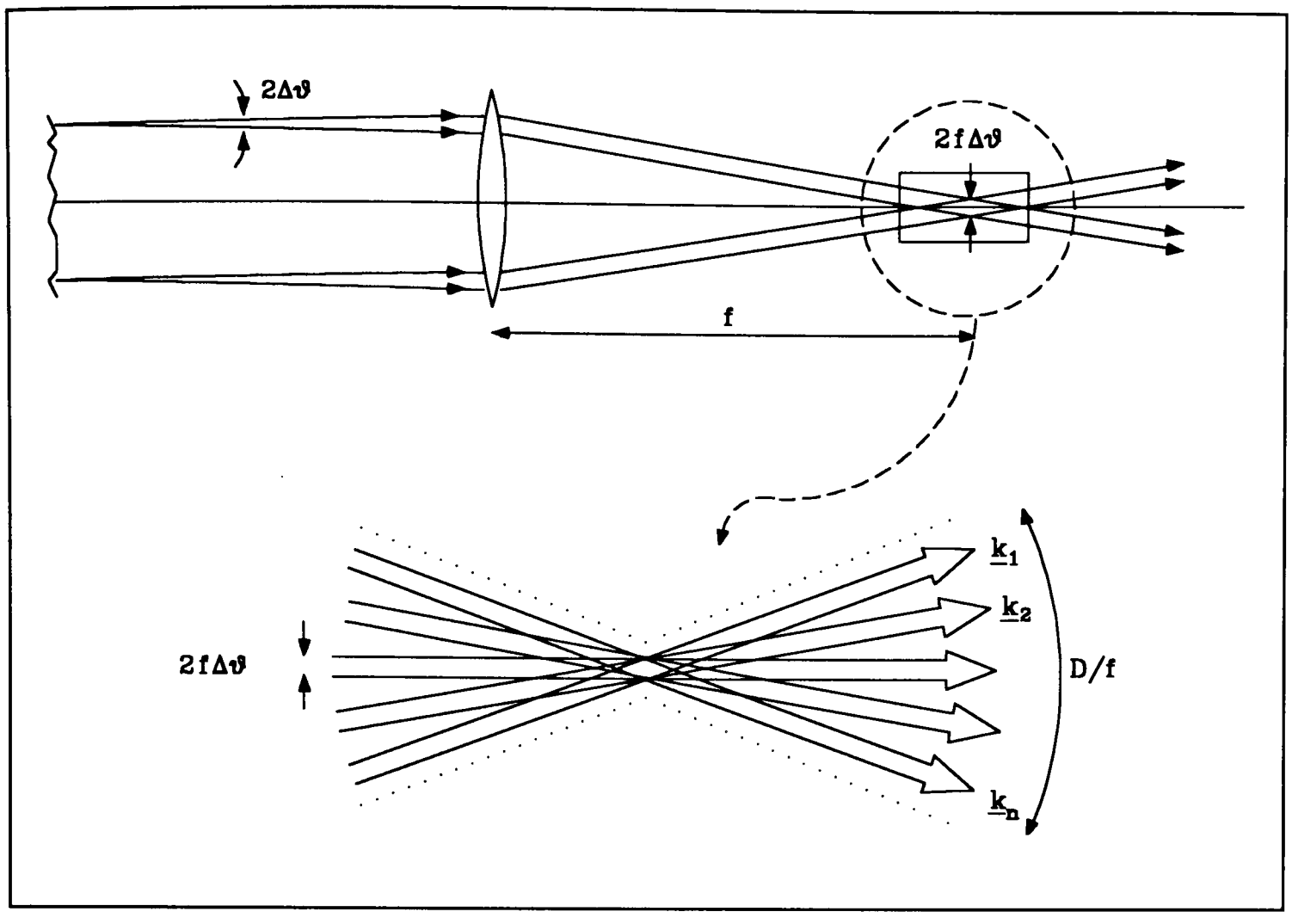


Figure 6.19 : The CVL is considered as being made up of a series of "ray-bundles" of linear dimension $w_0 = 2\Delta\theta f$.

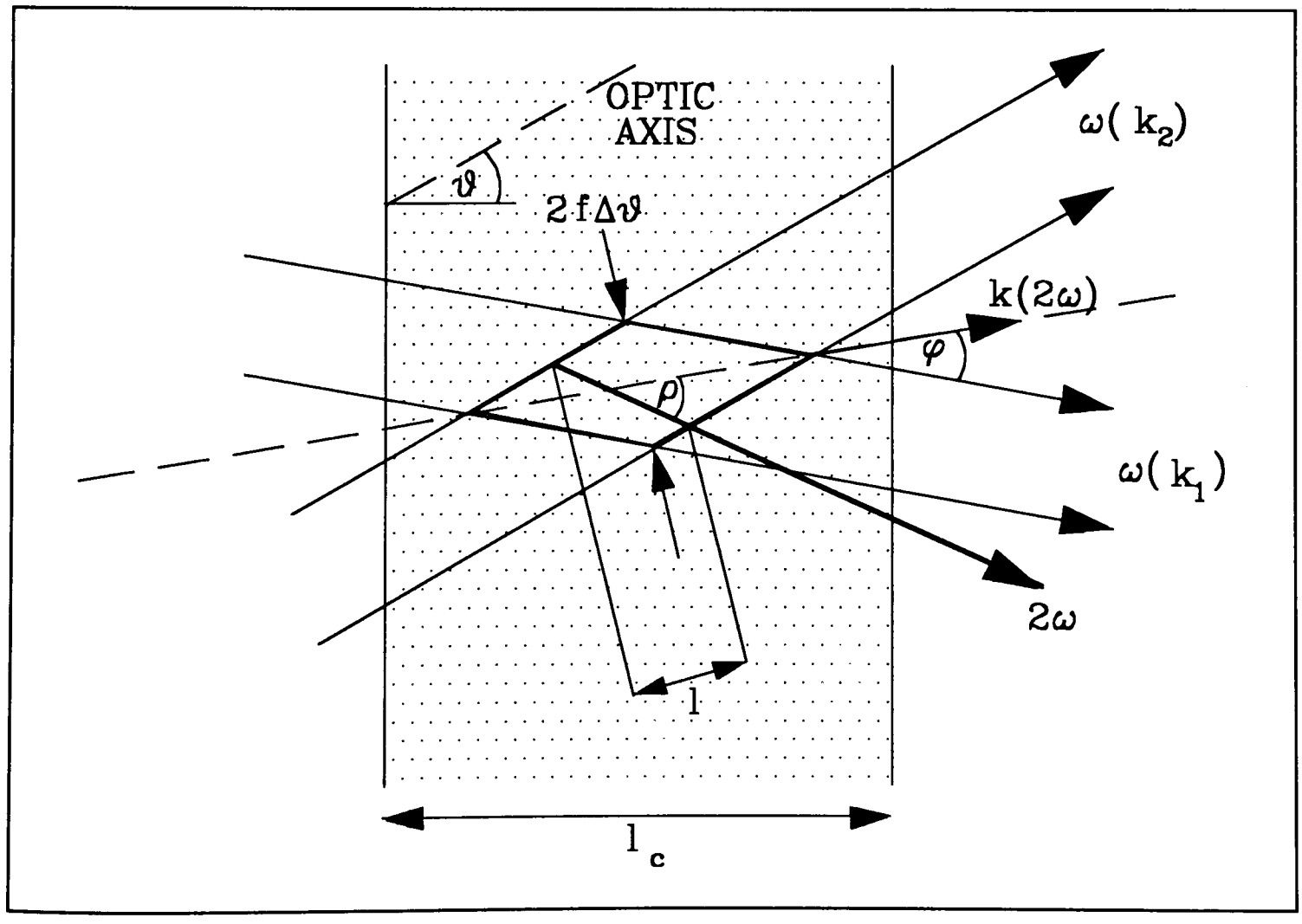


Figure 6.20 : Detail of the interaction region within a nonlinear crystal of length l_c, cut at an angle θ for phase-matching perpendicular to its surface. The interaction length, $l \leq l_c$, is limited by walk-off.

$$\Delta I_{2\omega} = 8\pi^2\left(\frac{\mu_0}{\epsilon_0}\right)^{1/2}\frac{d_{eff}^2 L^2}{n^3\lambda^2}G(1,2)(\Delta I_\omega)_1(\Delta I_\omega)_2\frac{\sin^2(\Delta kL/2)}{(\Delta kL/2)^2}\ , \qquad (60)$$

where L is the interaction length determined by beam walk-off in the region of overlap between the ray-bundles (but limited by the physical length of the nonlinear crystal such that $L \leq l_c$); $(\Delta\ I_\omega)_1$ and $(\Delta\ I_\omega)_2$ are the intensities of the interacting ray-bundles; and *G(1,2)* is a normalized second order correlation function describing the coherence of the laser beam. Otherwise, the symbols have their usual meanings. The total second harmonic power is then given by :

$$P_{2\omega} = \sum_{(all\ pairs\ of\ pencils)} \int \Delta I_{2\omega}\, d(interaction\ region)\ . \qquad (61)$$

The evaluation of the second harmonic power using the non-collinear model is, unfortunately, difficult, and requires not an inconsiderable amount of computing power - additionally, the peak instantaneous power and transverse coherence vary during the CVL pulse, making the model input parameters ambiguous. However, with a few simplifying assumptions, the theory can be translated into a viable computer model to usefully predict the variation of the normalized second harmonic power as a function of focusing. The main assumptions are :-

1. BBO is a negative uniaxial crystal, and phase-matching limits only the angle between the optic axis and the direction of propagation - the azimuthal angle around the z axis remains arbitrary. Strictly, the effective nonlinear coefficient is a function of the azimuthal angle, but the small dependence is neglected here. Therefore, the calculation is simplified to a one dimensional problem.
2. The intensity distribution and divergence of the CVL is assumed to be uniform and constant throughout the pulse; additionally, the CVL beam is assumed to be coherent $G(i,j)=1+|\gamma(i,j)|^2=1$.

Translation of the theory into a computer model involves dividing the energy from the two dimensional CVL beam into a one dimensional line of ray bundles. This is conveniently accomplished by ascribing the energy of bundle j, $P_{\omega j}$, to the

energy of the corresponding line segment of the CVL beam. The phase mismatch between the second harmonic and the ray bundles *i,j* can be shown to be :

$$\Delta k = \frac{4\pi}{\lambda}\left[n_o(\omega)\cos\phi - n_e(2\omega,\psi)\right], \qquad (62)$$

where $\psi=\alpha_1-\phi+\theta$, θ being the angle at which the crystal is cut relative to the optic axis, and α_1 is the angle the lower ray bundle makes with the crystal face normal. In the one dimensional approximation, Omatsu shows that the harmonic power is conveniently divided into three components, and the total harmonic power generated by the non-collinear interaction of ray bundles i and j is :

$$P_{2\omega}(i,j) = 4\beta_0 P_{\omega i} P_{\omega j}\left[\frac{\sin^2\left(\frac{\Delta k.w_0}{2(\rho+\phi)}\right).w_0}{\Delta k^2} + 2.\int_{\frac{(w_0-\rho.l_f)}{2}}^{0} \frac{\sin^2\left(\frac{\Delta k.\phi.y}{(\rho^2-\phi^2)}\right)}{\Delta k^2} dy\right] \qquad (63)$$

where

$$\beta_0 = 8\pi^2\left(\frac{\mu_0}{\epsilon_0}\right)^{1/2}\frac{d_{eff}^2}{\lambda^2 n^3 S^2} \qquad (64)$$

and S is the spot area of the ray-bundle. Using equations (61) to (64), the present author has constructed a Mathcad computer model [Appendix A.11] to investigate the variation of the SH power with focusing for CVL divergences in the region 1-1.3 mrads. The model assumes the CVL to be operating at 3.7kHz with a pulselength of 40ns; the CVL is asumed to deliver 4W of green,511nm, avaerage power in a 10mm diameter beam. Whilst the absolute SHG powers predicted by the model are not accurate, the variation of the normalized SH efficiency with focusing and divergence are qualitatively correct. The model suggests that the greatest efficiency is offered by optimally-focused low divergence radiation, and that the greatest SH power generated by radiation of higher divergence requires stronger focusing than that of lower divergence. The results from the model are shown in figure 6.21. A contour map of the normalized SH efficiency/power showing the line of optimum focusing as a function of divergence is shown in figure 6.22.

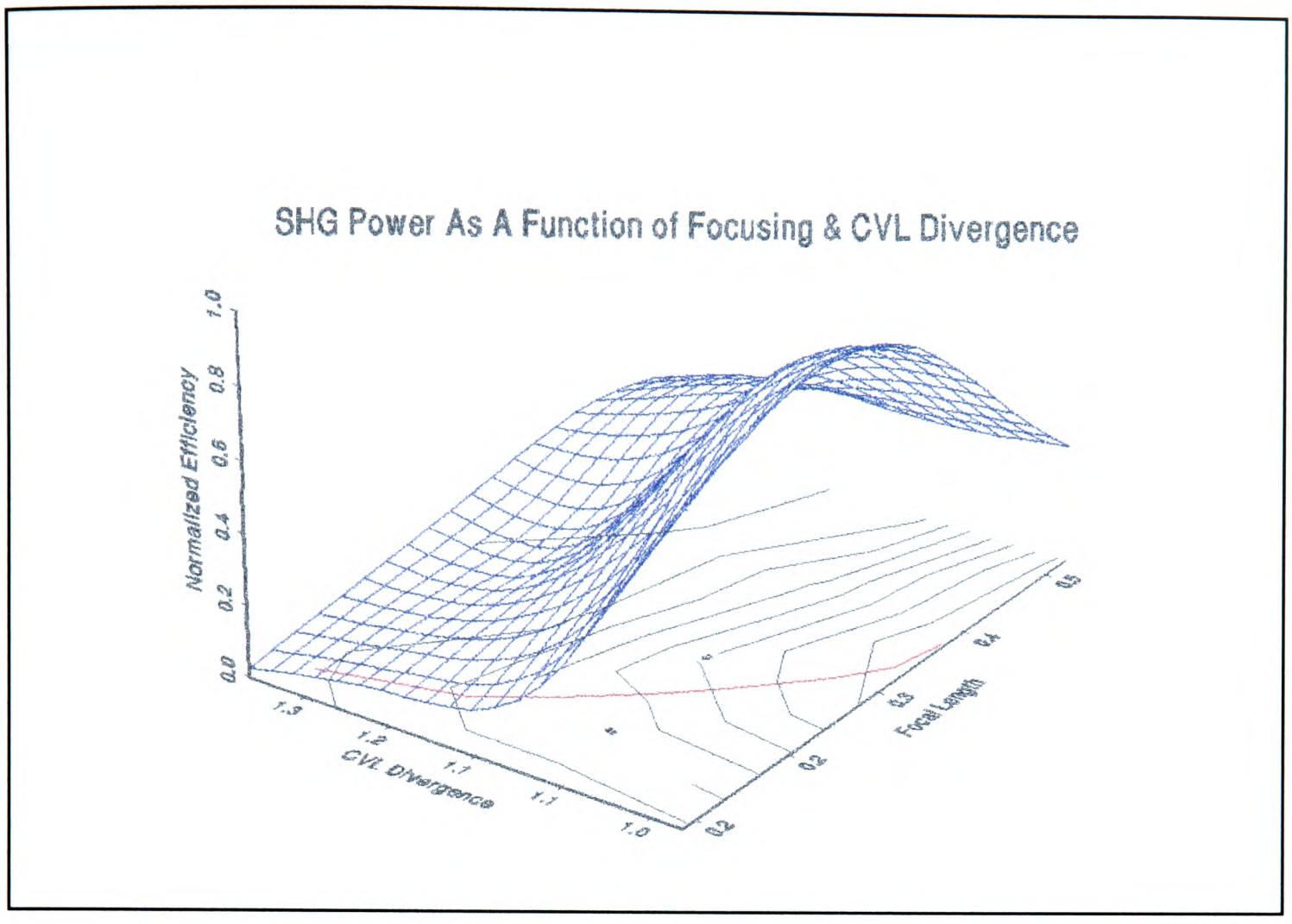


Figure 6.21 : Variation of the normalized second harmonic intensity with divergence and strength of focusing for a 10mm diameter CVL beam interacting in a 7.5mm BBO crystal.

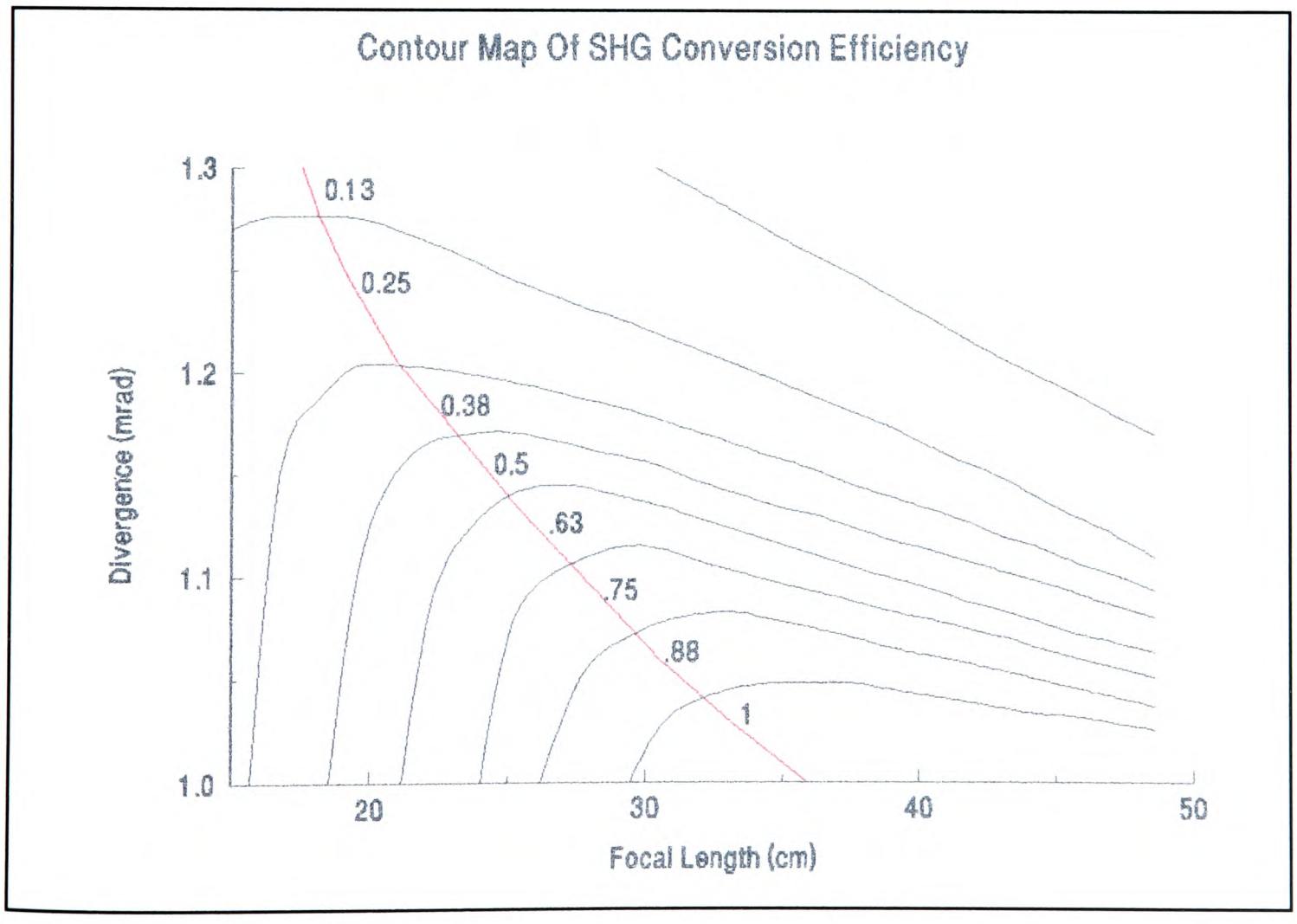


Figure 6.22 : Contour map of the above 3-D surface, illustrating the optimum strength of focusing as a function of CVL beam divergence.

6.6 Concluding Remarks

Three models for harmonic generation have been presented. The Boyd and Kleinman theory is based on the interaction of ideal Gaussian beams, and is expected to offer the best description of the harmonic generation with the near diffraction - limited CVL-pumped dye laser beams. The non-collinear interaction model caters for divergent laser beams of non-Gaussian intensities, and is expected to offer the best description of SHG with the CVL. Whilst these models offer a guide to the choice of crystal and focusing geometry, in practice several practical constraints must be also considered. Such constraints include the crystal damage threshold, the absorption coefficients for the fundamental and SH radiation, and the susceptibility of the crystal to thermal dephasing. The practice of harmonic generation is reported in the next chapter where all three theories will be compared, and the practical and efficiency limiting constraints will be detailed.

Appendix 6.1 : The Effective Nonlinear Coefficient

The second order polarization in a particular direction, P_i, generated by the fields $E_j(\omega_2)$ and $E_k(\omega_1)$ may be written as :

$$P_i(\omega_3) = \epsilon_0 \chi^{(2)}_{ijk} E_j(\omega_2) E_k(\omega_1 = \omega_3 - \omega_2) \ . \qquad \textbf{A.1}$$

By considering the effect of an inversion operation in the case of $\omega_1 = \omega_2 = \omega$, it can be seen that if the material possesses a centre of symmetry, the polarizability has to be the same for **E** and -**E** and, consequently, $\chi_{ijk}^{(2)} = 0$. Thus, this second order polarization only occurs in materials which do not possess a centre of symmetry (non-centrosymmetric crystals). Additionally, one cannot physically distinguish between $E_j(\omega_1)\ E_k(\omega_2)$ and $E_k(\omega_2) E_j(\omega_1)$, so that :

$$\chi^{(2)}_{ijk} = \chi^{(2)}_{ikj} \ , \qquad \textbf{A.2}$$

and so $\chi_{ijk}^{(2)}$ only contains 18 independent terms, which are conveniently written as a 3×6 matrix [6.3], as for the piezoelectric tensor. Thus :-

$$\begin{pmatrix} P_1 \\ P_2 \\ P_3 \end{pmatrix} = \begin{pmatrix} d_{11} & d_{12} & d_{13} & d_{14} & d_{15} & d_{16} \\ d_{21} & d_{22} & d_{23} & d_{24} & d_{25} & d_{26} \\ d_{31} & d_{32} & d_{33} & d_{34} & d_{35} & d_{36} \end{pmatrix} \cdot \begin{pmatrix} E_1(\omega_1)E_1(\omega_2) \\ E_2(\omega_1)E_2(\omega_2) \\ E_3(\omega_1)E_3(\omega_2) \\ E_2(\omega_1)E_3(\omega_2)+E_3(\omega_1)E_2(\omega_2) \\ E_1(\omega_1)E_3(\omega_2)+E_3(\omega_1)E_1(\omega_2) \\ E_1(\omega_1)E_2(\omega_2)+E_2(\omega_1)E_1(\omega_2) \end{pmatrix} . \qquad \textbf{A.3}$$

The form of the effective nonlinear coefficient is a function of the type of phase-matching and the crystal type; let us consider the case of type I phase-matched SHG in the negative uniaxial crystal BBO. The fundamental beam propagation direction is defined by the azimuthal angle, ϕ, and the inclination, θ, and is polarized in the ordinary direction (in the plane *xy*); the electric field may be written as :

$$(E_x\ E_y\ E_z) = E_1(\sin\phi, -\cos\phi, 0) \ , \qquad \textbf{A.4}$$

and so, the second order polarization will be :

$$\underline{P}(2\omega) = \epsilon_0 E(\omega_1)^2 \begin{pmatrix} d_{11} & d_{12} & d_{13} & d_{14} & d_{15} & d_{16} \\ d_{21} & d_{22} & d_{23} & d_{24} & d_{25} & d_{26} \\ d_{31} & d_{32} & d_{33} & d_{34} & d_{35} & d_{36} \end{pmatrix} . \begin{pmatrix} \sin^2\phi \\ \cos^2\phi \\ 0 \\ 0 \\ 0 \\ -\sin 2\phi \end{pmatrix} \qquad \textbf{A.5}$$

$$\underline{P}(2\omega) = \epsilon_0 E(\omega_1)^2 \begin{pmatrix} d_{11}\sin^2\phi + d_{12}\cos^2\phi - d_{16}\sin 2\phi \\ d_{21}\sin^2\phi + d_{22}\cos^2\phi - d_{26}\sin 2\phi \\ d_{31}\sin^2\phi + d_{32}\cos^2\phi - d_{36}\sin 2\phi \end{pmatrix} . \qquad \textbf{A.6}$$

For coherent second harmonic addition in the type I phase-matching scheme, the harmonic must be polarized along the extraordinary direction ($\cos\phi\cos\theta$, $\sin\phi\cos\theta$, $-\sin\theta$). Thus, the component of the induced second order polarization of interest is:

$$P_e(2\omega) = \epsilon_0 E(\omega_1)^2 (\cos\phi\cos\theta \;\; \sin\phi\cos\theta \;\; -\sin\theta) . \begin{pmatrix} d_{11}\sin^2\phi + d_{12}\cos^2\phi - d_{16}\sin 2\phi \\ d_{21}\sin^2\phi + d_{22}\cos^2\phi - d_{26}\sin 2\phi \\ d_{31}\sin^2\phi + d_{32}\cos^2\phi - d_{36}\sin 2\phi \end{pmatrix} \qquad \textbf{A.7}$$

and so, upon comparison with the definition of the effective nonlinear coefficient in equation (25), we may write:

$$d_{eff} = \begin{array}{r} \cos\phi\cos\theta\,(d_{11}\sin^2\phi + d_{12}\cos^2\phi - d_{16}\sin 2\phi) \\ +\sin\phi\cos\theta\,(d_{21}\sin^2\phi + d_{22}\cos^2\phi - d_{26}\sin 2\phi) \\ -\sin\theta\,(d_{31}\sin^2\phi + d_{32}\cos^2\phi - d_{36}\sin 2\phi) \end{array} . \qquad \textbf{A.8}$$

In the case of BBO, a class 3 crystal (trigonal, with one three-fold rotation axis) in which Kleinman symmetry applies, the second order susceptibility tensor is

$$\begin{pmatrix} d_{11} & -d_{11} & 0 & 0 & d_{31} & -d_{22} \\ -d_{22} & d_{22} & 0 & d_{31} & 0 & -d_{11} \\ d_{31} & d_{31} & d_{33} & 0 & 0 & 0 \end{pmatrix} . \qquad \textbf{A.9}$$

Thus, for type I phase-matching in BBO the effective nonlinear coefficient is:

$$d_{eff} = \cos\theta\,(d_{22}\sin 3\phi - d_{11}\cos 3\phi) - d_{31}\sin\theta \ . \qquad \textbf{A.10}$$

The values of d_{11}, d_{22}, d_{31} have been measured by Chen [6.15] to be 1.6, 0 and 0.1 pm/V respectively, and so :

$$d_{eff} = -1.6\cos\phi\cos\theta - 0.1\sin\theta \times 10^{-12}\ m.V^{-1} \ . \qquad \textbf{A.11}$$

Thus, d_{eff} is maximized if our waves propagate along the crystallographic x axis (ϕ=0). In a similar manner, the effective nonlinear coefficient for type II phase-matching in BBO can be shown to be:

$$d_{eff} = d_{11}\cos^2\theta\sin 3\phi \ . \qquad \textbf{A.12}$$

In the case of the biaxial crystal LBO, point group mm2, the second order susceptibility tensor is :

$$\begin{pmatrix} 0 & 0 & 0 & 0 & d_{15} & 0 \\ 0 & 0 & 0 & d_{24} & 0 & 0 \\ d_{31} & d_{32} & d_{33} & 0 & 0 & 0 \end{pmatrix} . \qquad \textbf{A.13}$$

The general form of the nonlinear coefficient is complex, but for type I phase-matching at θ=90°, the effective nonlinear coefficient can be shown to be :

$$d_{eff} = d_{32}\cos\phi \ . \qquad \textbf{A.14}$$

where the components of the second order susceptibility tensor have been measured by Chen [6.16].

Chapter 6 : References

6.1 G.D. Boyd & D.A. Kleinman
Parametric interaction of focused Gaussian light beams
J. Appl. Phys. ***39*** *3597-3639 (1968)*

6.2 T. Omatsu *et al.*
Non-collinear interaction model of the second harmonic generation of a copper vapor laser
Opt. Comm. ***79*** *125-130 (1990)*

6.3 A. Yariv
Introduction to non-linear optics - second harmonic generation
Quantum Electronics 2nd Edition, Wiley & Sons (1975)

6.4 R.L. Byer
Parametric oscillators and nonlinear materials
Nonlinear optics, Ed. P.G.Harper & B.S. Wherrett, Academic Press (1977)

6.5 P.A. Franken & J.F. Ward
Optical harmonics & nonlinear phenomena
Rev. Mod. Phys. ***35*** *23-39 (1963)*

6.6 M. Born & E. Wolf
Principles of Optics 6th Edition
Pergamon Press, Oxford (1986)

6.7 J.F. Nye
Physical Properties of Crystals - their representation by tensors and matrices
OUP (1967)

6.8 D. Eimeral *et al.*
Optical, mechanical, and thermal properties of barium borate
J. Appl. Phys. ***62*** *1968-1983 (1987)*

6.9 M.V. Hobden
Phase-matched second-harmonic generation in biaxial crystals
J. Appl. Phys. ***38*** *4365-4372 (1967)*

6.10 J.Q. Yao & T.S. Fahlen

Calculations of optimum phase match parameters for the biaxial crystal $KTiOPO_4$

J. Appl. Phys. ***55*** *65-68 (1984)*

6.11 S.P. Velsko, M Webb, L Davies & C. Huang

Phase-matched harmonic generation in lithium triborate (LBO)

IEEE J.Q.E. 27 2182-2192 (1991)

6.12 T.G.M. Freegarde

Spectroscopic applications of pulsed metal vapour lasers

D.Phil. Thesis, Oxford 1989

6.13 S.Blit, E.G.Weaver & F.K.Tittel

Wavelength temperature and angle bandwidths in SHG of focused beams in nonlinear crystals.

Appl. Opt. ***18*** *733-736 (1979)*

6.14 R.C.Eckardt, M.Masuda, Y.X.Fan & R.L. Byer

Absolute and Relative Nonlinear Coefficients of KDA, KD^*P, BaB_2O_4, $LiIO_3$, $MgO:LiNbO_3$, and KTP Measured by Phase-Matched Second-Harmonic Generation.

IEEE J.Q.E. ***26*** *922-933 (1990)*

6.15 C. Chen, B. Wu, A. Jiang & G. Yan

A new type of ultraviolet SHG crystal - β-BaB_2O_5

Sci. Sin. B ***28*** *235-243 (1985)*

6.16 C.Chen et al.

New nonlinear-optical crystal : LiB_3O_5

J.O.S.A. B ***6*** *616-621 (1989)*

6.17 F. Zernike Jr.

Refractive Indices Of Ammonium Dihydrogen Phosphate and Potassium Dihydrogen Phosphate Between 2000Å and 1.5μ.

JOSA ***54*** *1215-1220 (1964)*

6.18 H. Buesener, A. Renn, M. Brieger, F. Von Moers, A. Hese

Frequency Doubling of cw Ring-Dye-Laser Radiation in Lithium Iodate Crystals.

Appl. Phys. B ***39*** *77-81 (1986)*

6.19 S. Lin, Z. Sun, B. Wu & C. Chen
The Nonlinear Optical Characteristics of a LiB_3O_5 Crystal.
J. Appl. Phys. ***67*** *634-638 (1990)*

6.20 A. Borsutzky, R. Brunger, Ch. Huang & R. Wallenstein
Harmonic and Sum-Frequency Generation of Pulsed Laser Radiation in BBO, LBO and KD^*P
Appl. Phys. B ***52*** *55-62 (1991)*

Chapter 7

Second Harmonic Generation and Sum Frequency Mixing : Practical Results

7.1 Introduction.

7.2 CVL Second Harmonic Generation.

7.2.1 Calibration.

7.2.2 Results.

7.2.3 Elliptical Focusing.

7.3 SHG of CVL-Pumped Dye Laser Radiation.

7.3.1 Results.

7.4 Sum Frequency Mixing The Dye Laser and CVL Radiation.

7.5 Comparison With Theory.

7.5.1 CVL SHG : Comparison With Theory.

7.5.2 Dye Laser SHG : Comparison With Theory.

7.6 Conclusion and Discussion.

7.7 Future Design Considerations and Suggested Work.

7.7.1 SHG With Air-Cooled CVLs.

7.7.2 Enhancement Cavities and Parametric Oscillation.

References.

Chapter 7 : Second Harmonic Generation and Sum Frequency Mixing : Practical Results

7.1 Introduction

High average power, high repetition rate laser sources in the ultra-violet are of interest for a variety of applications, including the micro-machining of polymeric materials, photolithography, and fluorescence mapping. Such UV sources may be effectively provided by the nonlinear frequency conversion of the CVL. Furthermore, nonlinear frequency conversion of CVL pumped dye lasers offers a valuable source of high repetition rate, tunable radiation for UV spectroscopy, resonance ionization mass spectrometry, and laser induced fluorescence.

Prior to the start of the present research in 1989, the highest reported CVL SHG conversion efficiency was 11% (Freegarde and Naylor [7.1]). However, this efficiency could only be realized at low CVL powers, and at the higher CVL powers generated by an oscillator amplifier configuration, the same researchers reported a reduced efficiency of 7%. It was clear at the time that the limiting factor in the pursuit of high conversion efficiencies was the relatively poor CVL beam quality. Experimentally, it was observed that a substantially lower SHG conversion efficiency was achieved by the highly divergent light at the CVL pulse onset, as compared with the near diffraction-limited radiation found towards the pulse termination. To address this problem, much of the ensuing research has concentrated on CVL cavity design and improving the beam quality. Recent efforts by Pini *et al* [7.2] have achieved nearly 20% SHG conversion efficiency when using a diffraction-limited CVL beam generated by a self-filtering unstable resonator (SFUR). Here, the conversion coefficient ($c=P_{2\omega}/P_{\omega}^2$), a good measure of the beam quality, was nearly constant throughout the CVL pulse; however, the overall system efficiency was small, owing to the poor extraction efficiency of the SFUR cavity. Improvements to the CVL beam quality have been pursued in a different manner at the Lawrence Livermore National Laboratory [7.3], where, recently, by using an injection controlled oscillator amplifier CVL configuration, in excess of 3.2 W of UV has been generated at 17%

efficiency in BBO. In general, however, whilst high magnification unstable resonators and self-filtering designs offer the greatest amount of diffraction-limited output, they sacrifice some of the potentially useful low divergence power, to produce the greatest output with diffraction-limited beam divergence.

This chapter reports investigations into the second harmonic generation of the CVL using spherical, and the hitherto untried elliptical, focusing geometry. Conversion efficiencies in excess of 18% in BBO have been demonstrated, and the pursuit of even higher efficiencies has been limited only by the amount of available CVL 511 nm power, which was limited to 3-4 Watts at the time of the SHG investigations. Comparisons are made with theory and the limitations restricting further improvements are discussed. Type I and type II SHG geometries in BBO are compared with type I SHG in LBO for both the 511nm and 578nm lines.

In a similar manner, a series of experiments has been undertaken to investigate frequency doubling CVL-pumped dye laser radiation. Little research has been conducted in this area, and published results report very poor efficiencies and UV powers, with only a few milliwatts having been achieved at a few percent conversion efficiency [7.4]. The research reported in this chapter demonstrates that the superior beam quality and coherence of CVL-pumped dye lasers, as compared to the CVL, results in efficient second harmonic generation. SHG efficiencies approaching 40% have been demonstrated, and are limited only by the available pump power; these results easily represent the highest efficiencies presently reported. An experimental comparison of frequency conversion in LBO, BBO and $LiIO_3$ has been made, and sum frequency mixing of the dye laser with the CVL has been demonstrated to yield a valuable source for UV spectroscopy.

Whilst BBO and LBO offer excellent nonlinear properties for critically phase-matched SHG of the CVL and CVL-pumped dye lasers, the only nonlinear crystal available facilitating temperature-tuned non critical phase-matched SHG of the CVL is ADP (ammonium dihydrogen phosphate). Unfortunately, previous investigations by several researchers [7.5,7.6] have demonstrated that only transient phase-matching is possible in ADP, because of thermal dephasing effects; additionally, ADP

possesses a prohibitively low damage threshold, and so the present investigations have concentrated upon critically phase-matched geometries.

7.2 CVL Second Harmonic Generation

The efficiency of the second harmonic process is a sensitive function of the beam quality of the fundamental radiation. In the case of CVL SHG, Freegarde [7.6] has demonstrated that whilst the transverse coherence, beam divergence and SHG efficiency improve with increasing unstable cavity magnifications, the power extraction from the CVL decreases. Clearly, there is an optimum to be found between improving the CVL beam quality by the use of high magnification unstable cavities, and efficiently extracting the available power from the CVL. In his investigations, Freegarde demonstrated that a cavity magnification of 40 provided the greatest SH power (from a 15W air cooled CVL), even though the efficiency with this cavity magnification was significantly less than that offered by cavity magnifications of order 150. There is, however, one further means of improving the beam quality from a CVL unstable cavity - that is by decreasing the repetition rate. At low repetition rates, the CVL pulse length increases, which results in more cavity round trips, and a greater fraction of the CVL pulse possessing low, or near diffraction-limited divergence. Additionally, at low repetition rates, the pulse energy increases, and so the peak fluence, an important factor for efficient SHG, can be more than a factor of two greater than the fluence at high repetition rates.

Thus, for the CVL SHG investigations carried out here, an unstable cavity magnification of 40 was used, and by increasing the capacitance in the CVL thyratron tank, and across the laser head, to 16nF and 4nF respectively, the CVL was configured to run at 3.7 kHz. The CVL beam was polarized by an intra-cavity Glan-Taylor polarizing cube inserted into a miniature cavity side-arm, as described in chapter 5. For SHG investigations (rather than SFM) the 511 nm line was separated from the 578 nm line by the use of multiple dichroic filters in the beam delivery path. The optical layout shown in figure 7.1, illustrates the lengthy optical path used [~ 30ns] in order to prevent optical feedback into the CVL cavity, and so maintain beam quality. The CVL beam was focused into the BBO/LBO crystal by a lens of focal

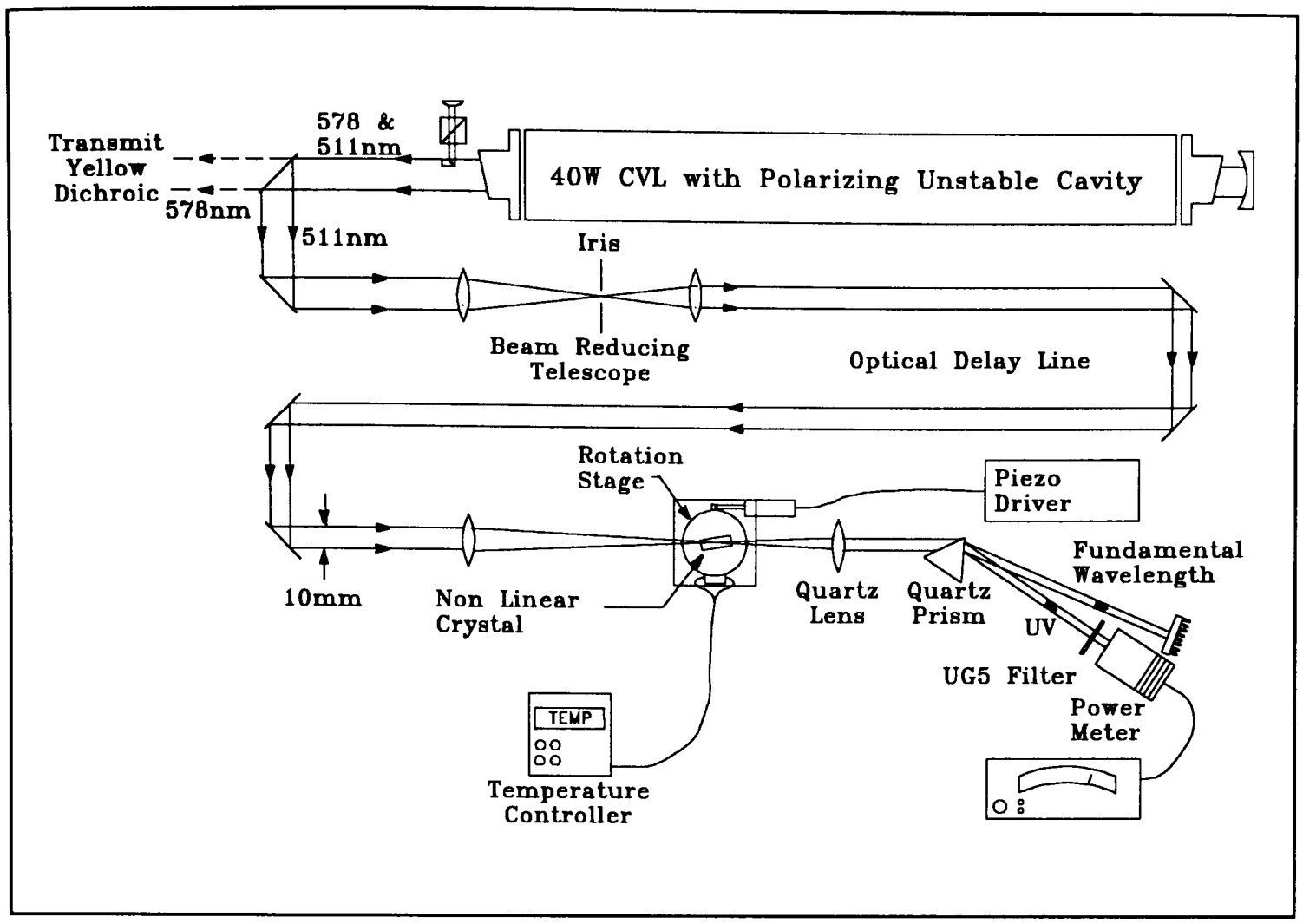


Figure 7.1 : Optical geometry used for the second harmonic generation of the CVL wavelengths using conventional spherical focusing.

length f, and the diverging radiation emerging from the crystal was collimated by a silica lens which was transparent to both the fundamental and harmonic radiation (BK7 and many other optical glasses absorb at wavelengths below $\sim$400nm). The UV was separated from the fundamental by a 60° silica prism and passed through an UG5 (transmit UV only) optical filter, before being incident upon a power meter. The fundamental power was recorded using a second power meter inserted between the focusing lens and the crystal.

The BBO and LBO crystals used in the present studies of second harmonic generation were obtained from Fujian Castech Crystals Inc. P.R.C. The BBO crystal used was cut at 51° to allow phase-matching of the CVL 511 nm line at normal incidence to its uncoated surfaces; BBO is slightly hygroscopic, and so the $5\times3\times10$mm crystal was supported on a temperature-stabilized mount maintained above room temperature. Whilst phase-matching in BBO is relatively insensitive to

temperature change[1], in the case of LBO a temperature-stabilized crystal mount was found to be necessary, owing to the sensitivity of phase-matching to temperature changes ($l\Delta T[°C.cm]=3.9°$). The LBO crystal used measured some $6\times3\times10.4$ mm and was cut at $\theta=90°$, $\phi=74°$ to allow near normal incidence phase-matching of the CVL 578 nm line.

The **E**-Field polarization of the CVL beam was vertical, and that of the generated harmonic was horizontal - this orientation allowed convenient crystal rotation about a vertical axis for the critical phase-matched geometries, and minimized surface reflection losses of the SH associated with the dispersing prism. To avoid crystal damage, initial alignment of the CVL beam through the crystal was performed using an apertured beam; this was especially necessary when the beam focus was near one of the crystal surfaces, since the surface damage threshold is approximately an order of magnitude less than the damage threshold of the crystal bulk. When aligning the focusing lens, great care was taken to finely optimize the phase-match angle for each lens position - this corresponds to the optimization of the Boyd and Kleinman σ-parameter which is a function of the strength of focusing and focus position in the crystal. The temporal variation of the CVL, frequency doubled CVL, and depleted CVL beam were recorded using vacuum photodiodes, and the pulse shapes were displayed on a Tektronix 2440 digital oscilloscope.

7.2.1 Calibration

The power meter used for measuring the UV power consisted of a Laser Instrumentation model 9000 thermopile head and model 9350 meter. The CVL power, however, was measured using an Ophir power meter which was calibrated against the Laser Instrumentation unit for the purpose of the present experiments. The transmission of the Schott UG5 colour glass filter was measured using a spectrophotometer and was found to vary from 58% transmission at 255 nm to 82%

[1] For BBO $l\Delta T[°C.cm]=55°$ - ie a temperature change of 55° causes the SHG power of an optimally phase-matched 10 mm BBO crystal to fall to one half of its original power.

at 289 nm. The transmission losses associated with the prism and silica collimating lens for the UV were determined by measuring the UV power transmitted through the UG5 filter with and without the prism and lens in the optical path to the power meter. (Note that the absorbing UG5 glass filter cannot be used as a long term substitute for the dispersing prism since it is prone to thermal fracture at high CVL powers.) The transmission loss of the prism/lens combination to both 255 nm and 289 nm was found to be 12%. By solving Fresnels' equations for the appropriate polarizations at the CVL fundamental and harmonic frequencies, the reflection losses associated with the nonlinear crystal surfaces at the phase-matching angular orientation may be estimated. For BBO, these losses may be shown to be 6% for the fundamental radiation at the entrance surface, and 5% for the harmonic at the exit surface.

The results presented later in this chapter have been corrected to allow for the losses associated with the prism, lens, UG5 filter and crystal surfaces. No attempt, however, has been made to account for any scattering or absorption losses associated with the crystal, since these are likely to be both intensity and wavelength dependent.

7.2.2 Results

BBO Type I Phase-matching

The variation of the 255 nm harmonic power as a function of the strength of focusing, at a fixed CVL power of 3 W, is plotted in figure 7.2. The harmonic power is seen to increase with increasing strength of focusing up to f=250mm, whereafter the harmonic power decreases until the onset of crystal damage, witnessed as a string of self-focusing bubbles, at a focal lengths less than 150mm.

The scaling of the harmonic power and efficiency with respect to the fundamental input power under optimum focusing conditions (f=250 mm) can be seen in figure 7.3; here, the CVL power arriving at the crystal was varied using calibrated reflective neutral density filters. The best recorded efficiency was some 15%, limited only by the CVL 511nm power available at the time of 3 W.

The recorded pulse shapes of the CVL 511 nm line, the depleted CVL 511 nm line (ie. the 511 nm radiation measured after the crystal) and the 255 nm second

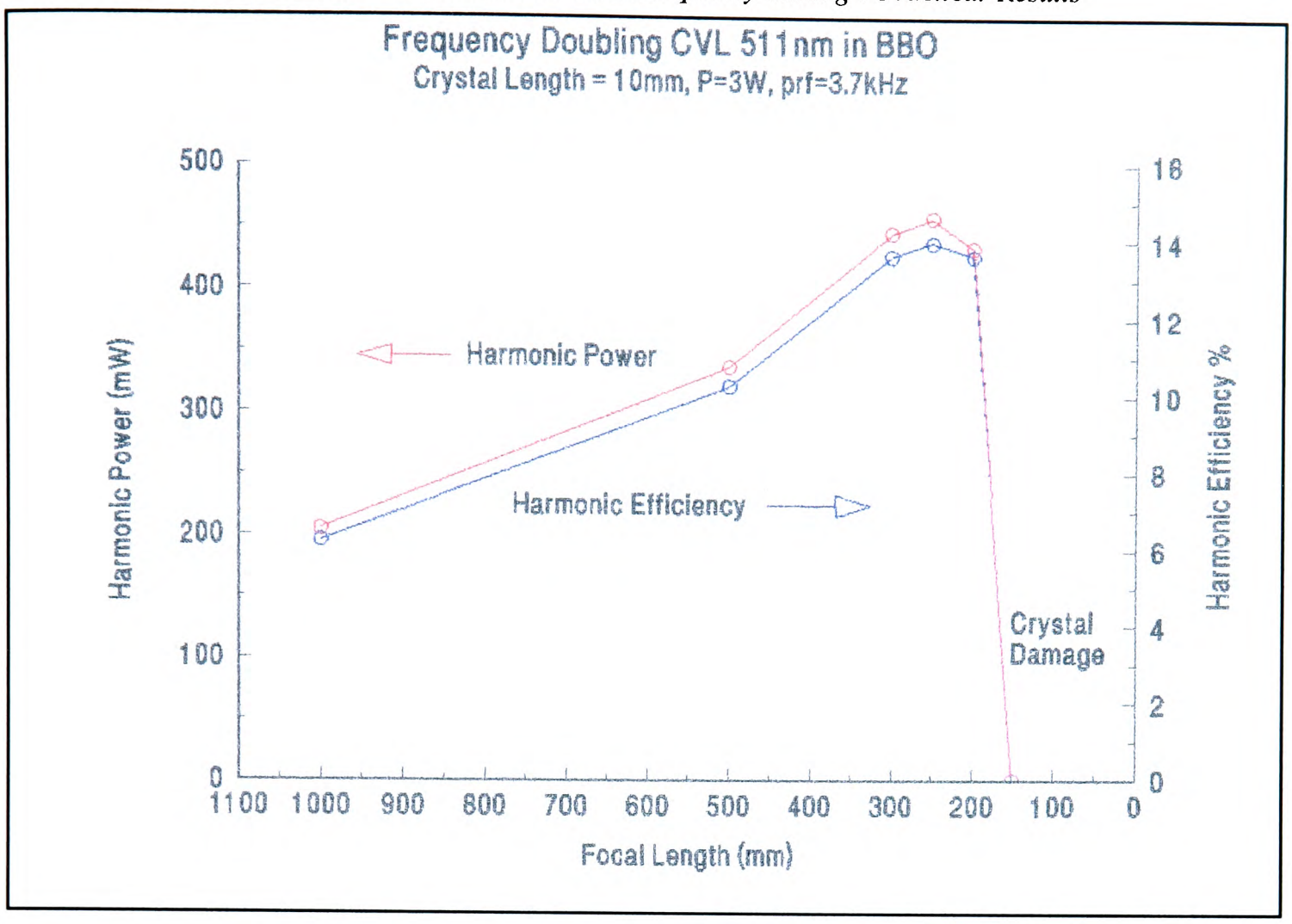


Figure 7.2 : Variation of the harmonic power and efficiency as a function of focusing in the SHG of the CVL 511nm line in a 10mm long BBO crystal.

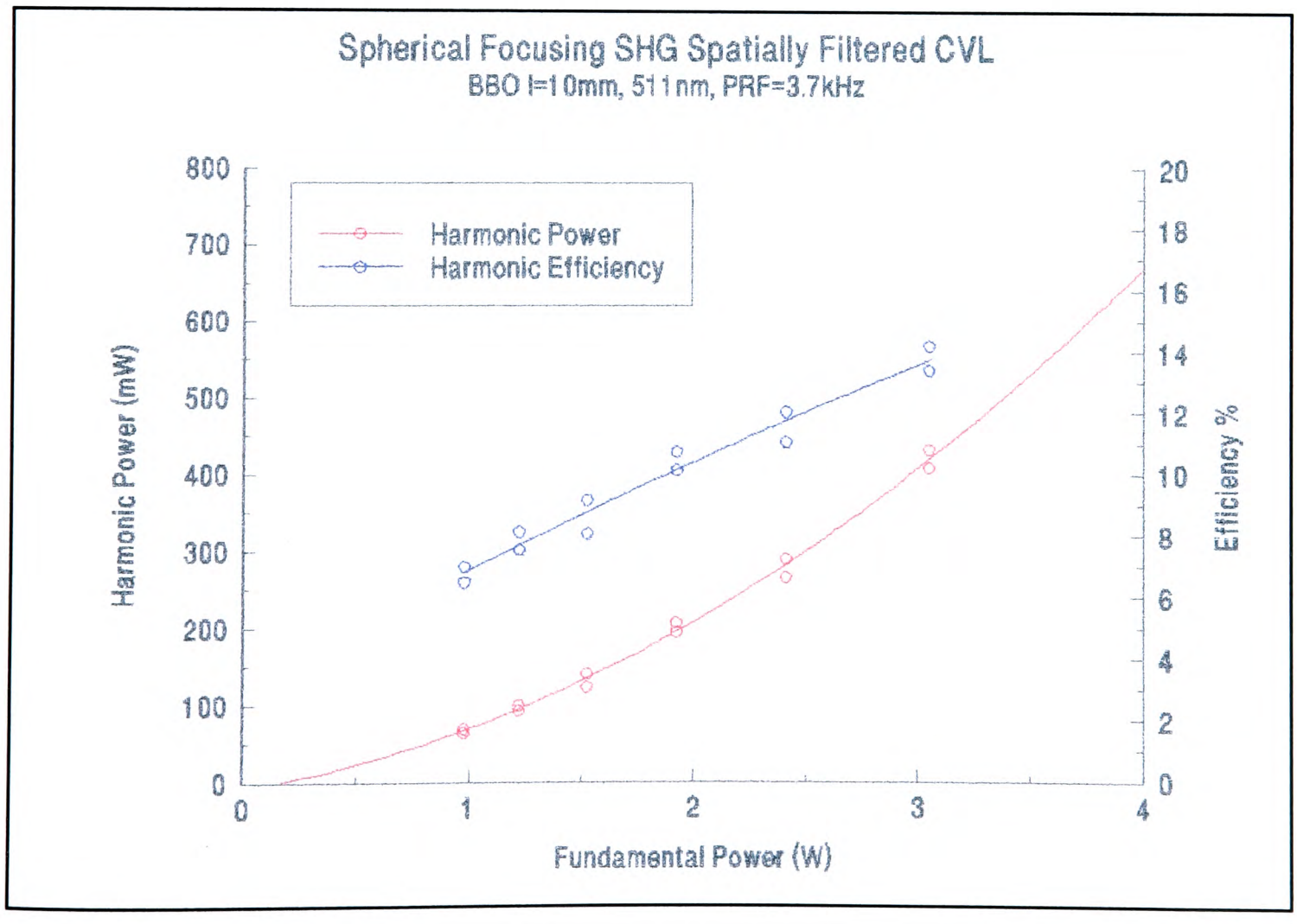


Figure 7.3 : SHG power scaling of the CVL 511nm line in BBO.

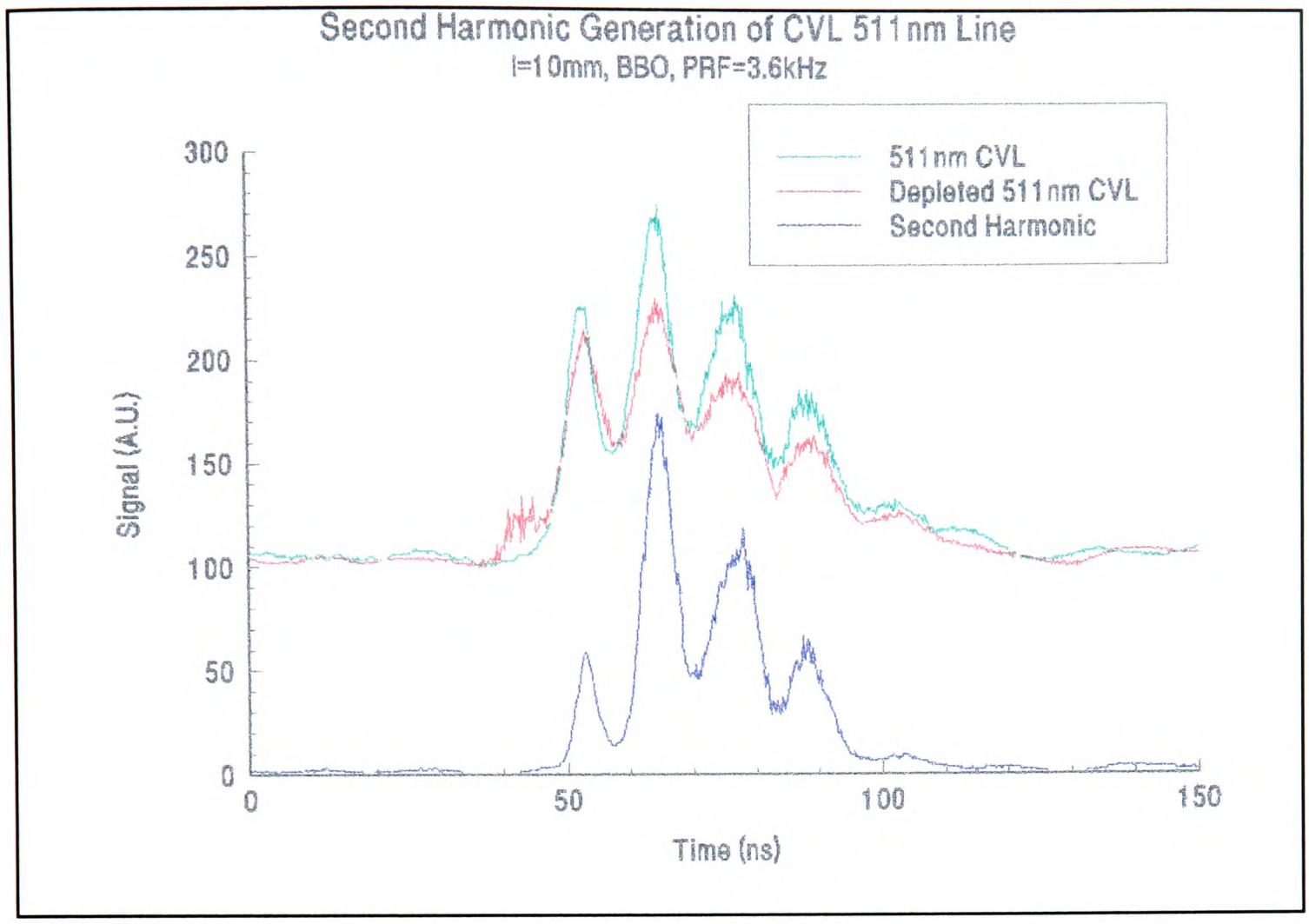


Figure 7.4 : Pulse shapes of the CVL, depleted CVL and second harmonic when the CVL 511nm line is frequency doubled in BBO.

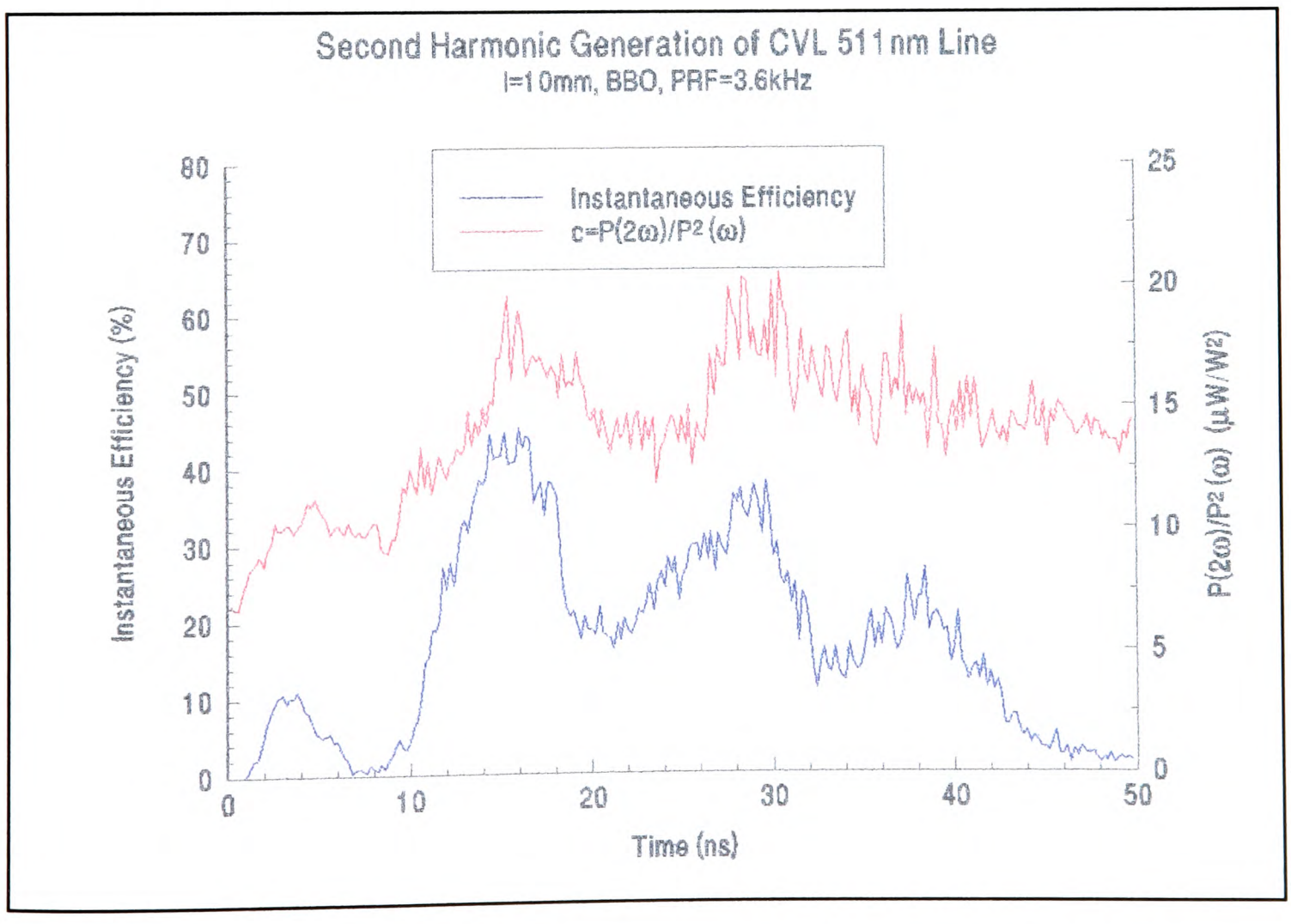


Figure 7.5 : Instantaneous conversion efficiency and conversion coefficient for the SHG of CVL 511nm radiation in BBO.

harmonic are shown in figure 7.4; from these pulse shapes, the instantaneous efficiency and the conversion coefficient, $c=P(2\omega)/P(\omega)^2$, may be calculated, and are displayed in figure 7.5. The second harmonic power and efficiency show a similar temporal dependence to the CVL pulse, in so much as when the CVL microstructure (owing to the cavity round trip time) exhibits a peak, so, too, does the SHG pulse. It is interesting to note that, whilst the average SHG conversion efficiency is 15%, the peak instantaneous efficiency mid-pulse approaches 50%; the efficiencies at the pulse onset and pulse termination are, however, somewhat lower, owing to the initially poor CVL beam divergence and low CVL peak power respectively. The SHG conversion coefficient, $c=P_{2\omega}/P_{\omega}^2$, is closely related to the beam divergence, since the quadratic SHG power dependence is incorporated in its definition. Figure 7.5 shows the conversion coefficient to increase in steps of 10 ns, corresponding to the cavity round trip time - this gives an indirect measure of the temporal evolution of the CVL beam divergence and transverse coherence. This form of the temporal evolution of the transverse coherence is exactly that which has been directly measured using interferometric techniques by several researchers [7.7,8]. The slight fall in the conversion coefficient towards the end of the pulse may be attributable to measurement errors associated with the very small signals at the pulse termination.

Similarly, the efficiency and power scaling of frequency doubling the CVL 578nm line to 289 nm can be seen in figure 7.6; the best recorded efficiency, just in excess of 12%, is again limited by the available CVL power. By comparing figures 7.3 and 7.6, the SHG of the CVL 578nm line can be seen to be more efficient than the 511 nm line at the same power level, owing to the superior divergence and transverse coherence of the 578nm laser transition. The CVL yellow, depleted yellow and SHG pulse shapes were recorded and are plotted in figure 7.7, whilst the calculated instantaneous efficiency and conversion coefficient are plotted in figure 7.8.

BBO Type II Phase-matching

The birefringence of BBO is such that phase-matched Type II SHG is not possible for the CVL green line (the type II SHG cut-off occurs at 527nm) but is,

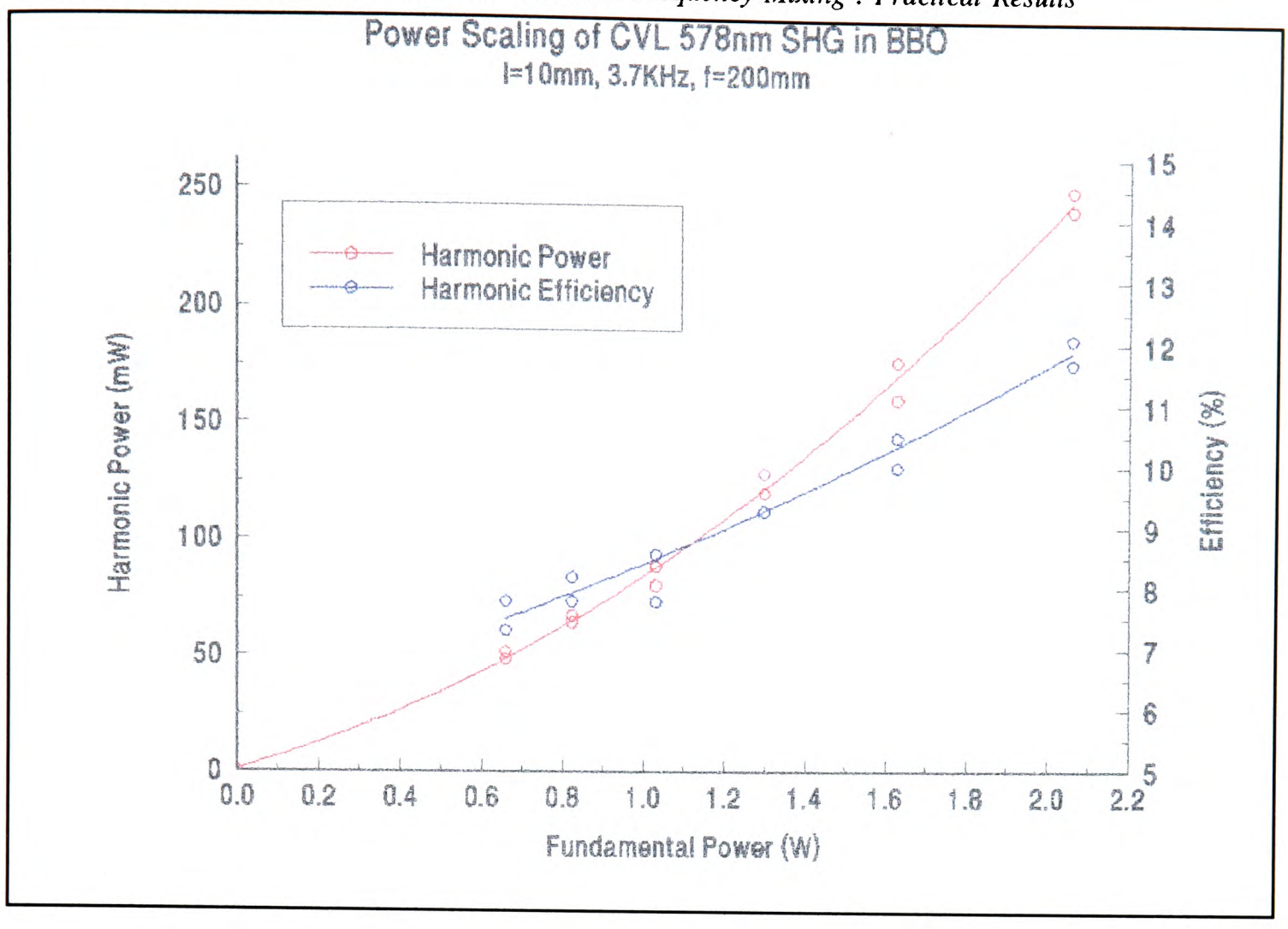


Figure 7.6 : SHG efficiency and power scaling for type I SHG of the CVL 578nm line in a 10mm BBO crystal.

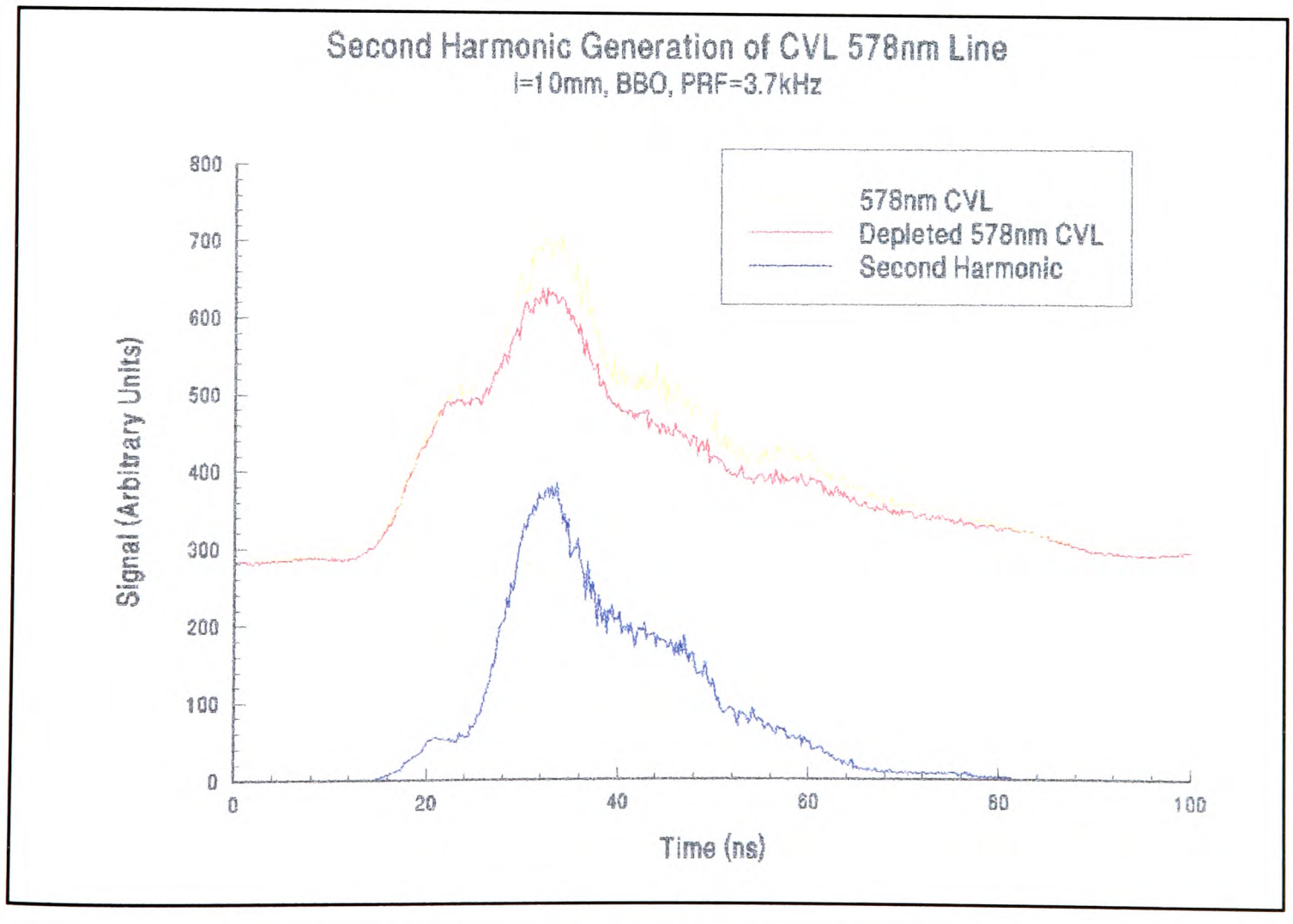


Figure 7.7 : Pulse shapes of the CVL 578nm line, depleted 578nm line and the 289nm radiation resulting from SHG in BBO.

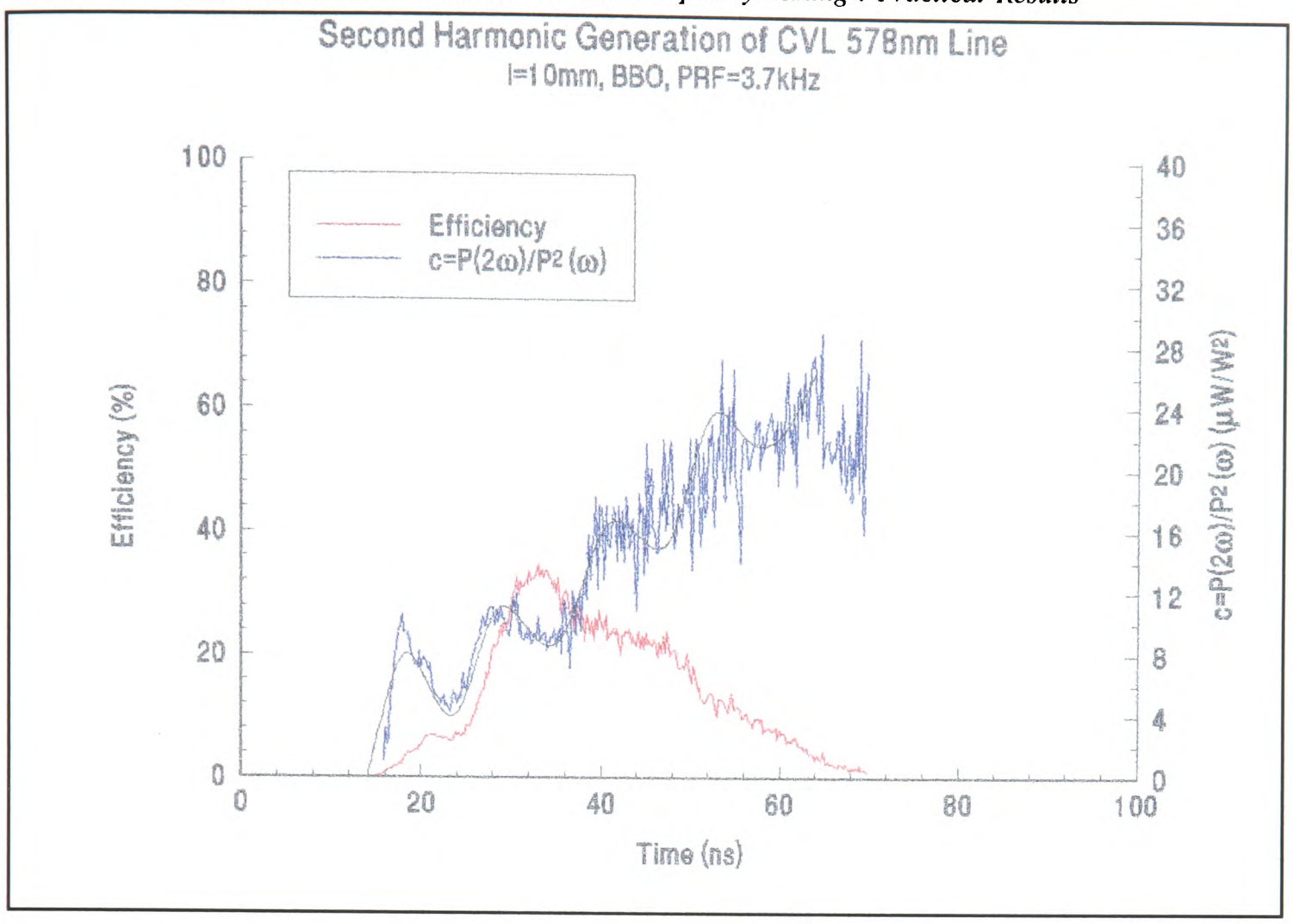


Figure 7.8 : Instantaneous conversion efficiency and SHG conversion coefficient during the 578nm laser pulse. Here the unstable cavity mode evolution is quite marked as step increases in the conversion coefficient with a period of ~10ns (the cavity round trip time).

however, possible for the 578nm line, occurring at $\theta=65°$. Type II SHG of the CVL yellow line was investigated using the $5\times3\times10$mm BBO crystal ($\theta=51°$) orientated at $\sim22.5°$ relative to the incident CVL beam, such that the internal angle of laser beam propagation was 65°. The vertically polarized CVL radiation was rotated through 45° by a suitably orientated multiple-order half wave plate. Thus, with equal horizontal (e-wave) and vertical (o-wave) CVL components arriving at the crystal, the piezo-driven rotary crystal mount was carefully scanned.

Unfortunately, no evidence of any SHG (II) was seen with the available 2W of yellow CVL radiation. A variety of focusing lenses were tried, but at no time was any UV observed. In this case, however, despite greater angular and temperature phase-matching tolerances of the type II geometry, type II SHG was not observed because of the behaviour of the effective nonlinear coefficient. For type II SHG in BBO, the effective nonlinear coefficient may be shown to be :

$$d_{eff}(II) = d_{11}\cos^2\theta\sin 3\phi \ . \qquad (1)$$

Unfortunately, the BBO crystal was cut at $\phi=0^o$ which, whilst maximising d_{eff} for type I SHG, precluded any type II interaction.

LBO

The birefringence of the biaxial crystal LBO is such that phase-matched type II SHG is not possible for either the 511nm or 578nm CVL lines. Also, phase-matched type I SHG is not possible for the 511nm line, but is possible for the CVL 578nm line at crystal orientations close to $\theta=90^o,\phi=69^o$. The dependence of the SHG efficiency upon focusing for the 578 nm radiation was investigated, and the optimum focal length was found to be $f=25$cm, the same as that for SHG in BBO. The UV output power was seen to vary quite markedly in time due to thermal dephasing - on imaging the UV beam onto a piece of card the refractive index changes were clearly seen as intensity fluctuations across the beam profile. The scaling of the harmonic power and efficiency with respect to the fundamental CVL power under optimum focusing conditions ($f=25$cm) was investigated and is displayed in figure 7.9. The best efficiency of 8.2% was limited by the available yellow power of 1.5W. A comparison of SHG in BBO and LBO is made later in this chapter (§7.5).

7.2.3 Elliptical Focusing

As detailed in the previous chapter, when the Gaussian beam SHG theory of Boyd and Kleinman is modified to include elliptical focusing, higher conversion efficiencies are predicted than for conventional spherical focusing. However, no experimental comparison of SHG using elliptical and spherical focusing has previously been reported. In addition to offering improved SHG powers and efficiencies, elliptical geometries may alleviate several problems associated with CVL SHG, namely :-

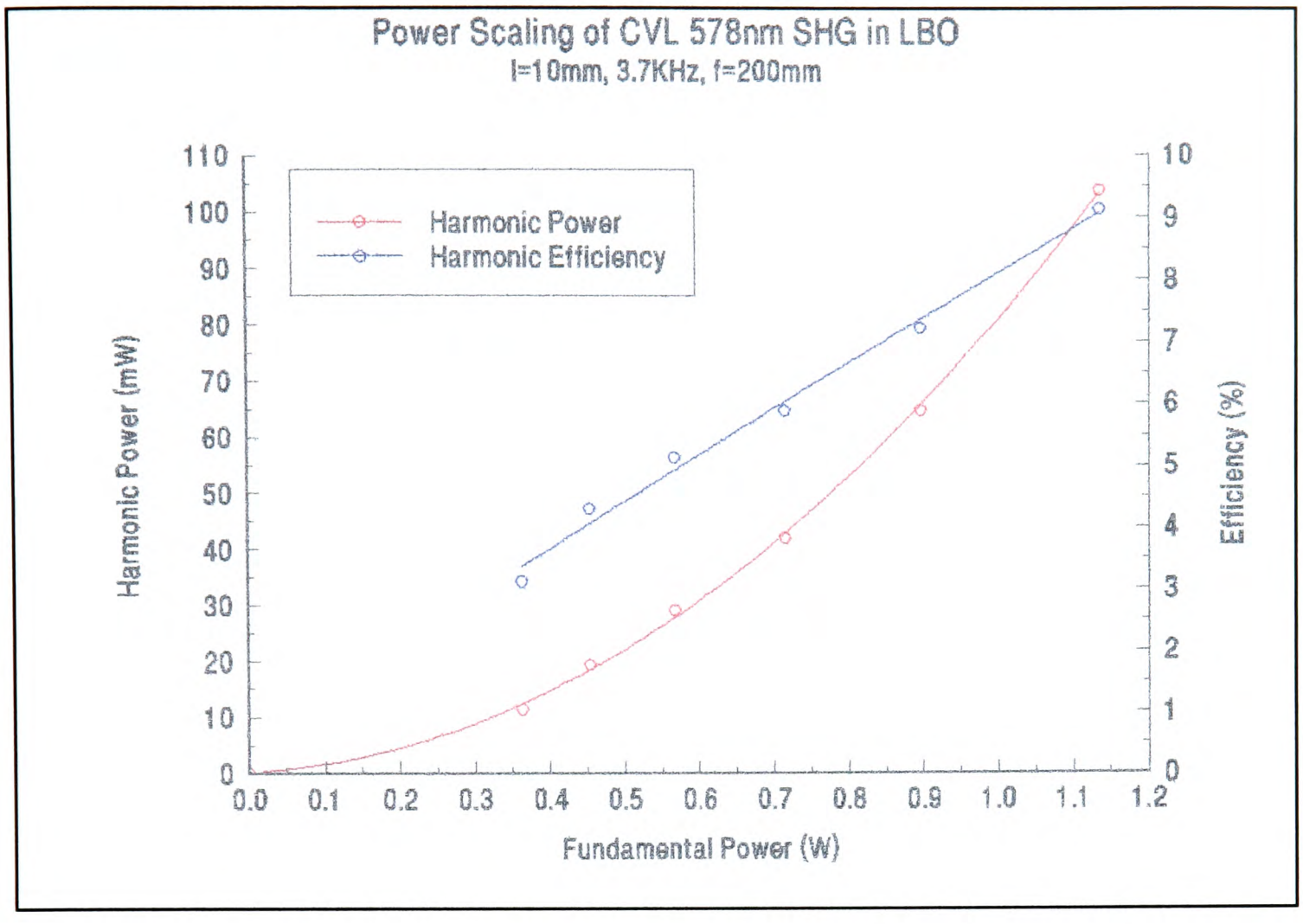


Figure 7.9 : Scaling of the SHG efficiency and power for type I phase-matching in a 10.4mm LBO crystal.

1. Many efficient non-linear crystals such as BBO possess narrow acceptance angles, and so long focal length lens systems must be employed. In order to achieve efficient doubling with such focusing, a good CVL beam quality is required to achieve high focal power densities within the crystal. This, however, leads to correspondingly high power densities at the crystal surfaces, which generally possess a damage threshold ($< 1 GWcm^2$) one order of magnitude below that for bulk damage. Thus, to achieve efficient doubling with the power density well above the threshold for non-linear frequency conversion ($\sim 100 MWcm^{-2}$), there is a danger of causing crystal surface damage. Elliptical focusing has the potential of spreading the energy density over a greater area at the crystal surfaces, so avoiding damage problems.
2. Spherically focused SHG geometries suffer from restricted efficiencies through beam walk-off because of the small transverse dimension of the CVL circular focus. In the case of elliptical focusing, however, the focus is extended in the direction of beam walk-off, and so the effect is greatly reduced.
3. Finally, owing to the high optical power densities, thermal dephasing and detuning

are a problem in sustaining stable UV output powers - again, due to the extended focus, heat conduction out of the irradiated area is improved and thermal dephasing is less of a problem with elliptical focusing.

Additionally, when using highly eccentric elliptical geometries, the focus resembles a line. The peak power density of such one-dimensional line focus is proportional to the divergence of the CVL rather than to the square of the divergence, as in the case of spherical focusing. Thus, potentially greater use of the non-diffraction-limited CVL radiation is made, with both diffraction-limited and $\sim 5\times$diffraction-limited beam components contributing effectively to the SHG process.

In the experiments conducted here, an elliptical focus was produced by the combination of a cylindrical telescope with a spherical focusing lens. The cylindrical telescope is used to expand the CVL beam in the horizontal plane (the direction of beam walk-off in the crystal) and the spherical lens is used to focus the elliptical CVL beam into the crystal. This geometry produces an elliptical beam that approximates the anisotropy of the UV far-field intensity pattern when conventional spherical focusing is used. The optical arrangement is schematically represented in figure 7.10. The collimation of the cylindrical telescope provides the extra degree of freedom in SHG optimization of varying the elipticity of the focus formed in the crystal.

Maximization of the SHG efficiency is achieved by simultaneously optimizing the strength of focusing, focus elipticity, focus position and crystal orientation. Thus, with careful alignment for each focusing lens, elliptical SHG of both CVL lines was investigated using the same detection and calibration procedures as detailed earlier.

The best SHG results were obtained with a CVL elipticity of ~ 2.5 and a $f=200$mm focusing lens. In this case, the scaling of the conversion efficiency and UV power for SHG of the CVL green line were recorded, and are shown in figure 7.11. Despite the reduced CVL power incident at the crystal, owing to reflection losses at the cylindrical telescope, both the efficiency and generated UV power were greater than those achieved with conventional focusing geometries. Also, the SHG power was observed to be more stable than that produced by spherical focusing,

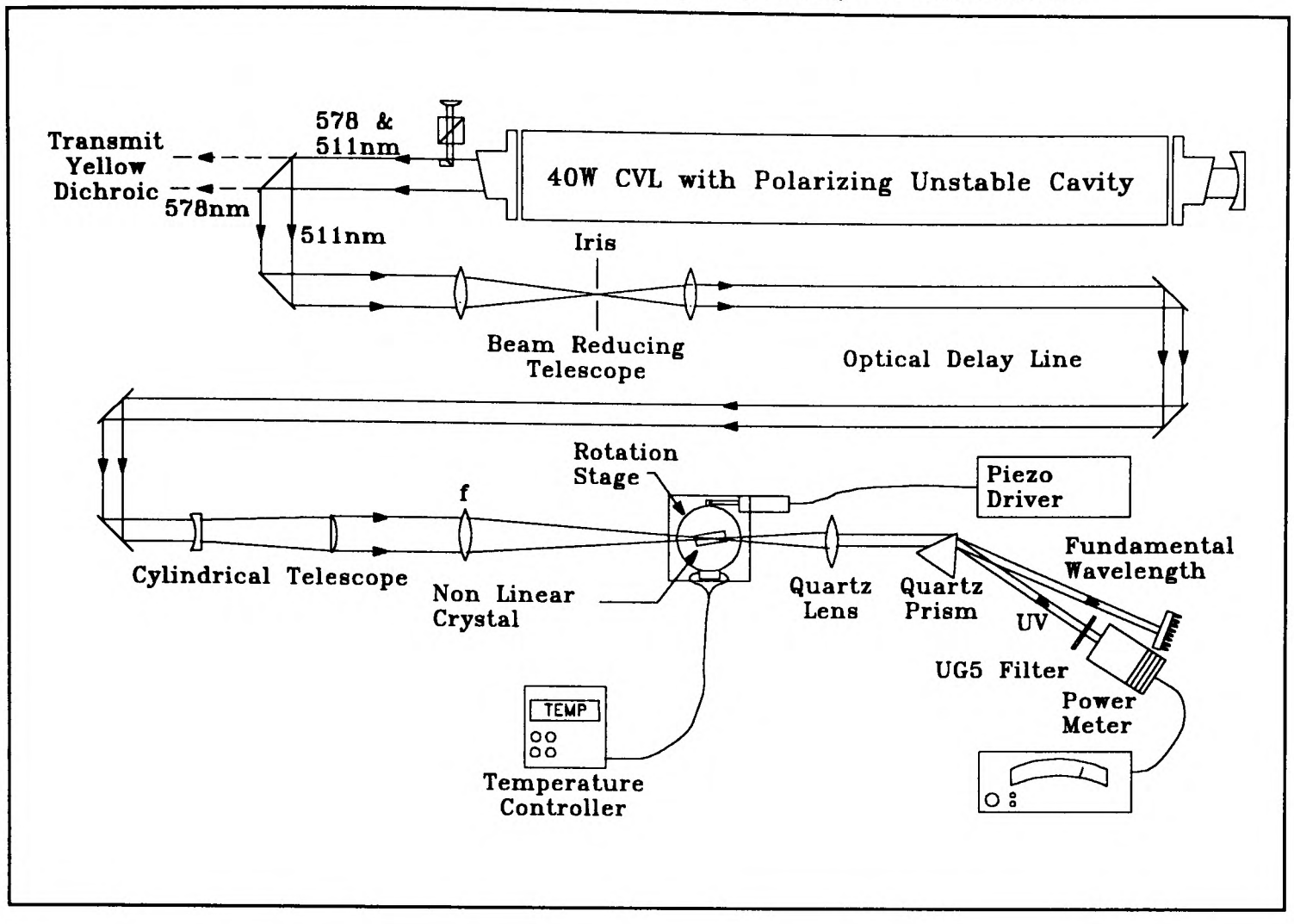


Figure 7.10 : Schematic of the optical arrangement used for type I elliptical SHG of the CVL radiation in BBO.

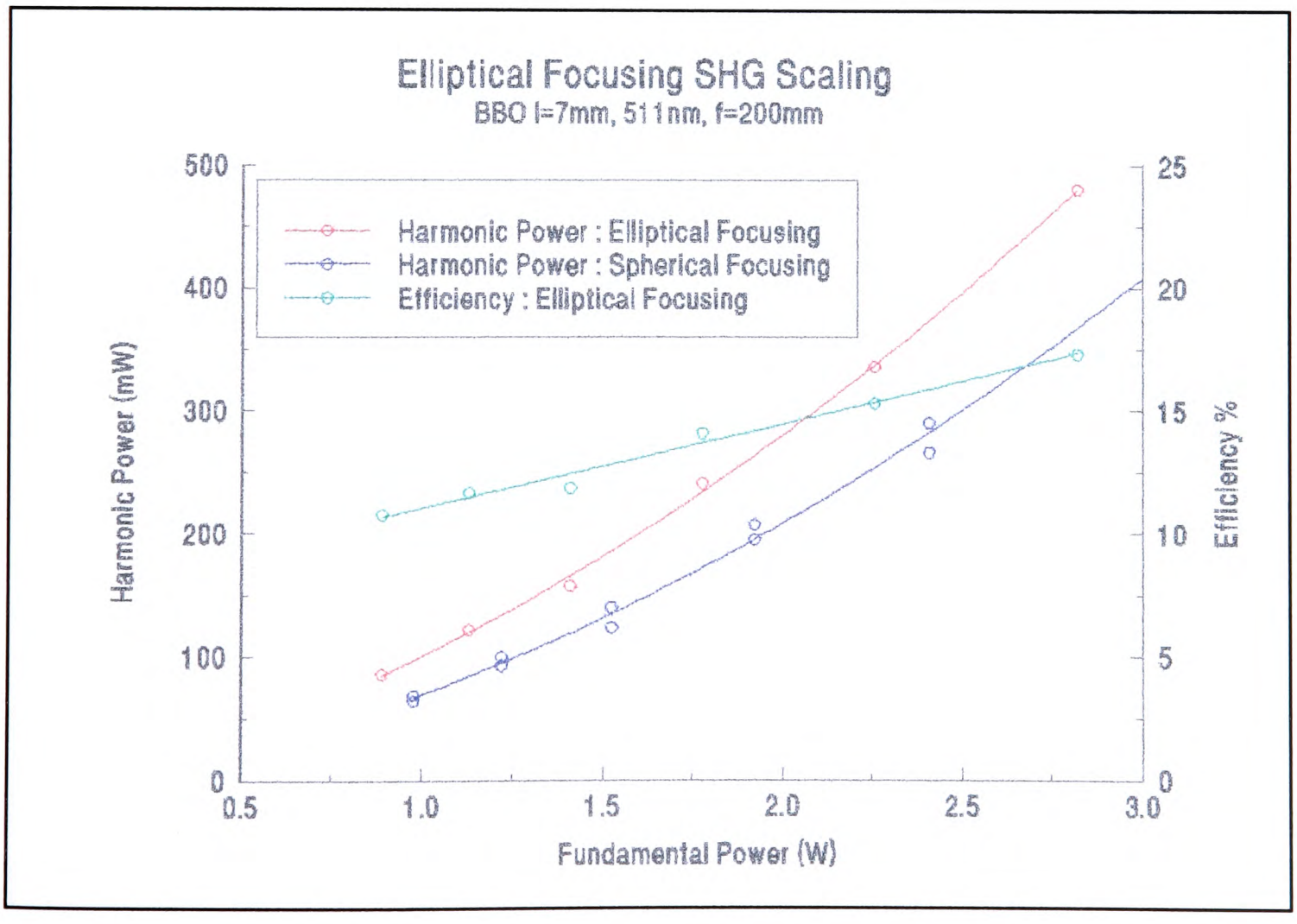


Figure 7.11 : Scaling of the harmonic power and efficiency for the elliptical SHG of the CVL 511nm line in BBO. Also shown for comparison is the harmonic power achieved in the same crystal using spherical focusing.

owing to the reduced thermal dephasing caused by the extended line focus. Thermal dephasing effects were still apparent, however, since the UV power would decrease over a period of several tens of seconds, before further angle-tuning of the crystal was necessary to restore the original power. Eventually, a steady state thermal profile is established in the crystal and a constant UV power is achieved.

The pulse shapes of the CVL green line, depleted CVL green line and UV are shown in figure 7.12, whilst the calculated instantaneous efficiency and conversion coefficient are presented in figure 7.13. The UV power and efficiency at the pulse onset are seen to be considerably greater those for with conventional spherical geometries (figures 7.4 and 7.5). This shows that greater use of the low, but non-diffraction-limited, radiation is made with elliptical focusing. It can also be noted that the peak SHG efficiency generated with the elliptical geometry is somewhat less than with the spherical geometry, owing to the reduced peak fluence of the extended focus. A full comparison between spherical and elliptical focusing and theory is made later

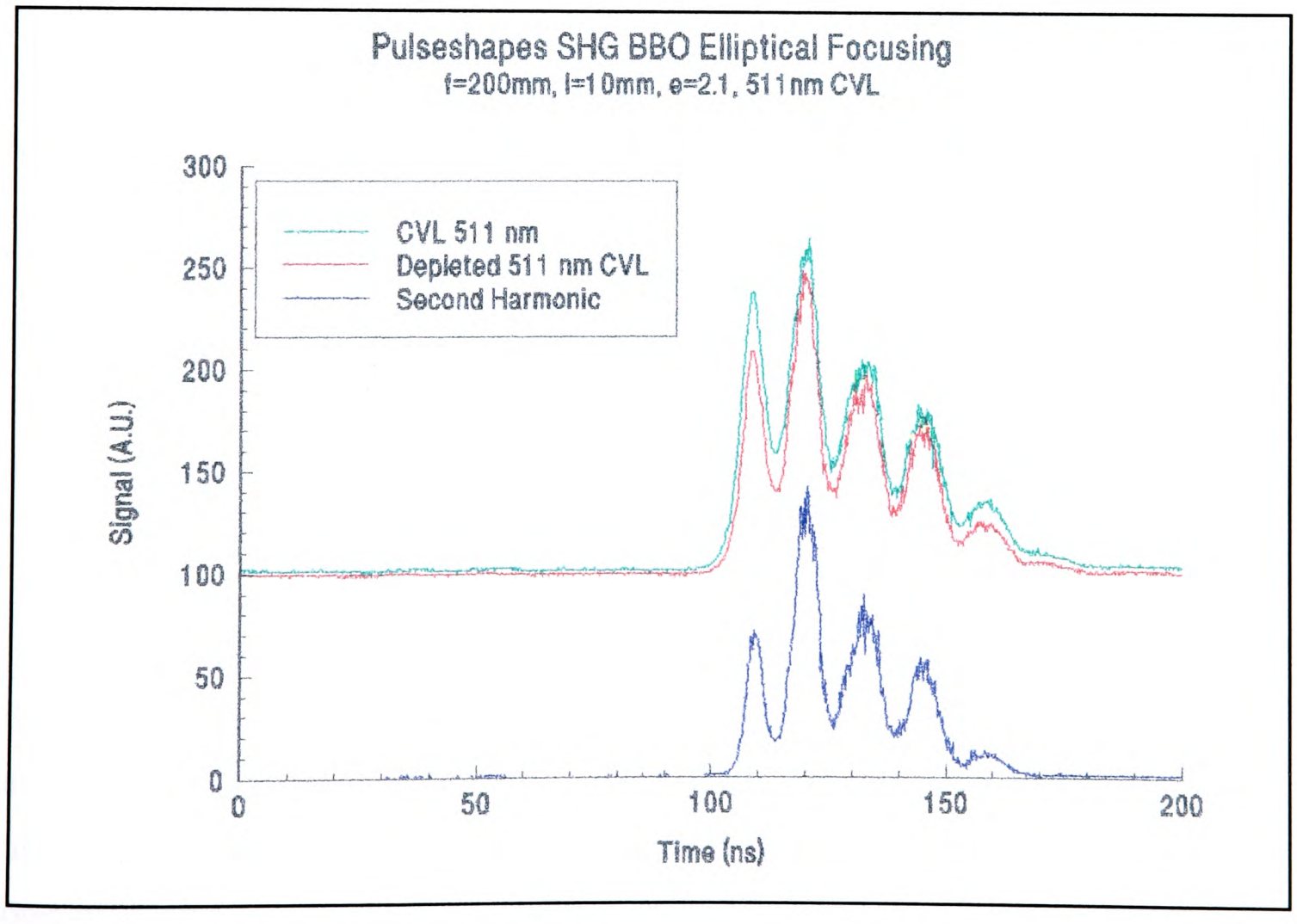


Figure 7.12: Pulseshapes of the CVL, depleted CVL and SH radiation generated using an elliptical focusing geometry in BBO. Note the increased SH power at the pulse onset as compared with spherical focusing.

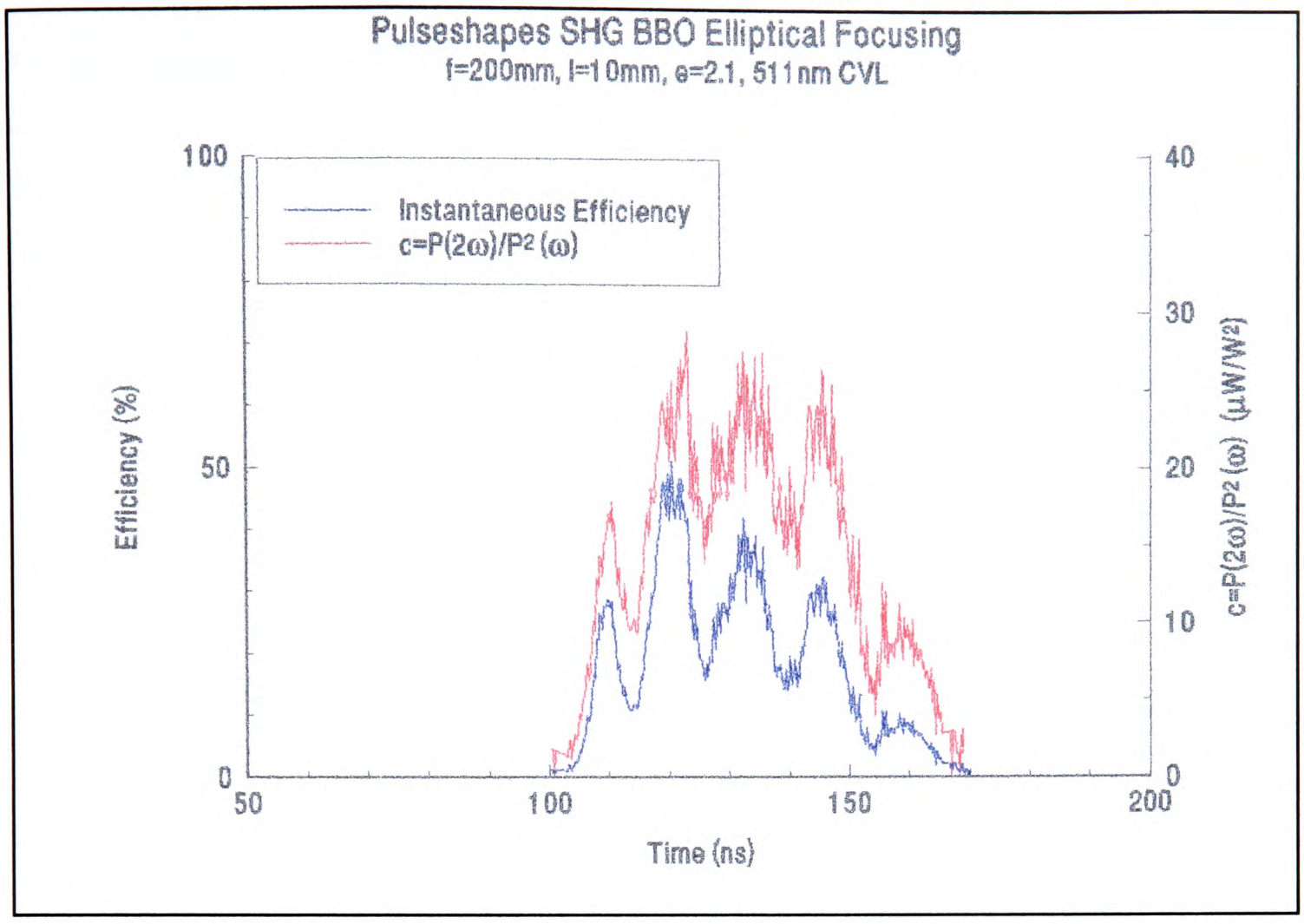


Figure 7.13 : The calculated instantaneous efficiency and conversion coefficient for elliptically focused SHG of the CVL 511nm line using the pulse shapes of figure 7.12.

in this chapter (§7.5).

7.3 SHG of CVL-Pumped Dye Laser Radiation

As detailed in the previous chapter, CVL pumped dye lasers offer narrow bandwidth radiation, typically a few gigahertz, with good beam quality, usually between 1.5-2×diffraction limit, and with good frequency and beam pointing stability. All of these properties combine to give a laser beam "ideally suited" to harmonic conversion in nonlinear crystals.

Since the beam quality of CVL pumped dye lasers is largely independent of the repetition rate of the pump laser, for these investigations, the CVL was operated at 6.5kHz, which gave the greatest average power from the dye laser. The SHG investigations were performed using a modified Lambda Physik FL2001 dye laser operating using a "dye cocktail" of Rhodamine 6G and Rhodamine 640 Perchlorate, designed to give the maximum output power at 616nm. At this wavelength, a comparison of second harmonic generation in LBO, BBO and Lithium Iodate ($LiIO_3$)

was conducted using the same calibration and crystal mounting techniques detailed earlier in this chapter for CVL SHG. The uniaxial lithium iodate crystal measured 10×10×10mm, and was cut at $\theta=68°$ relative to the optic axis, to allow 616 nm phase-matched SHG at normal incidence to its uncoated crystal surfaces. Similarly the 5×3×7mm BBO crystal was cut at $\theta=39°,\phi=0°$ so as to maximise $d_{eff}(I)$, and enable phase-matching at normal incidence to the crystal. The LBO crystal was the same one as used for the CVL SHG investigations, but was rotated such that the dye laser beam made an angle $\theta=58°,\phi=90°$ with the optic axis to satisfy the phase-matching condition.

The experimental configuration is shown in figure 7.14. The output beam from the dye laser was greater than 95% vertically polarized, and so type I phase-matching in all three crystals could be realized by angular changes about a vertical axis. No attempt was made to collimate the dye laser radiation and compensate for the thermal lensing in the dye cuvette - to first order, this does not alter the quality of focus produced in the nonlinear crystal, but merely changes the focus position. The SHG power was critically dependent upon the dye laser beam quality, and, hence, upon the alignment of the dye laser. The best beam quality and SHG power did not correspond to aligning the dye laser for maximum output power. Instead, to achieve the best beam quality, the dye laser was aligned by monitoring the UV, rather than fundamental power. When the dye laser was so aligned for maximum UV power, the fundamental output power coincided with 80-85% of the potential maximum. One of the key factors in generating a good quality dye laser beam was to optimize the oscillator, and to slightly defocus the amplifier, as compared to the set-up for optimum fundamental power extraction.

7.3.1 Results

The variation of the conversion coefficient, $c=P(2\omega)/P^2(\omega)$, for BBO and LBO as a function of the strength of focusing is plotted in figure 7.15. The scatter of the data illustrates the critical dependence of the SH power upon dye laser alignment, focusing alignment, and crystal orientation. Because the fundamental power was rarely constant over the period of investigation, but drifted between 700 and 800mW,

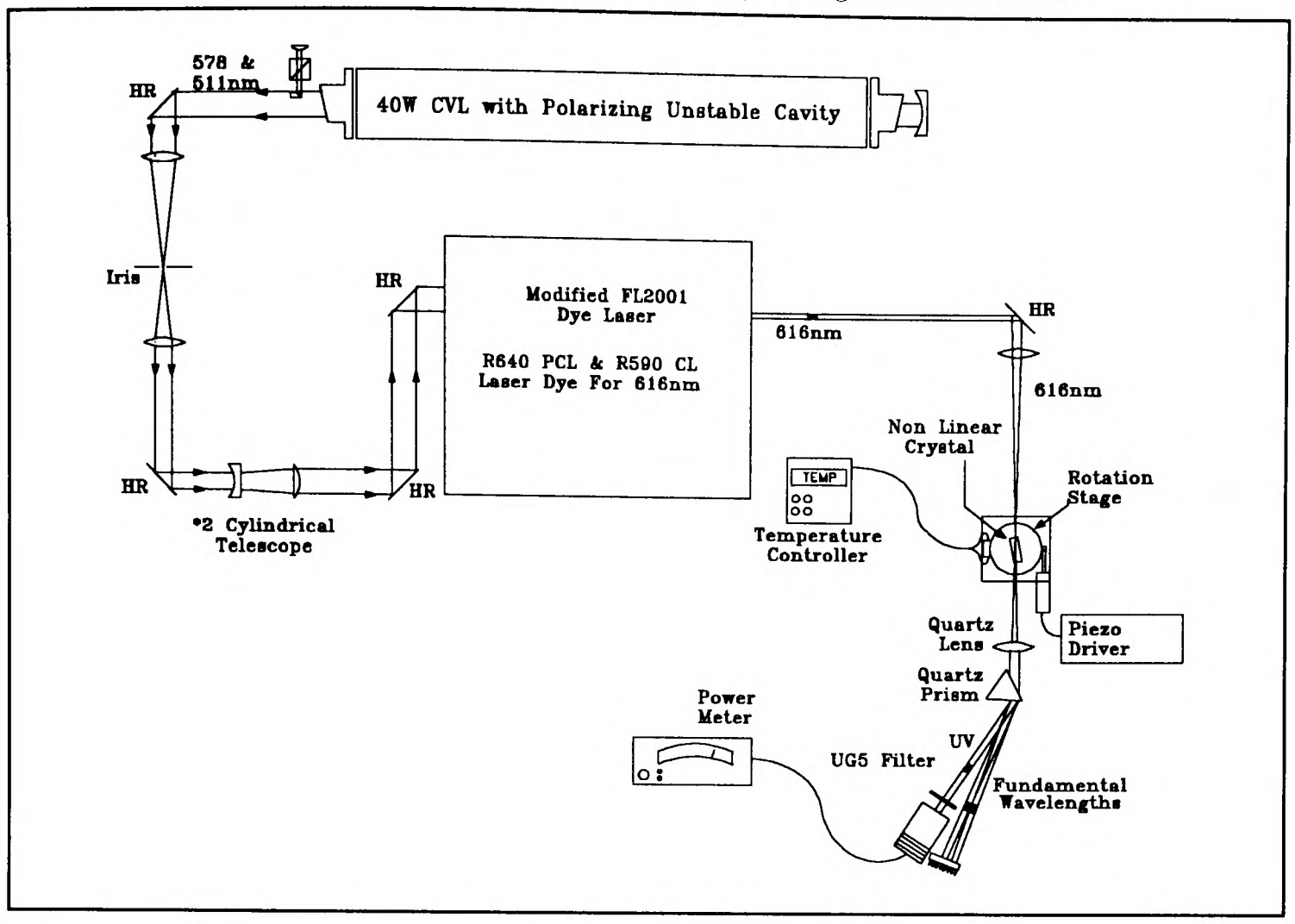


Figure 7.14 : Optical geometry used for the SHG of CVL-pumped dye laser radiation.

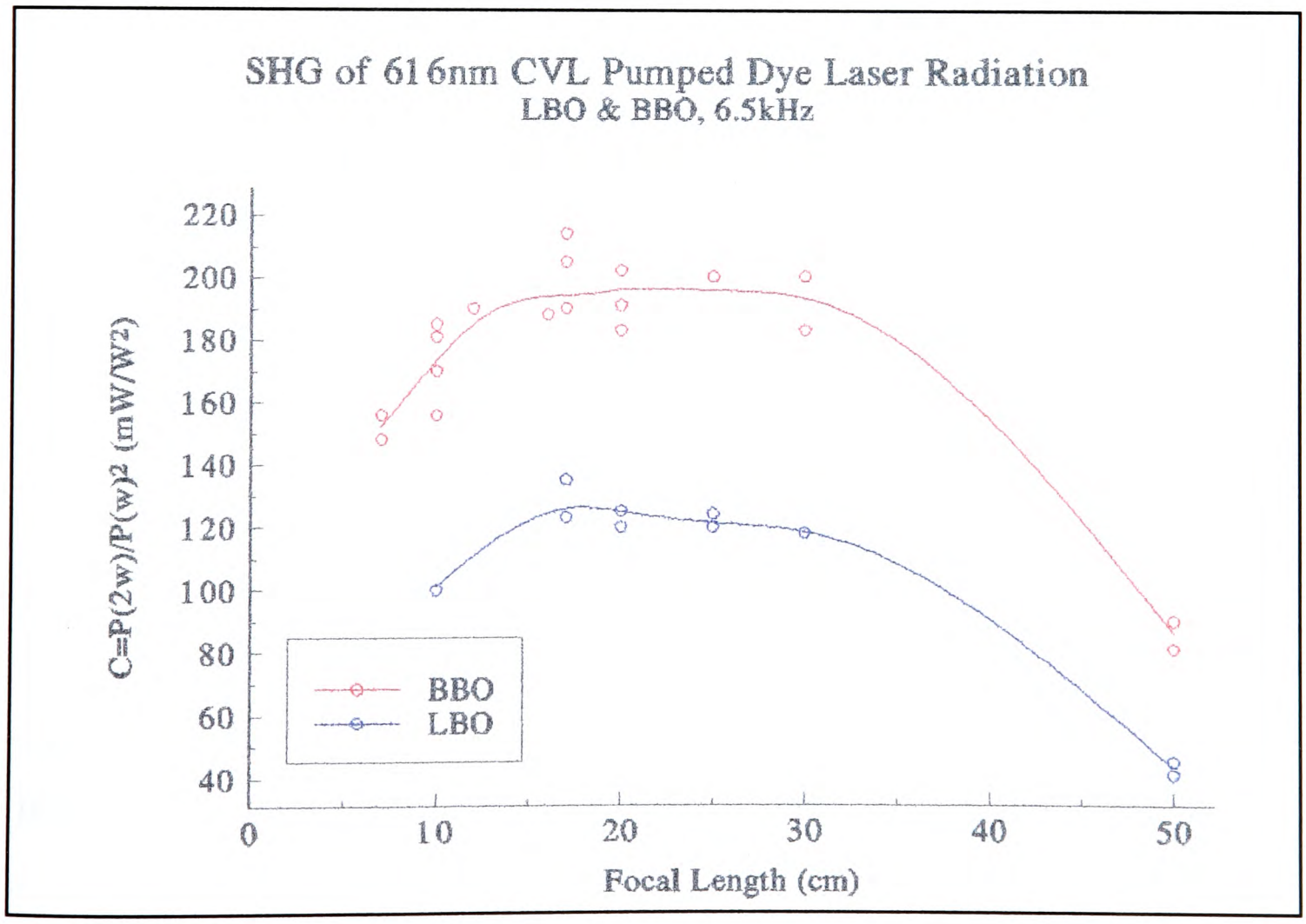


Figure 7.15 : Dependence of the harmonic conversion coefficient upon strength of focusing for LBO and BBO. In both cases a least squares curve fit is used to the data.

the conversion coefficient rather than the harmonic efficiency was used as a measure of the merit of the various focusing geometries. The justification in assuming that the conversion coefficient is a valid measure of the performance of a given strength of focusing will be discussed later. The dependence of the conversion coefficient on the strength of focusing can be seen to be less critical than for the CVL, and near maximum SHG efficiency was achieved over the range $f=15$cm to $f=30$cm. The optimum focusing lens for both LBO and BBO was found to be $f=17$cm, although the comparative insensitivity of the SHG efficiency to focusing enabled investigations with slightly softer focusing than optimum to avoid crystal damage. With lithium iodate, however, the crystal was damaged by all focal geometries stronger than $f=30$cm, and even with softer focusing, the crystal damaged at appreciable power levels.

By using calibrated reflective neutral density filters to attenuate the dye laser beam, the scaling of the harmonic power and efficiency were recorded as a function of the fundamental power under optimum focusing ($f=17$cm) in LBO and BBO. The results are plotted in figure 7.16 and illustrate the quadratic dependence of the second harmonic power on the fundamental. The best efficiency of 12.5% for LBO is limited only by the dye laser power available. Whilst the same limitation of efficiency is true in BBO, the plot of efficiency versus fundamental power shows signs of saturation at efficiencies greater than 20%. No damage was evident in either crystal at the power levels investigated, and the SH power was stable, indicating the absence of any thermal dephasing problems.

In a similar manner, the scaling of the harmonic power and efficiency as a function of fundamental dye laser power were recorded for SHG in lithium iodate, but this time for $f=30$cm and $f=50$cm focusing. The results plotted in figure 7.17 illustrate the superior nonlinear properties of the crystal, as compared with LBO or BBO. Efficiencies approaching 40% were achieved at low powers when using $f=30$cm focusing, and average powers approaching 300mW in the UV were achieved at 35% efficiency with $f=50$cm focusing. However, the crystal is not without its problems. Its damage threshold is relatively low, and limits harmonic generation to dye laser powers less than 350mW in the case of $f=30$cm focusing, and 850mW in

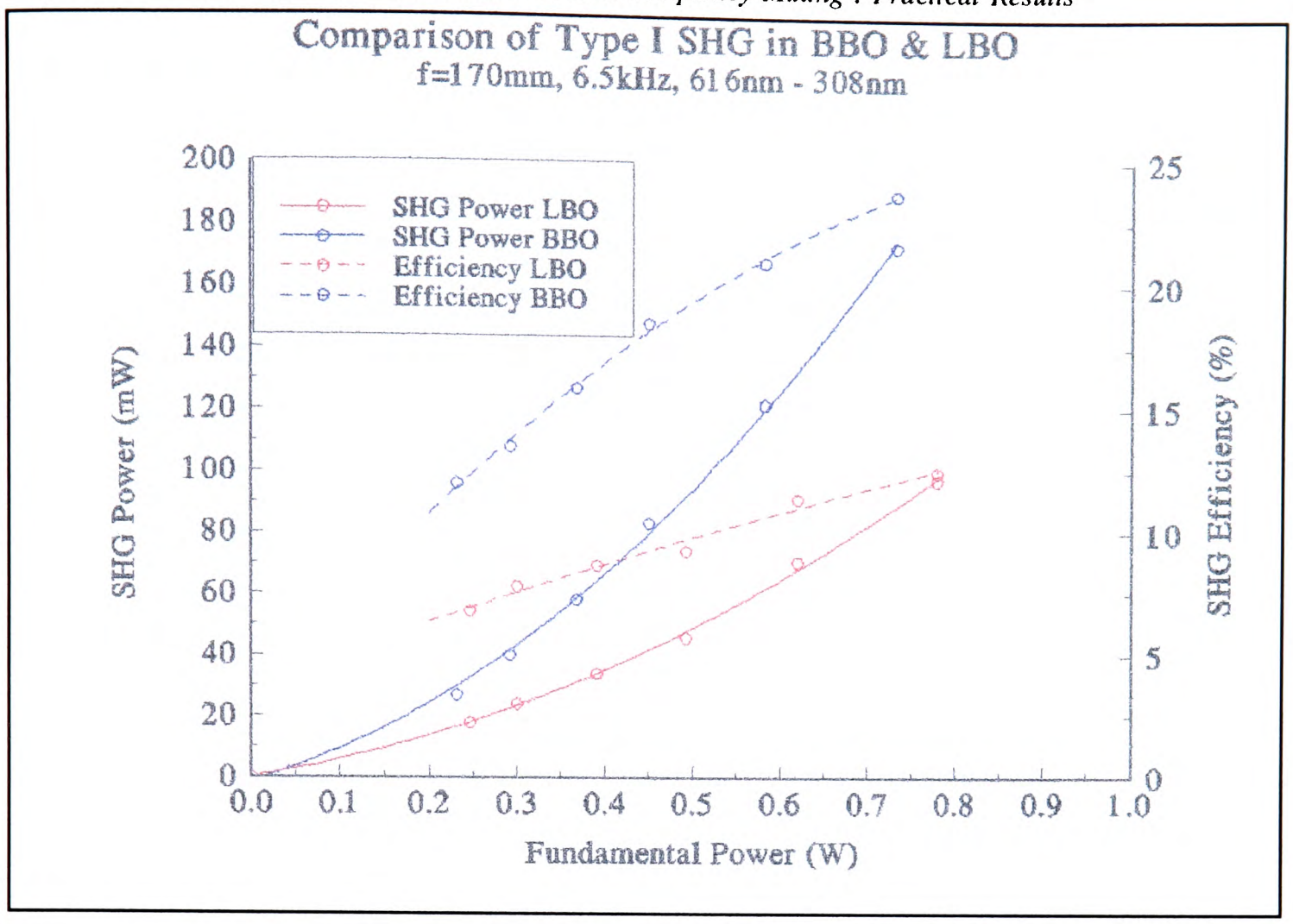


Figure 7.16 : SHG power and efficiency scaling as a function of the fundamental 616nm CVL pumped dye laser radiation in BBO and LBO.

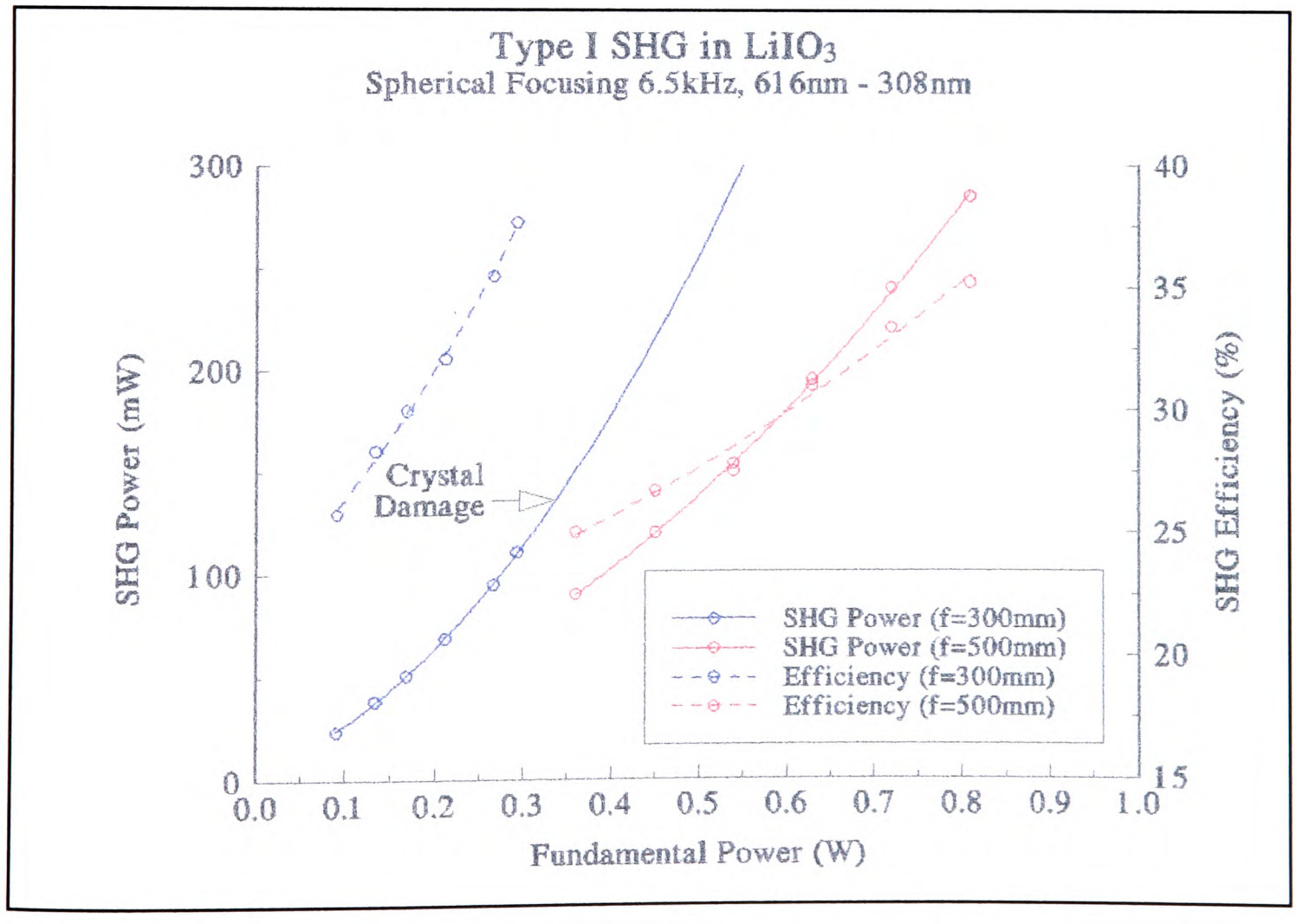


Figure 7.17 : SHG power and efficiency scaling as a function of the fundamental 616nm CVL pumped dye laser radiation in lithium iodate for f=300mm and f=500mm focusing.

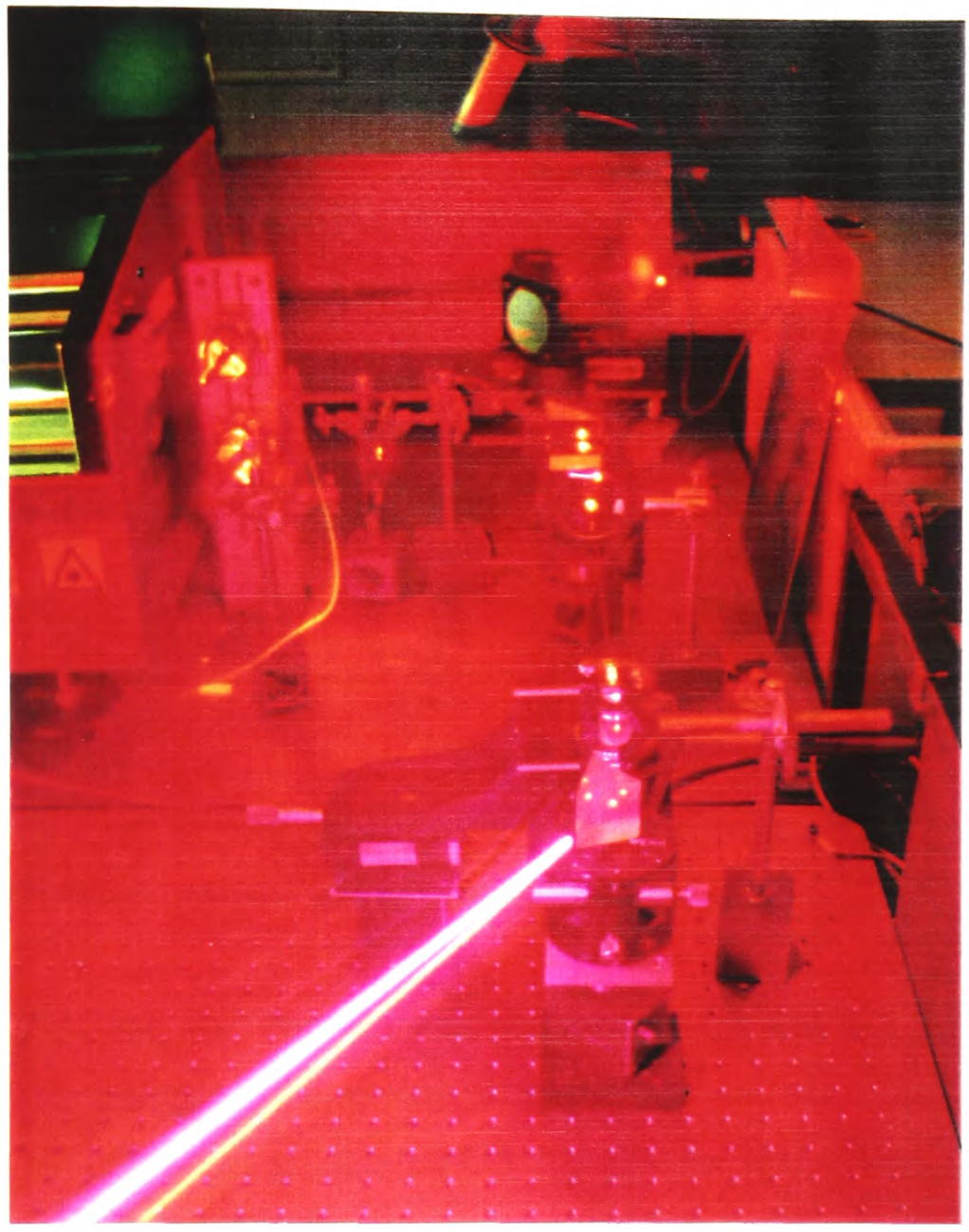


Plate 7.1 : Second harmonic generation with CVL-pumped dye laser 616nm radiation in β-barium borate. Here, the fundamental and second harmonic are dispersed using a 60° prism. The UV can be seen to be very much wider (in the horizontal plane) than the fundamental as a result of the large beam walk-off in BBO.

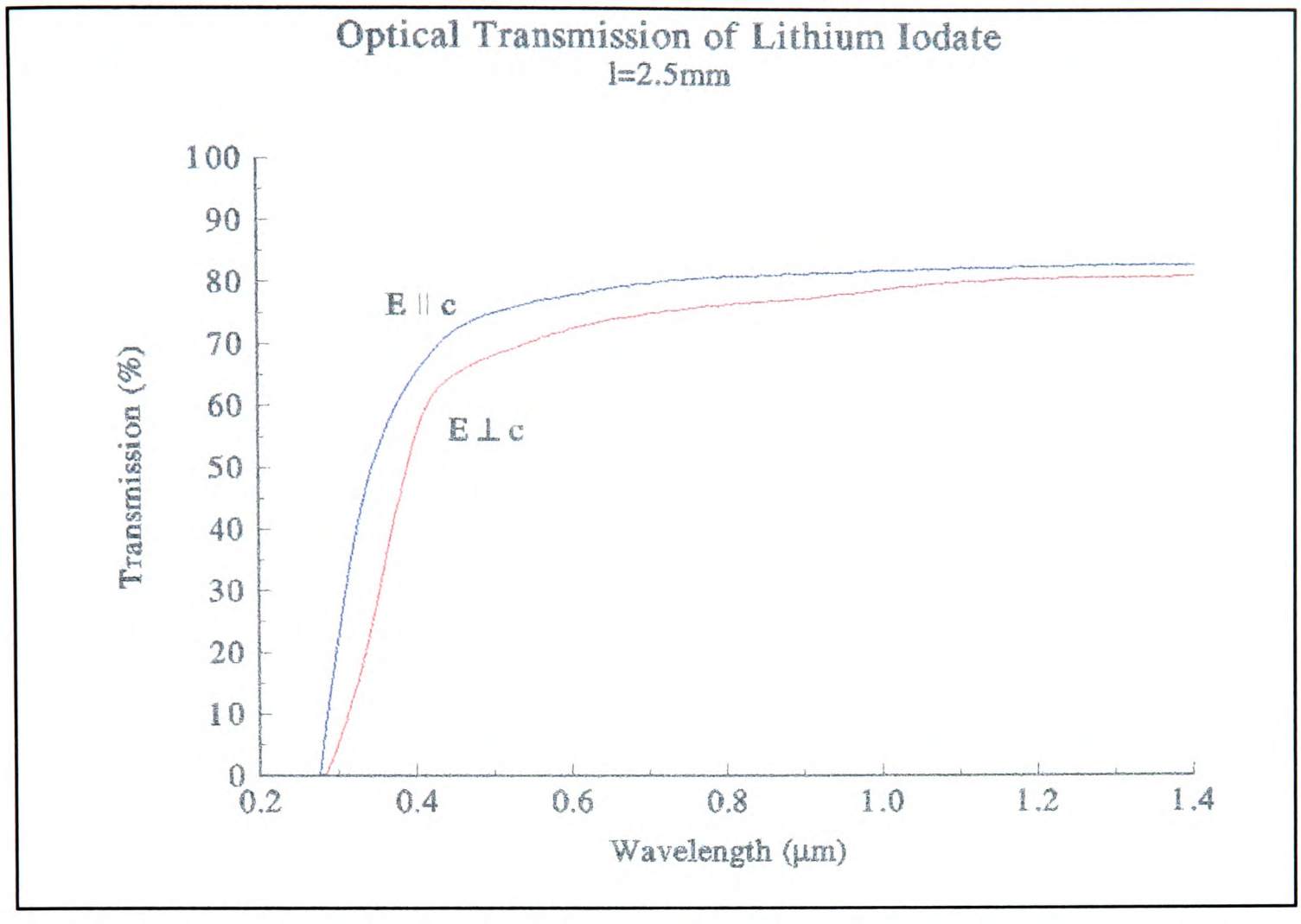


Figure 7.18 : Absorption spectra of lithium iodate. Taken from [7.9].

the case of f=50cm focusing. It was observed that it was not the fundamental radiation which instigated the crystal damage, but the harmonic - the crystal transparency cut-off occurs at 280nm [7.9] and absorbs nearly 15% at 308nm in a 10mm crystal (figure 7.18). Damage to the crystal was seen to occur, not when the fundamental 616nm radiation was incident, but as the crystal was angle tuned into the phase-matching orientation, and the harmonic signal started to grow. This absorption at the harmonic also gave rise to severe thermal dephasing problems, with the output power falling over a period of seconds before crystal reorientation/ repositioning was necessary to restore the harmonic power.

The pulse shapes of the 616nm dye radiation, the depleted dye radiation and the UV were recorded using fast response vacuum photodiodes and are plotted in figure 7.19. As before, from these pulse shapes the instantaneous efficiency and conversion coefficient were calculated, and are shown in figure 7.20. The UV pulse and harmonic efficiency can be seen to be in sympathy with the microstructure of the dye pulse. It is interesting to note, however, that the conversion coefficient is

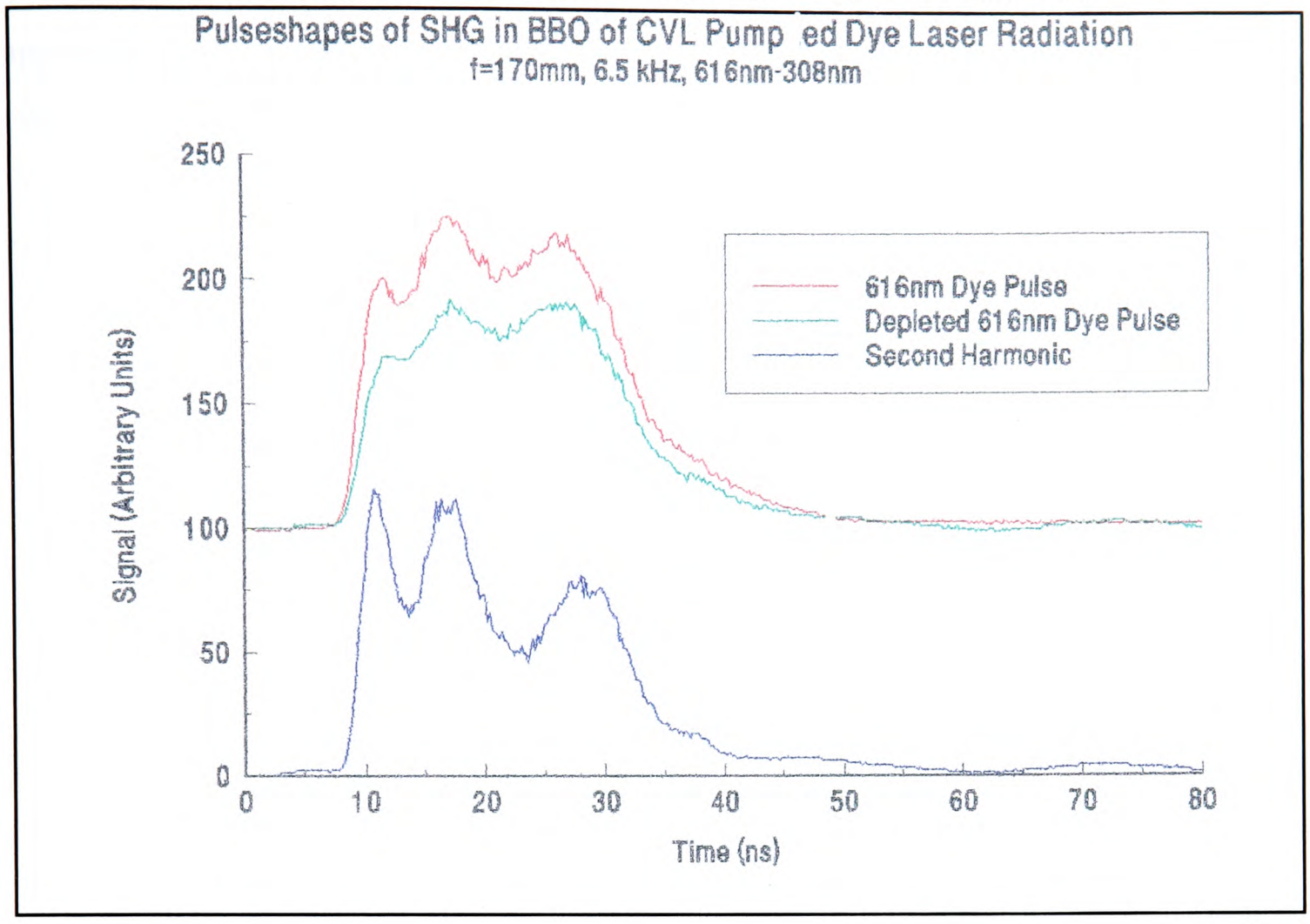


Figure 7.19 : Pulse shapes of the fundamental 616nm radiation, depleted 616nm radiation and 308nm SH radiation.

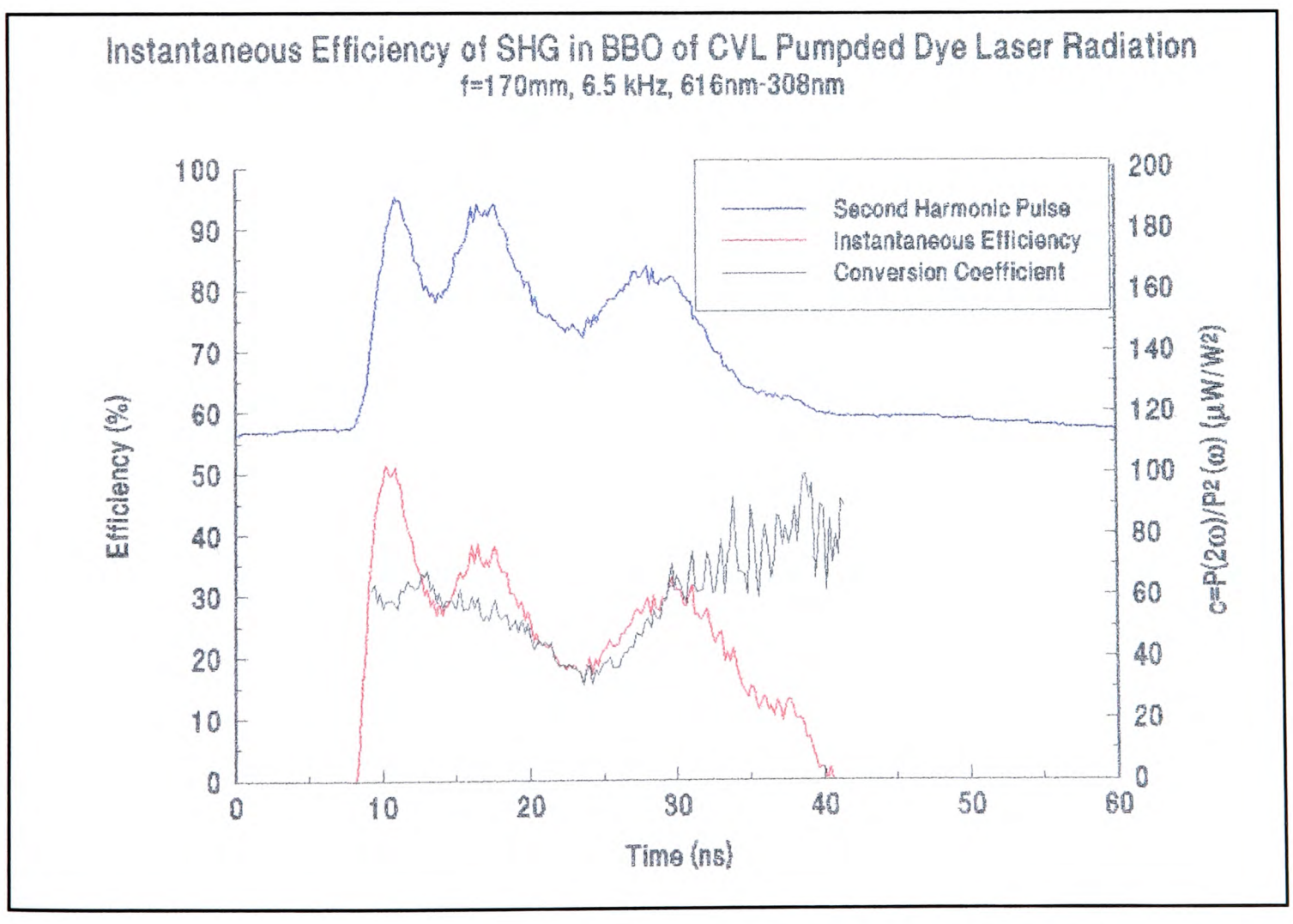


Figure 7.20 : Instantaneous SHG efficiency and conversion coefficient for SHG of 616nm CVL-pumped dye laser radiation in BBO (calculated from the above wave forms).

approximately uniform throughout the pulse, in contrast to the 10ns step variations characteristic of the unstable cavity mode evolution seen when performing SHG with the CVL. This implies that the dye laser beam quality is uniform throughout the duration of the laser pulse, as might intuitively be expected from a short oscillator cavity.

The transformation of the dye laser bandwidth by the second harmonic process was investigated by simultaneously measuring the fundamental and UV spectral profiles. The UV bandwidth was analyzed using an ultra-violet pulsed wavemeter (on loan from Burleigh Instruments), whilst the fundamental bandwidth was measured using a visible wavemeter. The fundamental bandwidth of 8GHz was seen to transform into an UV bandwidth of 16GHz (figure 7.21), indicating a doubling of the bandwidth by the SHG process. This was also found to be the case when an intra-cavity etalon was inserted into the dye oscillator cavity, resulting in a fundamental bandwidth of 3GHz, and a SH bandwidth of 6GHz.

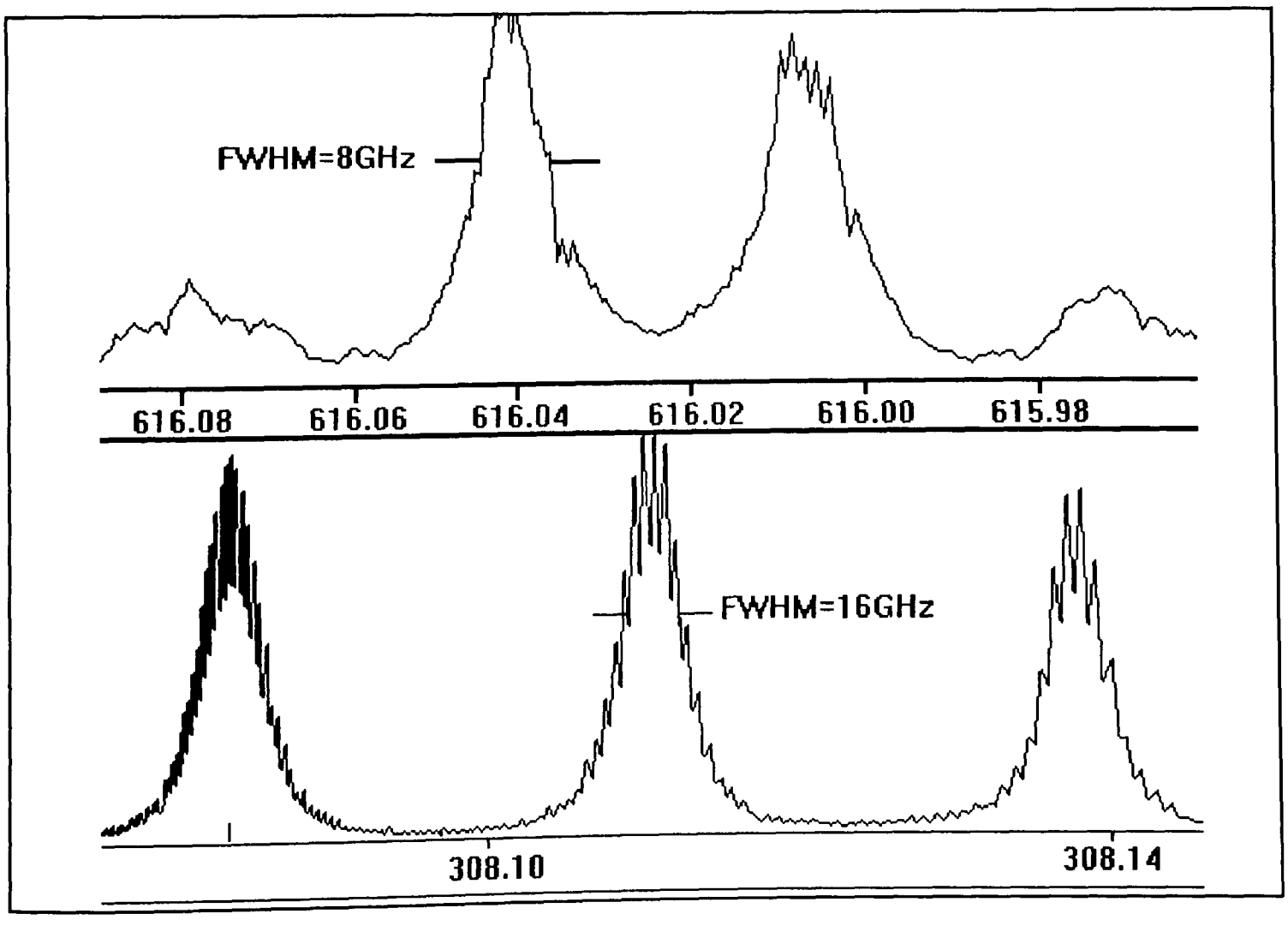


Figure 7.21 : The fundamental dye laser and second harmonic radiation bandwidths measured using visible and UV Burleigh wavemeters.

For both circular and elliptical focusing, the UV beam resulting from second harmonic generation was no longer circular, but approximated a highly eccentric ellipse, or line, reflecting the beam walk-off within the crystal. When used for UV spectroscopy, where a circular beam might be required, the elliptical UV beam can easily be converted to a circular one by using a cylindrical telescope.

7.4 Sum Frequency Mixing The Dye and CVL Radiation.

The process of sum frequency mixing (SFM) is akin to SHG, but now, instead of two fundamental photons of the same frequency "combining" to make one at the second harmonic, two photons of different frequencies (from different laser beams) "combine" to make one at the sum frequency according to :

$$\omega_3 = \omega_1 + \omega_2 , \tag{2}$$

and

$$\underline{k_3} = \underline{k_1} + \underline{k_2} . \tag{3}$$

These equations may be solved in a similar manner to those for phase-matched SHG described in the previous chapter. Thus, using published Sellmier data for BBO, a Mathcad model was created [Appendix A.13] to calculate the sum frequency mixing phase-match curves plotted in figure 7.22; the plot shows the variation of the crystal orientation (to achieve phase-matching) with wavelength when one of the signals to be mixed with is supplied by the CVL. In much the same way as the SHG power is proportional to the fundamental power squared, $P(\omega_1).P(\omega_1)$, (in the low conversion limit), the theoretical SFM power is proportional to $P(\omega_1).P(\omega_2)$. Thus, by mixing the dye laser radiation with the high power available from the CVL, SFM can be seen to have the potential to provide high average power tunable UV radiation.

SFM of the CVL 511nm line with dye laser 616nm radiation was investigated using the experimental arrangement shown in figure 7.23. In this arrangement 20% of the CVL pump beam to the dye laser was split off and combined with the 616nm dye radiation, using a dichroic mirror. The dichroic mirror was transparent to the dye radiation but was highly reflecting at the CVL

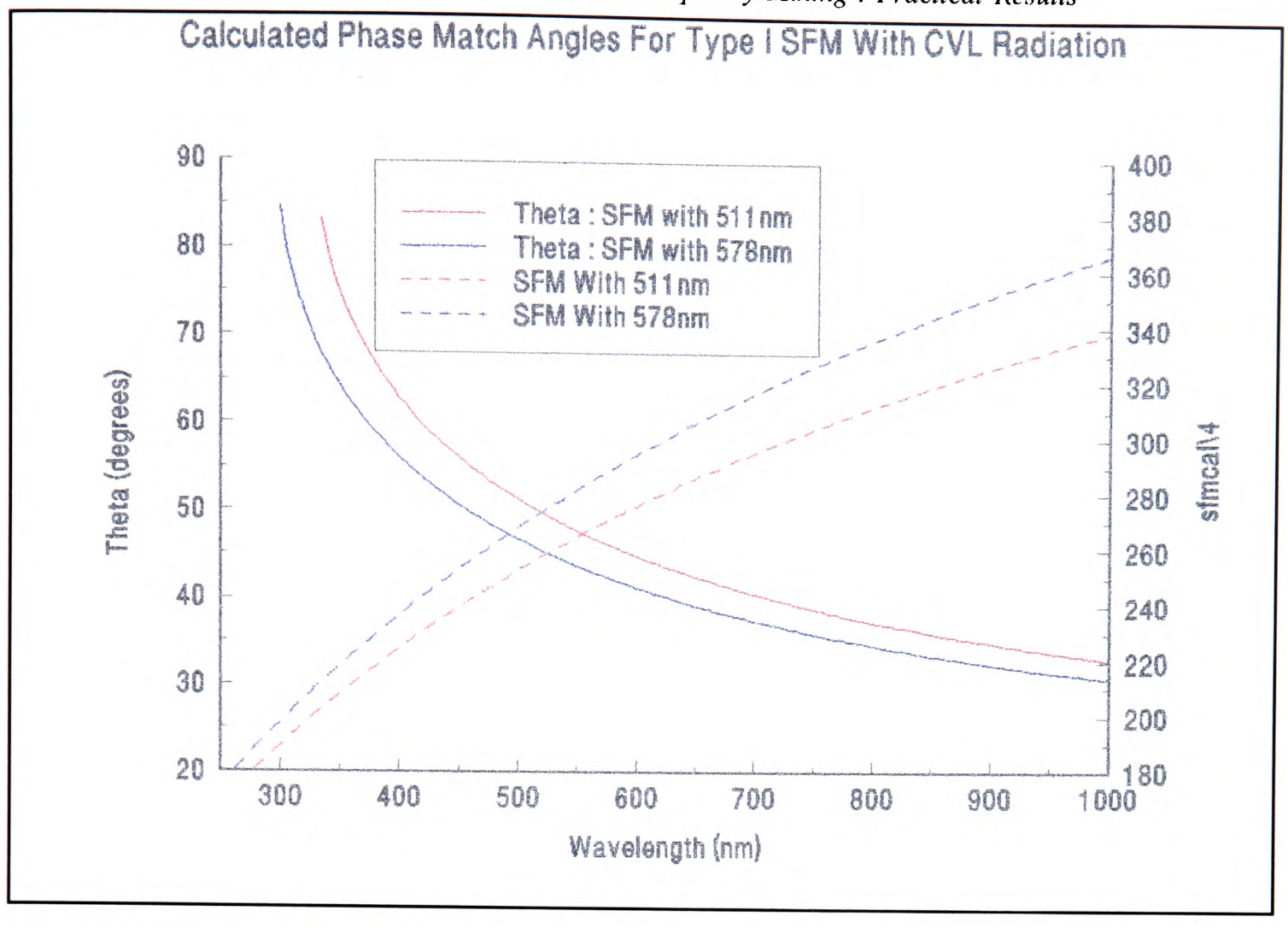


Figure 7.22 : Calculated phase-matching angles for type I SFM of the CVL 511nm radiation in BBO as a function of wavelength.

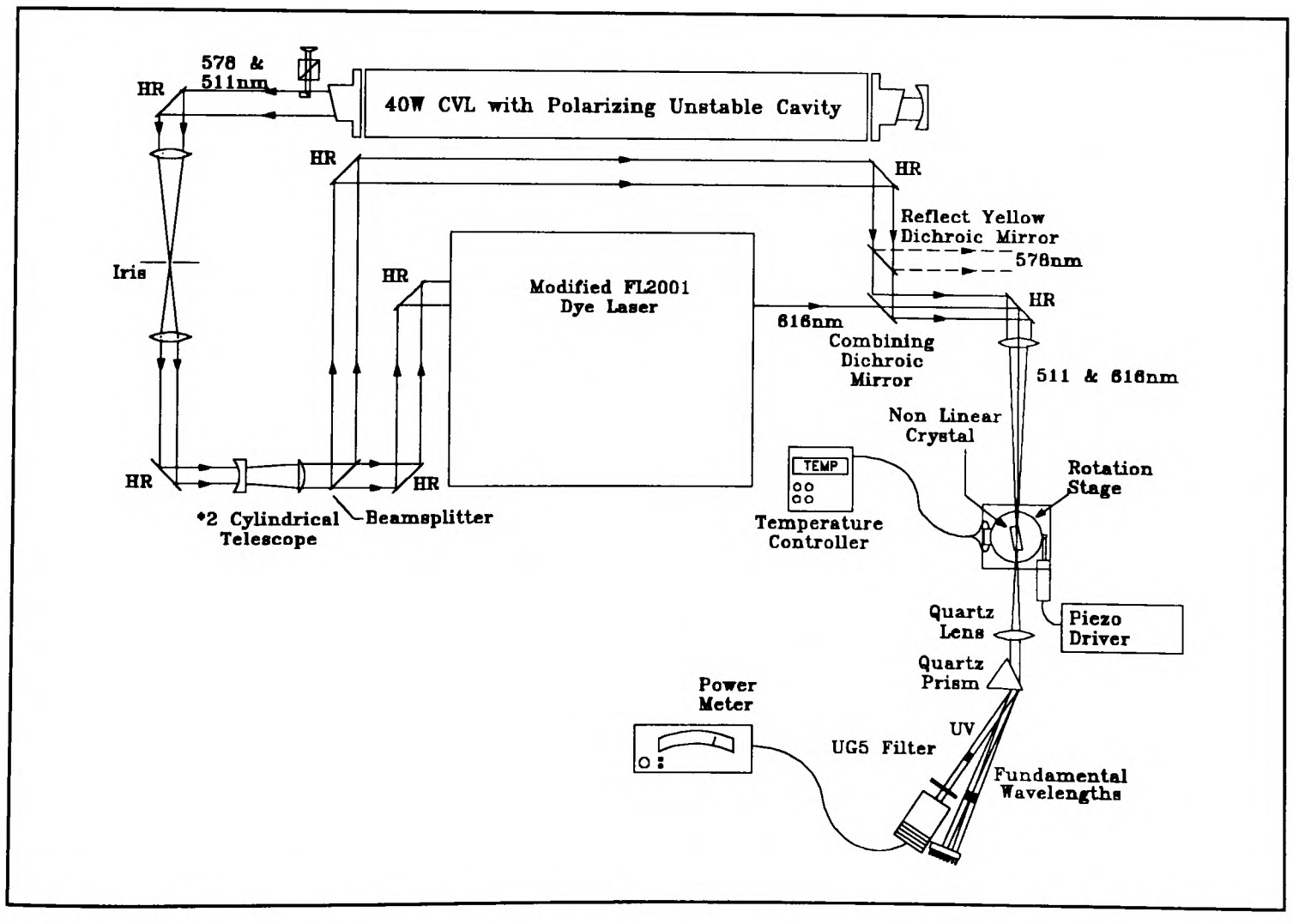


Figure 7.23 : Experimental configuration used for the SFM of CVL 511nm radiation with 616nm radiation from a CVL pumped dye laser.

wavelengths, and allowed the combination of the dye laser and CVL beams with any polarization orientation. The laser beams were carefully aligned so that they overlapped and were collinear with each other. The polarizations of both laser beams were arranged to be vertical, and were focused into the nonlinear crystal using an achromatic lens, in an effort to ensure that the foci were coincident in the type I SFM geometry. A number of problems were encountered :-

1. Firstly, because of the thermal lensing in the dye laser, the 616nm radiation does not focus at the same position as the CVL light, even though achromatic focusing is used. This was overcome by inserting a $f=1$m lens into the dye laser beam and adjusting its position until the dye and CVL foci were coincident.

2. The second major problem is one of synchronization. The dye and CVL pulses do not arrive at the nonlinear crystal at the same time because of the build-up time associated with the dye laser. This was overcome by building a suitable optical delay line into the CVL beam path to the nonlinear crystal such that the 25ns dye laser pulse overlapped with the latter half of the CVL pulse (corresponding to the better quality, low divergence light).

Once these problems had been overcome, the BBO crystal was rotated carefully about the vertical axis. UV was seen to be generated at three separate crystal orientations; two of these orientations coincide with SHG of the 616nm and 511nm laser beams respectively, whilst the third orientation results from SFM. SFM could be verified by blocking either one of the 616/511nm laser beams, which extinguished the UV. The power of the SFM radiation was, however, rather disappointing and was critical not only upon the crystal position and orientation, but also on the overlap of the laser beams at the focus position within the crystal. A number of different focusing geometries were tried and $f=20$cm focusing was found to produce the best output of 25mW when 300mW of 616nm radiation and 1W of CVL 511nm power were incident at the crystal. The pulse shapes of the CVL and dye radiation at the crystal were recorded together with the SFM output, and are displayed in figure 7.24. Despite vigorous efforts, SFM at high efficiencies was not achieved; it is thought that the disappointing efficiencies achieved are due to the poor

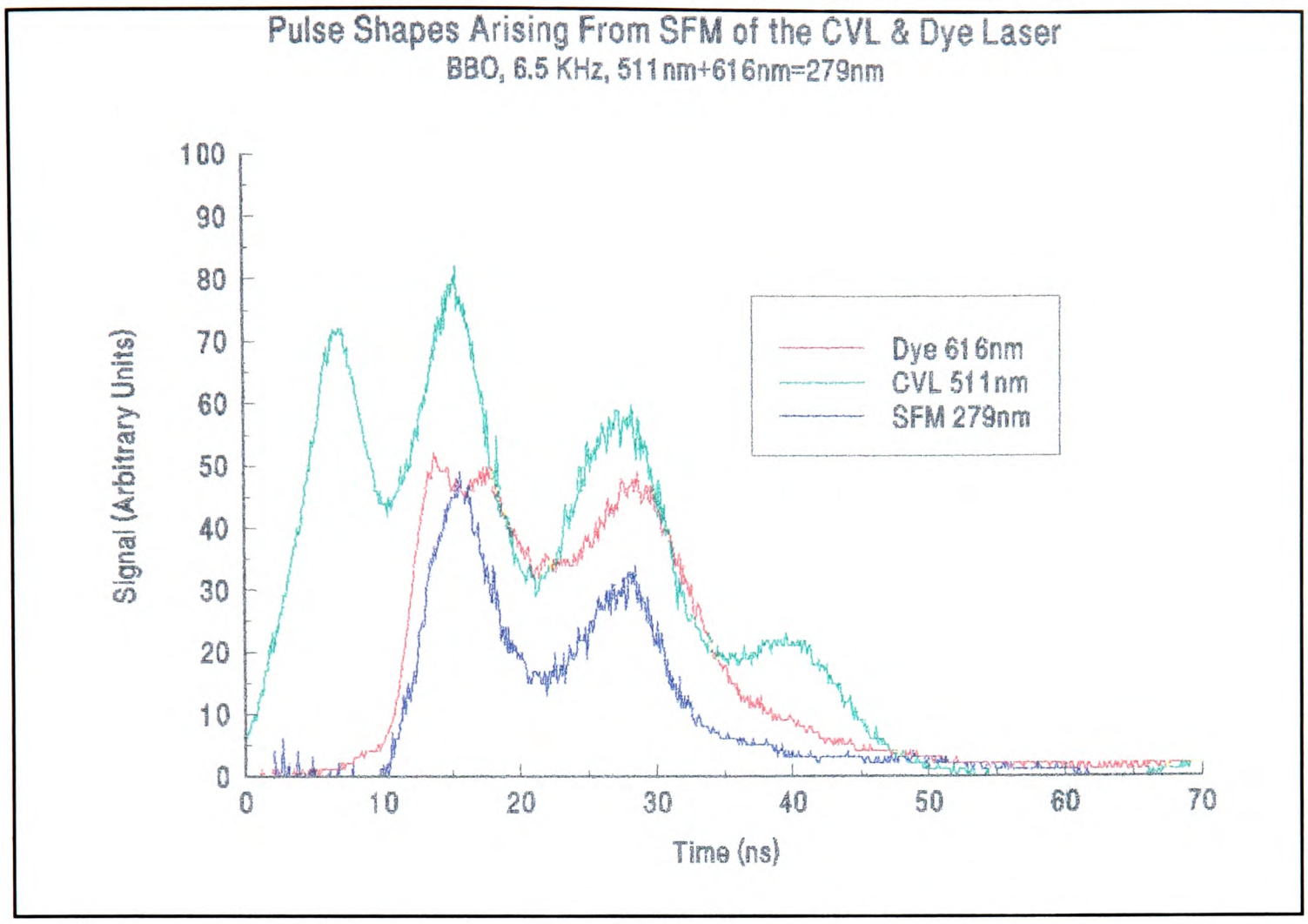


Figure 7.24 : Pulse shapes of the CVL 511nm, 616nm dye radiation, and the resulting SFM radiation at 279nm.

temporal overlap between the CVL and dye laser pulses, and the critical alignment sensitivity of the SFM process. Also, the beam pointing instability of the CVL relative to the dye laser limits focus overlap in the crystal and has the effect of restricting the SFM efficiency.

7.5 Comparison With Theory

At the elevated SHG powers and efficiencies reported in this chapter, significant depletion of the fundamental beam occurs, which is contrary to the assumptions of the SHG models presented in the previous chapter. A rigorous evaluation of the reduction in harmonic power at elevated powers presents a complex problem. However, in the case of harmonic generation with plane waves, the coupled polarization equations 5.27 and 5.28 may be solved by invoking energy conservation such that $E^2(\omega)+E^2(2\omega)=E_{inc}^2$, where E_{inc} is the incident electric field at $z=0$. The solution for perfect phase-matching is the well known result :

$$\frac{I(2\omega)}{I(\omega)} = \tanh^2(\kappa E_{inc} z) , \tag{4}$$

where

$$\kappa^2 |E(\omega)|^2 l^2 = \frac{2\omega^2 |d_{eff}|^2 l^2 I(\omega)}{n^3 c^3 \epsilon_0} , \tag{5}$$

and the symbols have their usual meanings. By expanding the *tanh*^{2} function, and with a little algebraic manipulation, it can be shown that the initial departure of the harmonic conversion coefficient from its low power limit is given by :

$$\frac{I(2\omega)}{I(\omega)^2} = \frac{I(2\omega)}{I(\omega)^2}\bigg|_0 \left(1 - \frac{2}{3}\frac{I(2\omega)}{I(\omega)^2}\bigg|_0 I(\omega)\right) . \tag{6}$$

Thus, the harmonic conversion coefficient is expected to decrease linearly with increasing fundamental intensities; however, by the same token, if the conversion coefficients for the present results are extrapolated back to I(ω)=0, then the SHG theories of chapter 5 can be tested.

7.5.1 CVL SHG : Comparison With Theory

The conversion coefficients for CVL SHG, under optimum spherical and elliptical focusing conditions, can be calculated from figures 7.3, 7.6, 7.9 and 7.11 to give the plots shown in figures 7.25 and 7.26. As shown in chapter 5, the Boyd and Kleinman theory predicts the harmonic conversion coefficients for type I SHG of the CVL to be 56μW/W^2, 54μW/W^2 and 47μW/W^2 for the 511nm and 578nm lines in BBO, and 578nm line in LBO respectively. At 3.7kHz, the CVL pulse length is 50ns, and so the laser has a duty cycle of $\sim$0.0002, whereupon the peak power will be some 5400 times the mean power. Thus, assuming the CVL pulse has a rectangular temporal profile, the expected average power harmonic conversion coefficients are transformed to 300mW/W^2, 290mW/W^2 and 252mW/W^2 respectively. From figure 7.25 the conversion coefficients for 511nm and 578nm in BBO can be seen to be 93W/W^2 and 126W/W^2 whilst the conversion coefficient of the 578nm line in LBO

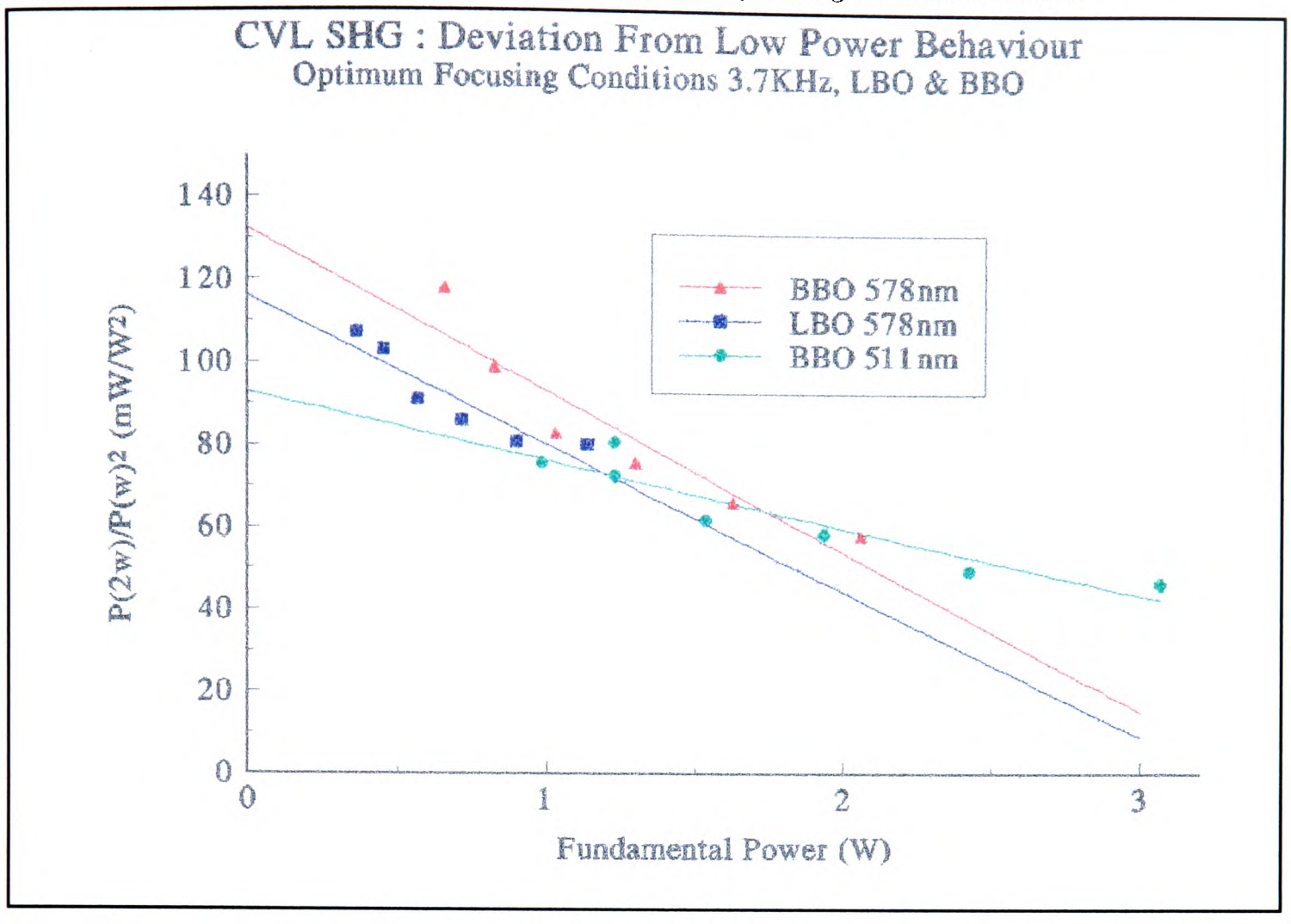


Figure 7. 25 : Extrapolation of the conversion coefficients back to zero intensity for optimally focused type I SHG of the CVL wavelengths in BBO and LBO using spherical focusing.

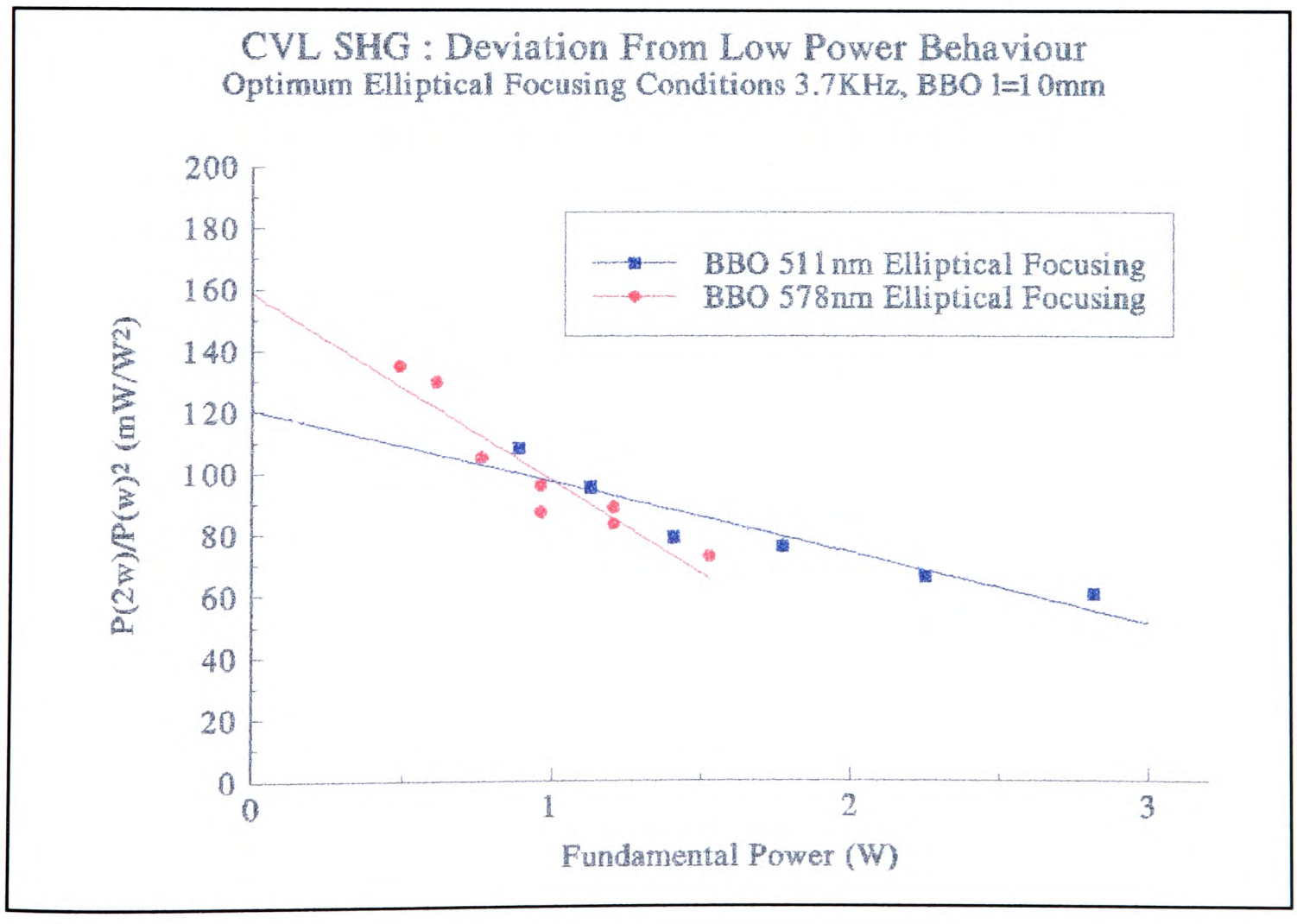


Figure 7. 26 : Extrapolation of the conversion coefficients back to zero intensity for optimally focused type I SHG of the CVL wavelengths in BBO using elliptical focusing.

can be seen to be $117W/W^2$. Not only are the conversion coefficients considerably smaller than those predicted by theory, but SHG of the yellow line in BBO can be seen to have the greatest conversion coefficient, whilst SHG in BBO of the green line has the lowest conversion coefficient, in contradiction to theory.

BBO possesses a large walk-off angle, and the corresponding Boyd and Kleinman *B* parameter is about 14 for a 10mm crystal. According to the elliptical focusing theory of Freegarde, by using an optimally focused elliptical beam with a high *B* crystal such as BBO, the SHG power may be increased by up to 30% over that offered by conventional focusing geometries. Indeed, by comparing the SHG conversion coefficients resulting from spherically and elliptically focused CVL laser beams in figures 7.25 and 7.26, it can be seen that, for the 511nm line, $c=93mW/W^2$ for spherical focusing and $c=120mW/W^2$ for elliptical focusing. Similarly, for elliptical SHG with the 578nm line, $c=159mW$, as compared to $126mW/W^2$ for conventional focusing. Whilst the experimentally achieved elliptical conversion coefficients are less than those theoretically predicted ($390mW/W^2$ for the green and $377mW/W^2$ for the yellow), the 25-30% improvement in the conversion coefficients as compared with the results obtained using spherical focusing is in agreement with Freegarde's theory.

The Boyd and Kleinman theory also predicts an optimum strength of focusing through the parameter $\xi(B)=l/b$, where l is the crystal length, and b is the confocal parameter of the laser beam *inside* the crystal. A Gaussian beam with a waist w_1, a distance $d_1=f$, away from a lens of focal length f, is focused to a new beam waist w_2 , in the focal plane of the lens, where :

$$w_2 = \frac{\lambda . f}{\pi . w_1} \quad . \tag{7}$$

Under these focusing conditions, the optimum focal length, f_{opt}, predicted by the Boyd and Kleinman theory may be shown to be :

$$f_{opt} = \left(\frac{l k_1 w_1^2}{4 n_1 \xi_m} \right)^{\frac{1}{2}} , \tag{8}$$

where w_1 is the CVL beam waist, n_1 is the refractive index of the nonlinear crystal at the fundamental wavelength, and ξ_m is the optimum focusing parameter predicted by the Boyd and Kleinman theory. In the case of CVL SHG, the optimum focusing parameters for the 511nm and 578nm lines in BBO, and 578nm line in LBO, are 1.4,1.4 and 1.6 respectively. The corresponding optimum focal length lenses for a 10mm CVL beam are $f=$ 57cm, 54cm and 52cm respectively. From the experimental investigations, the optimum focal length lenses have been found to be $f=25\pm3$cm irrespective of the CVL wavelength or crystal; also, the variation of SHG power with strength of focusing can be seen to be quite rapid - again in contrast to that suggested by the Boyd and Kleinman theory.

The results of the theoretical predictions and experimental observations are summarized in table 7.1.

Table 7.1

	θ_m	ρ	B	h_m	ξ_m	d_{eff} pmV	c_{theory} mW/W^2	f_{theory} cm	c_{expt} mW/W^2	f_{expt} cm
BBO 511nm	50.5	4.1	10.5	0.068	1.4	1.1	**300**	**57**	**93**	**25**
BBO 578nm	42	4.2	10.1	0.071	1.4	1.3	**290**	**54**	**126**	**25**
LBO 578nm	69	0.7	1.9	0.37	1.6	0.4	**251**	**52**	**117**	**25**

The errors associated with the experimental results may be estimated to be 10%, reflecting the sensitivity of the SHG process to fine alignment.

It is not entirely surprising that the achieved conversion coefficients fall rather short of those predicted by theory, since the CVL is only partially coherent, and its divergence evolves during the laser pulse to give an average divergence many times the diffraction-limit. The improved conversion coefficient of SHG of the yellow line as compared with the green line may be ascribed to the superior divergence and transverse coherence of the 578nm line as compared with the 511nm line [7.8].

In a similar manner, owing to the divergence of the CVL, the focusing predictions of the Boyd and Kleinman theory are seen to fail. The non-collinear interaction model, however, predicts optimum focusing strengths in the region of f=20-30cm for the CVL in reasonable agreement with experiment. However, since the non-collinear model only offers normalized efficiencies at present, further work is required to test its validity in offering a complete description of SHG with the CVL. It is interesting to note, however, that Pini's research into CVL SHG indicates that the Boyd and Kleinman theory is applicable when the CVL is diffraction-limited and if, instead of assuming a Gaussian intensity profile, a top-hat profile is used.

7.5.2 Dye Laser SHG : Comparison with Theory

In contrast to the CVL, CVL-pumped dye lasers offer near diffraction-limited divergence for almost the whole duration of the laser pulse. Thus, using the Boyd and Kleinman analysis to calculate the conversion coefficient and optimum focusing strength, a comparison with the experimental results for SHG of 616nm dye radiation in BBO, LBO and $LiIO_3$ may be made. The results are summarized in table 7.2:

Table 7.2

	θ_m	ρ	B	h_m	ξ_m	d_{eff} pmV	c_{theory} mW/W^2	f_{theory} cm	c_{expt} mW/W^2	f_{expt} cm
BBO 616nm	39	4.16	11.6	0.062	1.4	1.3	**475**	**20**	**550**	**17**
LBO 616nm	58	0.87	2.4	0.295	1.53	0.6	**341**	**20**	**340**	**17**
$LiIO_3$ 616nm	67.6	3.15	8.8	0.081	1.4	3.8	**2300**	**21**	**2400**	**≤30**

Again, a 10% uncertainty in the experimental figures may be estimated due to alignment sensitivities.

Here, the experimental conversion coefficients are the extrapolated values at

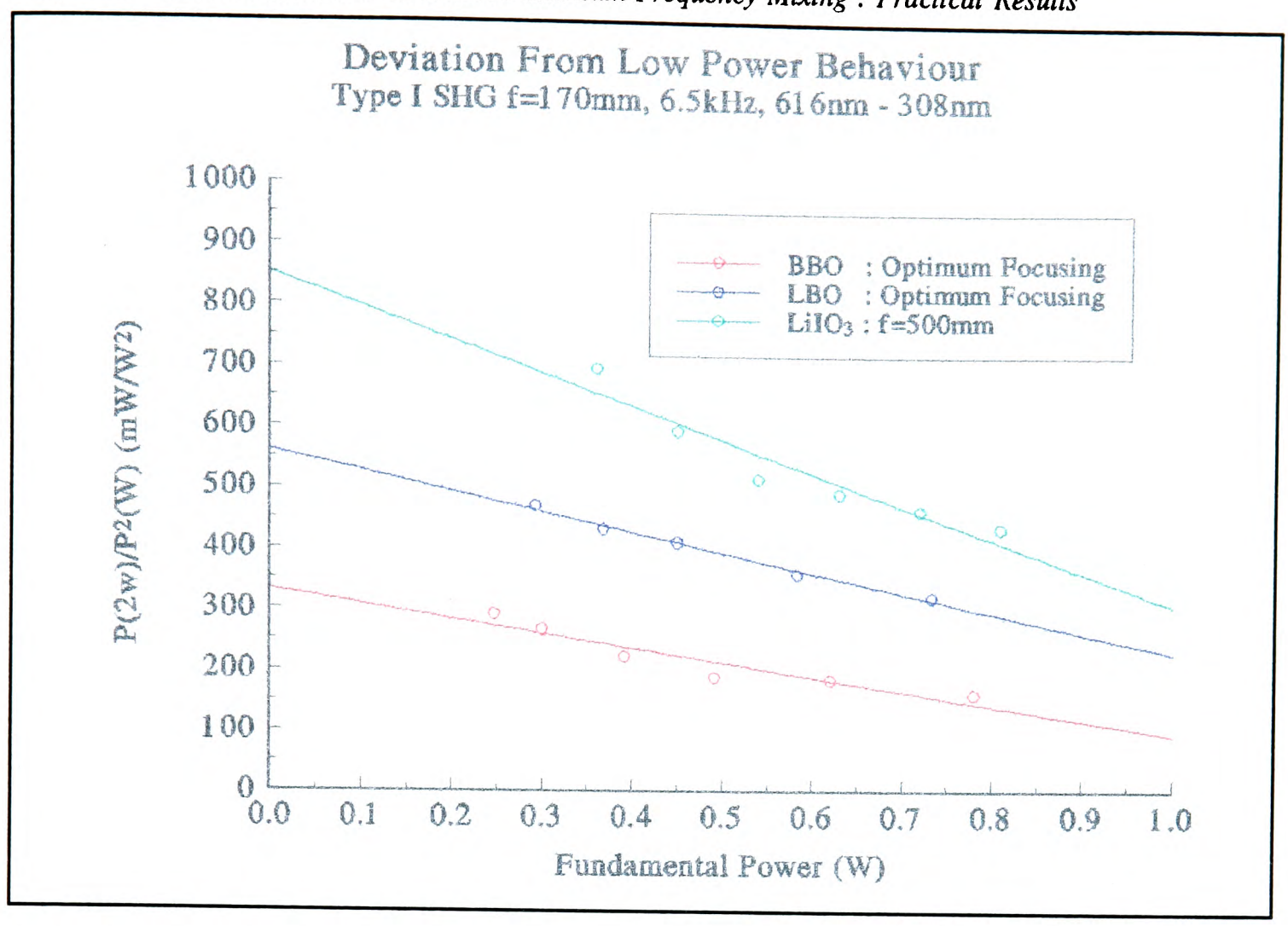


Figure 7.27 : Extrapolation of the conversion coefficient back to zero fundamental intensity for the SHG of CVL-pumped dye laser radiation in BBO and LBO.

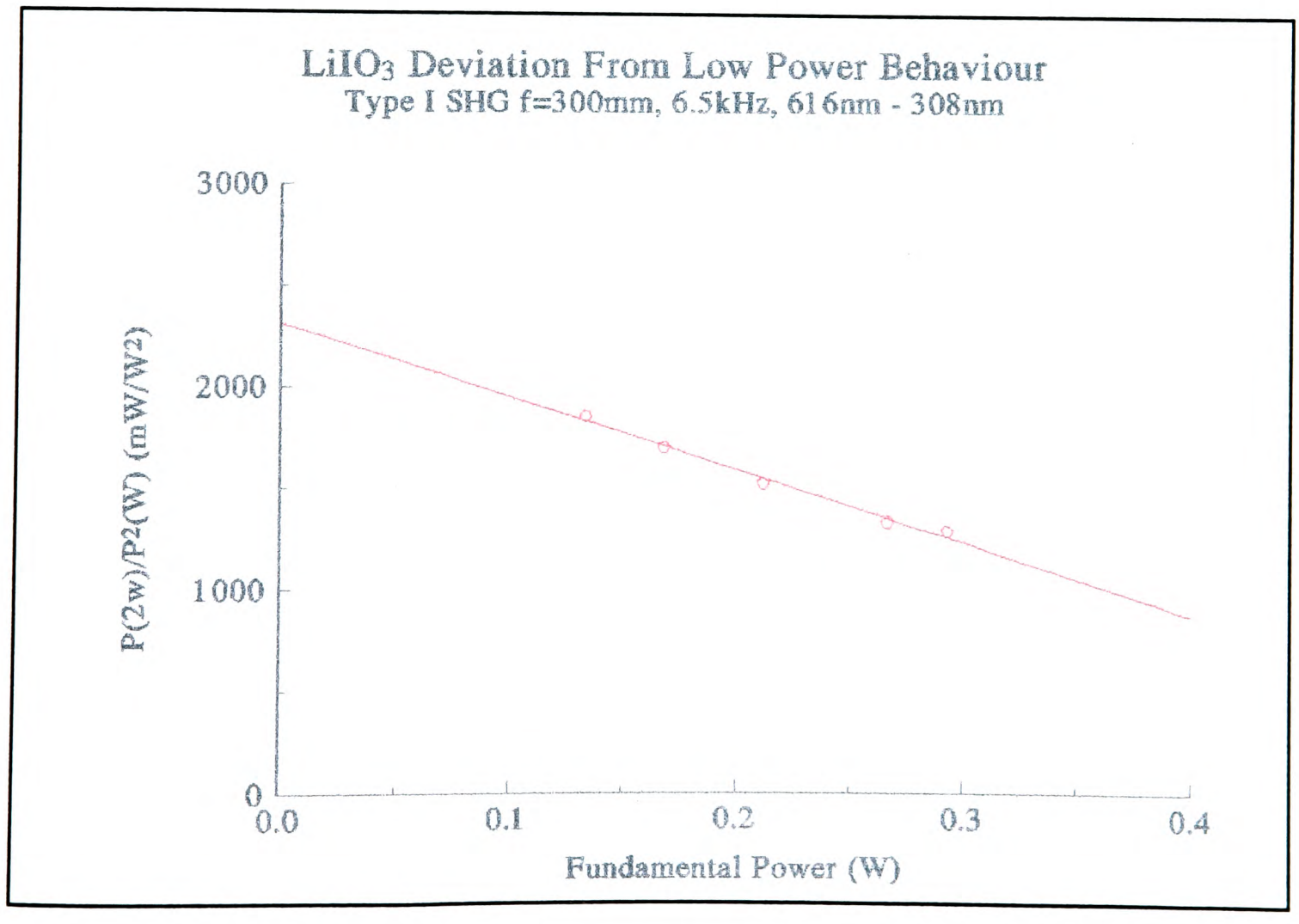


Figure 7.28 : Extrapolation of the conversion coefficient back to zero fundamental intensity for the SHG of CVL-pumped dye laser radiation in $LiIO_3$.

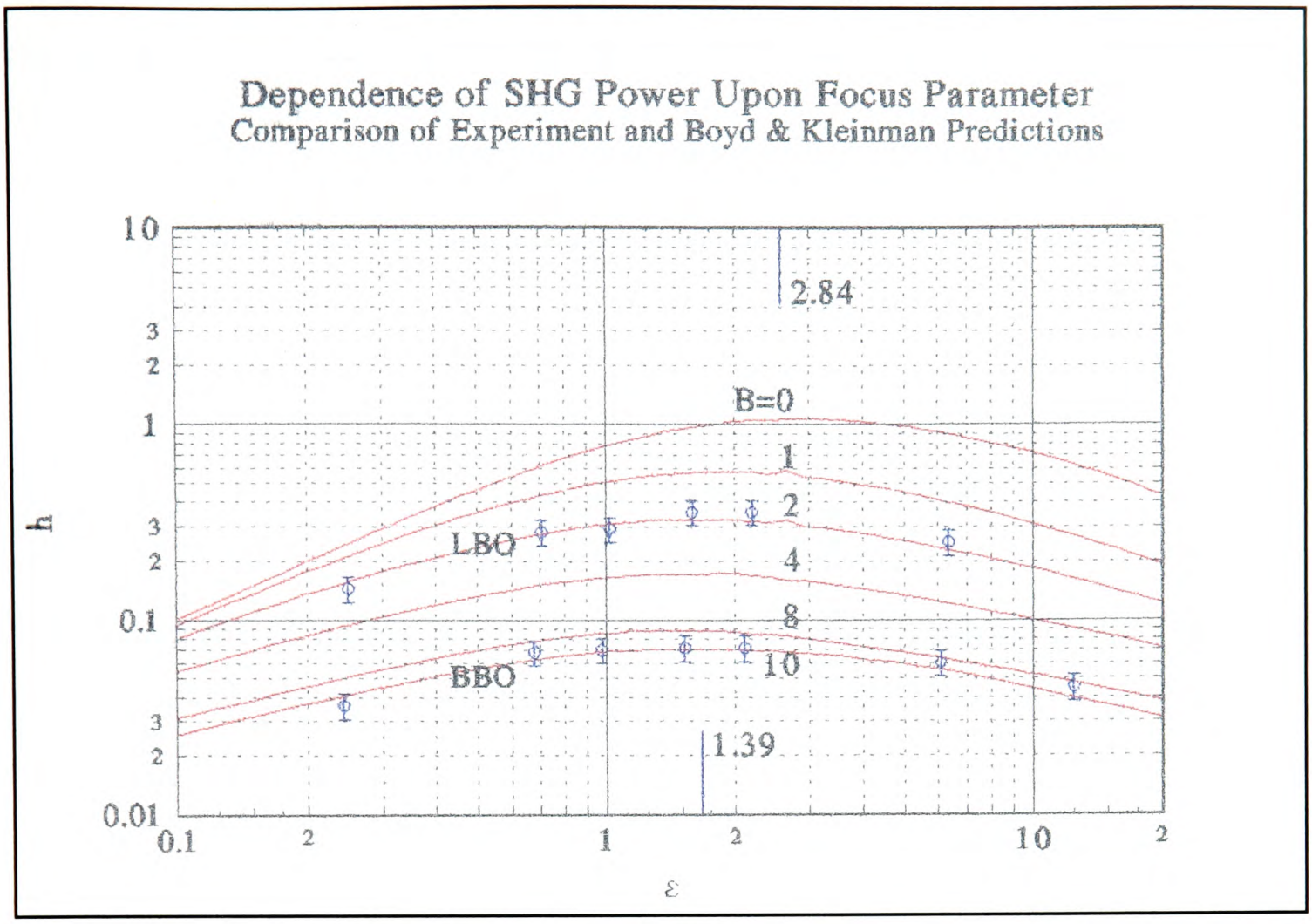


Figure 7.29 : Comparison of the conversion coefficient $c=P(2\omega)/P^2(\omega)$ predicted by theory with experiment. Plotted as a function of the focusing parameter ξ

zero fundamental intensity derived from figures 7.27 and 7.28. The agreement between the Boyd and Kleinman theory and experiment is excellent, with both the predicted strength of focusing and the predicted conversion coefficients agreeing with experiment within the associated measurement errors. Furthermore, the variation in the SHG efficiency / conversion coefficient with respect to strength of focusing is close to that theoretically predicted as shown in figure 7.29. Thus, it may be concluded that the Boyd and Kleinman theory provides a good description of SHG with CVL-pumped dye laser radiation at low powers, and that the conversion coefficient departs from the theoretical predictions linearly with fundamental intensity.

7.6 Conclusion and Discussion

High average power, high efficiency, second harmonic generation has been demonstrated with both the CVL and CVL-pumped dye laser radiation. When using spherical focusing, SHG with CVL radiation at efficiencies in excess of 15% has been demonstrated; elliptical focusing has proved to be advantageous, with efficiencies in

excess of 18% being achieved. In both cases even higher conversion efficiencies are possible, with the availability of increased fundamental power. CVL-pumped dye lasers have proved to be well suited to harmonic conversion, and conversion efficiencies approaching 40% have been demonstrated.

Very recently, research using highly eccentric elliptical ($e \sim 10$) focusing has been conducted by Coutts *et al* [7.10], which has resulted in conversion efficiencies approaching 24% for the CVL 511nm line with 5.5W of fundamental light. It is interesting to note, however, that the optimum ellipse eccentricity predicted by Freegarde's theory is 3, in close agreement with the results presented here, and that if the elliptical focusing efficiency trend in figure 7.11 is extrapolated to 5.5W, then efficiencies approaching 30% would be possible.

The Boyd and Kleinman SHG theory has proved to provide a good account of SHG with dye laser beams, but fails to describe the CVL SHG process owing to the evolving beam quality. The non-collinear interaction model shows promise of accurately describing the CVL SHG interaction, although more theoretical and experimental development and testing is necessary.

7.7 Future Design Considerations and Suggested Work

7.7.1 SHG With Air-Cooled CVLs

The process of SHG is sensitive to the angle the laser beam makes with the crystal rather than the transverse position of the beam at the crystal face (providing of course that the laser beam does not clip the crystal sides). This angular sensitivity has previously restricted the SHG conversion efficiencies achieved by air-cooled CVLs, where air currents near the plasma tube windows cause beam pointing instabilities, and consequently angular changes at the nonlinear crystal for SHG. However, by careful optical design, the angular component of the beam pointing instability may be translated into beam position wander, but without any angular dither. (This is, in fact, the opposite of what is required when launching laser beams into optical fibres, when angular changes are unimportant, but the focus position is.) Consider the ray matrix for a beam propagating through a lens of focal length f as

described in appendix 5.2.

$$\begin{pmatrix} A & B \\ C & D \end{pmatrix} = \begin{pmatrix} 1-\frac{d_2}{f} & d_1+d_2-\frac{d_1 d_2}{f} \\ -\frac{1}{f} & 1-\frac{d_1}{f} \end{pmatrix}$$

For no angular variation in the crystal, we require that element D vanishes, and consequently $d_1=f$. That is, if the CVL plasma tube window (strictly the confocal point of the unstable cavity) is a distance $d_1=f$ from the focusing lens, then the focus generated in the focal plane is free from angular dither. Whilst the beam pointing stability is good with water-cooled CVLs, such a focusing geometry could yield beneficial results with small air-cooled systems.

7.7.2 Enhancement Cavities and Parametric Oscillation

A commonly used approach to improve the SHG efficiency with cw lasers is to enclose the nonlinear crystal in a high finesse "enhancement" cavity. Sometimes the enhancement cavity is the laser cavity itself, in which case, the crystal is exposed to the much higher intra-cavity flux. The UV is conveniently coupled out of such a system by a dichroic output coupler or intra-cavity dispersive element. In the case of the CVL, however, the high gain enables external efficiencies nearly as high as those intra-cavity. Also, there is a more fundamental problem with the use of enhancement cavity techniques with CVL SHG: because of the bandwidth of the laser transitions are so broad (the structure of the 511nm and 578nm lines are determined by Doppler broadening of the hyperfine multiplets, and have been measured to be 6.8 and 8.9GHz respectively), the temporal coherence is limited to times of order 0.1ns, and this, in turn, limits the coherence length to distances less than 0.03m. For reasonable length cavities, this limits the finesse to only 1 or 2.

The laser bandwidth is also a major problem in attempting an optical parametric oscillator, where a high finesse cavity is required to achieve the parametric build-up of a signal and idler waves from noise. However, there may be a possibility of both cavity enhancement SHG and parametric oscillation, depending upon the

outcome of current research at the Clarendon by Andrews. Andrews [7.11] is currently investigating the nature of the CVL spectral profile - if a significant proportion of the bandwidth is homogeneously broadened, then a small CVL air-cooled unit may be spectrally filtered (by an etalon) before amplification in a larger CVL unit. Such a configuration could provide high power, low divergence, narrow-bandwidth radiation suitable for pumping a parametric oscillator or a SHG enhancement cavity.

It would be possible to use an external enhancement cavity to promote the SHG efficiency of narrow-bandwidth CVL-pumped dye laser radiation, although this avenue of research has not been pursued with the 7GHz bandwidth dye laser used for the present studies (for coherence length reasons).

Chapter 7 : References

7.1 T.G.M. Freegarde & G.A. Naylor

Efficient High Average Power Harmonic Generation Using Copper Vapour Lasers

Tech. Dig. CLEO (1990) ***CTHK3***

7.2 R. Pini, R. Salimbeni, G. Toci & M. Vannini

Efficient Second Harmonic Generation in β-Barium Borate By a Diffraction Limited Copper Vapour Laser.

Appl. Opt. ***31*** *2747-2751 (1992)*

7.3 W. Molander, M. Norton & J. Chang

Improved Efficiency of Second Harmonic Generation in BBO Using the 511nm Line of an Injection Seeded Copper Laser.

LLNL Internal Report

7.4 M. Broyer, J. Chevaleyre, G. Delacrétaz & L. Wöste

CVL - Pumped Dye Laser For Spectroscopic Application.

App. Phys. B ***35*** *31-36 (1984)*

7.5 A.A. Isaev, G. Yu Lemmerman & G.L. Malafeeva

Second Harmonic Generation From Pulsed Copper Vapour Radiation

Sov. J.Q.E. ***10*** *983-985 (1980)*

7.6 T.G.M. Freegarde

Spectroscopic Applications of Pulsed Metal Vapour Lasers.

D.Phil Thesis, Oxford (1989)

7.7 D.W. Coutts, M.D. Ainsworth & J.A. Piper

Observation of The Temporal Evolution of Transverse Coherence in Copper Vapour Lasers

Opt. Commun. ***87*** *245-248 (1992)*

7.8 T. Omatsu & K. Kuroda

Time Resolved Measurements of Spatial Coherence of a Copper Vapour Laser Beam Using a Reversal Shear Interferometer.

Opt Commun. ***87*** *278-286 (1992)*

7.9 G. Nath & S. Haussühl

Large Nonlinear Optical Coefficient and Phase Matched Second Harmonic Generation In $LiIO_3$.

Appl. Phys. Lett. ***14*** *154-156 (1969)*

7.10 D.W. Coutts & J.A. Piper

One Watt Average Power by Second Harmonic and Sum Frequency Generation from a Single Medium Scale Copper Vapour Laser.

IEEE J.Q.E. ***28*** *1761-1764 (1992)*

7.11 A.J. Andrews

Clarendon Laboratory

Private Communication.

Chapter 8
Applications of High Repetition Rate Lasers and Conclusions

8.1 Introduction.

8.2 RIMS - Resonant Ionization Mass Spectrometry.

8.3 Tropospheric Hydroxyl Radical Detection.

8.4 Conclusion.

8.5 The Future Direction For High Repetition Rate Tunable Laser Research.

References.

Chapter 8
Applications of High Repetition Rate Tunable Lasers

8.1 Introduction

The high repetition rate tunable laser research detailed in the present work was originally undertaken as part of a collaborative programme to develop a resonant ionization mass spectrometry (RIMS) apparatus. However, the applicability of the laser sources developed is by no means restricted to RIMS and, in the course of the research programme, the author has been involved in the application of CVL-pumped dye lasers and the nonlinear conversion of their radiation to a number of interesting areas. These applications have included the detection of tropospheric hydroxyl radicals, and the development of a laser projection TV system.

The chapter reviews some of the applications to which CVL-based high repetition rate tunable lasers have been applied, and provides illustration of their unique properties as a spectroscopic tool. In addition, the current research is summarized, and conclusions are drawn about the future direction for research in the field.

8.2 RIMS - Resonant Ionization Mass Spectrometry.

RIMS is a highly sensitive and selective technique for the trace analysis of materials. Its applications include the detection of trace amounts of impurities, such as carbon and iron, in the silicon used for the semiconductor industries, and the detection of trace amounts of environmental pollutants such as plutonium [8.1]. The technique involves the selective multi-step excitation of one particular atomic (or isotopic) species with resonant laser radiation, followed by an ionization process, which may also be selective. The resulting photoions are analyzed and quantified by a time-of-flight (TOF) mass spectrometer, which also enables isotopic qualification, and discriminates against any non-resonant background.

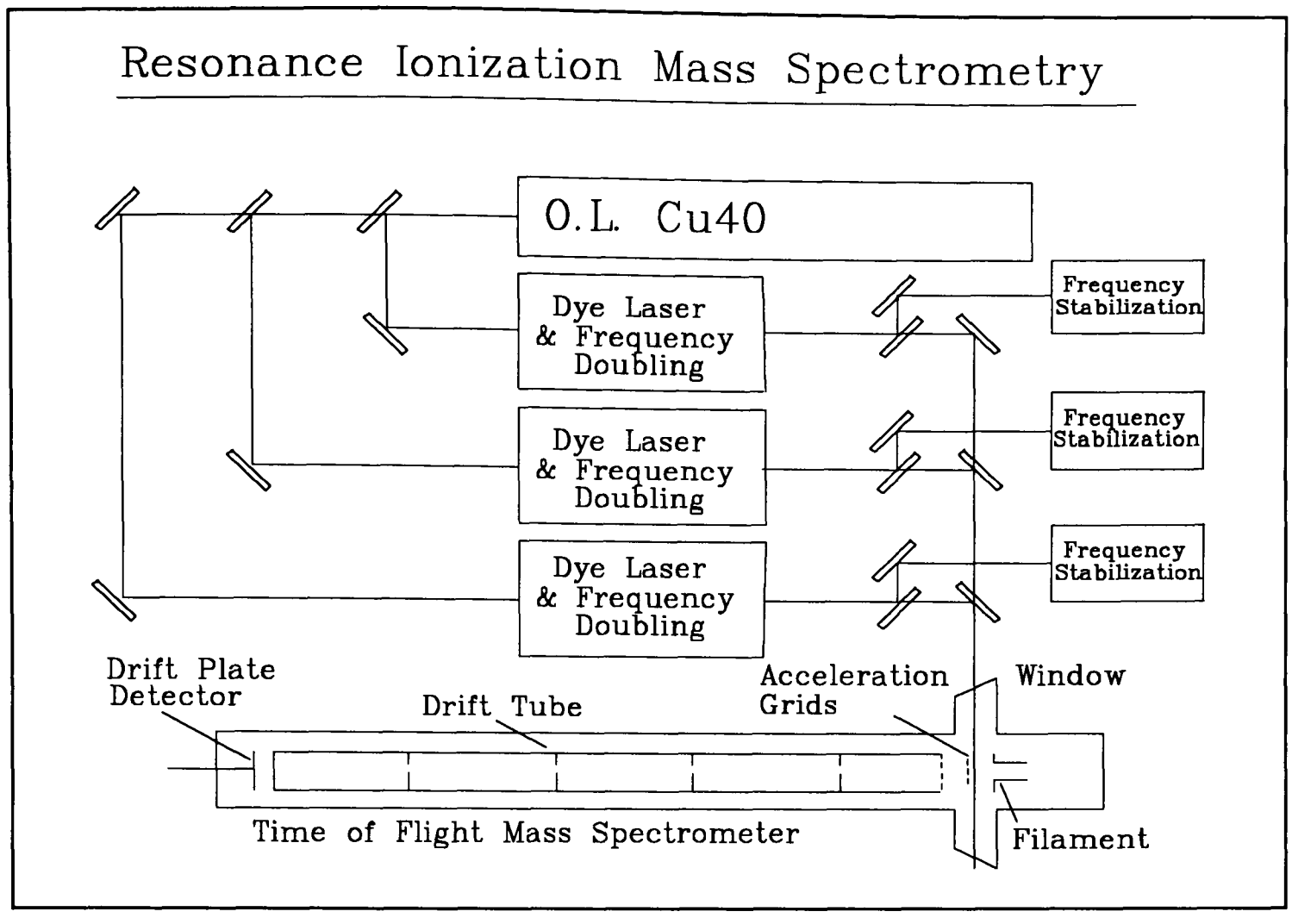


Figure 8.1: Integration of the laser and TOF mass spectrometer for RIMS.

A schematic illustrating how the laser and mass spectrometry sub-systems are integrated is shown in figure 8.1. The sample under investigation is introduced into the mouth of a time-of-flight mass spectrometer. A small fraction of the sample is vaporized by an ion gun, and an electric sweep field is applied to remove any secondary ions created. The remaining cloud of neutral atoms is exposed to laser radiation resonant at one or more wavelengths in the multi-photon/multi-step resonance ionization scheme of the element under investigation. Since the energy levels of each particular element (or isotope) are unique, in general only one of the many atomic species present in the cloud of neutral atoms will be ionized for a particular combination of laser frequencies. Hurst *et al* [8.2] have shown that, in general, nearly any element may be resonantly ionized using one of five characteristic resonance ionization schemes (figure 8.2). The exceptions to Hurst's scheme are helium, fluorine and neon, where the photon energies associated with transitions from the ground state are unattainable by current laser technology, even by two-photon absorption.

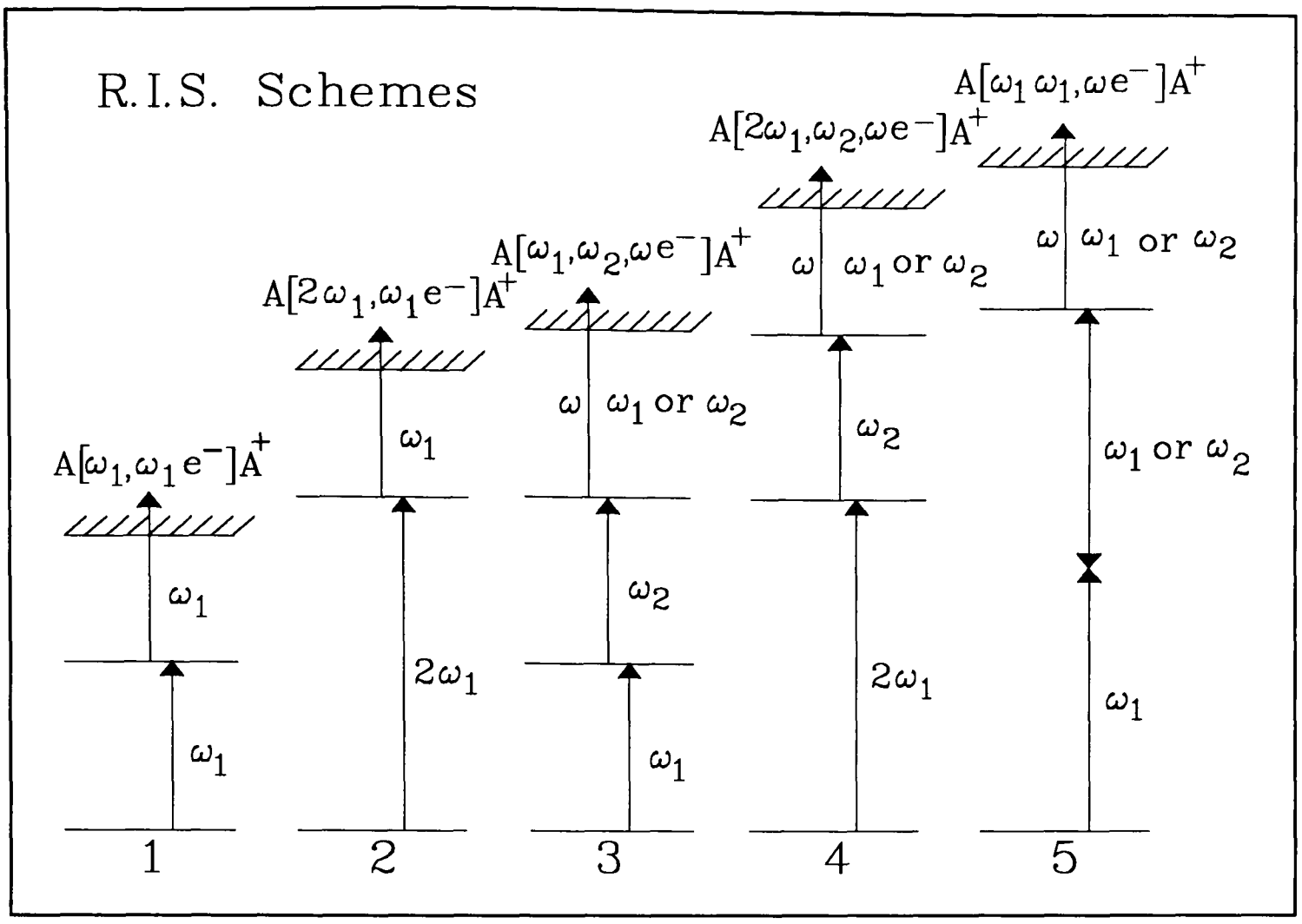


Figure 8.2 : Resonance ionization of nearly any element may be achieved by one of the above five schemes. Exceptions are helium, fluorine and neon, where, because of the high photon energy associated with the first transition, resonant ionization cannot be achieved by currently available laser and nonlinear sources.

For instrument sensitivity, each of the resonant transitions must be saturated if all of the atomic species under investigation are to be ionized. For a homogeneously broadened transition, the saturation intensity may be shown to be :

$$I_{sat}(\omega) = \frac{\hbar\omega}{\sigma\tau} , \qquad (1)$$

where σ is the absorption cross-section, and τ is the lifetime of the upper level to spontaneous emission. For typical atomic cross-sections and lifetimes, laser intensities of hundreds of kilowatts per square centimetre are required to saturate the transitions. To achieve saturation over a reasonable volume dictates the use of pulsed laser systems. Pulsed lasers are capable of peak powers of order tens or hundreds of kilowatts, as compared to the tens of watts available from cw laser systems. However, too high a laser intensity does not increase instrumental sensitivity through over-saturating the resonant transitions, but increases the non-resonant background signal. The neutral atoms released from the sample surface by ion sputtering have thermal energies close to 2000K, and, thus, have a mean velocity of about 10^4cm/s.

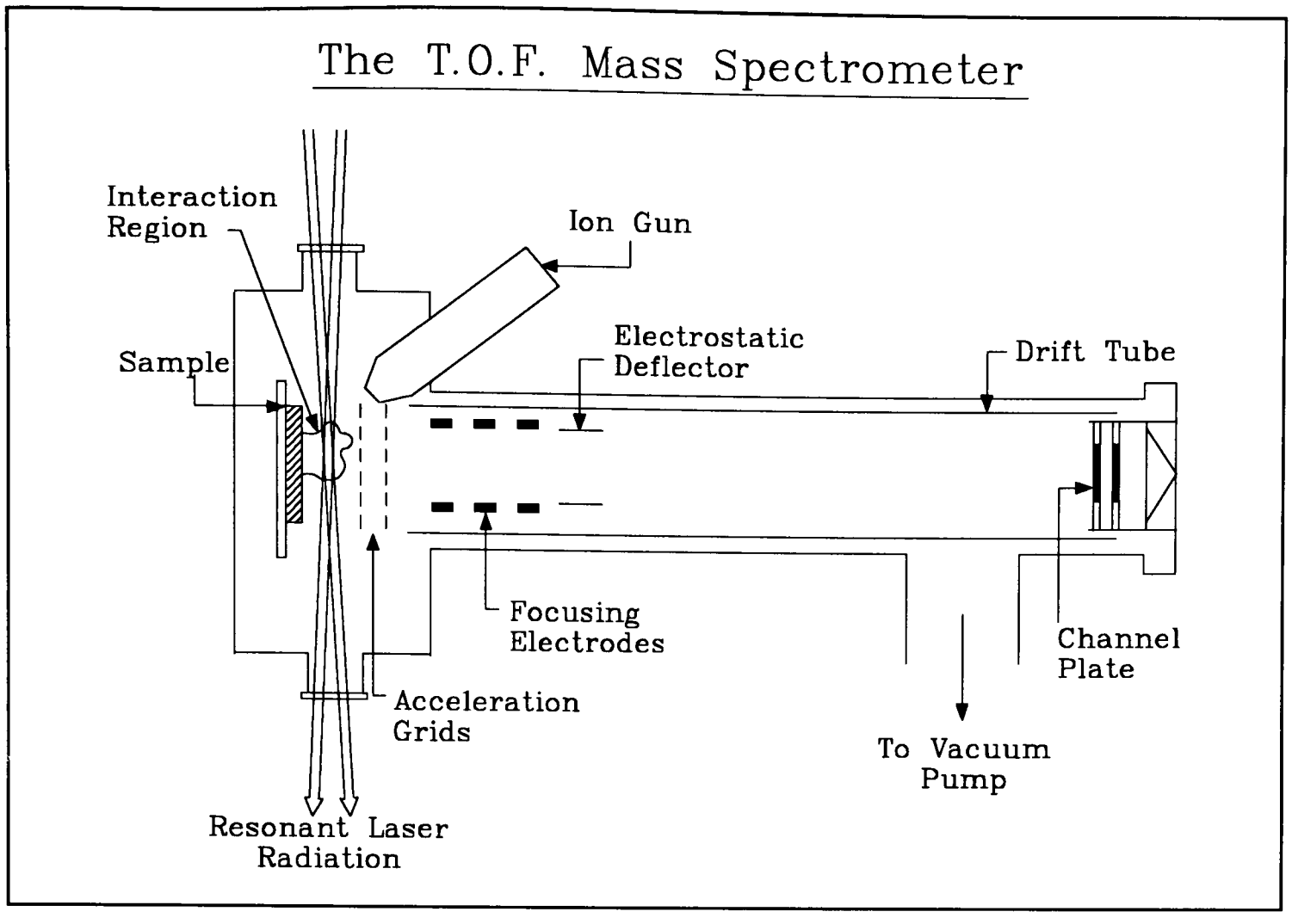


Figure 8.3 : Detail of the time-of-flight mass spectrometer.

These atoms will traverse the irradiation zone, typically 1mm in diameter, on sub-millisecond timescales, and, if every atom is to be exposed to laser radiation, it is necessary to pulse the tunable laser at several kilohertz. This means that CVL-based high repetition rate lasers, of the kind developed during the present studies, are the laser sources best suited to this application.

The photoions, generated by resonance ionization, are accelerated by the electric field created by a pair of acceleration grids, and pass into the drift tube of the time of flight mass spectrometer. The drift tube is typically 1m long, and at its end is situated a channel plate detector, as shown in figure 8.3. Since all the photoions created experience the same electric acceleration field, their transit time to the detector, via the drift tube, depends upon their masses. Thus, by monitoring the channel plate detector signal as a function of time, the ions may be qualified according to their isotopic mass. However, qualification ambiguity associated with photoion-transit-time measurement errors may arise due to a number of factors :

1. Photoions are created at different spatial positions within the laser beam and, thus, follow different path lengths to the detector - this may be overcome by designing the electrostatic accelerating fields such that the ion orbits are isochronous between the source and detector, and a time focus is produced at the detector. In this case, the further away from the detector the ions are produced, the greater the electrostatic potential they experience, so allowing them to catch up with the slower ions, which have a shorter drift length.
2. Photoions are created at different times - this is determined by the laser pulse length, and is less of a problem for the relatively brief pulse from the CVL.
3. The neutral species from which the ions are created will have a non-zero initial velocity distribution in addition to that acquired by the accelerating electric field. This is a more difficult problem to overcome, and in general requires the design of an electrostatic velocity-specific reflector.

Once these possible qualification ambiguities have been overcome, using the laser pulse to define a time origin, t=0, detection gates between 50 and 100ns are set electronically at times corresponding to the transit times of the elemental ion, its oxide and dioxide etc. Between laser pulses, a gate of several microseconds duration is opened to monitor the background noise. The kilohertz repetition rate of the CVL enables fast data acquisition rates, and if the ion beam sample sputtering is spatially confined, then by translating the sample, a matrix of the material composition may rapidly be acquired.

As part of the LINK collaboration, a CVL-pumped dye laser developed at the Clarendon (a modified Lambda Physik LPD3000) has been integrated with an Oxford Lasers Cu40 and a Fisons Surface Science TOF mass spectrometer at UC Swansea. Researchers there are currently trying to demonstrate RIMS in iron using, in the first instance, a single excitation wavelength at 302nm, corresponding to the first resonance ionization scheme of figure 8.2.

8.3 Tropospheric Hydroxyl Radical Detection

The oxidizing capacity of the atmosphere is primarily determined by the

concentration of hydroxyl radicals (OH). These radicals control the removal of most naturally- and anthropogenically-produced atmospheric trace gases; for example, the greenhouse gas methane, and the hydrogen containing CFC-substitutes, are exclusively removed by reaction with OH. Due to its high reactivity, the concentration of OH radicals is extremely low (of order 10^5 radicals/cc), and its measurement has proved a notoriously difficult problem for atmospheric chemists for over a decade. However, a leading research group at the KFA Jülich, Germany, have recently devised a scheme capable of the sensitive detection of OH based on laser induced fluorescence (LIF) techniques. A prototype experiment using a low repetition rate Nd:YAG pumped tunable laser has demonstrated the suitability of the technique [8.3], but to improve data acquisition times from hours to tens of seconds, the German group have sought high repetition rate tunable lasers of the kind developed here at the Clarendon Laboratory.

The LIF technique (figure 8.4) involves laser excitation of OH radicals

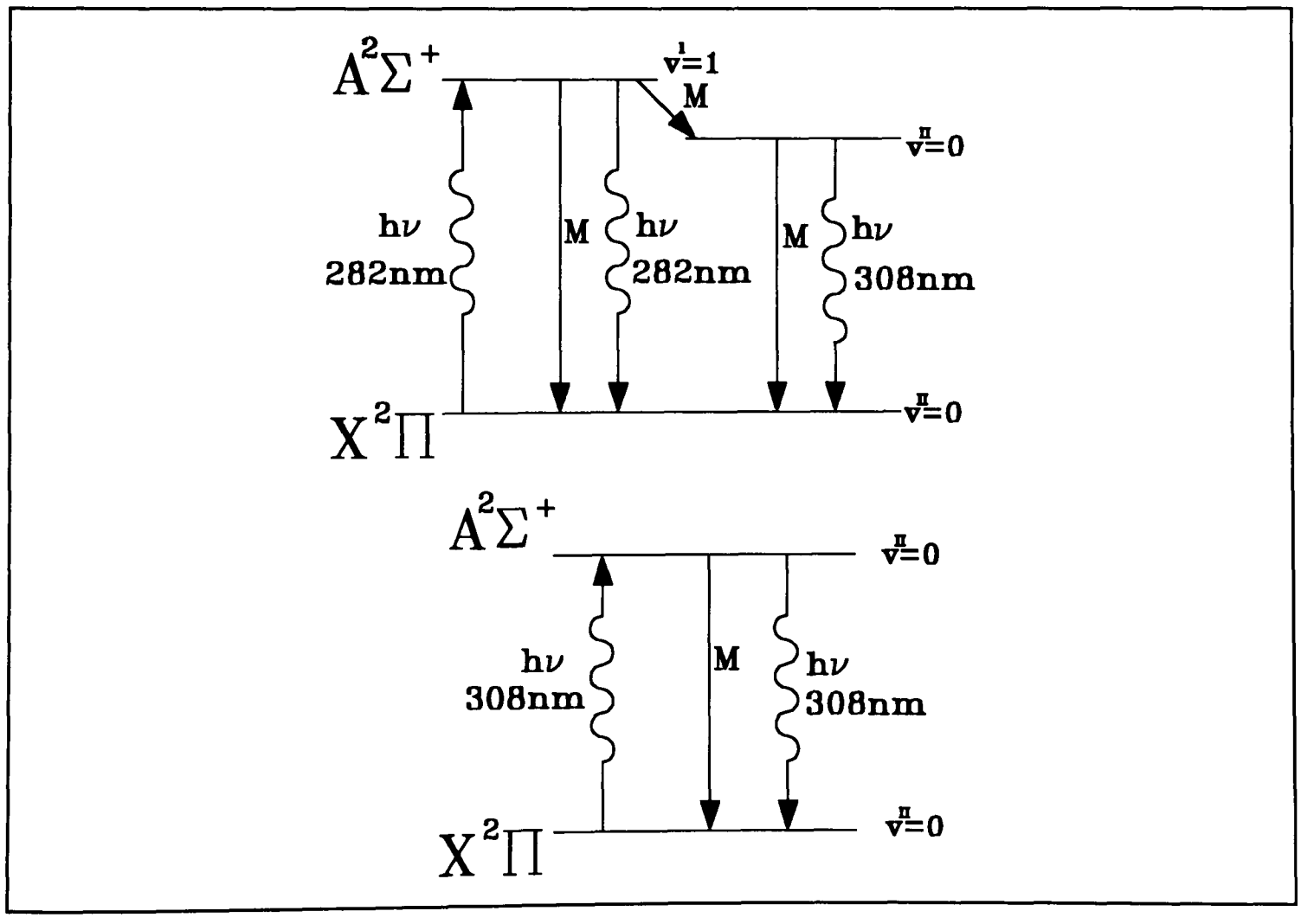


Figure 8.4 : LIF schemes for OH detection. Here M symbolizes a radiationless decay process (eg. collisional quenching).

($A^2\Sigma^+ \leftarrow X^2\Pi_i$) at wavelengths near 282nm (1-0 band), or near 308nm (0-0 band). The amount of fluorescence subsequently emitted around 309nm (0-0 band in the A←X transition) by the excited OH radicals is used as a measure of the OH concentration. Whilst excitation at 282nm enables easy spectroscopic discrimination between the excitation and fluorescence signals, at 282nm the photon energy is sufficient to photolyze ozone, and the ensuing reaction between $O(^1D)$ and atmospheric water vapour produces OH radicals at greater concentrations than are naturally present [8.4]:

$$O_3 + h\nu \rightarrow O(^1D) + O_2(^1\Delta_g)$$

$$O(^1D) + H_2O \rightarrow OH + OH$$

Laser excitation at 308nm offers two advantages over excitation at 282nm. Firstly, the cross section for ozone photolysis is some 29 times smaller at 308nm than that at 282nm, and secondly, the OH absorption cross-section is 4 times larger at 308nm as compared to 282nm [8.5]. The laser induced fluorescence corresponding to excitation at 308nm is, however, more difficult to detect because of the near spectral coincidence between the excitation and fluorescence wavelengths. The fluorescence signal, detected by photon counting, is discriminated from the excitation laser signal by its time signature. The lifetime against pressure quenching of excited OH radicals at atmospheric pressure is about 7ns, but by decreasing the pressure in the detection chamber to $\sim$2mbar, the fluorescence lifetime can be extended to hundreds of nanoseconds. Thus, by gain-switching the photomultiplier, and gating the photon counting system for the duration of the excitation laser pulse, the weak OH fluorescence signal can be distinguished from the scattering of the laser beam from the detection chamber walls and the Rayleigh scattering off the air molecules.

The integration of the laser system, detection chamber with air inlet, and photon counting system is illustrated in figure 8.5. Here, a small fraction of the 308nm laser radiation is split off and passed through a flame for calibration purposes. OH radicals are created with large abundances in flames, and by monitoring the absorption of the laser beam in such a flame, the laser can be accurately tuned on- and off-resonance with the OH absorption.

As for RIMS, in order to saturate the OH absorption, and potentially detect

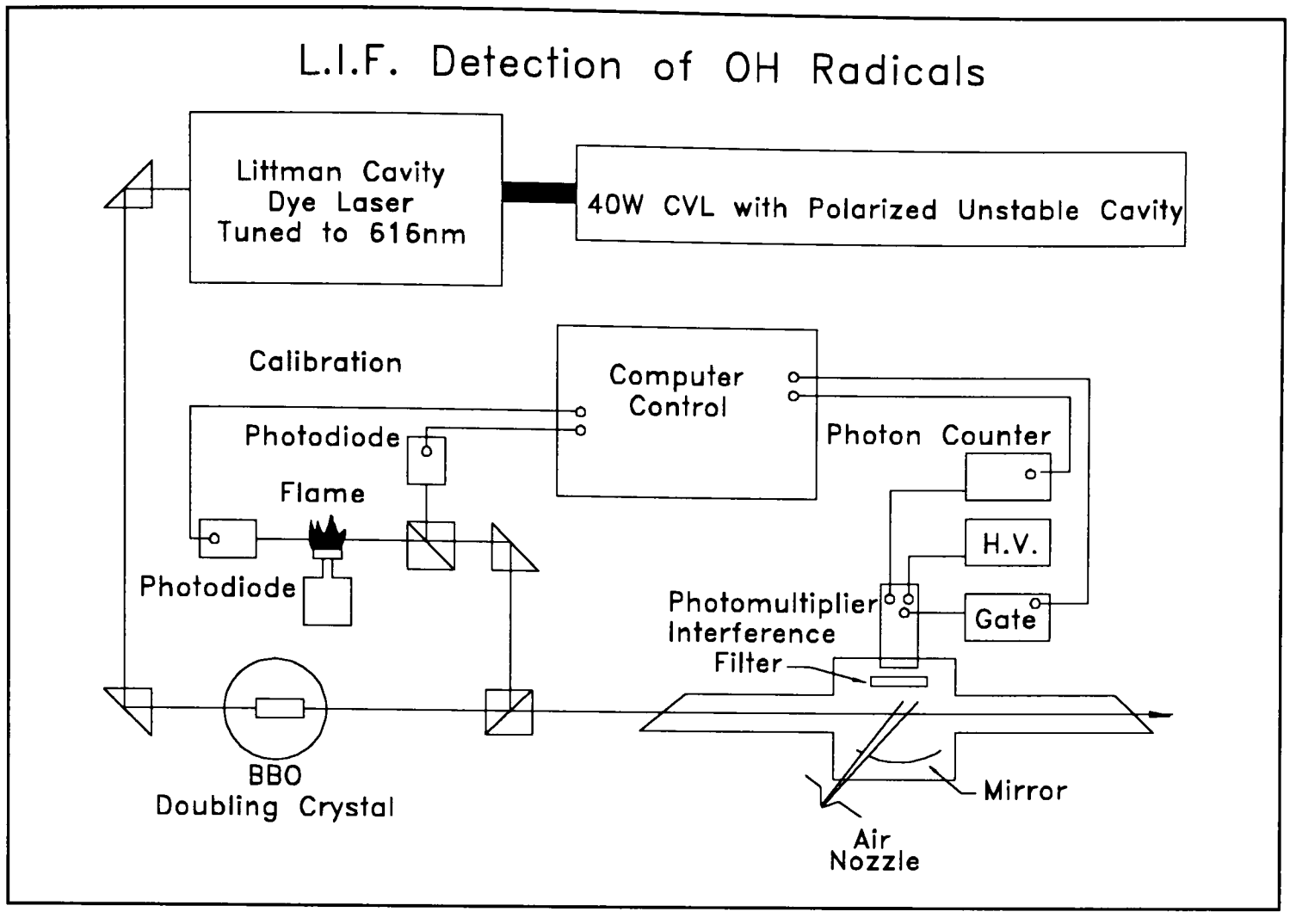


Figure 8.5 : Schematic of the OH-LIF detection system.

every OH radical which enters the detection chamber, the high peak powers of a pulsed laser are needed. Even so, the efficiency of the detection system is rather low owing to the finite integration time available to the photon counting system (the laser pulse and photomultiplier noise experienced during gain-switching limits detection duty cycles to ~ 0.5), and the small solid angle of the photomultiplier subtended at the LIF region. When coupled with the very low densities of OH present in the atmosphere ($\sim 10^5$ radicals/cc), typically only one photon is counted for every 10^4 laser pulses. Thus, extremely long sampling periods are required when using anything other than a CVL-pumped tunable laser operating at 308nm. The 308nm ($Q_1(2)$) absorption in OH starts to saturate at intensities of 15MW/cm^2 ($\sim 70\mu$J/cm^2 for a 50ns pulse length), and any increased pulse energy does not contribute to increased detection efficiency, but only to generate more instrumentally produced OH through ozone photolysis. Thus, a frequency doubled CVL-pumped dye laser operating at 616nm, of the kind described in chapters 4 and 6, is ideally suited to OH detection. Such a laser source supplies sufficient peak intensity to just saturate the OH absorption cross-section at kilohertz repetition rates, and does not over-saturate the

transition, so ensuring that ozone photolysis is kept to a minimum.

Laser dyes fluorescing at 616nm generally offer good absorption to the CVL yellow line, but do not fully utilize the CVL green line, which contains most of the laser power. Therefore, a number of dye mixtures were investigated, and a solution of Rhodamine 6G (0.3mM) and Rhodamine 640 Perchloride (0.17mM) in methanol was found to be the optimum for 616nm generation. In this "dye cocktail", the Rhodamine 6G acts as a fluorescence converter into the yellow for the CVL 511nm line, and enables the efficient pumping of the Rhodamine 640 Perchloride dye, which is responsible for fluorescing at 616nm.

Thus, to examine the feasibility of OH detection using a CVL-based laser system, a modified Lambda Physik LPD3000 dye laser incorporating an intra-cavity etalon, pumped by an Oxford Lasers ACL35, was set up by the present author at the KFA laboratory, Jülich. The 616nm dye laser radiation was frequency doubled in BBO, to give 750mW of 308nm radiation after separation from the fundamental beam using a set of four Pellin-Broca silica prisms. By sampling 1000 laser pulses, the root-mean-square pulse energy jitter of the 308nm radiation was estimated to be less than 3%, and by synchronously scanning the phase-match angle of the BBO crystal, and the oscillator grating and etalon, the 308nm radiation could be scanned over the 308nm OH absorption profile with constant intensity.

Thus, using a small fraction of the UV beam (20mW), the absorption spectrum of OH was recorded by measuring the intensity change of the UV laser beam passing through a bunsen burner flame as the wavelength was scanned. The 308nm power passing through the flame was measured using a calibrated photodiode, and the absorption spectrum recorded over the region 308.2nm - 307.5nm is presented in figure 8.7. This illustrates the spectroscopic potential of CVL-based high repetition rate tunable lasers, and their suitability for OH detection.

The integration of a CVL-based high repetition rate tunable laser with the aforementioned low pressure LIF detection chamber is currently under way, and joint EC-funded experiments between the KFA and the Clarendon Laboratory into

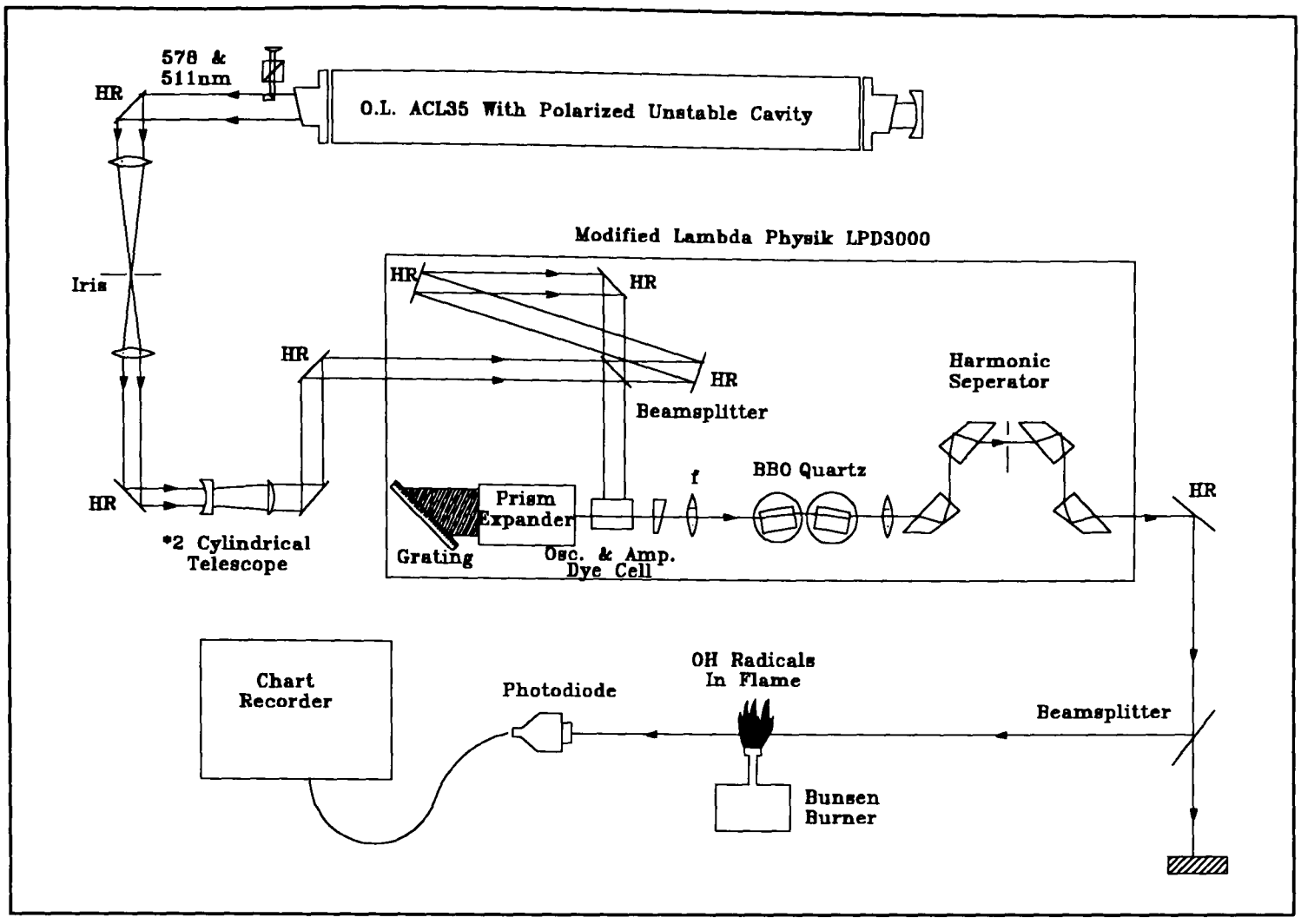


Figure 8.6 : Schematic of the laser and detection system used to record the absorption spectrum of OH in a bunsen burner flame.

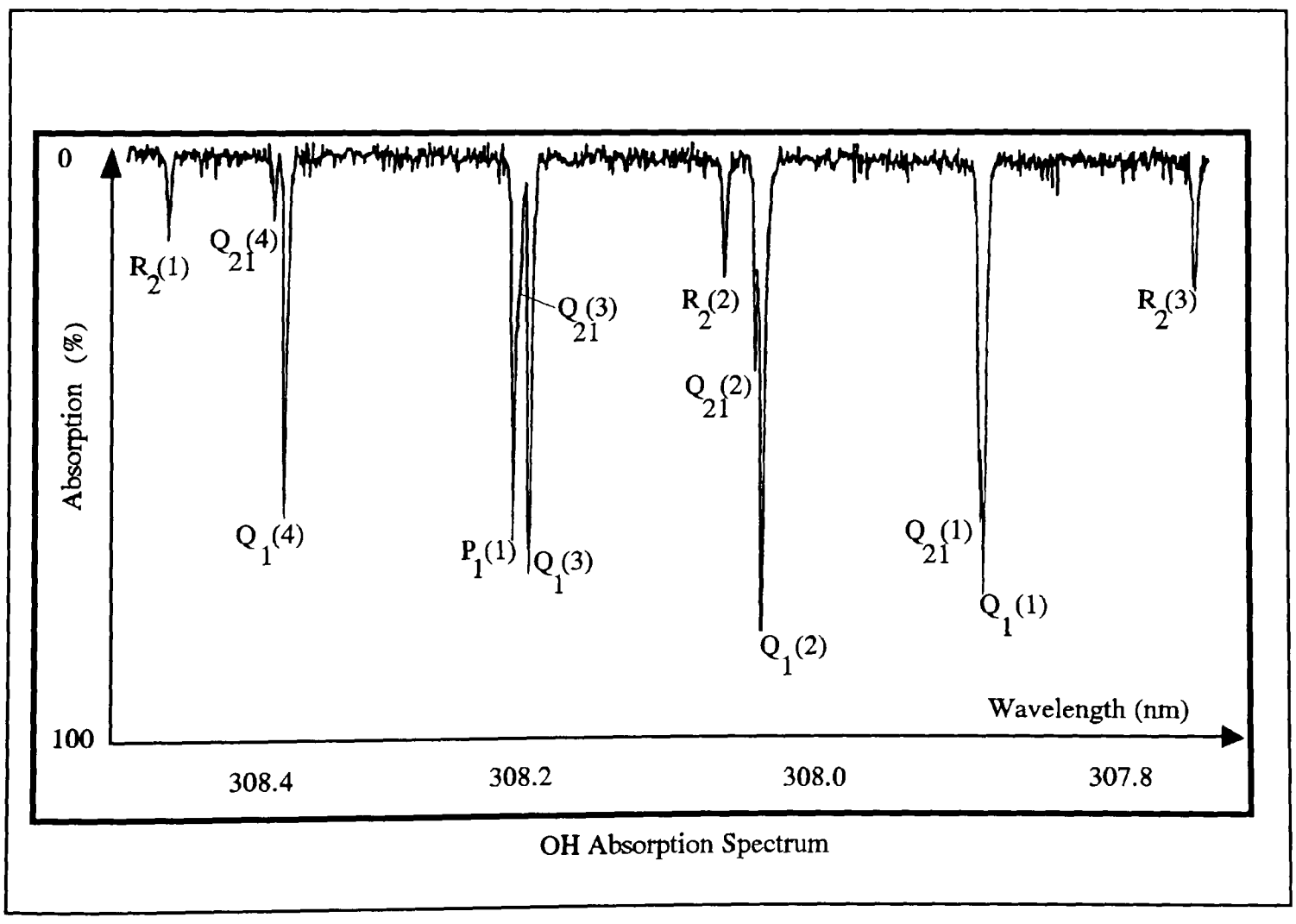


Figure 8.7 : The OH absorption spectrum recorded with a frequency doubled CVL-pumped dye laser.

tropospheric OH measurements on board an aircraft are planned.

8.4 Conclusion

Before the present work was started in 1989, whilst CVLs promised to be an effective source for pumping dye lasers and achieving a source of high repetition rate tunable radiation, very little published research was available to suggest how to design, or optimize, such a laser system. The same was true for the second harmonic conversion of the CVL, and CVL-pumped dye lasers, where, in both cases, harmonic conversion efficiencies were previously restricted to values below 10%. Thus, in designing a high repetition rate tunable laser source for RIMS, the initial research goals were to achieve 10% conversion of the CVL into narrow-bandwidth tunable dye radiation, and then to achieve 10% conversion of the dye radiation into its second harmonic. The reported efficiencies, bandwidths, beam-qualities, frequency stabilities, and powers are somewhat better than the targets set, and in many cases represent the best currently published data.

A series of experiments has been conducted to gain a physical understanding of the fundamental parameters necessary for optimization of the CVL-pumping of dye lasers. It has been concluded that the optimum dye laser performance is achieved when the CVL is fitted with a polarized unstable cavity, whose polarization is matched to the preferred polarization of the dye laser. In addition, dye laser performance is enhanced by removing the ASE present in the CVL beam, and by ensuring that the whole length of the dye cuvette is pumped. When using dyes which fluoresce in the range 560-600nm, it has been shown to be detrimental to use the CVL 578nm line in the pumping scheme because of gain-quenching.

For efficient pulsed dye laser operation, the clearing ratio of the dye must be greater than unity, and when using a kilohertz repetition rate pump laser, this necessitates the use of a high speed circulator and laminar flow dye cells. By choosing dye oscillator materials which offer a better reflectivity than the conventionally-used aluminium toward the red region of the spectrum (the region of laser operation limited by the CVL 511nm line), conversion efficiencies can be

improved by up to 30%. High power, narrow-bandwidth dye laser operation is best achieved using a master oscillator power amplifier (MOPA) configuration. The beamsplitter optimization in such a MOPA system is critical to the overall performance, and must be chosen simultaneously to provide the maximum amount of power for efficient amplification, and to ensure a good temporal match between the oscillator and pump laser pulses arriving at the amplifier. A number of ASE suppression techniques have been investigated, and careful laser design has been shown to give signal to noise ratios better than $1:10^5$ (the instrument detection limit).

The dye laser systems investigated have been exhaustively characterized, and the beam characteristics of CVL-pumped dye lasers have been measured for the first time. The analysis of asymmetric dye laser beams has required a novel analysis technique to be developed, which negates errors associated with beam astigmatism and thermal lensing in the dye laser beam. Typically the dye laser beams have possessed near diffraction-limited divergence, although the asymmetry of the single sided transverse pumping schemes used is evident in the beam profiles.

A new rate equation analysis of the kinetic processes relevant to optical amplification in laser dyes has been presented, and the corresponding computer model predictions are in excellent agreement with experiment. The rate equation model predicts that optimum amplification is realized when the seed input is focused into the dye cell, so as to saturate the gain throughout the whole length of the amplifier. The model also predicts that the optimum gain length for a CVL-pumped dye laser amplifier is close to 10mm, in contrast to the 20-40mm dye amplifiers typically used. Using the physical understanding gleaned from the theoretical model, conversion efficiencies approaching 45% have been realized when using Rhodamine 6G dye close to its fluorescence peak.

As a result of the aforementioned investigations, three commercially available dye lasers have been successfully optimized for CVL pumping for the first time. Once modified, these dye lasers have typically shown conversion efficiencies in excess of 20%, with bandwidths as narrow as 800MHz, and beam qualities approaching the diffraction-limit. The design modifications necessary for the

optimum operation of the commercial dye lasers at kilohertz repetition rates are detailed. The modified units show themselves to be ideally suited for spectroscopy and as an ideal high repetition rate source of tunable laser radiation for RIMS.

The theory of second harmonic generation with plane waves, Gaussian beams and partially coherent beams has been reviewed, and a suite of corresponding computer models developed to predict the optimum focusing, expected harmonic conversion coefficients, and the phase-matching angles for both uniaxial (BBO and lithium iodate) and biaxial crystals (lithium tri-borate). These models have been used to form a basis for a coherent experimental investigation of UV generation using the CVL and CVL-pumped dye laser.

Second harmonic generation of both CVL lines has been extensively investigated in both beta-barium borate (BBO) and lithium tri-borate (LBO). With a polarized unstable cavity of magnification M=40, and optimum spherical focusing, conversion efficiencies approaching 15% have been demonstrated. In the middle of the CVL pulse, instantaneous efficiencies approaching 50% are evident, although the evolving divergence and transverse coherence of the CVL unstable cavity limits the usefulness of the Boyd and Kleinman Gaussian beam SHG theory. The dependence of the SHG efficiency upon strength of focusing shows good agreement with a non-collinear interaction model, although further theoretical and computer model development is necessary to test whether this model provides a full description of SHG with the CVL.

For the first time, a comparison of SHG with elliptical and spherical focusing has been undertaken. When the major ellipse axis is in the direction of beam walk-off in the crystal, optimum elliptical focusing has been found to yield 25-30% more UV power than with optimized spherical focusing. This is in good agreement with the result predicted by theory, and by analysis of the instantaneous conversion coefficient, elliptically focused SHG can be seen to make better use of the non-diffraction-limited radiation found in the early part of the CVL pulse.

In a similar manner, a thorough investigation of second harmonic generation

using CVL-pumped dye lasers in BBO, LBO and lithium iodate has been undertaken. The superior beam quality and coherence of the dye laser, as compared to the CVL, enables efficient nonlinear conversion into the UV, and provides an efficient source of high repetition rate tunable radiation in the ultra-violet. Conversion efficiencies approaching 40% in $LiIO_3$ have been demonstrated, with conversion coefficients approaching 2400mW/W^2 realized at low input powers. At high powers conversion efficiencies in excess of 35% have been demonstrated - these results represent by far the best published. The Boyd and Kleinman theory is found to provide an excellent description for the low power SHG of the near diffraction-limited dye laser beams, and accurately predicts the conversion coefficient and the optimum focusing strength. For the first time, sum-frequency mixing of the CVL with a dye laser has been demonstrated, and found to provide a potentially efficient source for tunable UV radiation.

Finally, the acquired high repetition rate laser physics and technology has been applied to record the absorption spectrum of OH in a flame, and some of the laser systems developed here are currently being used for on-going investigations for RIMS and tropospheric hydroxyl radical detection.

8.5 The Future Direction For High Repetition Rate Tunable Laser Research.

It is desirable to re-examine much of the CVL and CVL-pumped dye laser second harmonic generation at higher CVL powers. At the power levels available to the present research, in most cases the SHG conversion efficiency scales linearly with the fundamental power, and so, substantially greater efficiencies should be possible at higher CVL powers. Also, the resonant cavity enhancement of a sub-gigahertz CVL pumped dye laser may provide attractive conversion efficiencies.

The design of a laser system to be used on an airborne platform for the tropospheric detection of hydroxyl radicals is currently under way. To ensure compactness and minimum weight, the proven CVL-pumped dye laser design is to be substituted with a CVL-pumped solid state laser. It is hoped to mix the output of

a CVL-pumped diode-injected Ti:sapphire/Cr:LiCAF laser operating at 776nm with the 511nm line of the CVL, so achieving the 308nm OH excitation wavelength. In this way, the added weight and complexity of the dye circulation system and oscillator tuning mechanism may be obviated.

Undoubtedly, a future direction of research with high repetition rate tunable lasers must lie with tunable solid-state hosts, such as titanium-doped sapphire, and chromium-doped LiSAF and LiCAF. The efficient CVL pumping of a narrow-bandwidth Ti:Sapphire laser has been demonstrated in this laboratory by Knowles and Webb [8.6]. However, the maximum doping level of titanium ions in the sapphire host is limited to 0.15% weight; this, in turn, limits the maximum single pass gain of the laser, and results in long, if not erratic, build-up times. This time synchronization problem poses potential difficulties for many spectroscopic applications, especially those where the output of the Ti:Sapphire laser is to be mixed with that from another laser source. Modelling by the present author shows that the increased doping level available to Cr:LiCAF/LiSAF offers an alternative to Ti:Sapphire where the build-up times may be substantially reduced.

A cursory examination of the frequency doubling of a CVL-pumped Ti:Sapphire laser has been attempted by Knowles and the present author. Initial conversion efficiencies in excess of 20% in LBO have been demonstrated, although intra-cavity SHG of the near SLM diode-seeded CVL-pumped Ti:Sapphire laser appears to be the most promising method for generating narrow-band tunable radiation in the range 350-500nm.

Chapter 8 : References

[8.1] U. Krönert *et al.*
Laser Resonant Ionization of Plutonium
Appl. Phys. B 38 65-70 (1985)

[8.2] G.S. Hurst, M.G. Payne, S.D. Kramer & J.P. Young
Resonance Ionization Spectroscopy and One Atom Detection
Rev. Mod. Phys. 51 767-819 (1979)

[8.3] A. Hofzumahaus, H-P. Dorn & U. Platt
Tropospheric OH radical measurement techniques : Recent Developments.
Physico-Chemical Behaviour of Atmospheric Pollutants Ed. G. Restelli, G. Angeletti. Kluwer Academic Press (1990)

[8.4] C.C. Wang, L.I. Davies Jr., C.H. Wu & S. Japar
Laser-Induced Dissociation Of Ozone And Resonance Fluorescence Of OH In Ambient Air
Appl. Phys. Lett. 28 14-16 (1976)

[8.5] A. Hofzumahaus & F. Holland
KFA Jülich, Germany
Private Communication.

[8.6] M.R.H. Knowles & C.E. Webb
Efficient High-Power Copper-Vapour-Laser Pumped Ti:Al_2O_3 laser.
Opt. Lett. 18 607-609 (1993)

Appendix A : Mathcad Model Listings.

A.1 Longitudinally Pumped Amplifier Calculations.

A.2 Optimum Gain Length For Transversely Pumped Amplifiers.

A.3 Seed Power Scaling For Transversely Pumped Amplifiers.

A.4 Pump Power Scaling For Transversely Pumped Amplifiers.

A.5 Type I Phase-Match Calculations in BBO.

A.6 Type II Phase-Match Calculations in BBO.

A.7 Type I Phase-Match Calculations in Lithium Iodate.

A.8 Type I Phase-Match Calculations in The Biaxial Crystal LBO.

A.9 Type II Phase-Match Calculations in The Biaxial Crystal LBO.

A.10 Type I Phase-Match Calculations in LBO at $\theta=90°$.

A.11 Boyd & Kleinman Theory : Variation of The SHG Efficiency With Phase-Mismatch and Strength of Focusing.

A.12 Non-Collinear Interaction Model.

A.13 Type I SFM Calculations in BBO.

Longitudinally Pumped Amplifier Calculations

Define Dye and Laser Parameters

$\sigma ol := 1.25 \cdot 10^{-18}$ absorption cross section 0-1 for the dye laser

$\sigma op := 1.66 \cdot 10^{-16}$ absorption cross section 0-1 for the pump laser

$\sigma e := 1.76 \cdot 10^{-16}$ stimulated emission cross section of the dye laser

$\sigma 12 := 0.9143 \cdot 10^{-16}$ absorption cross section 1-2 for the dye laser

$\sigma eff := \sigma e - \sigma 12$ effective stimulated emission cross section

$\tau := 4.8 \cdot 10^{-9}$ natural decay lifetime of the first excited singlet

$N := 6 \cdot 10^{17}$ density of dye molecules 1mM (no./cc)

$Pp := 10$ pump power

$Pos := 0.05$ oscillator power

$Posl := 0.02$

$f := 6500$ repetition rate

$h := 1.05 \cdot 10^{-34}$ Planck's constant

$\omega p := 3.69 \cdot 10^{15}$ Pump angular frequency

$\lambda p := 511 \cdot 10^{-9}$

$\omega l := 3.28 \cdot 10^{15}$ Oscillator angular frequency

$\lambda l := 570 \cdot 10^{-9}$

$\delta t := 50 \cdot 10^{-9}$ Pulselength

$\delta tl := 30 \cdot 10^{-9}$ oscillator pulselength

$wL := 0.05$ pump laser focus width

$wl := 0.001$ oscillator beam area

$\rho := 0.000001$ $\rho 1 := 0.25$ $\rho 2 := 0.5$ Different values of the rho parameter

$Ip := \frac{Pp}{f \cdot h \cdot \omega p \cdot \delta t \cdot 0.001}$ Pump Intensity

$G := 50$ Gain

$T := e^{-3}$ Dye Transmission

$j := 1 .. 100$

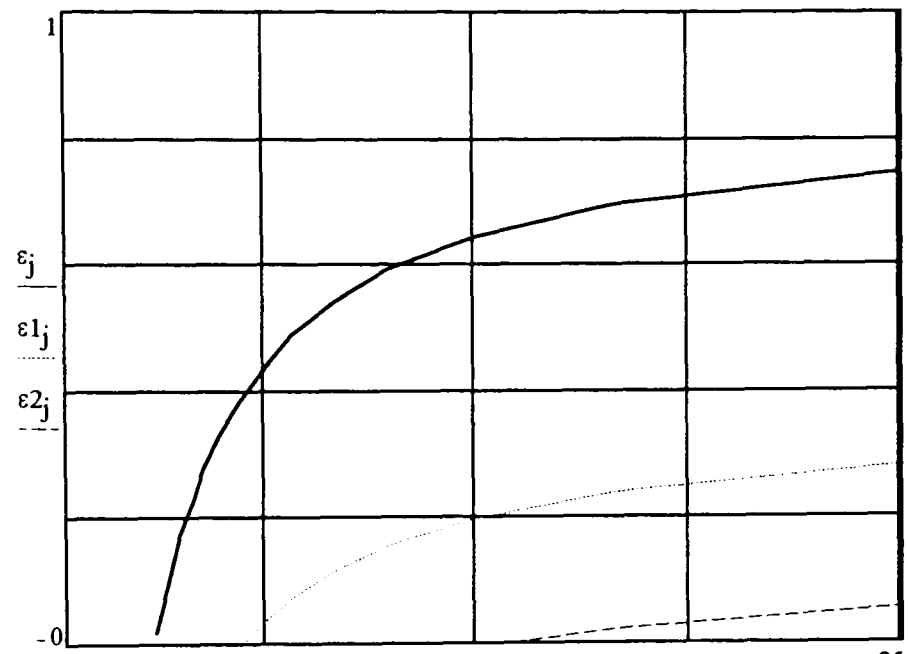
$Ip_j := Ip \cdot \frac{1}{j}$

$$\varepsilon_j := \frac{\lambda p}{\lambda l}\cdot(1+\rho)\cdot\frac{G-1}{G^{1+\rho}-1}\cdot\left(1-T\cdot G^{\rho}-\frac{G^{\rho}-1}{\rho\cdot\sigma e\cdot\tau\cdot Ip_j}\right)$$

$$\varepsilon 1_j := \frac{\lambda p}{\lambda l}\cdot(1+\rho 1)\cdot\frac{G-1}{G^{1+\rho 1}-1}\cdot\left(1-T\cdot G^{\rho 1}-\frac{G^{\rho 1}-1}{\rho 1\cdot\sigma e\cdot\tau\cdot Ip_j}\right)$$

$$\varepsilon 2_j := \frac{\lambda p}{\lambda l}\cdot(1+\rho 2)\cdot\frac{G-1}{G^{1+\rho 2}-1}\cdot\left(1-T\cdot G^{\rho 2}-\frac{G^{\rho 2}-1}{\rho 2\cdot\sigma e\cdot\tau\cdot Ip_j}\right)$$

Scaling of The LPA Extraction Efficiency Vs. Pump Intensity



OPTIMUM GAIN LENGTH FOR PULSED DYE AMPLIFIER

$\sigma ol := 1.25 \cdot 10^{-18}$ absorption cross section 0-1 for the dye laser

$\sigma op := 1.66 \cdot 10^{-16}$ absorption cross section 0-1 for the pump laser

$\sigma e := 1.76 \cdot 10^{-16}$ stimulated emission cross section of the dye laser

$\sigma 12 := 0.9143 \cdot 10^{-16}$ absorption cross section 1-2 for the dye laser

$\sigma eff := \sigma e - \sigma 12$ effective stimulated emission cross section

$\tau := 4.8 \cdot 10^{-9}$ natural decay lifetime of the first excited singlet

$N := 6 \cdot 10^{17}$ density of dye molecules 1 mM (no./cc)

$Pp := 4$ pump power

$Pos := 0.05$ oscillator power

$Pos1 := 0.02$

$f := 6500$ repetition rate

$h := 1.05 \cdot 10^{-34}$ Planck's constant

$\omega p := 3.69 \cdot 10^{15}$ Pump angular frequency

$\omega l := 3.28 \cdot 10^{15}$ Oscillator angular frequency

$\delta t := 50 \cdot 10^{-9}$ Pulselength

$\delta tl := 30 \cdot 10^{-9}$ oscillator pulselength

$wL := 0.05$ pump laser focus width

$wl := 0.001$ oscillator beam area

$$Ios := Pos \cdot \frac{0.493}{f \cdot h \cdot \omega l \cdot \delta tl \cdot wl}$$ Oscillator Intensity

$$Ios1 := Pos1 \cdot \frac{0.493}{f \cdot h \cdot \omega l \cdot \delta tl \cdot wl}$$

$l := 1 .. 50$ Dye gain length * 100

$L_l := l \cdot \frac{1}{25}$ Actual dye gain length

$$Ip_l := Pp \cdot \frac{0.415}{f \cdot h \cdot \omega p \cdot \delta t \cdot wL \cdot L_l}$$ Pump Intensity

$$\alpha 0_l := \sigma eff \cdot N \cdot \frac{\sigma op \cdot Ip_l \cdot \tau - \frac{\sigma ol}{\sigma eff}}{1 + \sigma op \cdot Ip_l \cdot \tau}$$

SamII Signal Gain

$$\Gamma := \tau \cdot (\sigma e + \sigma ol)$$

$$Is_l := \frac{1 + \sigma op \cdot Ip_l \cdot \tau}{\Gamma}$$

Saturation Intensity

$$\xi_l := \sigma ol \cdot \sigma 12 \cdot N \cdot \frac{\tau}{1 + \sigma op \cdot Ip_l \cdot \tau}$$

ESA Parameter

Calculate The Gain Using The ESA Theory

$G := 1 \qquad G1 := 1$

$$G_l := root\left[G - \frac{\alpha 0_l}{Ios \cdot \xi_l} + \left(\frac{\alpha 0_l}{Ios \cdot \xi_l} - 1 \right) \cdot \exp\left[\frac{\ln(G) - \alpha 0_l \cdot L_l}{1 + \frac{\alpha 0_l}{\xi_l \cdot Is_l}} \right], G \right]$$

$$G1_l := root\left[G1 - \frac{\alpha 0_l}{Ios1 \cdot \xi_l} + \left(\frac{\alpha 0_l}{Ios1 \cdot \xi_l} - 1 \right) \cdot \exp\left[\frac{\ln(G1) - \alpha 0_l \cdot L_l}{1 + \frac{\alpha 0_l}{\xi_l \cdot Is_l}} \right], G1 \right]$$

Calculate The Gain Using The Hargrove & Kan Theory

$G2 := 1 \qquad G3 := 1$

$$G2_l := root\left[\alpha 0_l \cdot L_l - \frac{Ios}{Is_l} \cdot (G2 - 1) - \ln(G2), G2 \right]$$

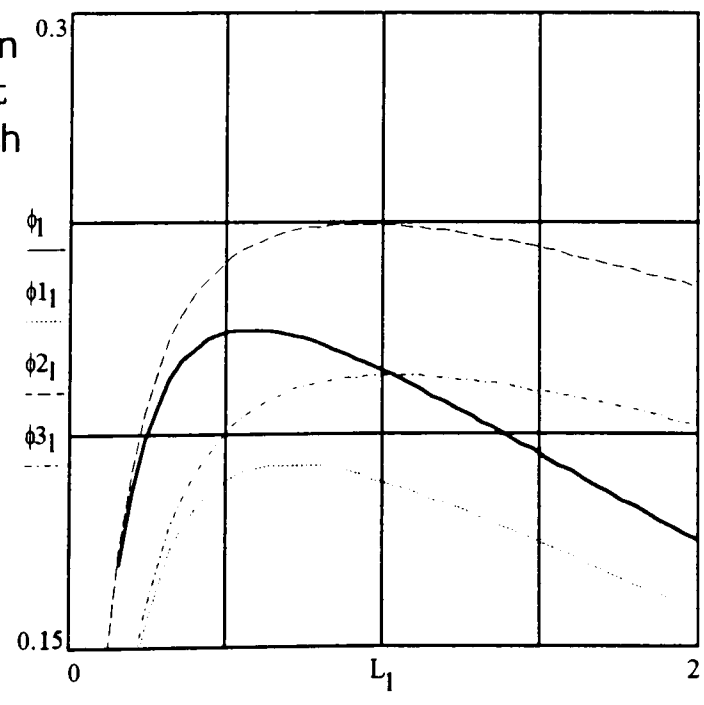
$$G3_l := root\left[\alpha 0_l \cdot L_l - \frac{Ios1}{Is_l} \cdot (G3 - 1) - \ln(G3), G3 \right]$$

Calculate The Corresponding Extraction Efficiencies

$$\phi_l := (G_l - 1) \cdot \frac{Pos}{Pp} \qquad \phi 1_l := (G1_l - 1) \cdot \frac{Pos1}{Pp}$$

$$\phi 2_l := (G2_l - 1) \cdot \frac{Pos}{Pp} \qquad \phi 3_l := (G3_l - 1) \cdot \frac{Pos1}{Pp}$$

Scaling Of The Extraction Efficiency With Respect To Amplifier Gain Length



OSCILLATOR SEED POWER SCALING IN A PULSED DYE AMPLIFIER

$\sigma ol := 1.25 \cdot 10^{-18}$ absorption cross section 0-1 for the dye laser

$\sigma op := 1.66 \cdot 10^{-16}$ absorption cross section 0-1 for the pump laser

$\sigma e := 1.76 \cdot 10^{-16}$ stimulated emission cross section of the dye laser

$\sigma 12 := 0.9143 \cdot 10^{-16}$ absorption cross section 1-2 for the dye laser

$\sigma eff := \sigma e - \sigma 12$ effective stimulated emission cross section

$\tau := 4.8 \cdot 10^{-9}$ natural decay lifetime of the first excited singlet

$N := 6 \cdot 10^{17}$ density of dye molecules 1 mM (no./cc)

$Ppl := 2$
$Pp := 5$ pump power

$Pos := 0.5$ oscillator power

$f := 6500$ repetition rate

$h := 1.05 \cdot 10^{-34}$ Planck's constant

$\omega p := 3.69 \cdot 10^{15}$ Pump angular frequency

$\omega l := 3.28 \cdot 10^{15}$ Oscillator angular frequency

$\delta t := 50 \cdot 10^{-9}$ Pulselength

$\delta tl := 30 \cdot 10^{-9}$ oscillator pulselength

$wL := 0.03$ pump laser focus width

$wl := 0.001$ oscillator beam area

$j := 1 .. 100$

$Pos_j := Pos \cdot \frac{j}{100}$ Oscillator Power

$Ios_j := Pos_j \cdot \frac{1}{f \cdot h \cdot \omega l \cdot \delta tl \cdot wl}$ Oscillator Intensity

$L := 2$ Actual dye gain length

$Ip := Pp \cdot \frac{0.632}{f \cdot h \cdot \omega p \cdot \delta t \cdot wL \cdot L}$

$Ipl := Ppl \cdot \frac{0.632}{f \cdot h \cdot \omega p \cdot \delta t \cdot wL \cdot L}$ Pump Intensity

$$\alpha 0 := \sigma eff \cdot N \cdot \frac{\sigma op \cdot Ip \cdot \tau - \frac{\sigma ol}{\sigma eff}}{1 + \sigma op \cdot Ip \cdot \tau} \qquad \alpha 01 := \sigma eff \cdot N \cdot \frac{\sigma op \cdot Ip1 \cdot \tau - \frac{\sigma ol}{\sigma eff}}{1 + \sigma op \cdot Ip1 \cdot \tau}$$

Small Signal Gain

$$\Gamma := \tau \cdot (\sigma e + \sigma ol)$$

$$Is := \frac{1 + \sigma op \cdot Ip \cdot \tau}{\Gamma} \qquad Is1 := \frac{1 + \sigma op \cdot Ip1 \cdot \tau}{\Gamma}$$

Saturation Intensity

$$\xi := \sigma ol \cdot \sigma 12 \cdot N \cdot \frac{\tau}{1 + \sigma op \cdot Ip \cdot \tau} \qquad \xi 1 := \sigma ol \cdot \sigma 12 \cdot N \cdot \frac{\tau}{1 + \sigma op \cdot Ip1 \cdot \tau}$$

ESA Parameter

Calculate The Gain Using The ESA Theory

$G := 1 \qquad G1 := 1$

$$G_j := root\left[G - \frac{\alpha 0}{Ios_j \cdot \xi} + \left(\frac{\alpha 0}{Ios_j \cdot \xi} - 1 \right) \cdot \exp\left(\frac{\ln(G) - \alpha 0 \cdot L}{1 + \frac{\alpha 0}{\xi \cdot Is}} \right), G \right]$$

$$G1_j := root\left[G1 - \frac{\alpha 01}{Ios_j \cdot \xi 1} + \left(\frac{\alpha 01}{Ios_j \cdot \xi 1} - 1 \right) \cdot \exp\left(\frac{\ln(G1) - \alpha 01 \cdot L}{1 + \frac{\alpha 01}{\xi 1 \cdot Is1}} \right), G1 \right]$$

Calculate The Gain Using The Hargrove & Kan Theory

$G3 := 0.9 \qquad G4 := 1$

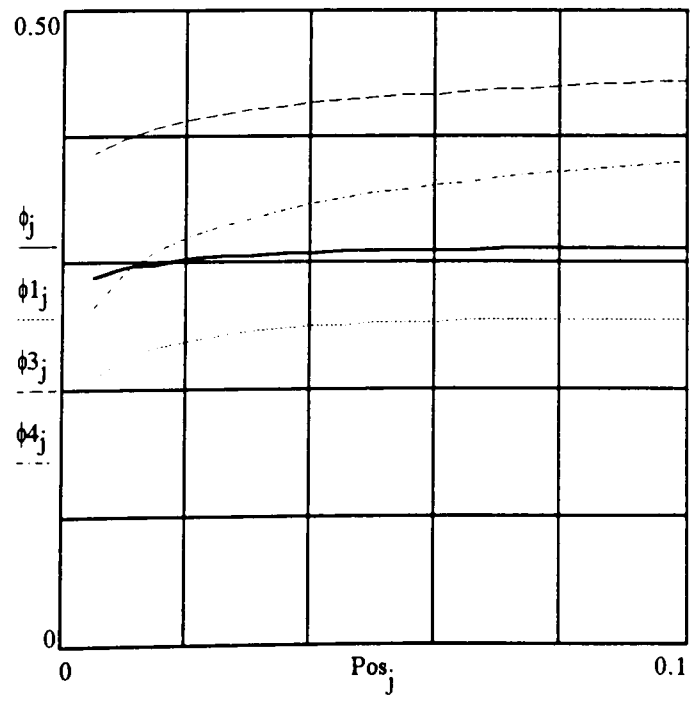
$$G3_j := root\left[\alpha 0 \cdot L - \frac{Ios_j}{Is} \cdot (G3 - 1) - \ln(G3), G3 \right]$$

$$G4_j := root\left[\alpha 01 \cdot L - \frac{Ios_j}{Is1} \cdot (G4 - 1) - \ln(G4), G4 \right]$$

Calculate The Corresponding Extraction Efficiencies

$$\phi_j := (G_j - 1) \cdot \frac{Pos_j}{Pp} \qquad \phi 1_j := (G1_j - 1) \cdot \frac{Pos_j}{Pp1}$$

$$\phi 3_j := (G3_j - 1) \cdot \frac{Pos_j}{Pp} \qquad \phi 4_j := (G4_j - 1) \cdot \frac{Pos_j}{Pp1}$$



PUMP POWER SCALING IN A PULSED DYE AMPLIFIER

$\sigma ol := 1.25 \cdot 10^{-18}$ absorption cross section 0-1 for the dye laser

$\sigma op := 1.66 \cdot 10^{-16}$ absorption cross section 0-1 for the pump laser

$\sigma e := 1.76 \cdot 10^{-16}$ stimulated emission cross section of the dye laser

$\sigma 12 := 0.9143 \cdot 10^{-16}$ absorption cross section 1-2 for the dye laser

$\sigma eff := \sigma e - \sigma 12$ effective stimulated emission cross section

$\tau := 4.8 \cdot 10^{-9}$ natural decay lifetime of the first excited singlet

$N := 6 \cdot 10^{17}$ density of molecules 1mM (no./cc)

$Pp := 5$ pump power

$Pos := 0.1$ oscillator power

$Pos1 := 0.02$

$f := 6500$ repetition rate

$h := 1.05 \cdot 10^{-34}$ Planck's constant

$\omega p := 3.69 \cdot 10^{15}$ Pump angular frequency

$\omega l := 3.28 \cdot 10^{15}$ Oscillator angular frequency

$\delta t := 50 \cdot 10^{-9}$ Pulselength

$\delta tl := 30 \cdot 10^{-9}$ oscillator pulselength

$wL := 0.03$ pump laser focus width

$wl := 0.001$ oscillator beam area

$Ios := Pos \cdot \frac{1}{f \cdot h \cdot \omega l \cdot \delta tl \cdot wl}$ Oscillator Intensity

$Ios1 := Pos1 \cdot \frac{1}{f \cdot h \cdot \omega l \cdot \delta tl \cdot wl}$

$L := 2$ Actual dye gain length

$j := 1 .. 50$

$Pp_j := Pp \cdot \frac{j}{50}$ Pump Power

$Ip_j := Pp_j \cdot \frac{0.632}{f \cdot h \cdot \omega p \cdot \delta t \cdot wL \cdot L}$ Pump Intensity

$$\alpha 0_j := \sigma eff \cdot N \cdot \frac{\sigma op \cdot Ip_j \cdot \tau - \frac{\sigma ol}{\sigma eff}}{1 + \sigma op \cdot Ip_j \cdot \tau}$$ Small Signal Gain

$$\Gamma := \tau \cdot (\sigma e + \sigma ol)$$

$$Is_j := \frac{1 + \sigma op \cdot Ip_j \cdot \tau}{\Gamma}$$ Saturation Intensity

$$\xi_j := \sigma ol \cdot \sigma 12 \cdot N \cdot \frac{\tau}{1 + \sigma op \cdot Ip_j \cdot \tau}$$ ESA Parameter

Calculate The Gain Using The ESA Theory

$G := 1 \qquad G1 := 1$

$$G_j := root\left[G - \frac{\alpha 0_j}{Ios \cdot \xi_j} + \left(\frac{\alpha 0_j}{Ios \cdot \xi_j} - 1 \right) \cdot \exp\left[\frac{\ln(G) - \alpha 0_j \cdot L}{1 + \frac{\alpha 0_j}{\xi_j \cdot Is_j}} \right], G \right]$$

$$G1_j := root\left[G1 - \frac{\alpha 0_j}{Ios1 \cdot \xi_j} + \left(\frac{\alpha 0_j}{Ios1 \cdot \xi_j} - 1 \right) \cdot \exp\left[\frac{\ln(G1) - \alpha 0_j \cdot L}{1 + \frac{\alpha 0_j}{\xi_j \cdot Is_j}} \right], G1 \right]$$

Calculate The Gain Using The Hargrove & Kan Theory

$G3 := 1 \qquad G4 := 1$

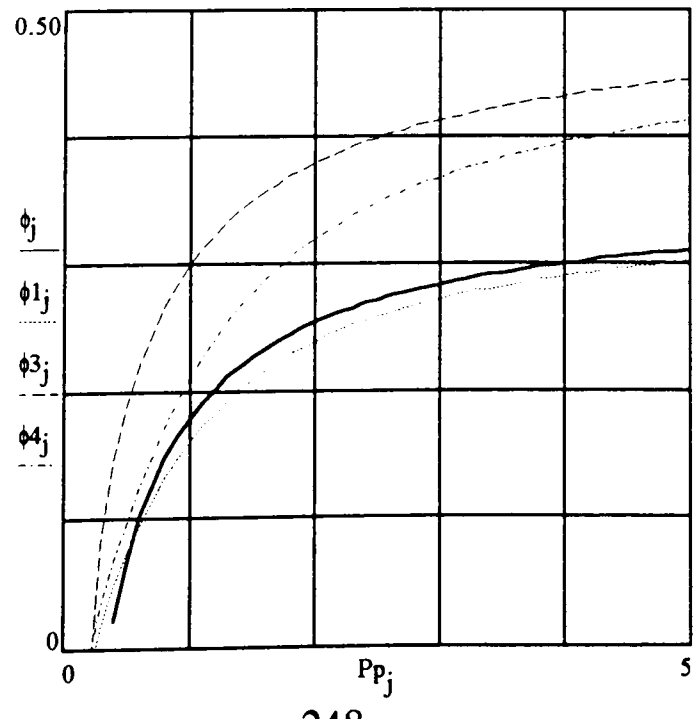
$$G3_j := root\left[\alpha 0_j \cdot L - \frac{Ios}{Is_j} \cdot (G3 - 1) - \ln(G3), G3 \right]$$

$$G4_j := root\left[\alpha 0_j \cdot L - \frac{Ios1}{Is_j} \cdot (G4 - 1) - \ln(G4), G4 \right]$$

Calculate The Corresponding Extraction Efficiencies

$$\phi_j := \left(G_j - 1\right) \cdot \frac{Pos}{Pp_j} \qquad \phi 1_j := \left(G1_j - 1\right) \cdot \frac{Pos1}{Pp_j}$$

$$\phi 3_j := \left(G3_j - 1\right) \cdot \frac{Pos}{Pp_j} \qquad \phi 4_j := \left(G4_j - 1\right) \cdot \frac{Pos1}{Pp_j}$$



Calculation of the Phase Match Angles for Type I SHG in β-BBO

$Ane := 2.3730$

$Bne := 0.0128$

$Cne := -0.0156$

$Dne := -0.0044$

Sellmier Coefficients for the Extraordinary Polarization

$Ano := 2.7405$

$Bno := 0.0184$

$Cno := -0.0179$

$Dno := -0.0155$

Sellmier Coefficients for the Ordinary Polarization

Calculate The e- and o-wave Refractive Indices as a Function of Wavelength

$i := 1 .. 600$

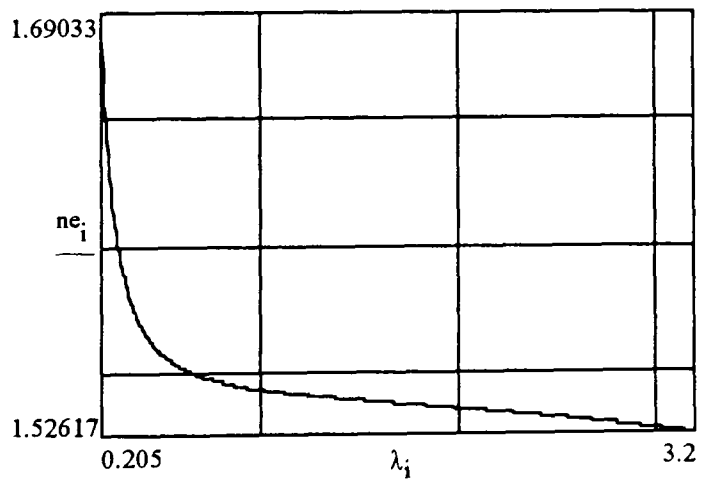
$\lambda_i := 200 \cdot 10^{-3} + i \cdot 5 \cdot 10^{-3}$ Wavelength

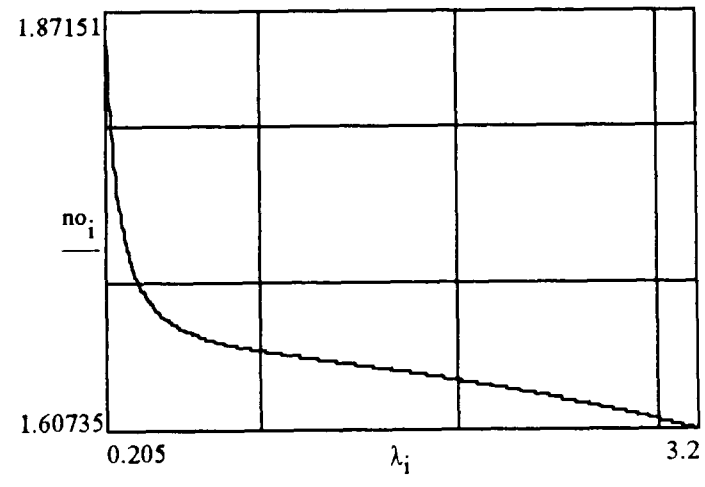
$$ne_i := \sqrt{Ane + \frac{Bne}{(\lambda_i)^2 + Cne} + Dne \cdot (\lambda_i)^2}$$

n(e-wave)

$$no_i := \sqrt{Ano + \frac{Bno}{(\lambda_i)^2 + Cno} + Dno \cdot (\lambda_i)^2}$$

n(o-wave)





Calculate The Phase Matching Angle

$l := 1 .. 150$

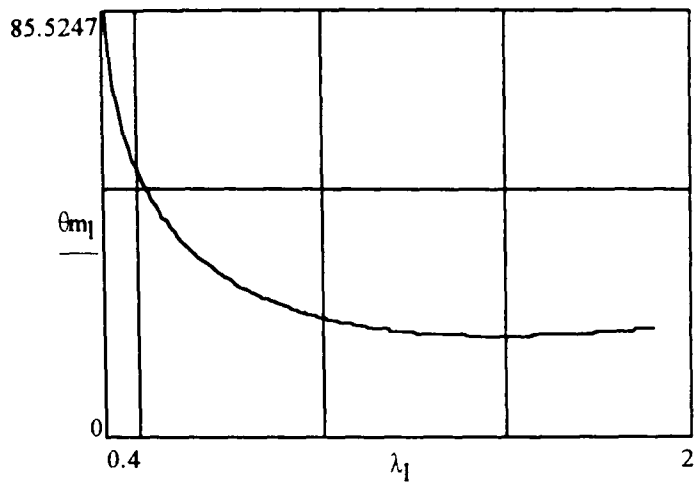
$$\theta m_l := \operatorname{acos}\left[\sqrt{\frac{(no_{l \cdot 2 + 40})^{-2} - (ne_l)^{-2}}{(no_l)^{-2} - (ne_l)^{-2}}}\right]$$

Phase Match Angle

$\lambda_l := 400 \cdot 10^{-3} + 10 \cdot 10^{-3} \cdot l$

$$\theta m_l := \theta m_l \cdot \frac{180}{3.142}$$

Plot of Phase Match Angle Vs. Wavelength For Type I SHG



1 := 10.. 25

θm_1	λ_1
52.154	0.5
50.545	0.51
49.061	0.52
47.686	0.53
46.407	0.54
45.212	0.55
44.093	0.56
43.041	0.57
42.05	0.58
41.115	0.59
40.23	0.6
39.392	0.61
38.596	0.62
37.84	0.63
37.12	0.64
36.433	0.65

Calculation of the Phase Match Angles for Type II SHG in β-BBO

Ane := 2.3730

Bne := 0.0128

Cne := - 0.0156

Dne := - 0.0044

Sellmier Coefficients for the Extraordinary Polarization

Ano := 2.7405

Bno := 0.0184

Cno := - 0.0179

Dno := - 0.0155

Sellmier Coefficients for the Ordinary Polarization

Calculate The e- and o- wave Refractive Indices as a Function of Wavelength

i := 1 .. 600

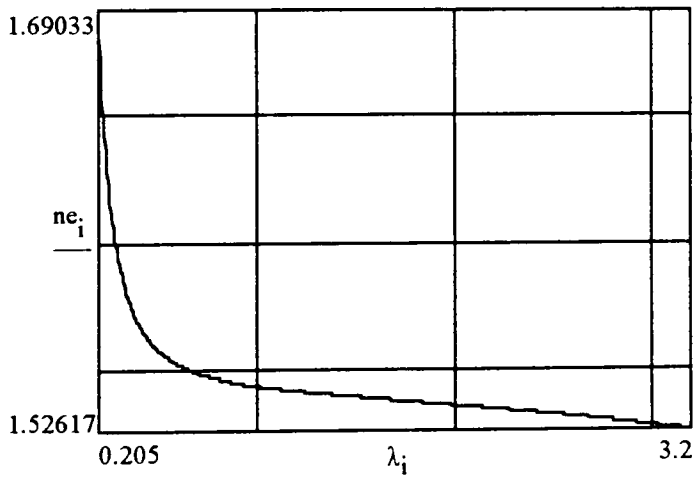
$\lambda_i := 200 \cdot 10^{-3} + i \cdot 5 \cdot 10^{-3}$ Wavelength

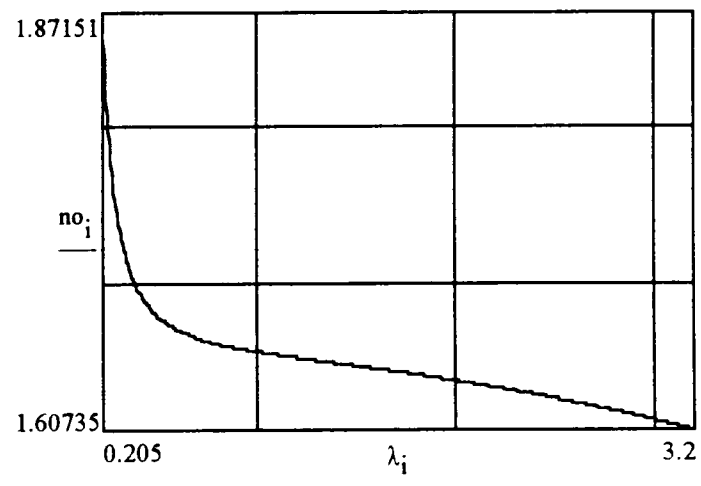
$$ne_i := \sqrt{Ane + \frac{Bne}{(\lambda_i)^2 + Cne} + Dne \cdot (\lambda_i)^2}$$

n(e-wave)

$$no_i := \sqrt{Ano + \frac{Bno}{(\lambda_i)^2 + Cno} + Dno \cdot (\lambda_i)^2}$$

n(o-wave)





Calculate The Type II Phase Matching Angles

l := 1 .. 150

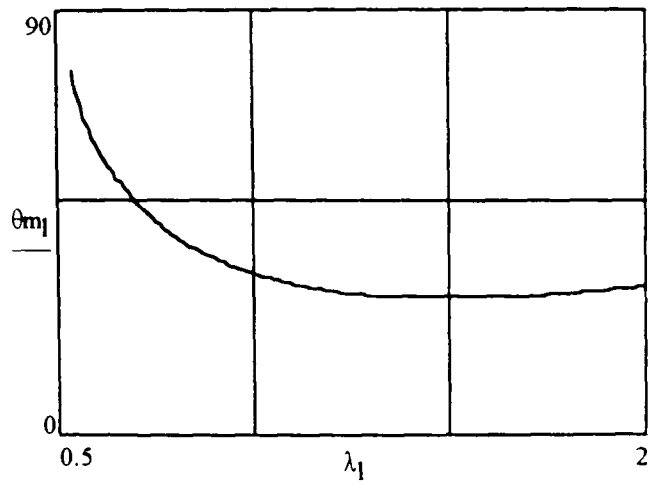
θ := 0.4

$$\theta m_l := \text{root}\left[\frac{2 \cdot ne_{l+13} \cdot no_{l+13}}{\sqrt{(no_{l+13})^2 \cdot \sin(\theta)^2 + (ne_{l+13})^2 \cdot \cos(\theta)^2}} - \frac{no_{l \cdot 2+66} \cdot ne_{l \cdot 2+66}}{\sqrt{(no_{l \cdot 2+66})^2 \cdot \sin(\theta)^2 + (ne_{l \cdot 2+66})^2 \cdot \cos(\theta)^2}} - no_{l \cdot 2+66}, \theta\right]$$

$\lambda_l := 400 \cdot 10^{-3} + 10 \cdot 10^{-3} \cdot (l + 13)$

$$\theta m_l := \theta m_l \cdot \frac{180}{3.142}$$

Plot of the Phase Match Angle For Type II SHG



l := 1 .. 15

θm_l	λ_l
77.218	0.54
72.968	0.55
69.792	0.56
67.198	0.57
64.971	0.58
63.002	0.59
61.227	0.6
59.605	0.61
58.109	0.62
56.72	0.63
55.424	0.64
54.209	0.65
53.504	0.66
52.304	0.67
51.183	0.68

Calculation of the Phase Match Angles for Type I SHG in LiIO3

$Ane := 2.913366$

$Bne := 0.034267$

$Cne := -0.033230$

$Dne := -0.00$

Sellmier Coefficients for the Extraordinary Polarization

$Ano := 3.425834$

$Bno := 0.046664$

$Cno := -0.032155$

$Dno := -0.010334$

Sellmier Coefficients for the Ordinary Polarization

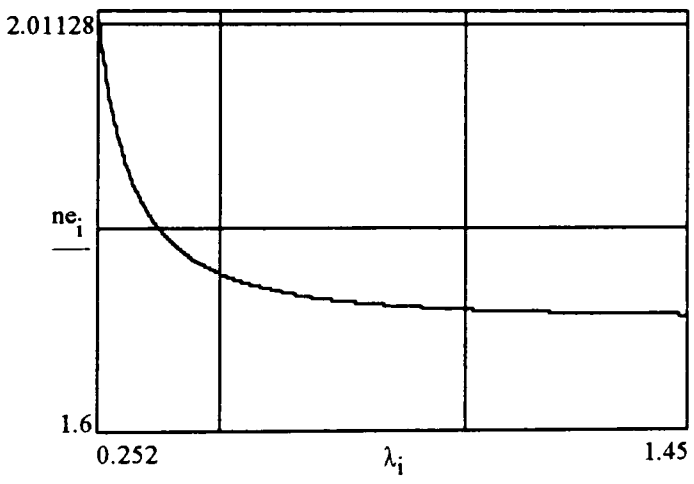
Calculate The e- and o-wave Refractive Indices as a Function of Wavelength

$i := 1 .. 600$

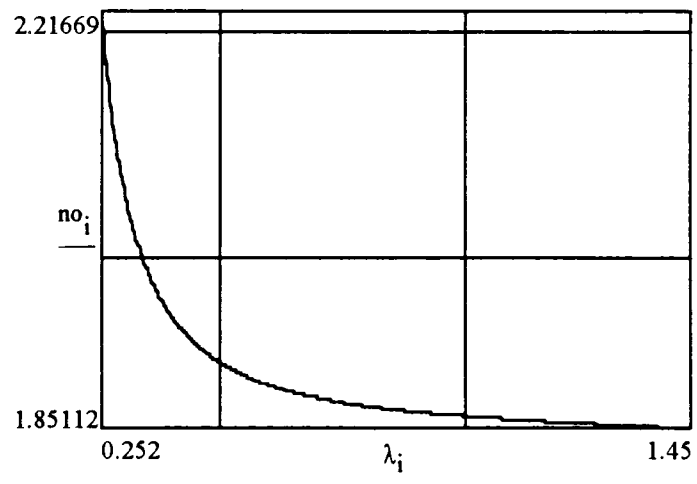
$\lambda_i := 250 \cdot 10^{-3} + i \cdot 2 \cdot 10^{-3}$

$$ne_i := \sqrt{Ane + \frac{Bne}{(\lambda_i)^2 + Cne} + Dne \cdot (\lambda_i)^2} \qquad no_i := \sqrt{Ano + \frac{Bno}{(\lambda_i)^2 + Cno} + Dno \cdot (\lambda_i)^2}$$

n(e-wave)



n(o-wave)



Calculate The Type I Phase Matching Angles

$l := 1 .. 150$

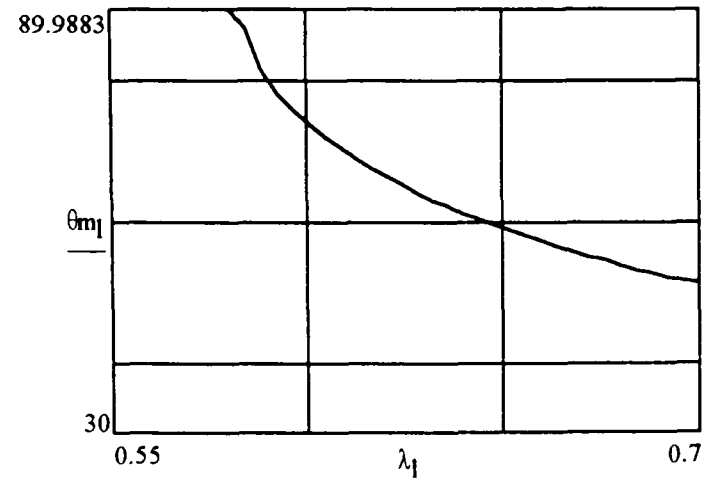
$$\theta m_l := \operatorname{acos}\left[\sqrt{\frac{(no_{l \cdot 2 + 125})^{-2} - (ne_l)^{-2}}{(no_l)^{-2} - (ne_l)^{-2}}}\right]$$

Phase Match Angle

$\lambda_l := 500 \cdot 10^{-3} + 4 \cdot 10^{-3} \cdot l$

$\theta m_l := \theta m_l \cdot \frac{180}{3.142}$

Plot of Phase Match Angle For Type I SHG in Lithium Iodate



$i := 21 .. 50$

θm_i	λ_i
87.181	0.584
81.356	0.588
78.169	0.592
75.724	0.596
73.681	0.6
71.903	0.604
70.316	0.608
68.877	0.612
67.555	0.616
66.331	0.62
65.188	0.624
64.116	0.628
63.106	0.632
62.149	0.636
61.241	0.64
60.376	0.644
59.551	0.648
58.76	0.652
58.003	0.656
57.275	0.66
56.575	0.664
55.9	0.668
55.25	0.672
54.621	0.676
54.013	0.68
53.425	0.684
52.855	0.688
52.302	0.692
51.765	0.696
51.244	0.7

Phase Match Calculations For Type I SHG In The Biaxial Crystal LBO

Sellmeir Coefficients

$Anx := 2.4543$ $Cnx := -0.0094981$

$Any := 2.5382$ $Cny := -0.011387$

$Anz := 2.5854$ $Cnz := -0.011617$

$Bnx := 0.011413$ $Dnx := -0.013900$

$Bny := 0.012830$ $Dny := -0.017034$

$Bnz := 0.013065$ $Dnz := -0.018146$

Calculate The Principal Refractive Indices as a Function of Wavelength

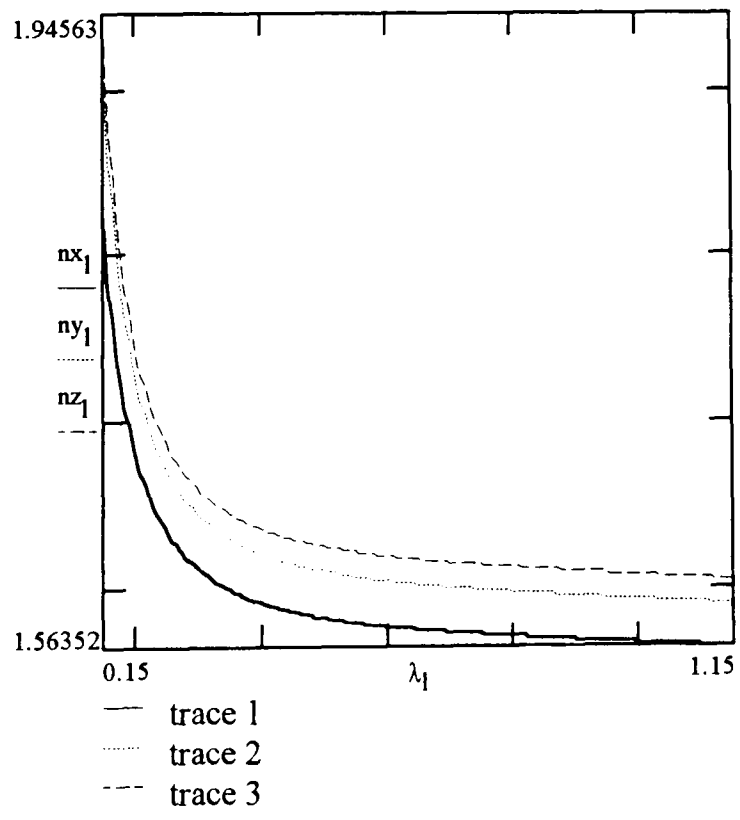
$l := 0 .. 200$

$\lambda_l := \frac{150 + 5 \cdot l}{1000}$ Wavelength in Microns 150nm,160,170..

$$nx_l := \sqrt{Anx + \frac{Bnx}{(\lambda_l)^2 + Cnx} + Dnx \cdot (\lambda_l)^2} \qquad ny_l := \sqrt{Any + \frac{Bny}{(\lambda_l)^2 + Cny} + Dny \cdot (\lambda_l)^2}$$

$$nz_l := \sqrt{Anz + \frac{Bnz}{(\lambda_l)^2 + Cnz} + Dnz \cdot (\lambda_l)^2}$$

nx, ny, nz



Choose The Fundamental Laser Wavelength

$Nx := nx_{86}$ $Ny := ny_{86}$ $Nz := nz_{86}$ $\lambda_{86} = 0.58$

$Nx2 := nx_{28}$ $Ny2 := ny_{28}$ $Nz2 := nz_{28}$ $\lambda_{28} = 0.29$

Set Up Dummy Variables For The Phase Match Transcendental

$a1 := Nx^{-2}$ $\quad b1 := Ny^{-2}$ $\quad c1 := Nz^{-2}$

$a2 := Nx2^{-2}$ $\quad b2 := Ny2^{-2}$ $\quad c2 := Nz2^{-2}$

$m := 90..55$

$\theta_m := m \cdot \frac{\pi}{180}$

$\alpha 1_m := \sin(\theta_m)^2 \cdot (b1 + c1)$ $\quad \beta 1_m := \sin(\theta_m)^2 \cdot (a1 + c1)$

$\delta 1_m := \cos(\theta_m)^2 \cdot (a1 + b1)$ $\quad \varepsilon 1_m := \sin(\theta_m)^2 \cdot b1 \cdot c1$

$\Gamma 1_m := \sin(\theta_m)^2 \cdot a1 \cdot c1$ $\quad \Phi 1_m := \cos(\theta_m)^2 \cdot a1 \cdot b1$

$\alpha 2_m := \sin(\theta_m)^2 \cdot (b2 + c2)$ $\quad \beta 2_m := \sin(\theta_m)^2 \cdot (a2 + c2)$

$\delta 2_m := \cos(\theta_m)^2 \cdot (a2 + b2)$ $\quad \varepsilon 2_m := \sin(\theta_m)^2 \cdot b2 \cdot c2$

$\Gamma 2_m := \sin(\theta_m)^2 \cdot a2 \cdot c2$ $\quad \Phi 2_m := \cos(\theta_m)^2 \cdot a2 \cdot b2$

Solve Transcendental For Type I SHG

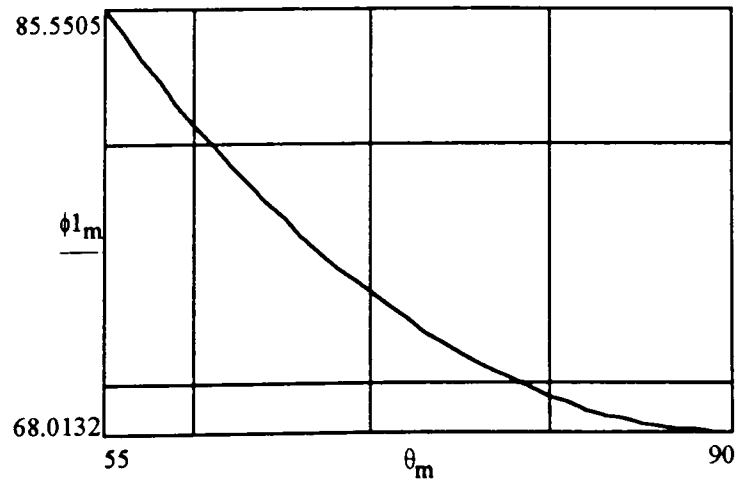
$\phi := 1.3$

$$\phi_m := \text{root}\left[\left[\left[\begin{array}{l} -\left(-\alpha 1_m \cdot \cos(\phi)^2 - \beta 1_m \cdot \sin(\phi)^2 - \delta 1_m\right) \ldots \\ +-\sqrt{\left(-\alpha 1_m \cdot \cos(\phi)^2 - \beta 1_m \cdot \sin(\phi)^2 - \delta 1_m\right)^2 - 4 \cdot \left(\varepsilon 1_m \cdot \cos(\phi)^2 + \Gamma 1_m \cdot \sin(\phi)^2 + \Phi 1_m\right)} \ldots \\ +\left(-\alpha 2_m \cdot \cos(\phi)^2 - \beta 2_m \cdot \sin(\phi)^2 - \delta 2_m\right) \end{array}\right] \ldots \right] \ldots \right] \ldots \right]$$

$$+-\sqrt{\left(-\alpha 2_m \cdot \cos(\phi)^2 - \beta 2_m \cdot \sin(\phi)^2 - \delta 2_m\right)^2 - 4 \cdot \left(\varepsilon 2_m \cdot \cos(\phi)^2 + \Gamma 2_m \cdot \sin(\phi)^2 + \Phi 2_m\right)} \Bigg], \phi \Bigg]$$

$\phi 1_m := \phi_m \cdot \frac{180}{\pi}$ $\quad \theta_m := m$

Theta & Phi Variation For Phasematching 578nm.



Phase Matching Calculations In The Biaxial Crystal LBO

Sellmeir Coefficients

$Anx := 2.4543$ $\quad Cnx := -0.0094981$

$Any := 2.5382$ $\quad Cny := -0.011387$

$Anz := 2.5854$ $\quad Cnz := -0.011617$

$Bnx := 0.011413$ $\quad Dnx := -0.013900$

$Bny := 0.012830$ $\quad Dny := -0.017034$

$Bnz := 0.013065$ $\quad Dnz := -0.018146$

Calculate The Principal Refractive Indices as a Function of Wavelength

$l := 0 .. 200$

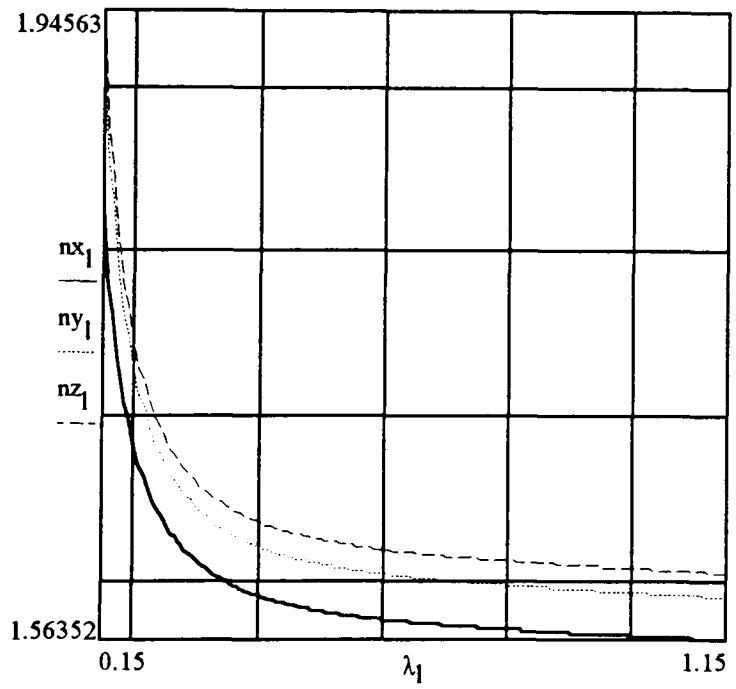
$\lambda_l := \frac{150 + 5 \cdot l}{1000}$ Wavelength in Microns 150nm,160,170..

$$nx_l := \sqrt{Anx + \frac{Bnx}{(\lambda_l)^2 + Cnx} + Dnx \cdot (\lambda_l)^2}$$

$$ny_l := \sqrt{Any + \frac{Bny}{(\lambda_l)^2 + Cny} + Dny \cdot (\lambda_l)^2}$$

$$nz_l := \sqrt{Anz + \frac{Bnz}{(\lambda_l)^2 + Cnz} + Dnz \cdot (\lambda_l)^2}$$

nx,ny,nz



Choose The Fundamental Wavelength

$Nx := nx_{182}$ $\quad Ny := ny_{182}$ $\quad Nz := nz_{182}$ $\quad \lambda_{182} = 1.06$

$Nx2 := nx_{76}$ $\quad Ny2 := ny_{76}$ $\quad Nz2 := nz_{76}$ $\quad \lambda_{76} = 0.53$

$a1 := Nx^{-2}$ $\quad b1 := Ny^{-2}$ $\quad c1 := Nz^{-2}$

$a2 := Nx2^{-2}$ $\quad b2 := Ny2^{-2}$ $\quad c2 := Nz2^{-2}$

$m := 90..18$

$\theta_m := m \cdot \frac{\pi}{180}$

Set Up Dummy Variables

$\alpha 1_m := \sin(\theta_m)^2 \cdot (b1 + c1)$

$\beta 1_m := \sin(\theta_m)^2 \cdot (a1 + c1)$

$\delta 1_m := \cos(\theta_m)^2 \cdot (a1 + b1)$

$\varepsilon 1_m := \sin(\theta_m)^2 \cdot b1 \cdot c1$

$\Gamma 1_m := \sin(\theta_m)^2 \cdot a1 \cdot c1$

$\Phi 1_m := \cos(\theta_m)^2 \cdot a1 \cdot b1$

$\alpha 2_m := \sin(\theta_m)^2 \cdot (b2 + c2)$

$\beta 2_m := \sin(\theta_m)^2 \cdot (a2 + c2)$

$\delta 2_m := \cos(\theta_m)^2 \cdot (a2 + b2)$

$\varepsilon 2_m := \sin(\theta_m)^2 \cdot b2 \cdot c2$

$\Gamma 2_m := \sin(\theta_m)^2 \cdot a2 \cdot c2$

$\Phi 2_m := \cos(\theta_m)^2 \cdot a2 \cdot b2$

Solve Transcendental For Type II SHG

$\phi := 0.5$

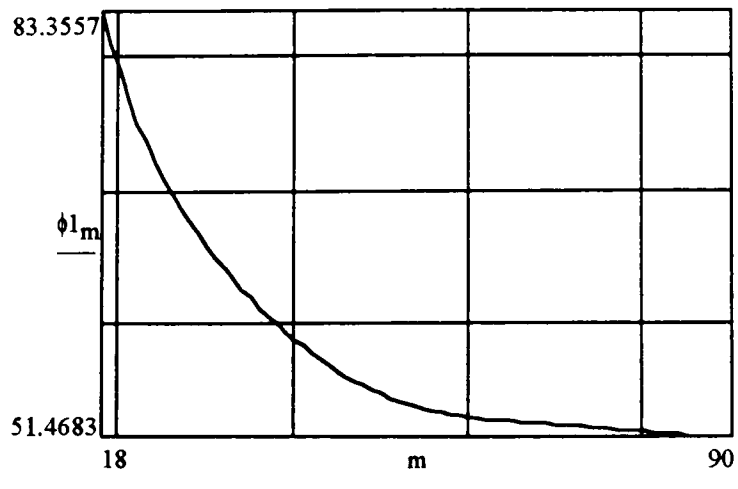
$$\phi_m := \text{root}\left[\left[\frac{1}{2}\cdot\left[\frac{\sqrt{2}}{\sqrt{-\left(-\alpha 1_m\cdot\cos(\phi)^2-\beta 1_m\cdot\sin(\phi)^2-\delta 1_m\right)-\sqrt{\left(-\alpha 1_m\cdot\cos(\phi)^2-\beta 1_m\cdot\sin(\phi)^2-\delta 1_m\right)^2\ldots}}}\ldots\right]\ldots\right],\phi\right]$$

$$+\frac{\sqrt{2}}{\sqrt{-\left(-\alpha 1_m\cdot\cos(\phi)^2-\beta 1_m\cdot\sin(\phi)^2-\delta 1_m\right)+\sqrt{\left(-\alpha 1_m\cdot\cos(\phi)^2-\beta 1_m\cdot\sin(\phi)^2-\delta 1_m\right)^2\ldots}}}$$

$$+\frac{-\sqrt{2}}{\sqrt{-\left(-\alpha 2_m\cdot\cos(\phi)^2-\beta 2_m\cdot\sin(\phi)^2-\delta 2_m\right)+\sqrt{\left(-\alpha 2_m\cdot\cos(\phi)^2-\beta 2_m\cdot\sin(\phi)^2-\delta 2_m\right)^2\ldots}}}$$

$$\phi 1_m := \phi_m \cdot \frac{180}{\pi}$$

Theta & Phi Variation For Type II SHG In LBO (1.06micron)



Calculation of the Phase Match Angles for Type I SHG in LBO (Theta = 90)

Sellmeir Coefficients

Anx := 2.4543

Bnx := 0.011413

Sellmier Coefficients for the x axis

Cnx := - 0.0094981

Dnx := - 0.013900

Any := 2.5382

Bny := 0.01283

Sellmier Coefficients for the y axis

Cny := - 0.011387

Dny := - 0.017034

Anz := 2.5854

Bnz := 0.013065

Sellmeir Coefficiencts for the z axis

Cnz := - 0.011617

Dnz := - 0.018146

Calculate The Principal Refractive Indices as a Function of Wavelength

i := 1 .. 400

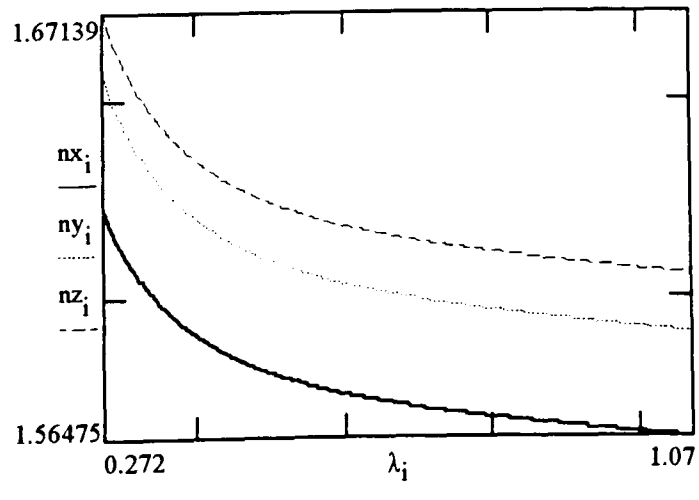
$\lambda_i := 270 \cdot 10^{-3} + i \cdot 2 \cdot 10^{-3}$ $\lambda 2_i := 2 \cdot \lambda_i$

$$nx_i := \sqrt{Anx + \frac{Bnx}{(\lambda_i)^2 + Cnx} + Dnx \cdot (\lambda_i)^2} \qquad nx2_i := \sqrt{Anx + \frac{Bnx}{(\lambda 2_i)^2 + Cnx} + Dnx \cdot (\lambda 2_i)^2}$$

$$ny_i := \sqrt{Any + \frac{Bny}{(\lambda_i)^2 + Cny} + Dny \cdot (\lambda_i)^2} \qquad ny2_i := \sqrt{Any + \frac{Bny}{(\lambda 2_i)^2 + Cny} + Dny \cdot (\lambda 2_i)^2}$$

$$nz_i := \sqrt{Anz + \frac{Bnz}{(\lambda_i)^2 + Cnz} + Dnz \cdot (\lambda_i)^2} \qquad nz2_i := \sqrt{Anz + \frac{Bnz}{(\lambda 2_i)^2 + Cnz} + Dnz \cdot (\lambda 2_i)^2}$$

nx,ny,nz



Calculate The Type I Phase Match Angles For Type I SHG (Theta = 90)

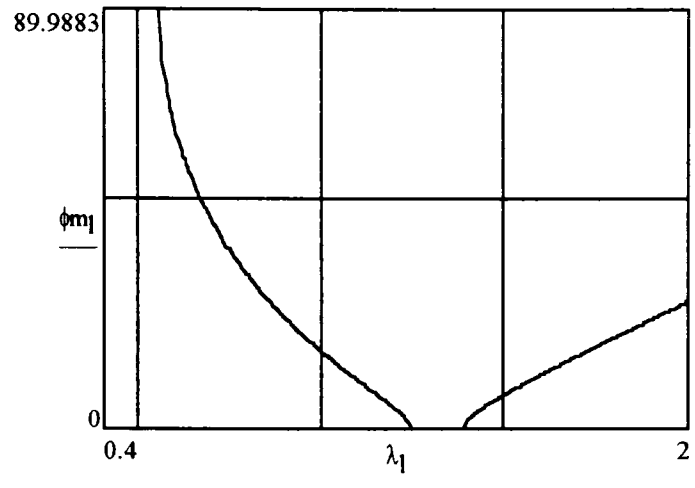
$l := 1 .. 400$

$$\phi m_l := \operatorname{asin}\left[\left[\frac{(ny_l)^2 - (nz2_l)^2}{(ny_l)^2 - (nx_l)^2}\right]^{0.5} \cdot \frac{nx_l}{nz2_l}\right]$$

$$\lambda_l := 540 \cdot 10^{-3} + 4 \cdot 10^{-3} \cdot l$$

$$\phi m_l := \phi m_l \cdot \frac{180}{3.142}$$

Plot of Phase Match Angle In LBO For Type I SHG (Theta = 90)



$l := 1 .. 20$

ϕm_l	λ_l
89.988 – 11.379i	0.544
89.988 – 7.993i	0.548
88.865	0.552
81.866	0.556
78.575	0.56
76.056	0.564
73.941	0.568
72.085	0.572
70.415	0.576
68.886	0.58
67.47	0.584
66.147	0.588
64.901	0.592
63.722	0.596
62.6	0.6
61.53	0.604
60.505	0.608
59.521	0.612
58.573	0.616
57.659	0.62

Boyd & Kleinman Parametric Interaction of Focused Gaussian Beams

Variation of The SHG Power As A Function Of Focusing And Phase Matching

$\rho := 0.12$ Walk Off Angle in LBO @ 570nm SHG

$l := 0.01$ Length of crystal

$\lambda := 616 \cdot 10^{-9}$ Wavelength

$k1 := 2 \cdot \frac{\pi}{\lambda}$ Wavenumber

$\delta := 15 .. 29$

$\alpha := 0 .. 10$ Iteration Variables

$\xi_\delta := \frac{\delta}{10}$ Boyd & Kleinman Focusing Parameter

$\beta_\delta := \rho \cdot \frac{(l \cdot k1)^{0.5}}{2} \cdot (\xi_\delta)^{0.5}$ Boyd & Kleinmand Birefringence Parameter

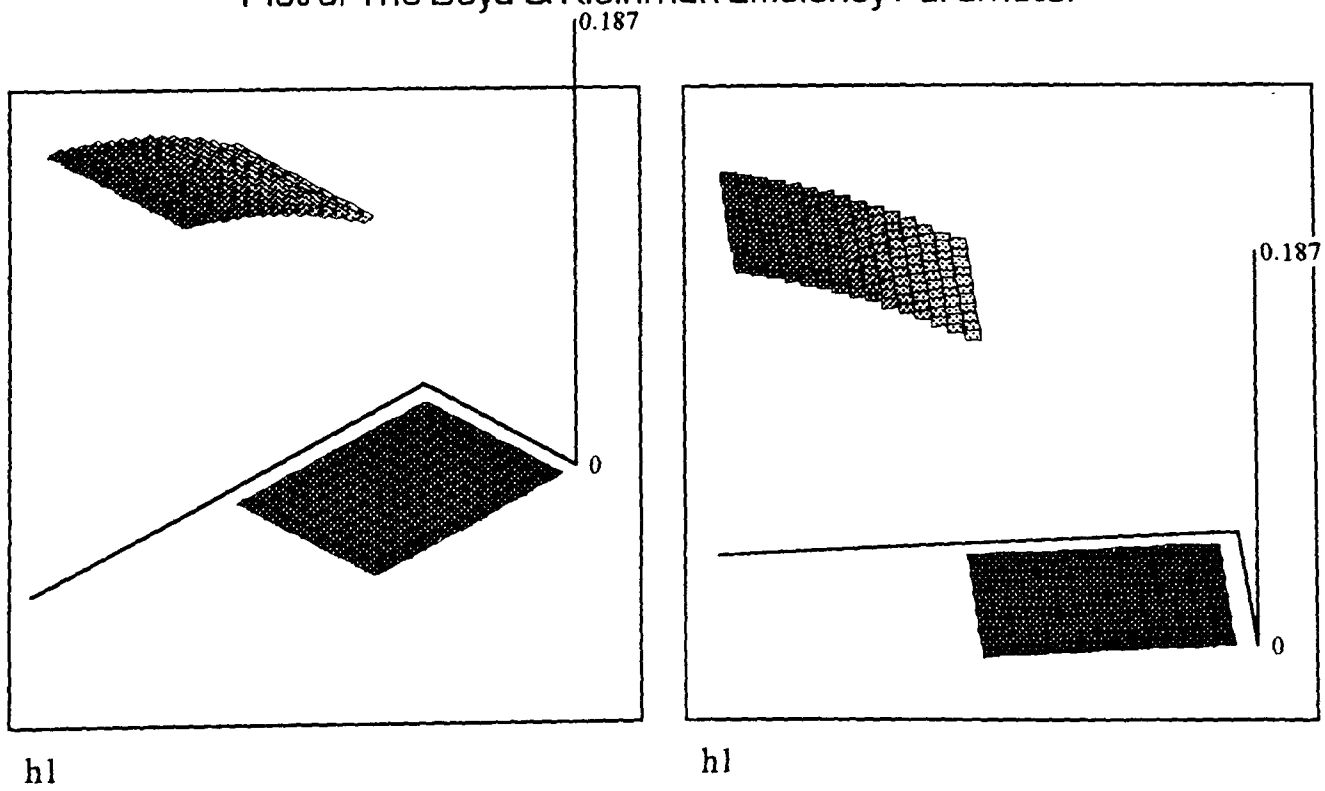
$i := \sqrt{-1}$

$\sigma_\alpha := \frac{\alpha}{50} + 0.55$ Boyd & Kleinmand Phase Mismatch Parameter

$$hl_{\delta,\alpha} := \left[\frac{1}{\xi_\delta} \cdot \int_{-\xi_\delta}^{\xi_\delta} \int_{-\xi_\delta}^{\xi_\delta} \frac{\exp\left[-(\beta_\delta)^2 \cdot (\tau - \tau l)^2 + i \cdot \sigma_\alpha \cdot (\tau - \tau l) \right]}{(1 + i \cdot \tau) \cdot (1 - i \cdot \tau l)} \, d\tau \, d\tau l \right]$$

Boyd & Kleinman Efficiency Parameter

Plot of The Boyd & Kleinman Efficiency Parameter



Calculation of the Non-Collinear SHG Interaction of a CVL in BBO

$Ane := 2.3730$

$Bne := 0.0128$

Sellmier Coefficients for the Extraordinary Polarization

$Cne := -0.0156$

$Dne := -0.0044$

$Ano := 2.7405$

$Bno := 0.0184$

Sellmeir Coefficients for the Ordinary Polarization

$Cno := -0.0179$

$Dno := -0.0155$

$\lambda 1 := 511 \cdot 10^{-3}$ CVL Wavelength

$\lambda 2 := 255 \cdot 10^{-3}$ 2nd Harmonic Wavelegth

Calculate The e- and o-wave Refractive Indices

$$ne1 := \sqrt{Ane + \frac{Bne}{\lambda 1^2 + Cne} + Dne \cdot \lambda 1^2} \qquad no1 := \sqrt{Ano + \frac{Bno}{\lambda 1^2 + Cno} + Dno \cdot \lambda 1^2}$$

$$ne2 := \sqrt{Ane + \frac{Bne}{\lambda 2^2 + Cne} + Dne \cdot \lambda 2^2} \qquad no2 := \sqrt{Ano + \frac{Bno}{\lambda 2^2 + Cno} + Dno \cdot \lambda 2^2}$$

$D := 10 \cdot 10^{-3}$ Diameter of CVL Beam

$f := 0.4$ Focal Length of Lens

$\delta\theta := 0.6 \cdot 10^{-3}$ Divergence of CVL

$wO := 2 \cdot \delta\theta \cdot f$ Bundle Size

$N := \frac{D}{wO}$ Number of Bundles across CVL Beam

$i := 1 .. N$ $N = 20.833$ $centre := ceil\left(\frac{N}{2}\right)$

$$a_i := \int_{(i-1)\cdot wO}^{i \cdot wO} \sqrt{\left[\frac{D^2}{4} - \left[\left(\frac{D}{2} - y\right)^2\right]\right]} \cdot 2 \, dy$$ Area Of 1-D Strips Across Beam

$P := 4$ CVL Average Power

$\tau := 40 \cdot 10^{-9}$ Pulse Length

$\omega := 4000$ Pulse Repetition Rate

$Pp := \frac{P}{\omega \cdot \tau}$ Peak Power

$S := \frac{\pi \cdot \delta\theta^2 \cdot f^2}{4}$ Spot Size in Focal Plane

$Pbp_i := a_i \cdot 4 \cdot \frac{Pp}{\pi \cdot D^2}$ Peak Power of Each Bundle

$ZO := 377$ Impedance of Free Space

$n := 1.6$ Average Refractive Index

$deff := 1.6 \cdot 10^{-12}$ Effective Non-Linear Coefficient

$\beta := 8 \cdot \pi \cdot ZO \cdot \frac{deff^2}{\lambda 1^2 \cdot n^3 \cdot S^2}$ Lumped Harmonic Constants

$\rho := 0.0833$ Walk-Off Angle

$lc := 10 \cdot 10^{-3}$ Crystal Length

$k := 1 .. N$

$j := 1 .. N$

$\theta_{(k,j)} := \operatorname{atan}\left[(k - j + 1) \cdot \frac{w0}{f} \cdot \frac{1}{2} \right]$ $\theta_{k,j} := \sqrt{(\theta_{k,j})^2}$ Angle between ray bundles always +ve

$\psi 1_k := \operatorname{atan}\left[(centre - k) \cdot \frac{w0}{f} \right]$ $\psi 2_j := \operatorname{atan}\left[(centre - j) \cdot \frac{w0}{f} \right]$

$\psi 3_{k,j} := \psi 1_k - \theta_{k,j} + \frac{51}{180} \cdot \pi$ Angle Of Resulting Wavevector (w.r.t. xtal axes when cut for perpendicular Type I phasematching in BBO)

$\delta k_{(k,j)} := 4 \cdot \frac{\pi}{\lambda 1} \cdot \left[\cos(\theta_{k,j}) \cdot no1 - \frac{ne2 \cdot no2}{\sqrt{(no2^2 \cdot \sin(\psi 3_{k,j})^2 + ne2^2 \cdot \cos(\psi 3_{k,j})^2)}} \right]$ Phase Mismatch

$lf_{k,j} := (\theta_{k,j} \neq 0) \cdot \frac{w0}{\theta_{k,j}} + (\theta_{k,j} = 0) \cdot lc$

$il_{k,j} := lf_{k,j} \cdot (lf_{k,j} \leq lc) + lc \cdot (lf_{k,j} > lc)$

Ensure that the interaction length is less than the crystal length

$$P1 := \sum_k \sum_j (j \geq k) \cdot 4 \cdot \beta \cdot Pbp_k \cdot Pbp_j \cdot \left[\left[\sin\left[\delta k_{k,j} \cdot \frac{w0}{(\rho + \theta_{k,j})} \right] \right]^2 \cdot \frac{w0}{\left[\delta k_{(k,j)} \right]^2} \right]$$

$$P2 := \sum_k \sum_j (j \geq k) \cdot 4 \cdot \beta \cdot Pbp_k \cdot Pbp_j \cdot \left[\int_{\frac{w0 - \rho \cdot lf_{k,j}}{2}}^{0} \left[\sin\left[\delta k_{k,j} \cdot \theta_{k,j} \cdot \frac{y1}{\left[\rho^2 - (\theta_{k,j})^2 \right]} \right] \right]^2 \cdot \frac{1}{(\delta k_{k,j})^2} \, dy1 \right]$$

$Pt := P1 + P2$

Calculation of the Phase Match Angles for Type I SFM in β-BBO

$Ane := 2.3730$

$Bne := 0.0128$

Sellmier Coefficients for the Extraordinary Polarization

$Cne := -0.0156$

$Dne := -0.0044$

$Ano := 2.7405$

$Bno := 0.0184$

Sellmier Coefficients for the Ordinary Polarization

$Cno := -0.0179$

$Dno := -0.0155$

$\lambda 1 := 578.2 \cdot 10^{-3}$ CVL yellow line to be mixed with

$i := 1 .. 200$

$\lambda 2_i := 500 \cdot 10^{-3} + i \cdot 5 \cdot 10^{-3}$ Wavelength

$\lambda 3_i := \dfrac{\lambda 1 \cdot \lambda 2_i}{\lambda 1 + \lambda 2_i}$ The Sum-Frequency Wavelength

Calculate The Refractive Indices For The e- and o- Waves

$$ne1 := \sqrt{Ane + \frac{Bne}{\lambda 1^2 + Cne} + Dne \cdot \lambda 1^2}$$

$$no1 := \sqrt{Ano + \frac{Bno}{\lambda 1^2 + Cno} + Dno \cdot \lambda 1^2}$$

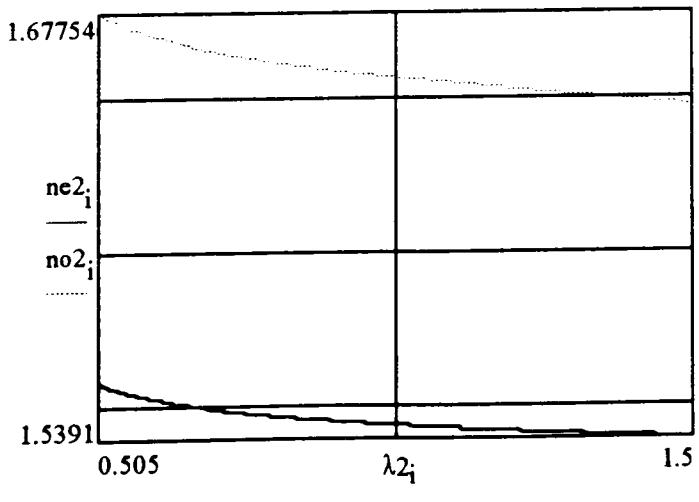
$$ne2_i := \sqrt{Ane + \frac{Bne}{(\lambda 2_i)^2 + Cne} + Dne \cdot (\lambda 2_i)^2}$$

$$no2_i := \sqrt{Ano + \frac{Bno}{(\lambda 2_i)^2 + Cno} + Dno \cdot (\lambda 2_i)^2}$$

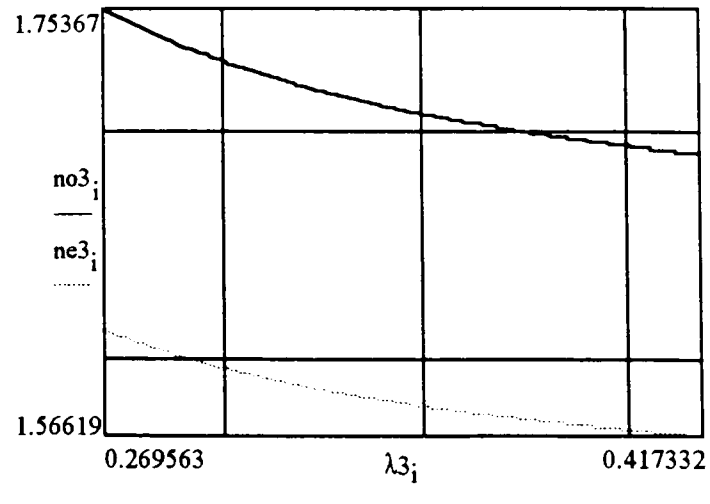
$$ne3_i := \sqrt{Ane + \frac{Bne}{(\lambda 3_i)^2 + Cne} + Dne \cdot (\lambda 3_i)^2}$$

$$no3_i := \sqrt{Ano + \frac{Bno}{(\lambda 3_i)^2 + Cno} + Dno \cdot (\lambda 3_i)^2}$$

nε and no For The Mixing Wavelength



ne and no For The Sum Frequency



Calculate The Phase Match Angles For Type I SFM

$l := 1 .. 200$

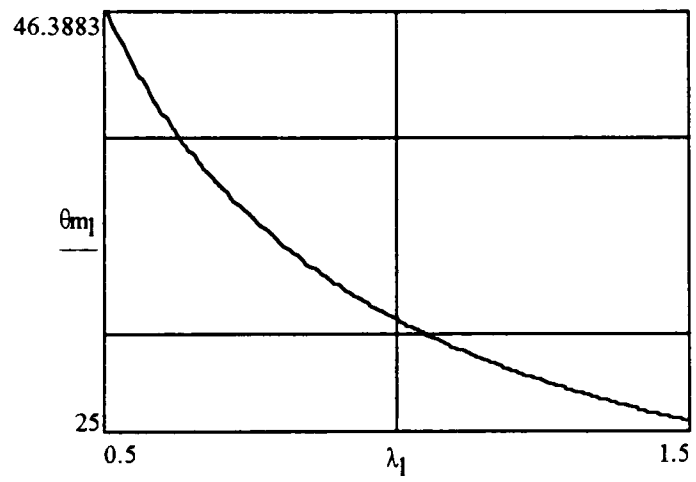
$L_l := l$

$$\theta m_l := \operatorname{acos}\left[\sqrt{\frac{\left(no3_l\right)^2\cdot\left(ne3_l\right)^2}{\left[\frac{\frac{no1}{\lambda 1}+\frac{no2_l}{\lambda 2_l}}{\frac{1}{\lambda 1}+\frac{1}{\lambda 2_l}}\right]^2}-\left(no3_l\right)^2}{\left(ne3_l\right)^2-\left(no3_l\right)^2}}\right]$$

$\lambda_l := 500\cdot 10^{-3} + 5\cdot 10^{-3}\cdot l$

$\theta m_l := \theta m_l \cdot \frac{180}{3.142}$

Phase Match Angles for SFM 578.2nm with wavelength λ in BBO



$l := 1 .. 20$

θm_l	λ_l
46.388	0.505
46.058	0.51
45.736	0.515
45.421	0.52
45.114	0.525
44.813	0.53
44.519	0.535
44.232	0.54
43.95	0.545
43.675	0.55
43.405	0.555
43.141	0.56
42.883	0.565
42.629	0.57
42.381	0.575
42.137	0.58
41.898	0.585
41.663	0.59
41.433	0.595
41.207	0.6